Seismic anisotropy in siliciclastic reservoir rocks

Jamie Stewart Maddock

Submitted in accordance with the requirements for the degree of PhD.

The University of Leeds
School of Earth and the Environment
September 2006

Optimis parentibus

Acknowledgements

Many people have in one way or another contributed significantly to this work, and I am very grateful to them all. I particularly wish to thank my advisors: Mike Kendall, Quentin Fisher, Geoff Lloyd, and Martin Casey.

As ever thanks also to Kerry for her endless support, extraordinary understanding and encouragement without which I am sure I would never have made it this far.

I would also like to show my appreciation to those people who have contributed to the experimental results in this study: Walid Ben-Ismaïl, Steve Covey-Crump, and Ernie Hailwood.

Financial support for this project was provided by an Industry Technology Facilitator (ITF) grant. The sponsors included: BG, BP, ChevronTexaco, DTI, Hess, Kerr-McGee, Shell and Total.

I also wish to extend my most sincere gratitude to Dan, my office mate, who single handedly dealt with all my ups and downs.

Thanks also to Prof. John Wheeler and Prof. Rob Knipe for kindly agreeing to act as examiners.

Abstract

The interpretation of geophysical field measurements of seismic anisotropy is presently limited by our knowledge of the controls of the elastic anisotropy of sedimentary rocks in the subsurface. Traditionally, laboratory ultrasonic velocity measurements have been used to provide important information on bulk aggregate seismic anisotropy, however, they do not allow the discrimination of the contribution from the various microstructural parameters (e.g., crystallographic lattice preferred orientation (LPO), preferentially aligned porosity, aligned fractures and the non-random spatial distribution of mineral phases). In this study the results from scanning electron microscope-electron backscattered diffraction (SEM-EBSD), quantitative X-ray diffraction (QXRD), image analysis, ultrasonic velocity measurements, palaeomagnetism, anisotropic magnetic susceptibility, and numerical modelling are combined to elucidate the controls of the elastic anisotropy of siliciclastic sedimentary rocks from an oil reservoir.

SEM-EBSD was used to measure both the overall and individual constituent mineral phase LPO (Maddock et al. 2004). As phyllosilicates are both very fine-grained, with a high aspect-ratio and low crystallinity, their LPO contribution was established via a combination of image analysis and numerical modelling (Bingham approximation). These analytical and predictive methods for determining phyllosilicate fabric intensity produced consistent results. For the first time, the azimuthally preferred orientation of elongate grains within sedimentary rocks was determined using anisotropic magnetic susceptibility of ferrous minerals and were compared to those predictions obtained using EBSD.

The strength of the fabric-texture (J), as determined by EBSD, is proportional to the maximum compressional and shear-wave anisotropy, as calculated from the Christoffel equation, by taking a Hill average of the bulk aggregate elastic constants. The quartz and feldspar velocity maxima aligned in a constructive fashion throughout most of the

samples. It is possible that the preferred alignment of crystals detected by EBSD reflects the palaeoflow direction. The predicted symmetries of velocity anisotropy ranged from orthorhombic in the phyllosilicate-free, well-sorted, mature sandstones to strong vertical transverse isotropy in the unfractured phyllosilicate-rich mudstones. Vertical transverse isotropy is predicted to be oriented, such that, the plane of azimuthal isotropy is aligned parallel to bedding i.e., parallel to the horizontally aligned clays and micas. Similarly, orthorhombic symmetry is predicted to be oriented, such that, one plane of symmetry is aligned approximately parallel to bedding whilst the other symmetry plane is aligned parallel to the single most dominant fracture set. The results from this study provide the input needed for a general mathematical model for the reservoir allowing the prediction of seismic anisotropy for any rock in the reservoir given accurate modal proportions. The resulting model is an advance on the empirical correlations that are usually used to determine how seismic velocities are affected by factors such as clay content and porosity. In particular, the bulk aggregate elastic stiffness tensor obtained during this study can be integrated with high-pressure ultrasonic measurements to enable the prediction of the additional contribution from grain-scale effects such as shape-preferred orientations, and grain boundary compliances (Hall et al. 2007). The results from this study have also provided the basic data to allow field seismic data to be inverted to obtain estimates of *in situ* fracture density and orientation (Kendall et al. 2006).

In summary, analysis of a suite of siliciclastic hydrocarbon reservoir rocks has shown that the LPO of constitutive minerals can offer information about the nature of a reservoir. The results suggest that seismic anisotropy is not only indicative of lithology but can also be an indicator of reservoir quality and palaeoflow direction.

Contents

List of Tables

List of Figures

Abbreviations

4C	Four component
AI	Acoustic impedance
AMS	Anisotropic magnetic susceptibility
AVOA	Amplitude variation with offset and azimuth
CTI	Cylindrical transverse isotropy
EBSD	Electron backscattered diffraction
EWT	Extended well test
HTI	Transverse isotropy with a horizontal symmetry axis
LPO	Lattice preferred orientation
MAD	Mean angular deviation
OBS	Ocean bottom seismic
ODF	Orientation distribution function
PTL	Periodic thin layering
QXRD	Quantitative X-ray diffraction
SEM	Scanning electron microscope
SPO	Shape preferred orientation
TTI	Tilted transverse isotropy
VRH	Voigt-Reuss-Hill averaging scheme
VSP	Vertical seismic profile
VTI	Transverse isotropy with a vertical symmetry axis
XTG	X-ray texture goniometry

Chapter 1

Fundamentals

1.1 Introduction

Hydrocarbon production from siliciclastic reservoirs varies considerably, and is of great importance in an era of rapidly declining oil stocks and ever harder to find commercially producable reservoirs. Seismic data is currently used to help guide such exploration as it contains information about the geological structure, and the lithologies present beneath the subsurface (Strandness 1991, Grechka et al. 2002, Olofsson et al. 2002). Recent advances in acquisition and processing have seen the development of a range of seismic techniques for inferring reservoir properties (Hall et al. 2002, Kommedal et al. 2004, Tabti et al. 2004). These include time-lapse seismic surveys, converted-wave and shear-wave surveys, and passive seismic monitoring (Kendall & Kendall 1996, Caley et al. 2001, Sayers 2002*a*). The conventional use of seismic lithology analysis aims to estimate lithological, and reservoir properties from seismic-wave attributes alone, such as, velocity analysis and amplitude variation with offset (AVO)(Blangy 1992, Alkhalifah & Rampton 2001). These technologies are based upon the simple yet extremely effective assumption of isotropy. Whereby, the various properties of the medium are not dependent upon direction. Regardless of the location of the transmitter or receiver the exact same properties are recorded at all locations for an isotropic medium. However, seismic-wave attributes can also possess a directional dependence, known as seismic anisotropy. A number of methods have been developed for estimating seismic anisotropy using a wide range of attributes in seismic data (Winterstein 1986, Van der Baan & Kendall 2002, Helbig & Thomsen 2005). However, the anisotropy itself is an indicator of a wide range of properties and as such is a seismic attribute that is sensitive to both past and

present processes (Raymer et al. 2000*a*, Smith & McGarrity 2001, Thomsen 2002). A key challenge with its interpretation is untangling the various contributions to the anisotropy (Wendt et al. 2003, Valcke et al. 2006).

In sedimentary rocks there are many factors which control seismic anisotropy: alignment of sets of fractures, mineralogy, partial grain alignment, and layering. However, the relative contributions of these various parameters towards observations of seismic anisotropy are presently not well understood. The SAIL project (seismic anisotropy as an indicator of lithology) was designed to address this issue. The aim of the SAIL project was to determine the causes of seismic anisotropy through linked analyses of core, and seismic data to aid the understanding of seismic interpretation. The SAIL project was a joint industrial consortium funded through an Industry Technology Facilitator (ITF) Grant. SAIL was designed to be a joint research project combining experience and technical ability between Manchester University and Leeds University. This thesis which represents a component of the SAIL project is concerned with the link between petrofabric properties of siliciclastic hydrocarbon reservoir rocks and seismic anisotropy.

In general, siliciclastics constitute approximately 75% of basin in-fill, and therefore are of foremost importance to hydrocarbon production (Hornby 1998). Recent improvements in the data acqusition and processing techniques used in exploration seismic surveys mean that observations of seismic anisotropy are better characterised than ever before. Therefore, it is a good time to attempt to discriminate the various contributions made by fractures, lithological layering and lattice prefered orientation in producing seismic anisotropy. Information obtained from seismic anisotropy analyses could in the future provide valuable information on reservoir attributes, such as, preferential flow directions, *in situ* stress distributions, fracture orientation, and lithology.

1.2 Overview of seismic anisotropy

Seismic anisotropy is considered here to be the variation of the seismic wave vector velocity with angle. The term angle covers a wide range of meanings but specifically here refers to the polar angle (angle from the vertical) and the azimuthal angle. Seismic anisotropy can also be due to the angle of propagation and the angle of polarisation of shear-waves. Seismic anisotropy is principally a result of some order in the arrangement of sub-seismic wavelength heterogeneities (Babuska & Cara 1991). Ordered heterogneities include, the

partial alignment of anisotropic minerals, grains, microcracks, fractures, and bedding planes. Hence, seismic anisotropy is simply the larger-scale manifestation of smaller scale ordering (Thomsen 2002). Therefore, anisotropy in sedimentary basins can be considered as being indicative of some physical phenomenon, for example, horizontal or oblique shortening due to tectonic compression (Kendall 2000).

Seismic anisotropy effects seismic wave propagation in a wide variety of ways. These include azimuthal variation in seismic properties such as stacking velocities, AVO (amplitude variation with offset), and converted wave amplitudes. Shear-wave splitting, or the propagation of two independent shear waves, is the most unequivocal evidence of the presence of anisotropy (Figure 1.1). If a shear-wave enters a medium that is anisotropic it splits into fast and slow shear-wave components. Shear-wave splitting is commonly quoted in terms of percent and generally refers to the lag between the first arriving shear-wave (fast) and the second arriving shear-wave (slow). Shear-wave splitting (S-wave anisotropy) can not only depend on the intrinsic properties of the aggregate but also on the propagation and polarisation angle. P-wave anisotropy is very different to S-wave anisotropy as a P-wave is a compressional, non-longitudinal wave it is not affected by polarisation angle. On the other hand,to be able to calculate a P-wave anisotropy requires several different angles of measurements positioned at various locations throughout and across the sample. Whilst, P- and S-wave anisotropy mat seem very similar the controlling parameters can be very different.

Seismic anisotropy and it's effects on various seismic wave attributes have been used in the investigation of a variety of rock properties. For example, Crampin & Lovell (1991) used shear-wave splitting to characterise aligned fractures. Moreover, Kendall & Kendall (1996) observed that there existed direct correlations between shear-wave amplitude anomalies and areas containing high hydrocarbon production. It has long been recognised that AVO could also be used as a useful indicator of lithology and fluid fill (Ostrander 1984). P-wave amplitude variation with offset and azimuth (AVOA) has also been identified as a useful tool in the identification of fracture alignment as it provides good vertical resolution (Hall et al. 2002). The limited availability of useful data sets meant that the SAIL project primarily concentrated upon the effects of amplitude variation with offset and azimuth (AVOA).

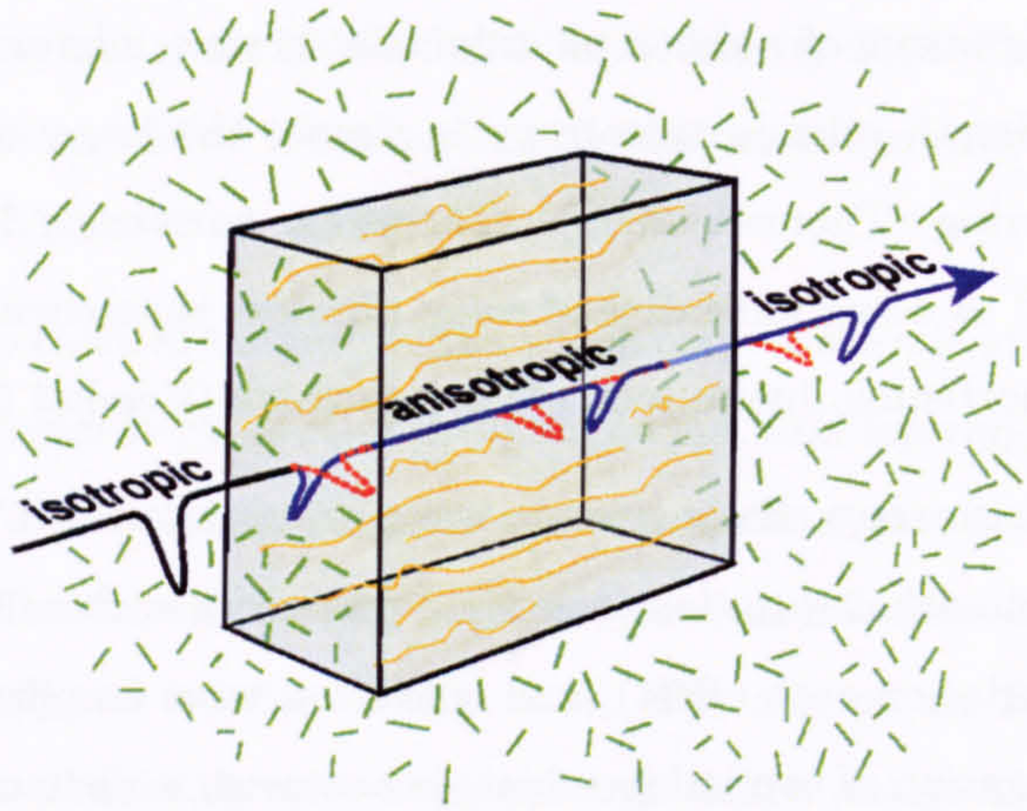

Figure 1.1: *A diagram illustrating shear-wave splitting. Shear-wave splitting is the most unequivocal evidence of the presence of anisotropy. If a shear-wave enters a medium which is anisotropic it splits into fast and slow shear-wave components (Crampin 1981).*

1.3 Elasticity

The degree of order within a medium can be described mathematically through the elastic stiffness tensor (C_{ijkl}). Stress (σ_{ij}) and strain (ϵ_{kl}) are second-order symmetric tensors. For an infinitesimal deformation of an elastic body, Hooke's law for a general anisotropic, linear elastic solid states that σ_{ij} is linearly proportional to ϵ_{kl} via the fourth-order C_{ijkl} elastic tensor (Mavko et al. 1998). Where,

$$\sigma_{ij} = C_{ijkl}\epsilon_{kl}, \tag{1.1}$$

in which, summation is implied over the repeated subscripts k and l.

Or, where the stress and strain tensors are related to the compliance (s_{ijkl}),

$$\epsilon_{ij} = s_{ijkl}\sigma_{kl}, \tag{1.2}$$

such that,

$$c_{ijkl} = s^{-1}_{ijkl}. \tag{1.3}$$

Strain is defined as,

$$\epsilon_{kl} = \frac{1}{2}\left(\frac{\partial u_k}{\partial x_l} + \frac{\partial u_l}{\partial x_k}\right), \tag{1.4}$$

for displacement u_i and spatial reference coordinate x_i.

The C_{ijkl} elastic tensor is a four-dimensional array and has 81 components, however, not all 81 components are independent. Since,

$$C_{ijkl} = C_{jikl} = C_{ijlk} = C_{jilk}, \tag{1.5}$$

because,

$$\sigma_{ij} = \sigma_{ji} \quad and \quad \epsilon_{kl} = \epsilon_{lk}. \tag{1.6}$$

Therefore, reducing the number of significant (distinct, independent, and non-vanishing) constants to 36. Furthermore, the existence of an unique strain energy potential requires that,

$$C_{ijkl} = C_{klij}, \tag{1.7}$$

further reducing the number of constants to 21. Therefore, 21, is the maximum number of elastic constants that are required to describe any medium. Isotropic elastic materials such as volcanic glass, which have maximum symmetry are completely characterised by 2 independent constants. In comparison plagioclase feldspar has the lowest possible symmetry, and requires all 21 constants.

It is, however, easier to use an abbreviated notation, sometimes called the Voigt notation when dealing with elasticity, which reduces the number of subscripts of the stiffness and compliance tensors to two (Thomsen 2002). Each pair of indices $ij(kl)$ is simply replaced by one index I(J) as follows,

$ij(kl)$	I(J)
11	1
22	2
33	3
23, 32	4
13, 31	5
12, 21	6

In the two-index notation, C_{IJ}, is represented by a *2D*, 6x6 matrix. Note the symmetry, $C_{ij} = C_{ji}$,

$$\begin{pmatrix} c_{11} & c_{12} & c_{13} & c_{14} & c_{15} & c_{16} \\ c_{12} & c_{22} & c_{23} & c_{24} & c_{25} & c_{26} \\ c_{13} & c_{23} & c_{33} & c_{34} & c_{35} & c_{36} \\ c_{14} & c_{24} & c_{34} & c_{44} & c_{45} & c_{46} \\ c_{15} & c_{25} & c_{35} & c_{45} & c_{55} & c_{56} \\ c_{16} & c_{26} & c_{36} & c_{46} & c_{56} & c_{66} \end{pmatrix}. \tag{1.8}$$

The ability to transform the elastic tensor into two-dimensions enables the simplified comparison, visualisation and manipulation of fourth-order tensors.

1.3.1 Anisotropic symmetry systems

The least symmetric system is triclinic, with 21 independent elastic constants (Babuska & Cara 1991). In reality rocks generally show more symmetry. A simple *semi-realistic* symmetry in sedimentary rocks is vertical transverse isotropy (VTI), otherwise known as polar anisotropy or as hexagonal symmetry with a vertical symmetry axis. VTI symmetry is characterised by seismic velocities azimuthally symmetrical about a single axis, which vary with declination from the axis (Array 1.9). c_{11} and c_{22} can be considered as being contained within the horizontal plane (parallel to the plane of bedding and rotationally invariant) with c_{33} therefore perpendicular to bedding (vertical).

$$\begin{pmatrix} c_{11} & c_{12} & c_{13} & 0 & 0 & 0 \\ c_{12} & c_{11} & c_{13} & 0 & 0 & 0 \\ c_{13} & c_{13} & c_{33} & 0 & 0 & 0 \\ 0 & 0 & 0 & c_{44} & 0 & 0 \\ 0 & 0 & 0 & 0 & c_{55} & 0 \\ 0 & 0 & 0 & 0 & 0 & c_{66} \end{pmatrix} \tag{1.9}$$

The same principles hold for tilted transverse isotropy (TTI) where the axis of symmetry is inclined to the vertical. Both VTI and TTI are commonly associated with the symmetry pattern of a horizontally finely-layered sequence, e.g., shale. CTI (cylindrical

transverse isotropy) can be thought of as when there is a single vertical set of fractures that are azimuthally isotropic (have an almost perfectly equal radial distribution). This type of fracture set is commonly observed in cylindrical samples which have been subjected to non-hydrostatic stresses aligned parallel to the long axis of the sample.

However, a combination of multiple fracture sets, layering, inclusions, and crystal alignment will generate anisotropy with a lower degree of symmetry. A common example in crustal rocks is orthorhombic symmetry which is typically associated with horizontal layering and a single set of vertically aligned fractures (Figure 1.2). Nine independent elastic constants are required to define an orthorhombic elastic tensor. C_{11} and c_{22} can be considered as being contained within the horizontal plane (parallel to the plane of bedding and rotationally variant) with c_{33} therefore perpendicular to bedding (vertical).

$$\begin{pmatrix} c_{11} & c_{12} & c_{13} & 0 & 0 & 0 \\ c_{12} & c_{22} & c_{23} & 0 & 0 & 0 \\ c_{13} & c_{23} & c_{33} & 0 & 0 & 0 \\ 0 & 0 & 0 & c_{44} & 0 & 0 \\ 0 & 0 & 0 & 0 & c_{55} & 0 \\ 0 & 0 & 0 & 0 & 0 & c_{66} \end{pmatrix} \tag{1.10}$$

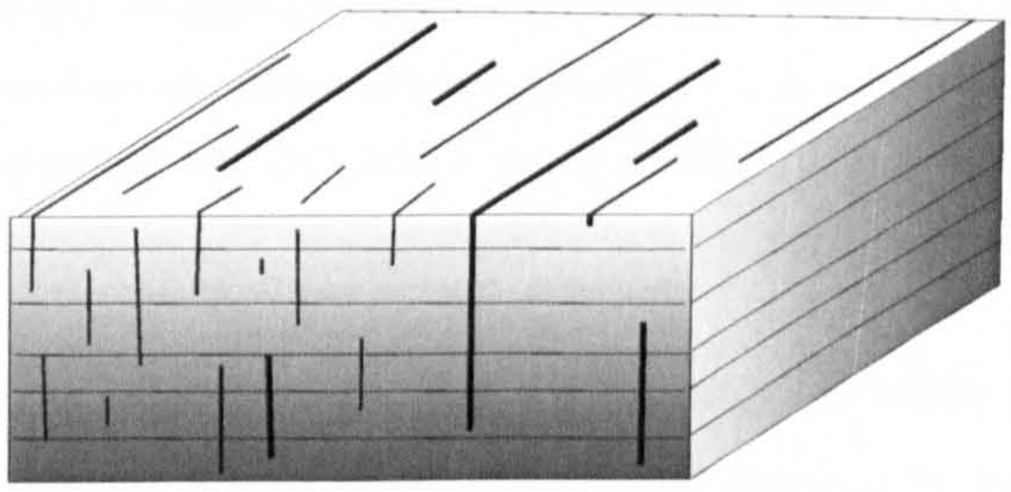

Figure 1.2: *The combination of horizontal layering and a vertically aligned fracture set leads to an orthorhombic style of symmetry.*

1.3.2 Calculation of seismic velocities from the stiffness tensor

Single crystal or bulk aggregate seismic velocities are calculated by solving the Christoffel equation (Christoffel 1910).

The equations of motion for elastic media, are writtten,

$$\frac{\partial \sigma_{ij}}{\partial x_j} = \rho \frac{\partial^2 u_i}{\partial t^2}, \tag{1.11}$$

at time t, where ρ is the density of the medium, σ_{ij} is the $3D$ stress tensor, u_i is the displacement, and x_j is the spatial coordinate system (Kendall 2000). Substitution of Equations (1.1 and 1.4) into Equation (6.7) gives for homogeneous media,

$$c_{ijkl} \frac{\partial^2 u_l}{\partial x_j \partial x_k} = \rho \frac{\partial^2 u_i}{\partial t^2}. \tag{1.12}$$

A plane-wave harmonic solution of (6.8) takes the form,

$$u_i = A_i e^{i\omega(t \pm x_i n_i / v_n)}, \tag{1.13}$$

where A is the amplitude and ω the frequency of a plane wave with unit normal, n_i and phase velocity, v_n. Substituting Equation (6.9) into Equation (6.8) gives,

$$c_{ijkl}(n_i n_l - \rho v_n^2 \delta_{jk} A_k) = 0, \tag{1.14}$$

where δ_{jk} is the Kronecker delta. Assuming A gives non-zero terms,

$$det|c_{ijkl} n_k n_l - \rho v_n^2 \delta_{ij}| = 0 \tag{1.15}$$

and

$$det|c_{ijkl} p_k p_l - \rho \delta_{ij}| = 0. \tag{1.16}$$

Thus the phase velocities of the three wave fronts can be determined from the three eigenvalues of $c_{ijkl} p_i p_j$ which correspond to one quasi-P wave and two quasi-S waves (Love 1944, Nye 1957).

1.3.3 Seismic wave theory

In isotropic media a P-wave will propagate with a velocity that is parallel to the wavefront normal and is also coincident with the ray direction and particle motion. In homogeneous, anisotropic media, however, the P-wave particle motion is not, in general, parallel to the wavefront normal or the ray direction. Additionally, the shear-wave particle motions will not be orthogonal to the wavefront normal or ray direction. Therefore, waves propagating

in an anisotropic media should strictly be defined as quasi-P and quasi-S-waves. From this description of wave propagation in anisotropic media three significant directions can be defined, the wavefront normal, the polarisaton and the ray direction (Figure 1.3). The wavefront normal, defined by vector n_i corresponds to the direction of the slowness p_i and the phase velocity v_n of the propagating phase. A further velocity must be defined in anisotropic media, the group velocity which is parallel to the ray direction and direction of energy transport.

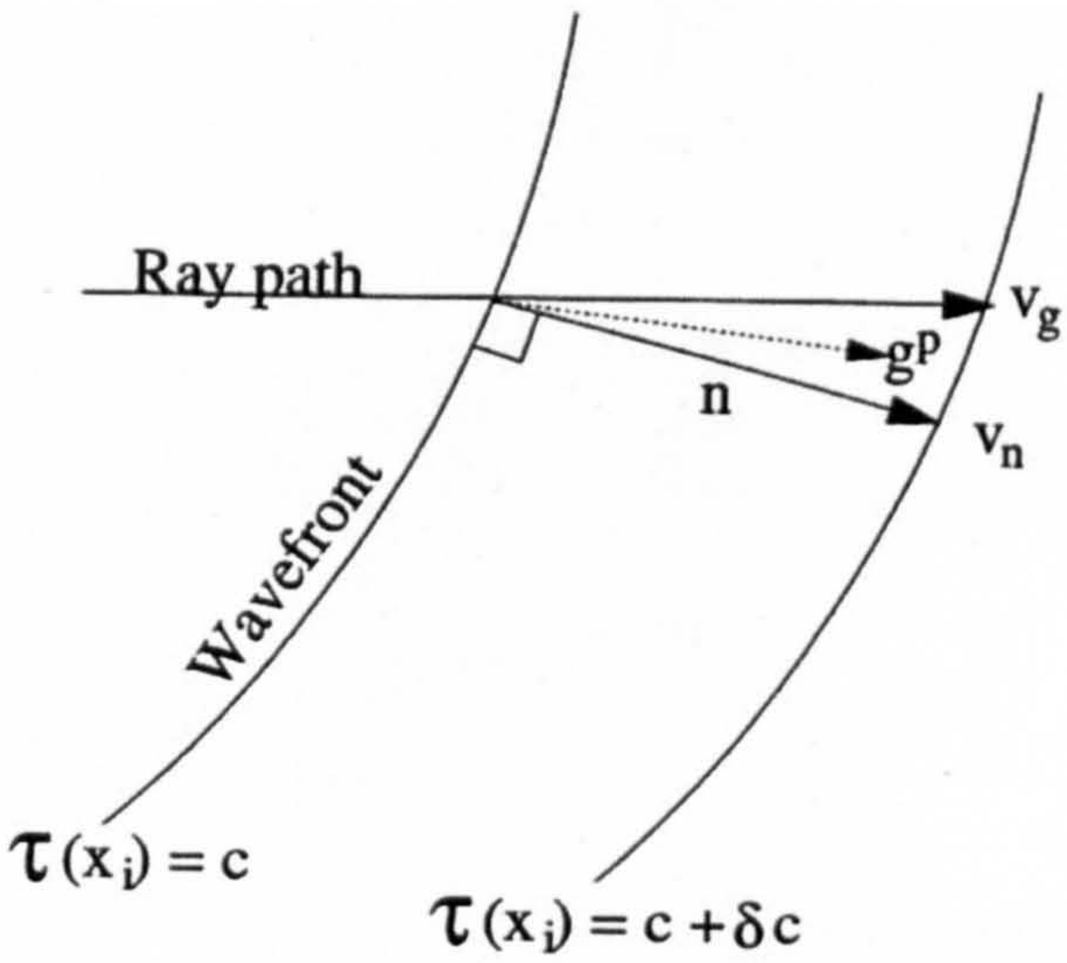

Figure 1.3: *Relationship between wavefront, ray direction, phase velocity, group velocity and particle motion. A wavefront has constant phase ($\tau(x_i) = c$ c is a constant), phase velocity (v_n), aligned with the wavefront normal (n), and a group velocity (v_n) along the ray direction. The particle motion or polarisation (g^p) is at an angle to both the ray direction and wavefront normal (Sheriff & Geldart 1999).*

In anisotropic media, pure S- and P-waves may exist only in certain directions. In transversely anisotropic media SV- and P-modes of propagation are coupled. Wavefronts are not in general orthogonal to the directions of wave propagation. Phase velocity is velocity perpendicular to a surface of constant phase (wavefront), and group velocity is the velocity with which the energy travels is in a different direction (Figure 1.4)(Sheriff & Geldart 1999).

As stated previously layering and parallel fracturing tend to produce transverse isotropy. The symmetry axis is perpendicular to the bedding with the velocities of P- and S-

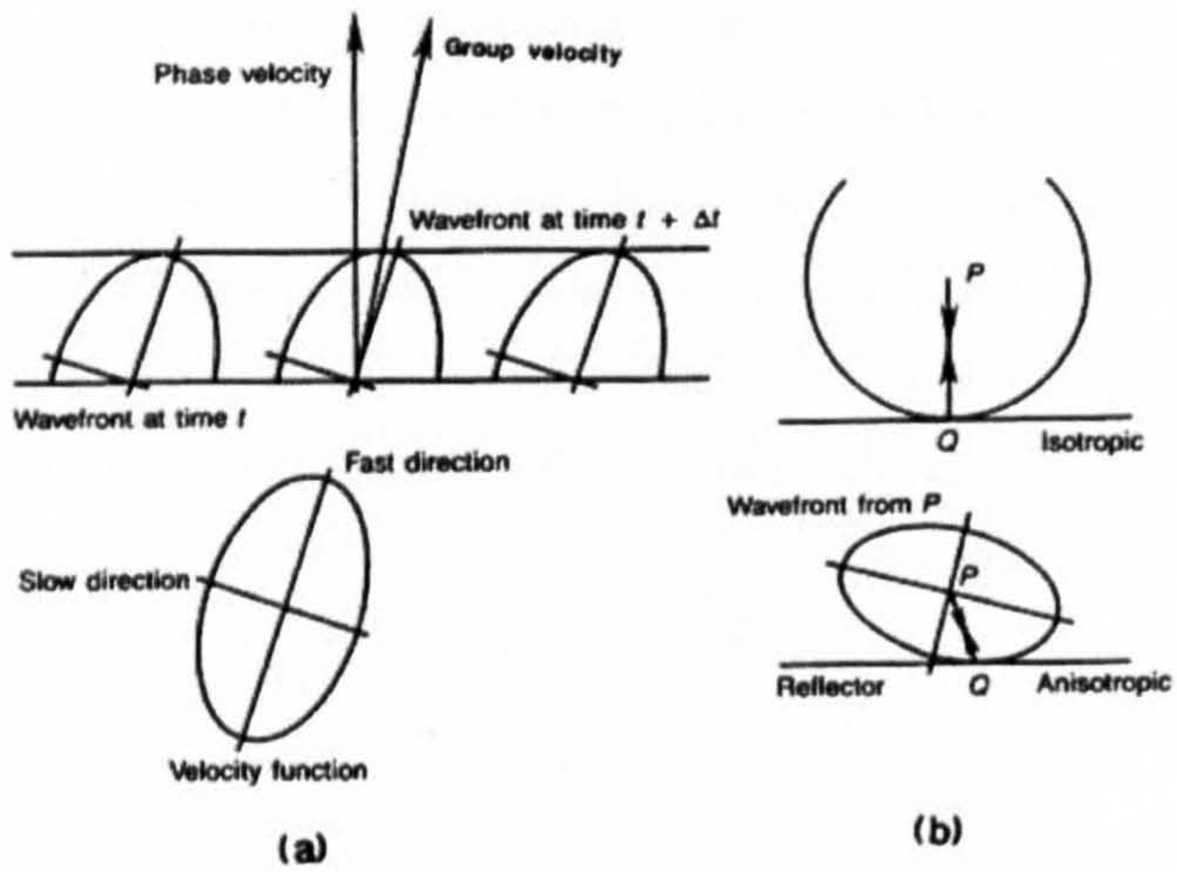

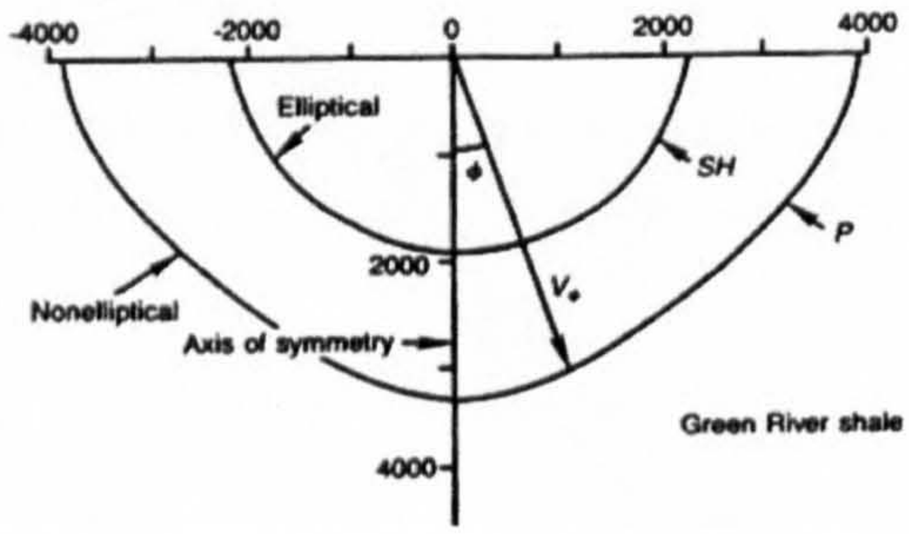

Figure 1.4: *Wavefronts in anisotropic media. a) Application of Huygen's principle to an anisotropic medium illustrates direction and magnitude differences between phase and group velocity. c) SH wavefronts in transversely isotropic media are elliptical. P and SV-wavefronts are not elliptical except in special instances.* $V_H > V_V$ *with a vertical axis of symmetry.* V_ϕ *is the group velocity as a function of the angle with the symmetry axis (Sheriff & Geldart 1999).*

waves that involve motion parallel to the bedding larger than those involving motion perpendicular to the bedding. The velocity parallel to the bedding is greater because the higher-velocity layers carry the energy first whereas for wave motion perpendicular to the bedding, each layer contributes in proportion to the time taken to traverse it.

Non-horizontal fracturing and micro-cracks produce azimuthal anisotropy with a symmetry axis perpendicular to the fracturing. The velocity of the waves that involve motion parallel to the fracturing (S_1) is larger than that of waves with motion perpendicular to the fracturing (S_2)(Sheriff & Geldart 1999). If the motion is neither parallel nor perpendicular to the fracturing, an S-wave splits into two waves with orthogonal polarisations (Figure 1.5).

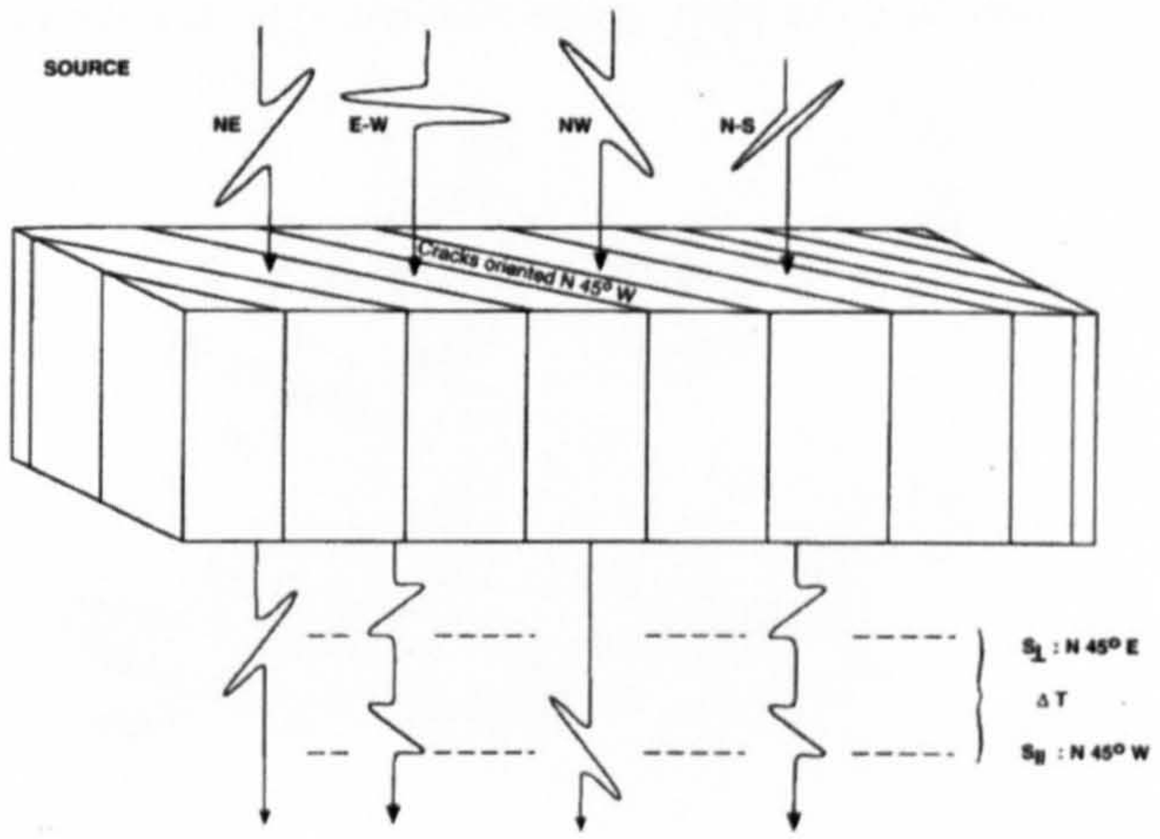

Figure 1.5: *Shear-wave propagation in a fractured medium with cracks oriented $N45^oW$. An S-wave travelling parallel to fracturing, the velocity (S_2) is slower for a component involving motion perpendicular to the fracturing than for one involving motion parallel to the fracturing (S_1).*

1.4 Causes of anisotropy

1.4.1 Lattice preferred orientation

Almost every rock forming mineral is to some extent intrinsically anisotropic (Mainprice et al. 2000). Phyllosilicates, for example, can exhibit up to 60% and 72% P-wave and S-wave anisotropy (shear-wave splitting), respectively, whereas halite has a maximum P-wave anisotropy of 7.4% and 15.9% S-wave anisotropy.

For an aggregate to exhibit elastic anisotropy due to a lattice preferred orientation (LPO), the constituent mineral phases are required to have a non-random orientation and significant intrinsic anisotropy. Aggregates are thought to develop a LPO in a variety of different ways. For example, through plastic and viscous flow in the upper and lower mantle (Hess 1960, Kendall 2000) or by depositional processes in sedimentary basins (Kaarsberg 1959).

Upon deposition the predominant mechanism orienting individual mineral grains is gravity. Platy mineral phases (phyllosilicates) tend to align their basal planes parallel to sub-parallel to bedding. Immediately after deposition the fabric is relatively disordered and contains a large amount of space. It is upon mechanical compaction that the pore

space is reduced and the platy grains re-align to form a strong LPO (Figure 1.6) (Helfing 1970).

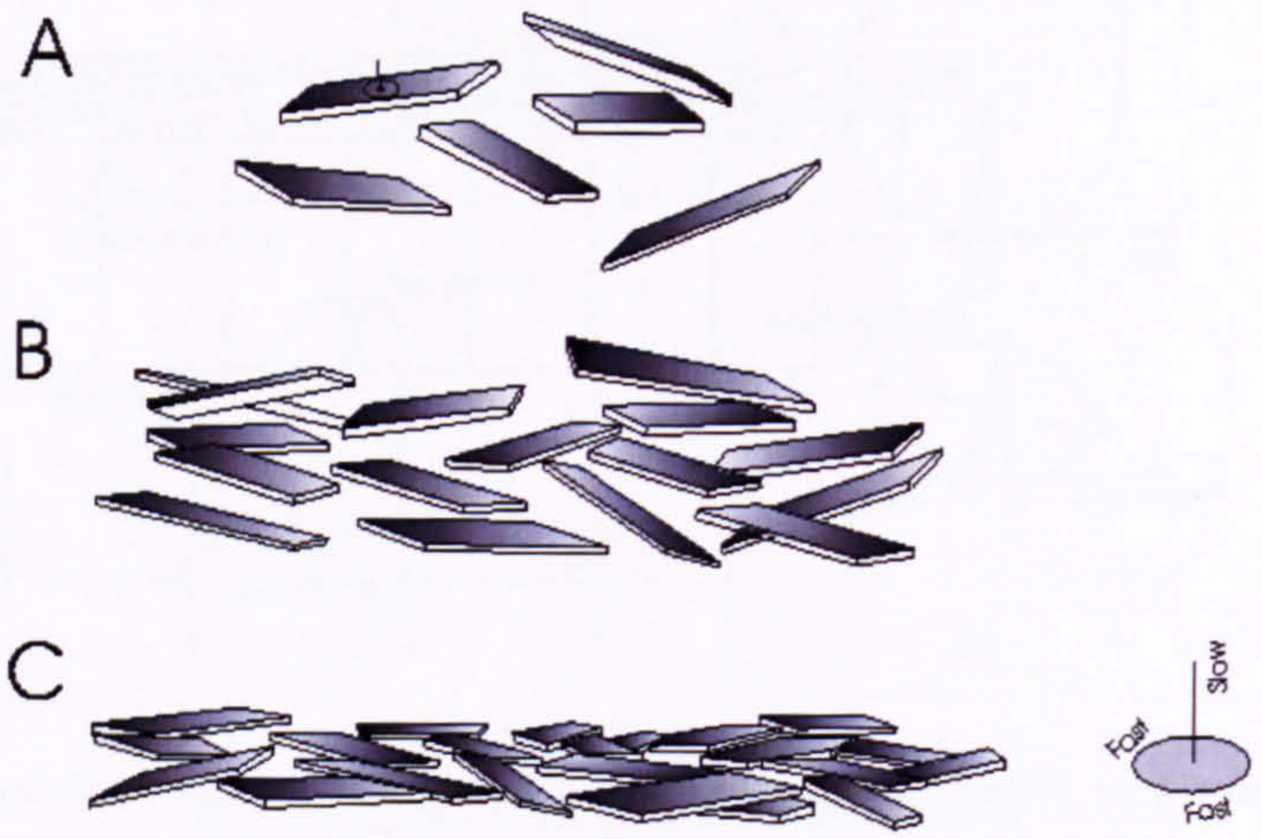

Figure 1.6: *Schematic diagram of settling detrital phyllosilicate platelets.* ***A*** *- phyllosilicate platelets drop out of suspension and settle through the water column.* ***B*** *- the platelets are randomly deposited upon the plane of bedding with a large amount of inter-grain pore space.* ***C*** *- during mechanical compaction the platelets reorient their basal plane parallel to bedding. Such deposition results in a vertical transverse isotropy style of symmetry.*

Similar to the flow that can occur in igneous rocks, which re-orientates elongated crystallites, sedimentary rocks can exhibit an azimuthally non-random distribution of grain axes due to a depositional flow direction (Figure 1.7)(Hailwood & Ding 2000). This type of preferred depositional flow direction might be expected to occur in submarine (turbidites) and subaqueous environments (slope debris flows).

1.4.2 Grain fabric

The affect of grain morphology on seismic anisotropy in sedimentary environments is inextricably linked to the effect grain boundaries have on bulk aggregate elastic properties. If grain boundaries, and therefore crack-like discontinuities, are preferentially aligned by some extrinsic mechanism (e.g., tectonic activity) they can significantly affect the bulk aggregate seismic anisotropy (Figure 1.8). Oriented systems of cracks can cause a velocity anisotropy even if the matrix of the rock is isotropic (Babuska & Cara 1991). The velocity is reduced most significantly in the direction normal to the long-axis of the plane of oriented cracks (parallel to the maximum compressive stress). It was shown

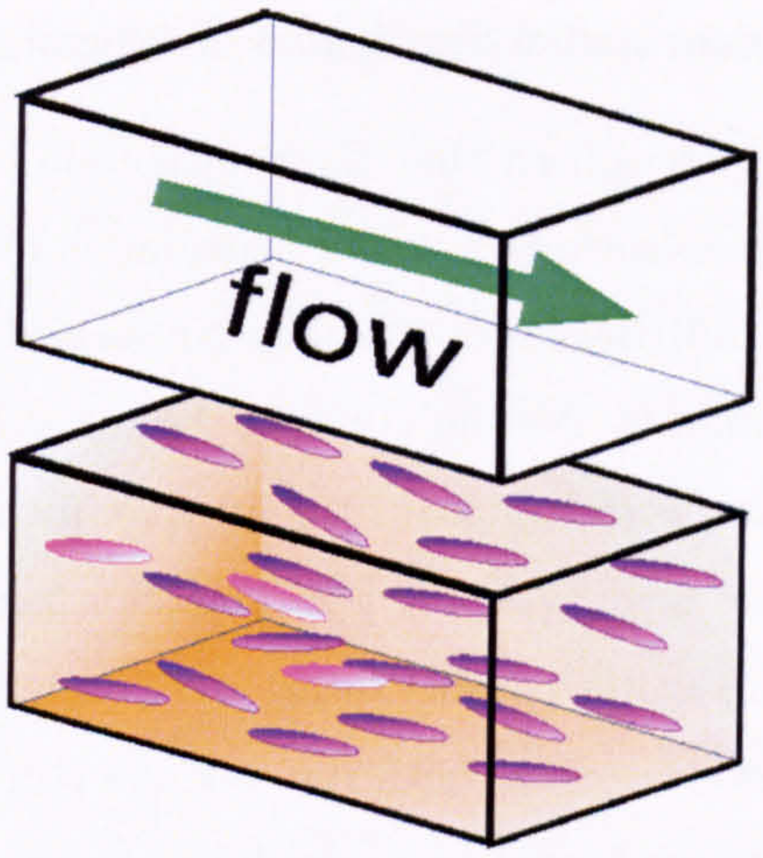

Figure 1.7: *Diagram illustrating the development of azimuthal anisotropy due to a preferred depositional flow direction. Azimuthal anisotropy is commonly found in depositional environments which have a predominant direction of flow, such as in submarine and subaqueous settings (Modified from Garnero, E.).*

by Burlini & Kunze (2000) that the measured seismic anisotropy of the Carrara marble could not simply be explained by the LPO of calcite and phyllosilicates alone. It was, however, shown to be related to grain boundary effects. The results of this qualitative correlation demonstrate that the nature of microdiscontinuities in crustal rocks plays a vital role on seismic anisotropy.

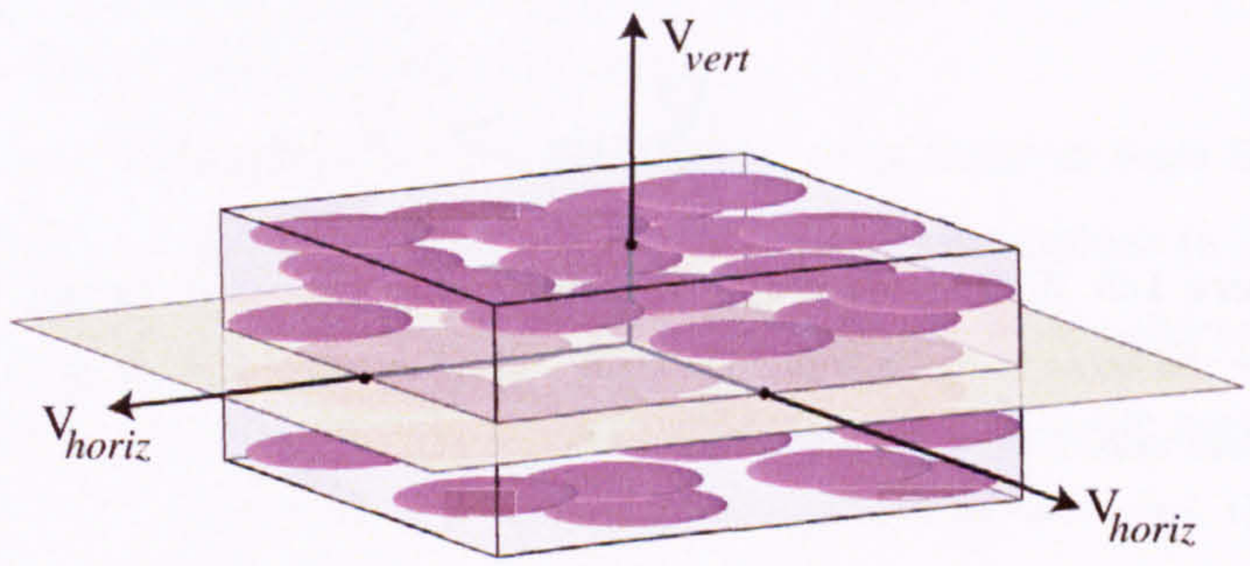

Figure 1.8: *Diagram illustrating the preferential alignment of grains during tectonic deformation. Horizontal or vertical shortening of the crust due to tectonic activity, such as during periods of mountain building can cause grains to realign in parallel with the maximum compressive stress.*

1.4.3 Non-random spatial distribution of mineral phases

It has long been recognised that the propagation of elastic waves in layered media is likely to have an anisotropic velocity distribution for wavelengths longer than the layer spacing (Figure 1.9)(Backus 1962). Observations of layer-induced anisotropy led to two independent studies by Postma (1955) and Krey & Helbig (1956). For example, when a P-wave propagates perpendicular to a layered sequence the softer, more compliant, layers compress and the wave experiences a compliant formation. On the other hand, when a similar wave propagates parallel to layering, both rigid and compliant layers compress with great resistance. Since both the soft and stiff layers compress concomitantly, the wave experiences the formation as much less compliant and the wave propagates faster. Anisotropy is greatest when the layering is thin and the difference in rigidity between the layers is large (Backus 1962, Berryman 1979).

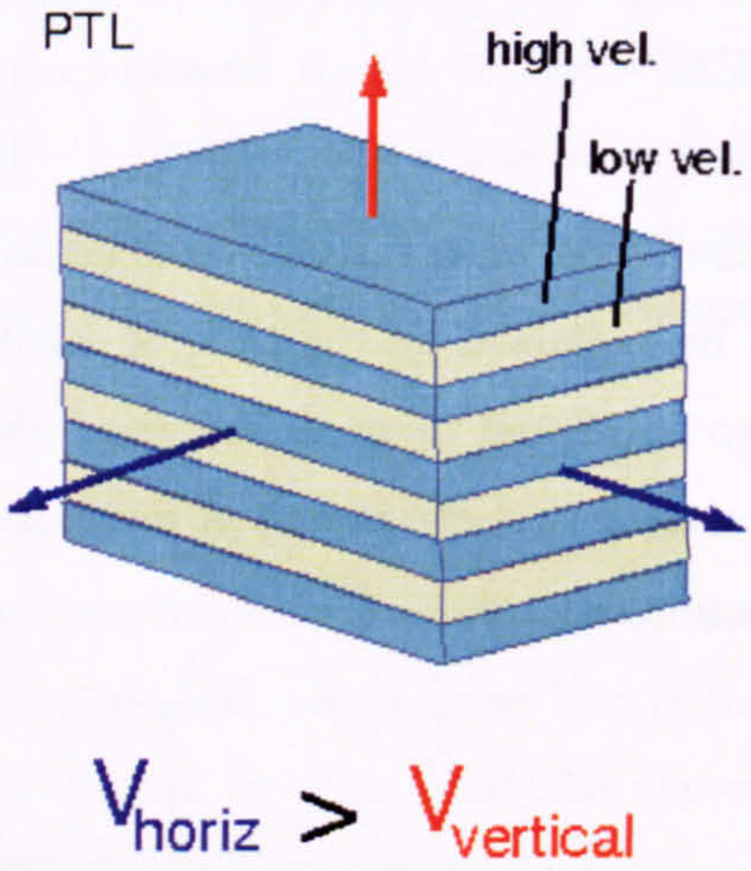

Figure 1.9: *Seismic anisotropy as a result of periodic thin layering only ever occurs when the layer thickness is significantly less than that of the seismic wavelength.* V_{horiz} *and* V_{vert} *refer to P-wave velocities in the horizontal and vertical.*

1.4.4 Preferentially aligned fractures, pores, and cracks

Fractures often have a significant impact on reservoir performance and consequently are the most commonly studied cause of seismic anisotropy in sedimentary rocks. Fractures can occur in a range of different sizes, from grain boundary micro-discontinuitities (μm), to large-scale regional faults ($km's$). Deformation-induced fracturing is usually asso-

ciated with a significant maximum regional stress in a single direction with fractures generally appearing to align in sets (Crampin 1985). In these situations each set of preferentially aligned fractures will contribute to the overall anisotropy of the rock. In the simplest scenario where there is a single direction of fracture alignment, wave propagation will be slower perpendicular to the fracturing than parallel. A vertically propagating shear wave in an azimuthally anisotropic medium will split into two components with different polarisations if the source polarisation is not aligned with the principal axes of the medium. So in the case of a single set of aligned vertical fractures the fast shear wave for vertical propagation has particle motion parallel to the fracture planes, whilst the slow shear wave has particle motion perpendicular to the fracture planes (Sayers 2002*a*).

1.5 Observations of seismic anisotropy

Seismic data analysis is one of the key technologies used in the characterisation of reservoirs and monitoring of subsurface fluids. While there have been significant advances in *3D* seismic data processing, effective media modeling, and laboratory investigations of the data, rock property interpretations still pose an exceptional challenge. The relative importance of each feature in producing the anisotropy in any given rock type is not presently known. This is an important limitation, because were it possible to determine what is responsible for the anisotropy that is observed in exploration seismic surveys, a great deal of information relevant to the exploration and extraction of petroleum could be recovered from the seismiological data alone.

Observations of seismic anisotropy in sedimentary rocks range in scale from field wide studies (e.g., Krey & Helbig 1956) to laboratory based investigations (e.g., Nur & Simmons 1969). A substantial amount of evidence has already been collected which highlights the occurrence of anisotropy in the subsurface. Although in the past this has been primarily shown to exist within core samples examined in laboratories, there have also been observations of field wide seismic anisotropy.

1.5.1 Field observations of seismic anisotropy

Even though the ideas behind anisotropy were first formulated about 175 years ago (Fresnel 1821, Green 1837) it has only been through the advancement of technology that it has become of significant importance in seismic exploration. Including among others: longer offset P-wave data (shows nonhyperbolic moveout), *3C*x*3C* data (highlights shear-

wave splitting), wide-azimuth *3D* data (shows azimuthal anisotropy), and OBS data (incorporates all the previous effects).

One of the earlier references to anisotropy was following a field study by **?**. As a result of velocity anisotropy it was shown that the depths calculated from S-wave stacking velocities always exceeded the actual depths by up to 25%, and those calculated from P-waves by 10%. Alkhalifah & Rampton (2001) conducted a study in Trinidad that showed a VTI media induced nonhyperbolic moveout of reflections. It was also found that processing the data using algorithms that took anisotropy into account improved the resolution when compared to those from isotropic processing. Similarly, Grechka et al. (2002) concluded that ignoring seismic anisotropy could cause serious errors in processing, and interpretation of multicomponent seismic data. They went on to say that the CCP (common-conversion-point) stacks of PS-waves generated by the VTI model had much higher quality than those by the isotropic model. Accounting for anisotropy was deemed essential for obtaining an accurate AVO (amplitude variation with offset) response for the PS reflections.

It was shown by Hall et al. (2002) and Hall & Kendall (2003) that anisotropy simply could not be ignored in wide-azimuth P-wave surveys. It was suggested that, because fractures are often vertically aligned and produce azimuthal anisotropy, directional dependence in seismic properties (AVOA) could provide information about fracture density and orientation. The AVOA observations showed considerable spatial variability in both orientation and magnitude (Figure 1.10) and were further shown to correlate well with independent fracture pattern analysis (Figure 1.11) (Hall et al. 2002).

It was also noticed by Caley et al. (2001) that the anisotropy of the overburden may have a time-dependence relating to production of a hydrocarbon reservoir (Figure 1.12). The production of oil from a highly compliant chalk reservoir (such as Valhall) causes collapse of the reservoir formation, deformation of the overburden, and subsidence of the sea floor (Olofsson et al. 2002) (Figure 1.13). Helbig & Thomsen (2005) also believed that the Valhall reservoir would be very sensitive to small changes in reservoir conditions, and thus exhibit dramatic time-dependent anisotropy effects.

Raymer et al. (2000*a*) suggested that part of the difficulty associated with finding hydrocarbon targets near salt structures could be not only due to the highly *3D* nature of salt bodies and their large velocity contrasts but also because salt structures primarily

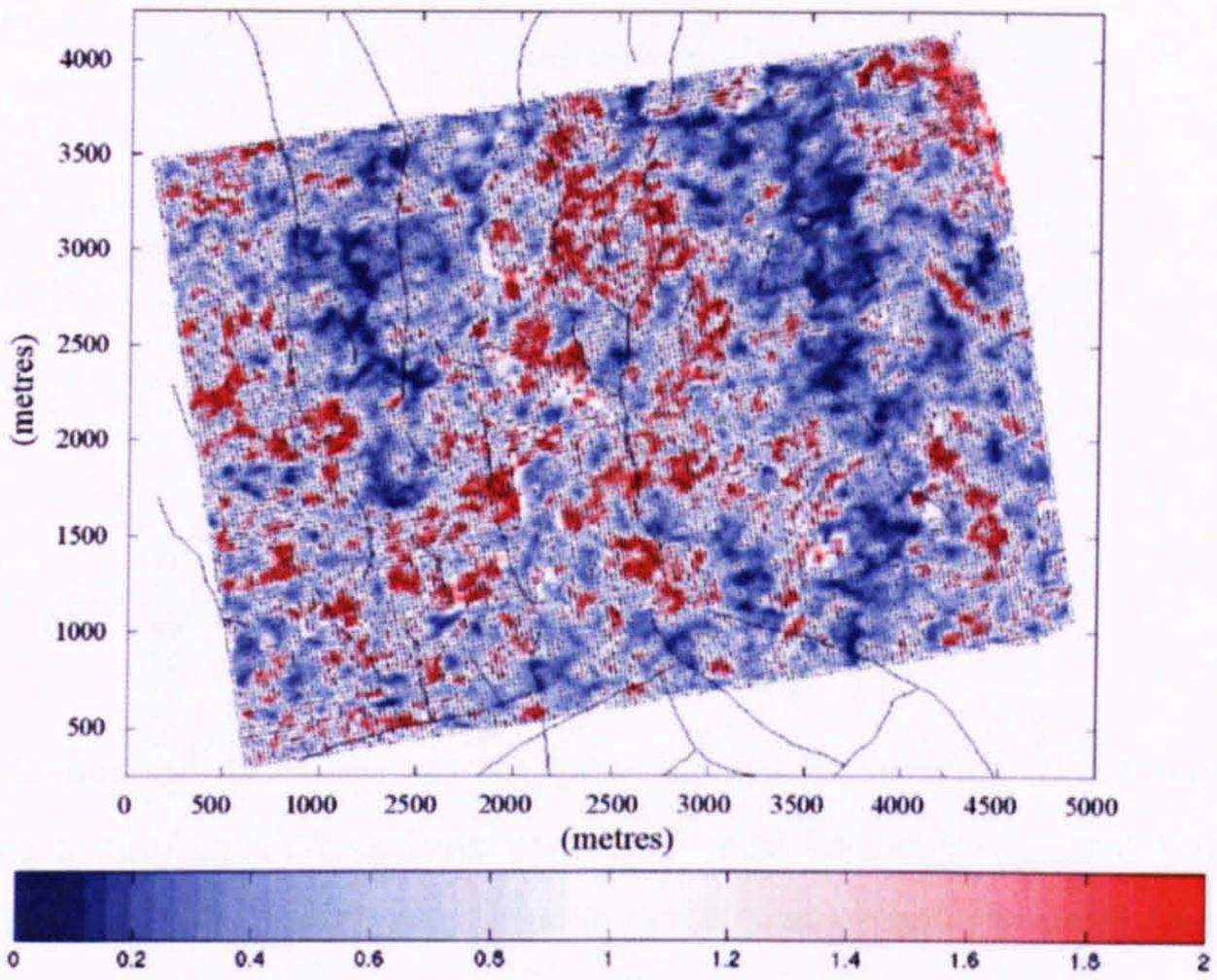

Figure 1.10: *Fracture orientations and anisotropy magnitude from the northern flank of Valhall derived from AVOA analysis. The magnitude is the normalised difference of the two principal gradients. The areas of high anisotropy magnitude and directions of fracturing (large-scale faulting marked by solid lines) are related (Hall et al. 2002).*

consist of halite which is elastically anisotropic. Numerical simulations as determined by Raymer et al. (2000*b*), and based upon a visco-plastic self-consistent approach, predicted that a 600m thick salt sill could produce up to 20ms P-wave anomalies, and 60ms S-wave anomalies with respect to isotropic models. The resulting mis-interpretation of salt velocities and thickness would potentially result in a costly mistake that could have been avoided if an anisotropic Earth model was applied.

1.5.2 Laboratory studies of seismic anisotropy

An objective in many rock-physics experiments is to determine how lithology, porosity, pore fluid type, saturation, and anisotropy effect P- and S-waves in sedimentary rocks. Experimental studies in laboratories in the 1950's and 1960's showed that the best way of determining velocity and attenuation on reservoir rock specimens was to employ the pulse first arrival or pulse echo technique using sensitive ceramic piezoelectric transducers (Birch 1960, King 1966).

Numerous studies have been conducted with the intention of determining the relationship between rock type and velocity (e.g., Tosaya & Nur 1982, Castagna et al. 1985, Han 1986).

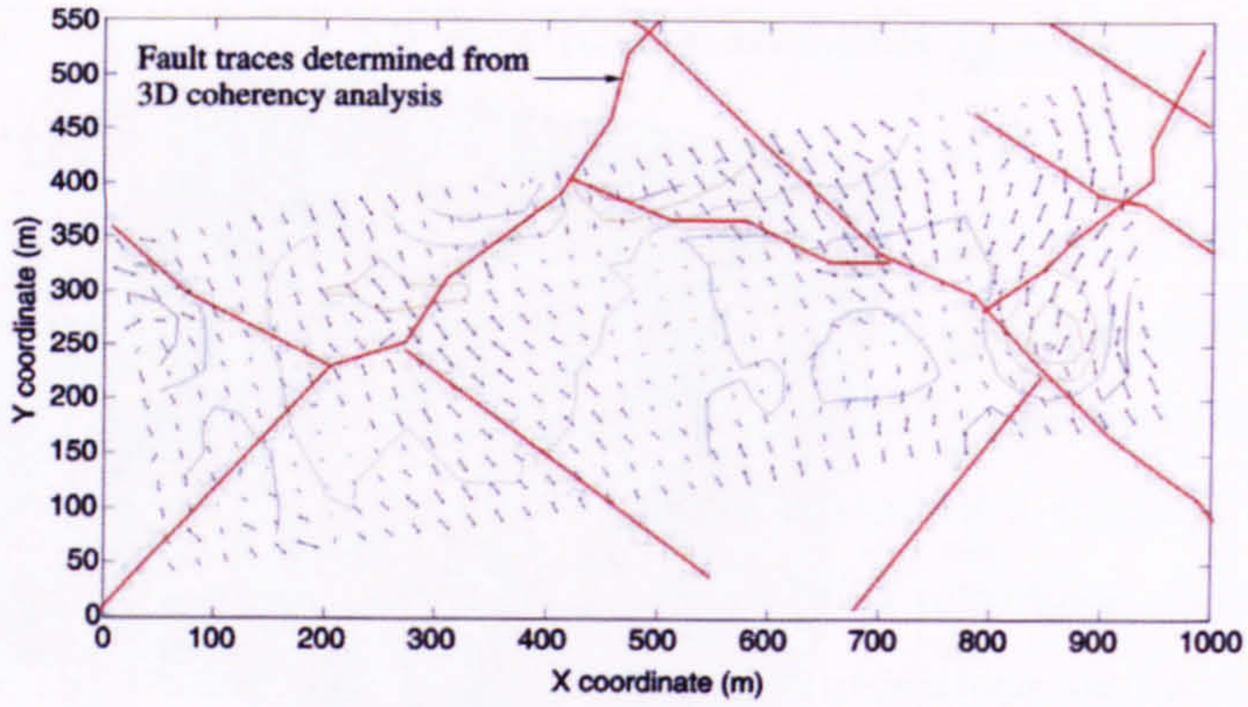

Figure 1.11: *Interpreted fracture map for the top chalk horizon at the Valhall field compared to fault traces determined from coherency analysis. This shows a good correlation between the inferred fracture patterns and the large scale faulting (Hall et al. 2002).*

It is commonly understood that shales exhibit intrinsic seismic anisotropy (Tosaya & Nur 1982, Vernik & Nur 1992*b*). Kaarsberg (1959) first linked the alignment of clay particles to observed laboratory P-wave anisotropy. It was shown that as compaction increased, the strength of clay particle alignment increased; concomitantly, there was an increase in the difference between the bedding parallel and bedding perpendicular P-wave velocities.

Since the publication of the earliest work significant progress has been made on accurately measuring and quantifying seismic anisotropy in sedimentary rocks and at *in situ* conditions (e.g., Wang 2002). Previous studies, however, have concentrated largely upon observations of velocity anisotropy in shales and hydrocarbon source rocks (Vernik & Nur 1992*b*, Vernik & Liu 1997). Both studies record levels of seismic anisotropy in the region of 40% to 50%, which they attribute to kerogen content, microstructure and maturation levels. In an investigation conducted by Wang (2002), an unfractured reservoir rock such as carbonates and massive sandstones were considered to have insignificant levels of anisotropy at around 2%. Whereas, tight-sands, shaly-sands, siltstones and shales exhibited in excess of 10% anisotropy.

Jones & Wang (1981) measured both P-wave and S-wave velocities in typically VTI shales. It was qualitatively inferred from SEM image analysis that the VTI symmtery was caused by clay particle alignment. Furthermore, they also suggested that an increase in preferred orientation with compaction might cause an increase in seismic wave velocity, but not necessarily an increase in seismic anisotropy, as previously suggested

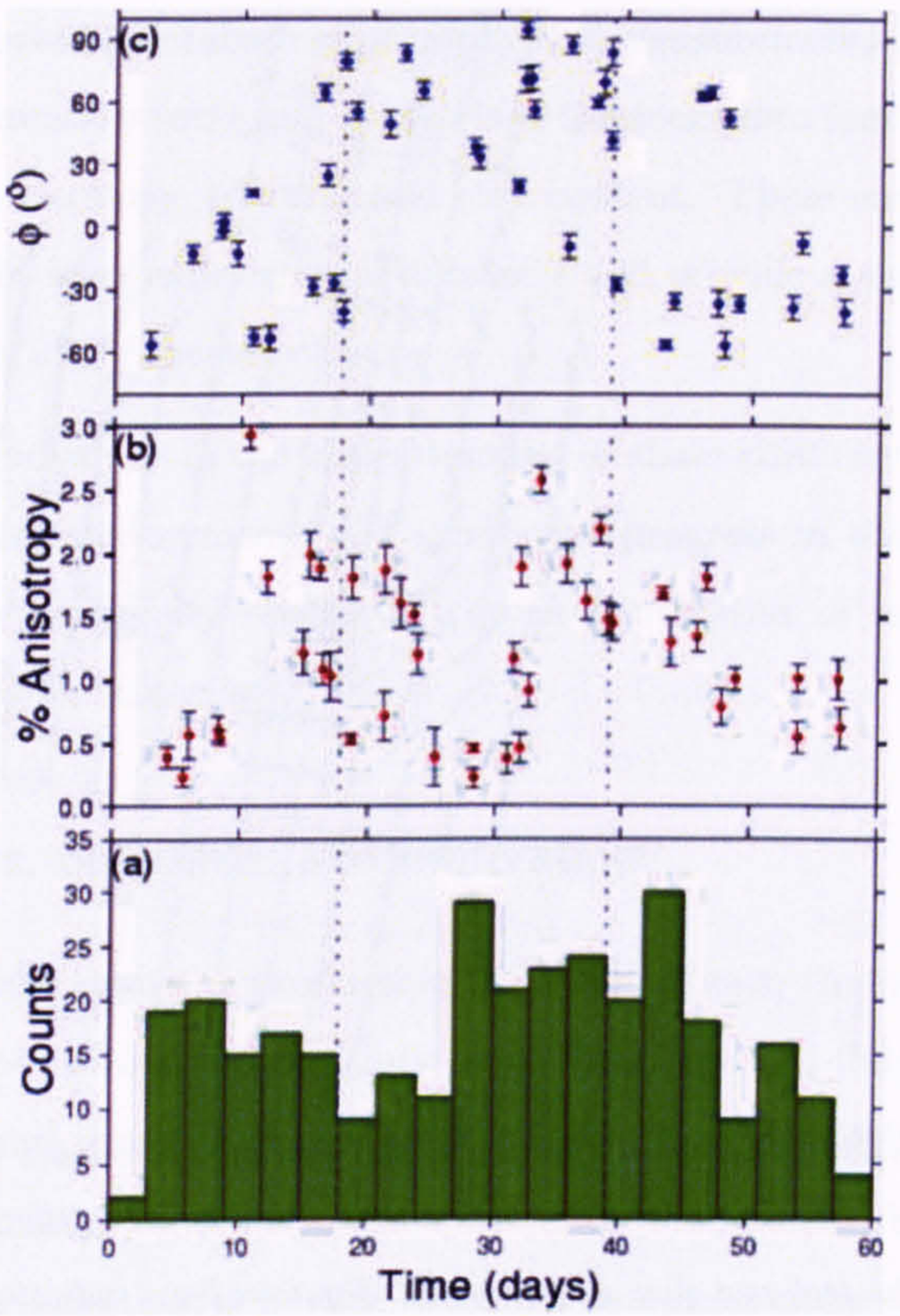

Figure 1.12: *Variations in shear-wave splitting with time. (a) histogram of Valhall seismicity. (b) variations in the estimated shear-wave anisotropy. (c) measurements of the fast shear-wave polarisation. Note the ninety-degree shift in azimuth of the fast shear-wave polarisation during the eight week period. Time in days goes from left to right (0 - 60 days)(Caley et al. 2001).*

by Kaarsberg (1959).

Sayers (1994) presented a theoretical model of the elastic anisotropy of a shale resulting from the partial orientation of clay particles also derived qualitatively by SEM image analysis. It was one of the first studies to use estimates of preferred orientation of clay particles to calculate seismic anisotropy. It was suggested that only two of the expansion coefficients of the ODF (orientation distribution function) affect seismic anisotropy of shales with VTI symmetry. By adjusting the values of these two parameters, the study investigated the anellipticity of shale anisotropy i.e., the degree of anisotropy. Results of the modelling showed that shales could develop strong anelliptic anisotropy due to intrinsic textural properties.

Carlson et al. (1984) measured the preferred orientation of calcite c-axes in carbonate-

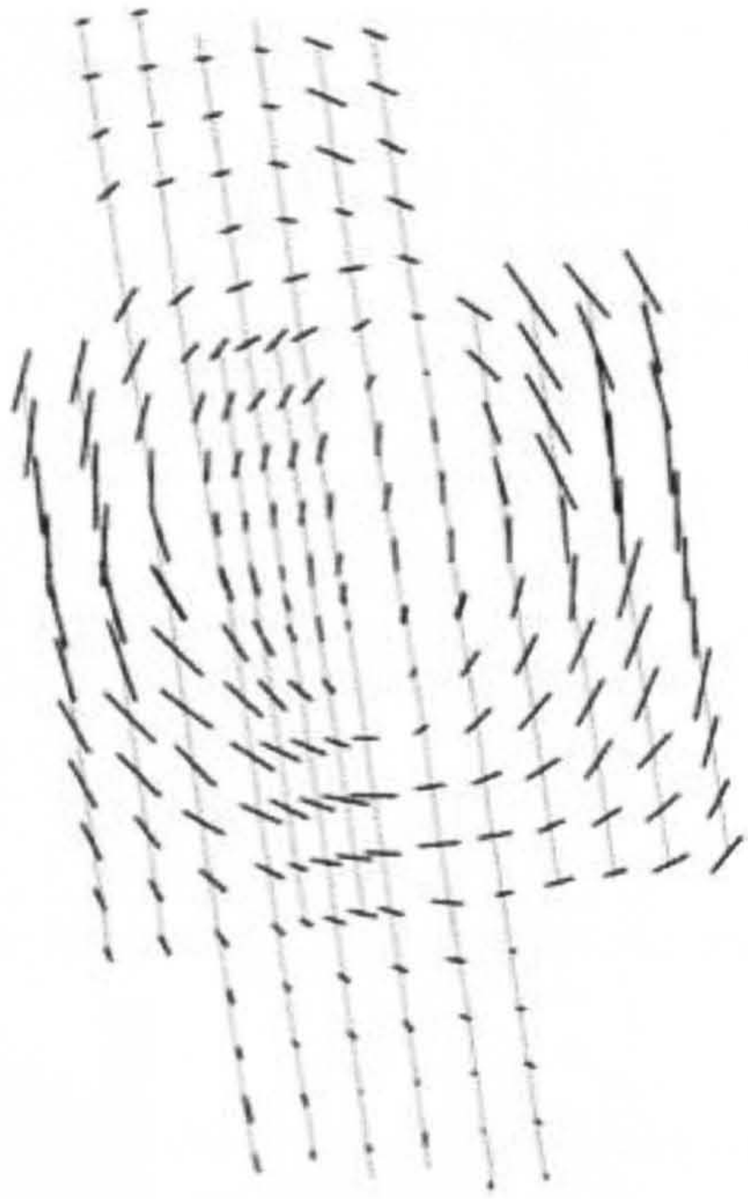

Figure 1.13: *Shear-wave splitting in the shallow overburden at the Valhall field, Norway. The ticks show the fast shear-wave direction, and the length of tick is proportional to the time delay between the fast and slow shear-waves. The thin lines indicate the receiver lines. Production at Valhall causes the reservoir to collapse which deforms the overburden, and causes subsidence of the sea floor (Olofsson et al. 2002).*

bearing deep-sea sediments using XTG and compared the results to the observed P-wave anisotropy. They concluded that the concentrations of calcite c-axes normal to bedding seemed insufficiently strong to contribute appreciably to the seismic anisotropy of calcareous deep-sea sediments.

In one of the most comprehensive studies of ultrasonic velocity anisotropy in sedimentary rocks, Wang (2002) conducted measurements on a suite of shales, sandstones, and carbonates under fluid saturated and *in situ* confining pressures. It was postulated that clay content and fine layering in siliciclastic sedimentary rocks could be one of the main causes of the observed seismic anisotropy. Furthermore, Wang (2002) observed that unfractured sandstones and carbonates show very little intrinsic anisotropy in comparison to some of the very clay and organic-rich shales.

It has been suggested by some of the earlier empirical studies that relatively simple relationships exist between seismic velocities and rock parameters. For example Vernik &

Nur (1992*a*) constructed a database of petrophysical measurements at high pressure on a suite of clastic sedimentary rocks and categorised the rocks into four petrological groups, based upon their mineralogy, texture, and clay content. These empirical formulas are obtained statistically from experimental data sets and provide a simple, yet convenient form of summarising experimental data.

Despite substantial advances in the understanding of shale elasticity based on numerous laboratory ultrasonic measurements and significant progress in the modelling of shale elasticity, significant ambiguity related to the *in situ* causes of seismic anisotropy in other sedimentary rocks still exists.

1.6 Thesis aims, objectives and motivation

In exploration, as well as in the production of hydrocarbons, the overall goal is to extract information and estimate uncertainty about lithology and fluid in the subsurface. Traditionally, standard prospect evaluation has focused on identifying structural traps. To fully enable the utilisation of seismic-wave velocities in hydrocarbon exploration and rock property characterisation, it is vital to have a complete understanding of what the seismic waves can tell us about the intrinsic and extrinsic parameters of the rocks *in situ*. Understanding the interaction between the various parameters that control rock properties is crucial to better interpretation of geophysical measurements. With the rapid advancement and inclusion of anisotropic processing algorithms in seismic data it is now an appropriate time to see whether it is possible to determine the relative importance of the different factors that control anisotropy. Evidence of seismic anisotropy in sedimentary rocks clearly has the potential to provide important information on the relative contributions of the controls of elastic anisotropy of rocks in the subsurface. This project was intended to investigate the relative contributions to elastic anisotropy from grain fabric alignment, fracture alignment, and crystal alignment.

Accurately predicting petrophysical properties requires a quantitative description of the complex microstructure of the medium. In the absence of a full structural characterisation, attempts to relate the elastic properties of rocks to petrological properties have been limited to empirical relationships and effective medium theories. Furthermore, previous studies have largely failed to quantify the intrinsic and extrinsic variables that control seismic anisotropy. Moreover, studies that have attempted to quantify the intrin-

sic anisotropy of sedimentary rocks have concentrated largely upon shales and clay-rich mudstones.

The structure of the SAIL project, and the role which this thesis played within it, meant that it was ideally positioned to tackle the issues outlined above. This thesis combined the results of a variety of different analytical and computational techniques to be able to fully understand the extrinsic and intrinsic controls of seismic anisotropy of siliciclastic hydrocarbon reservoir rocks. The experimental techniques employed included: electron microscopy, X-ray diffraction, palaeomagnetics, anisotropic magnetic susceptibility and ultrasonic velocity analysis. The results of the experimental techniques were integrated, utilised, and verified through a variety of geomathematical models, which included, among others: crack density tensor inversion, Bingham distribution modeling, empirical relations, and upscaling techniques.

1.6.1 Project goals

The principal goals of this project were to:

1. Develop methodologies to characterise petrofabric using complementary analytical and numerical techniques.
2. Compare results obtained from petrofabric analysis with laboratory based investigations into velocity anisotropy.
3. Interpret results determined from petrofabric analyses, ultrasonic measurements, and palaeomagnetics.
4. Identify how measurements of seismic anisotropy can be used to make inferences about rock and fluid type in the subsurface.

1.7 Thesis outline

Chapter 1 provides an introduction to the SAIL project which this thesis was a fundamental part of. It further goes on to describe why seismic anisotropy could be an important attribute to understand in the hydrocarbon industry. The latter parts of this introductory chapter address the parameters controlling seismic anisotropy. The chapter concludes with examples of observed seismic anisotropy in both laboratory experiments and field wide seismic surveys.

Chapter 2 presents a detailed background of the field area that this project was based upon. It provides a complete background of the location, structural setting, and structural history of the Clair field, N.W. Scotland. The reservoir geology of the Clair Group is also presented with accompanying details regarding the main sedimentological horizons (I-X), and their respective Supercycles (I-II-III). A review of the most recent seismic surveys conducted are also examined and the details of their results are also presented. The chapter concludes with the mineralogy (as determined by QXRD) of the samples analysed.

Chapter 3 contains detailed descriptions of the various commonly employed methods used to determine modal mineralogy. The techniques that are described include: point counting, image analyses, EBSD, and QXRD. Each of the techniques are then critically assessed with any associated uncertainties highlighted. A detailed description of XRD is presented with information regarding the theory and analytical set up for use as QXRD. The chapter concludes with the results of the QXRD analyses.

Chapter 4 describes the techniques, and methodologies used to determine the ultrasonic velocity of cylindrical rock samples at atmospheric and at high pressure (approximately *in situ*). The chapter begins with the core sampling technique used to investigate seismic anisotropy in heterogeneous siliciclastic rocks. For comparison, the same core samples were used for atmospheric and high pressure analyses. Details are presented of the high pressure (potentially very high) pressure vessel set-up and position of the piezoelectric transducers. Furthermore, an interesting technique using split-shear wave transducers and the method of Silver & Chan (1988) is applied to determine orientation and magnitude of shear-waves at high pressure. The chapter concludes with the results of the atmospheric and high pressure ultrasonic analyses.

Chapter 5 is primarily concerned with electron microscopy techniques. It begins with an overview of the SEM that includes, its workings, set-up, and sample-electron interaction. It further describes the application of the SEM to high-resolution imaging using BSE's. Electron backscattered diffraction (EBSD) is a technique for obtaining crystallographic information in the SEM. EBSD is then introduced, with an overview of the fundamentals of orientation determination, and the specific analytical set-up. Problems are encountered, however, when attempting to index low symmetry and weak crystalline mineral phases, such as feldspar and phyllosilicates, respectively. The problem of mis-indexing is addressed within this chapter and a possible solution proposed. The methodology

used to display and quantify the results obtained from EBSD analyses are presented (texture-index). The chapter goes on to present the results of the analyses for the predominant mineral phases present, in frequency histograms, and crystallographic pole figure distributions.

Chapter 6 begins with an explanation of how the data obtained from EBSD analyses is used to determine an estimate of seismic anisotropy of a polycrystalline aggregate using Voigt-Reuss-Hill averaging, and the Christoffel equation. Problems can be encountered when using EBSD to index low crystallinity mineral phases, such as muscovite. The Bingham method is presented as an analytical methodology of determining the orientation distribution of phyllosilicates. The results obtained from the Bingham model were compared to those obtained from EBSD analyses for verification. The single crystal seismic properties for quartz, feldspar, calcite and muscovite are also presented to aid interpretation of the predictions of bulk aggregate seismic anisotropy. The chapter also contains the bulk aggregate seismic anisotropy pole figure predictions based on the results obtained from QXRD, and EBSD analyses. Moreover two different models were developed that could be used to determine velocity and anisotropy from modal proportions alone. The first model was based upon an understanding that the texture-index for the constituent mineral phases did not vary systematically throughout the reservoir. It used a simple average of the single mineral phase elastic tensors to predict velocity and anisotropy from modal proportions alone. The second model was based upon empirical relations. The model used an ANOVA analysis and a multiple linear-regression to determine formulae to predict P- and S-wave anisotropy from modal proportions alone. The ability of these two models to predict P- and S-wave anisotropy was investigated using a paired *t*-test and the Wilcoxon signed rank test. Comparisons of the different models can be observed in tables presented at the end of the chapter.

Chapter 7 uses the results obtained from ultrasonic analyses and the bulk aggregate elastic tensor predictions from EBSD to invert for crack density. The theory of microcracks and their ability to control seismic anisotropy is presented along with the possible uses of remotely determining crack magnitude and orientation. The theory and equations of Sayers & Kachanov (1991) and the orthorhombic generalisations are presented in detail (Hall et al. 2007). Contained within the results of this chapter are inversion schemes using, α_{ij}, β_{ijkl}, P-wave, and S-wave ultrasonic data.

Chapter 8 is principally concerned with palaeomagnetism and AMS. The chapter begins

with an introduction as to why palaeomagnetism is a useful technique. It goes onto to deal with the methodologies, techniques, and apparatus used to determine palaeomagnetism and AMS. The theory and methodology behind the determination of grain fabric is also presented. Similarly so methodologies, techniques, and results used in the determination of pore fabric, permeability anisotropy, palaeomagnetism core orientation, horizontal anisotropy, degree of anisotropy, and permeability anisotropy are also described. The concluding parts of this chapter describe a study into the scale dependence of the analyses of grain fabric measurements.

Chapter 9 brings together the results obtained from various SAIL project investigators to enable broad conclusions to be drawn from the results of this project. For example, as a result of this project we now have a framework for interpreting anisotropy on various length scales: crystal (LPO), intergrain (SPO), and fracture or bedding scale (seismics). The data obtained from LPO analyses has been used in determination of an expected AVOA response from crystal alignment alone and therefore allows more confidence in interpreting fracture induced anisotropy.

Chapter 2

Clair field, N.W. Scotland

2.1 Overview

The Clair field is located approximately 75km West of the Shetland Islands, and for twenty years was the largest undeveloped oil discovery on the UK Continental Shelf (Smith & Lappin 1997)(Figure 2.1). The Clair field consists of Old Red Sandstone rocks that were deposited over a Lewisian basement at the end of the Caledonian Orogeny (c. 350-400Ma)(Coney et al. 1993). Sedimentation was largely controlled by the closure of the Iapetus Ocean.

2.2 Structural history

The Clair field is located on the SE flank of the NE-SW trending Rona Ridge. The field consists of a Lewisian basement onlapped by Devonian-Carboniferous sediments (Allen & Mange-Rajetzky 1992) and can be divided into three main structural elements: Core-Graben, Horst, and Ridge (Figure 2.1) (Smith & Lappin 1997).

The Ridge forms the highest part of the field's structure and is a continuation of the Rona Ridge. The Core-Graben area lies to the SE of the Ridge in the southern half of the field and is in the hanging wall of the eastern bounding fault of the Ridge. To the SE of the Core-Graben is the Horst (Figure 2.2).

The NE-SW regionally trending faults that run parallel to the ridge are associated with the opening of the Clair basin during the Caledonian orogeny. The predominant movement on these Caledonian faults is dip-slip, but their is some evidence to suggest both sinistral and dextral strike-slip movement (Smith & Lappin 1997). The fractures which

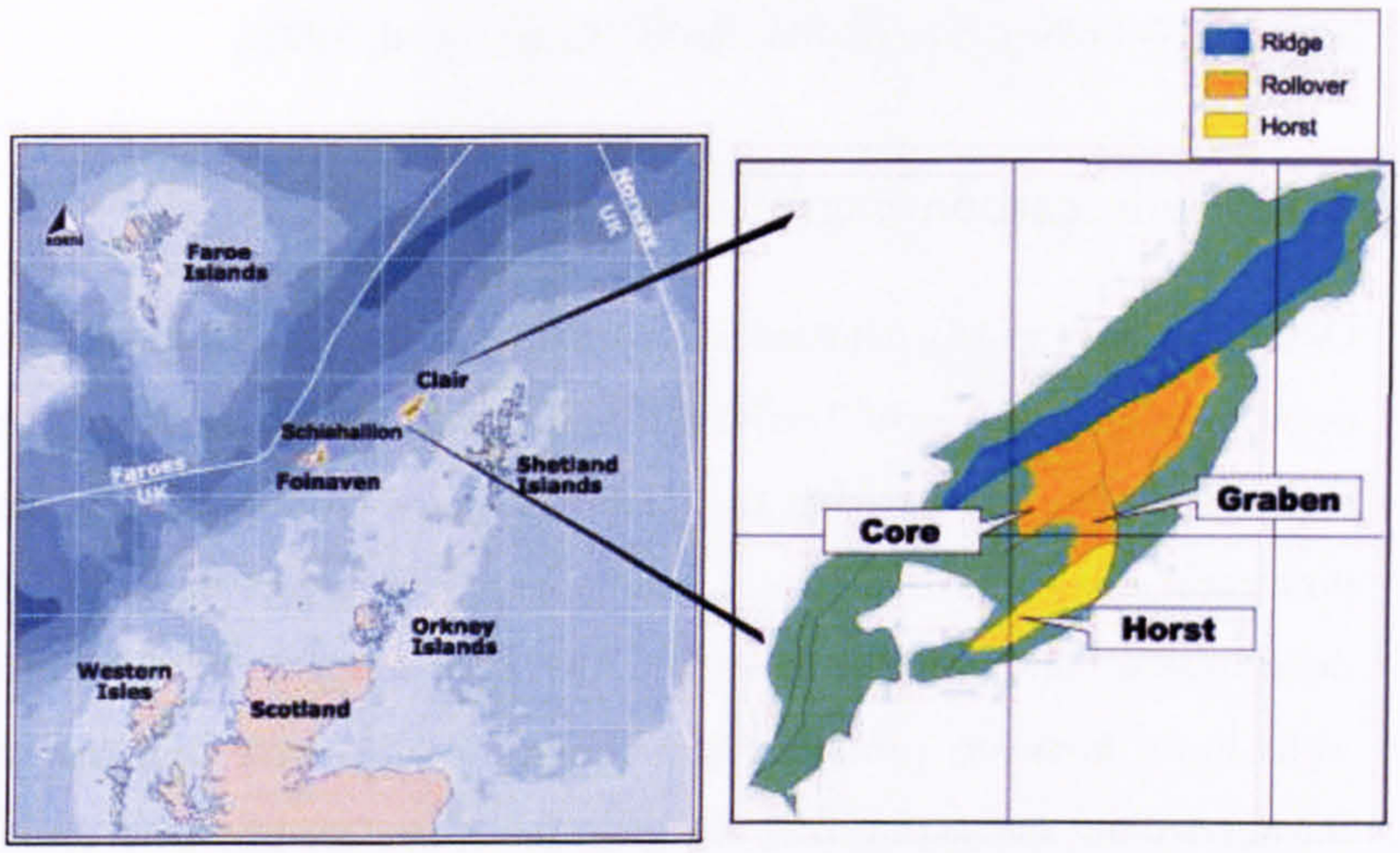

Figure 2.1: *Location, and structural configuration of the Clair field, N.W. Scotland - UKCS. The field is located in water depths of up to 150m and extends over* $220km^2$ *covering five licence blocks - 206/7a, 206/12, 206/8, 206/13a and 206/9. One block is approximately 75km wide and 150km long.*

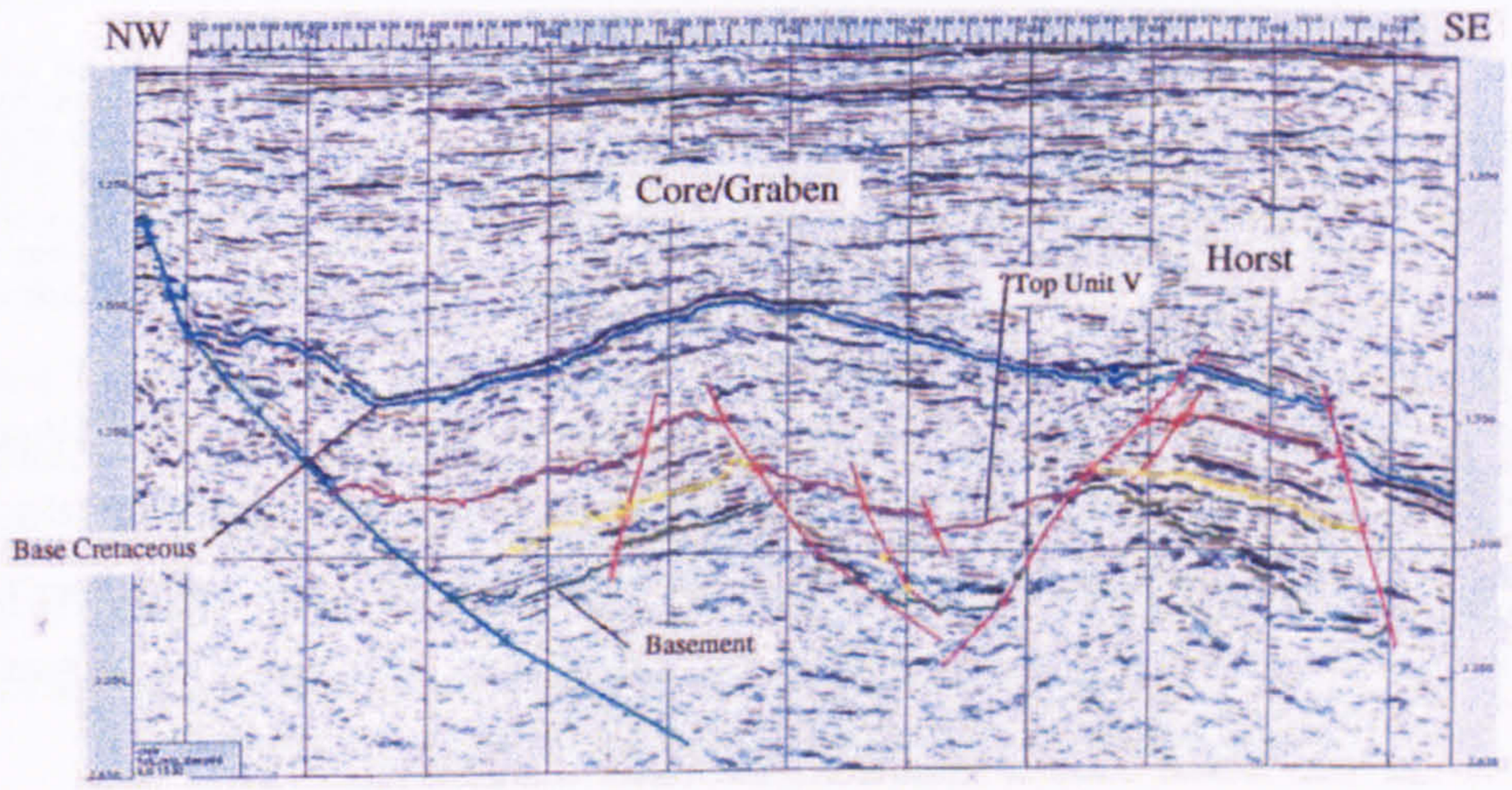

Figure 2.2: *Dip-line section through the Ridge (left hand-side), Core-Graben, and Horst. The section is presented in two-way-time. The entire depth of the section is 2.5secs TWT which is approximately 3000m.*

run parallel to the Caledonian faults tend to be closed, whilst a second set of faults oriented N-S offset the NE-SW faults (Coney et al. 1993).

2.3 Hydrocarbon migration

Oil migration is widely believed to have begun in the Late Cretaceous with filling actively occurring until the early Tertiary (Coney et al. 1993). However, the majority of the appraisal wells drilled within the Clair field have produced disappointing hydrocarbon flow rates due to poor reservoir quality and a high concentration of low permeability deformation bands (Smith & Lappin 1997, Knipe et al. 1998). Three recent appraisal wells have, however, produced economic flow rates with well test data and mud loss during drilling suggesting that the good flow rates are probably associated with breccia zones and open fractures. The breccia zones are thought to have formed by the linkage and brecciation of closely spaced tension fractures during strike-slip motion. It has been suggested that the breccia zones developed in response to transtensional shearing during dextral strike-slip movement along the Rona Ridge and Southern Horst faults (Knipe et al. 1998).

2.4 Reservoir geology

The overall stratigraphic framework for the Clair field was first established by Blackbourn (1987) and later revised by Allen & Mange-Rajetzky (1992) (Figure 2.3). The best quality reservoirs are found in Units III and V. But there are also some good quality reservoirs within Units IV and VI (Coney et al. 1993).

The Clair field can be divided into two main groups; the Lower Clair Group (Units I to VI), and the Upper Clair Group (Units VII to X) (Allen & Mange-Rajetzky 1992). There are two field-wide unconformities. One separates the Lower and Upper Clair Groups. The second is at the top of the Clair Group, and is overlain by the Cretaceous Shetland Group (shales) that form the regional seal (Coney et al. 1993).

Lower Clair Group

The Lower Clair Group consists of the following units:

Unit I - Fluvial mudstones, both cross, and uni-directional laminations with thin fining upwards units. Mainly composed of shales similar to those found in modern day lakes.

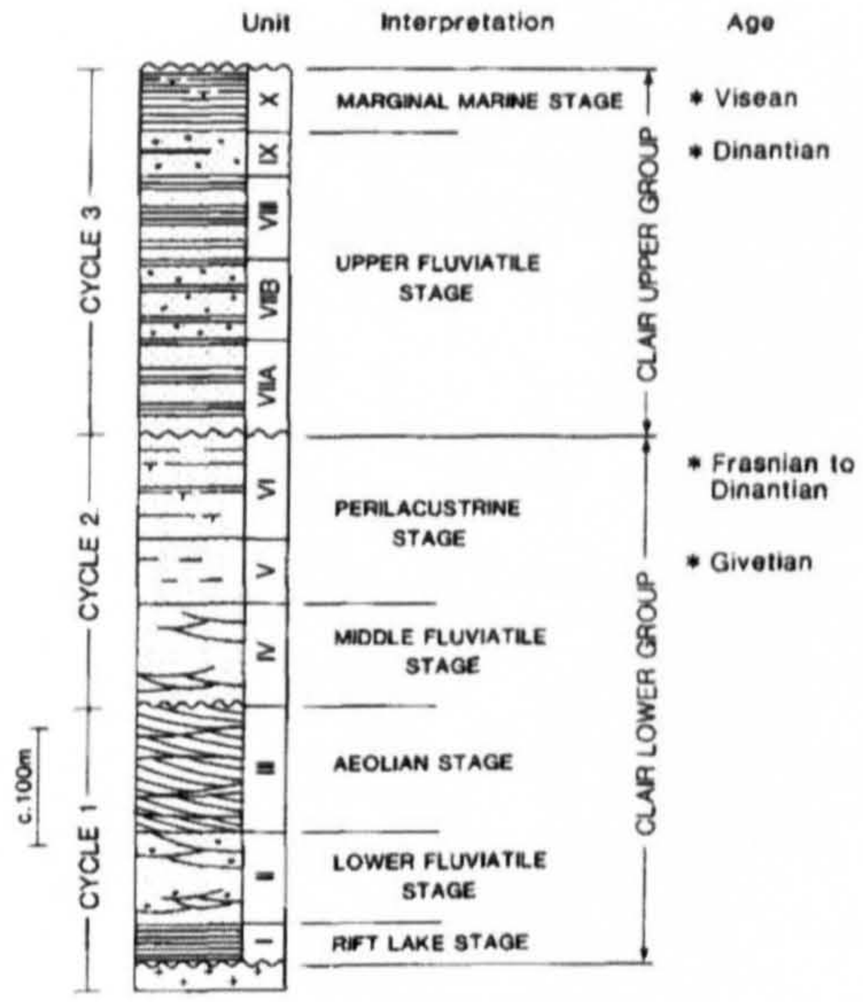

Figure 2.3: *Summarised Clair Group stratigraphy (Allen & Mange-Rajetzky 1992).*

Unit II - Lower fluviatile, matrix supported conglomerates, with cross-stratified medium to coarse grained sandstones.

Unit III - Aeolian environment with irregularly laminated siltstones, cross-stratified fine to medium grained sandstones and mudstones. This unit is probably associated with aeolian dune facies, with interdune sabkhas, and sporadic river floods.

Unit IV - Middle fluviatile stage composed of interbedded breccias, coarse, and compositionally immature sandstones. This unit is thought to have been deposited by bed-load dominated rivers with aeolian interactions in the dried up beds.

Unit V and VI - The main lithologies contained within Unit V are cross-stratified sandstones, and finely laminated sandstones, interbedded with silty sandstones. Whilst the main lithologies within Unit VI are horizontally and wave-rippled fine grained sandstones, and mudstones. It is thought to have been deposited in a perilacustrine environment with aeolian, and river activity, with fringing sabkhas, and playas.

Upper Clair Group

The Upper Clair Group consists of the following units:

Units VII to IX - Upper fluviatile stage. Sediments include: arkosic, texturally immature medium-coarse grained sandstones, pebbly sandstones, and horizontally laminated

mudstones. The depositional environment is thought to be a high-sinuosity river containing low angle point bars, and chute channels.

Unit X - Marginal marine environment containing mudstones, coarse, rubbly sandstones, and rippled sandstones. These sediments are thought to represent mouth bars, and distributary channels.

Allen & Mange-Rajetzky (1992) identified three major supercycles within the lithostratigraphic units. Cycle 1 (Units I-II-III) is thought to represent a change from rift, floodplain lakes to sand laden streams. This suggests a change from external drainage in the rift basin to internal drainage. Cycle 2 (Units IV-V-VI) is believed to reflect a similar trend towards internal drainage, with sand-rich streams being replaced by shallow lakes. Cycle 3 (Units VII-VIII-IX-X) is held to be representative of a change from high sinuosity river systems to fluvio-deltaic, and marine environments representing a further increase in river discharge.

Broadly, the Clair sequence is thought to have evolved during two phases with contrasting provenance and drainage patterns (Morton et al. 2002). Cycles 1 and 2 are believed to have been deposited by small intra-rift drainage networks, while Cycle 3 represents an enlargement of the watershed, with river systems draining back into Shetland, the Scottish mainland, Scandinavia, and Greenland (Allen & Mange-Rajetzky 1992).

2.4.1 Matrix mineralogy and reservoir quality

It was demonstrated by Pay et al. (2000) that the depositional facies of the Clair Group (CG) were an important control upon the abundance of clay minerals. It was found that the fluvial sediments generally exhibited a higher clay mineral content compared to those deposited in aeolian settings. Matrix porosity and permeability was determined to be severely restricted where pore-lining clays were in abundance ($> 15\%$), and where the clays bridge or fill pores. Figure (2.4) illustrates the direct correlation between low permeability zones and clay mineral abundance. Moreover, where calcite cement is in abundance, clay mineral content inversely constitutes only a minor proportion of the overall modal content, and vice versa.

The following clay minerals have been identified within the Clair field reservoir:

Smectite - grain coating and pore filling, typically $c.10 - 30\mu$m long, and occurs exclu-

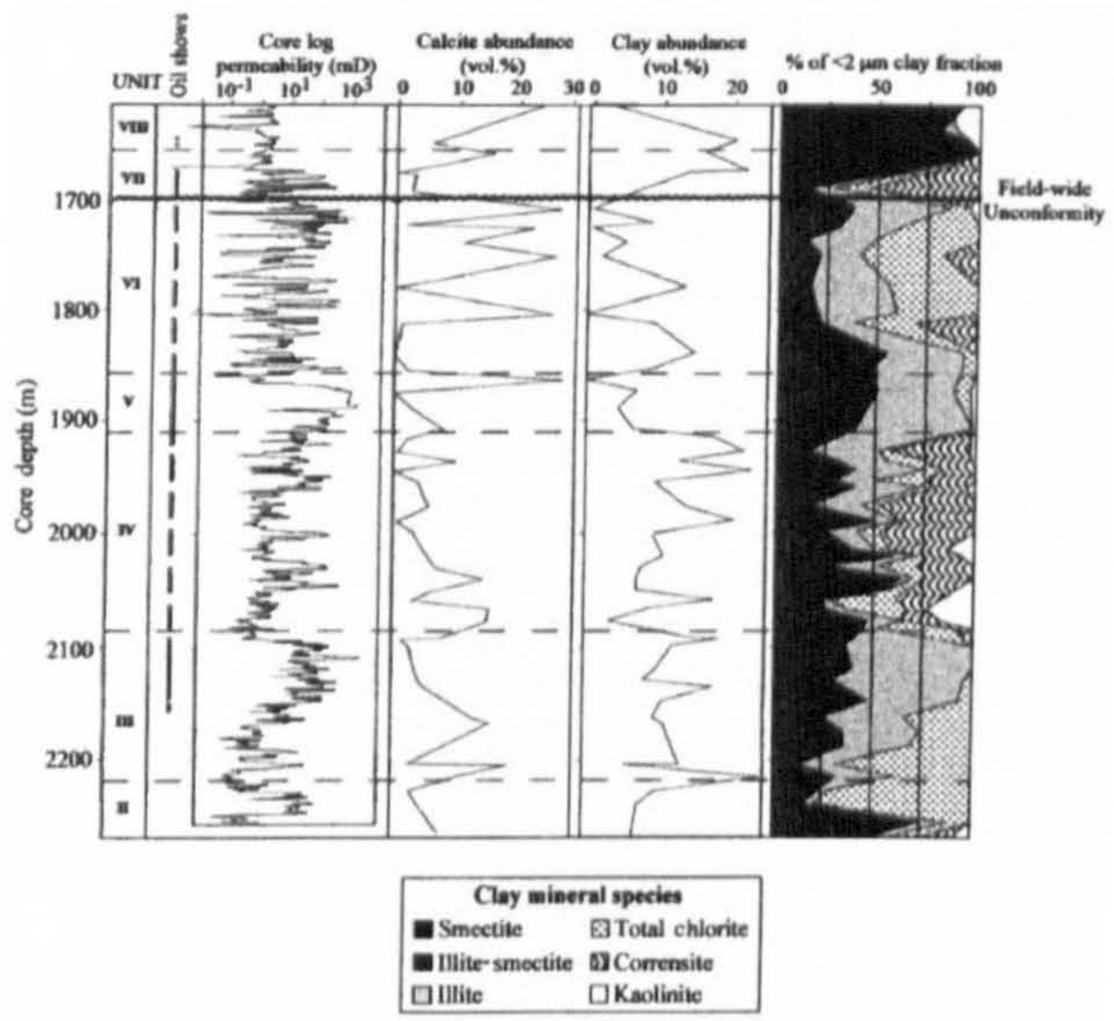

Figure 2.4: *Distribution of permeability, authigenic carbonate, and clay mineral type with depth - Well 206/8-8 (Pay et al. 2000).*

sively in the UCG (Upper Clair Group).

Kaolinite - vermiform kaolinite is found randomly distributed throughout the CG, typically $c.1 - 30\mu$m long, and $c.5 - 10\mu$m wide.

Illite - occurs sporadically throughout the LCG (Lower Clair Group) as grain coatings or pore bridging ribbons $< 5 - 10\mu$m thick, and $\leq 40\mu$m long.

2.5 Provenance

Lower Clair Group - Heavy mineral assemblages with good sorting and high sphericity suggests that the detritus was shed mainly from pre-existing sediments, mostly low-grade metasediments and high-grade metamorphics of the Precambrian crystalline basement (Morton et al. 2002).

Upper Clair Group - The heavy mineral assemblage of the UCG is dramatically different to that of the LCG. An abundance of coarse, poorly-sorted, unstable species suggests a considerable change in both sedimentation and palaeogeography. It is believed by Allen & Mange-Rajetzky (1992) that the combination of structural events exposing complex lithologies and an enlarged drainage network contributed to the significant change in mineral assemblage.

Ultimately, it is thought that the sediments can be considered as having derived from the Precambrian and Caledonian complexes of West Shetland, Shetland Islands, Greenland, and Scandinavia. At that time the larger rivers may well have reached into areas of Greenland, which was in close proximity, whilst also draining regions of Shetland (Figure 2.5).

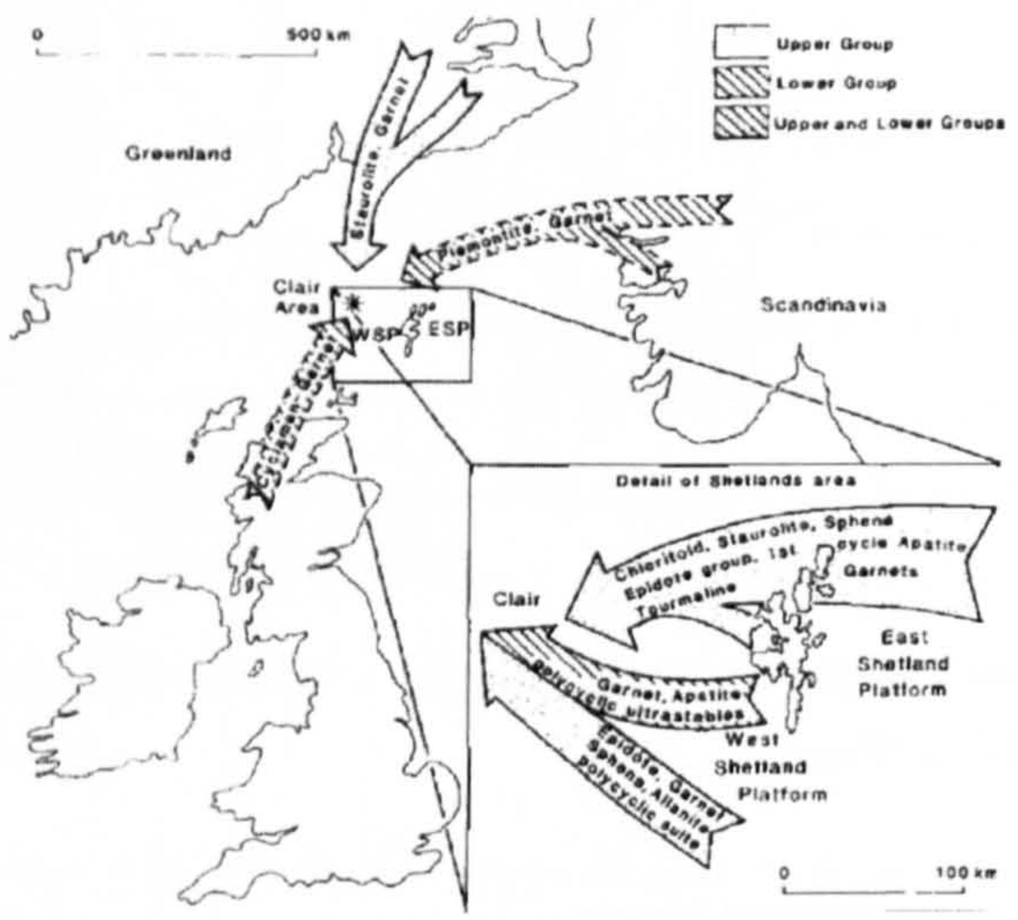

Figure 2.5: *Provenance of minerals comprising the Devonian-Carboniferous Clair reservoir. Arrows with broken lines are minor sources. WSP - West Shetland Platform; ESP - East Shetland Platform; asterisk marks location of Clair field (Allen & Mange-Rajetzky 1992).*

2.6 Clair field seismic data review

Seismic interpretation is largely based upon the fully migrated *3D* stack volume, which comprises the 1990, 1992, and 1996 *3D* surveys, covering approximately $350km^2$ (Smith & Lappin 1997). The seismic data shows good agreement with both the well and VSP (vertical seismic profile) data. Although the Clair *3D* seismic data set is acknowledged as having an optimal acquisition geometry, new technologies such as OBC (ocean bottom cable) have been investigated to aid field development.

It was proposed after the initial extended well test (EWT) that an intimate understanding of Clair's complex fracture network would be crucial to achieving the fields full potential. The primary investigation comprised of a multiazimuth walkaway VSP and was intended to characterise fracture orientations and densities (Smith & McGarrity 2001). It was, however, demonstrated by Smith & McGarrity (2001) that the technol-

ogy would not prove significantly beneficial without a wider azimuthal coverage and consistent signal-to-noise levels.

Consequently, three *2D* ocean bottom seismic (OBS) lines were acquired in 2000 in preparation for a *3D* OBS study (Kommedal et al. 2004). The *3D-4C* OBS data was acquired in 2002 with a view to characterisng azimuthal variations in elastic properties (Kommedal et al. 2004, Tabti et al. 2004). The *3D-4C* OBS survey was also used to improve the imaging resolution within the Clair field, which has high levels of water layer multiple contamination. A comparison between the OBS image and the streamer data image can be seen in Figure (2.6). The *3D-4C* OBS survey improved signal-to-noise ratio and enabled a reduction in uncertainty in the structural imaging, resulting in modification of the geological model.

2.7 Samples analysed

A suite of siliciclastic sedimentary rocks were collected from two wells: 206/8-8 and 206/13a-2, located within the Core and Horst, respectively (Figure 2.7). The samples were chosen to be representative of both Clair field lithotypes and typical siliciclastic hydrocarbon reservoir rocks. More specifically, the samples were extracted from the three main horizons of the Clair field Units I-III, V, and VI (Tables 2.1 and 2.2). Unit IV was not sampled because the lithotypes present within it had been sampled previously (Figure 2.3).

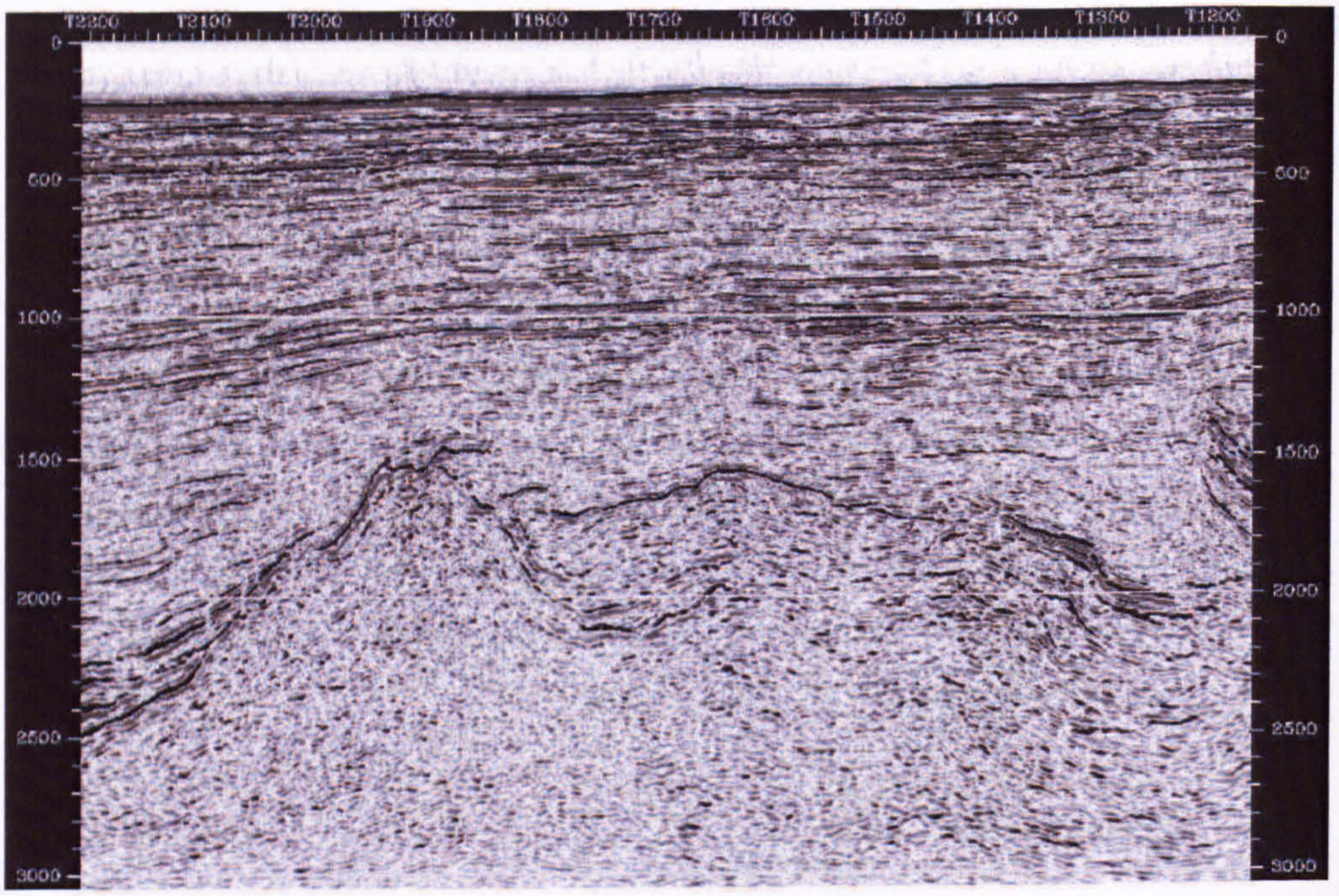

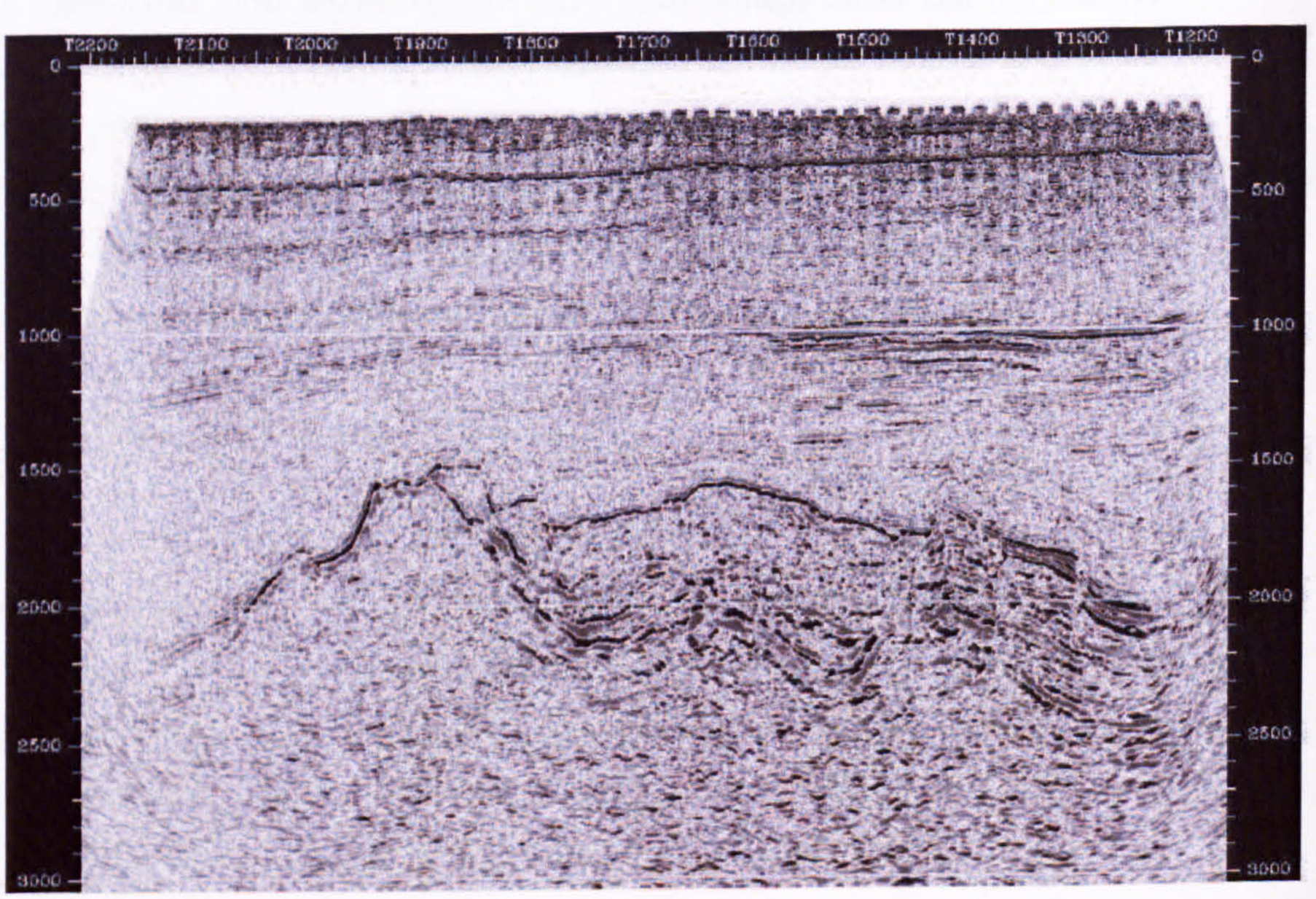

Figure 2.6: *Clair reservoir streamer data (top) compared with OBS (ocean bottom seismic) data (bottom). The main reflectors in the OBS data are: Base Tertiary 1s, Base Cretaceous unconformity 1.6s, intra-reservoir reflector 1.8s, and Top Basement 2s (Kommedal et al. 2004). The section is presented in two-way-time. The entire depth of the section is 3.0secs TWT which is approximately 3300m.*

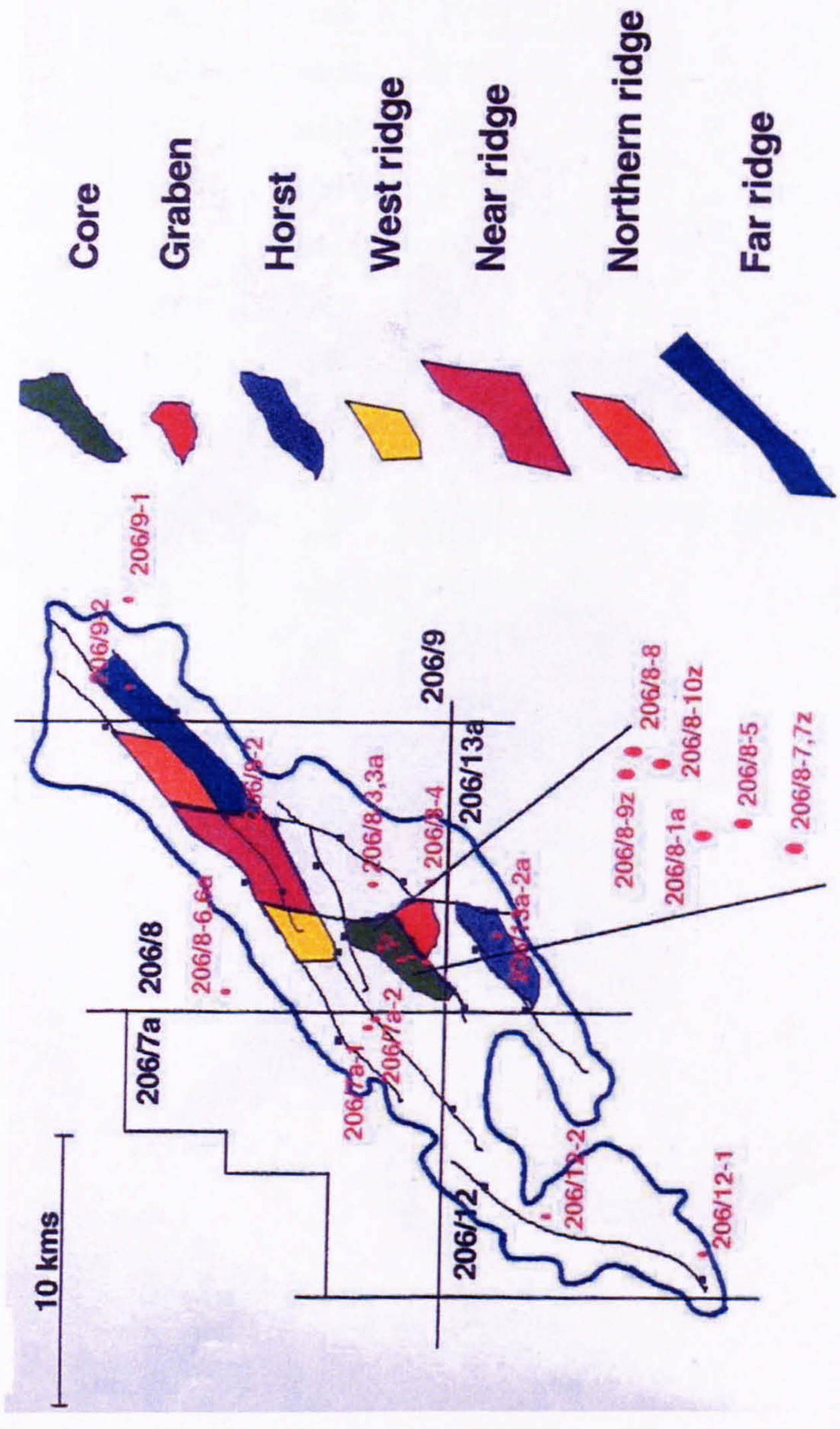

Figure 2.7: *Clair field, N.W. Scotland, UKCS - Well locations. Wells 206/8-8 and 206/13a-2 are situated within the Core and Horst respectively.*

Table 2.1: *Samples analysed from Well 206/8-8. Sample number also refers to core depth. Sst - sandstone, Mdst - mudstone.*

Unit	Lithology	Sample
VI	Sst	1663
VI	Mdst	1763
VI	Mdst	1784
VI	Mdst	1788
VI	Mdst	1841
V	Sst	1909
V	Sst	1950
V	Sst	2073
V	Sst	2088
I-III	Sst	2129
I-III	Sst	2192
I-III	Sst	2194
I-III	Sst	2198

Table 2.2: *Samples analysed from Well 206/13a-2. Sample number also refers to core depth. Sst - sandstone, Mdst - mudstone.*

Unit	Lithology	Sample
V	Mdst	1959
V	Mdst	1963
V	Sst	2015
V	Sst	2023
V	Sst	2028
V	Sst	2034
V	Sst	2070

A description of the various lithotypes typical of each unit sampled is provided as follows:

Unit VI

A medium-grained, moderately-well sorted, weakly laminated, clean sandstone that has been extensively cemented by calcite. The ductile components comprise rare quantities of partially grain-rimming brown detrital clays and isolated and deformed illitic mudclasts (Figure 2.8). Authigenic minerals are dominated by pore-filling non-ferroan calcite and fine-grained calcite, which is possibly in part, replacing detrital clays and mudclasts (Figure 2.9). The macropore system comprises well connected primary interparticle macropores that are typically $c.150 - 300\mu m$ in diameter and are distributed in discrete laminae that are free from authigenic minerals. Micropores will be present between detrital clays and within mudclasts but may also be present within finely crystalline calcite patches. The layered nature of the calcite cement will seriously reduce vertical permeability.

Unit V

A medium-grained and moderately well sorted massive sandstone, displaying a weakly compacted fabric (Figure 2.10). Ductile minerals are typically rare and comprise very thin, discontinuous, green and brown detrital clay rims on a significant proportion of grains. The macropore system comprises moderately to moderately-well connected primary interparticle macropores which range in size from $c.50 - 300\mu m$ in diameter and are evenly distributed throughout the section. Secondary oversized macropores are poor to moderately connected to the primary pore system and range in size up to $c.450\mu m$ in diameter (Figure 2.11).

Unit I-III

A fine-grained and moderately well sorted laminated sandstone, which displays an open to weakly compacted fabric (Figure 2.12). Laminae are defined by grain size, detrital clay and K-feldspar abundance differences. Ductile grains comprise relatively continuous, but thin illitic clay coatings on the majority of the framework grains. Finer grained laminae are typically dominated by ductile grains and contain a higher proportion of pore filling detrital clays. Authigenic minerals are dominated by non-ferroan calcite, which is present principally within coarser grained and cleaner laminae. The pore system comprises moderate to moderately-well connected primary interparticle macropores, which are typically $c.15 - 50\mu m$ in diameter and are distributed throughout the section but are less abundant within calcite cemented horizons (Figure 2.13). Micropores are distributed

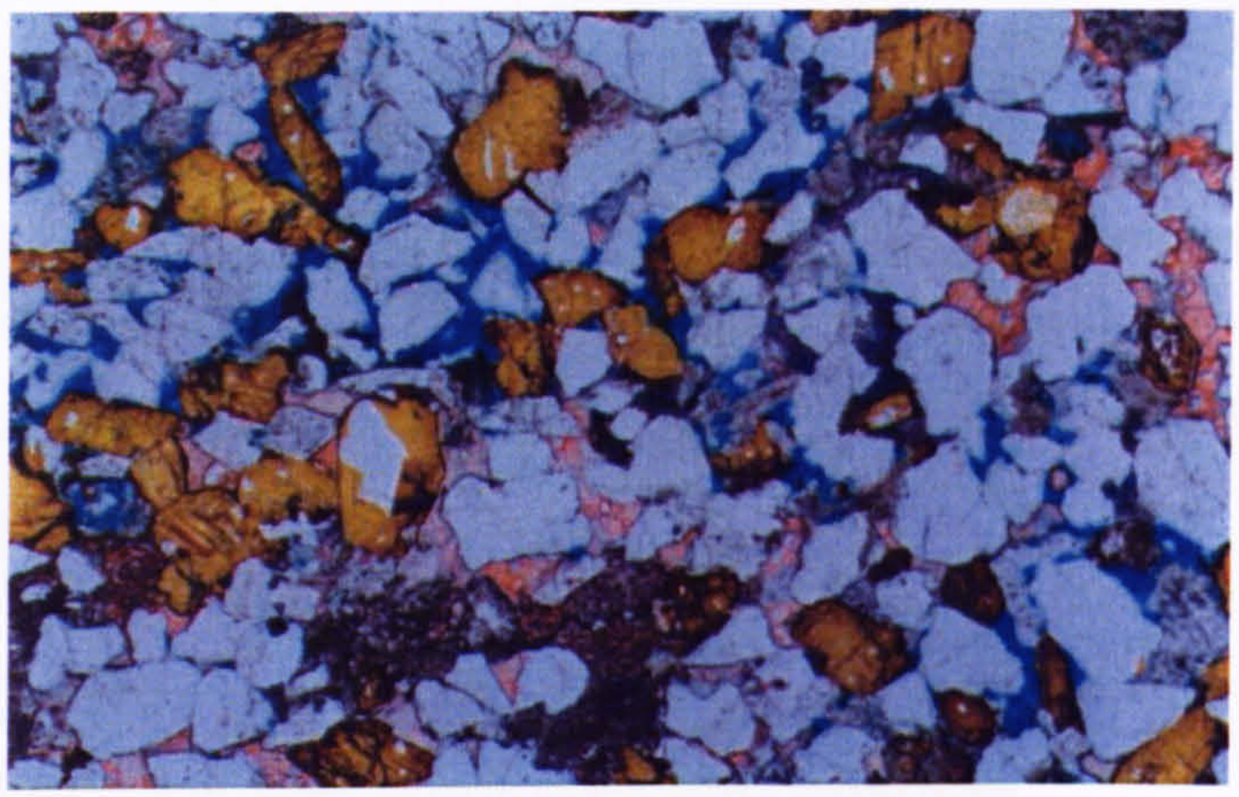

Figure 2.8: *Optical microscope image of a medium-grained, moderately-well sorted, weakly laminated clean sandstone. The lithotype presented typifies Unit VI within Well 206/8-8 (Sample - 1663m). Quartz grains appear clear and colourless. Undifferentiated feldspars are yellow in colour. The calcite cement is stained blue for ease of identification. Slide is 3cm long and oriented perpendicular to bedding.*

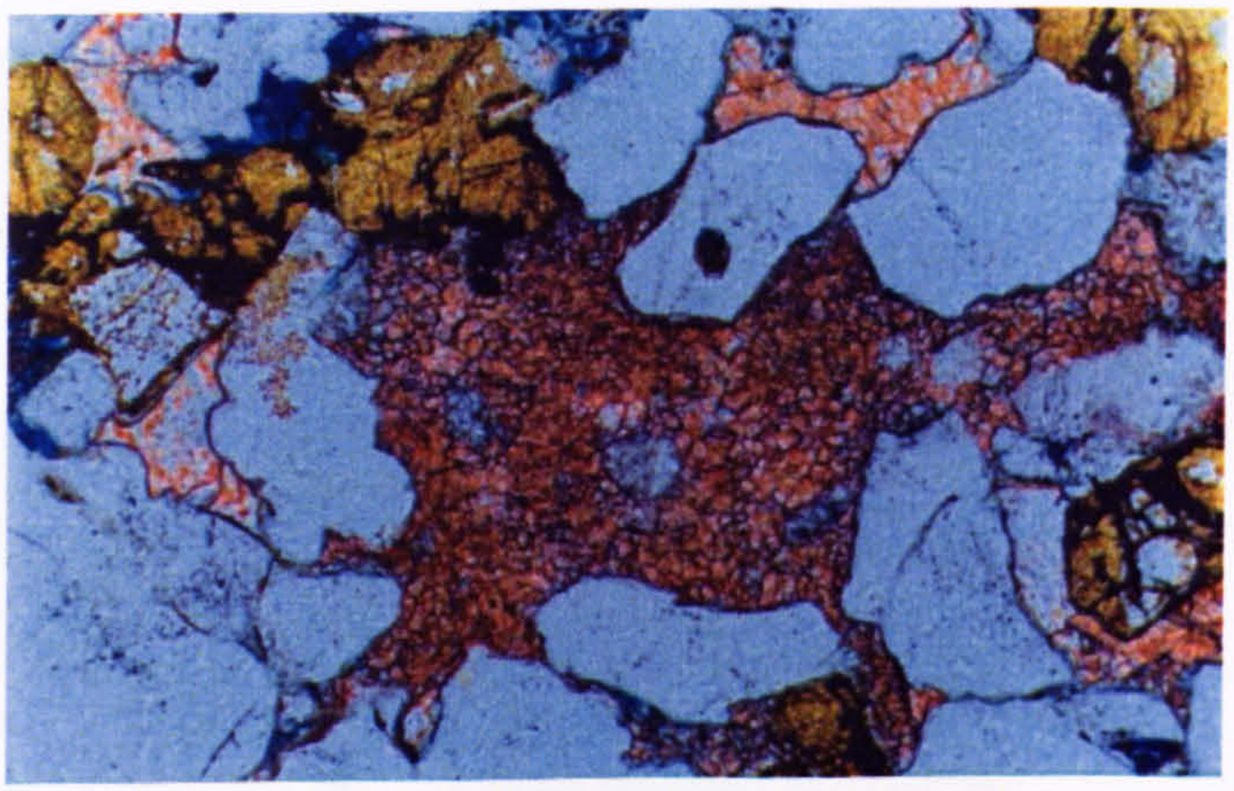

Figure 2.9: *High resolution optical microscope image of the authigenic pore filling minerals from a Unit VI lithotype from Well 206/8-8 (Sample - 1663m). The pore-filling material is dominated by calcite spar and fine grained calcite. Quartz grains appear clear and colourless. Undifferentiated feldspars are yellow in colour. The calcite cement is stained blue for ease of identification. Slide is 1.3cm long and oriented perpendicular to bedding.*

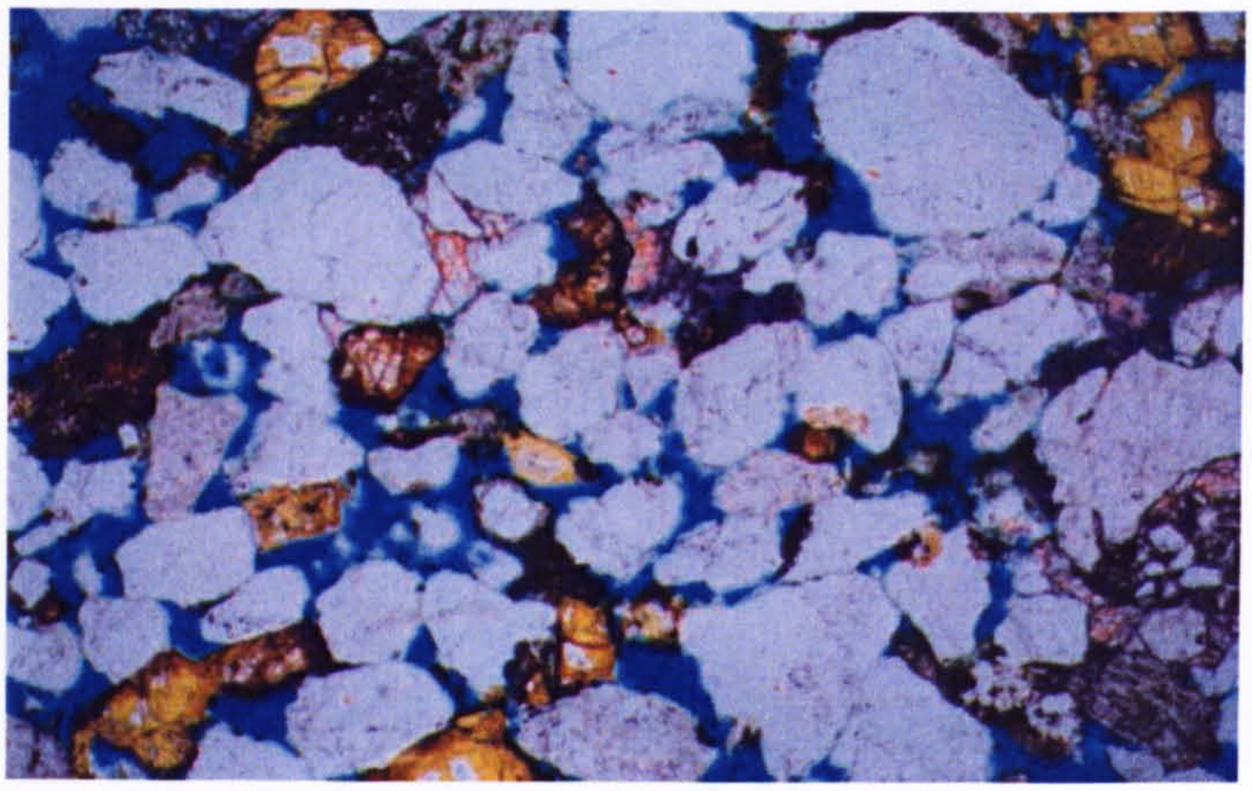

Figure 2.10: *Optical microscope image of a medium-grained, well-sorted clean sandstone. The lithotype presented typifies Unit V within Well 206/8-8 (Sample - 1909m). Quartz grains appear clear and colourless. Undifferentiated feldspars are yellow in colour. The calcite cement is stained blue for ease of identification. Slide is 3cm long and oriented perpendicular to bedding.*

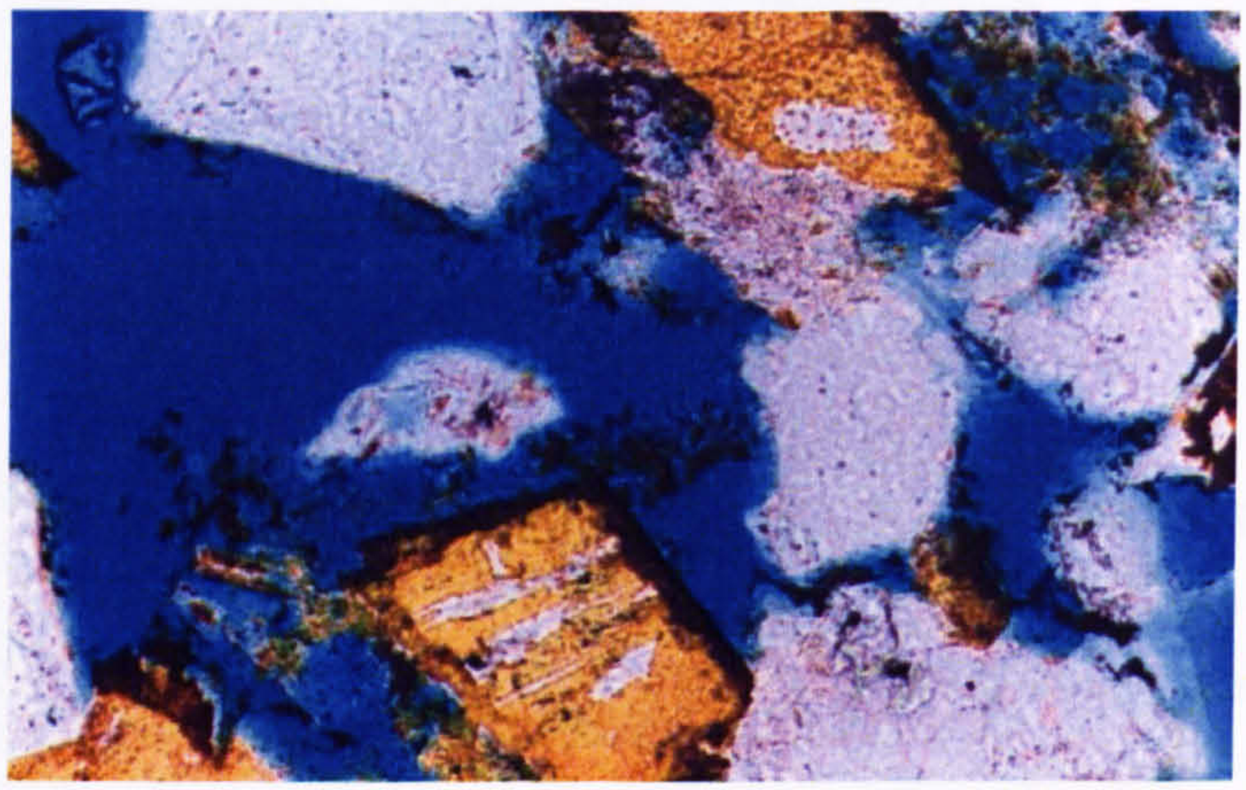

Figure 2.11: *High resolution optical microscope image of the macropore space from a Unit V lithotype from Well 206/8-8 (Sample - 1909m). Quartz grains appear clear and colourless. Undifferentiated feldspars are yellow in colour. The calcite cement is stained blue for ease of identification. Slide is 1.3cm long and oriented perpendicular to bedding.*

throughout the section being principally held within detrital clays. The discontinuous calcite cemented horizons will form local baffles to vertical fluid movement.

In general, the samples range from medium grain sized, mature sandstones (quartzo-feldspathic rich) to fine-grained, finely-laminated mudstones (phyllosilicate rich). The samples are broadly classified as arenites, arkoses, and wackes. To illustrate the variation in modal proportion, individual sample mineralogy is conveniently plotted on a ternary diagram (Figure 2.14).

Figure 2.12: *Optical microscope image of a fine-grained, moderately well sorted sandstone. The lithotype presented typifies Unit I-III within Well 206/8-8 (Sample - 2194m). Quartz grains appear clear and colourless. Undifferentiated feldspars are yellow in colour. The calcite cement is stained blue for ease of identification. Slide is 3cm long and oriented perpendicular to bedding.*

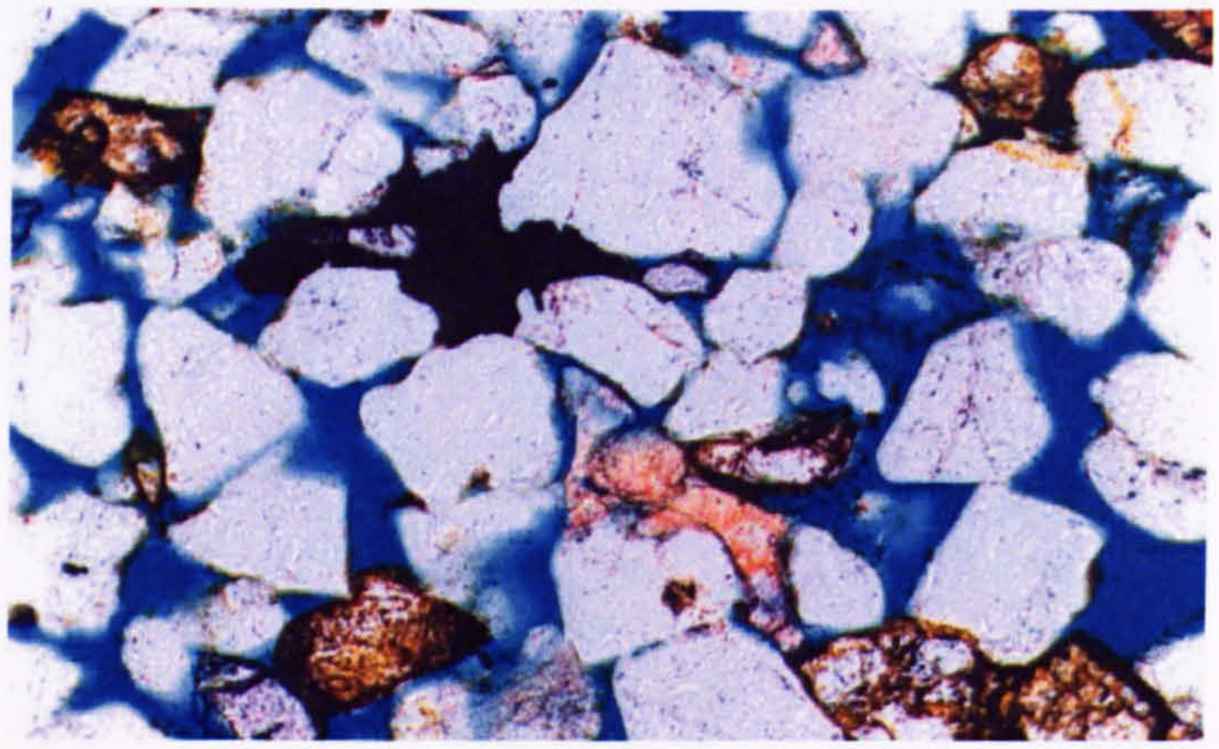

Figure 2.13: *High resolution optical microscope image of interparticle macropores and calcite cemented horizons from Unit I-III of Well 206/8-8 (Sample - 2194m). Quartz grains appear clear and colourless. Undifferentiated feldspars are yellow in colour. The calcite cement is stained blue for ease of identification. Slide is 1.3cm long and oriented perpendicular to bedding.*

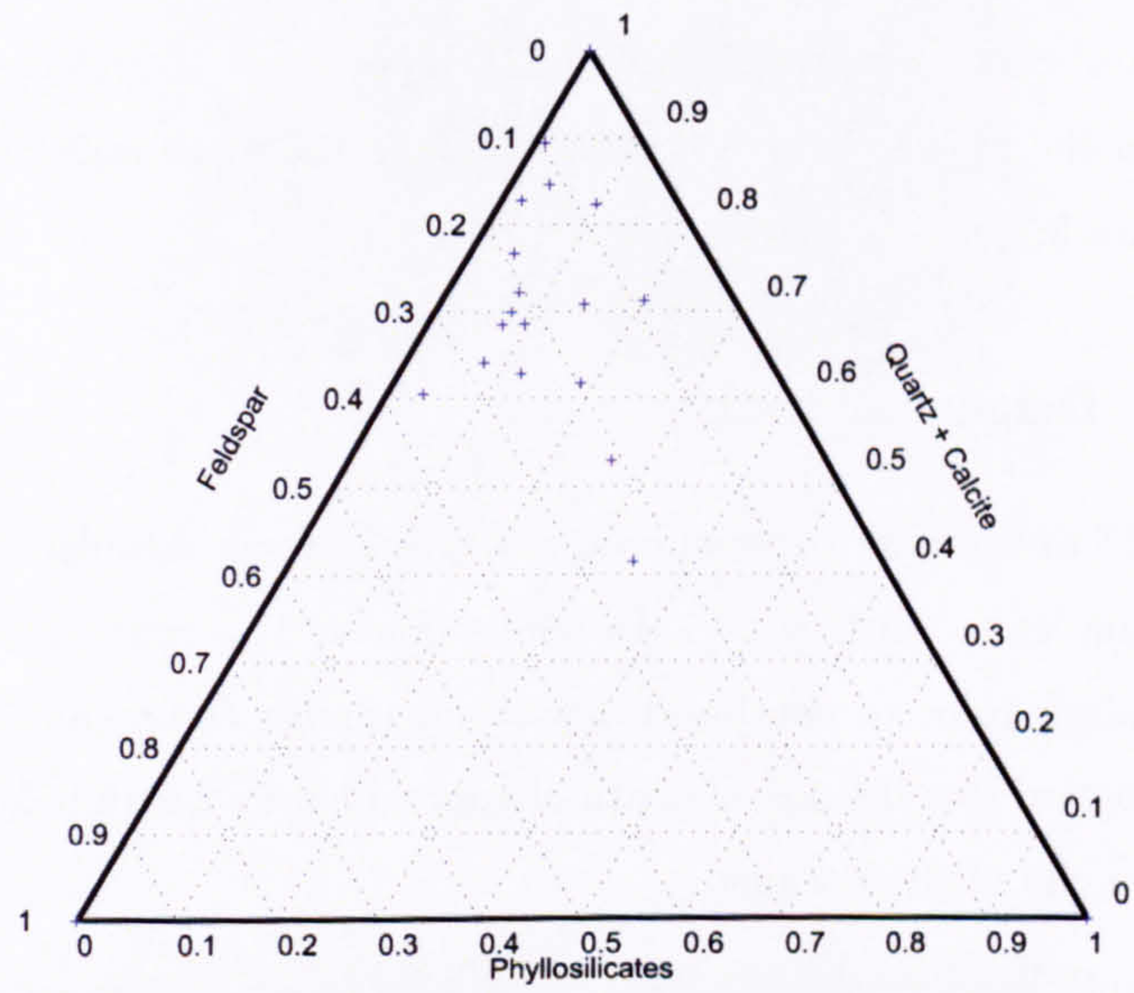

Figure 2.14: *A ternary diagram illustrating the variation in modal proportion throughout the samples. Phyllosilicates include biotite, muscovite, and illite. Based on quantitative X-ray diffraction results from Chapter (3). The side which contains the label represents 100%.*

The mature sandstones have an average porosity and permeability of 15% and 50mD respectively. The clean sandstones were often relatively massive with only minor variations in mineralogy and subtle bedding features (Figure 2.15). BSE imaging indicates that the clean sandstones have a simple mineralogy, with lots of pore space and rounded to sub-rounded grains with a high sphericity (Figure 2.16).

In complete contrast are the mudstones which have a much lower porosity and permeability of approximately 7% and 1mD respectively (Figure 2.17). The microtextures observed at high magnification are typical of mudstones, with poor sorting, low porosity, and strongly aligned phyllosilicates (Figure 2.18). During mechanical compaction the phyllosilicate grains re-align to form a high degree of preferred orientation but are broken in the process as they are bent around the much stiffer quartz and feldspar grains (Figure 2.19).

2.8 Diagenetic history

The Clair reservoir experienced prolonged tectonic subsidence during the Devonian and Carboniferous with a period of inversion at the time of the Carboniferous-Permian boundary prior to continued deposition (Smith & Lappin 1997). The Clair reservoir was buried to a maximum depth of approximately 2.6km before it was uplifted to 0.6km at the end of the Permian.

The mineralogy and poroperm properties of the reservoir sandstones within the Clair field have undergone significant diagenetic modification (Table 2.3). Authigenic K-feldspar occurs as $\leq 15\mu m$ wide overgrowths on detrital K-feldspar grains with petrographic evidence suggesting that it occured during shallow burial. Most calcite observed occurs as a coarse grained pore filling cement which precipitated after the authigenic quartz. Calcite was also observed in association with pyrite as a vein filling cement. Moreover, the presence of authigenic corrensite is also important because it appears to have suppressed quartz overgrowth precipitation, which in turn may have suppressed K-feldspar dissolution (Smith & Lappin 1997). In general, the undeformed sandstones within the Clair field are well lithified despite the lack of quartz cement. This reflects the fact that it has experienced some pressure solution. It is possible that the silica generated by pressure solution may have been utilised during clay mineral transformation within the reservoir (Knipe et al. 1998).

Figure 2.15: *Half-core colour photograph of a typical Clair sandstone, with the four cores removed prior to ultrasonic testing. Sample number 2198m (Y-core) from Well 206/8-8.*

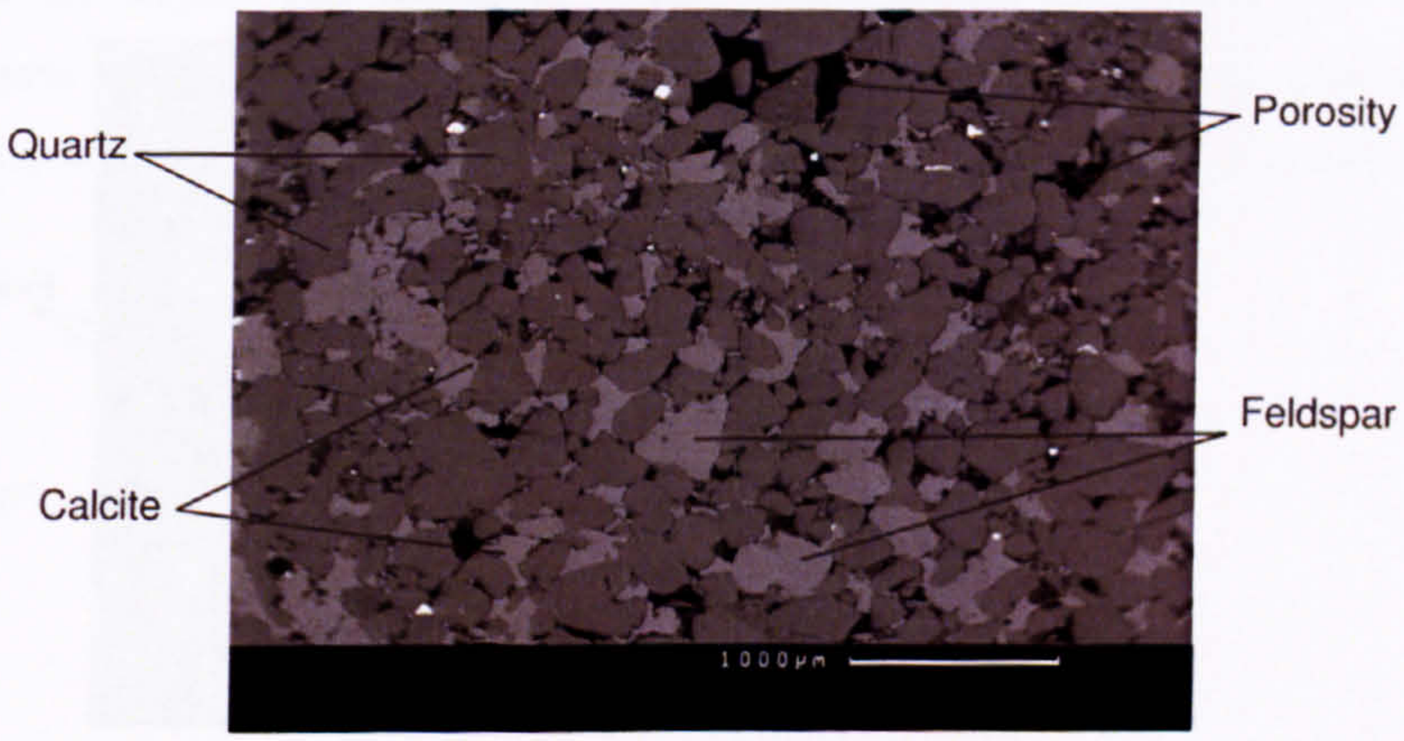

Figure 2.16: *BSE photomicrograph of a typical Clair sandstone: mature, well sorted, moderate porosity with authigenic calcite. Sample number 2129m (Y-core) from Well 206/8-8.*

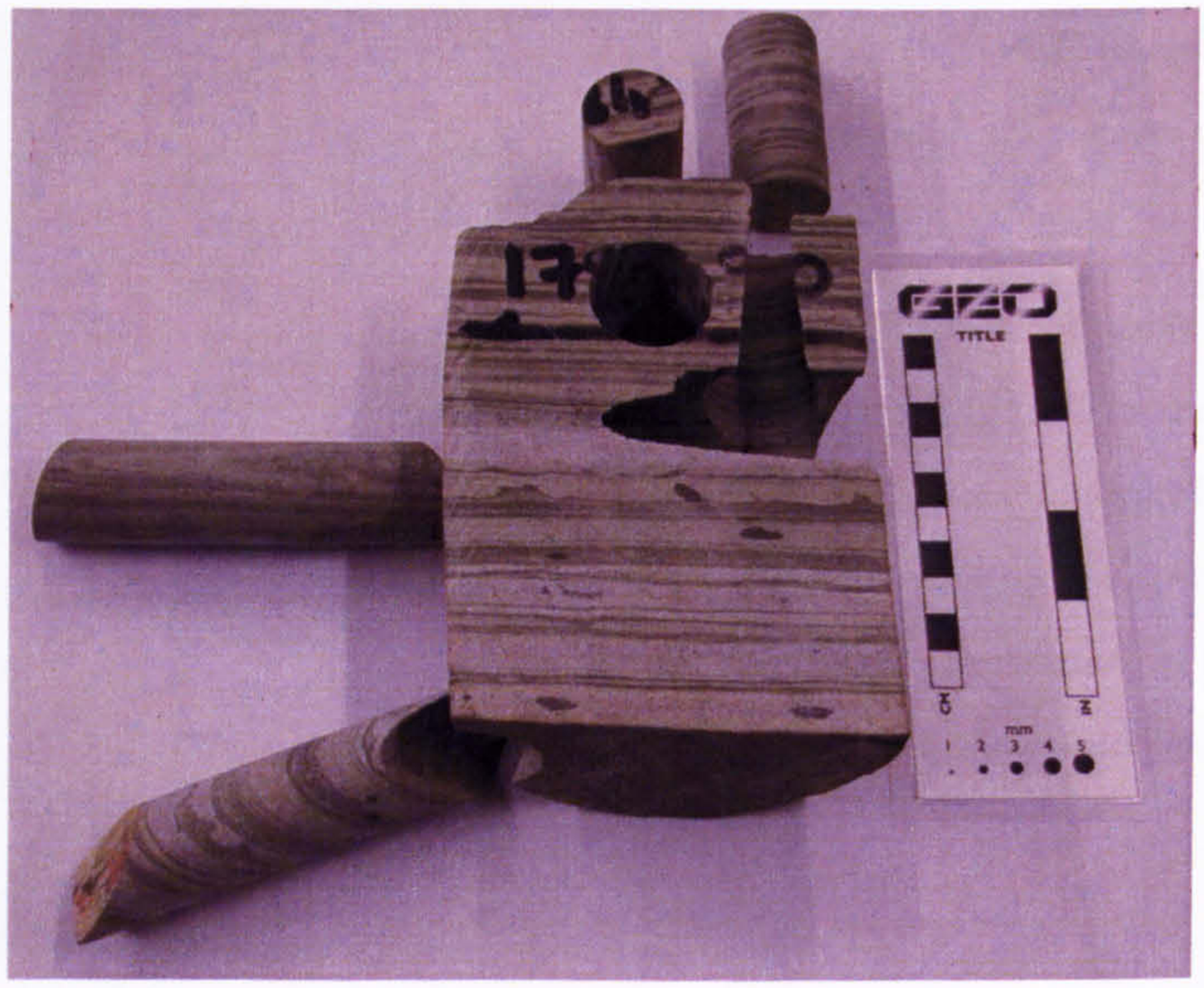

Figure 2.17: *Half-core colour photograph of a typical Clair mudstone, with the four cores removed for ultrasonic analyses. Sample number 1784m (Y-core) from Well 206/8-8.*

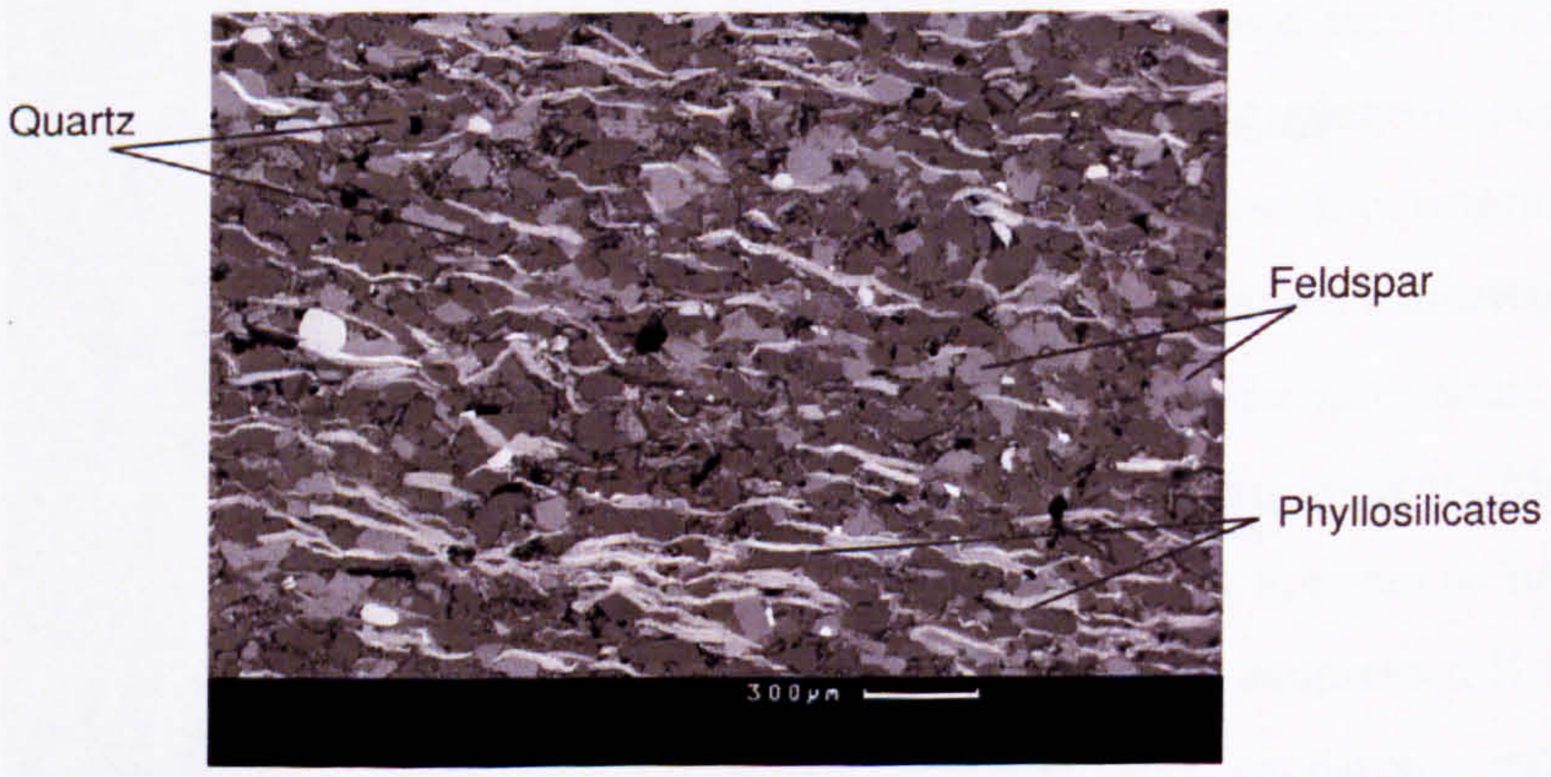

Figure 2.18: *BSE photomicrograph typical of the Clair mudrocks: poorly sorted, low porosity, well aligned phyllosilicates. Sample number 1841m (Y-core) from Well 206/8-8.*

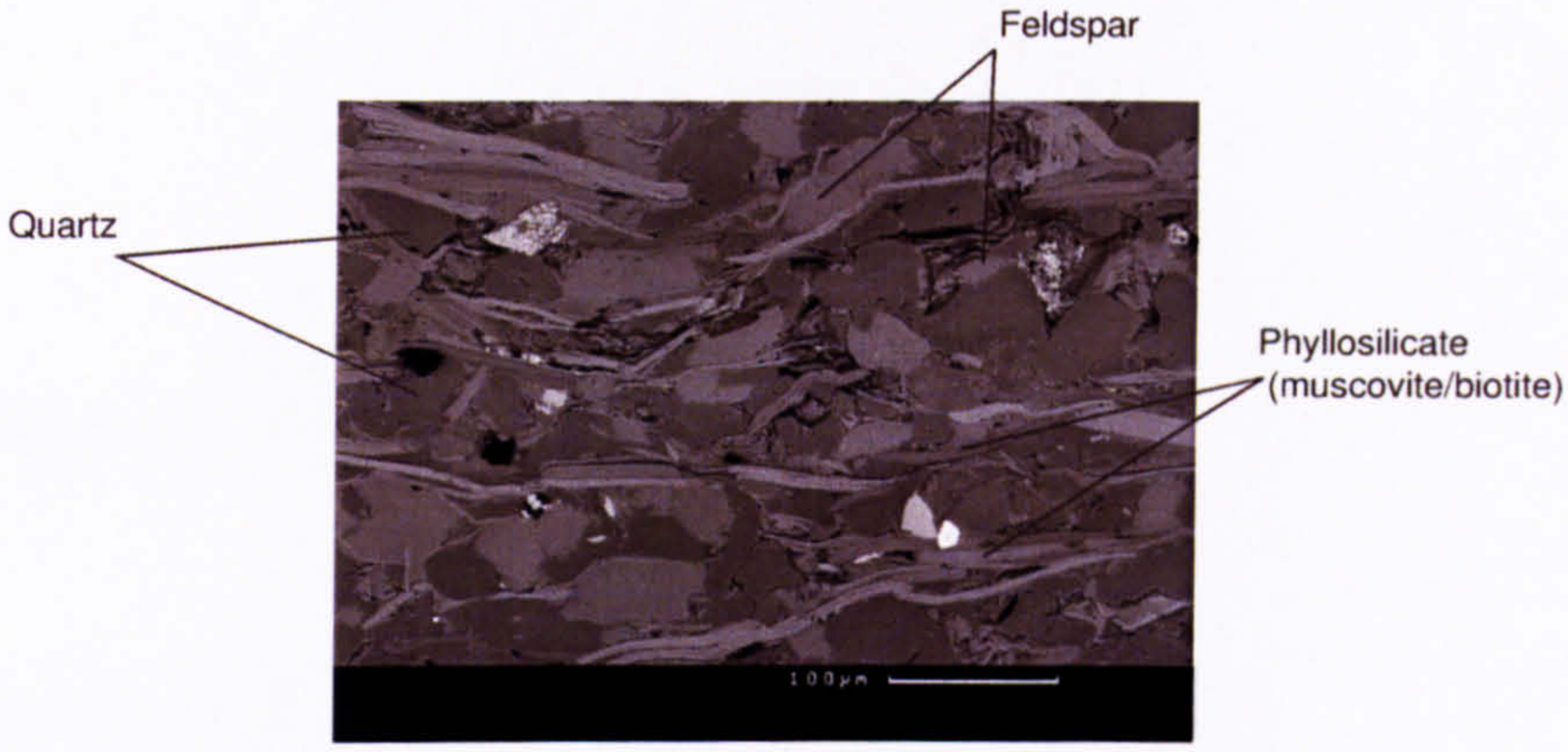

Figure 2.19: *High magnification BSE photomicrograph of a typical Clair mudstone. Softer phyllosilicates bend around the stiffer quartz and feldspar grains. Sample number 1784m (Y-core) from Well 206/8-8.*

2.9 Summary

Presented within this chapter is a brief introduction to the Clair field's geology, structural history and location. Furthermore, this chapter also elaborates upon the structural complexity of the Clair field addressing the location and structural significance of the Core, Graben and Horst. It also identifies the reservoir geology detailing the environmental interpretation of the different horizons, and the three major super-cycles within which the lithologies were deposited. Later in the chapter the most recently acquired seismic data for the Clair field is presented, and reviewed. The chapter concludes with sample descriptions, photomicrographs, and locations of the samples analysed.

Table 2.3: *Summary of the diagenetic and deformational history of the Clair Group. Time increases from left (E. Devonian) to right (Present day). K-fspr. - potassium feldspar, Press. soln. - pressure solution and Oil mig. - oil migration. The position of the asterisk marks the timing of the event.*

Burial depth	Shallow					Deep		Intermediate
K-fspr.	*					*		
Calcite		*			* *	*		
Smectite		* *						
Corrensite			* * *					
Quartz					* *	*		
Press. soln.			* * *					
Oil mig.							*	
Deformation			* *			*	*	*

Chapter 3

Quantification of mineralogy

3.1 Introduction

In the majority of studies of seismic anisotropy bulk aggregate properties have been investigated using ultrasonic laboratory measurements. Although direct analysis of a sample's seismic anisotropy is informative it does not allow the discrimination of the various factors that control the measured anisotropy. The aim of this project was to assess and understand both the intrinsic and extrinsic controls of seismic anisotropy of siliciclastic rocks. The intrinsic seismic properties of a sample are controlled by the bulk aggregate elastic properties which are in turn controlled by individual grain orientation, grain distribution, and porosity. For the purposes of this study understanding the mineralogy is important because it provides the basis for the calculations of intrinsic seismic anisotropy due to grain orientation. Moreover, accurate and reliable quantification of the mineralogy of petroleum bearing rocks provides a fundamental understanding on the controls of reservoir quality so that it is possible to predict reservoir quality away from the borehole. Presented in Chapter (5) is the microstructural investigation of the intrinsic properties of siliciclastic hydrocarbon reservoir rocks. To accurately calculate the elastic stiffness tensor requires both an accurate assessment of a rocks modal mineralogy and it's individual mineral phase orientation distribution. Hence, this then provides a means with which to begin to investigate the relevance and importance of the various properties that ultimately control the seismic anisotropy of rocks.

Presented within this chapter is a review of the most commonly used techniques to determine modal composition, these include: point counting, image-analysis (optical and

electron acquired), EBSD, and X-ray diffraction. The modal composition of the sample's analysed in this project were determined by QXRD (quantitative x-ray diffraction) analysis. QXRD was used because of its ability to quickly, and accurately quantify the sample's modal mineralogy including the fine-grained clay mineral content.

3.2 Review of techniques used to determine modal composition

3.2.1 Point counting

Point counting is a relatively accurate method of establishing modal composition albeit a very time consuming one (Galehouse 1971). It must first be assumed that the thin-section used for the point counting is representative of the bulk rock modal composition. Moreover, with point counting it must be remembered that values are computed from *2D*. For inhomogeneous sediments, particularly those with a strong fabric, total measurement of modal composition should be a combination from three perpendicular thin-sections. To highlight porosity, and hence ease identification of calcite cement optical microscopy thin-sections are usually impregnated with a blue-dye. The most commonly used technique for point counting is spot identification (Van der Plas & Tobi 1965). Essentially, there are two methods for determining modal composition using spot identification. Both methodologies use the same basic approach the only difference is that one uses a systematic grid whilst the other relies upon random sampling.

Using the approach of the systematic grid the thin-section is usually placed on a mechanical stage which is screwed to the rotating stage of the optical microscope. The mechanical stage is also connected to a counting unit that controls the movement of the stage over a predetermined distance. The distance is dependent upon grain size; the finer the grain size, the smaller the interval. The mineral phases are represented by a key on the counting stage which is pressed each time that mineral phase is visible under the cross hairs of the microscope. Several traverses are made for each thin section and a total of c.250-300 points per thin-section are required to give accurate percentages of the components present. The only difference with the random-walk is that the thin-section is moved manually in a random fashion, otherwise, both methods use the same basic counting principals. Thus, for the *ith* mineral, found at x_i points out of a total of N points counted, the best estimate of its percentage in a rock is $\hat{p} = 100x_i/N$. An awareness of the error associated with this type of counting procedure is essential.

Chayes (1956) estimated that the total error would be the sum of the counting errors and the size of the sample taken from the rock. Chayes (1956) approximated the error to be of a binomial distribution even though the Bernoulli criteria would not be satisfied during point counting. To be considered a Bernoulli trial, an experiment must meet each of three criteria. There must be only two possible outcomes, such as: black or red, sweet or sour. One of these outcomes is called a success, and the other a failure. Each outcome has a fixed probability of occurring; a success has the probability of p, and a failure has the probability of $1 - p$. Each experiment and result are completely independent of all others. The basic problem is that the counting process depends on two unrelated factors. The operator selects the grid size distance, it could be bigger than the grain size or smaller than the grain size. The second factor affecting the counting error is that the rocks constituent minerals could be stochastically independent or dependent. The error can be calculated a number of ways either by using the graph of Van der Plas & Tobi (1965) or by the empirical relationships as devised by Bayly (1965). However, the graph as devised by Van der Plas & Tobi (1965) only relates to Bernoulli sampling processes and even if the operator selects a grid distance greater than the diameter of the largest grain there is no assurance that the observations are stochastically independent. The relationships calculated by Bayly (1965) are based upon a select number of samples and would not necessarily apply to any other rock.

It is recommended that the following procedure should be followed to minimise errors: determine the largest diameter of crystal and fix the grid size separation to slightly exceed it, collect k sets of a total N points whereby each traverse contains $\sqrt{N}$ points on a square grid of $\sqrt{N}$ traverses and use a random point to get the x, y coordinates for the counting stage (Chayes 1956, Bayly 1965) .

3.2.2 Image analysis

Determining modal composition from image analysis broadly involves the post-acquisition evaluation of a digital image. Image analysis can be conducted using digital photomicrographs either collected from optical microscopy thin-sections or backscattered electron images. Typically, however, atomic number contrast BSE photomicrographs are used to determine modal composition. Prior to conducting image analysis it is useful to have *a priori* knowledge of the mineral phases present.

The digital image is first imported into one of the many publicly available image anal-

ysis programs, such as Scion Image and ImageJ. The images are then processed in the following procedure:

1. The photomicrographs are cropped to 512 x 1024 pixels, and greyscaled (if not already) - software prerequisites (Figure 3.1);
2. Upper and lower thresholds are defined within the greyscale that correspond to the mineral phases required to be calculated. The image is then converted to a binary image (Figure 3.2);
3. The binary image is then processed using a *closure* function. This function performs a *dilation* operation followed by an *erosion*, which in effect smooths the object outlines, fills holes, and removes any wildspikes;
4. Using the *analyse* function and then the *measure particle* function, the number of pixels that the greyscale thresholded image occupies is calculated. Knowing that the image measures 512 x 1024 pixels, the modal proportion of that particular mineral phase can thus be determined.

Image analysis has numerous drawbacks. It is time-consuming because of the cutting and preparation of the orthogonal sections. Problems can also occur when; the contrast between mineral phases is low, the grain size is similar to that of the image resolution, there is a non-random spatial distribution of mineral phases, and when the sample has a range of different grain sizes (Schofield et al. 2002).

3.2.3 Electron backscattered diffraction

Automated EBSD has proven its utility in the characterisation of microstructure in polycrystalline materials (Schwartz et al. 2000). For a full description of the technique see Chapter (5). Orientation imaging microscopy differentiates between phases by indexing a pattern using the pertinent structure parameters for each phase. The phase that provides the best fit to the pattern is assumed to be the correct phase. EBSD determines modal mineralogy and composition in the following manner:

1. An EBSD pattern is obtained from the region of interest;
2. The chemistry is qualitatively determined by EDS (X-ray energy dispersive spectrom-

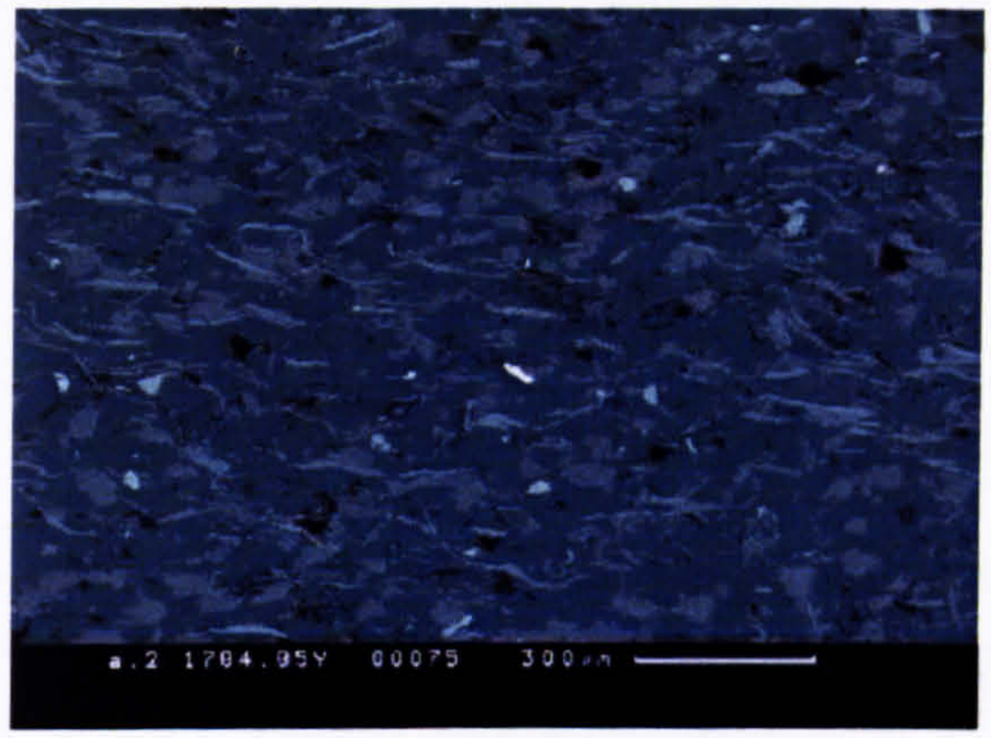

Figure 3.1: *Electron backscattered atomic contrast image of a clay-mica rich specimen. Sample 1784m (Y-core) from Well 206/8-8.*

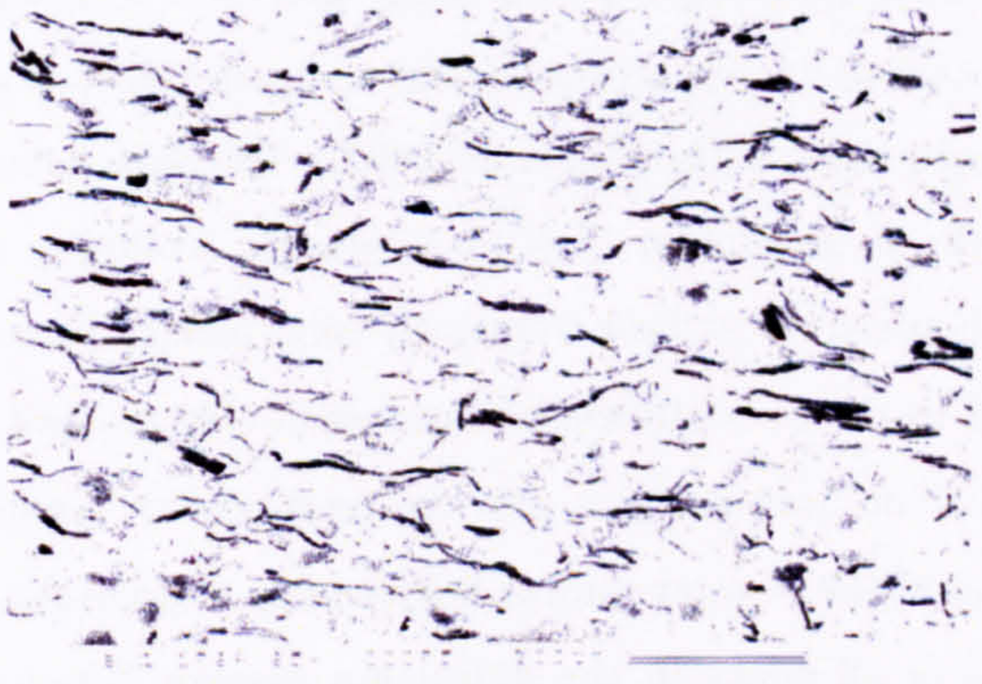

Figure 3.2: *Binary converted electron backscattered atomic contrast image of a clay-mica rich specimen. Sample 1784m (Y-core) from Well 206/8-8.*

etry);

3. The chemistry is then used to search the crystallographic database for the correct reflector file. The search takes only a few seconds and returns approximately 20 possible matches;

4. The pattern is then indexed using the database information and a comparison is made between the simulated and experimental pattern until a consistent set of indices are found.

EBSD is well suited to differentiate between phases that are similar in chemical composition but dissimilar in crystallographic structure (Schmidt & Olesen 1989, Schwartz et al. 2000). It is postulated that EBSD cannot correctly and repeatedely identify poorly crystallised phases, and fine-grained mineral phases, such as clay minerals and phyllosilicates. Moreover, modal determination using EBSD is also time consuming in that the samples are required to be prepared to a high standard. Furthermore, the actual sample modal proportion determined is also very small in comparison to that analysed by other techniques, for example, image analysis, and XRD.

3.2.4 X-ray diffraction

XRD (X-ray diffraction) is a commonly used tool in the mineralogical analysis of sediments because of its rapid, precise, and accurate ability to quantify phases in fine-grained polymineralic rocks (Schofield et al. 2002). The determination of the modal proportions of the phyllsilicate content (biotite, muscovite, kaolinite, and illite) on whole-rock XRD analysis, however, is at best frequently semi-quantitative (Hillier 2000). This is largely attributed to the difficulties associated with clay mineral compositional variation, mineralogical structural disorder, and the tendency for phyllosilicates to adopt a preferred orientation in the powder sample holder prior to analysis. To obtain the correct relative intensities of all peaks in the diffraction pattern X-ray powder diffraction completely relies upon the preparation of a random powder sample.

Sample preparation issues can be almost entirely eliminated by using spray dried samples (Hillier 1999). This arguably provides the most effective preparation technique for the quantitative analysis of modal mineralogy. Spray drying essentially involves spraying a sample as an aqueous solution into a heated chamber so that it dries in the form of

spherical droplets. Spray drying is not currently a widely used method of sample preparation for X-ray powder diffraction because of the high cost of commercially available equipment and because it is not suitable for samples of less than 1g.

X-rays are produced by bombarding a metal anode (copper, iron or silver) with high energy electrons from a heated filament. The X-rays are then collimated before passing through a divergence slit, which controls the angle at which the analysis will be carried out, for example, $\frac{1}{12}^0$ or 4^0 for low and wide angle work respectively. The beam is directed towards the sample and any X-rays that satisfy the Bragg equation will therefore diffract according to this law (Equation 3.1). Bragg's Law states that,

$$n\lambda = 2d\sin\theta. \tag{3.1}$$

The Bragg equation explains why the cleavage faces of crystals appear to reflect X-ray beams at certain angles of incidence (θ). The variable d is the distance between atomic layers in a crystal, λ is the wavelength of the incident X-ray beam, and n is an integer.

Consider the conditions necessary to make the phases of the incident beams (e.g., ions, electrons and neutrons) coincide, i.e., when the incident angle equals the reflecting angle (Figure 3.3). The rays of the incident beam are always in phase and parallel up to the point at which the top beam strikes the top layer at atom, z. The second beam continues to the next layer where it is scattered by atom, B. The second beam must travel AB+BC if the two beams are to continue travelling adjacent and parallel. This extra distance must be an integral (n) multiple of the wavelength (λ) for the phases of the two beams to be the same,

$$n\lambda = AB + BC. \tag{3.2}$$

Therefore,

$$AB = d\sin\theta, \tag{3.3}$$

and because AB=BC, Equation (3.2) becomes

$$n\lambda = 2AB. \tag{3.4}$$

Substituting Equation (3.3) into Equation (3.4) we get,

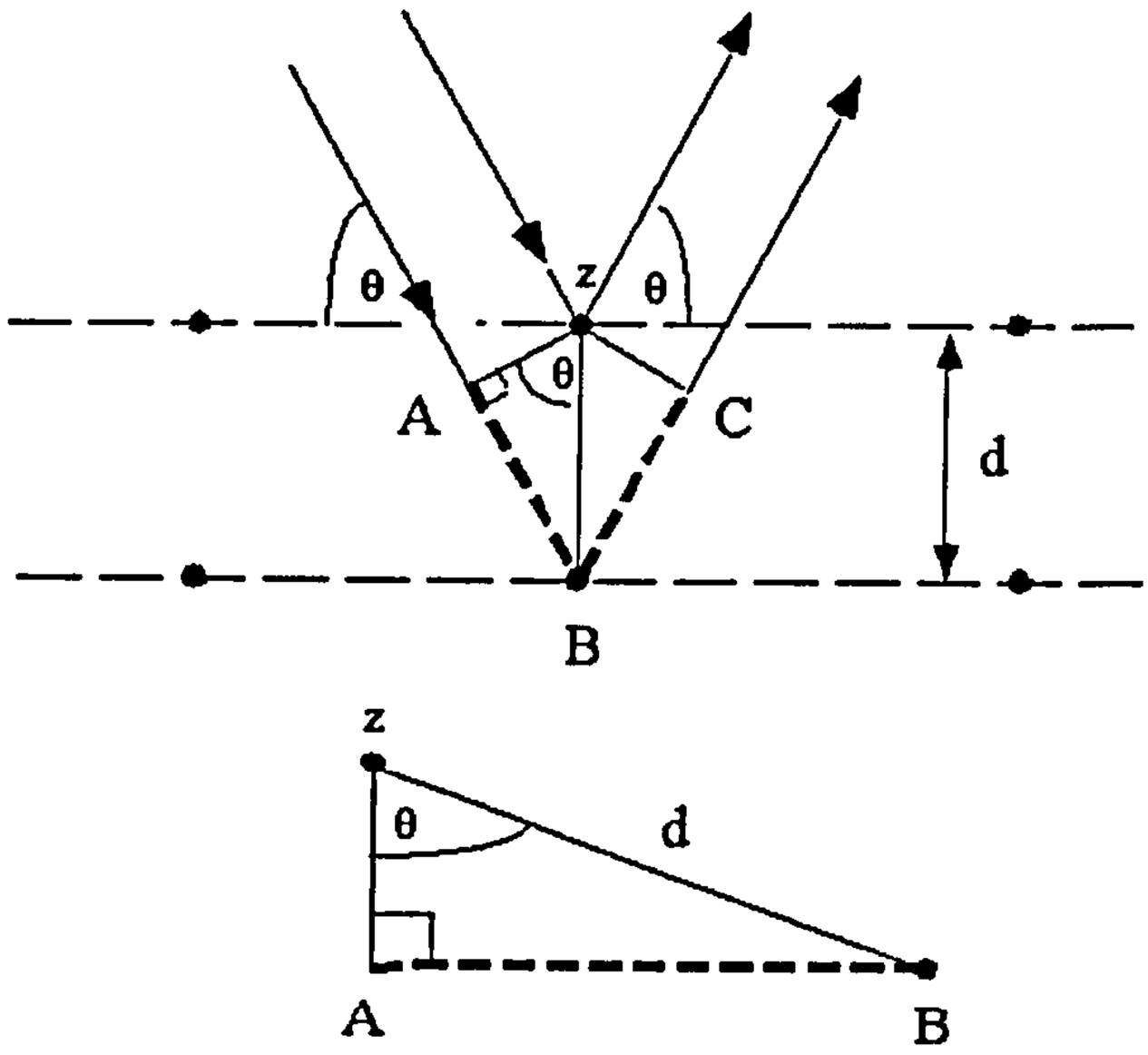

Figure 3.3: *Deriving Bragg's Law using reflection geometry and trigonometry.*

$$n\lambda = 2d\sin\theta. \tag{3.5}$$

The reflected beam is then passed through a collimator to reduce its scatter before entering the final detector (Figures 3.4 and 3.5). The output is a strip chart, which is synchronised with the detector so that the x-axis is in $2\theta^0$ (Figure 3.7).
Good sample preparation is absolutely fundamental to obtaining good quality results. The ideal specimen is a statistically infinite amount of randomly oriented powder with crystallite size less than $10\mu m$.

XRD analysis requires that corundum is added to the finely ground specimen, this is known as a *spike*. The crushed rock specimen and corundum mixture is then combined with 1% aqueous PVA (polyvinyl alcohol), with a solid to liquid ratio of 1:1.5 to 1:2.3. The PVA acts as a binder giving strength to the dried product. A single drop of 1-octanol is then added to the slurry to stop the sample foaming during grinding.

The slurry mixture is then dispersed (ground) for 12 minutes using a McCrone Mill. The resulting solution is then sprayed into the drying chamber at 5-10 psi allowing small droplets to form (c.$50\mu m$) and fall to the bottom. Operating at such low pressures

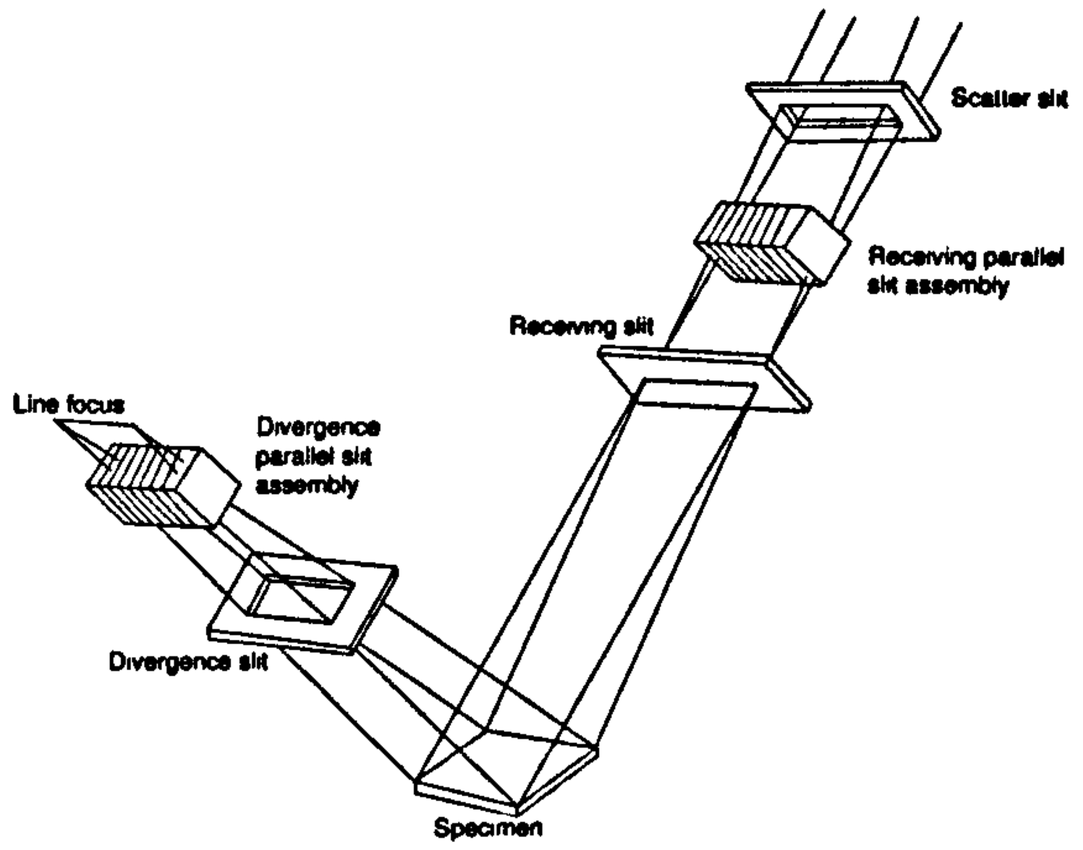

Figure 3.4: *Geometry of the X-ray diffractometer, sample, and electron source.*

means that even clay fractions consisting of smectites can be successfully spray dried with recovery of up to 70%. The aim of spray drying materials for X-ray powder diffraction is to produce a sample which can be loaded into a powder holder without inducing a preferred orientation and to present a relatively constant bulk density to the X-rays (Figure 3.6) (Hillier 1999). The data obtained from the XRD analysis is output as a strip-chart (Figure 3.7). The 2θ angle increases from left-to-right on the horizontal scale and intensity of the diffracted peak above background is given by the vertical scale. The various large peaks at different 2θ spacings are indicative of a particular mineral phase. Spray-dried X-ray powder patterns are completely reproducible and operator independent and do not exhibit any preferred orientation.

3.2.5 Quantitative X-ray diffraction

Quantitative analysis of diffraction data refers to the determination of the amounts of different phases in multi-phase samples. In quantitative analysis, an attempt is made to determine phase proportions with quantifiable numerical precision from the experimental data itself.

The X-ray powder diffraction data was collected using a Philips PW1050 Goniometer with a Philips PW1730 CuKα X-ray tube (graphite monochromator). A 1^o divergence and anti-scatter slit was used with a receiving slit of 0.2^0. The data was collected over a range of $3 - 70^o$, with a step size of 0.02^o and a counting time of 2 sec per step. The data was analysed using Hiltonbrooks HBX data acquisition software and

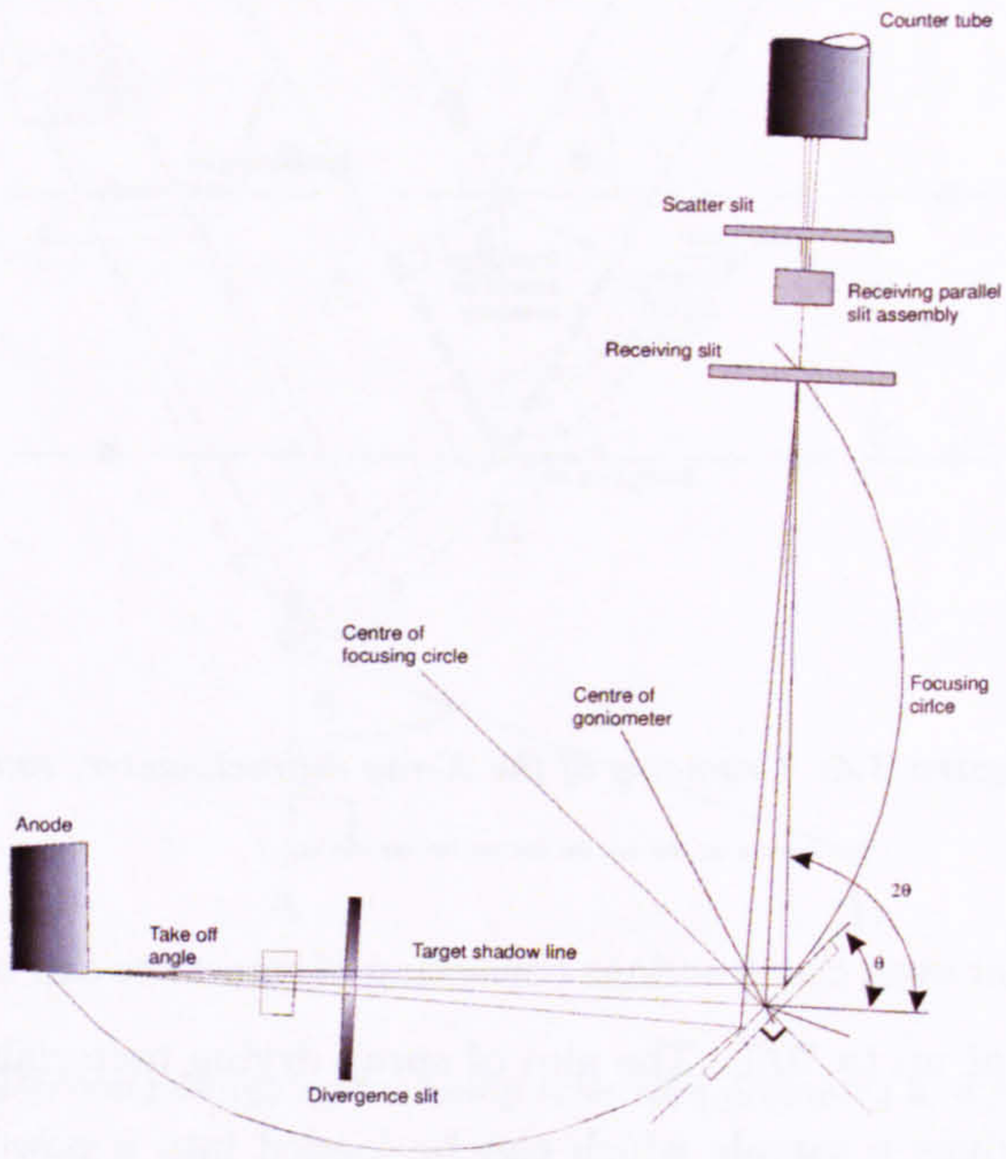

Figure 3.5: *Geometry of the angular relationships within a diffractometer.*

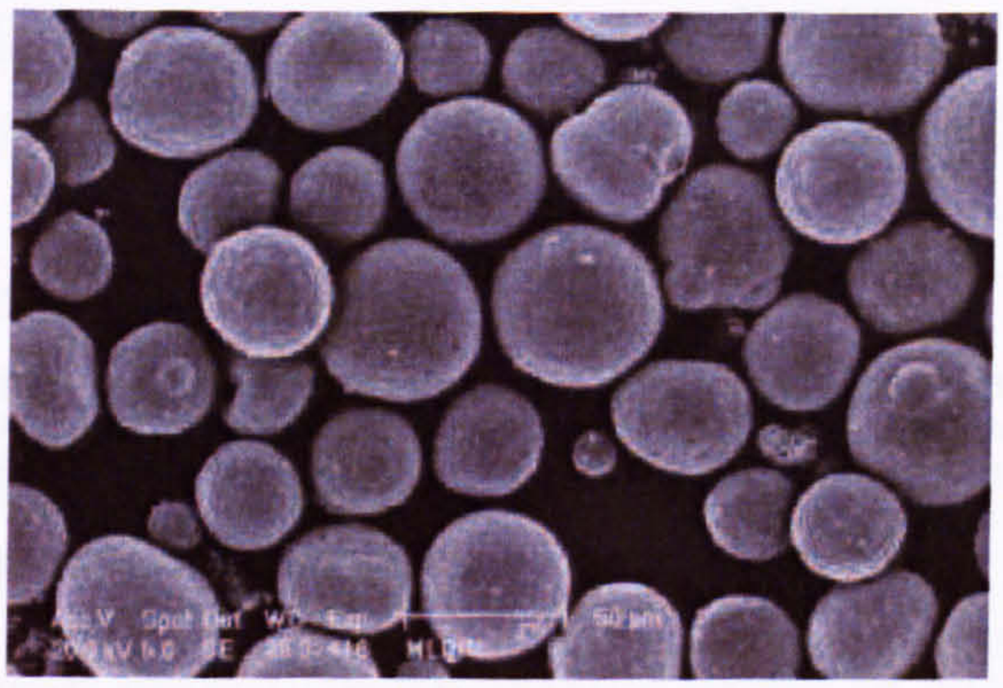

Figure 3.6: *Secondary electron photomicrograph of spray-dried kaolinite. The spheres present a relatively constant bulk density to the X-rays and do not acquire a preferred orientation during mounting into the XRD specimen holder.*

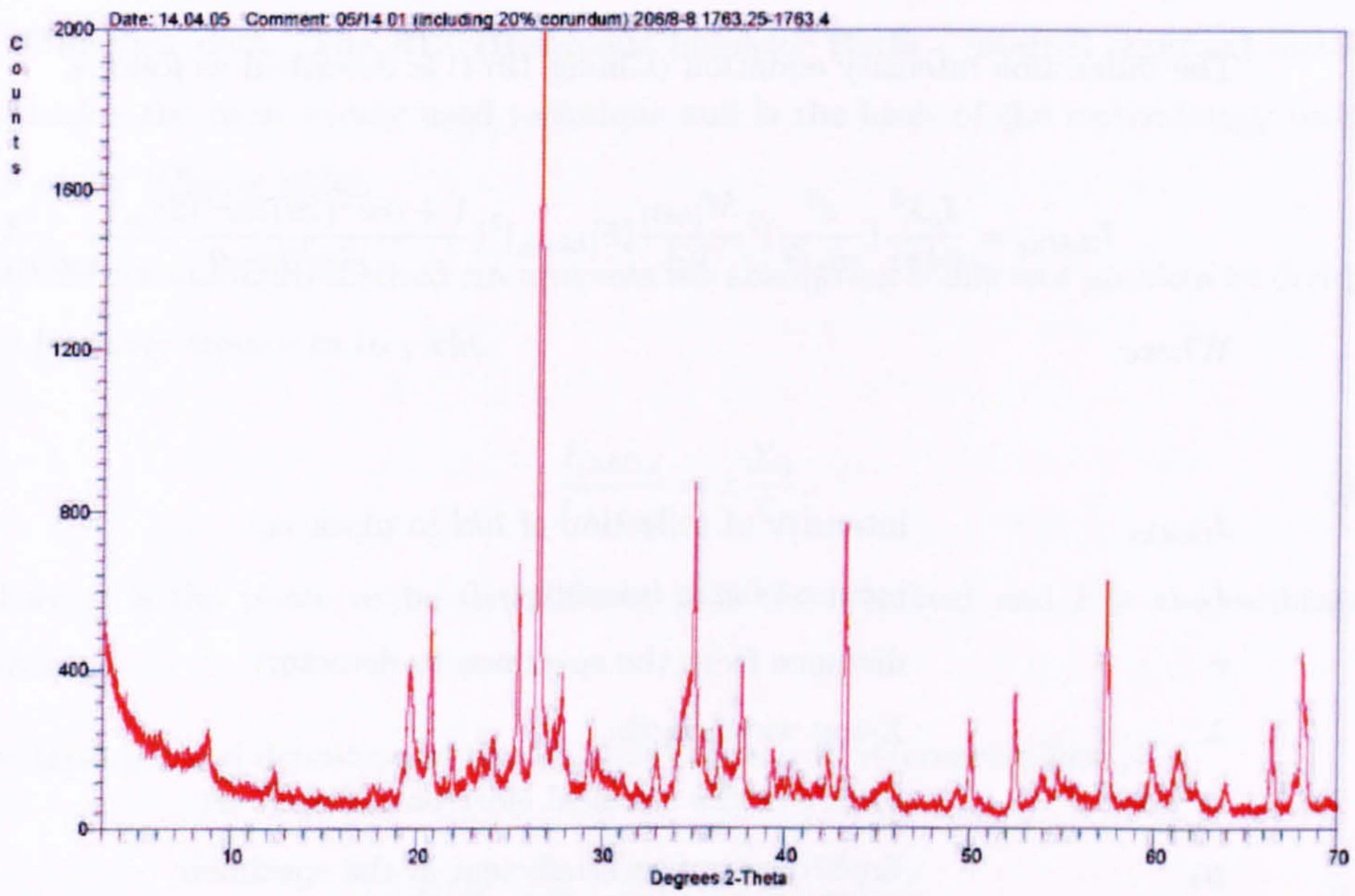

Figure 3.7: *X-ray diffraction strip chart diffraction pattern. The 2θ angle increases from left-to-right on the horizontal scale and intensity of the diffracted peak above background is given by the vertical scale. The various large peaks at different 2θ spacings are indicative of a particular mineral phase.*

Diffraction Technology's TRACES software using the International Centre for Diffraction Data Powder Diffraction Files for the database of phase identification.

The diffraction pattern includes information about peak intensity and positions (Figure 3.7). The peak positions are indicative of the crystal structure and the symmetry of the contributing phase. The peak intensities reflect the total scattering from each plane in the phase's crystal structure and are directly dependent on the distribution of particular atoms in the structure. Thus intensities are ultimately related to both the structure and composition of the phase (Jenkins & Synder 1996).

The diffraction intensity equation (Chung 1974) is described as follows,

$$I_{(hkl)\alpha} = \frac{I_o \lambda^3}{64\pi r}\left(\frac{e^2}{m_e c^2}\right)^2 \frac{M_{(hkl)}}{V_\alpha^2}|F_{(hkl)\alpha}|^2\left(\frac{1+cos^2(2\theta)cos^2(2\theta_m)}{sin^2\theta cos\theta}_{hkl}\right)\frac{\nu_\alpha}{\mu_s}. \qquad (3.6)$$

Where:

$I_{(hkl)\alpha}$	intensity of reflection of hkl in phase α;
I_o	incident beam intensity;
r	distance from the specimen to detector;
λ	X-ray wavelength;
$(e^2/mc^2)^2$	square of the classical electron radius (cm);
μ_s	linear absorption coefficient of the specimen;
V_α	volume fraction of phase α;
M_{hkl}	multiplicity of reflection hkl of phase α;
o	Lorentz-polarisation correction;
ν_α	volume of the unit cell of phase α;
$2\theta_m$	the angle between the goniometer and electron source (diffraction angle);
$F_{hkl}\alpha$	structure factor for reflection hkl of phase α.

As many of the terms remain constant for a particular experimental set-up we can define an experimental constant, K_e. For a given phase it is possible to define another constant, $K_{(hkl)\alpha}$. Substituting the weight fraction X_α for the volume fraction, the density of the phase for the volume and the mass absorption coefficient for the linear absorption coefficient yields,

$$I_{(hkl)\alpha} = \frac{K_e K_{(hkl)\alpha} X_\alpha}{\rho_\alpha} (\mu/\rho)_s \tag{3.7}$$

This equation describes in simpler terms the intensity of peak hkl for phase α.

If the mass absorption coefficient $(\mu/\rho)_s$ is known, the calculations are simple. However $(\mu/\rho)_s$ is a function of the amount of the constituent phases present, and hence is the object of the experiment (Jenkins & Synder 1996).

Numerous methods have been developed to use peak intensities for quantitative analysis of diffraction data. The RIR (Reference Intensity Ratio - internal standard method) method is the most widely used technique and is the basis of the methodology used in this study (Chung 1974).

The internal standard method circumvents the absorption coefficient problem by dividing two intensity equations to yield,

$$\frac{I_{(hkl)\alpha}}{I_{(hkl)'\beta}} = k \frac{X_\alpha}{X_\beta}. \tag{3.8}$$

Where α is the phase to be determined, β is the standard and k is the calibration constant.

The most general definition of the RIR for phase α to reference phase β is,

$$RIR_{\alpha,\beta} = \left(\frac{I_{hkl}\alpha}{I'_{hkl}\beta}\right)\left(\frac{I'_{hkl}\beta^{rel}}{I_{hkl}\alpha^{rel}}\right)\frac{X_\beta}{X_\alpha}. \tag{3.9}$$

Where the I_{rel} term ratios the relative intensities of the peaks used. RIRs may be experimentally determined for any phase using any material as a standard.

Rearranging the above equation yields,

$$X_\alpha = \left(\frac{I_{(hkl)\alpha}}{I_{(hkl)'\beta}}\right)\left(\frac{I^{rel}_{(hkl)'\beta}}{I_{(hkl)\alpha}}^{rel}\right)\left(\frac{X_\beta}{RIR_{\alpha,\beta}}\right). \tag{3.10}$$

The RIR value is then obtained through careful calibration. Best results are obtained if as many possible variables (RIR and I^{rel}) are experimentally determined. Each phase determined is independent of the whole, this method works well for complex mixtures including unidentified or amorphous phases (Jenkins & Synder 1996).

3.3 Results - Modal Composition

The results obtained from the QXRD modal proportion analysis are presented in Table (3.1).

3.4 Conclusions

There are several techniques which quantify modal composition, these include, among others: point counting, image analysis, EBSD and QXRD. The accuracy and speed, however, at which these various procedures determine modal proportions varies dramatically. Presented within this chapter are the advantages and disadvantages of using anyone of the particular techniques. For example, point counting can provide results relatively quickly when compared to some other techniques. Furthermore, it doesn't require particularly sophisticated equipment or a high level of training to be able to apply the technique. However, it does not accurately quantify the modal composition in *3D*, which requires the cutting and preparation of numerous orthogonal sections. Moreover, it does not accurately and repeatedly quantify the fine-grained mineral content of aggregates, such as, clays or mineral phases in highly-deformed rocks. Image analysis requires either a selection of digital images acquired using electron microscopy or optical light microscopy. As with point counting to ensure an accurate representation of the rocks mineralogy in *3D* orthogonal sections are required. The most prominent draw back of image analysis is that if the minerals within the sample have very similar properties. For example, in BSE imaging both quartz and certain types of feldspar have approximately the same atomic contrast (Z-contrast), which makes identification and quantification of these two very different minerals extremely difficult. Furthermore, if the grain size of the constituent minerals are particularly small this can cause problems with pixelation and identification of grain boundaries. Among the main benefits of image analysis is that there are numerous open source software packages available for the post-acquisition processing of the images. EBSD has been shown here and in previous studies to be a good way of determining modal proportion (Goldstein et al. 1992, Randle 2003, Prior et al. 1999). However, it does have some serious drawbacks, the basic understanding of electron microscopy analytical techniques required to conduct this type of analysis is very high. Moreover, the area of which EBSD determines the modal composition is also very small, with a maximum of usually $1cm^2$, which is not necessarily represen-

Table 3.1: *Sample mineralogy, porosity, permeability, and stratigraphic location. The Well refers to the number the samples was extracted from 206/8-8 or 206/13a2. Stratigraphic unit devised by Allen & Mange-Rajetzky (1992), sample depth (m), individual sample mineralogy (%), porosity (%) and permeability (mD). Qtz.- quartz, Fspr. - feldpsar, Clc./Dol. - calcite + dolomite, Phyllo. - muscovite + biotite + illite and Kaol. - kaolinite. Por. - Porosity was determined using helium porosimetry and Perm. - permeability by air porosity (Smith & Lappin 1997). Tech. - technique used to measure modal proportion.*

Well	Unit	Sample	Qtz.	Fspr.	Clc./Dol.	Phyllo.	Kaol.	Por.	Perm.	Tech.
8-8	VI	1663	57.60	6.81	12.37	8.13	0.00	15.10	0.65	QXRD
8-8	VI	1763	17.02	20.64	1.90	47.35	1.18	11.90	0.00	QXRD
8-8	VI	1784	38.64	18.26	18.26	6.20	6.65	12.00	24.00	QXRD
8-8	VI	1788	30.89	25.41	1.32	34.38	0.00	8.00	0.02	QXRD
8-8	VI	1841	30.97	21.77	5.92	30.24	0.00	11.10	0.07	QXRD
8-8	V	1909	54.95	16.07	10.48	3.73	1.78	13.00	2.80	QXRD
8-8	V	1950	44.19	30.46	7.45	3.10	0.00	14.80	84.00	QXRD
13a2	V	1959	39.11	23.36	14.30	6.54	0.00	16.70	5.48	QXRD
13a2	V	1963	45.77	7.69	16.46	17.43	5.55	7.10	0.15	QXRD
13a2	V	2015	54.54	17.12	5.57	5.97	0.00	16.80	177.00	QXRD
13a2	V	2023	54.00	19.88	2.53	6.15	1.35	16.10	12.30	QXRD
13a2	V	2028	49.60	19.98	0.71	9.72	1.18	18.80	4.84	QXRD
13a2	V	2034	39.96	16.02	0.32	19.86	5.45	18.40	138.00	QXRD
8-8	V	2070	47.46	17.57	7.75	7.75	7.06	12.40	3.80	QXRD
8-8	V	2073	46.78	16.85	6.13	15.95	3.79	10.50	0.05	QXRD
8-8	V	2088	53.79	14.57	2.30	19.34	0.00	10.00	1.20	QXRD
8-8	I-III	2129	74.30	8.22	2.51	0.78	0.00	14.20	79.00	QXRD
8-8	I-III	2192	63.76	9.51	6.43	3.17	1.63	15.50	55.00	QXRD
8-8	I-III	2194	61.05	12.62	8.06	1.70	4.48	12.10	1.40	QXRD
8-8	I-III	2198	58.49	13.58	6.32	13.11	0.00	8.50	0.36	QXRD

tative of the larger sample. In this study it was decided that QXRD would provide the most reliable and quick method of accurately determining modal composition. The advantages include: it's ability to accurately and repeatedly quantify fine-grained clay content, operator independence, and the speed of data collection and analysis.

Using the results obtained from the QXRD modal mineralogy analyses combined with the helium porosimetry measurements it was possible to categorise the various samples into three groups. Group 1 was defined as having a high phyllosilicate and clay-mineral (c.15 - 20%) content combined with relatively low permeability (c.0.05mD). Group 2 was defined as having a dominant quartz, feldspar and calcite mineral assemblage (c.75%) with a highly variable permeability (0.4 - 84.0 mD) and relatively high porosity(> 15%). Group 3 was defined as having a high proportion of quartz, feldspar and calcite (c.75%) but with a low permeability (c.0.01 - 10.0mD) and generally moderate porosity (c.10 - 14%).

Chapter 4

Ultrasonic analyses

4.1 Introduction

Recent developments, such as, vertical multi-component seismic, VSP (vertical seismic profiling), and cross-well seismic methods, mean that it is now possible to measure the seismic anisotropy of reservoir rocks in the subsurface. Such measurements offer a potentially powerful tool for determining rock and fluid properties. The interpretation of such data is, however, presently limited by our understanding of the causes of seismic anisotropy in sedimentary rocks. For example, it is well known that the presence of oriented fractures, aligned grain-boundaries, and an alignment of mineral grains can result in anisotropy. There is, however, relatively little understanding of the relative contributions of each of these to the overall anisotropy of sedimentary rocks.

It is possible to theoretically calculate the amount of seismic anisotropy resulting from some of the individual contributory elements. For example, effective media modeling allows an estimation of the effect of cracks on seismic anisotropy (e.g., Eshelby 1957, Castañeda & Willis 1995). However, other causes of anisotropy, such as the contribution from aligned grain boundaries, are more difficult to model. Therefore, laboratory measurements are required to better quantify the amount of anisotropy resulting from such causes. Unfortunately, the interpretation of laboratory data in terms of the causes of anisotropy is often non-unique. It is therefore important to integrate laboratory measurements with microstructural analysis. Very few studies have been published that combine laboratory and microstructural analysis (e.g., Louis et al. 2003, Wendt et al. 2003). In this study compressional and shear-wave velocity measurements have been

conducted on a suite of samples obtained from the Clair field, N.W. Scotland whose microstructure and mineralogical composition have been rigorously established (Chapter 5 and Chapter 3, respectively). Samples ranged from clean, porous sandstones to clay-mica-rich siltstones. An extensive set of laboratory ultrasonic analyses was carried out under dry conditions at both atmospheric and elevated confining pressures. Atmospheric (bench-top) measurements were conducted to provide a method of rapidly obtaining a large set of acoustic velocity measurements that could be compared to elevated confining pressure results. Measurements have been made at a variety of confining stresses to gain information on the stress-dependence of seismic anisotropy, which may be of value in understanding how pressure depletion affects the seismic properties of reservoirs during production and extended life programs.

The following chapter begins by describing the experimental techniques (Section 4.2).

Sampling methods are described in Section (4.2.1) before the results are presented in Section (4.3). The results are discussed in Section (4.3) and then the results of the chapter are summarised in Section (4.4).

4.2 Ultrasonic analysis technique

To assess the influence of subsurface environmental conditions on the physical properties of rocks, it is necessary to exert strict control over certain key laboratory parameters in order to detect interesting seismic responses in the rocks. Ultrasonic velocity experiments at the Rock Deformation Laboratory at Manchester University use the pulse transmission technique with a central frequency close to one megahertz. This technique is widely recognised and accepted in both mechanical non-destructive evaluation and rock physics testing. Efficient piezoelectric transducers combined with electrical impedance matched pulse generator, millivolt sensitivity pre-amplifier and oscilloscope allow the pulse transmission technique to be used as an accurate estimation of velocity in rock physics testing. Using the pulse transmission technique of Birch (1960) measurements of travel times of a compressional (P-wave) and a tangential pulse (S-wave) through a short cylindrical rock specimen were used to calculate velocity. The best way to evaluate the anisotropy of any physical property in the laboratory is to work on spherical samples to avoid uncertainties due to rock heterogeneity between multiple samples (Vickers & Thill 1969). Due to the difficulty of machining spheres from a block, it is generally easier to work on cylindrical

cores.

The basic methodology is to use piezoelectric transducers to produce and measure ultrasonic waves. Essentially, a piezoelectric transducer is a piece of polarised material with electrodes attached to its opposite faces, with some parts of its positively and other parts of it negatively charged. Application of an electric field causes the piezoelectric transducer to change its dimensions, which produces an electric field (this is known as the piezoelectric effect). The opposite is also true. In particular, application of a strain to a piezoelectric transducer produces an electrical signal. The method of Birch (1960) takes advantage of the piezoelectric effect by placing a transducer on either side of the rock sample. A piezoelectric transducer is used to convert electrical pulses into mechanical vibrations and back into electrical signals again. A transducer identical to the one used to initiate the mechanical wave is then used to convert the waves received at the other end of the rock sample back into a measurable electrical signal.

In the ultrasonic pulse transmission technique, the wave velocity is not measured directly. Instead, the travel time of an ultrasonic transient pulse wave is measured. The velocities are then calculated with the following equation,

$$V_{ij} = \frac{L}{t_M - t_T} \tag{4.1}$$

where V_{ij} is either P-velocity or S-velocity, L is the length of the sample, t_M and t_T are pulse wave travel times with the sample under measurement in place and without the sample in place (the transmitter in direct contact with the receiver), respectively.

Then, the error may be analysed by partial differentiation,

$$\Delta V = \frac{\delta V}{\delta L}\Delta L + \frac{\delta V}{\delta t_M}\Delta t_M + \frac{\delta V}{\delta t_T}\Delta t_T \tag{4.2}$$

and the absolute error can be evaluated as,

$$\Delta V = \Delta L|\frac{1}{t_m - t_T}| + \Delta L|\frac{\Delta t_M}{(t_M - t_T)^2}| + \Delta L|\frac{\Delta t_T}{(t_M - t_T)^2}| \tag{4.3}$$

where Δt_T and Δt_M are the oscilloscope's time resolution, ΔL is the absolute error in sample length measurement, which can be less than 0.05mm.

Since $t_M - t_T$ is usually larger than $10\mu s$ and typically nearer $15\mu s$, the second and third terms in Equation (4.3) may be neglected. Then, the maximum absolute error ΔV could

be less than $50m/sec$, and the corresponding relative error could be estimated to be less than 3% in P-wave velocity estimation and 5% in S-wave velocity estimation.

In this study a 100V sinc-wave with a 5ms repeat rate was used to excite a piezoelectric (lead-zirconate titanate) transducer with resonant frequency of approximately 1MHz. The time-of-flight along the length of the sample was determined using a 300MHz digital storage dual-trace oscilloscope. The P- and S-wave transducers were randomly oriented with respect to each individual sample.

At 1MHz the wavelength is approximately 3 to 4mm, comparable to the dimensions of the grains in many of the coarser samples analysed. Under these conditions, scattering becomes important in reducing the amplitude especially of the high-frequency components of the pulse. This is due to heterogeneities at the scale of the ultrasonic wavelength, which results in diffraction of the waves and as a consequence, high attenuation values (Lucet & Zinszner 1992). This leads to the problem of accurately recognising the first break of the first arriving wave in many of the coarser samples analysed. In the coarse grained samples it is often the case that the first break is obscured by noise and even when the first motion is strong it is found to arrive gradually even at high amplification.

4.2.1 Sample preparation

Considering all significant parameters in the pulse transmission experiments, it is essential to minimise pulse-wave energy dissipation caused by diffraction, scattering, mode conversion, and reflective phenomena. In the pulse-transmission experiments, the deleterious effect by these phenomena are reduced through judicious optimisation of the transient pulses, in view of all that is known of a given rock sample's relevant physical characteristics. The following parameters may be considered when preparing rock samples for laboratory ultrasonic measurements.

1. To avoid waveguide effect, the geometric diffraction, the sample radius r should exceed the wavelength λ of the ultrasonic pulse wave that is transmitted along the sample. When $r < \lambda$, the waveguide effect attenuates and slows the propagating waves, which causes the wave to travel at a reduced velocity (Schreiber 1973).

2. To ensure that the ultrasonic pulse waves are transmitted through the sample rather than displacing the sample uniformly, the path of the pulse wave from the source to receiver, usually the rocks sample's length L, should be greater than one wavelength

of the pulse wave, $L/\lambda > 1$ (Kolsky 1953).

3. To avoid scattering of the ultrasonic wave by the pores or grains in a rock sample, the wavelength of the transmitted pulse should be at least three times longer than the largest grain size d_s or pore size in the sample, $\lambda_s/d_s > 3$ (Plona & Tsang 1979).

4. To avoid cancellation of the direct first arrival amplitude by interference with waves reflecting off of the sample sidewalls, the sample length should be less than five times sample diameter d, $L < 5d$, to assure a more distinct first arrival for an accurate velocity estimation.

In general, the cylindrical specimens were 1-inch in diameter and 2 to 3 inches long (dependent upon original core length). The samples were cored in water using a steel diamond-tipped drill, then ground to right circular cylinders with flat ends to within 0.01mm, and dried in an oven at 100°C for at least twenty-four hours before analysing. Four cores were drilled from each half-core: two in the horizontal bedding plane (X and Y), one parallel to the long axis of the borehole (Z), and one inclined at forty-five degrees to the long axis of the borehole (XYZ) (Figure 4.1). The core orientations were chosen with a TI (transverse isotropy) set of properties in mind with the core parallel to the Y direction used as a check on the isotropy in the XY plane. Transverse isotropy is considered to be the simplest semi-realistic symmetry system that could be observed by field wide seismic surveys. It has long been known, however, than natural rocks can and do exhibit far more complex symmetry patterns the next simplest being orthorhombic. Nonetheless, the non-transverse components of anisotropy (i.e., the variation of velocity within the bedding plane) are often very weak and currently difficult to quantify using field wide seismic data. Hence, to enable a direct comparison between laboratory and field wide measurements of seismic anisotropy a simple TI system of anisotropy was used.

Some of the samples were oil stained, acoustic measurements were conducted on these samples before and after cleaning with dicholoromethane (a solvent that removes oil).

4.2.2 Ultrasonic core evaluation

Experimentally the measurements commonly used to evaluate the five independent elastic stiffnesses in TI materials are (Figure 4.2):

1. measurement of V_p in the XY plane ($V_p(90^o)$) and measured on a core oriented with

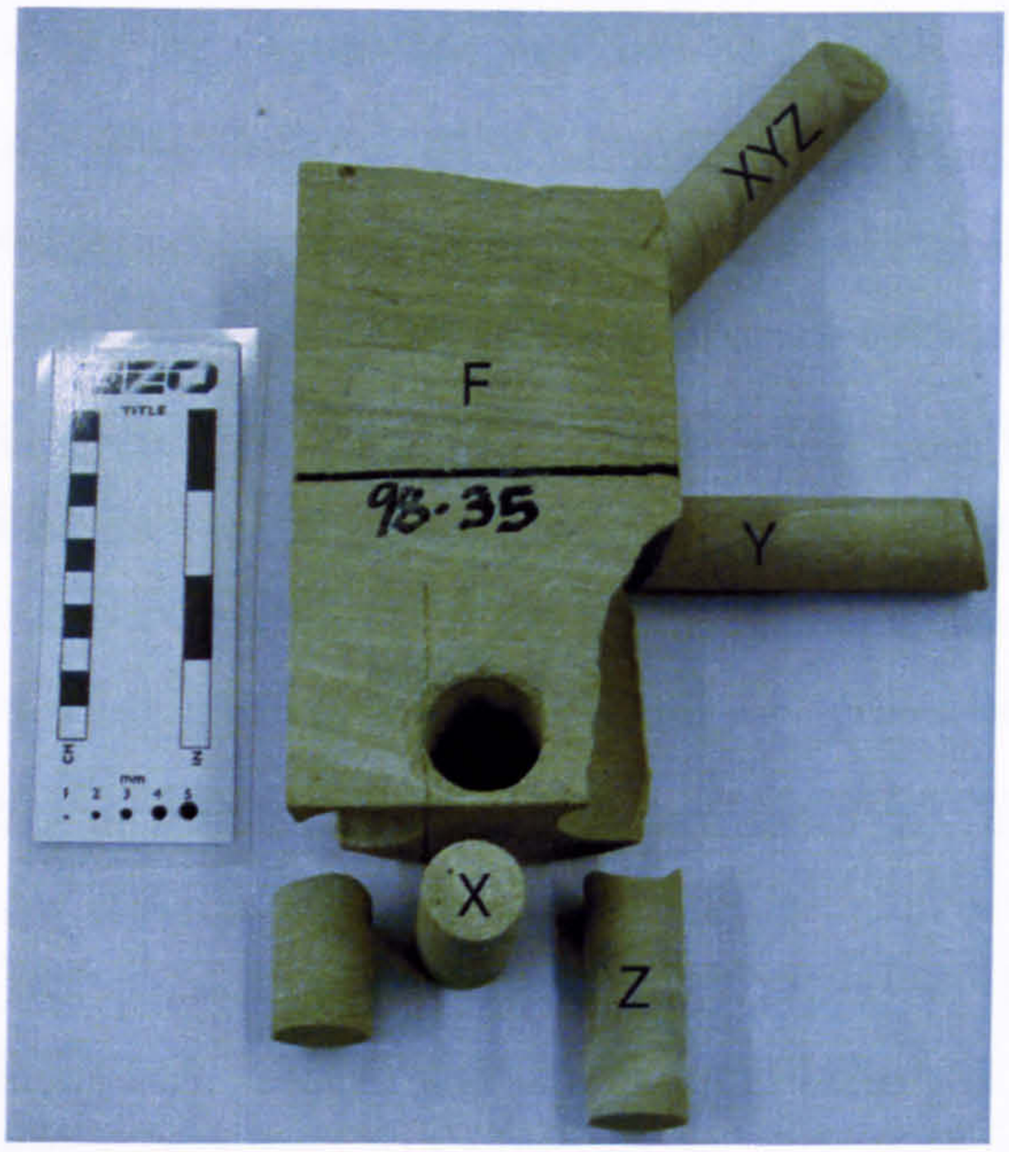

Figure 4.1: *The core sampling strategy used in determining the velocity anisotropy. X - parallel to bedding and perpendicular to F (the fiducial direction and flat face of the half-core), Y - parallel to bedding, perpendicular to F but also in the same plane as X, Z - perpendicular to the plane XY (parallel to the borehole core axis), and XYZ - 45° to the borehole core axis.*

the core axis parallel to bedding providing c_{11};

2. measurement of V_p parallel to the Z axis ($V_p(0^o)$) and measured on a core oriented with the core axis normal to bedding providing c_{33};

3. measurement of V_s for a shear-wave polarisation plane which contains the Z axis often measured on a core oriented with the core axis normal to bedding, so that the propagation direction is parallel to the Z axis ($V_{sv}(0^o)$) providing c_{44};

4. measurement of V_s for a shear-wave polarisation plane parallel to the XY plane ($V_{sh}(90^o)$) and measured on a core with the core axis parallel to bedding providing c_{66};

5. measurement of V_p in a propagation direction at 45^o to the Z axis ($V_p(45^o)$) and measured on a core oriented with the core axis at 45^o to bedding which provides c_{13} when c_{11}, c_{33} and c_{44} are known.

Since this suite of measurements requires three differently oriented cores (cored normal, parallel, and at 45^o to bedding) it is easy experimentally to recover one P-wave velocity and two orthogonal S-wave velocities. Rather more velocity measurements are acquired than is necessary, so a selection of what is deemed to be the most reliable measurement is

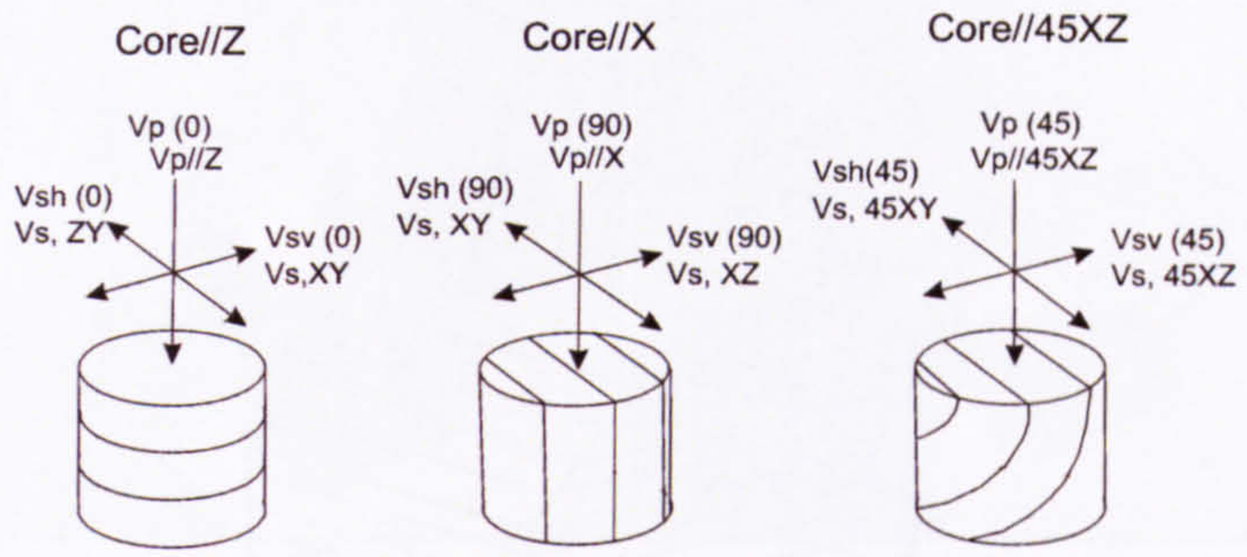

Figure 4.2: *Elastic tensor as determined from ultrasonic analyses. Single ended arrows show propagation direction; double ended arrows show polarisation direction.*

used (Figure 4.3). Reliability and consistency are inter-related, if a set of measurements provides a good apparent consistency of results it is deemed to be reliable and thus used in the calculations of P- and S-wave anisotropy. Generally, the P-wave data sets provided more reliable data due to high attenuation problems associated with shear-waves.

Using the results of the ultrasonic analysis it is possible to calculate the elastic stiffness tensor under the assumption of transverse isotropy as follows:

c_{11} $[(V_p)_{//x} + (V_p)_{//y}]/2$;

c_{33} $(V_p)_{//z}$;

c_{44} $average(V_s)_{//z}$;

c_{66} $[(V_s)_{xy} + (V_s)_{//z}]/2$;

c_{12} $c_{11} - 2c_{66}$;

c_{13} $(V_p)_{//45xz}$.

4.2.3 Atmospheric conditions velocity measurements

Compressional-wave measurements were conducted both radially at atmospheric conditions at intervals of twenty-degrees (Figure 4.4). The sample is rotated about its long-axis when conducting P-wave radial measurements, thereby varying the propagation direction in a plane that has the core axis as its normal. Anisotropy is determined from V_{max} and V_{min}, where,

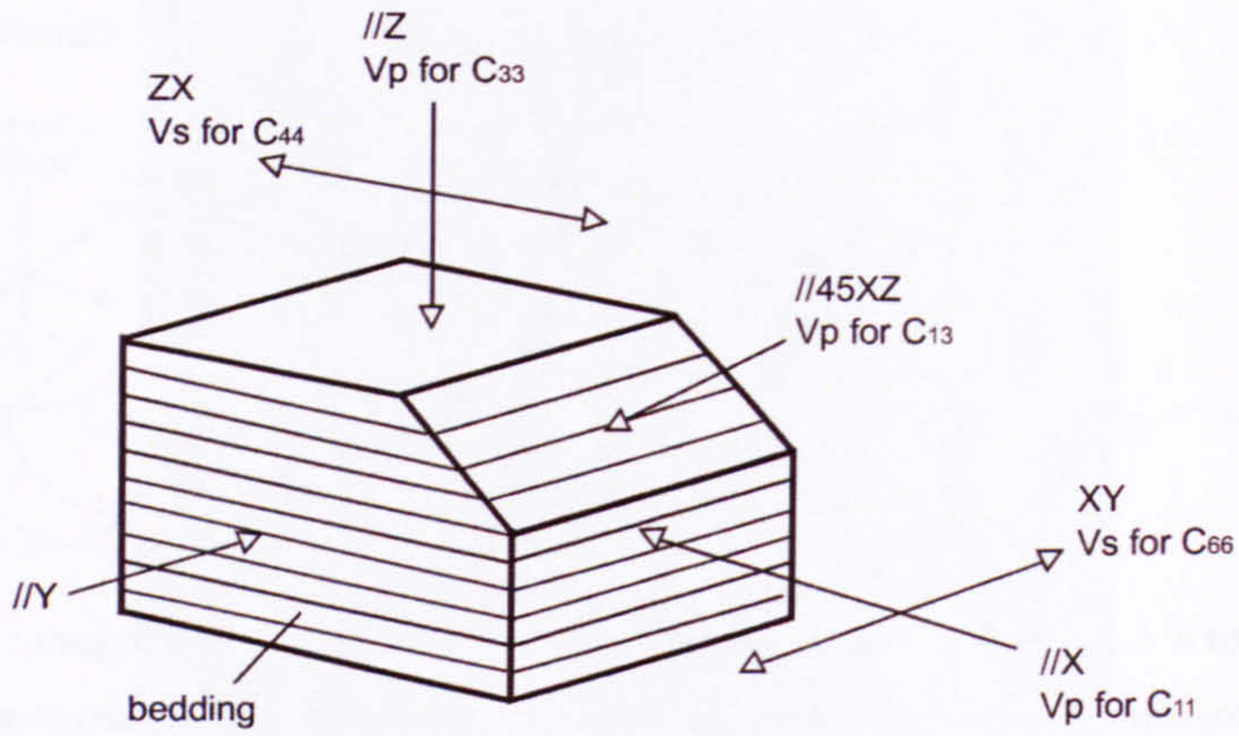

Figure 4.3: *Core sample orientation with respect to elastic tensor components. Single-ended arrows show propagation direction; double-ended arrows show polarisation direction.*

$$A\% = 200(V_{max} - V_{min})/(V_{max} + V_{min}) \tag{4.4}$$

and where

$$V_{max} = (V_{//X} + V_{//Y})/2, \tag{4.5}$$

and

$$V_{min} = V_{//Z}. \tag{4.6}$$

In determining V_{max} and V_{min} the average of measurements 180^o apart were used.

S-wave measurements were conducted axially at bench top conditions at intervals of twenty-degrees. The sample was rotated about its long axis, thereby varying the orientation of the polarisation plane while keeping the propagation direction constant. Anisotropy was determined as for the radial P-wave measurements by finding V_{max} and V_{min} in this propagation direction (Equations 4.4 and 4.5). It is important to remember that in P-wave analyses the propagation direction is incrementally changed whilst in S-wave analyses it is the polarisation orientation that is being altered.

The results of the atmospheric ultrasonic velocity analysis for P- and S-waves for each individual sample were plotted on polar diagrams. The X-, Y- and Z-core were plotted to show the azimuthal variation in velocity with each assigned a different colour

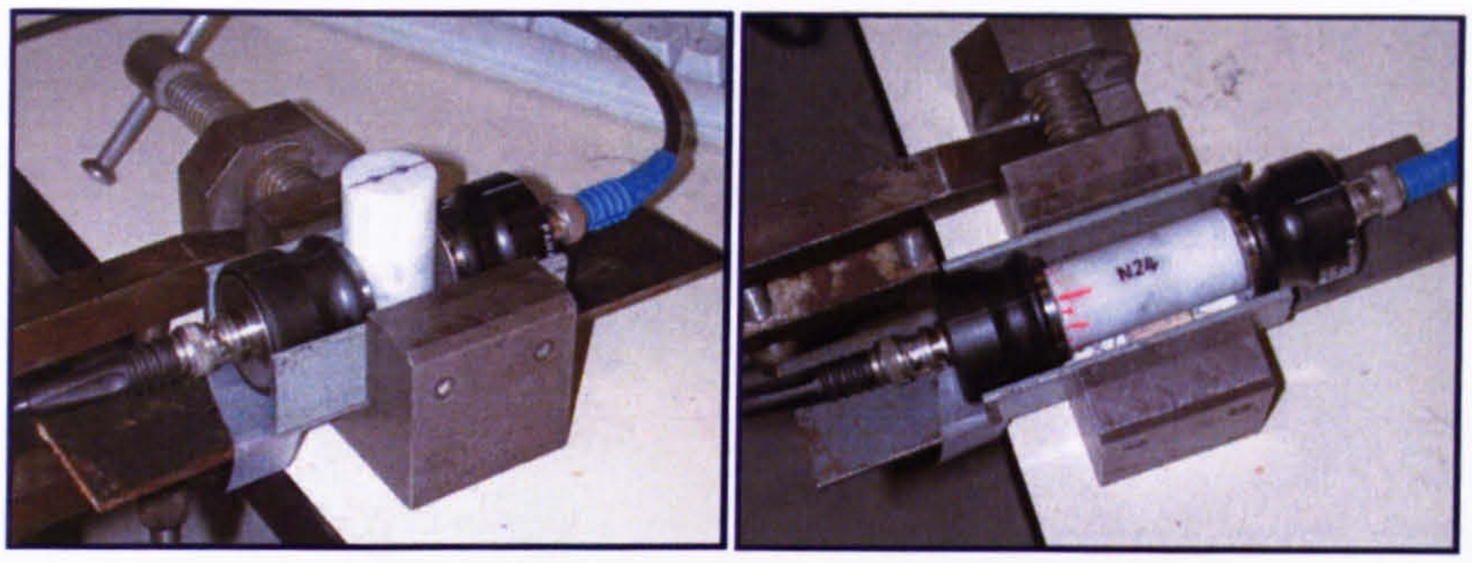

Figure 4.4: *Illustration of the atmospheric conditions set up for radial (L), and axial (R) ultrasonic velocity measurements. It is important to remember that in P-wave analyses the 'propagation direction' is incrementally changed whilst in S-wave analyses it is the polarisation orientation that is being altered. The transducers at either end of the rock sample were rotated through 360 degrees with measurements conducted every 20 degrees. The transducers and rock sample were clamped in place to ensure a good contact and accurate alignment of transducers.*

and notation. P-wave anisotropy is with respect to the wave vector whereas S-wave anisotropy is with respect to the polarisation vector. The S_x, S_y and S_z measurements were determined by conducting S-wave measurements axially on the sample's three core orientations X, Y and Z.

4.2.4 High-pressure velocity measurements

Seismic velocities in rocks are sensitive to stress (Sayers 2002*b*). The presence of microcracks, and microporosity along grain boundaries greatly affects the velocity of elastic waves in rocks (Sayers 1994). This is generally attributed to the closing of compliant cracks and grain boundaries. Cracks are pushed together as the confining pressure increases. As more and more of the cracks are closed the mechanical stiffness and hence velocities of the rock increase (Sayers et al. 1990). The apparatus used for the high-pressure ultrasonic velocity measurements was designed and built in the Rock Deformation Laboratory at Manchester University (Figure 4.5). Porous materials, such as reservoir rocks, are prone to high attenuation problems. To reduce these effects it is necessary to put as much energy as possible into the sample, hence the transducers had to be placed inside the pressure vessel (Figure 4.6). The high-pressure rig was designed to perform velocity measurements at room temperature and hydrostatic pressures ranging from 0 to 700MPa, far exceeding *in situ* conditions.

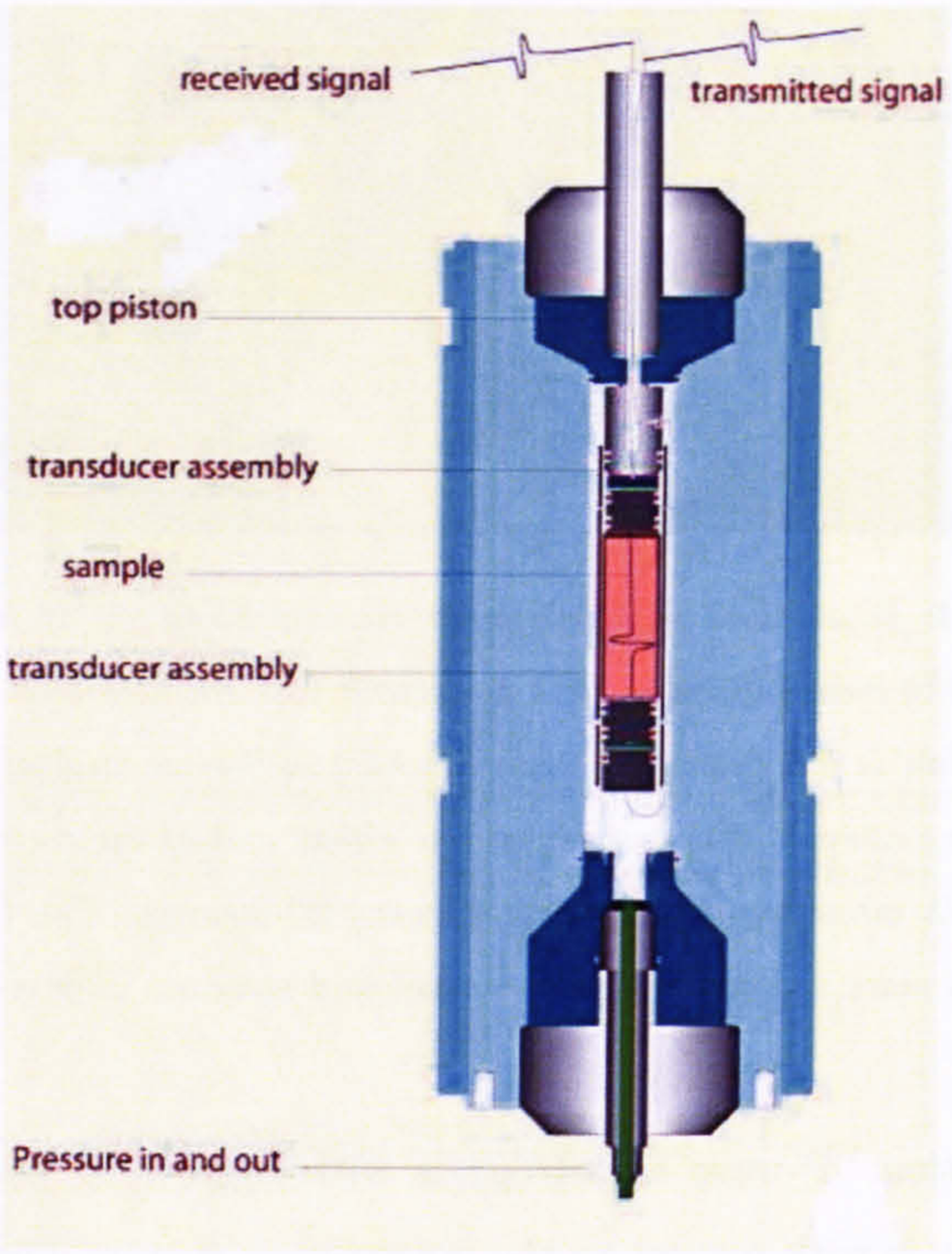

Figure 4.5: *Diagram of the high-pressure rig that was designed and built in the Rock Deformation Laboratory at Manchester University.*

In this study P- and S-wave velocities were measured between 0-50MPa (approximately maximum *in situ* pressure) at increments of 5-10MPa. Several sets of analyses were collected at both increasing and decreasing pressures to ensure reliable results were obtained and averages could be easily determined. In general, a sample will be subjected to four cycles of increasing and decreasing confining pressure with measurements conducted at a variety of pressures. It was noticed that hysteresis seemed to be insignificant and did not noticeable affect the velocity of a sample with respect to the repeated cycling of increasing and decreasing confining pressures. The samples were arranged with the P-wave propagation direction parallel to the sample axis, and the S-wave propagation direction parallel to the sample axis with the polarisation plane rotated through intervals of 45^o.

The specimens were enclosed within a rubber jacket and mounted between the two transducers as shown in Figure (4.7). The rubber jacket was used to exclude the pressurised hydraulic fluid from the spaces between transducers, backing pieces, and the specimen.

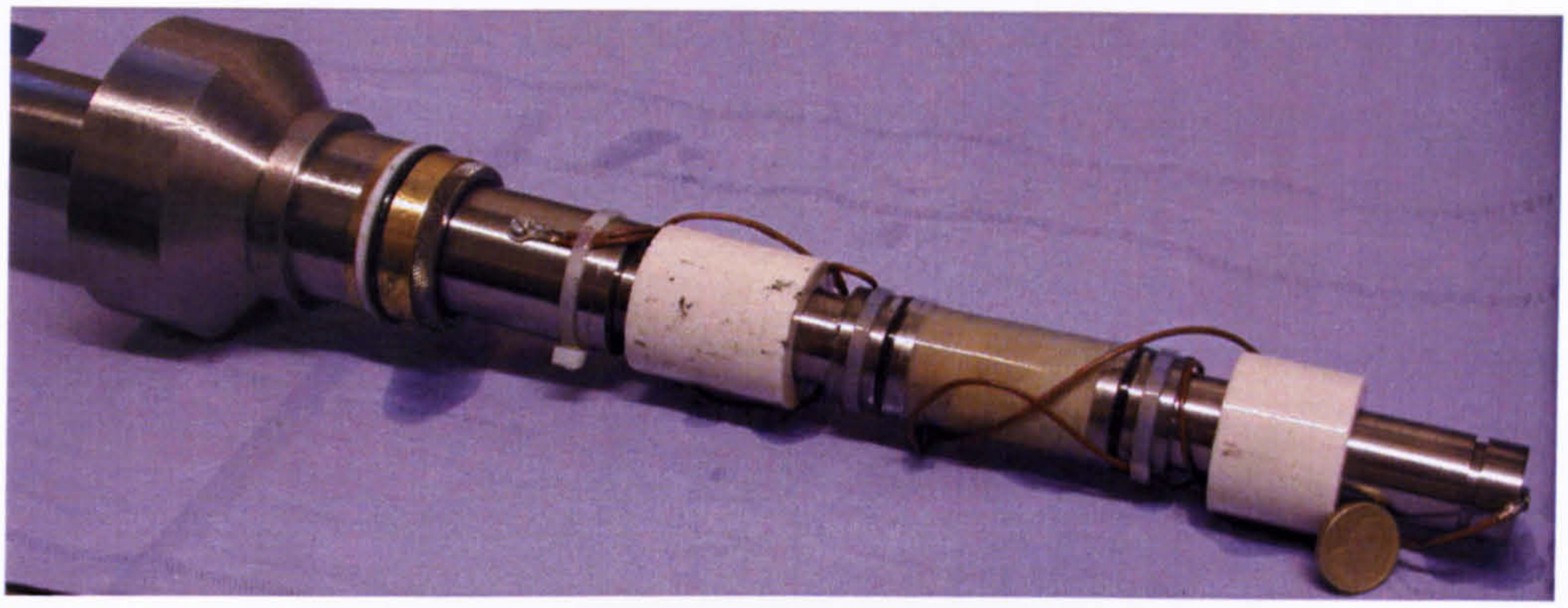

Figure 4.6: *Close up of the high-pressure rig piston.*

As the pressure is raised these pieces clamp together with normal stresses nearly equal to hydrostatic pressure. A light film of honey is also applied to the surfaces of the specimen and transducers to fill small irregularities that may be present on the ends of the specimen. The zero setting of the delay was obtained by finding the settings corresponding to the first arrivals through steel samples of different lengths and extrapolating to zero length. The zero setting is the approximate time taken for the ultrasonic wave to travel from one transducer to the other when no sample is present. The steel standards were cut from the same bar of 1-inch steel to avoid the complexities associated with heterogeneity.

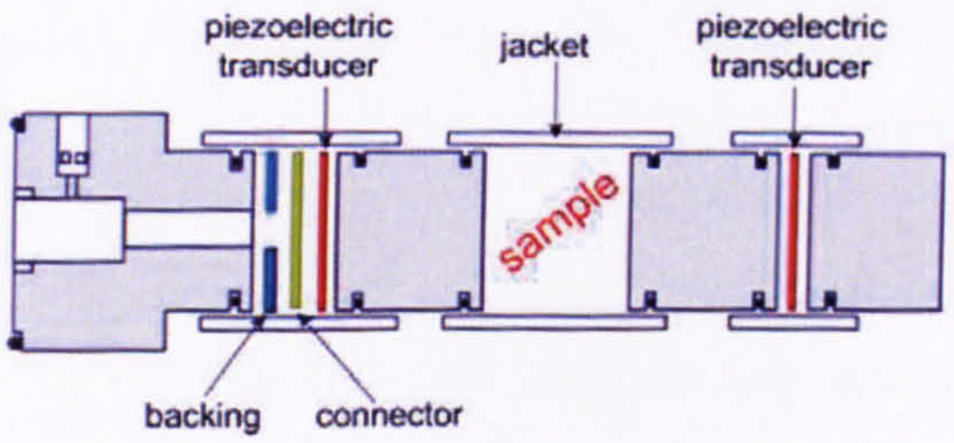

Figure 4.7: *Illustration of the high-pressure piezoelectric transducer assembly. The backing is made of pyrophyllite (which was used to insulate the connector from the piston and suppress signals from the back of the transducer) and the connector was made from brass.*

In calculating the anisotropy, the velocities used at any given pressure in a given direction were determined from cubic polynomial fits to velocity and pressure data in that direction. The use of the cubic polynomial strategy was employed because velocities

measured on different cores were not all measured at identical pressures. The cubic polynomial fit provides a good approximation of the velocity magnitudes throughout the pressure intervals analysed within experimental error and measurement reproducibility (Figure 4.8).

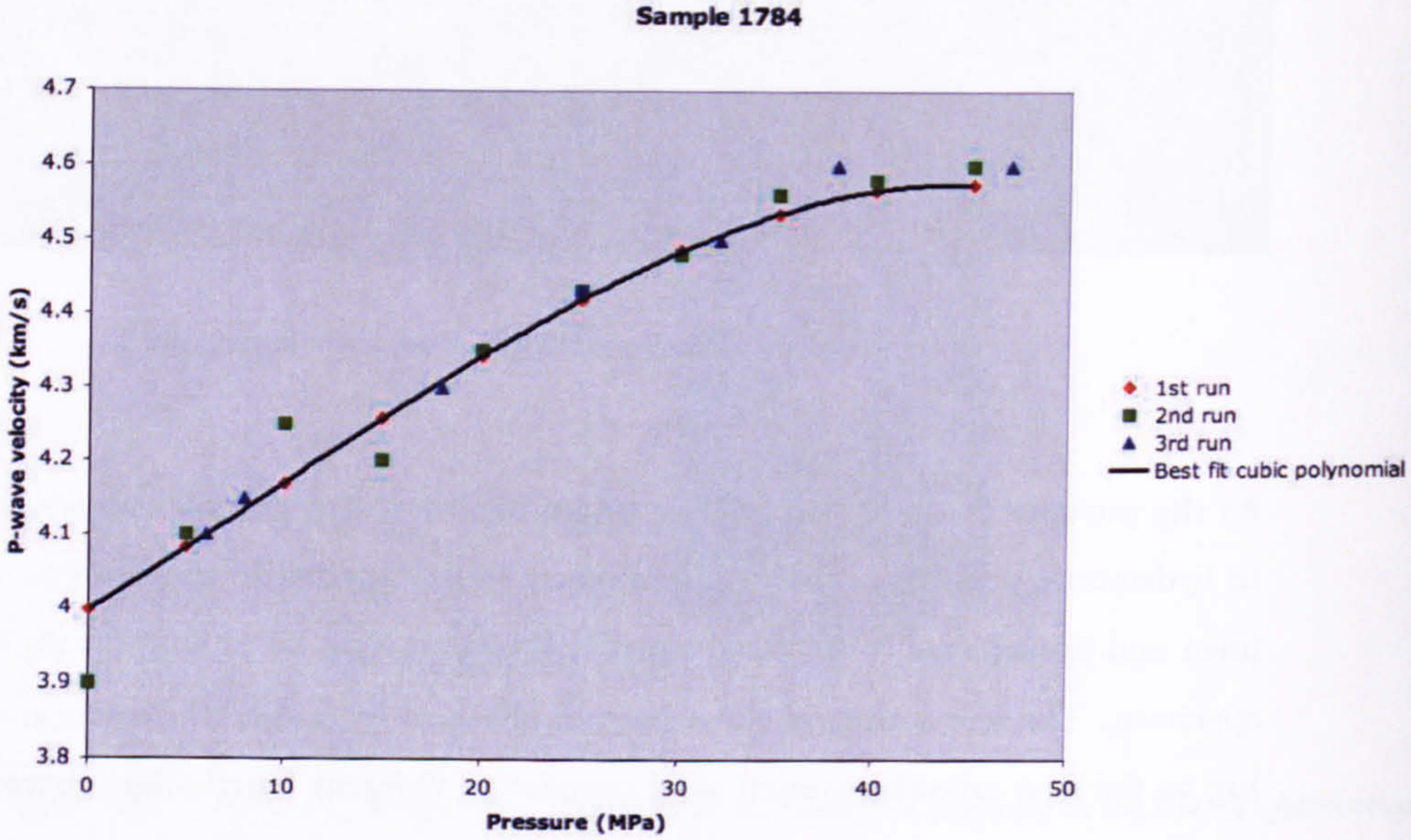

Figure 4.8: *An example of the best fit cubic polynomial trend line using all of the data obtained for sample 1784m. It can be seen that the cubic polynomial fit provides a good approximation of the velocity magnitudes throughout the pressure intervals analysed within experimental error and measurement reproducibility.*

4.2.5 Split transducer shear-wave analysis

It is possible to propagate two orthogonally polarised shear-waves at elevated confining pressure through modification of the piezoelectric transducer assembly. This is done by carefully splitting two conventional shear-wave transducers into two and then taking one half, and rotating it through ninety-degrees and joining them back together (Figure 4.9). Furthermore, by taking advantage of the methodology devised by Silver & Chan (1988) it is possible to determine the degree of shear-wave splitting (% anisotropy) and orientation of anisotropy (in degrees) in one single measurement (Figure 4.10). Whilst this methodology would have undoubtedly yielded very interesting results unfortunately due to time restraints the analysis was not performed. The technique and methodology is presented so as to provide future researchers with assistance.

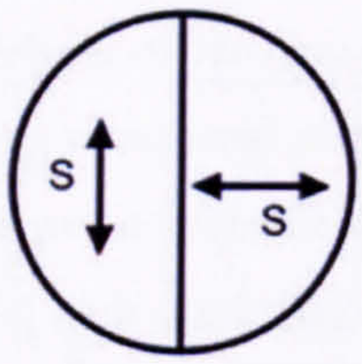

Figure 4.9: *Assembly of the combined split shear-wave transducers used to analyse shear-wave splitting in one measurement. The double headed arrows indicate the polarisation plane of the shear-wave.*

It is possible to describe the Silver & Chan (1988) relatively briefly, as in the following statement, however, should the reader require further details of the technique and mathematical equations used here it is recommended that they refer to the original paper Silver & Chan (1988). The Silver & Chan (1988) method attempts to minimise the effect of anisotropy (i.e., remove the shear-wave splitting) by correcting for a range of possible lag times (δt) and the fast directions (ϕ) implemented as a grid search. For each pair of values (each node on the grid) the eigenvalues of the covariance matrix of the two shear-waves recorded on the horizontal components are calculated. The best-fitting δt and ϕ correspond to the point of smallest λ_2 (the smallest eigenvalue). These parameters best linearise the ellipticity of the particle motion. The error in the results is estimated by applying a statistical F-test, and using the extent of the 95% confidence interval (Silver & Chan 1988, Wookey et al. 2002).

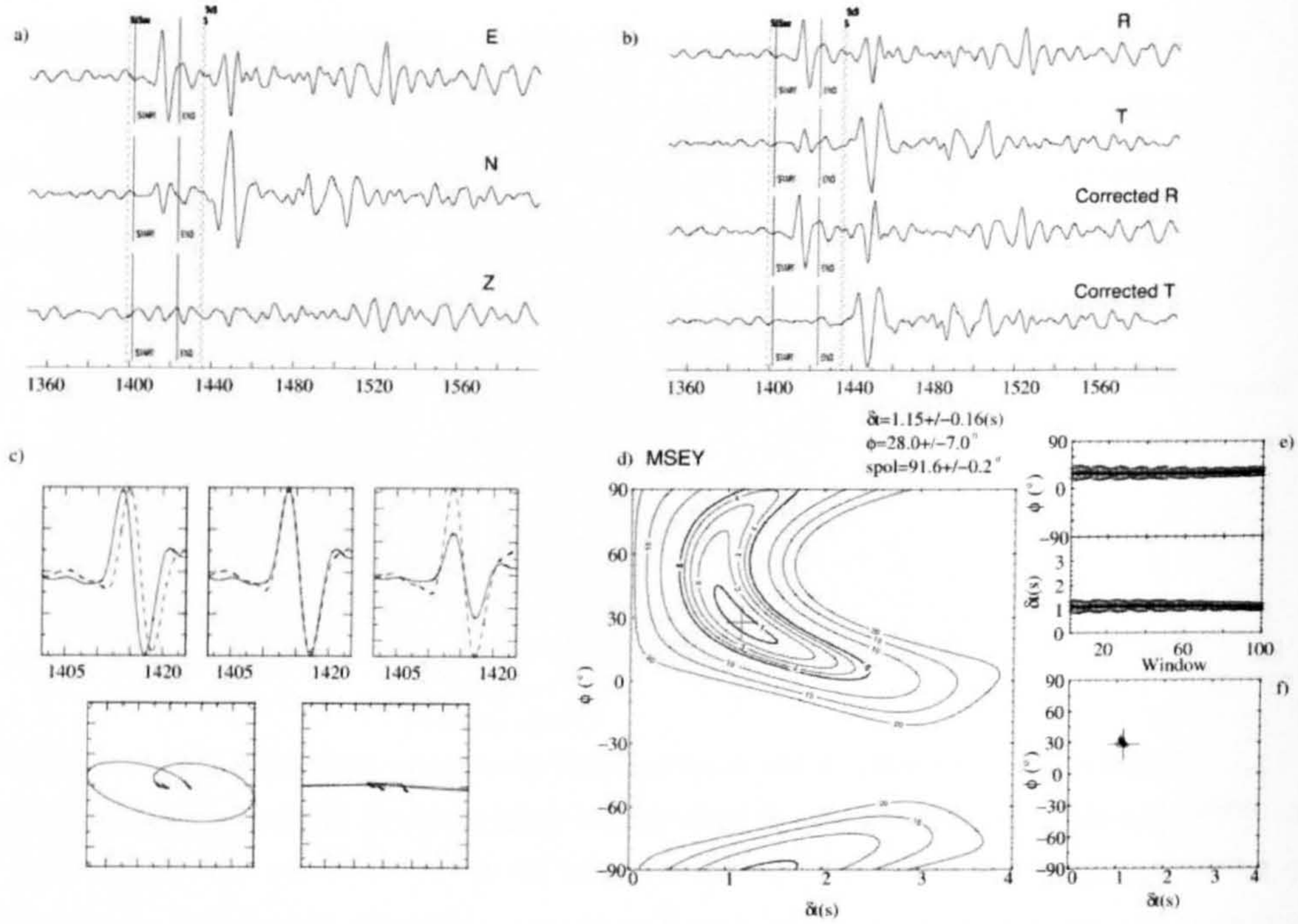

Figure 4.10: *This figure shows an example of the output of the Silver and Chan method for analysing shear-wave splitting for a direct S-wave arrival. a) Original traces (E, N, Z). b) Traces rotated into R and T directions before and after the anisotropy correction. R component is the initial shear wave polarisation before entering the anisotropic region. c) Top traces show the fast/slow shear waveforms for uncorrected (left) and corrected (right) seismograms. The bottom panels show the particle motion for uncorrected (left) and corrected (right) seismograms. A good result will show similar fast/slow shear waveforms and any elliptical particle motion will have been linearised. d) Results of the grid search over δ_t and ϕ. The optimum splitting parameters are represented by the cross and the first surrounding contour denotes 95% confidence region.*

4.3 Ultrasonic analyses results

Polar plots are used in this study to conveniently illustrate the azimuthal variation in velocity, and are annotated as follows: X-core = red/dashed line; Y-core = blue/dotted line; Z-core = green/dash-dot line. The point the data was acquired from and is located on the polar plot is indicated by the asterisk and cross, this is dependent upon which core is analysed. A list of the samples analysed using both atmospheric and elevated confining pressure ultrasonic analyses is presented in Table (3.1).

The complete set of results obtained from the individual samples are presented in Appendices (N; O; P). The P-wave polar diagrams are determined from radially acquired measurements on the three core directions (X, Y and Z). Whereas, the S-wave measurements are acquired from axial measurements of the three core directions (X, Y and Z) with the variation of polarisation angle of the transducers. In this study the P-wave velocity measurements (3% error) are considered as being more reliable than the S-wave measurements (5% error). The S-wave measurements are considered to be less reliable than the P-waves due to problems of high attenuation levels of shear-waves propagating through highly porous media and coupling. The main restraint on the amount of energy that is transferred into the sample is the coupling of the transducer to the sample surface. The more energy that can be transferred into the sample the more reliable the results should be. Nevertheless, P-waves are less affected by poor or bad coupling hence S-waves are considered to provide less reliable data sets because of the limit on the energy that can be exerted onto the sample.

Well 206/8-8, sample 1663m The azimuthal variation in P-wave velocity at atmospheric pressure: X-core c.3.0km/s, Y-core c.3.0km/s and Z-core c.3.0-3.2km/s. The azimuthal variation in S-wave velocity at atmospheric pressure: X-core c.2.0km/s, Y-core c.2.0km/s and Z-core c.1.8km/s. Both the P- and S-wave measurements show good correlation, a high level of confidence in the analysis and within experimental error. The P-wave analysis shows that the sample is approximately isotropic except for some minor variations. The S-wave analysis is slightly different in that the Z-core which is still isotropic is about 0.25km/s slower than the X- and Y-cores. It is most likely that the sample analysed was atypical when compared to the others analysed from 1663. This sample did not have any elevated confining pressure ultrasonic velocity analysis conducted upon it.

Well 206/8-8, sample 1784m The azimuthal variation in P-wave velocity at atmospheric pressure: X-core c.3.0-4.0km/s, Y-core c.2.5-4.0km/s and Z-core c.4.0km/s. The azimuthal variation in S-wave velocity at atmospheric pressure: X-core c.2.0-2.5km/s, Y-core c.2.0-2.5km/s and Z-core c.1.5km/s. High pressure P-wave velocities from 0MPa to 50MPa: X-core 4.0-4.5km/s, Y-core 4.2-4.5km/s, XYZ-core 3.8-4.5km/s and Z-core 2.4-3.4km/s. At low confining pressures (up to 30MPa) the X- and Y-cores have noticeably different velocities. As hydrostatic pressure increases from 10MPa to 50MPa the bulk P-wave anisotropy decreases very rapidly from c.50% to c.28%. The initially very high P-wave anisotropy is likely to be due to crack and grain boundary microcrack relaxation. The resulting anisotropy at 50MPa is considered to be representative of the intrinsic anisotropy of the sample after all the cracks have been closed. The sample has an orthorhombic symmetry at low pressures but becomes approximately VTI at *in situ* pressures (50MPa). There is also a small amount of hysteresis which is probably due to the partial closure of small bedding parallel fractures within this heterogeneous sample.

Well 206/8-8, sample 1788m The azimuthal variation in P-wave velocity at atmospheric pressure: X-core c.2.5-3.5km/s, Y-core c.2.5-3.2km/s and Z-core c.3.2km/s. The azimuthal variation in S-wave velocity at atmospheric pressure: X-core c.2.0-3.0km/s, Y-core c.2.0-2.5km/s and Z-core c.1.5km/s. High pressure P-wave velocities from 0MPa to 50MPa: X-core 3.5-4.0km/s, Y-core 3.5-4.0km/s, XYZ-core 3.1-3.6km/s and Z-core 2.5-3.2km/s. At both atmospheric conditions and at elevated confining pressures the X- and Y- cores have almost identical velocity-pressure profiles, whilst the Z-core (which is perpendicular to bedding) is significantly slower and azimuthally isotropic. The S-wave atmospheric pressure analysis shows some variability within the X- and Y-cores, which is most likely due to the highly attenuative nature of the bedding parallel phyllosilicates. Generally, all the high-pressure P-wave core samples show good consistency of results and little variance due to heterogeneities or hysteresis. As hydrostatic pressure increases from 10MPa to 50MPa the P-wave anisotropy decreases very rapidly from c.35% to c.20%. The initially very high P-wave anisotropy is likely to be due to crack and grain boundary microcrack relaxation (as in sample 1784). The resulting anisotropy at 50MPa is considered to be representative of the intrinsic anisotropy of the sample after all the cracks have been closed. As with 1784 the velocity perpendicular to bedding is much slower than the others at all pressures. Furthermore, the sample has a simple VTI symmetry pattern across all pressures.

Well 206/8-8, sample 1841m The azimuthal variation in P-wave velocity at atmospheric pressure: X-core c.2.0-3.5km/s, Y-core c.1.8-4.0km/s and Z-core c.4.0km/s. The azimuthal variation in S-wave velocity at atmospheric pressure: X-core c.2.0-3.0km/s, Y-core c.1.5-2.5km/s and Z-core c.1.7km/s. High pressure P-wave velocities from 0MPa to 50MPa: X-core 4.2-4.7km/s, Y-core 4.2-4.5km/s, XYZ-core 3.4-4.0km/s and Z-core 2.0-3.1km/s. As hydrostatic pressure increases from 10MPa to 50MPa the P-wave anisotropy decreases very rapidly from c.70% to c.32%. The scatter in S-wave measurements at atmospheric conditions is likely to be as a result of one or more of these problems: noise, high-attenuation, and scattering effects. Fortunately, the P-wave data collected at atmospheric conditions appear to be far more robust. The X- and Y-core show a high degree of ellipticity and give approximately coincident results. The Y-, XYZ, and Z-cores all show a nice cubic polynomial type curve of increase in P-wave velocity with increasing pressure. The X-core, however, after a gradual increase in P-wave velocity over the first c.25MPa from 4.2km/s all of a sudden jumps up c.0.25km/s to 4.5km/s. This particular phenomenon is not observed throughout any of the other samples analysed. It is postulated here that the sudden jump in velocity is due to the abrupt closure of cracks and fractures within the sample as the confining pressure is gradually increased. Sample 1841 is certainly an extreme case, whereby, at low confining pressures there is a substantial amount of layer parallel microcracks as a result of the opening up of grain boundaries due to stress relaxation. However, over the first 20MPa almost half of the total P-wave anisotropy has been reduced. The slowest velocity is perpendicular to bedding. At lower pressures it has a distinct VTI symmetry whilst at higher pressures it tends towards an orthorhombic symmetry, $V_{p33} << V_{p22} < V_{p11}$.

Well 206/8-8, sample 1909m with oil The azimuthal variation in P-wave velocity at atmospheric pressure: X-core c.3.8km/s, Y-core c.3.8km/s and Z-core c.3.8km/s. The azimuthal variation in S-wave velocity at atmospheric pressure: X-core c.2.25km/s, Y-core c.2.25km/s and Z-core c.2.25km/s. Both the P- and S-wave measurements show good correlation, a high level of confidence in the analysis and within experimental error no observable anisotropy. The sample is completely isotropic throughout all cores under both P- and S-wave analysis. This sample did not have any elevated confining pressure analysis conducted upon it.

Well 206/8-8, sample 1909m without oil The azimuthal variation in P-wave velocity at atmospheric pressure: X-core c.3.0km/s, Y-core c.3.2km/s and Z-core c.3.4km/s. The

azimuthal variation in S-wave velocity at atmospheric pressure: X-core c.2.1km/s, Y-core c.2.1km/s and Z-core c.2.3km/s. High pressure P-wave velocities from 0MPa to 50MPa: X-core 3.25-4.4km/s, Y-core 3.3-4.25km/s, XYZ-core 3.1-4.2km/s and Z-core 3.2-4.25km/s. As hydrostatic pressure increases from 10MPa to 50MPa the P-wave anisotropy increases very rapidly from c.0% to c.8% at 15MPa before decreasing again at c.50MPa to 1%. Unusually, the P- and S-wave analysis shows that the core with the fastest velocity is the Z-core direction with the Y-core next and then the X-core direction the slowest. The elevated pressure analysis on the separate cores firmly supports the supposition that the sample is indeed isotropic. The X-core direction was analysed up to 120MPa with a P-wave velocity of 4.5km/s which all the core directions appear to be asymptotically approaching. This pressure is considerably higher than that it would have undergone at maximum burial depth. Moreover, it is to be noted that at this high a confining pressure the sample will have changed appreciably. The increase and then decrease in P-wave anisotropy with increasing confining pressure is thought to be due to the removal of the oil. That is, under an increasing hydrostatic confining pressure certain fracture directions will close preferentially when compared to other directions. The oil would likely be present within layer parallel porosity (i.e., intra- and interparticle microporosity) and after its removal it would leave small gaps between adjacent grains. This theory is supported by the fact that the Z-core direction (perpendicular to bedding) had the highest P- and S-wave velocities.

Well 206/8-8, sample 1950m The azimuthal variation in P-wave velocity at atmospheric pressure: X-core c.3.5km/s, Y-core c.3.8km/s and Z-core c.3.2km/s. The azimuthal variation in S-wave velocity at atmospheric pressure: X-core c.2.2km/s, Y-core c.2.5km/s and Z-core c.2.1km/s. High pressure P-wave velocities from 0MPa to 50MPa: X-core 3.6-4.2km/s, Y-core 4.1-5.5km/s, XYZ-core 3.7-5.0km/s and Z-core 3.6-4.2km/s. As hydrostatic pressure increases from 10MPa to 50MPa the P-wave anisotropy decreases from an initial c.6.6% to c.6% at 5-10MPa before increasing again to 1% at c.50MPa. At atmospheric conditions the sample is roughly isotropic. At elevated confining pressures the Y- and XYZ-cores are the fastest directions. that is to say that $V_{p22} >> V_{p11} \sim V_{p33}$. 1950 is very much an oddity in that the anisotropy decreases first before increasing again and that the X- and Z-cores are the slowest directions. This is the only sample that at elevated pressures there is still a significant difference in velocities between the various cores. Such is the difference between the X- and Y-cores it is likely that the X-core

intercepts layers of high-porosity or microfracturing.

Well 206/13a2, sample 1959m The azimuthal variation in P-wave velocity at atmospheric pressure: X-core 3.0-3.5km/s, Y-core c.4.0km/s and Z-core c.4.0km/s. The azimuthal variation in S-wave velocity at atmospheric pressure: X-core 2.2-2.8km/s, Y-core c.3.0km/s and Z-core c.3.0km/s. The sample is broadly isotropic except for the X-core direction which has a distinct azimuthal variation in P-wave velocity. On analysis of the results it appears that the data is reliable and consistent. Therefore, the X-core anomaly is likely to be as a result of intersecting a clay-mica rich band. This sample did not have any elevated confining pressure analysis conducted upon it.

Well 206/13a2, sample 1963m The azimuthal variation in P-wave velocity at atmospheric pressure: X-core c.3.0-3.5km/s, Y-core c.3.0-3.5km/s and Z-core c.3.5km/s. The azimuthal variation in S-wave velocity at atmospheric pressure: X-core c.2.0-2.5km/s, Y-core c.2.0-2.5km/s and Z-core c.2.0km/s. Unlike, previous samples both the P- and S-wave measurements appear to be quite consistent between each core analysed. This is most likely because the sample is well consolidated, and has less clays and micas in grain supporting locations. Sample 1963 did not have any elevated confining pressure analysis conducted upon it.

Well 206/13a2, sample 2015m The azimuthal variation in P-wave velocity at atmospheric pressure: X-core c.3.2km/s, Y-core c.3.2km/s and Z-core c.3.2km/s. The azimuthal variation in S-wave velocity at atmospheric pressure: X-core c.1.7km/s, Y-core c.1.9km/s and Z-core c.2.2km/s. There are notable discrepancies between the P- and S-wave analyses. P-wave analysis shows that all the cores have approximately similar velocity profiles. Whilst the S-wave analysis suggests that the X- and Y- directions are about 0.5km/s slower than the Z-direction. This sample did not have any elevated confining pressure analysis conducted upon it.

Well 206/13a2, sample 2023m The azimuthal variation in P-wave velocity at atmospheric pressure: X-core c.3.5km/s, Y-core c.3.5km/s and Z-core c.3.5km/s. The azimuthal variation in S-wave velocity at atmospheric pressure: X-core c.1.5km/s, Y-core c.1.5km/s and Z-core c.1.5km/s. Both the P- and S-wave results show good correlation and consistency across different core directions. This sample did not have any elevated confining pressure analysis conducted upon it.

Well 206/13a2, sample 2028m The azimuthal variation in P-wave velocity at at-

mospheric pressure: X-core c.3.1km/s, Y-core c.3.1km/s and Z-core c.3.1km/s. The azimuthal variation in S-wave velocity at atmospheric pressure: X-core c.2.0km/s, Y-core c.2.0km/s and Z-core c.2.0km/s. High pressure P-wave velocities from 0MPa to 50MPa: X-core 3.5-4.2km/s, Y-core 3.4-4.2km/s, XYZ-core 3.5-4.2km/s and Z-core 3.6-4.2km/s. Both the P- and S-wave atmospheric conditions azimuthal analyses show good consistency and reliability of data. The sample has only a very small anisotropy (5.5%) at low pressures (5MPa) which decreases to 0.5% at 45MPa. At atmospheric pressure the sample could be considered to have a very slight VTI symmetry but at elevated confining pressures becomes completely isotropic.

Well 206/13a2, sample 2034m The azimuthal variation in P-wave velocity at atmospheric pressure: X-core 2.5-3.5km/s, Y-core 2.5-3.5km/s and Z-core c.3.5km/s. The azimuthal variation in S-wave velocity at atmospheric pressure: X-core 2.0-2.5km/s, Y-core 2.0-2.5km/s and Z-core c.1.7km/s. The correlation between the P- and S-wave data is not entirely reliable as the S-wave data has considerable variability. The P-wave data indicates that the sample has a strong VTI symmetry which is not immediately apparent from core inspection. A more than likely explanation of the variability within the S-wave data and the high anisotropy is that the sample has a lot of layer parallel, horizontally aligned porosity. This sample did not have any elevated confining pressure analysis conducted upon it.

Well 206/8-8, sample 2070m The azimuthal variation in P-wave velocity at atmospheric pressure: X-core c.3.5-4.0km/s, Y-core c.3.5-4.0km/s and Z-core c.3.0km/s. The azimuthal variation in S-wave velocity at atmospheric pressure: X-core c.1.8-2.0km/s, Y-core c.1.8-2.0km/s and Z-core c.2.0km/s. Sample 2070 is not highly anisotropic but does show good cross-core agreement in velocities. This sample did not have any elevated confining pressure analysis conducted upon it.

Well 206/8-8, sample 2073m The azimuthal variation in P-wave velocity at atmospheric pressure: X-core c.1.8-3.5km/s, Y-core c.1.8-3.5km/s and Z-core c.3.5km/s. The azimuthal variation in S-wave velocity at atmospheric pressure: X-core c.2.0-2.5km/s, Y-core c.2.0-2.5km/s and Z-core c.1.6km/s. Both the P- and S-wave measurements show good correlation, a high level of confidence in the analysis and substantial anisotropy. The Z-core in the P-wave measurement is azimuthally isotropic and relatively fast in comparison to the X- and Y-cores. Whereas, the Z-core in S-wave analysis is significantly slower than both the X- and Y-cores but yet also has an isotropic distribution of

velocities. This sample did not have any elevated confining pressure analysis conducted upon it.

Well 206/8-8, sample 2088m The azimuthal variation in P-wave velocity at atmospheric pressure: X-core c.2.0km/s, Y-core c.2.0km/s and Z-core c.3.5km/s. Sample 2088 did not have any S-wave analysis performed upon it. As a result of the difference in velocities between the two horizontally aligned cores X- and Y- and the Z-core it is possible to determine that there is a significant difference between the horizontal and vertically aligned porosity, possibly grain boundary related. This sample did not have any elevated confining pressure analysis conducted upon it.

Well 206/8-8, sample 2129m without oil The azimuthal variation in P-wave velocity at atmospheric pressure: X-core c.2.5km/s, Y-core c.2.5km/s and Z-core c.2.1km/s. The azimuthal variation in S-wave velocity at atmospheric pressure: X-core c.1.5km/s, Y-core c.1.5km/s and Z-core c.1.5km/s. High pressure P-wave velocities from 0MPa to 50MPa: X-core 2.25-3.5km/s, Y-core 2.5-3.6km/s, XYZ-core 2.25-3.5km/s and Z-core 2.4-4.6km/s. At atmospheric conditions the sample is isotropic within experimental error. At elevated pressures V_{p33} is much faster than V_{p22}, V_{p33}, and $V_p^{45^0}$ leading to a CTI symmetry style (cylindrical transverse isotropy - single vertical set of fractures that have an azimuthally isotropic distribution in spacing, commonly observed in cylindrical samples which have been subjected to non-hydrostatic stresses aligned parallel to the long axis of the sample). This likely means then that there is at least one set of vertical fractures throughout sample 2129. The vertical fracturing could be as a result of a variety of natural and unnatural activities from *in situ* fracturing to drilling. As the Z-core direction is by far the fastest direction the P-wave anisotropy becomes increasingly more negative as the confining pressure is increased. At low confining pressure (0MPa) it has approximately 4% P-wave anisotropy which increases rapidly to a maximum of 26% at 25MPa, as the pressure continues to increase the anisotropy remains almost constant up to 45MPa.

Well 206/8-8, sample 2192m The azimuthal variation in P-wave velocity at atmospheric pressure: X-core c.2.2km/s, Y-core c.2.4km/s and Z-core c.2.5km/s. The azimuthal variation in S-wave velocity at atmospheric pressure: X-core c.1.5km/s, Y-core c.1.5km/s and Z-core c.1.5km/s. High pressure P-wave velocities from 0MPa to 50MPa: X-core 2.5-4.1km/s, Y-core 2.4-4.1km/s, XYZ-core 2.5-4.2km/s and Z-core 2.3-4.0km/s. P-wave anisotropy increases from approximately 6.5% at atmospheric pressure to a max-

imum of 9.5% at 17MPa before decreasing again until it reaches 0% at c.50MPa. At atmospheric conditions P-wave V_{p33} is faster than the other directions, whereas it is isotropic using S-wave analyses. Analysis of the P- and S-wave data suggests that the samples have a very slight VTI symmetry. This is is also supported by the elevated pressure P-wave analysis. Moreover, the P-wave data does appear to show good consistency and reliability of results. The increase and then decrease in anisotropy with increasing pressure is as a result of the bedding parallel cracks closing first and more rapidly than any other crack orientation. As the pressure continues to increase the other crack orientations also start to close thus giving elevated P-wave velocities at higher pressures. It is not until approximately 40MPa that the cracks oriented parallel to bedding and the Z-core direction appear to have closed fully thus leading to an isotropic symmetry system at high pressure.

Well 206/8-8, sample 2194m The azimuthal variation in P-wave velocity at atmospheric pressure: X-core c.2.5km/s, Y-core c.2.5km/s and Z-core c.2.5km/s. The azimuthal variation in S-wave velocity at atmospheric pressure: X-core c.1.6km/s, Y-core c.1.6km/s and Z-core c.1.6km/s. High pressure P-wave velocities from 0MPa to 50MPa: X-core 2.7-4.0km/s, Y-core 2.5-4.0km/s, XYZ-core 2.2-3.5km/s and Z-core 2.4-3.5km/s. The P-wave anisotropy increases from c.8% at low confining pressure (c.5MPa) to a maximum of 15% at 22MPa and then decreases again until reaching 12% at 45MPa. Even though their is a noticeable P-wave anisotropy when the sample is in the high-pressure rig their is not a noticeable difference within experimental error between the X-, Y-, and Z-core directions at atmospheric conditions on the bench-top. As the pressure increases both the X- and Y-core directions increase in velocity concomitantly. Even at 60MPa the Z-core direction is still almost 0.5km/s slower than the X- and Y-cores meaning that their could either be residual crack orientations that have not been fully closed or that the sample contains an inherent intrinsic anisotropy due to bedding parallel clays and micas or grain boundary parallel aligned pore space. The fact that even at *in situ* confining pressures their exists a relatively strong P-wave anisotropy suggests that the sample contains an inherent intrinsic anisotropy.

Well 206/8-8, sample 2198m The azimuthal variation in P-wave velocity at atmospheric pressure: X-core c.2.8km/s, Y-core c.2.5km/s and Z-core c.2.7km/s. The azimuthal variation in S-wave velocity at atmospheric pressure: X-core c.2.0km/s, Y-core c.1.6km/s and Z-core c.2.0km/s. In both the P- and S-wave analysis the Y-core direc-

tion is slightly slower than both the X- and Z-core directions. The data does seem to be reliable, and consistent suggesting that the difference in velocity might be as a result heterogeneities within the Y-core direction. These heterogeneities are likely to be bedding parallel cracks which just happen to be more abundant in the Y-core direction. Sample 2198 has a very slight P-wave anisotropy c.1-2%.

4.4 Discussion

4.4.1 Introduction

Presented within this section is a detailed discussion of the results obtained from atmospheric and elevated confining pressure ultrasonic analyses. The results of the elevated confining pressure ultrasonic data are conveniently summarised by a frequency histogram of the maximum P-wave anisotropy at what is estimated to be the approximate *in situ* confining pressure (Table 4.11). The results obtained from the elevated confining pressure analyses are used here because it is believed that they will most closely represent the maximum P-wave anisotropy observed by field wide seismic surveys in the reservoir. At low confining pressures the samples contain an abundance of horizontal relaxation cracks due to the sample coring process and removal from the subsurface which will significantly contribute to and exacerbate the maximum observed P-wave anisotropy at atmospheric conditions.

4.4.2 Discussion of atmospheric conditions velocity measurements

This section comprises a brief overview of the results obtained from the atmospheric pressure and temperature P- and S-wave ultrasonic velocity analysis. The results of the analysis are categorised into their three respective groups with overviews of both velocities and anisotropies provided.

On the basis of the room temperature and pressure velocity measurements the samples could be grouped into three main categories (Tables 4.1 and 4.2). Group 1 samples were typified by high velocities (c.3.8km/s) and strong anisotropy (> 20%). Group 2 samples had high velocities similar to Group 1 samples but had weak levels of anisotropy (< 10%). Group 3 samples had low velocities (c.2.5km/s) and intermediate amounts of anisotropy (10 – 20%).

Group 1 samples are typified by high velocities (c.4.0km/s) and strong anisotropy (c.

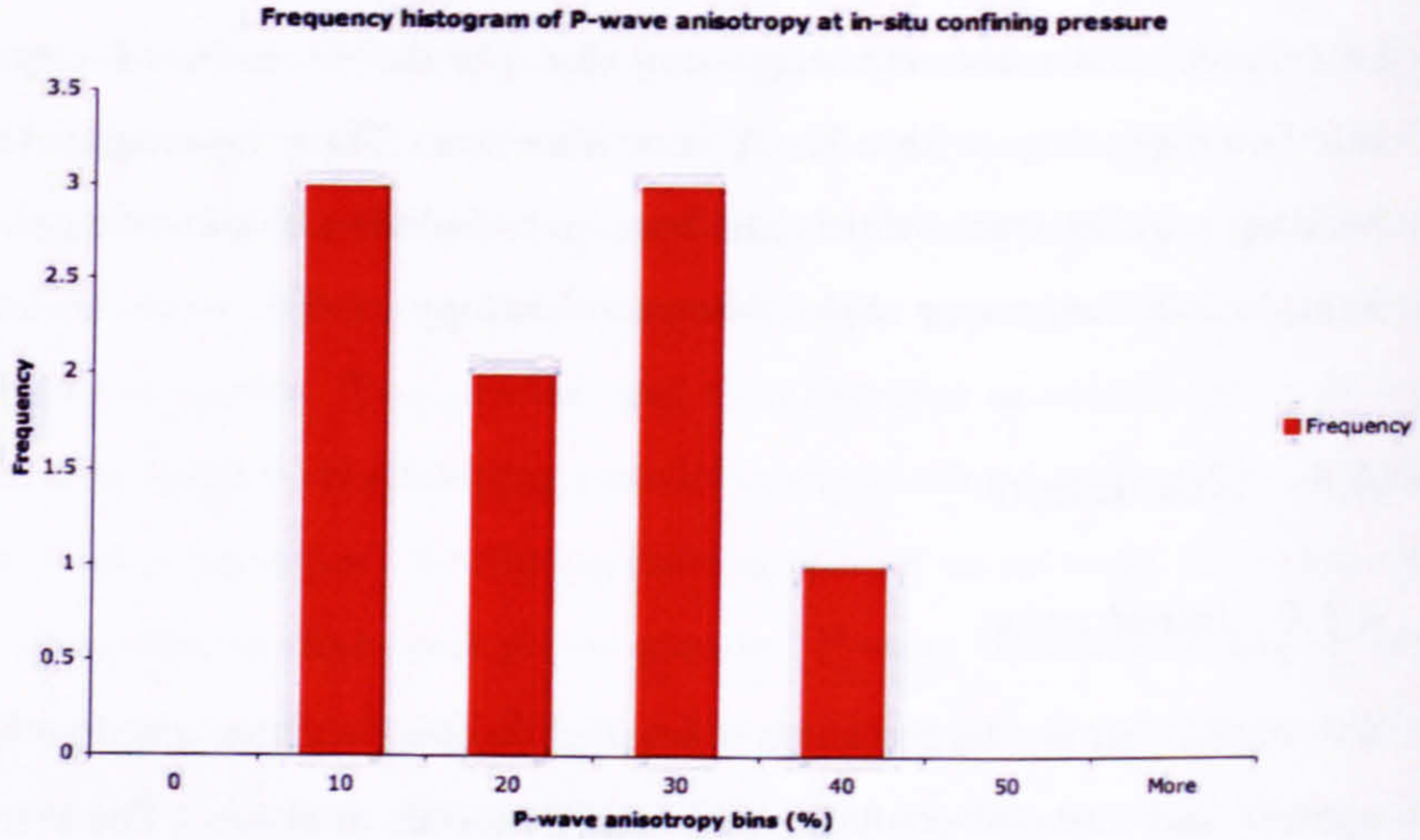

Figure 4.11: *Frequency histogram of the maximum P-wave anisotropy obtained using ultrasonic velocity measurements at in situ confining pressure. The X-axis represents maximum P-wave anisotropy binned into intervals of 10%. The Y-axis represents the frequency of occurrences within a specified bin.*

Table 4.1: *Ultrasonic analyses individual sample categories for Well 206/8-8.*

Sample	Group
1663	2
1784	1
1788	1
1841	1
1909	2
1950	2
2070	1
2073	1
2088	3
2129	2
2192	3
2194	3
2198	3

Table 4.2: *Ultrasonic analyses for Well 206/13a2.*

Sample	Group
1959	2
1963	1
2015	2
2023	2
2028	2
2034	3

> 20%). P-wave velocity measurements: X direction cores typically vary from 2.5km/s to 4km/s, Y direction cores typically vary from 2.5km/s to 4km/s (note X- and Y-cores were used to check for reliability of measurements) and Z direction cores typically varied from 3km/s to 4km/s. Whereas, S-wave velocity measurements: X direction cores typically vary from 2km/s to 3km/s, Y direction cores also typically vary from 2km/s to 3km/s and Z direction cores typically vary from 1.5km/s to 2km/s. The scatter and inconsistency of the S-wave velocity measurements is thought to be largely due to attenuation problems within highly porous and mica-rich samples.

Due to the bedding parallel microfabric of the phyllosilicates and associated bedding parallel micro-porosity the X- and Y-cores show a high-degree of P- and S-wave anisotropy ranging from 20 to 50% (typically illustrated by dumbbell shaped polar plots). Maximum P-wave and S-wave velocity is found when the layer parallel microfabric is aligned parallel to the propagation direction of the elastic wave. Minimum P-wave and S-wave velocity occurs when the microfabric is aligned perpendicular to the propagation direction of the waves. The Z-core can be considered as approximately azimuthally isotropic and shows minimal change in velocity with angle (circular velocity distribution). The samples are broadly termed as having strong VTI symmetry with weak components of orthorhombic symmetry as-well (Figures 4.12; 4.13). The small components of orthorhombic symmetry could however be due to natural heterogeneities within the X- and Y-core half-core.

Group 2 samples had high velocities similar to Group 1 samples (c.4.0km/s) but had weak levels of anisotropy (c. < 10%). P-wave velocity measurements: X direction cores typically vary from 2.5km/s to 3.5km/s, Y direction cores typically vary from 2.5km/s to 3.5km/s and Z direction cores typically vary from 2.5km/s to 4.0km/s. Whereas, S-wave velocity measurements: X direction cores typically vary from 1.5km/s to 3km/s, Y direction cores typically vary from 1.5km/s to 3km/s and Z direction cores typically vary from 1.5km/s to 3km/s.

The X-core of sample 1959 was the only specimen that had atypical velocity measurements for both P- and S-waves. Sample 1959 showed a significant overall decrease in velocity when compared to the other core directions and an element of P-wave anisotropy. Furthermore, when comparing the oil stained sample of 1909 with the cleaned sample it is evident that the velocities are approximately 0.5km/s slower in the clean sample than the oil stained sample. It is evident then that the removal of oil from the pore space and pore throats of a sandstone in a hydrocarbon producing reservoir measurably decreases

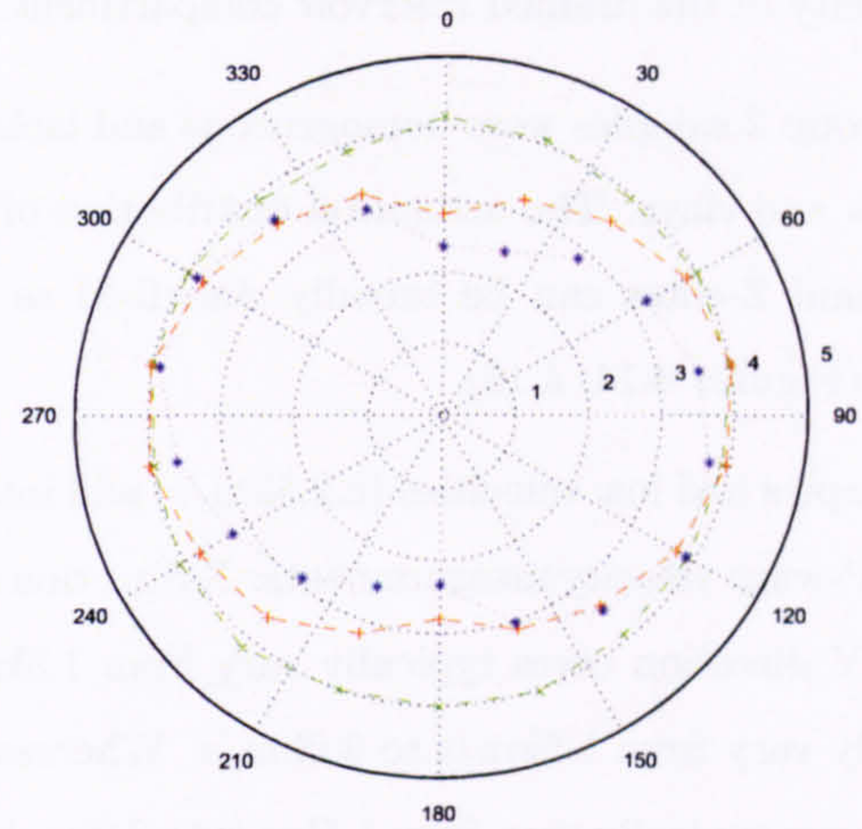

Figure 4.12: *Room temperature and pressure P-wave radial measurements on a Group 1 sample (1784). X-core = red/dashed line; Y-core = blue/dotted line; Z-core = green/dash-dot line. The P-wave polar diagrams are determined from radially acquired measurements on the three core directions (X, Y and Z). Whereas, the S-wave measurements are acquired from axial measurements of the three core directions (X, Y and Z) with the variation of polarisation angle of the transducers.*

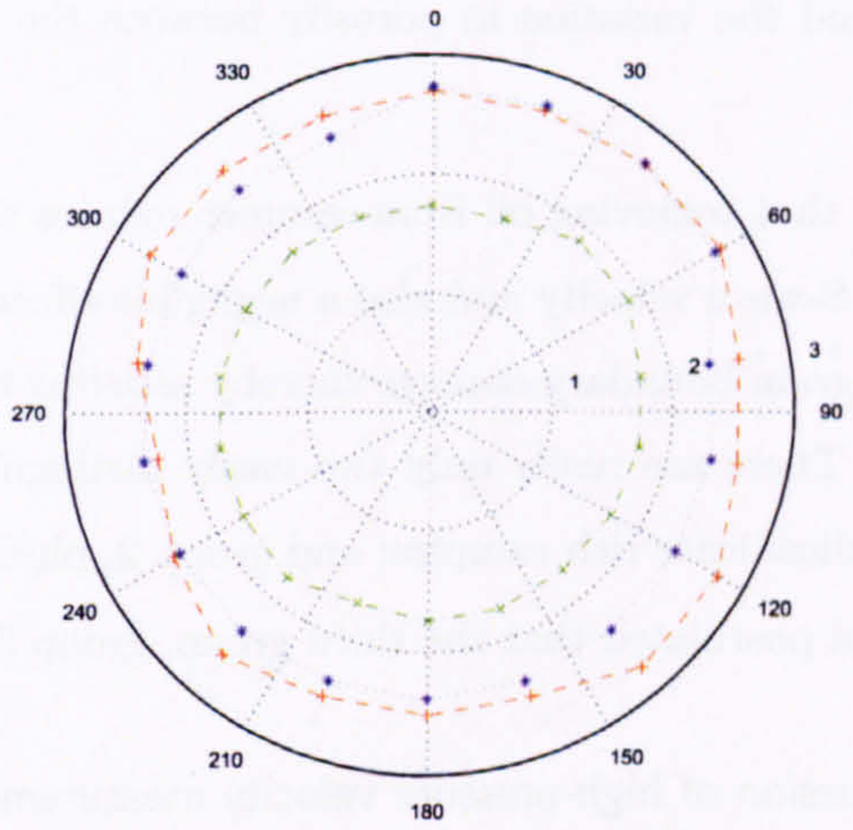

Figure 4.13: *Room temperature and pressure S-wave axial measurements propagating parallel to the core direction on a Group 1 sample (1784). X-core = red/dashed line; Y-core = blue/dotted line; Z-core = green/dash-dot line. The P-wave polar diagrams are determined from radially acquired measurements on the three core directions (X, Y and Z). Whereas, the S-wave measurements are acquired from axial measurements of the three core directions (X, Y and Z) with the variation of polarisation angle of the transducers.*

the bulk velocity of the drained reservoir compartment.

In general Group 2 samples were homogeneous and lacked any significant proportions of phyllosilicates and clays. The azimuthal distribution of P- and S-wave velocities within the X-, Y-, and Z-cores can be broadly described as isotropic with the exception of sample 1959 (Figures 4.14; 4.15).

Group 3 samples had low velocities (c.2.5km/s) and intermediate amounts of anisotropy (c.10-20%). P-wave velocity measurements: X direction cores typically vary from 1.5km/s to 3.0km/s, Y direction cores typically vary from 1.5km/s to 3.0km/s and Z direction cores typically vary from 1.5km/s to 3.0km/s. Whereas, S-wave velocity measurements: X direction cores typically vary from 1.5km/s to 2.0km/s, Y direction cores typically vary from 1.5km/s to 2.0km/s and Z direction cores typically vary from 1.5km/s to 2.0km/s.

Broadly, all the samples showed quite good P- and S-wave data correlation between the various cores. Except for the S-wave measurements in the X-core direction for sample 2034 which showed significant variability when compared to the Y-core direction. In general, Group 3 samples were broadly clean, high porosity sandstones. The low velocities and TI symmetry patterns in some of the samples reflect the high variability in porosity and the variation in porosity between the beds, respectively (Figures 4.16; 4.17).

It was found that removing oil from samples reduces the P-wave velocity but has little effect on the S-wave velocity and also a negligible effect on the anisotropy. The cleaning causes some grain boundary damage thereby assisting the lowering of velocities (Figures 4.18; 4.19). There are really only two easily distinguishable sample groups: group 1, clay and phyllosilicate rich samples; and group 2, phyllosilicate poor samples with high porosity. It is postulated that the third group, group 3, is down to the effect of oil.

4.4.3 Discussion of high-pressure velocity measurements

This section provides a brief overview of the results obtained from elevated hydrostatic confining pressure compressional-wave ultrasonic analysis. The results of the analysis are categorised into their respective groups with overviews of both velocities and anisotropies with respect to increasing confining pressure provided.

Group 1 samples have high levels of intrinsic anisotropy (30-50%), which rapidly decrease with increasing confining pressure. At elevated confining pressures P-wave velocity

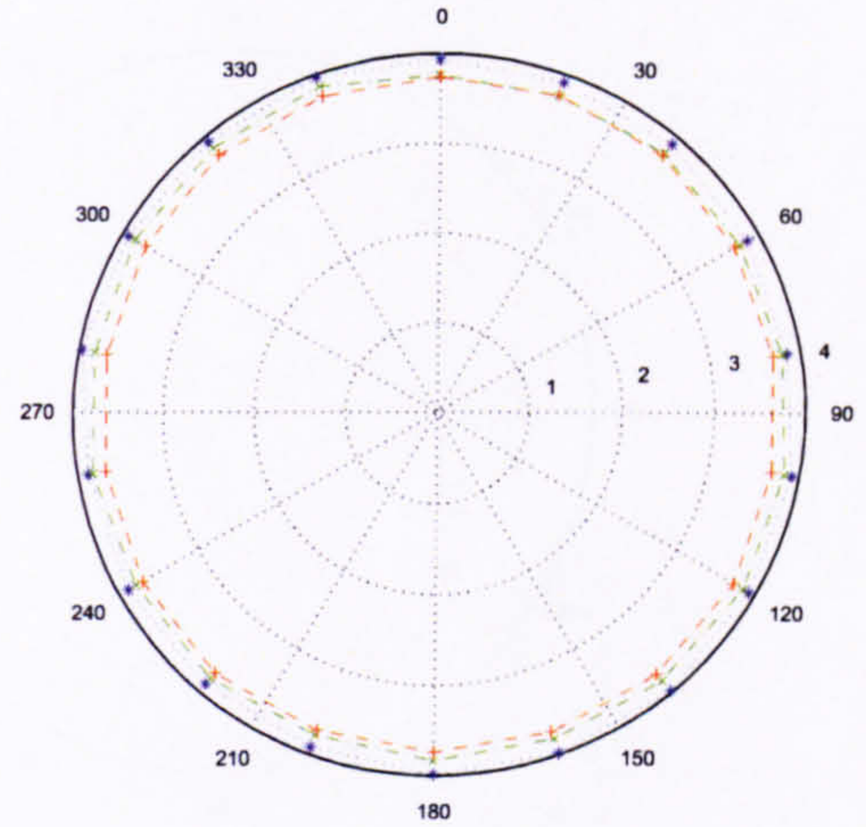

Figure 4.14: *Room temperature and pressure P-wave radial measurements on a Group 2 sample (1909). X-core = red/dashed line; Y-core = blue/dotted line; Z-core = green/dash-dot line. The P-wave polar diagrams are determined from radially acquired measurements on the three core directions (X, Y and Z). Whereas, the S-wave measurements are acquired from axial measurements of the three core directions (X, Y and Z) with the variation of polarisation angle of the transducers.*

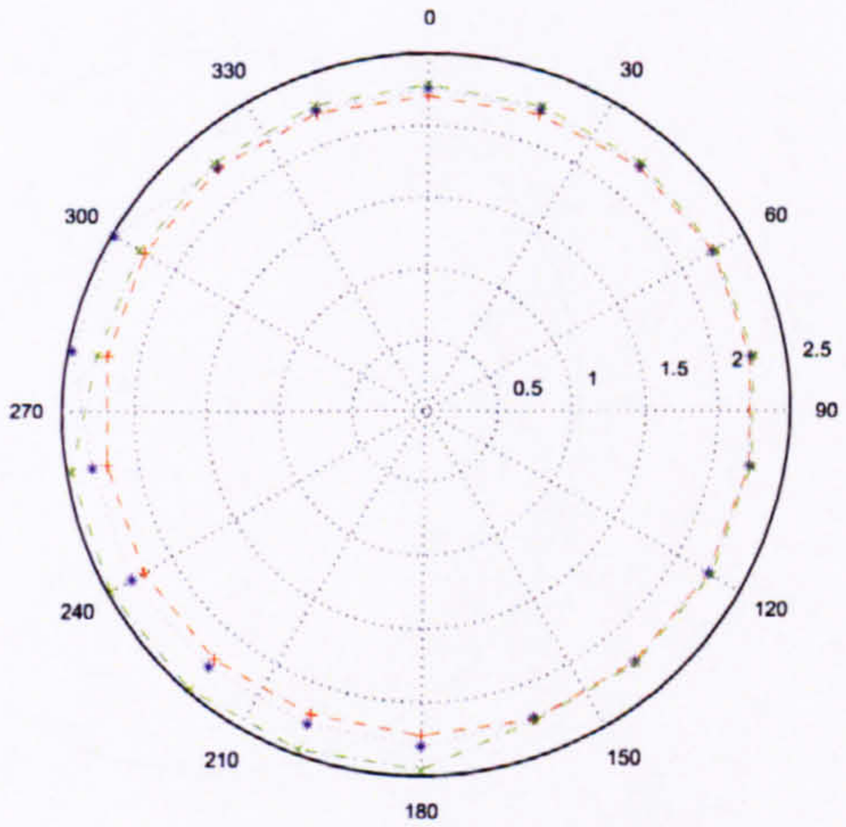

Figure 4.15: *Room temperature and pressure S-wave axial measurements propagating parallel to the core direction on a Group 2 sample (1909). X-core = red/dashed line; Y-core = blue/dotted line; Z-core = green/dash-dot line. The P-wave polar diagrams are determined from radially acquired measurements on the three core directions (X, Y and Z). Whereas, the S-wave measurements are acquired from axial measurements of the three core directions (X, Y and Z) with the variation of polarisation angle of the transducers.*

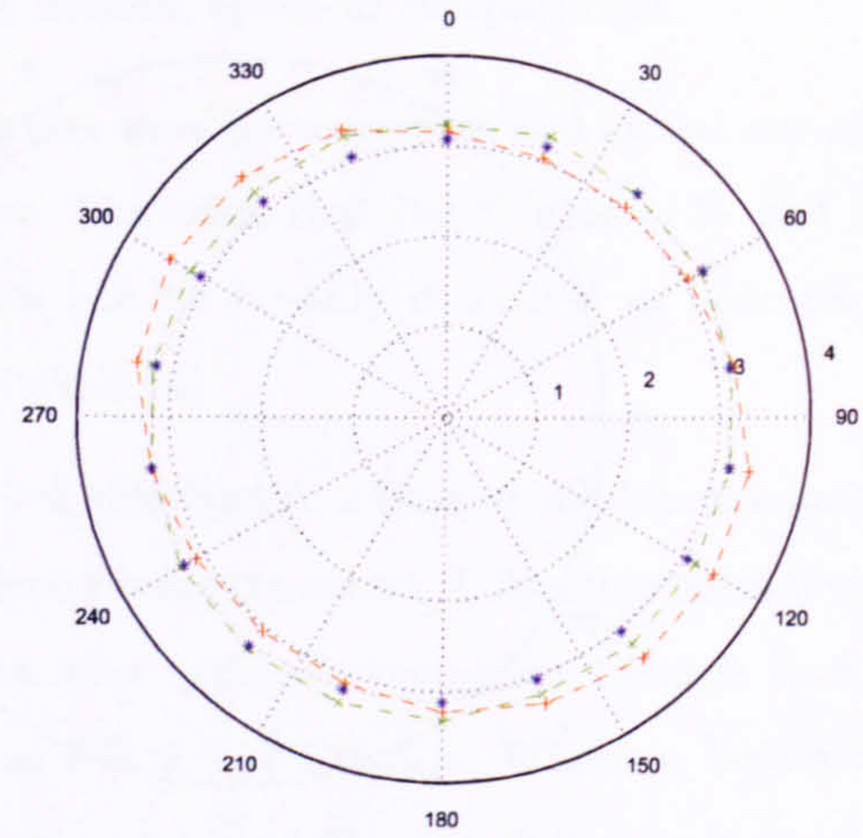

Figure 4.16: *Room temperature and pressure P-wave radial measurements on a Group 3 sample (2028). X-core = red/dashed line; Y-core = blue/dotted line; Z-core = green/dash-dot line. The P-wave polar diagrams are determined from radially acquired measurements on the three core directions (X, Y and Z). Whereas, the S-wave measurements are acquired from axial measurements of the three core directions (X, Y and Z) with the variation of polarisation angle of the transducers.*

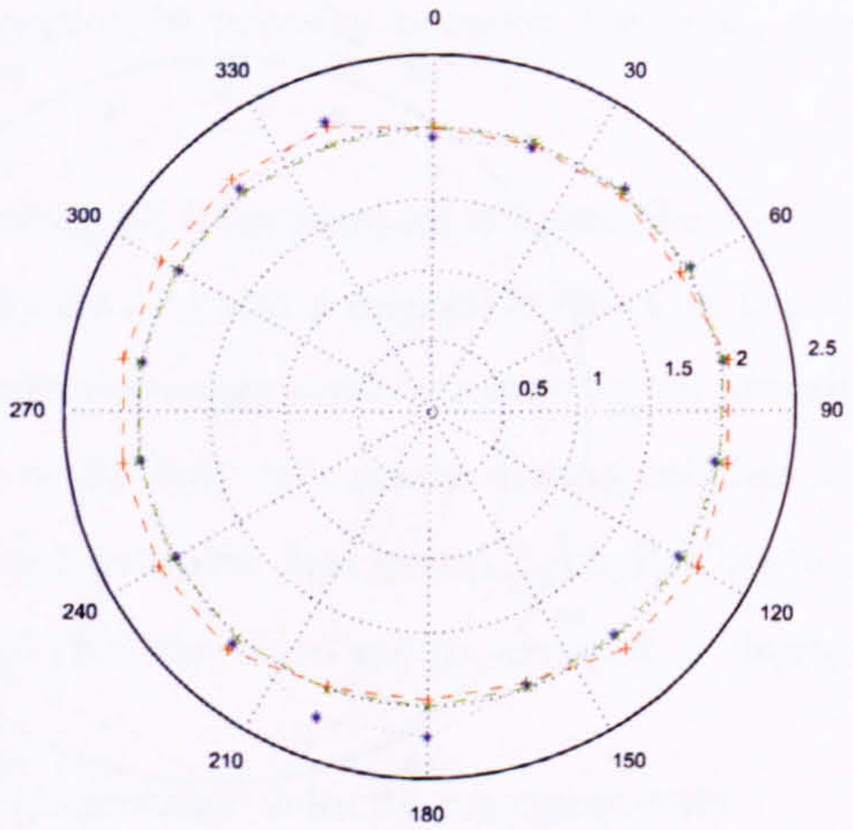

Figure 4.17: *Room temperature and pressure S-wave axial measurements propagating parallel to the core direction on a Group 3 sample (2028). X-core = red/dashed line; Y-core = blue/dotted line; Z-core = green/dash-dot line. The P-wave polar diagrams are determined from radially acquired measurements on the three core directions (X, Y and Z). Whereas, the S-wave measurements are acquired from axial measurements of the three core directions (X, Y and Z) with the variation of polarisation angle of the transducers.*

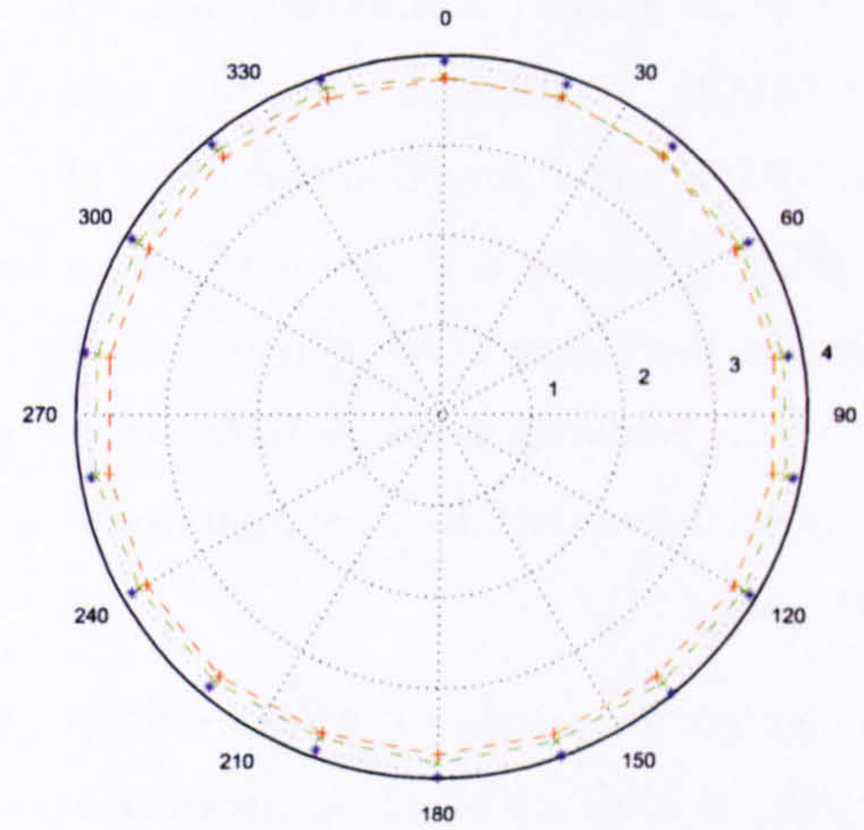

Figure 4.18: *Room temperature and pressure compressional-wave radial measurements on an oil-rich sample (1909 - oil). X-core = red/dashed line; Y-core = blue/dotted line; Z-core = green/dash-dot line. The P-wave polar diagrams are determined from radially acquired measurements on the three core directions (X, Y and Z). Whereas, the S-wave measurements are acquired from axial measurements of the three core directions (X, Y and Z) with the variation of polarisation angle of the transducers.*

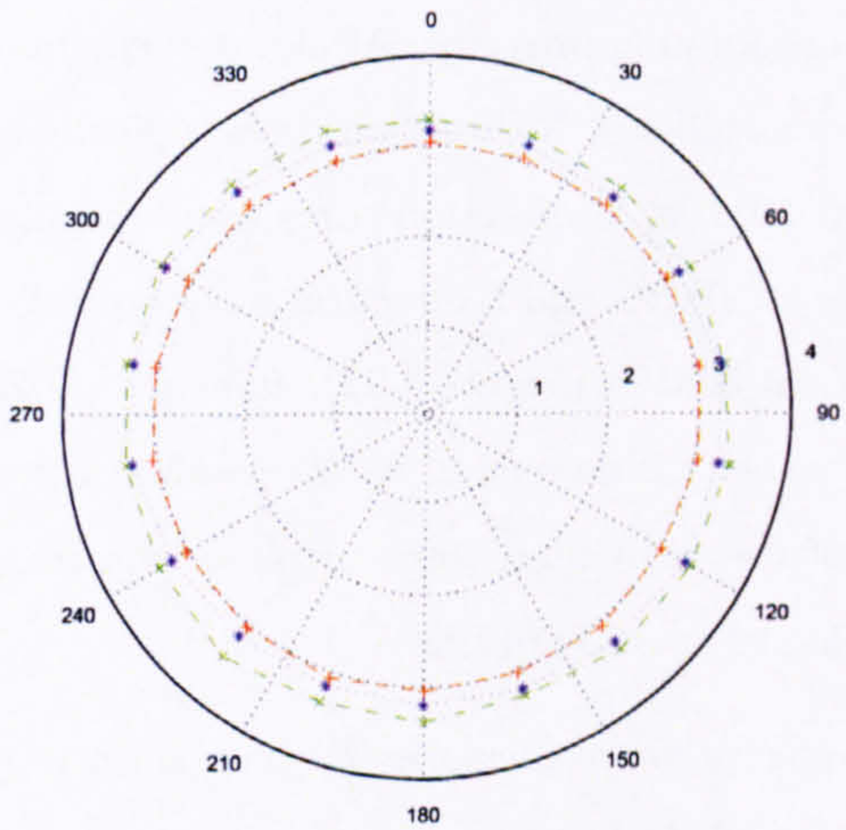

Figure 4.19: *Room temperature and pressure shear-wave radial measurements propagating parallel to the core direction on a sample which has been cleaned of all oil (1909 - no oil). X-core = red/dashed line; Y-core = blue/dotted line; Z-core = green/dash-dot line. The P-wave polar diagrams are determined from radially acquired measurements on the three core directions (X, Y and Z). Whereas, the S-wave measurements are acquired from axial measurements of the three core directions (X, Y and Z) with the variation of polarisation angle of the transducers.*

measurements vary as follows: X direction cores typically rise from 3.5km/s at 10MPa to 4.5km/s at 50MPa, Y direction cores also typically rise from 3.5km/s at 10MPa to 4.5km/s at 50MPa and Z direction cores typically vary from 2.5km/s at 10MPa to 3.2km/s at 50MPa (Figure 4.20). X- and Y-cores have almost unnoticeable velocity differences whereas the Z-core which is perpendicular to bedding is approximately half the velocity. As the confining pressure increases the rate at which the velocity of the individual cores increases decreases asymptotically reaching its maximum velocity at c.50-60MPa (Figure 4.21).

As the confining pressure increases P-wave anisotropy very quickly drops from 30-50% at 10MPa to 20-28% at 50MPa which is at approximately *in situ* conditions. As confining pressure increases the gradient of the slope of the percent anisotropy decreases rapidly over the first 20MPa before approaching an intrinsic value of individual sample anisotropy at 50MPa or approximately *in situ* conditions. Broadly, Group 1 samples have very high intrinsic anisotropy (c.50%) at approximately atmospheric conditions with very rapidly decreasing values as confining pressure increases before reaching a minimum value at stress equivalent to maximum burial depth.

Group 2 and 3 samples have relatively low levels of intrinsic anisotropy which decrease with increasing confining pressure. At elevated confining pressures P-wave velocity measurements vary as follows: X direction cores typically rise from 3.0-3.5km/s at 10MPa to 3.5-4.2km/s at 50MPa, Y direction cores also typically rise from 3.0-3.5km/s at 10MPa to 3.5-4.2km/s at 50MPa and Z direction cores typically vary from 3.2-4.2km/s at 10MPa to 4.2-4.6km/s at 50MPa (Figure 4.22). In sample 2028 X-, Y-, and Z-cores have almost unnoticeable velocity differences. As the confining pressure increases the rate at which the velocity of the individual cores increases, decreases, asymptotically approaching a maximum velocity at c.50-60MPa.

As the confining pressure increases P-wave anisotropy very quickly drops from 5% at 10MPa to 1% at 50MPa which is at approximately *in situ* conditions (Figure 4.23). As confining pressure increases the gradient of the slope of the percent anisotropy decreases rapidly over the first 40MPa before approaching an intrinsic value of individual sample anisotropy at 50MPa or approximately *in situ* conditions. The rapid decrease in anisotropy is thought to be primarily linked to the closure of micro-porosity (preferentially aligned grain boundary cracks) during the incremental increase in confining pressure. Determination of what was the principal cause of the micro-porosity is a non-

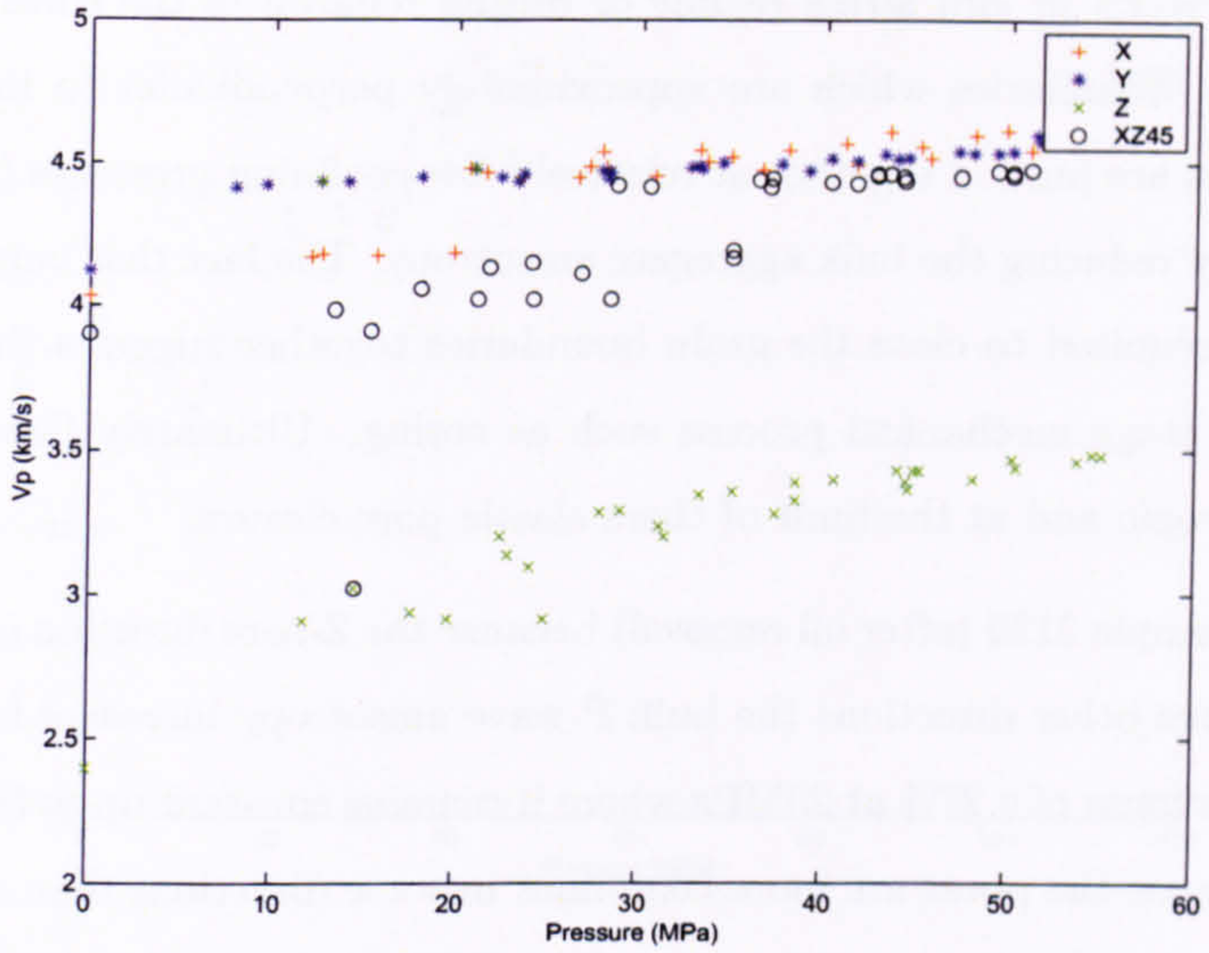

Figure 4.20: *High pressure P-wave velocity measurements typical of Group 1 samples. V_p//Z increases faster than //X and //Y relfecting a closure of bedding parallel porosity (1784). X - red cross, Y - blue star, Z - green cross, and XZ45 (XYZ) - black hollow circle.*

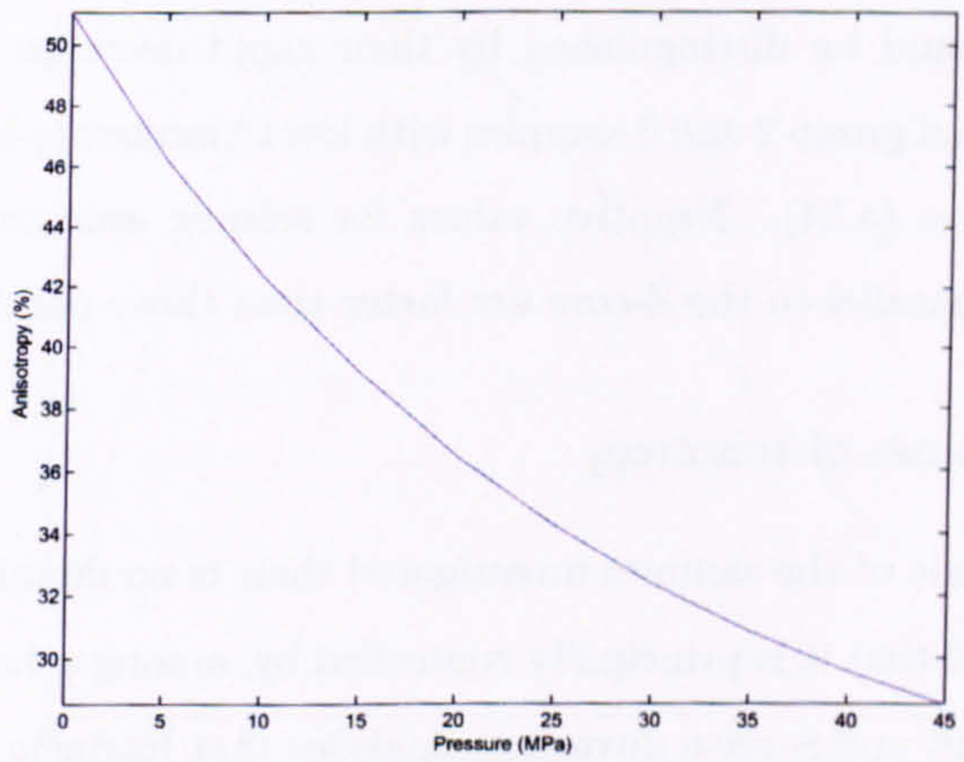

Figure 4.21: *Typical results for a Group 1 highly anisotropic sample. P-wave anisotropy with respect to increasing confining pressure (1784). As the pressure increases the degree of anisotropy quickly decreases before reaching an intrinsic anisotropy (due to microtexture) at in situ conditions. The initial very high level of P-wave anisotropy is probably due to layer parallel relaxation microfracturing.*

trivial matter. It is likely to be either related to stress relaxation on removal from the reservoir's *in situ* stress regime or during removal of the cores in the laboratory. The grain boundaries which are approximately perpendicular to the principal compressive stress are pushed together at relatively low confining pressures (< 20MPa) thus dramatically reducing the bulk aggregate anisotropy. The fact that only low confining pressures are required to close the grain boundaries together suggests that they are related to a late stage mechanical process such as coring. Ultimately Group 2 and 3 samples are isotropic and at the limit of there elastic pore closure.

In sample 2129 (after oil removal) because the Z-core direction is significantly faster than all the other directions the bulk P-wave anisotropy increases from c.5% at 10MPa to a maximum of c.27% at 20MPa where it remains constant up to 50MPa. It is believed that because the pores are more compliant in some directions than others there is a different rate of pore closure with pressure in different directions. Moreover, samples 2192 and 2194 have very similar velocity-pressure profiles. Both 2192 and 2194 exhibit an increase in P-wave anisotropy over the first 20MPa from c.6-9% to c.9-14% respectively. After approximately 20MPa P-wave anisotropy begins to decrease back to approximately its original values at 50MPa.

The results for all the samples are summarised in Figure (4.24). Generally, group 1 samples could be distinguished by their rapid decrease in anisotropy with increasing pressure and group 2 and 3 samples with low to moderate levels of anisotropy as is evident from Figure (4.24). Negative values for seismic anisotropy occur when the velocities recorded parallel to the Z-core are faster than those parallel to the X- and Y- cores.

4.4.4 Causes of anisotropy

On the scale of the samples investigated their is no doubt that wave-velocity anisotropy exists, and that it is principally controlled by, among other factors, stress. It is apparent from the P- and S-wave ultrasonic analyses that intrinsic wave-velocity anisotropy could be controlled by systems of micro-cracks which exist in planes parallel to bedding, and interbedded bedding parallel fine clay-mica rich layers (these are inextricably associated with inter-grain boundary micro-porosity and micro-cracks). For example, in samples which have a defined bedding parallel clay-mica rich layers. It is commonly observed during the hydrostatic loading of the X- or Y- and Z- orthogonal core directions that the Z-core direction is the slowest direction. It is believed therefore that the ultrasonic

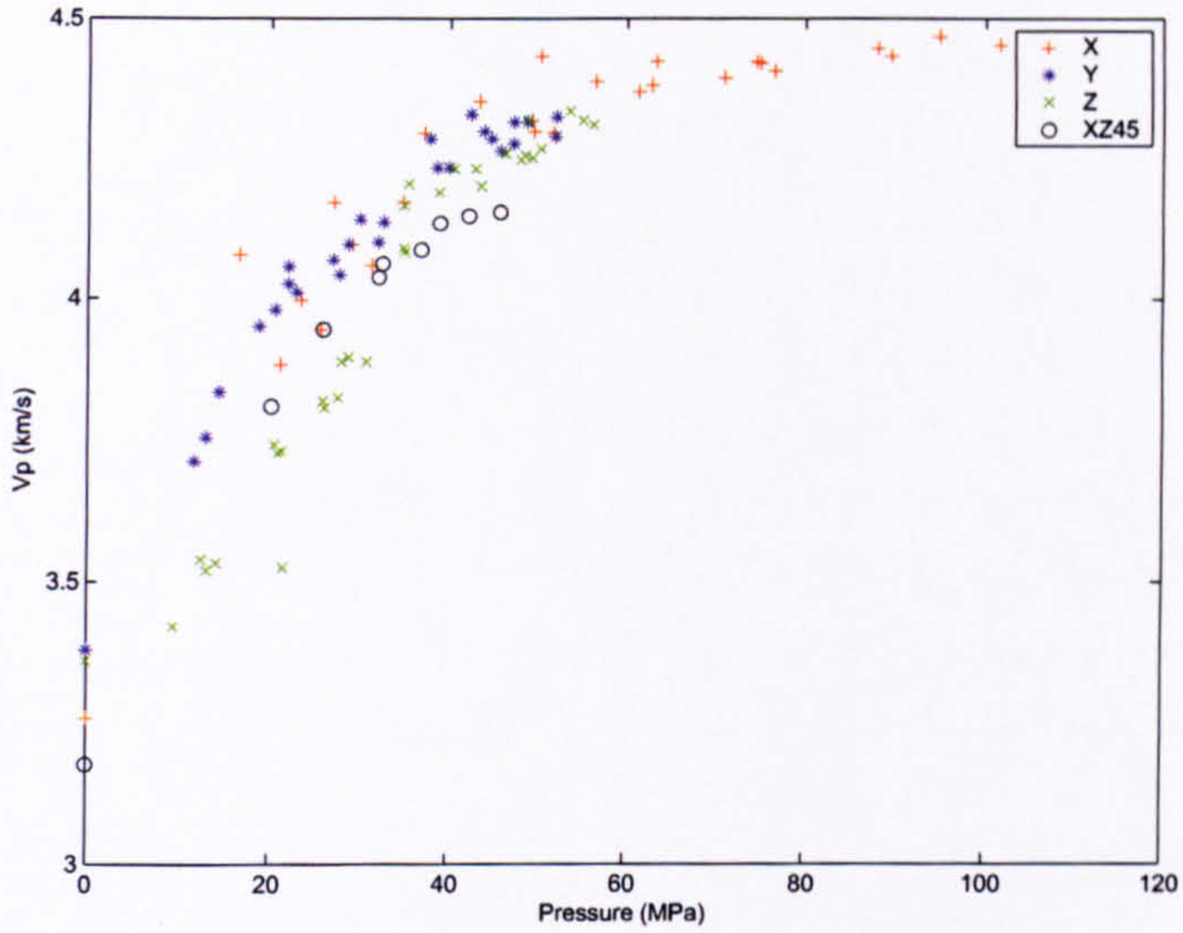

Figure 4.22: *Typical high pressure P-wave velocity measurements for the core plugs, X, Y, Z and XZ45 for a Group 2 and 3 sample (1909 - no oil). As the confining pressure increases, the P-wave velocity for all directions increases at the same rate as cracks and grain boundary fractures are closed concomitantly. X - red cross, Y - blue star, Z - green cross, and XZ45 (XYZ) - black hollow circle.*

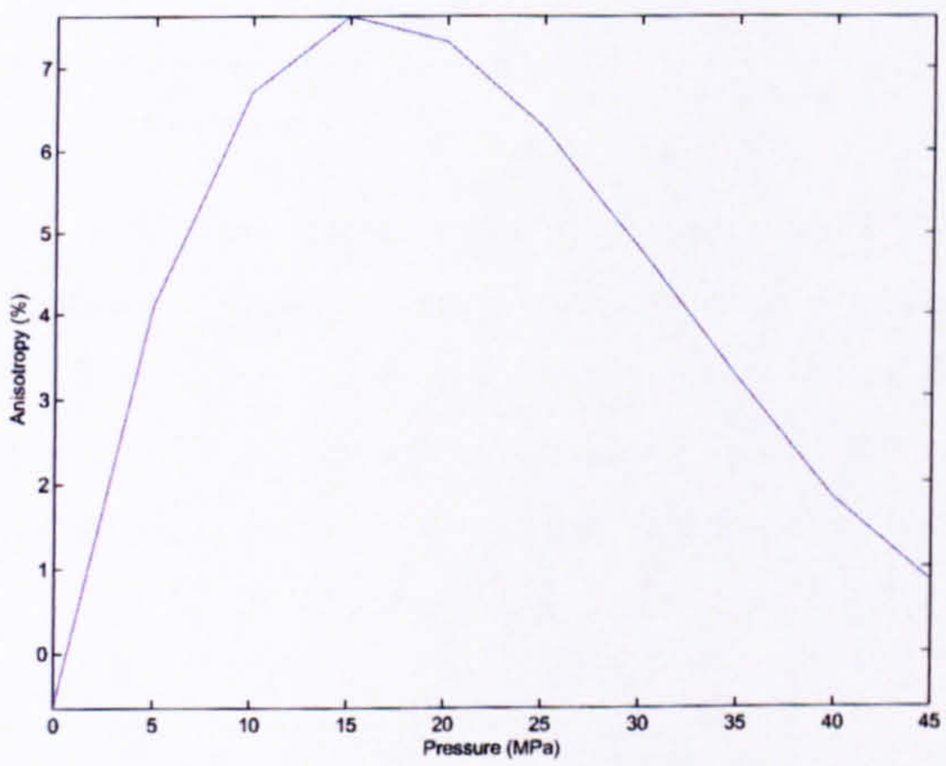

Figure 4.23: *Typical P-wave anisotropy with respect to increasing confining pressure for a Group 2 or 3 sample (1909 - no oil). The total anisotropy increased slightly at low confining pressures before decreasing to isotropy at in situ conditions. The increase in anisotropy at low pressures is believed to be related to the removal of oil from the pore space, thus resulting in additional micro-fractures.*

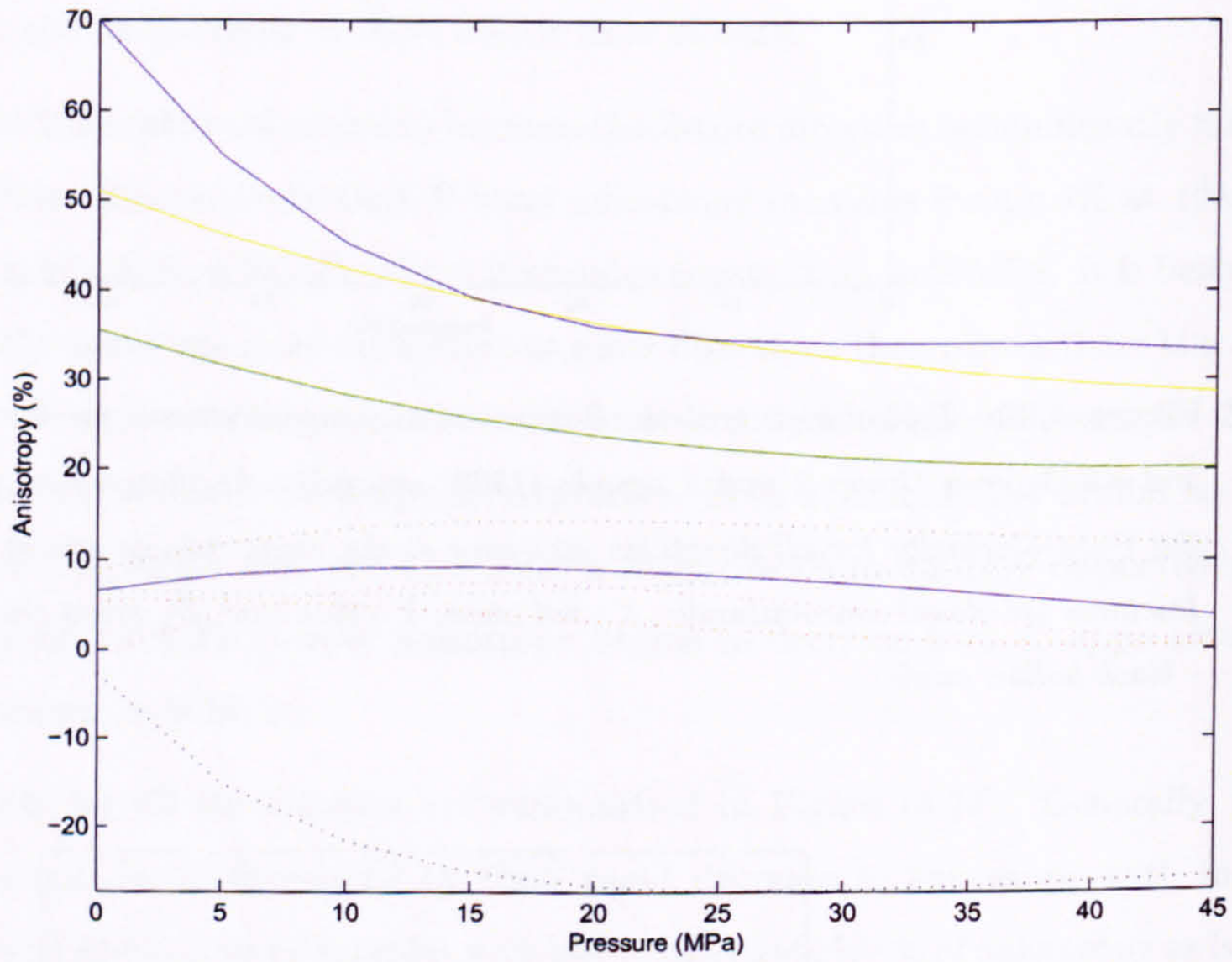

Figure 4.24: *P-wave anisotropy with respect to increasing confining pressure for all the samples. Group 1 samples = solid line, and Group 2+3 samples = dotted. Generally, Group 1 samples have high levels of initial anisotropy which decreases rapidly with the increasing confining pressure. In comparison, the Group 2 and 3 samples have initially low levels of anisotropy which remain approximately isotropic with increasing confining pressure. Group allocation in this diagram is based upon QXRD analyses.*

waves have to pass through bedding parallel micro-cracks, which are associated with grain boundary stress relaxation or through any mica-clay layers. During hydrostatic loading, however, the Z-core velocity can very quickly converge to within velocities which are very similar to those of the X- or Y-core directions. Therefore it can be postulated that the velocity anisotropy, in this case, was principally controlled by micro-cracks (i.e., grain boundaries) which are quickly closed up by the increase in confining pressure. This same theory can be applied to any of the core directions should another core intersect a principal fracture system orientation or identify any grain boundary alignment.

If after the sample has been returned to it's approximated *in situ* confining pressure there still exists a significant degree of anisotropy then it is likely that the sample has an inherent intrinsic anisotropy due to either clay-mica rich layers or a preferential grain boundary or micro-porosity alignment. Whether a sample's suspected intrinsic anisotropy is ultimately controlled by clay-mica layers (clay-mica grain mineral alignment) or by the associated inter-grain boundary micro-porosity at *in situ* confining pressures is not distinguishable as they are inextricably linked.

The results obtained from atmospheric and elevated confining pressure ultrasonic analysis provide useful complementary data sets. Atmospheric analysis provides a quick and easy way of understanding a sample's azimuthal anisotropy and style of symmetry of anisotropy. Whereas, in elevated pressure analysis it provides a fundamental understanding of what the sample would be like at depth, its variation in anisotropy with change in pressure and anisotropic symmetry style. Using apparatus similar to that of this project, where a single core direction is analysed, both bench-top and elevated confining pressure measurements are required to obtain a detailed and fundamental understanding of a sample's anisotropic properties. This is because it is far too time consuming to use the elevated pressure rig used in this study to conduct azimuthal anisotropy analysis at elevated pressures. In general the velocities obtained at atmospheric pressure agree well with the low confining pressure results obtained within the high-pressure rig. In general all high-pressure velocities are significantly faster than the bench top analysis possibly because of relaxation cracks which will be closed very quickly and easily at moderate confining pressures. Hence, in this study bench-top measurements did not provide a realistic representation of the sample's velocities but did provide a useful description of the sample's azimuthal variation in velocity which could not be determined from the high-pressure analysis. Consequently, the velocities obtained at what is approximately

in situ pressure will be used for comparison between previous studies of velocity and anisotropy.

Direct comparison between previous studies of velocity and anisotropy and this investigation will provide a useful guide as to whether the siliciclastic samples studied yield commensurate results. The rocks analysed within this study have never been previously analysed. Detailed mineralogical analyses was conducted on all the samples within this study which will allow for a quantitative comparison between similar samples in previously published work where accurately quantified mineralogical data is available.

When studying velocity anisotropy in the laboratory, it is generally held that observations of P-waves are more diagnostic than observations of S-waves. The sensitivity of response and the larger magnitude variation with changes in stress results from the sensitivities of P-waves to the longitudinal compressional stress along the wave front path. Whereas, S-waves depend equally on the longitudinal and transverse compressional stresses in the sense of wave propagation and polarisation and so show a convolved response to anisotropic stresses. A third principal stress parallel neither to an S-wave propagation direction nor to its polarisation direction has only a negligible effect on the S-wave anisotropy. Hence, in this study only P-wave velocity anisotropy measurements were calculated at elevated confining pressures.

When the results obtained from this study are compared with the P- and S-wave velocities from previous studies it can be seen that the three different groups approximately fall into the categories of weakly-consolidated sandstones and mudstones (Table 4.3). Moreover, there is no notable difference in velocities between Groups 1 and 2. Therefore, with the addition of measurements of seismic anisotropy it could be possible to further sub-categorise previously determined lithologies. For example, it could be possible to determine the difference between a sandstone which has horizontally as opposed to vertically aligned porosity or whether a sandstone is strongly cemented. Previous studies of P-wave velocity anisotropy in siliciclastic reservoir rocks vary from 37% for gas saturated tight-sands and shaly-sands to -0.07% for a brine-saturated sand (Wang 2002). The results obtained from this study show that Group 1 rocks (clay-mica rich) typically have on average 20-30% P-wave anisotropy at *in situ* confining pressure. Whilst Group 2 (clay-mica poor, low porosity) and 3 (clay-mica poor, highly variable porosity) have on average 4-8% and c.12% P-wave anisotropy respectively. The Bentheim sandstone is essentially a Quartzite with a porosity of c.24%. The Rothbach sandstone is also a

highly porous Quartzite but with pore filling clays (illite). Benson et al. (2005) in a recent publication calculated the Bentheim and Crab Orchard sandstones to have a P-wave anisotropy of 4.7% and 19.1% respectively. Benson et al. (2005) also calculated the Bentheim and Crab Orchard sandstones to have a S-wave of 3.0% and 7.6% respectively. It was also calculated that under a hydrostatic pressure the Crab Orchard sandstone decreases from 3% and 7%at 5MPa (P-wave and S-wave) to 1.5% and 1% respectively at effective pressures in excess of 40MPa. The Bentheim sandstone was calculated to have a significantly less decrease in anisotropy with increasing confining pressure (Benson et al. 2005). In comparison Louis et al. (2003) analysed the P-wave velocity and anisotropy of both the Bentheim and Rothbach sandstones under dry and saturated conditions. Louis et al. (2003) calculated the Bentheim and Rothbach sandstones to have a P-wave anisotropy under dry conditions of 11.6% and 4.1% respectively. Whereas, under saturated conditions Louis et al. (2003) calculated the Bentheim and Rothbach sandstones to have P-wave anisotropies of 4.7% and 7.0% respectively.

4.4.5 Application to the subsurface

A fundamental understanding of the variation in P- or S-wave anisotropy with lithology offers another way in which to remotely discriminate between the various properties of siliciclastics in the subsurface. For example, a velocity versus porosity plot is one of the most basic rock physics planes providing information about texture, mineralogy, lithology and diagenesis (Tosaya & Nur 1982). Nonetheless, this simple plot does not allow the accurate identification of the various microstructural properties of lithologies in the subsurface. A good rock physics plane for pore fluid analysis is V_p versus V_s crossplots. Where siliciclastic rocks tend to plot along the Mudrock line (Castagna et al. 1985), while gas saturated rocks fall on the line between quartz point and the origin where V_p/V_s is equal. Furthermore, one of the most well established relationships between velocity and the porosity and clay content of sandstones and shales is that published by Han (1986) which was based upon a series of laboratory studies. Han (1986) found empirical regressions relating ultrasonic velocities to porosity and clay content (Figure 4.25). These were determined from a set of eighty sandstones with porosity's ranging from 3 to 30% and clay fractions ranging from 0 to 55%.

The main problem with using the V_p/V_s ratio as an indicator of fluid and lithology is that various lithologically and microstructurally distinct rocks can have a very similar

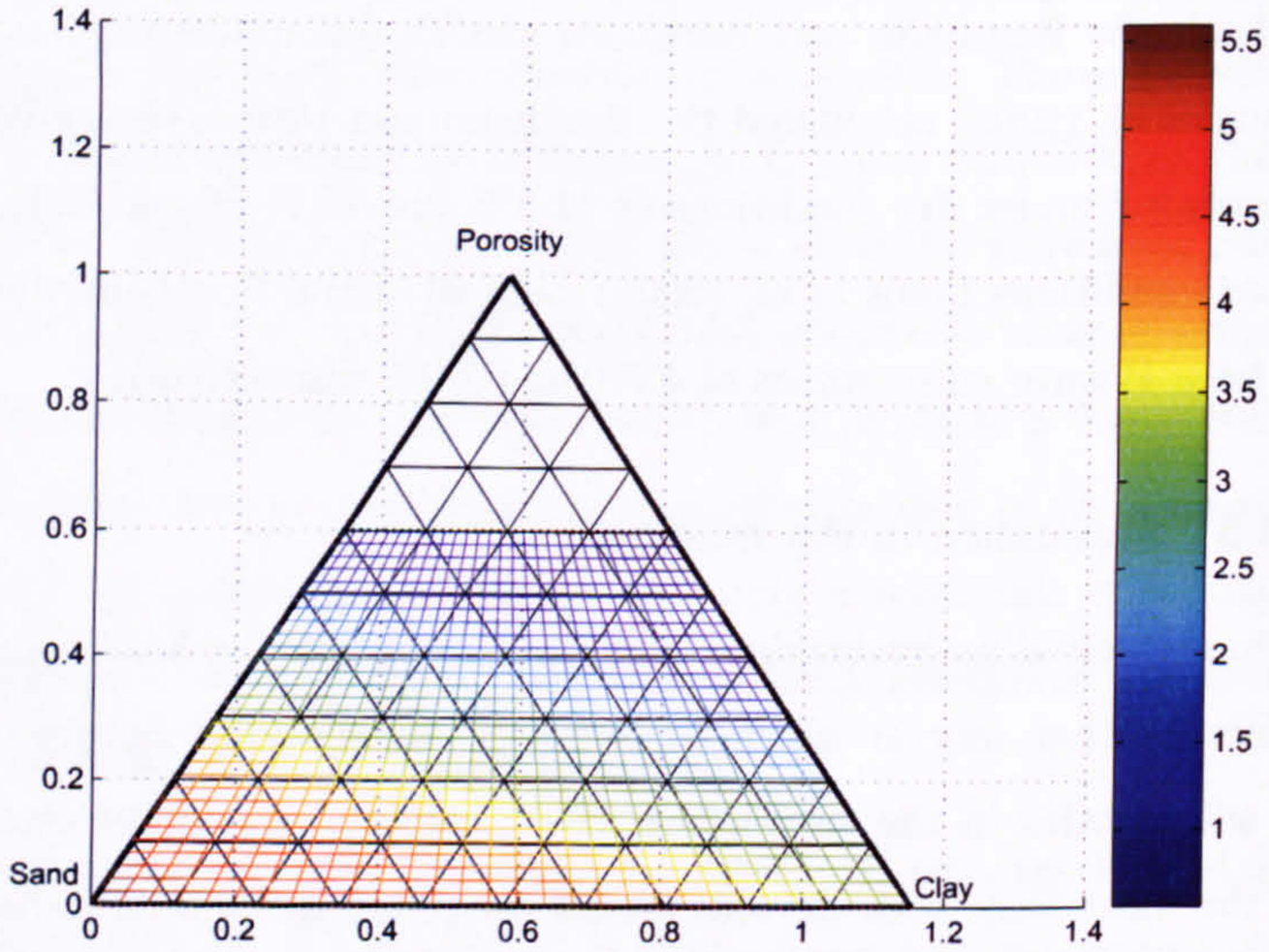

Figure 4.25: *Han's empirical relations for shaley-sandstones: velocity-porosity-clay models. A ternary diagram showing a set of Han's Vp's. The elevation of the mesh corresponds to the velocity values (km/s) and is contoured as shown by the colour bar. The Matlab software used to produce this diagram was written by the current author.*

Table 4.3: *Comparison between previous and current study of wave-velocity and V_p/V_s ratios of various sedimentary rocks. P- and S-wave velocity minimum and maximum (km/s). Group 1, 2, and 3 were calculated from atmospheric measurements. 1. Urmos & Wilkens (1993) and Brevik (1995) 2. Geertsma (1961) and Yale & Jamieson (1994) 3. Han (1986) 4. Jizba (1991) 5. Cadoret (1986), Lucet (1989) and Yale & Jamieson (1994) 6. Strandness (1991) 7. Blangy (1992) 8. Salisbury (2000) 9. Johnston & Christensen (1995).*

Type	V_p min.	V_p max.	V_s min.	V_s max.	V_p/V_s min.	V_p/V_s max.
Chalks 1	1.53	4.30	1.59	2.51	1.62	1.79
Dolomites 2	3.41	7.02	2.01	3.64	1.59	2.09
Sandstones 3	3.13	5.52	1.73	3.60	1.53	1.89
Tight sandstones 4	3.81	5.57	2.59	3.50	1.42	1.68
Limestone 5	3.39	5.79	1.67	3.04	1.72	2.04
High-porosity sandstones 6	3.46	4.79	1.95	2.66	1.68	1.88
Weak sandstones 7	2.43	3.14	1.21	1.66	1.88	2.24
Mudstone 8	2.61	4.49	2.35	3.79	1.11	1.18
Shale 9	3.89	4.89	1.89	2.63	2.05	1.85
Group 1	2.50	4.00	1.50	3.00	1.67	1.33
Group 2	2.50	4.00	1.50	3.00	1.67	1.33
Group 3	1.50	3.00	1.50	2.00	1.00	1.50

V_p/V_s ratio (Table 4.3). Analysis of Table (4.4) shows that having an understanding of the variation in P- or S-wave anisotropy provides more information about the structure and lithology of a sample in the subsurface than from analysis of the V_p/V_s ratio alone. For example, the V_p/V_s ratios of the Group 1 and Group 2 samples are both very similar and do not vary much throughout the samples within each group. By taking into consideration the bulk aggregate anisotropy it then becomes possible to differentiate between a clay-poor and clay-rich rock if the clays are grain supporting and not pore lining. Furthermore, it also provides detailed information on how the rock might respond to pressure variations caused by drilling or injection that V_p/V_s ratios would not provide any information on.

The observations of high-pressure ultrasonic velocity-anisotropy provide an insight into how a sample's anisotropy might vary with increasing depth. Moreover, in conjunction with the bulk aggregate elastic tensor predictions as determined by electron microscopy the data provides a methodology to determine crack density which in turn can be used to provide bedding scale data for reservoir models and intelligent well positioning programs. The elevated pressure ultrasonic analyses also provides a means of understanding how the observed anisotropy in a particular lithology in a reservoir might respond to a re-injection program. For example, if a time-lapse anisotropic survey was conducted the variation in anisotropy within the different horizons would provide a deeper understanding of the types of rocks present and the orientation of their fractures.

There a several known problems of using laboratory obtained ultrasonic data which must be considered when relating the results to a larger scale (i.e., reservoir or unit scale). All the ultrasonic tests in this study were conducted under dry conditions which is an unlikely assumption in the real world. Which means that ideally the dry laboratory results should be transformed using some known relation such as the Gassmann relation (Gassmann 1951). Gassmann's equations allow the prediction of saturated rock moduli from dry rock moduli and vice versa. Essentially, Gassmann's relations are used to estimate the change of low-frequency elastic moduli of porous media caused by a change of pore fluids. Moreover, the scale of the detected anisotropies in the laboratory is also far smaller than that which would be detected by field-wide or even wireline log scale seismic attribute analysis. Hence, upscaling presents itself as a major issue concerning the elastic properties of rocks. Not necessarily the best but has proved to be useful is the Effective Medium Theory (EMT) which is based upon the assumption that the average

Table 4.4: *Comparison between previous studies and the current study of wave-velocity anisotropy for different types of siliciclastics. Anisotropy is calculated in percent. Dry/Sat. refers to whether the ultrasonic analysis was conducted under dry or fluid saturated conditions. Low and high refers to the pressure at which the analysis was conducted. Low - atmospheric temperature and pressure; High - in situ confining pressure. 1. - Benson et al. (2005) and 2. - Louis et al. (2003).*

Name	P-wave Low	P-wave High	Dry/Sat.
Group 1	30-60	20-30	Dry
Group 2	0-10	0-2	Dry
Group 3	0-10	0-5	Dry
Bentheim 1	5	4	Dry
Bentheim 2	5	-	Sat.
Crab Orchard	19	1	Dry
Rothbach	7	-	Sat.

rock properties on a macroscopic scale are statistically homogeneous (Gueguen et al. 2006). Nonetheless, EMT becomes ineffective when the degree of heterogeneity is too large because basically EMT is a perturbation theory that fails beyond some point.

4.5 Conclusions

It is possible to draw the following conclusions from the experimental observations in this chapter.

On the basis of the atmospheric ultrasonic velocity analyses three distinct groups could be identified:

Group 1 - high velocities (c.3.8km/s), and strong anisotropy (> 20%). Probably due to the bedding parallel microfabric of the phyllosilicates, and associated bedding parallel micro-porosity.

Group 2 - high velocities (c.3.8km/s), and weak anisotropy (< 10%). These samples had high velocities and weak anisotropy. They were generally oil stained, homogeneous and lacked significant proportions of phyllosilicates and clays

Group 3 - low velocities (c.2.5km/s), and intermediate amounts of anisotropy (c.10-20%). These samples were broadly clean, high porosity sandstones.

The conclusions determined from the atmospheric ultrasonic analysis provide a detailed understanding of the azimuthal variation in velocity and anisotropy with respect to lithology. A clay-mica rich sample (> 15%) is expected to have no azimuthal variation in velocity within the bedding plane. Whereas, a quartz-feldspar rich sample could have a strong azimuthal variation in velocity due to mineral grain alignment and hence grain boundary or micro-porosity alignment. Furthermore, the bench top analyses allow a far more detailed investigation into lithology velocity-anisotropy relationships because of the speed of analysis. The bench top analyses provide a simple and convenient way to quickly characterise a samples group. The results of the atmospheric pressure ultrasonic analysis are in agreement with the high-pressure analysis.

On the basis of the high pressure ultrasonic velocity analyses two distinct groups could be identified. The third group is not identifiable at high pressure:

Group 1 - high velocities (c.3.5-4.5km/s), and strong intrinsic anisotropy (20-30%). Likely to be due to the high phyllosilicate, and clay content. P-wave anisotropy very

quickly decreases during an increase in confining pressure.

Group 2 - group 2 samples (likely contains both group 2 and 3 atmospheric determined samples) have low to moderate levels of anisotropy (c.1-5%). Ultimately isotropic at the limit of elastic pore closure. P-wave velocity anisotropy for the group 2 samples initially increases, and then decreases with increasing confining pressure (c.3.0-4.0km/s). Using the methodology of Silver & Chan (1988), and two split shear-wave transducers the orientation, and magnitude of shear-wave anisotropy could be quantified in one-single measurement. This novel approach described provides both a quick and very useful way of understanding a samples anisotropy, orientation of heterogeneity and a clever way of determining the magnitude of heterogeneity in a quantifiable manner. The approach as determined by Silver & Chan (1988) has been in use for some years within research into the deep-earth using seismological techniques. As a result of this study it has been shown that on the scale of ultrasonic analysis the main controlling parameter of wave-velocity anisotropy is grain boundary micro-porosity. This technique would most lend itself to the dynamic ultrasonic analysis of fractured or controlled-fractured samples during hydrostatic or anisotropic loading. This in turn would then provide a means of analysing the velocity-anisotropy stress dependence of different fracture systems on different lithologies.

Chapter 5

Petrofabric analysis

5.1 Introduction

It is commonly understood that seismic anisotropy is controlled by: LPO (lattice preferred orientation), the non-random spatial distribution of mineral phases, aligned porosity, and aligned fractures (Crampin 1981, Babuska & Cara 1991, Mainprice et al. 2000, Wendt et al. 2003, Kendall et al. 2006, Valcke et al. 2006). Therefore, in principle, any directional variation in these variables could then be inferred from seismic velocity anisotropy observations alone. Direct laboratory ultrasonic velocity measurements have traditionally been used to investigate the seismic velocity anisotropy of various rock properties. However, this type of investigation does not allow discrimination of the contributions from the various microstructural variables. Therefore, the relative contribution to observations of seismic anisotropy in sedimentary rocks from each of the individual causes is not well understood.

Hence, laboratory ultrasonic velocity measurements made on well microstructurally characterised rock aggregates could be used to improve the understanding of the controls of observations of seismic anisotropy. Until recently, the complex nature of the Earth's crust particularly when compared to the mantle has made it difficult to justify assumptions about the continuous microstructural elements on the scale of a seismic wavelength. Progress, however, in the resolution of controlled source seismic exploration and processing techniques have now made it possible to explore whether any link exists between microstructural observations and seismic data in crustal rocks. The aim of this part of the study was to quantify the LPO (fabric strength) of the constituent mineral phases

in a suite of siliciclastic hydrocarbon reservoir rocks using electron microscopy, EBSD (electron backscattered diffraction). Presented within this chapter is an overview of a SEM and its applications to BSE imaging and EBSD analysis. The results of EBSD petrofabric analyses are presented as lower hemisphere pole figure projections. In turn, the results of these analyses have been used to calculate the intrinsic seismic anisotropy due to the LPO of mineral phases alone (Chapter 6).

SEM-EBSD is a relatively robust technique to determine the lattice preferred orientation of sedimentary rock forming minerals (Valcke et al. 2006). SEM-EBSD, however, commonly encounters problems associated with the automated indexing of minerals which possess strong basal cleavage planes, such as, phyllosilicates and clay minerals (Ullemeyer et al. 2000). Phyllosilicates in sedimentary rocks are often very fine-grained, have poor crystal structure, and consistently align their foliation parallel to the SEM electron beam. This means that when the electron beam is incident upon a platy-mineral grain it does not reflect off any of the crystal's lattice planes, thus providing a diffraction pattern which has poor contrast and weakly identifiable Kikuchi bands. What is required, therefore, is an accurate and reliable technique that will allow the statistical determination of the *3D* orientation of phyllosilicates in thin-section.

The most commonly employed technique in the analysis of phyllosilicate mineral orientation is EBSD manual indexing. Manual indexing is simply the process of determining the mineral's orientation by hand and eye analysis of the Kikuchi band patterns. This methodology is particularly time consuming, nevertheless, in past experiments of this nature it has proven to be a very reliable technique (Valcke et al. 2006). The manual indexing of phyllosilicate-rich samples was used in this project as a means of not only determining the orientation but as a way of verifying the results obtained from alternative methodologies.

An alternative approach to the determination of phyllosilicate orientation is based upon the Bingham distribution. Bingham's distribution represents the portion of a trivariate Gaussian distribution that intersects the surface of a unit sphere, with varying ellipsoidal shapes of the underlying Gaussian contours hence producing a variety of distributional forms on the sphere (Cheeney 1983). The Bingham model is simplified here by making some underlying assumptions about the expected *3D* orientation distribution of phyllosilicate mineral phases. The first is that the preferred orientation produced by compaction has uniaxial symmetry (azimuthally symmetrical about a single axis). The second is

that the distribution can be described by two parameters in the Bingham distribution (Bingham 1974). Finally, that the distribution of orientations of lines of intersection of phyllosilicate basal planes is related to the uniaxial preferred orientation by projection.

5.2 Scanning electron microscope - fundamentals

The SEM (scanning electron microscope) uses a finely focused electron beam scanned across a sample's surface to produce high-resolution images. A SEM can resolve features much smaller than those of an optical microscope because it uses electrons to image the sample's surface as opposed to light waves. In the SEM, high-energy electrons are produced by a cathode filament (usually tungsten but other materials can be used e.g., LaB6) and are accelerated down the electron column (Goldstein et al. 1992). The electrons pass through a series of coils and electromagnetic condenser lenses progressively focusing the beam diameter (Figure 5.1) (Reed 1996). The spatial resolution is ultimately dependent upon the diameter of the incident electron beam on the sample surface and is approximately $1\mu m$ for a tungsten filament in a thermal emission SEM (Goldstein et al. 1992).

Upon incidence with the surface of the sample the electrons travel through the target in a random manner until they are either ejected from the sample through elastic scattering (no energy loss) or come to rest within the target by inelastic scattering (significant energy loss) (Goldstein et al. 1992). In either case the interactions can result in other electro-magnetic signals. The various types of signals produced from the interaction of the electron beam with the specimen include: secondary electron emission, backscattered electrons, Auger electrons, X-rays, and cathodluminescence (Figure 5.2). Typically the interaction depth for electrons is approximately $0.1 - 3\mu m$ (Reed 1996). One of the most widely utilised signals is the secondary electron emission. A secondary electron is produced when an electron from the SEM electron beam collides with a specimen's atom and losses energy to it. Secondary electron images are particularly useful for examining surface structure and provide the best resolution of any of the signals. A backscattered electron is defined as one which has undergone a single or multiple scattering events and escapes with an energy greater than 50eV (Reed 1996). Backscattered electrons are produced as the result of elastic collision with the atoms of the sample and usually retain 80% of their original energy. The number of backscattered electrons produced increases

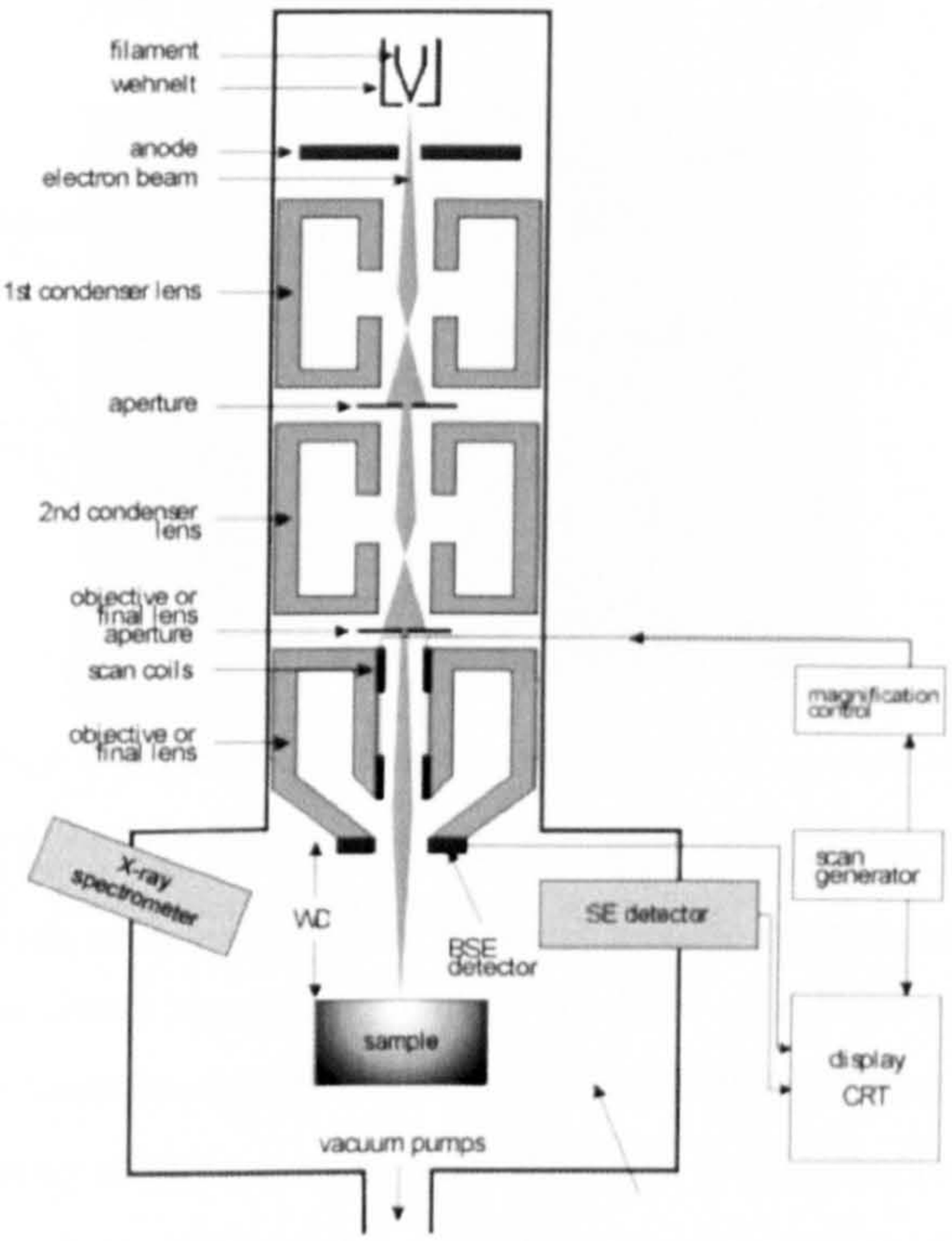

Figure 5.1: *Diagram of the main components of a scanning electron microscope (Goldstein et al. 1992).*

with increasing atomic number of the specimen (Goldstein et al. 1992). Elements that are of higher atomic number will produce more backscattered electrons and will therefore appear brighter (Figure 5.3) (Lloyd 1987). The detector for BSEs is very different to that used in the detection of secondary electrons, in that, it uses silicon devices. Only those electrons that travel in a straight path from the specimen to the detector go towards forming the backscattered image. So that enough electrons are collected to produce an image, SEMs use quadrant backscattered detectors positioned directly above the specimen. The most prominent draw back of BSEI (backscattered electron imaging) is that if the minerals within the sample have very similar properties. For example, in BSEI both quartz and certain types of feldspar (e.g., plagioclase) have approximately the same atomic contrast (sometimes referred to as Z-contrast), which makes identification of these two very different minerals extremely difficult without the use of an EDS (energy dispersive spectroscopy).

In summary SEM-BSE imaging can be used in conjunction with other techniques, such

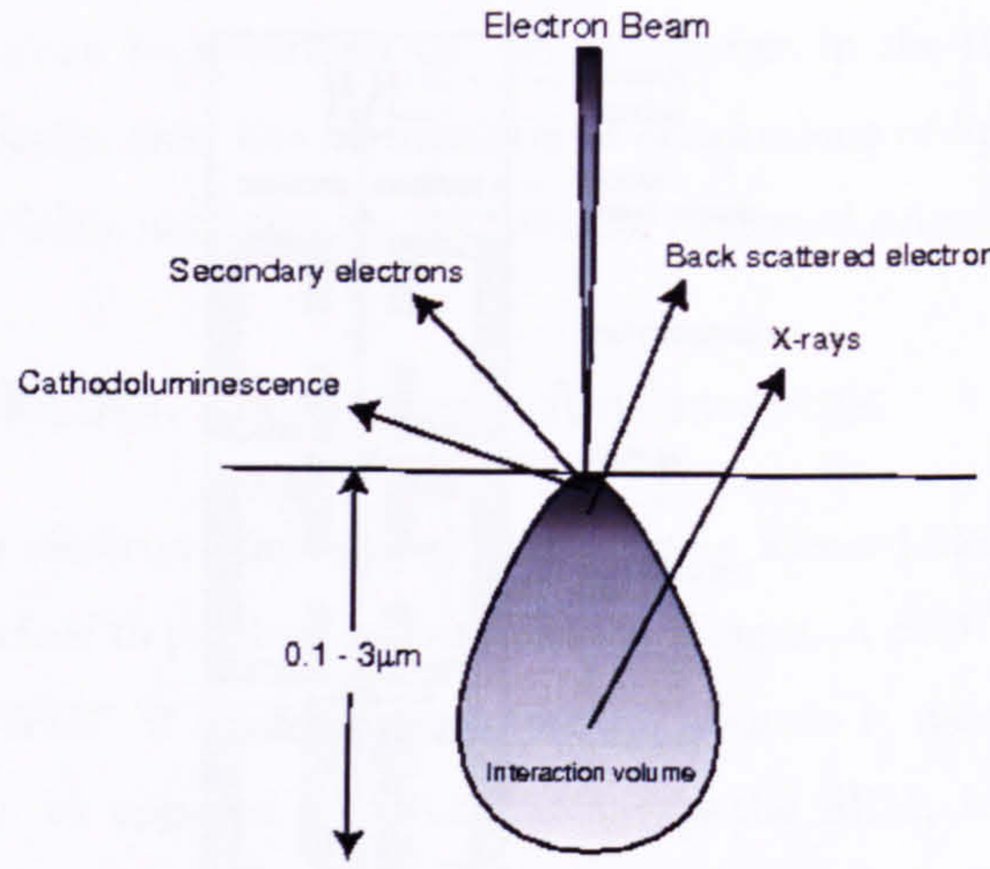

Figure 5.2: *Scanning electron microscope electron beam and sample interaction. Signals generated by interactions between specimen atoms and incident electron beam. Backscattered electrons (BSE) are SEM beam electrons that have undergone elastic scattering. The BSEs are produced from the uppermost third of the interaction volume.*

as optical microscopy, to provide a thorough understanding of the petrography and microtexture of an aggregate (Trimby & Prior 1999).

5.3 Electron backscattered diffraction - introduction

EBSD (Electron backscattered diffraction) is a technique for obtaining crystallographic information in the SEM. Basically, EBSD uses a beam of electrons which are directed onto a tilted crystalline sample. The electrons undergo various interactions with the atoms in the crystal's lattice and some of the electrons emerge from the sample to project onto a fluorescent screen. Projected onto the screen is the sample's diffraction pattern. The symmetry and appearance of the pattern is related to the crystal structure at the point where the beam meets the sample. EBSD has many uses, including the complete quantification, and characterisation of the crystallographic orientation of rock forming minerals (Venables & Harland 1973). Automated EBSD has now become a well established analytical technique to determine *3D* crystallographic orientation (e.g., Prior et al. 1999, Mainprice et al. 2000, Wendt et al. 2003, Lloyd & Kendall 2005, Valcke et al. 2006).

EBSD analysis can be conducted on most SEMs as the only requirements are a tilted

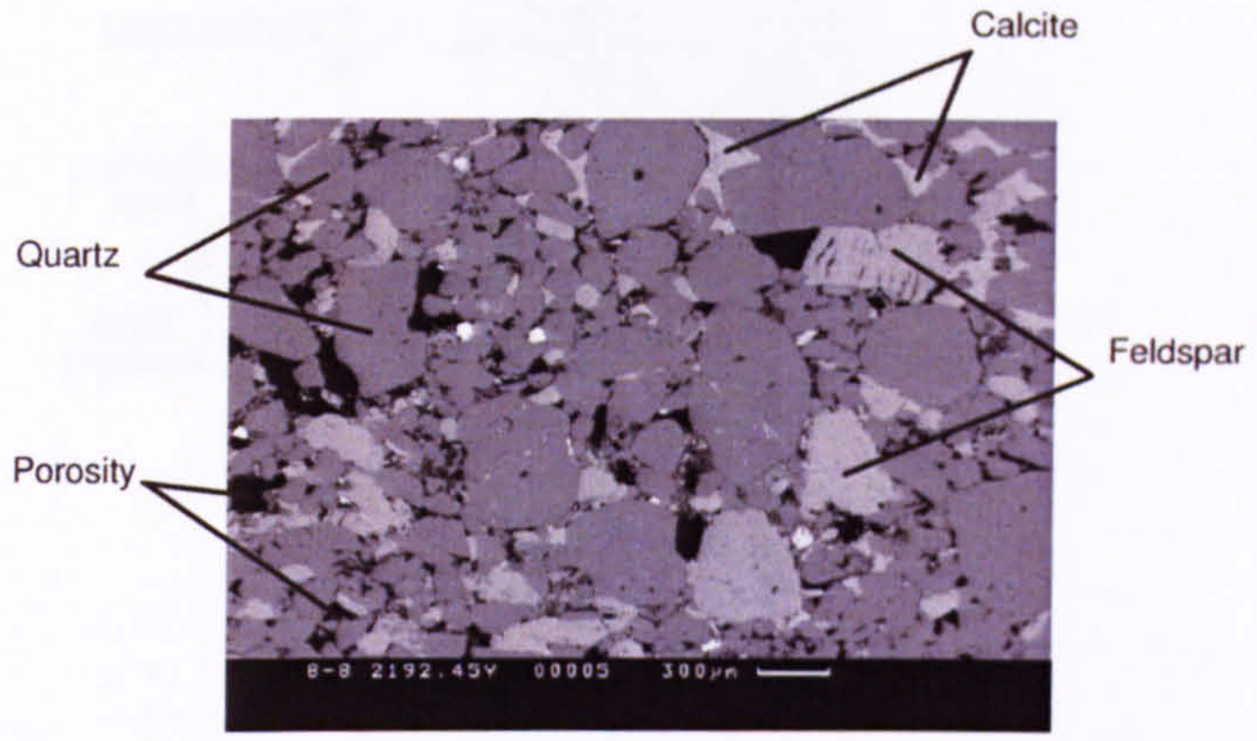

Figure 5.3: *Typical high quality backscattered electron image of a relatively mature sandstone which comprises of mainly quartz, feldspar, calcite, and minor proportions of zircon and apatite. The pore space is black. Sample number 2192m from Well 206/8-8.*

sample and a suitable detection system. The latter have been designed with the intention of completely optimising EBSD geometry and therefore performance. The system used in this study was a CamScan 4 SEM, with a low-light camera, FSED (forescatter electron detector) and HKL Technology Channel 5 software (including frame grabber i.e., non-digital).

5.3.1 Electron backscattered diffraction - fundamentals

The sample is placed in the SEM's specimen vacuum chamber and tilted to a high-angle to the electron beam (approximately 75^o). The SEM electron beam strikes the inclined sample surface. The BSE's that satisfy the Bragg Equation (Chapter 3; Equation 3.1), diffract to define two cones of electrons which project onto a fluorescent (phosphor) screen (Prior et al. 1999). Diffraction of these electrons occurs simultaneously on all of the sample's atomic lattice planes. The sample is tilted at a high angle to the electron beam, to optimise both the contrast in diffraction pattern and the fraction of backscattered electrons (Goldstein et al. 1992). These large angle cones are known as Kikuchi lines or bands. Each corresponds to a particular lattice plane within the incident mineral (Figure 5.4). The complete diffraction pattern consists of a set of Kikuchi lines that are indicative of the crystal structure (phase) and orientation (Figure 5.5). The crystal orientation of most minerals can now be measured with a spatial accuracy of $\geq 1\mu m$ and an angular resolution of $\geq 1\mu m$ (Day 1993).

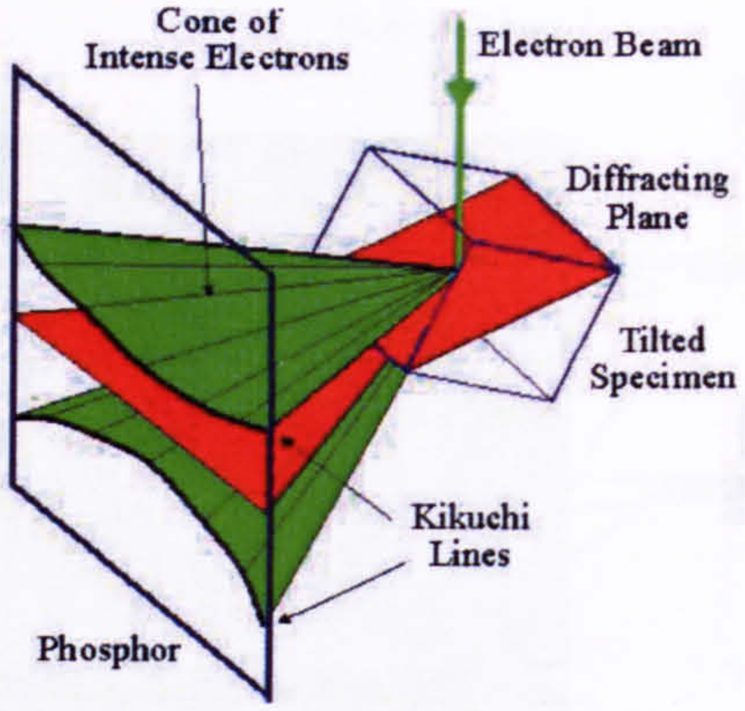

Figure 5.4: *This diagram illustrates the relationship between sample geometry, the paired diffracted electron cones, and the resulting Kikuchi lines (Modified from Day, A.).*

5.3.2 Automated electron backscattered diffraction

The advancement of computing power has facilitated complete automatism of EBSD (Schmidt & Olesen 1989). Numerical algorithms automatically detect complete sets of Kikuchi lines and then independently determine the *3D* crystallographic orientation and corresponding mineral phase.

The Kikuchi lines are projected onto a phosphor screen where a charged couple device camera captures the image, digitised, and transferred to a computer for analysis using HKL's Channel 5 program to calculate possible crystallographic orientations (Prior et al. 1999). The algorithm calculates all possible orientations of the crystal that give a match to the observed set of lattice planes of the target typically to within 3^o MAD (Mean Angular Deviation). The MAD can be thought of as the accuracy of the fit, that is, the difference between the observed Kikuchi band patterns and the nearest matching predictions.

The following information is required to accurately apply the indexing algorithm: unit-cell parameters, crystal symmetry, and a reflector file containing a list of the lattice planes that give rise to visible bands on electron backscattered patterns (Prior et al. 1999). Unit-cell parameters and crystal symmetry are widely available information in X-ray diffraction tables and in electronic crystallographic databases. Given the atomic positions in the unit-cell, kinematical theory can be used to determine the diffracting planes for electron diffraction (Schwartz et al. 2000). Determining the number of reflectors used to identify the mineral phase is not straight forward because the number

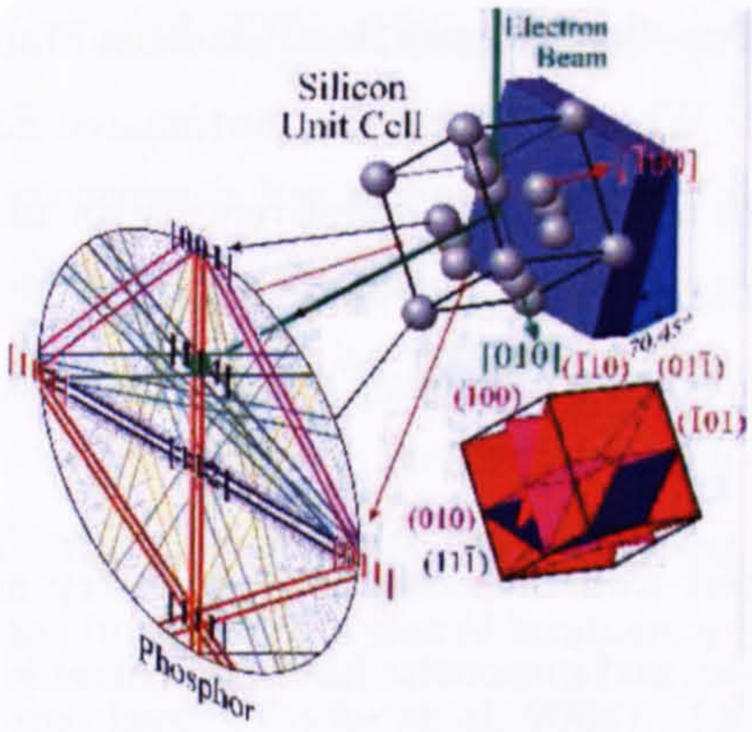

Figure 5.5: *Schematic diagram illustrating the formation of the electron backscattered diffraction pattern for a quartz unit cell. Electrons from a divergent source simultaneously interact with all of the crystal's lattice planes but only those electrons that obey Bragg's Law are diffracted into a pair of cones to form the Kikuchi lines of the diffraction pattern (Modified from Lloyd, G.E.).*

of reflectors per crystal structure is theoretically infinite. In general the more complex phases require more identifying reflectors (bands). Too many bands, however, will slow down the algorithm unnecessarily and too few bands will lower the indexing rate. In practice, however, modern EBSD software packages, such as, HKL's Channel 5 program contain pre-existing libraries of elements and common mineral phases (defaults).

In automated crystal orientation mapping, the electron beam steps over the sample, on a predetermined grid and at each point a diffraction pattern is obtained and the crystal orientation determined (Randle 2003). At each grid point the mineral phase, Euler angles, and MAD are recorded and saved in a data file.

Errors in crystal orientation measurements from the diffraction pattern will depend principally on the accuracy of the Kikuchi band position measurement and the system calibration (Schwartz et al. 2000). To ensure accuracy and reliability of the measured data, it is routine to remove indexed grid-points that have a MAD $\geq 1^o$ (Lloyd 2002, Xie et al. 2003).

5.3.3 Problems indexing low-symmetry mineral phases

Problems are commonly encountered when attempting to automatically index low-symmetry minerals, such as feldspars and phyllosilicates (Prior & Wheeler 1999, Ullemeyer et al. 2000). For example, diffraction patterns from muscovite are clearly of lower quality (low

contrast and diffuse band edges) than patterns from quartz or calcite. Moreover, it was shown in Prior & Wheeler (1999) that automated EBSD can correctly identify only 75% of EBSP patterns first time. The best remedy for minerals that have severe mis-indexing problems is manual indexing (Prior & Wheeler 1999, Valcke 2003). Manual indexing of mineral phases also acts as a good method of checking set-up calibrations and updated crystal files.

Experience gained from indexing low-symmetry and mineralogically complex phases, such as orthoclase, and muscovite has demonstrated the need to update crystal reference files. For example, micas in sedimentary rocks tend to be very fine-grained, and are generally a type $1M$ or $1Md$ (disordered) structure (Deer et al. 1999). By comparison, the indexing file traditionally used for micas is a $2M_1$ polytype more usually found in tectonites. Both, however, are common stacking sequences and lead to either one- or two-layered monoclinic polytypes (Deer et al. 1999). But, by not taking into the account the significant differences in space group between the different polytypes the operator is systematically restricting the ability of the algorithm to accurately and correctly identify the crystals orientation.

The indexing file used for the identification of the feldspar group of minerals present is that of pseudo-monoclinic orthoclase type $C2/m$. The orthoclase reflector file was chosen because it would best reflect the mineralogy of the constituent feldspar group. As shown by Prior et al. (1999), Prior & Wheeler (1999) the orthoclase indexing file will also act as a good general feldspar indexing file allowing the identification of orthoclase feldspar isotopes. Orthoclase is typically one of the more stable minerals from the feldspar family and therefore more likely to withstand the erosive and depositional processes. Moreover, the source region for the Clair field was likely to be from the North-West and thus the resulting mineralogy would likely reflect the catchment area of the Lewisian acid gneisses which commonly give rise to orthoclase as a detrital mineral phase (Allen & Mange-Rajetzky 1992). Finally, it was also observed after completing QXRD (quantitative x-ray diffraction) analyses that orthoclase feldspar was the most common feldspar phase present.

5.4 Electron backscattered diffraction sample preparation

EBSD as a technique in geosciences has previously been largely applied to tectonites (e.g., Mainprice et al. 2000, Wendt et al. 2003, Lloyd & Kendall 2005). However, there are exceptions, such as, Valcke et al. (2006). Sections are typically cut normal to foliation and parallel to lineation. In sediments, however, no such convenient reference plane exists. In microlayered sediments, sections normal to layering provide the best sampling strategy, where the cut plane intersects a series of laminae, whereas sections cut parallel to layering only intersect one layer (Valcke et al. 2006). Ideally the sample would be cut parallel to regional strike and perpendicular to the maximum dip of bedding. The samples in this study were extracted from well core, where it is not always possible to cut samples with respect to regional strike and dip. So they were cut and mounted with respect to the long axis of the borehole (Figure 5.6). This particular methodology of sample mounting was considered acceptable for three supporting reasons:

(1) the wells from which the samples were extracted were drilled vertically ($\pm 3^o$);
(2) bedding structures and laminae were approximately horizontal on the scale of the well core;
(3) due to the sampling strategy employed some samples intersected homogeneous sequences that did not possess any determinable sedimentary structures.

This method of sample mounting and analyses was conducted because a well-head trajectory and numerous seismic surveys had been carried out that provided detailed information about the regional structure and how much dip correction should be applied to any deviated well data (Crisp 1997, Smith & Lappin 1997).

A well prepared sample is an absolute prerequisite to obtaining good diffraction patterns as EBSD pattern recognition software is very sensitive to surface imperfections. Furthermore, diffracted electrons escape from within only a few tens of nanometres of the specimen surface. EBSD pattern formation can be severely impaired if material near the surface is deformed or has any surface contaminant (Prior et al. 1999). It is essential not to damage the surface during sample preparation.

Prior to undertaking any sample preparation, the samples containing oil were cleaned using dichloromethane, a solvent which removes oil contained within pore space. The

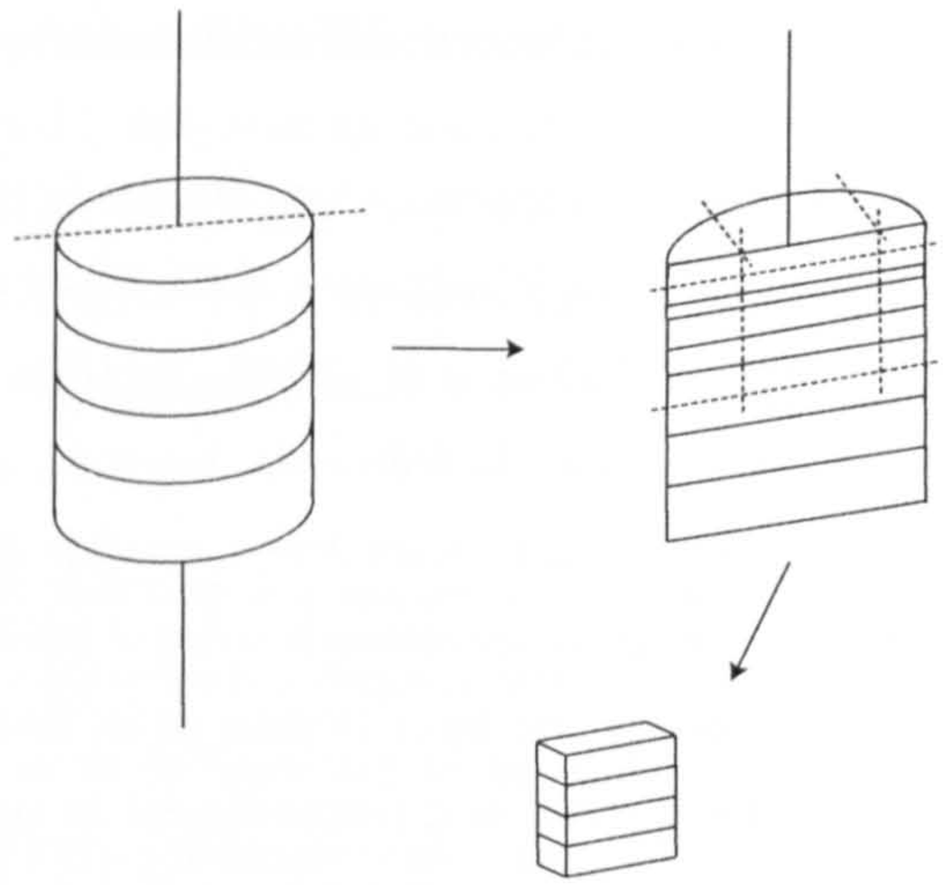

Figure 5.6: *Schematic diagram representing the relationship between the well-core, and prepared sample prior to analysis. To avoid errors associated with sample preparation inconsistency, all samples were cut perpendicular to the long axis of the well-core.*

samples were then impregnated with an epoxy-resin to hold the more porous samples together during the polishing process. Progressive mechanical polishing using increasingly finer abrasives (diamond or cubic boron nitride, then silicon carbide) does not provide a suitable surface for analysis with EBSD as it causes physical damage to the crystallographic lattice. So a further stage of polishing is required to remove the mechanically induced damage. This next stage in the polishing process uses a chemo-mechanical treatment of the surface to remove the mechanically induced damage (Fynn & Powell 1979).

In this study it has become evident that porosity content did not significantly affect the standard polishing process of SEM samples (Fynn & Powell 1979). Problems can be encountered, however, in samples that contain significant proportions of authigenic clays because the aqueous polishing solution reacts with the clays weakening their structure, causing them to loosen and wash away. Authigenic clays are extremely fine-grained, pore filling with low crystallinity and were therefore not analysed by EBSD and are assumed to have a random LPO. Clay minerals are often a result of diagenesis and usually grow within the pore space and hence are random in their crystallographic orientation. Therefore they do not adversely affect the LPO analyses results.

One of the problems with SEM imaging results from electrical currents developing on

the sample surface due to the interaction between the incident electron beam and the target specimen. The target surface can slowly develop an electrical charge if it is not appropriately earthed. Charging in non-conductive materials can be eliminated as for X-ray microanalysis by depositing a thin layer of carbon approximately 2 to 3nm thick on the sample surface (Reed 1996).

5.5 Stereological approach to the determination of phyllosilicate orientations

5.5.1 Introduction

In this section a stereological approach is presented as a method with which to statistically determine the orientation of phyllosilicate mineral phases. There are a variety of models available which would suffice, including among others those devised by March (1932) and Bingham (1974). Valcke et al. (2006) used a model that was determined originally by March (1932) which assumes that individual crystals (e.g., phyllosilicates) re-orient in the same manner under the same stress conditions, such as, compaction. The approach which was applied here, however, was that of Bingham (1974). The Bingham distribution is a general distribution of axial data and depending on the values of its parameters it may be used to describe a numerical summary of a wide variety of distributions (Cheeney 1983).

More specifically, the Bingham distribution is contained within the discipline of circular and directional statistics. Similar distributions exist on a *3D* sphere, such as the Kent distribution, Von-Mises-Fisher and 5-parameter Fisher-Bingham distributions which can be used to construct probability distributions over rotation matrices (Cheeney 1983). The Bingham distribution can be described as a trivariate Gaussian vector with zero mean and arbitrary covariance matrix, conditioned on the length of the vector being unity (Kenney & Keeping 1962*a*). Bingham's distribution thus represents the portion of a trivariate Gaussian distribution that intersects the surface of a unit sphere, with varying ellipsoidal shapes of the underlying Gaussian contours producing a variety of distributional forms on the sphere (Figure 5.7).

In this study the Bingham model is used to determine the probability of distribution of orientations under the following assumptions:

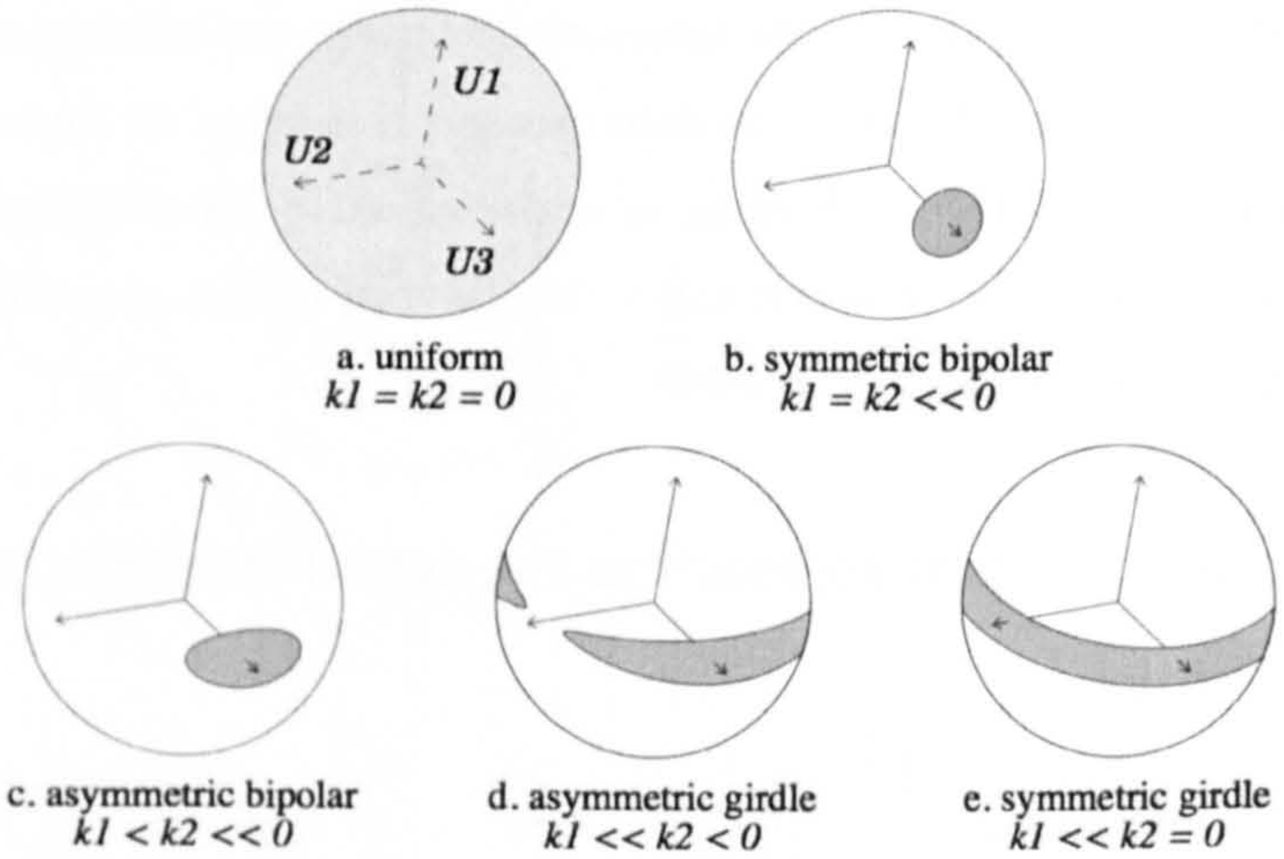

Figure 5.7: *Bingham's distribution - representative contours for varying shape parameter magnitudes.*

1. The preferred orientation produced by compaction has uniaxial symmetry (azimuthally symmetrical about a single axis);

2. The distribution can be described by two parameters in the Bingham distribution (Bingham 1974);

3. The distribution of orientations of lines of intersection of phyllosilicate basal planes is related to the uniaxial preferred orientation by projection.

5.5.2 Probability distribution of intersections of phyllosilicate basal planes and the surface of the specimen

The methodology which was used to determine the intersection probability profiles for sterelogically determined phyllosilicate orientations is outlined explicitly as follows.

Figure (5.8) is a backscattered atomic-contrast (Z-contrast) image of a mudstone, sample 1784m from Well 206/8-8. The phyllosilicates in Figure (5.8) show up as fairly light-grey grains with a high-degree of ellipticity. The phyllosilicate grains are then density sliced on their grey-scale level and converted to a binary image as shown in Figure (5.9). The analyse particles function of ImageJ (*ImageJ* National Institute of Health) was then used to obtain a table of values of orientation of the long axes and the area of the particles. The orientation of these axes were then taken to be the orientation of the line

of intersection of the phyllosilicate basal plane and the plane of the section.

The angle output by ImageJ is then the angle of the long axis from the positive x-axis (with a positive angle as an anti-clockwise rotation). The bedding plane normal was used as a frame of reference (long axis of borehole), and a clockwise angle of rotation was considered to be a positive value. The angle from bedding plane pole, θ, can then be considered to be related to the angle from the positive x-axis, ω whereby,

$$\theta = |180 - \omega|. \tag{5.1}$$

Each data point obtained from the image analysis is convoluted with a function of the angle from the measurement and added to profile points in the range 0 to $\frac{\pi}{2}$. The convolution is given by,

$$C_{\theta'} = exp(-(1 - cos(\theta - \theta^{'}))^2 F)A, \tag{5.2}$$

where, $C_{\theta'}$ is the contribution to the profile point $\theta^{'}$ of the data point at θ, F is a parameter determining the rate of fall of the contribution away from θ, and A is the area of the current elliptical particle (normalised counting circle procedure whereby an ODF can be determined from a set of discrete data points, i.e., the volume fraction of crystallites having the orientation g of their crystallographic axes with respect to a sample reference system)(Cheeney 1983). This procedure simply spreads the current data point over a certain range of the angular space. The function is only applied within a pre-determined distance, of the order of 12^o of the current measurement. All values are then taken into consideration and the results of applying (5.2) are accumulated for points on a 5^o mesh in the angle from the bedding plane normal. The value at θ is taken to be proportional to the probability of finding an intersection line perpendicular to θ, and the actual probability is estimated by normalising to unit probability over the range 0 to $\frac{\pi}{2}$,

$$p(\theta) = \frac{c(\theta)}{N} \tag{5.3}$$

where, $p(\theta)$ is the probability, $c(\theta)$ is the sum of convolutions, and N is the normalisation factor obtained from,

$$N = \int_0^{\frac{\pi}{2}} c(\theta) sin\theta d\theta. \tag{5.4}$$

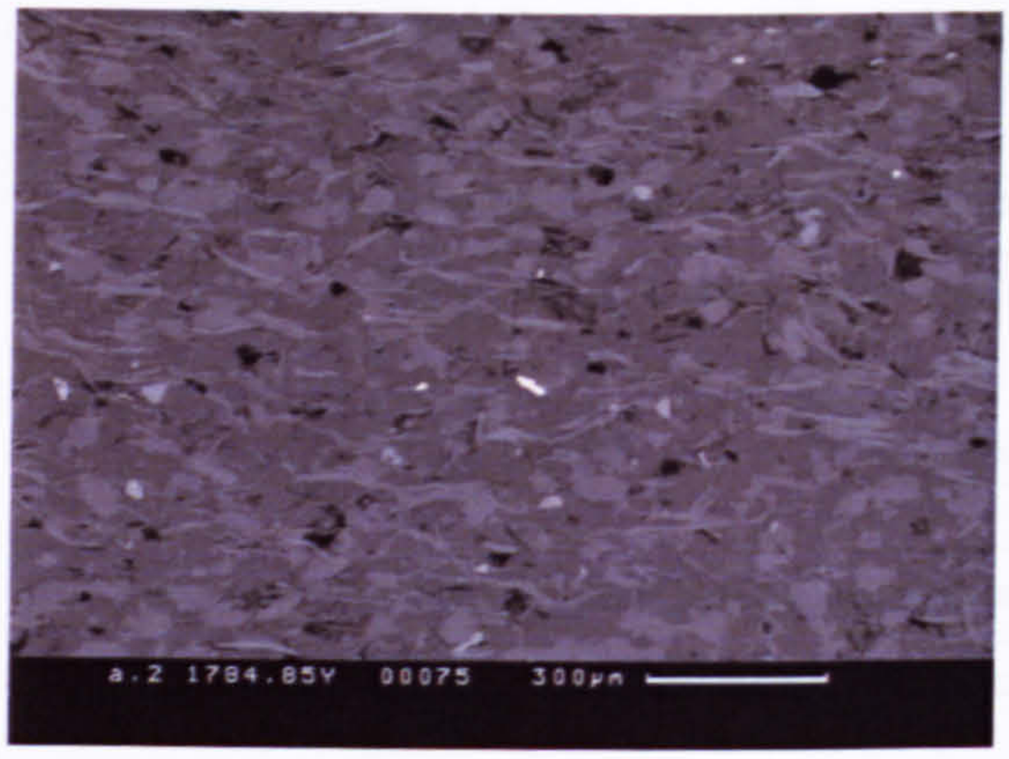

Figure 5.8: *Electron backscattered atomic-contrast (Z-contrast) image of a clay-mica rich specimen. Sample 1784m from Well 206/8-8. The image is approximately 2mm across.*

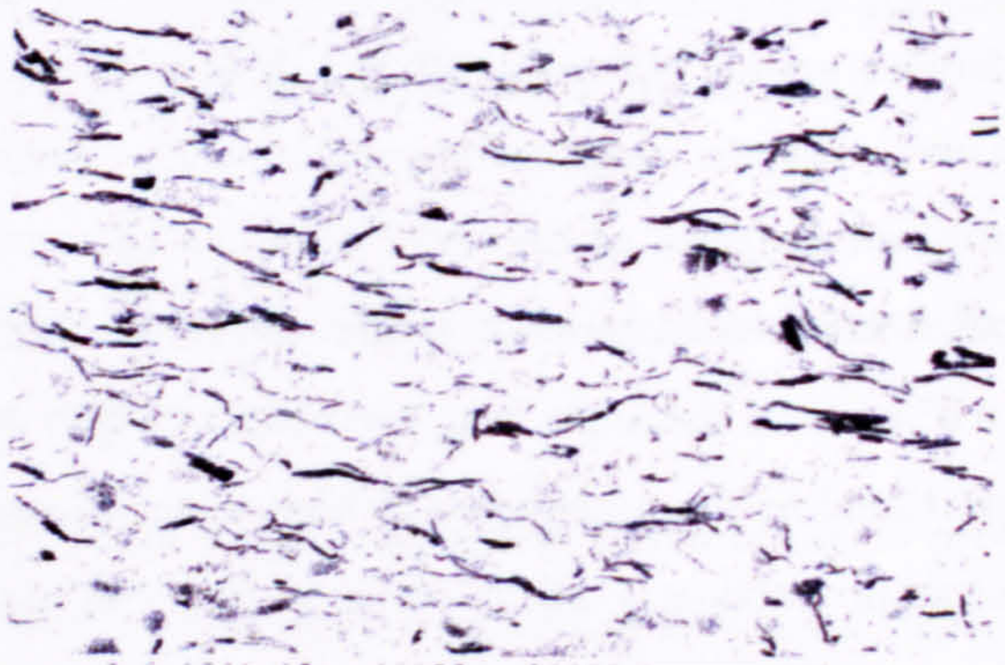

Figure 5.9: *Binary converted image of an electron backscattered atomic-contrast (Z-contrast) image of a clay-mica rich specimen. Sample 1784m from Well 206/8-8. The image is approximately 2mm across.*

5.5.3 Bingham model distribution

The Bingham distribution is simply a distribution of probability on a sphere obtained from the formula,

$$f(c) = N^{-1}(exp(K_1(c.t_1)^2) + exp(K_2(c.t_2)^2) + exp(K_3(c.t_3)^2)) \tag{5.5}$$

where, N is a normalisation factor, K_1, K_2, and K_3 are parameters of the distribution (K_n can be thought of as being broadly representative of the strength of alignment in a particular direction), t_1, t_2, and t_3 are the vectors corresponding to K_1, K_2, and K_3, and c is the orientation factor for which we wish to find the probability (Bingham 1974, Cheeney 1983).

For a uniaxial distribution the parameter K_1 is greater than K_2, which is equal to K_3, as shown by (e) in Figure (5.7). The vector for K_1 is considered here to be parallel to the bedding plane normal, with the other two other vectors lying within the bedding plane.

For a uniaxial distribution in the range of θ from 0 to $\frac{\pi}{2}$ the distribution is,

$$f(c) = N^{-1}(exp(K_1(c.t_1)^2) + exp(K_2(c.t_2)^2) \tag{5.6}$$

and the normalisation factor can be determined using (5.4). The full uniaxial pole figure can be obtained from the θ profile. The full distribution is based on spherical coordinates with polar angle, θ from 0 to $\frac{\pi}{2}$ and the longitude, ϕ, from 0 to 2π. It is usual to use a mesh with spacing of 5^o in each direction. The full uniaxial pole figure is then obtained from the 0 to $\frac{\pi}{2}$ profile by putting the single profile values at all mesh points with constant θ in the ϕ direction.

5.5.4 Model probability distribution of intersection orientation

In the full spherical coordinate distribution (Kenney & Keeping 1962a) the vector of the plane normal corresponding to θ, ϕ is given by,

$$n_x = sin\theta cos\phi, \tag{5.7}$$

$$n_y = sin\theta sin\phi, \tag{5.8}$$

$$n_z = cos\theta. \tag{5.9}$$

θ (angle of rotation) and ϕ (angle of inclination) specify an orientation in polar coordinates in *3D* space. The intersection angle in the x, z plane of a plane with normals (n_x, n_y, n_z) is given by,

$$tan\alpha = \frac{n_z}{n_x} \tag{5.10}$$

where α is the angle of the line perpendicular to the intersection line in the range 0 to $\frac{\pi}{2}$.

Equation (5.10) gives all values of the orientation of a phyllosilicate c-axis, in terms of spherical angles, that would give an orientation of the normal to the intersection in the x, z plane of α. To calculate the probability of finding this orientation α, we can integrate the probabilities on the line given by all those values of θ and ϕ through the full pole figure. This is expressed as,

$$p(\alpha) = \int_L p_c(\theta, \phi) dl; \tag{5.11}$$

where $p_c(\theta, \phi)$ is the probability of the uniaxial model Bingham distribution expressed in a full pole figure and the path of the integral L is given by the condition of Equation (5.10). The integration is carried out for α at 5^o intervals in the range 0 to $\frac{\pi}{2}$ (Figure 5.10).

The parameters that define the Bingham distribution were calculated as those that gave the best match between the model profile and that determined from the specimen. With only two parameters a direct search can be made by varying K_1 and K_2 over ranges with small intervals. The minimum is found by calculating the sum of the squares of the differences.

Presented are the results obtained from the intersection probability profile determined from the data (i.e., from the SEM-BSE image), the model intersection probability and the probability profiles of poles to basal planes corresponding to the model intersection probability profile (Figure 5.11). It can be seen from the probability profiles that the data and model have a good approximation.

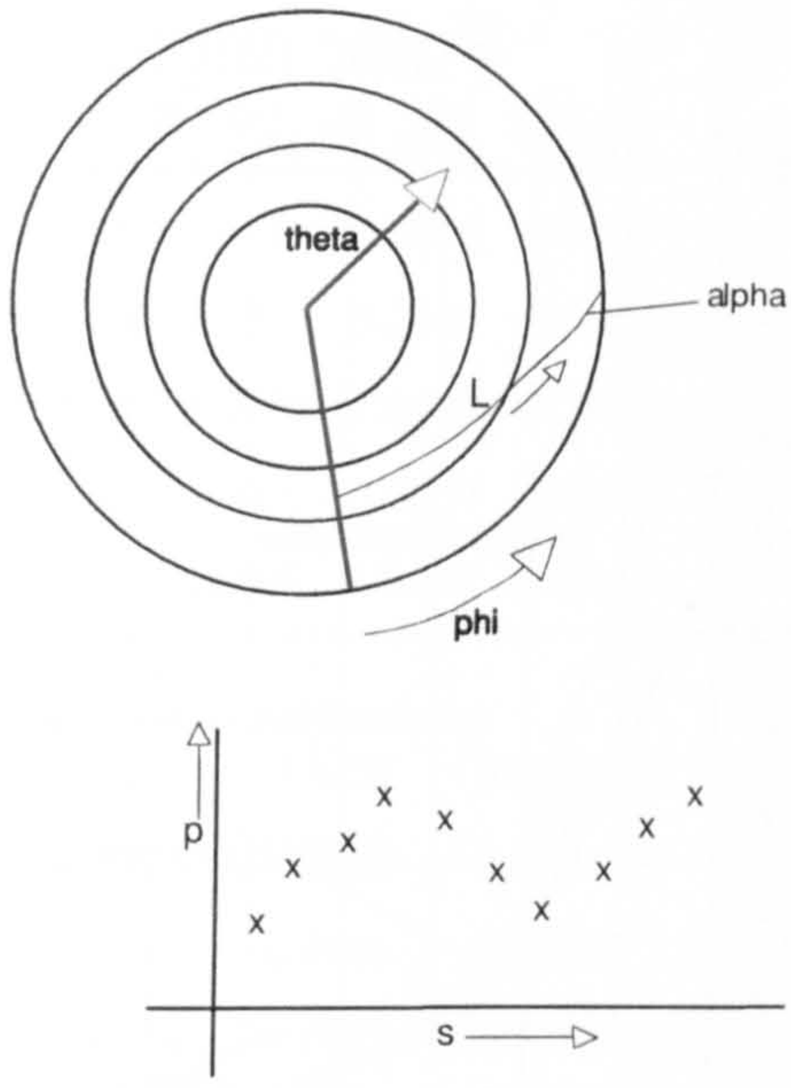

Figure 5.10: *Schematic diagram representing the calculation of the probability of finding a particular orientation. Theta and phi are the spherical coordinates, L is the path the integral follows (using five degree intervals), p is the probability of the orientation occurring in the Bingham distribution uniaxial pole figure, and s is the discrete data points where p is calculated at intervals of five degrees. The area under the discrete set of data points is the probability. The integration is carried out for* α *at* 5^o *intervals in the range* 0 *to* $\frac{\pi}{2}$ *and maps out the path integral L.*

The Bingham distribution is a convenient way of describing uniaxial probability distributions. In this instance the Bingham distribution can be considered to be described by two parameters. These two parameters effectively characterise the strength of the preferred orientation and could offer some advantages over the texture-index. In that these parameters are related to a particular distribution and do not just quantify the difference from the mean as in the texture-index (J).

5.5.5 Determination of a general phyllosilicate elastic stiffness tensor

The muscovite elastic stiffness tensor is then calculated by first expanding the probability profile into a full ODF (orientation distribution function). There is an implicit assumption that uniaxial symmetry exists about the pole normal to cleavage. Using intervals of five degrees, and based upon the probability profile obtained from the Bingham approximation a full ODF is populated at five degree intervals. The ODF is then integrated using a muscovite single crystal elastic stiffness tensor and a simple Voigt-

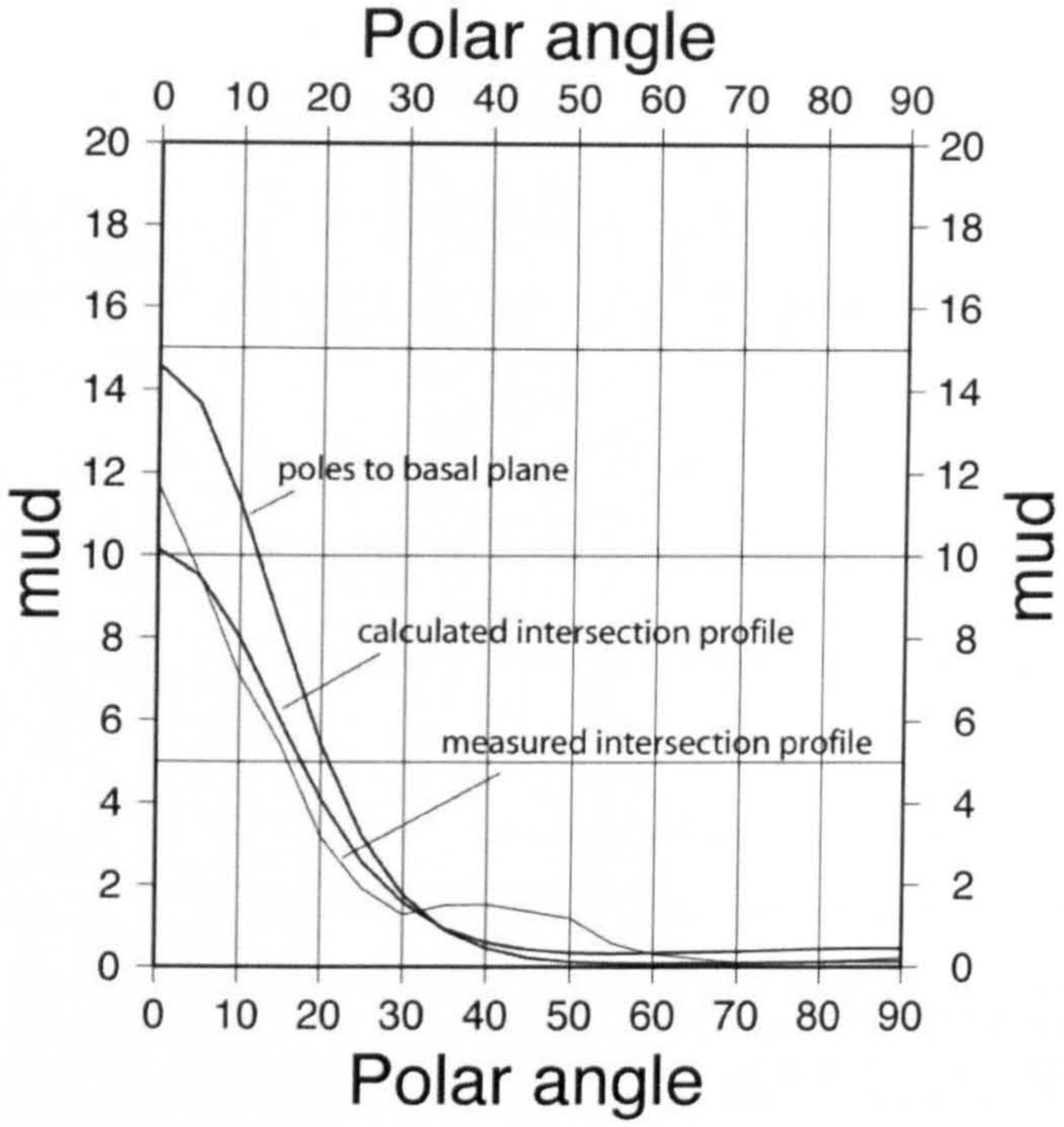

Figure 5.11: *Intersection probability profiles for stereologically determined phyllosilicate orientations. Intersection probability profile determined from data, the model intersection probability and the probability profiles of poles to basal planes corresponding to the model intersection probability profile. mud - mean uniform distribution (i.e., multiples of a uniform distribution); polar angle - is the angle from the vertical in degrees.*

Reuss-Hill average. Each component of the elastic stiffness tensor is multiplied by the individual value of the ODF. It was assumed in the calculations of the elastic stiffness tensor for phyllosilicates that biotite, muscovite, and chlorite would all be aligned similarly. The predicted elastic stiffness tensor of the phyllosilicate components of the Clair rocks as determined by using a Bingham approximation distribution is shown in (5.12). In comparison, the elastic tensor calculated from the manual EBSD indexing of 96 different muscovite grains is shown in (5.13). The elastic tensor as calculated from the manual indexing of phyllosilicate grains does not have a perfect VTI style of symmetry. To some extent this is to be expected with the analysis of a relatively small number of individual grains. Hence, the muscovite elastic stiffness tensor that was used in the bulk aggregate seismic anisotropy predictions was calculated by taking an average of the two independently derived tensors.

$$\begin{pmatrix} 1.4648 & 0.3907 & 0.2970 & 0.0000 & 0.0000 & 0.0000 \\ 0.3907 & 1.4648 & 0.2970 & 0.0000 & 0.0000 & 0.0000 \\ 0.2970 & 0.2970 & 0.6505 & 0.0000 & 0.0000 & 0.0000 \\ 0.0000 & 0.0000 & 0.0000 & 0.2432 & 0.0000 & 0.0000 \\ 0.0000 & 0.0000 & 0.0000 & 0.0000 & 0.2432 & 0.0000 \\ 0.0000 & 0.0000 & 0.0000 & 0.0000 & 0.0000 & 0.5371 \end{pmatrix} \tag{5.12}$$

$$\begin{pmatrix} 1.3287 & 0.3514 & 0.3403 & 0.0102 & 0.0009 & -0.0061 \\ 0.3514 & 1.3276 & 0.3403 & 0.0084 & -0.0061 & -0.0031 \\ 0.3403 & 0.3580 & 0.6926 & 0.0002 & 0.0100 & -0.0051 \\ 0.0102 & 0.0084 & 0.0002 & 0.3272 & -0.0049 & -0.0080 \\ 0.0009 & -0.0061 & 0.0100 & -0.0049 & 0.3259 & 0.0070 \\ -0.0061 & -0.0031 & -0.0051 & -0.0080 & 0.0070 & 0.4874 \end{pmatrix} \tag{5.13}$$

5.6 Samples analysed

Presented in Table (3.1) is a list of all the samples analysed using EBSD. The table contains data regarding: well number, unit number, depth, modal composition, porosity and permeability. The modal composition was determined by QXRD, the porosity by using helium porosimetry, and the permeability by air porosity analysis.

5.7 Petrofabric data presentation

Crystallographic texture's are commonly particularly complicated as they describe orientations in *3D* space of thousands or even millions of individual grains. It is possible to represent them graphically using either of two different tools, the pole figure based on the stereographic projection of the orientation distribution function (ODF) based on the three Euler angles of rotation required to coordinate a unit cell with a reference coordinate system.

The simplest and most convenient way to display the as-measured data points determined by EBSD is by stereographic projection. A stereographic projection is a graphical method of portraying *3D* geometrical data in *2D*. The raw data for a conventional macrotexture stereographic projection is a distribution of a family of directions or poles. A stereograph

that consists of discrete data points is the most direct and simple means of displaying the statistics of orientations (Schwartz et al. 2000). When the quantity of microtexture data is large, as in EBSD analyses, detail in the projection is lost because individual points are massed together. Therefore, it is more convenient to smooth the discrete data into contours (Randle 2003).

A random distribution of discrete orientations corresponds to a uniform distribution, therefore, the normalised, continuous densities in textured samples are multiples of uniform distribution. Hence, the contouring scheme employed throughout all the stereographic pole figure projections was in density of the orientation distribution function expressed as multiples of a uniform distribution (MUD) (Bunge 1982).

To visualise how a stereographic projection works it can be thought of as the plane of projection onto which everything is mapped. Points on the lower hemisphere are brought up to the plane of projection by moving them along lines which pass through the uppermost point of the sphere. In this way any point on the hemisphere projects to give a point on the plane of projection (Figure 5.12) (Leyshon & Lisle 1996). The crystallographic pole figures and contouring were calculated directly from the samples mineralogical ODF using a Fortran program originally developed by D. Mainprice (freely available at http://www.isteem.univ-montp2.fr/TECTONOPHY/petrophyiscs/software/petrophyiscs-software.html). The pole figure plotting software used to plot the individual mineral phase crystallographic pole figures used the following input parameters: bedding was aligned horizontally (X), bedding perpendicular was vertical (Z), mean angular deviation of 1^o, non-polar data, lower-hemisphere projections, rainbow coloured scale (red-blue-green), inverse colour scheme (blue - maximum and red - minimum), linear colour scale, Gaussian Half Width - 10, dashed line for the lowest value, automatic shading and an Euler angle cell size of 1^o. A real example of a series of crystallographic pole figures for quartz poles to lattice planes can be seen in Figure (5.13).

5.8 Petrofabric quantification

LPO is commonly presented in the form of pole figures that show the crystallographic distribution of orientations of individual data points with respect to a globally known reference frame. Although important variations in the distribution of the data can be determined qualitatively from individual crystallographic pole figures it is useful to have

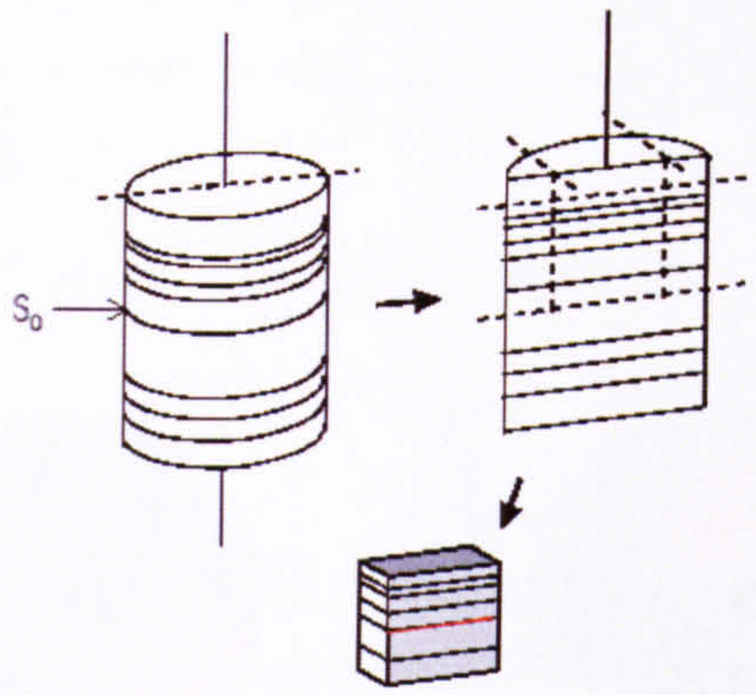

a.

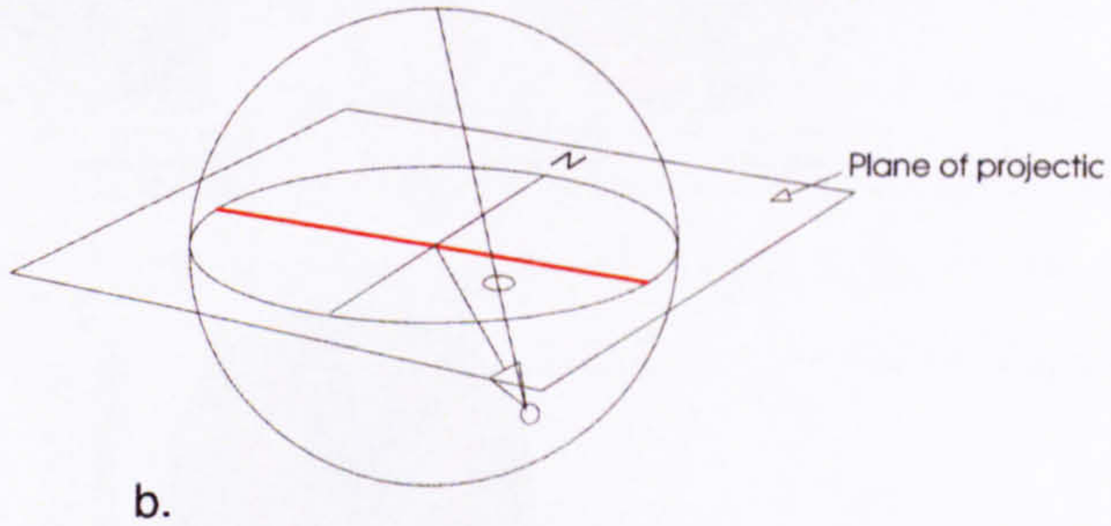

b.

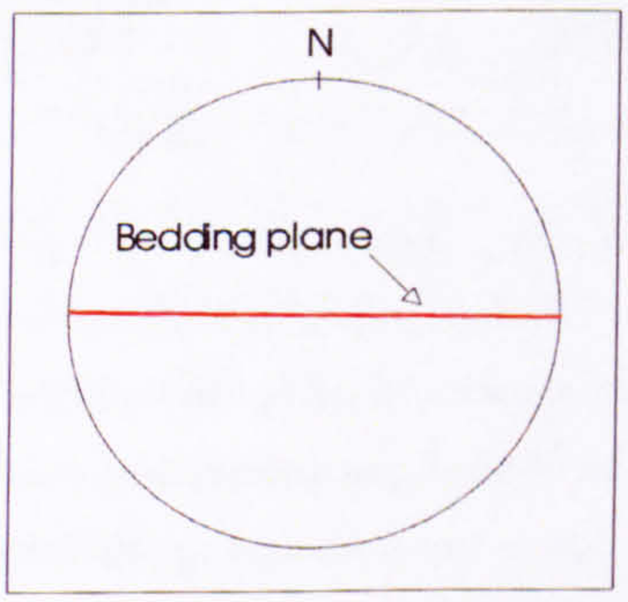

c.

Figure 5.12: *Stereographic projection - a. orientation of EBSD analysed sample with respect to bedding and the borehole core from which it was removed. S_0 represents bedding. b. the horizontal plane is the plane of projection and it is placed so that it passes through the centre of the sphere, points on the lower hemisphere are brought up to the plane of projection by moving them along lines which pass through the uppermost point of the sphere c. in this way any point on the hemisphere projects to give a point on the plane of projection. The final result of this projection is to produce a representation on a flat piece of paper of 3D orientations. N refers to the direction perpendicular to bedding (up).*

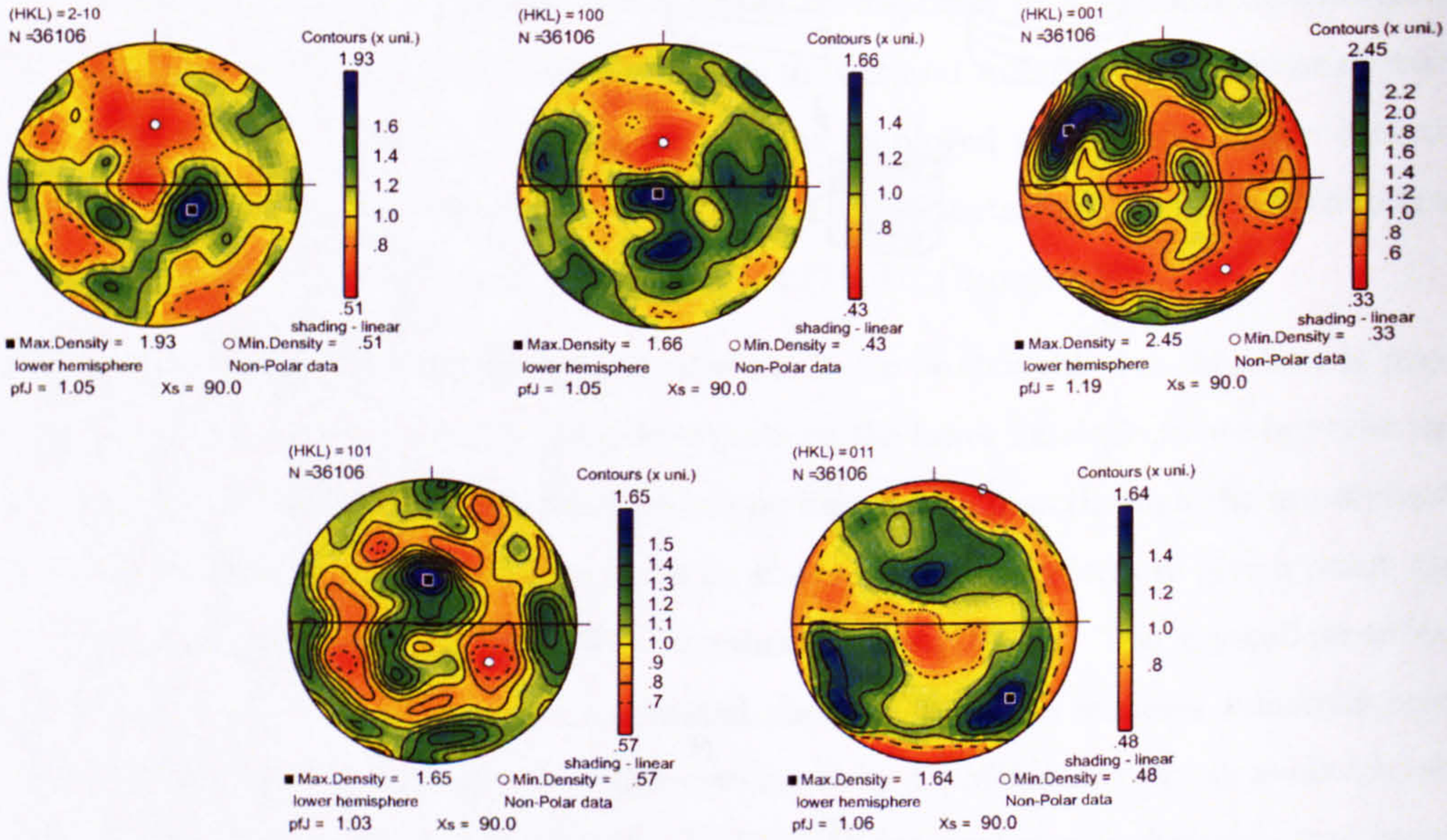

Figure 5.13: *Illustrative non-polar, lower-hemisphere, crystallographic stereonets of an individual mineral phase (quartz). Crystallographic pole figures are contoured stereographic plots of the poles to the crystallographic planes of a particular constituent mineral phase. Bedding is the horizontal line bisecting the pole figures and bedding perpendicular is at North (represented by the tick). The individual pole figures are contoured in multiples of uniform distribution (MUD). (HKL) = the pole to lattice plane. [uvw] = poles to crystallographic directions (not required here). N = the number of indexed points with a MAD of* ≤ 1*. The black square represents the maximum concentration of crystallographic orientations (blue), and the empty circle represents the minimum concentration of crystallographic orientations (red). Note different contour intervals between pole figures. pfJ refers to the individual pole figure fabric intensity (Equation 5.15).*

a quantitative description of the fabric intensity. Therefore, it becomes necessary to quantitatively characterise the strength of the fabric texture without considering the details of the distribution by using the texture-index (Equation 5.14) (Sturcken & Croach 1963).

The texture-index (J) is described by,

$$J = \oint [f(g)]^2 dg, \tag{5.14}$$

where, $f(g)$ is the ODF (orientation distribution function) ($f(\phi_1, \psi, \phi_2)$ with ϕ_1, ψ, ϕ_2 being Euler angle's) in the case of general texture, dg is the element of orientation (orientations in an infinitesimal element about a particular ψ_1, ϕ, ψ_2) and $\oint$ is the integral over the total orientation space. The texture index varies between 1 in the case of random orientation, and ∞ in the case of one or more ideal single crystals. See Appendix (A) for a full derivation of the texture-index (J), and individual crystal axis intensity (pfj)(Bunge 1982).

The texture-index is calculated by expanding the ODF into a series of spherical harmonics, which requires truncating the expansion at a finite number. A Gaussian smoothing function is also applied where each data point is replaced by a Gaussian probability distribution (Gaussian Half Width - GHW) and the bin size for the Euler angle space is defined. In this study the spherical harmonic expansion was set at 22, the GHW was set at 10, and the Euler angle cell size was set to 1^o degree. Truncation of the series expansion at a finite value of 22, has the effect of applying a noise filter. The harmonic method is also very stable, and gives good results even when the input data are of low quality, such as when the sample has a large grain size or low diffracted intensity. There is an implicit assumption in the harmonic method, however, that the orientation distribution is a smooth function, and that the truncation of an infinite series at a low order will not degrade the solution (Bunge 1982).

It is also possible to define a measure of the sharpness of individual pole figures, similar to that of the texture-index (J) by,

$$J_{hi} = \frac{1}{4}\pi \oint [P_{hi}(y)]^2 dy, \tag{5.15}$$

where, J_{hi} is the texture-index of the pole figure, P_{hi} is the pole figure associated with the crystal direction, y is the sample direction and dy is the element of solid angle

(Bunge 1982). It logically follows then that the measure of sharpness of an arbitrary pole figure can only be smaller than or at most equal to that of the *3D* ODF ($J_{hi} \leq J$). A pole figure represents the sum of probabilities along a path through the ODF, i.e., all those orientations which out the chosen critical crystal direction (HKL) parallel to one orientation in the pole figure. Thus, a summation, similar to that of the texture-index, will never produce a result with more variance than that of the ODF itself.

5.9 Mineral phase crystallographic pole figure distributions

Presented are the crystallographic pole figure distributions obtained from EBSD microstructural analyses for the principal constituent mineral phases. Plotting individual mineral phase pole figure distributions assist in the determination of the relevance and contribution of individual phases to bulk aggregate properties. Furthermore, it also provides another means of checking for anomalous data to ensure there is no bias in the results. Furthermore, by simply examining orthogonal sections for similarities, anomalous data can be determined and removed.

5.9.1 Quartz

An explanation of the notation used in the crystallographic pole figures for quartz are shown in Figure (5.14). The crystallographic pole figure distributions for each individual sample containing quartz is presented in Figures (E.1, E.2, E.3 and E.4) within Appendix (E). The (001) direction tends to align preferentially, whilst the other crystallographic directions are more randomly distributed. The maximum alignment of (001) directions in quartz is commonly found either parallel to the bedding plane, normal to the plane of the cut section, or oblique to the bedding plane, parallel to the plane of the the cut section. Similar patterns such as the location and shapes of girdles and maxima can broadly be observed throughout the other pole figures. However, it must be noted that the intensity of alignment of quartz's crystallographic axes is generally quite low. Patterns which appear to be quite striking in the pole figure projections can be as a result of the colouring scheme employed whereby red is the minimum value and blue is the maximum regardless of the number of intervals or specific maximum and minimum values. The colouring scheme employed does, however, provide a useful means of identifying trends and distributions which black and white would not show.

Using the Mainprice (standard) convention, Miller (101) and (011) are the same as Miller-Bravais (10-11) and (01-11). These are the r and z poles respectively. They are not equal but opposite, they are the rhomb terminations and are exchanged by a 60^o rotation about the c-axis, i.e., a Dauphine twin operator. If using the Channel (non-standard) convention they are not r and z but some combination based on the orthogonal crystal lattice. They occupy the same relative positions on the plane containing xz and yz respectively but these are not the same or equivalent and they may never be opposite.

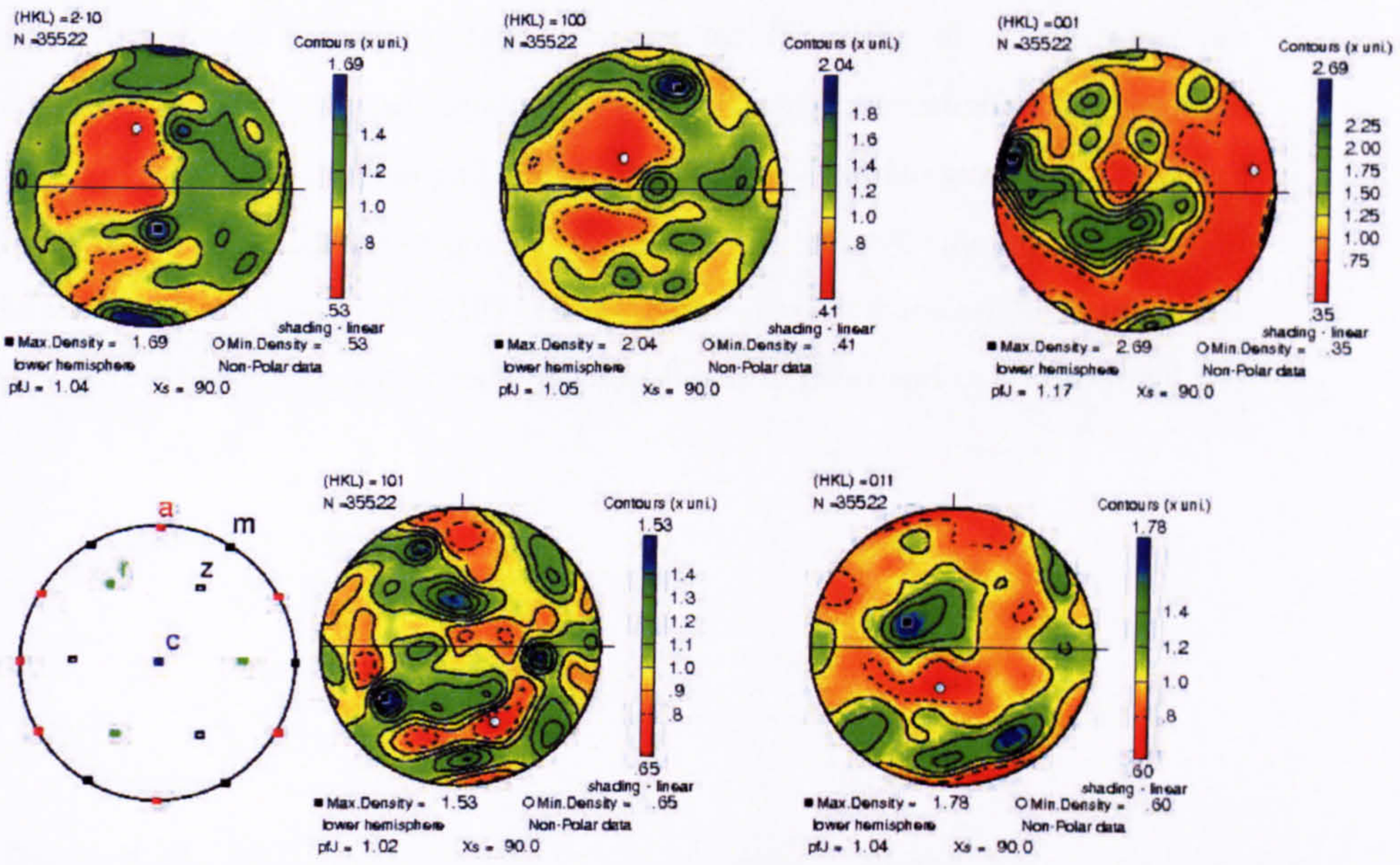

Figure 5.14: *Illustrative non-polar, lower hemisphere, crystallographic stereonets of quartz. HKL notation: (2-10) - a; (100) - c; (-001) - z; (101) - r and (011) - m. Bedding is the horizontal line bisecting the pole figures, and bedding perpendicular is at North (represented by the tick). The individual pole figures are contoured in multiples of uniform distribution (MUD). (HKL) = the pole to lattice plane. N = the number of indexed points with a MAD of* ≤ 1*. The black square represents the maximum concentration of crystallographic orientations (blue), and the empty circle represents the minimum concentration of crystallographic orientations (red). Note the different contour intervals between pole figures. pfJ refers to the individual pole figure fabric intensity (Equation 5.15). Samples which were analysed from cores extracted perpendicular to bedding (Z-direction cores) do not contain a horizontal line as the bedding plane is represented by the perimeter of the pole figure (Appendices E; F; G). For an explanation of sample number notation see Appendix (B).*

5.9.2 Feldspar

Figures (F.1, F.2, F.3 and F.4) in Appendix (F) contain the crystallographic pole figures for feldspar for all the samples analysed. Figure (5.15) is representative of the style of symmetry throughout all the samples analysed. There are two distinct systems of alignment, however, both of which generate the same style of grain alignment. In the [010] pole figure there is a single cluster in the upper-half of the circle which is related to the broad girdle in [001]. Similarly, the broad girdle in [010] is directly related to the tight cluster in [001]. It can be seen that in general the feldspar grains adopt a preferential alignment, whereby they are imbricated with the down-dip direction of imbrication varying azimuthally within the bedding plane. [uvw] represent the directions in a crystallographic system. Whereas, (HKL) represent the poles to lattice planes. In a monoclinic system, such as orthoclase, [010] = (010) (that is, they are coincident), hence, the [010] direction has been omitted in all further feldspar pole figure distributions.

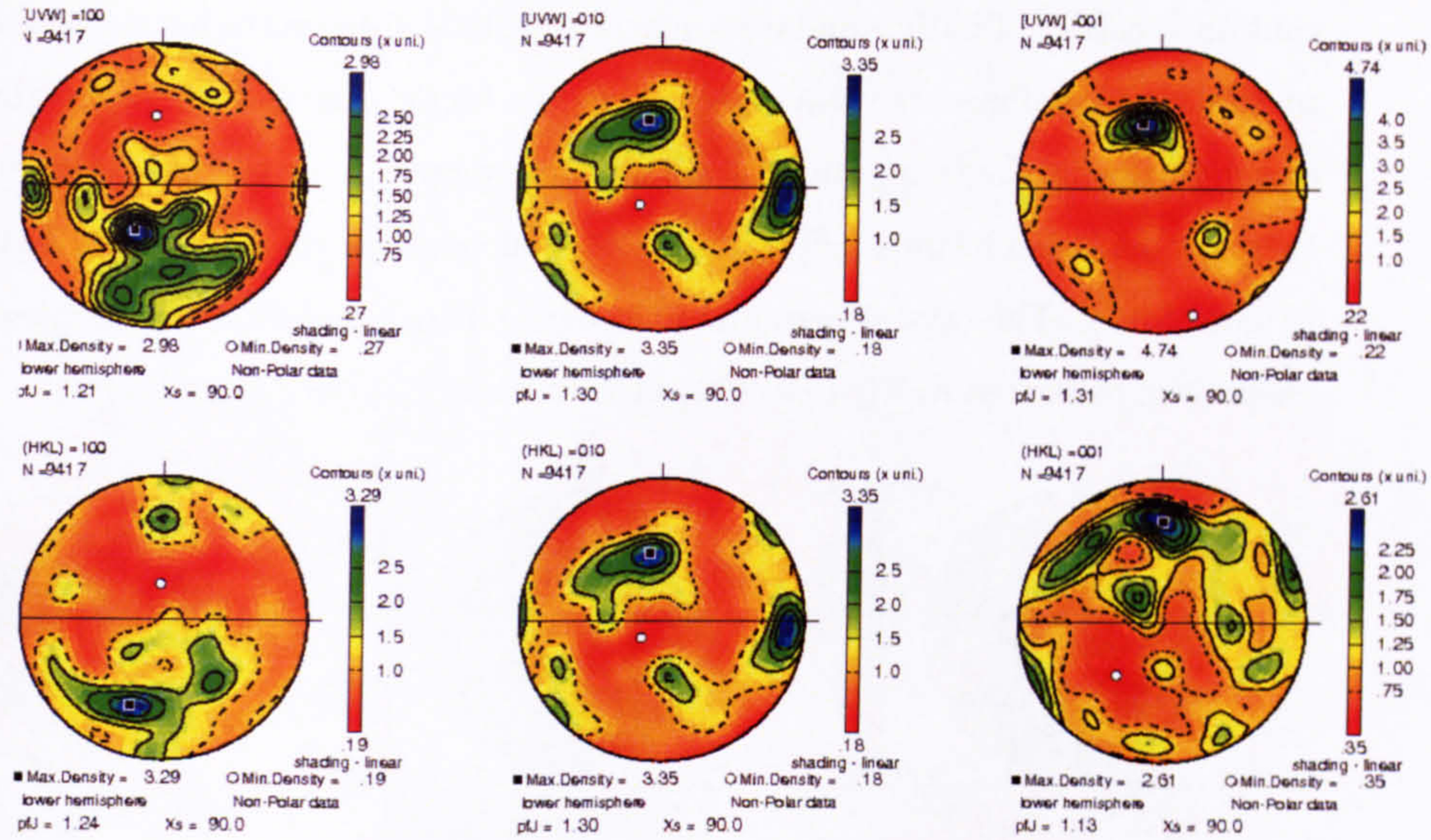

Figure 5.15: *Illustrative non-polar, lower hemisphere, crystallographic stereonets of feldspar. Bedding is the horizontal line bisecting the pole figures and bedding perpendicular is at North (represented by the tick). The individual pole figures are contoured in multiples of uniform distribution (MUD). [uvw] = directions in a crystallographic system. (HKL) = the poles to lattice planes. In a monoclinic system, such as orthoclase, [010] = (010) (that is, they are coincident), hence, the [010] direction has been omitted in all further feldspar pole figure distributions. N = the number of indexed points with a MAD of* ≤ 1*. The black square represents the maximum concentration of crystallographic orientations (blue), and the empty circle represents the minimum concentration of crystallographic orientations (red). Note the varying contour intervals between pole figures. pfJ refers to the individual pole figure fabric intensity (Equation 5.15). Z-direction samples are perpendicular to bedding, and therefore do not contain a horizontal line (bedding). The bedding plane is represented by the perimeter of the circle. For an explanation of sample number notation see Appendix (B).*

5.9.3 Calcite

Two distinct pole figure distributions were observed within the samples analysed which contained calcite. Firstly, similar to quartz, calcite is observed to have a very weak fabric texture and an almost random crystallographic fabric (Figure 5.16). Secondly, it is also observed that a single calcite crystal can occupy up to tens of mm's of pore space and therefore can significantly affect the LPO analyses over the scale of an EBSD sample (Figure 5.17). The crystallographic pole figure distributions for all samples containing calcite are presented in Figures (G.1, G.2, G.3 and G.4) in Appendix (G).

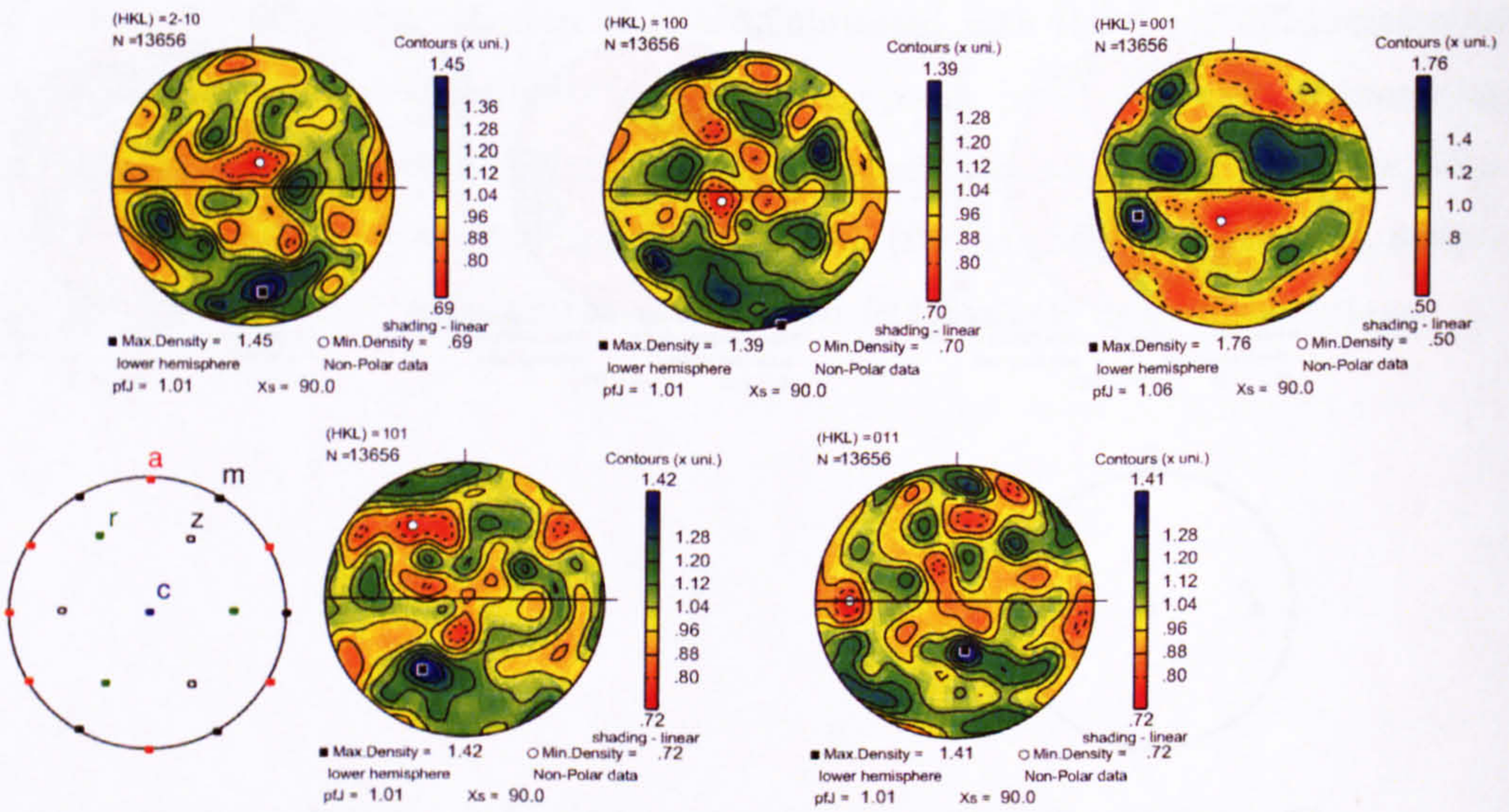

Figure 5.16: *Random fabric of detrital calcite. Illustrative non-polar, lower hemisphere, crystallographic stereonets of calcite. Bedding is the horizontal line bisecting the pole figures and bedding perpendicular is at North (represented by the tick). The individual pole figures are contoured in multiples of uniform distribution (MUD). (HKL) = the pole to lattice plane. N = the number of indexed points with a MAD of* ≤ 1*. The black square represents the maximum concentration of crystallographic orientations (blue), and the empty circle represents the minimum concentration of crystallographic orientations (red). Note the varying contour intervals between pole figures. pfJ refers to the individual pole figure fabric intensity (Equation 5.15). Z-direction samples are perpendicular to bedding, and therefore do not contain a horizontal line (bedding). The bedding plane is represented by the perimeter of the circle. For an explanation of sample number notation see Appendix (B).*

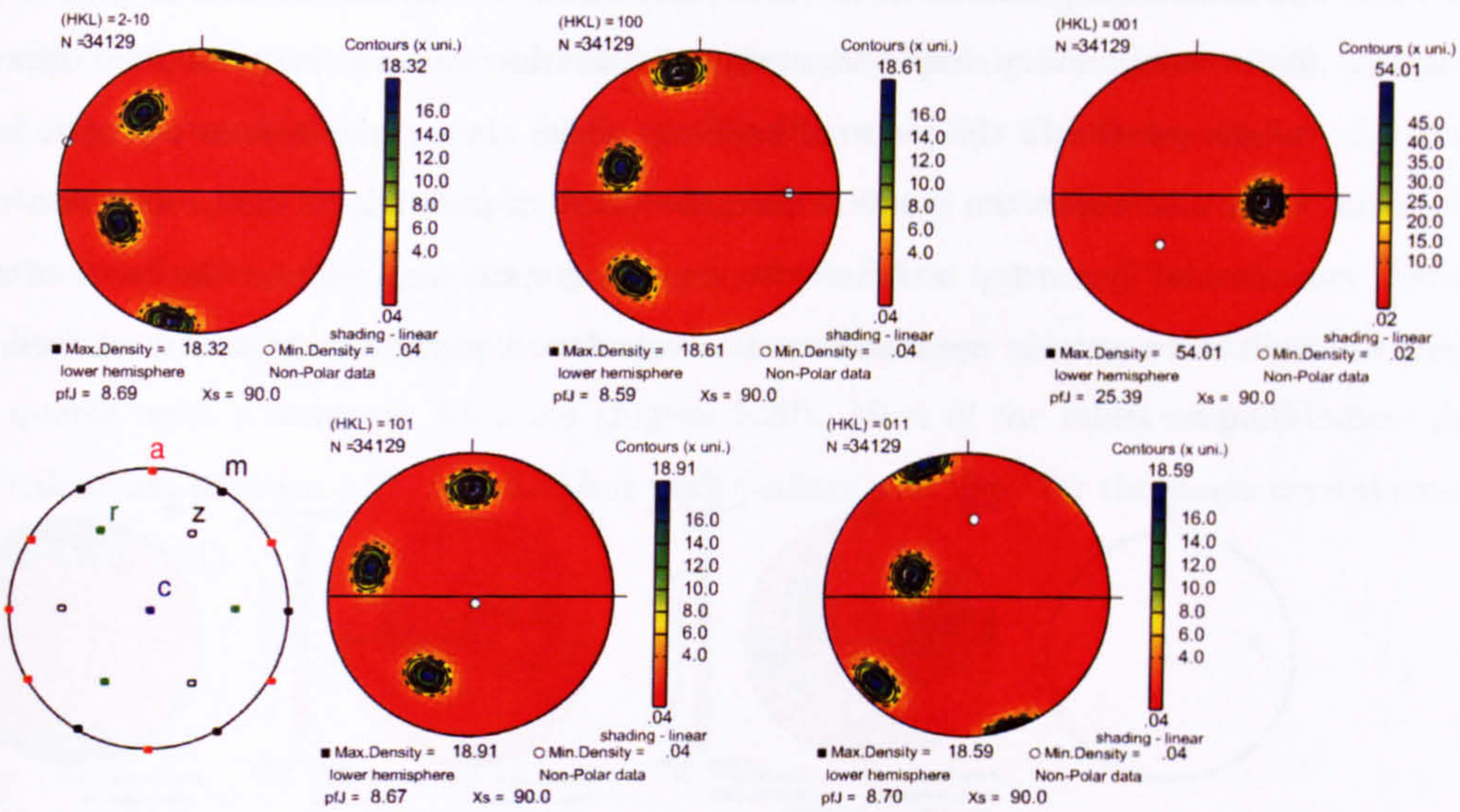

Figure 5.17: *Single crystal calcite pole figure after 34129 measurements on a 1cmx1cm polished block. Illustrative non-polar, lower hemisphere, crystallographic stereonets of calcite. Bedding is the horizontal line bisecting the pole figures and bedding perpendicular is at North (represented by the tick). The individual pole figures are contoured in multiples of uniform distribution (MUD). (HKL) = the pole to lattice plane. N = the number of indexed points with a MAD of* ≤ 1*. The black square represents the maximum concentration of crystallographic orientations (blue), and the empty circle represents the minimum concentration of crystallographic orientations (red). pfJ refers to the individual pole figure fabric intensity (Equation 5.15).*

5.9.4 Phyllosilicates

Using automated EBSD analyses muscovite crystallographic orientation determination was not successful primarily because of poor quality diffraction patterns. Manual EBSD indexing was, however, shown to be more successful in the determination of muscovite's crystallographic orientation. The results of manually indexing muscovite grains are presented in (Figure 5.18). Note that the results of the manual indexing are based upon 96 individual grains. Due to there platy structure, muscovite, and in general phyllosilicates, adopt a very simple orientation distribution whereby the basal plane approximately aligns parallel to the plane of bedding, whilst the a- and b- axes are more or less free to rotate about the c-axis within the plane of bedding. This observation of broadly uni-axial symmetry of muscovite crystallographic axes will be the basis of an analytical stereographic approach used to calculate a phyllosilicate elastic stiffness tensor in Chapter (6).

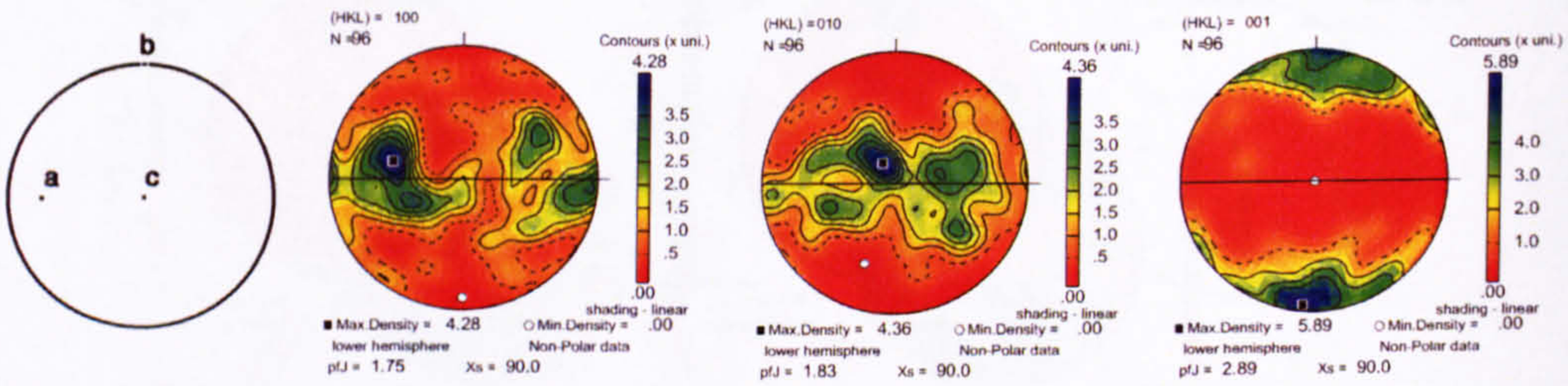

Figure 5.18: *Phyllosilicate pole figure. The c-axis is aligned approximately normal to the bedding plane, whilst the a- and b- axes freely rotate within this plane. Illustrative non-polar, lower hemisphere, crystallographic stereonets. Bedding is the horizontal line bisecting the pole figures and bedding perpendicular is at North (represented by the tick). The individual pole figures are contoured in multiples of uniform distribution (MUD). (HKL) = the pole to lattice plane. N = the number of indexed points with a MAD of ≤ 1. The black square represents the maximum concentration of crystallographic orientations (blue), and the empty circle represents the minimum concentration of crystallographic orientations (red). Note the variation in contour intervals between the pole figures. pfJ refers to the individual pole figure fabric intensity (Equation 5.15)*

5.10 Petrofabric results

Presented in Tables (5.1 and 5.2) is the raw data for the individual mineral phase texture-index calculations (J). Sample number notation is as follows; the small letter refers to

any number of repetitions of the same sample, X-Y-Z refers to the direction of core that it was removed from, a large letter followed by a number represents that a sample was also used for palaeomagnetic re-orientation. Where n/a appears, it means that the sample did not contain sufficient quantities of a mineral phase to enable its indexing. For example, 1663DY = sample number 1663, D the core was also used for palaeomagnetic re-orientation and was removed from core plug Y (parallel to bedding).

Frequency histograms have been plotted to facilitate the investigation of the relationship between mineral phase and absolute values of texture-indices (Figure 5.19, 5.20 and 5.21). Quartz has a very weak fabric texture (Figure 5.19). The texture-index of quartz throughout most of the samples (excluding any outliers) varies between 1, a completely random fabric, and 1.5, indicative of a very weak fabric texture. The frequency distribution of feldspar texture-indices suggest somewhat more clustered distributions than quartz, with a mean of 2.6 ± 0.8 (Figure 5.20). Most of the fabric texture-indices for calcite are between 1.25, and 2.50 but with outliers at c.12.50 for the single crystal cases (Figure 5.21).

Table 5.1: *Calculated texture indices for all samples within Well 206/8-8. Qtz. - quartz, Fspr. - feldspar and Clc. - calcite. See Appendix (B) for an explanation of the sample notation.*

Sample	Qtz.	Fspr.	Clc.
1663b	1.22	2.71	5.74
1663DY	1.43	2.86	12.20
1663Z	1.40	3.69	3.22
1784	1.31	2.30	2.43
1784a	2.26	3.31	n/a
1784b	1.28	1.92	1.49
1841	1.13	1.56	1.20
1909	1.21	2.55	6.73
1909L3	1.14	2.00	1.20
1950	1.46	3.24	1.41
1950NY1	1.40	2.83	1.30
2070X	1.20	2.06	1.14
2073	1.23	3.29	1.48
2073Z	1.53	2.69	1.90
2129	1.32	3.62	1.71
2129G3	1.36	3.62	1.71
2192	1.28	5.15	1.94
2194	1.18	2.21	1.11
2194KY2	1.20	2.94	1.52
2198	1.10	1.96	1.35
2198M1	1.07	1.76	1.41
2198Z	1.16	2.25	1.49
2198Za	1.11	1.84	1.47

Table 5.2: *Calculated texture indices for all samples within Well 206/13a-2. Qtz. - quartz, Fspr. - feldspar, and Clc. - calcite. n/a - not present. See Appendix (B) for an explanation of the sample notation.*

Sample	Qtz.	Fspr.	Clc.
1959	1.15	1.98	2.27
1963a	1.11	2.05	2.88
1963a2	1.27	3.00	1.75
1963AX	1.19	2.54	1.74
2015	1.25	2.19	1.75
2023	1.15	2.24	1.56
2028	1.28	3.31	1.83
2028B2	1.11	1.90	n/a
2034	1.21	2.10	n/a
2070X	1.20	2.06	1.14

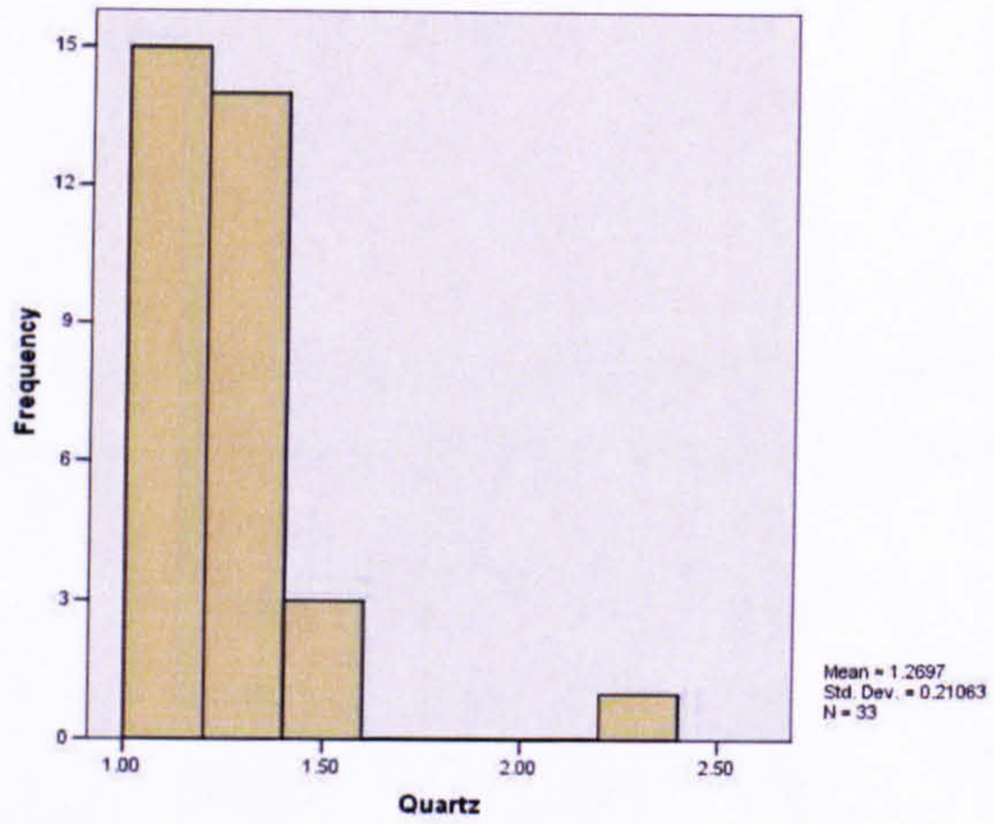

Figure 5.19: *Frequency histogram for the quartz texture-index for all samples analysed. The texture-index (J) is represented by the x-axis and increases from the left (random = 1) to the right (increased crystal alignment). Mean - 1.27, and standard deviation - 0.21.*

The mean, standard deviation (Kenney & Keeping 1962*a*), variance (Kenney & Keeping 1962*a*), minimum and maximum for the pre-processed (before removal of data outwith 1.5 standard deviations) data for the constituent mineral phases are presented in Table (5.3). Any problems encountered with anomalous data are identified and removed by applying a one and a half standard deviation (S.D.) filter to the data. After applying a 1.5 S.D. data filter quartz has the lowest mean fabric intensity, S.D., variance, minimum and maximum. Feldspar has the highest mean, S.D., variance, minimum and maximum, whilst, calcite has intermediate values of fabric intensity (Table 5.4). The random distribution of individual mineral phase texture-indices means that an approximation for the strength of fabric texture can be determined by taking the mean of all calculations (excluding outliers): quartz = 1.27, orthoclase = 2.49, and calcite = 1.73.

The texture-index (J) of all mineral phases is independent of both modal proportion and the texture-index and modal proportion of all other mineral phases (Figure 5.22). Given a set of variables $X_1, X_2, ...X_k$, the scatter plot matrix contains all the pairwise scatter plots of the variables on a single matrix format. If their are k variables, the scatter plot matrix will have k rows and k columns and the i_{th} row and j_{th} column of this matrix is a plot of X_i versus X_j. Since X_i versus X_j is equivalent to X_j versus X_i the plot is omitted. This observation is important because in multiple linear-regression when predictor variables are highly correlated, any one variable may act as a surrogate for any

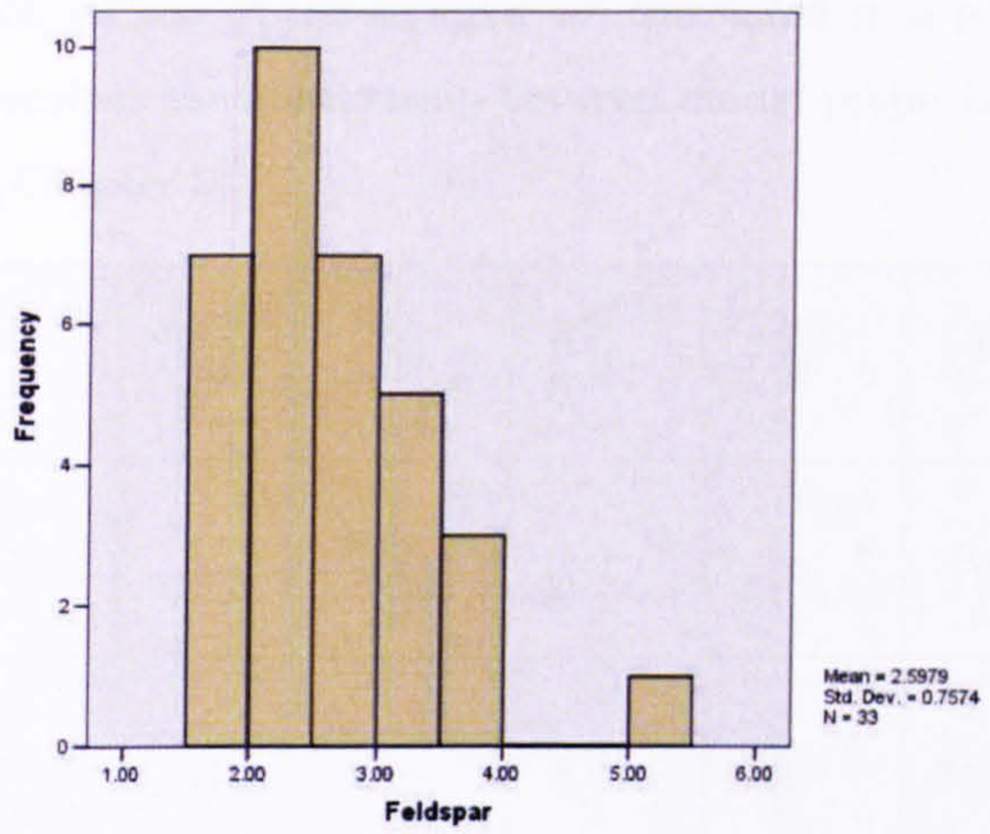

Figure 5.20: *Frequency histogram for the feldspar texture-index for all samples analysed (approximately log-normal). The texture-index (J) is represented by the x-axis and increases from the left (random = 1) to the right (increased crystal alignment). Mean - 2.60, and standard deviation - 0.76.*

Table 5.3: *Average texture-index properties for each constituent mineral phase. Qtz. = quartz, Fspr. = feldspar, and Clc. = calcite. S.D. = standard deviation, Var. = variance, Min.= minimum, and Max. = maximum.*

Phase	Mean	S.D.	Var.	Min.	Max.
Qtz.	1.27	0.21	0.05	1.08	2.26
Fspr.	2.92	2.05	4.20	1.56	13.4
Clc.	2.41	2.27	5.16	1.11	12.2

Table 5.4: *The texture-index for each constituent mineral phase with a 1.5 S.D. filter. Abbreviations - S.D. = standard deviation, Var. = variance, Min.= minimum and Max. = maximum. Bold type = new texture index due to the filter of anomalous data. Qtz. - quartz, Fspr. - feldspar, and Clc. - calcite.*

Phase	Mean	S.D.	Var.	Min.	Max.
Qtz.	1.27	0.21	0.05	1.08	2.26
Fspr.	**2.49**	**0.59**	**0.35**	1.56	**3.69**
Clc.	**1.73**	**0.53**	**0.29**	1.11	**3.22**

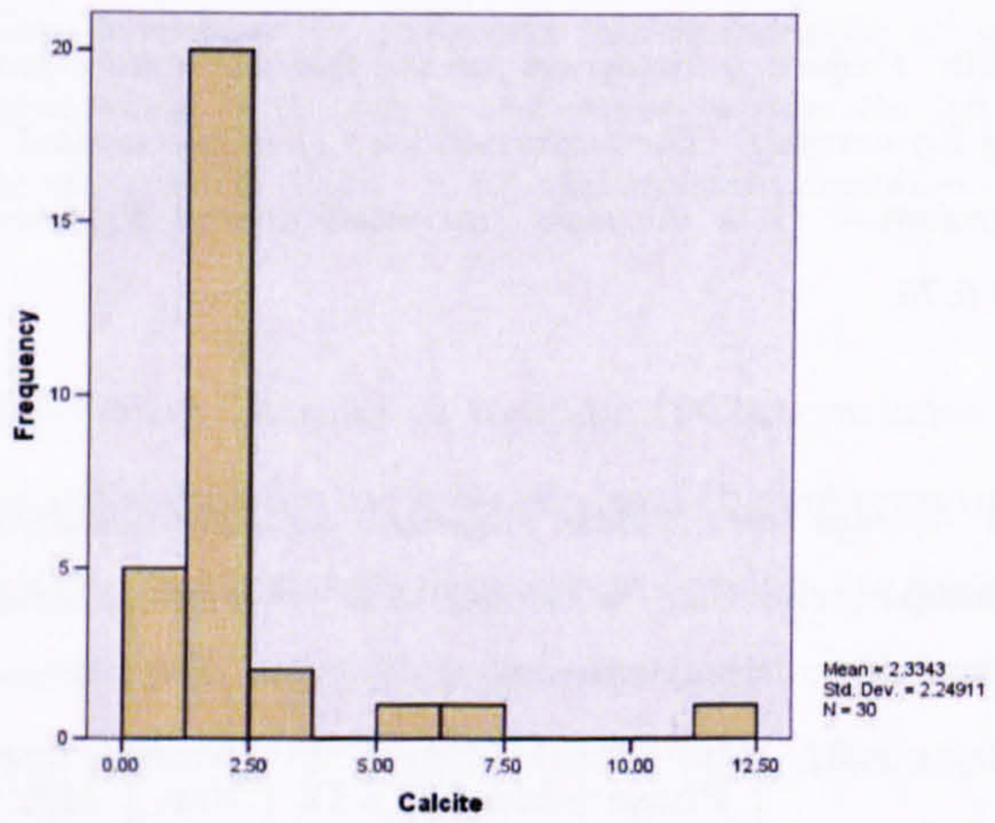

Figure 5.21: *Frequency histogram for the calcite texture-index for all samples analysed. The texture-index (J) is represented by the x-axis and increases from the left (random = 1) to the right (increased crystal alignment). Mean - 2.33, and standard deviation - 2.25.*

of the others. Hence, as non of the samples are correlated it is possible to determine a function which describes the relationship between modal proportion and the intrinsic seismic anisotropy (Chapter 6).

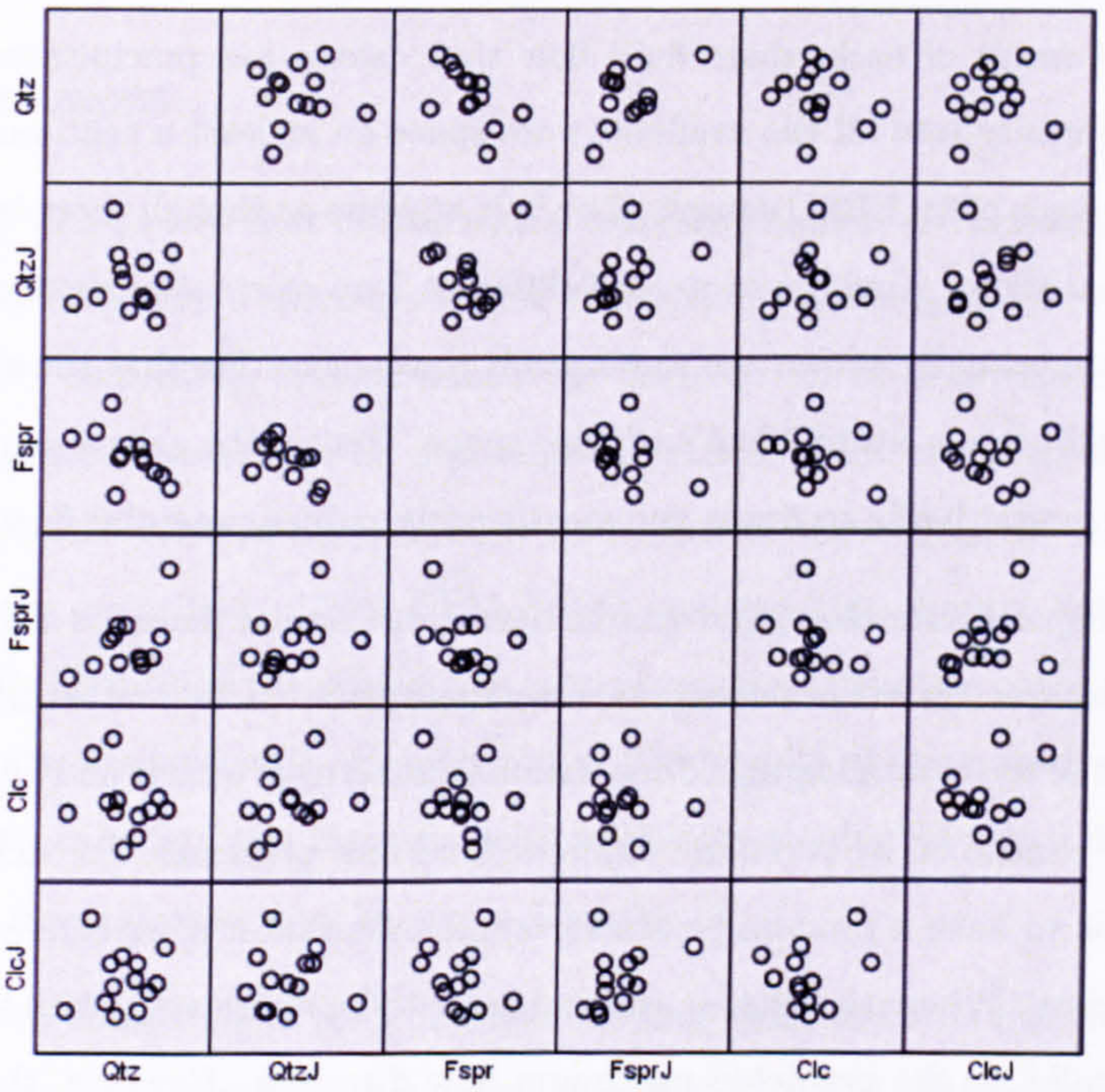

Figure 5.22: *Matrix scatter plot of each constituent mineral phase (Qtz = quartz, Fspr = feldspar, and Clc = calcite) and respective texture-index (mineral phase+J). Plotted within each individual cell is the modal proportion (increasing from left to right) for each sample with respect to its texture-index (increasing upwards within each cell) and every other sample's texture-index and modal proportion. The scatter plot shows whether any correlation exists between an individual sample's modal proportion and respective texture-index and when cross-correlated to all other sample's texture-indices and modal proportions. The matrix scatter plot assists the determination of independent variable dependence. Given a set of variables $X_1, X_2, ...X_k$, the scatter plot matrix contains all the pairwise scatter plots of the variables on a single matrix format. If there are k variables, the scatter plot matrix will have k rows and k columns and the i_{th} row and j_{th} column of this matrix is a plot of X_i versus X_j. Since X_i versus X_j is equivalent to X_j versus X_i the plot is omitted.*

5.11 Discussion

Calcite has been shown to generally exhibit a relatively weak fabric texture (c.1.5 - 2.0), however, one sample contains an almost single crystal orientation. It is believed that as a result of early stage fluid flow that calcite has precipitated in crystal orientation uniformity into all the available pore space on at least a centimetre scale. Therefore, on the scale of an EBSD sample ($1cm^2$) it appears as though there is only one calcite crystal orientation. Analysis of several different core orientations extracted from sample 1663 has repeatedly shown the same result thus suggesting that the single crystal orientation could occupy up to 10cm's of pore space. Hence, the calcite cementation could act as a horizontal baffle to fluids and significantly reduce potential flow rates.

Feldspar (orthoclase) and quartz have quite similar densities 2.57 and 2.65, respectively. Moreover, quartz is also significantly more resistant to weathering than orthoclase. Analysis of the crystallographic depositional patterns of quartz and feldspar suggests that they are controlled by two quite different fluid flow processes. For example, quartz grains appear to have a random crystallographic orientation irrespective of the depositional flow regime. Whereas, feldspar grains appear to be imbricated, with their longer axis oriented parallel to the predicted maximum flow direction. However, the alternative hypothesis is that the apparent difference in depositional patterns are actually only remnants of a biased sampling procedure. For example, the total number of orientation measurements for orthoclase ranged from four to eight thousand whereas for quartz the total number of orientation measurements varied between fifty and one hundred thousand. However, the law of large numbers states that the average of a randomly selected sample from a large population is likely to be close to the average of the whole population. On average each section contains approximately two to three hundred and fifty grains hence a sample selection of several tens of thousands is more than adequate sampling.

Confidence in the ability of EBSD to automatically index siliciclastic mineral phases correctly is a common concern within geosciences. SEM-EBSD in this study, however, has proven to be a relatively robust and reliable technique for analysing most mineral phases commonly found in siliciclastic hydrocarbon reservoir rocks. Minor problems were encountered on occasion when attempting to index low symmetry minerals (e.g., feldspars) and poorly-crystallised phases (e.g., phyllosilicates). In general, it has been found that feldspars provide relatively good Kikuchi patterns, that is, quite strong and

distinct band patterns whereas, phyllosilicates were found to produce weak, diffuse band patterns. The addition of two new indexing files for orthoclase and muscovite have proved to be of some benefit as demonstrated by the broadly improved indexing rate.

5.12 Conclusions

Although it is well known that clastic rocks, especially shales, are elastically and therefore seismically anisotropic there have been relatively few investigations into the various causes. Factors controlling seismic anisotropy include: LPO, non-random spatial distribution of mineral phases, SPO, and aligned cracks, pores or micro-discontinuities. However, as yet the relative contributions from each of these different factors has not been sufficiently quantified. Using SEM-EBSD analyses this chapter has investigated and successfully quantified the strength of fabric texture of the main constituent mineral phases of a suite of siliciclastic reservoir rocks. The results of these analyses have been further used to calculate the intrinsic seismic anisotropy due to the lattice preferred orientation of mineral phases, as shown in Chapter (6).

In general, when compared to some highly-deformed rocks the strength of fabric intensity for the three main constituent minerals was relatively low. Quartz has been shown to have an almost random crystallographic orientation in siliciclastic rocks, with most indices occurring between 1 and 1.5. Feldspar's crystallographic orientations have on average been shown to be more clustered and possess a log-normal frequency histogram distribution. Calcite can also be thought to have a random crystallographic orientation (usually between 1 and 1.5) except where it occurs as the dominant pore filling cement. When Calcite occurs as the pore filling cement it can grow freely and thus in crystallographic uniformity. The texture-index (J) after the removal of potentially anomalous results using a 1.5 standard deviation filter is as follows: quartz 1.27, feldspar 2.49 and calcite 1.73. Hence, apart from possibly phyllosilicates, feldspars are considered to have the greatest affect on the bulk aggregate seismic anisotropy. Even though on occasion calcite can have a very high fabric intensity these particular results have been shown to be anomalous and unrepresentative of the entire sample population.

The distributions of the quartz crystallographic axes are particularly weak and thus quite hard to determine. The c-axis of quartz (001) usually contains the strongest fabric alignment. The maximum alignment of (001) directions in quartz is usually either parallel

to the bedding plane, normal to the plane of the cut section, or oblique to the bedding plane, parallel to the plane of the the cut section. The location of girdles and position of the maximum crystal alignment are also broadly similar throughout all the quartz pole figures.

On aggregate the feldspar grains appear to have the strongest fabric alignment. Analysis of the individual feldspar pole figures suggests that the individual grains appear to be imbricated with their down dip direction varying with azimuth within the bedding plane (Appendix F). Two distinct yet similar systems of alignment can be identified, both of which generate the same style of grain alignment (grain imbrication). There is a single cluster within the [010] pole figure which is related to the girdle in [001]. Moreover, there is a single cluster in the upper-half of the [001] pole figure which is related to the broad girdle in [010]. These two different crystallographic orientations adopted by the feldspar grains both give rise to an imbricated style of grain fabric alignment.

Two very different pole figure distributions are observed within the samples analysed which contained calcite. Calcite is either observed to have a very weak fabric texture, almost random or a single calcite crystal orientation that can be up to tens of mm's and therefore significantly affect the LPO analyses. The single crystal orientation is likely to be due to cm scale pore occluding diagenetic calcite.

Automated EBSD analysis of the crystallographic orientation of muscovite was not particularly successful because of poor quality diffraction patterns. However, manual EBSD indexing was shown to be successful in the accurate determination of muscovite's crystallographic orientation. It is thought that due to muscovite's platy structure it adopts a very simple orientation distribution whereby the basal plane approximately aligns parallel to the plane of bedding, whilst the a- and b- axes are more or less free to rotate about the c-axis within the plane of bedding.

A matrix scatter plot of modal proportion versus strength of fabric intensity for every mineral phase against every other mineral phase demonstrates that their is no obvious linear correlation. This is an important observation in a number of ways. The fact that no relationship exists between modal proportion and strength of fabric intensity means that any model which is fitted to the data is not likely to be highly correlated.

Chapter 6

Seismic anisotropy

6.1 Introduction

Seismic anisotropy is controlled by: LPO (lattice preferred orientation), the non-random spatial distribution of mineral phases, aligned porosity, and aligned fractures (Crampin 1981, Babuska & Cara 1991, Mainprice et al. 2000, Wendt et al. 2003, Kendall et al. 2006, Valcke et al. 2006). Because of the control of microstructure on seismic anisotropy it follows that seismic anisotropy could be used as a diagnostic for specific rock types. The calculation of the physical properties of a bulk aggregate from microstructural information is fundamental to understanding the importance of the role microstructure plays in bulk rock seismic properties. To experimentally determine anisotropic bulk aggregate properties using ultrasonic analysis would require many different directions of measurement to characterise it fully. It would also be difficult to isolate a SPO effect from other grain scale effects. Although it is understood that sedimentary rocks can be seismically anisotropic, there have been relatively few investigations of the various individual underlying causes. The relative contribution from the various factors to observations of seismic anisotropy in sedimentary rocks is not well understood. In this part of the study the seismic anisotropy due to preferred mineral orientation will be investigated. Chapter (5) quantified the LPO (fabric strength) of the constituent mineral phases in a suite of siliciclastic hydrocarbon reservoir rocks using EBSD (electron backscattered diffraction). This Chapter will present the results of the calculations of seismic anisotropy due to the LPO of mineral phases alone.

To enable and constrain the interpretation of P- and S-wave anisotropy data a forward

model was devised. The model which is based upon a simple assumption about the nature of the fabric strength of the constituent mineral phases enables the prediction of anisotropy and velocity with different models of anisotropy and will in turn help guide the interpretation of the real data. The ability to quickly and accurately provide information about a rock's intrinsic seismic anisotropy from modal mineralogy alone is a useful tool to have. Assessment of the results obtained from SEM-EBSD analyses shows that the texture-index (J) or fabric strength of the individual mineral phases does not vary significantly or predictably throughout the reservoir. Therefore, with this observation in mind it is possible to take a simple-average of the individual texture-indices for each mineral phase and hence determine it's average elastic stiffness tensor. Then, with *a priori* knowledge of the modal mineralogy of a particular horizon as obtained from wireline logs or laboratory experiments it is then possible to predict the expected intrinsic elastic stiffness tensor. Using the prediction of expected elastic stiffness tensor it is then possible to calculate the expected P- and S-wave velocities in any direction from the Christoffel equation.

Several workers have supported the simple, if not obvious, idea that P- and S-wave velocities of rocks are related to mineralogy and porosity (Nur & Simmons 1969, Vernik & Nur 1992*a*). Han (1986) found empirical regressions relating ultrasonic (laboratory) velocities to porosity and clay content. Similarly, Eberhart-Phillips (1989) used a multivariate analysis to investigate the combined influences of effective pressure, porosity, and clay content on Han's measurements of velocities in water-saturated shaley-sandstones. Using this simple idea the results of the analyses obtained from SEM-EBSD measurements were assessed using a linear multivariate regression to determine models which would predict the intrinsic P- and S-wave anisotropy from modal mineralogy alone. This would then provide a means with which to estimate the expected intrinsic seismic anisotropy from *a priori* knowledge of the modal mineralogy of a particular reservoir unit. Nonetheless, these relations are only empirical and strictly speaking only apply to the rocks studied. Future studies will decide how generally applicable these relations are. By determining models which accurately predict intrinsic seismic anisotropy from modal mineralogy alone allows a quick assessment to be made of the expected anisotropy for a particular horizon without the effort of having to analyse it using SEM-EBSD.

6.2 Estimation of seismic anisotropy from polycrystalline properties

Given petrofabric characterisation a number of different methods are available to determine the effective macroscopic property, such as, Voigt-Reuss-Hill (VRH), self-consistent (SC), and differential effective medium (DEM) modelling. Each averaging technique deals with an increasing order of microstructural complexity but with each method predicting values that are progressively closer to those obtained by experimental methods (Mainprice et al. 2000, Wendt et al. 2003).

The simplest and best known averaging technique for determining the effective elastic bulk properties due to LPO alone is VRH. Where LPO is the sole microstructural feature under investigation the Voigt and Reuss averaging schemes are the best suited, in which upper and lower bounds are placed on material properties by taking weighted arithmetic and harmonic means respectively of the single crystal elastic stiffness tensors of each constituent phase. The VRH average is completely heuristic but does provide a useful approximation. These averages only use the: volume fraction, orientation, and individual crystal elastic constants of the constituent phases. No information regarding the shape or position of the grains is taken into consideration. The initial assumptions are that the aggregate is macroscopically uniform with microscopic heterogeneities and that the each constituent phase is isotropic, linear, and elastic. These basic assumptions can be justified to a certain degree because when the number of anisotropic grains is sufficiently large the orientations can be thought of as randomly distributed and thus the *effective* macroscopic behaviour will be isotropic (Mavko et al. 1998, Mainprice et al. 2000). Nonetheless, the samples are physically not isotropic and therefore the assumption is inaccurate. However, the simplicity of VRH and the accuracy of the calculated results to experimentally obtained values mean that it is a useful way of estimating the bulk aggregate properties.

The procedure for determining the aggregate elastic moduli devised by Voigt (1928) assumed that the strain was constant throughout the sample. In contrast, Reuss (1929) assumed that the stress was constant throughout the sample. Hill (1952) showed that the Voigt and Reuss estimates were upper and lower bounds, respectively. The Voigt average is very simply found by assuming that the strain is constant throughout the sample and that the strain is equal to the macroscopic strain of the sample (Mainprice et al. 2000). The effective macroscopic modulus, C^*, is then estimated by a volume

average of the local stiffnesses $C(g_i)$ with orientation g_i and volume fraction V_i, where,

$$C \approx C^{voigt} = [\sum_i V_i C_{(g_i)}]. \tag{6.1}$$

The Reuss average is then found by assuming that the stress is equal the macroscopic stress of the sample. C^* or S^* is then estimated by the volume average of the local compliances, $S_{(g_i)}$, where,

$$C^* \approx C^{Reuss} = [\sum_i V_i S_{(g_i)}]^{-1} \tag{6.2}$$

and,

$$S^* \approx S^{Reuss} = [\sum_i V_i S_{(g_i)}] \tag{6.3}$$

These two estimates are not equal for anisotropic solids where the Voigt is an upper bound and the Reuss a lower bound. A physical estimate should therefore be found somewhere between the bounds. Hill (1952) found that the arithmetic mean of the Voigt and Reuss bounds was often close to the experimental values. The Hill average is simply determined as the arithmetic mean of the Voigt and Reuss averages (Hill 1952) but has no theoretical justifcation.

6.3 Calculating seismic properties

Each indexed point obtained by EBSD analysis is associated with a set of Euler angles (according to Euler's rotation theorem, any rotation may be described using three angles). The ODF, $f(g)$, is defined as the volume fraction of crystal orientations with an orientation in the interval, g to $g + dg$ in a space containing all possible orientations,

$$\Delta V/V = \int f(g) dg, \tag{6.4}$$

where $\Delta V/V$ is the volume fraction of crystals with orientation g, $f(g)$ is the texture function, and $dg = \frac{1}{8}\pi^2 sin\phi d\varphi_1 d\phi d\varphi_2$ is the volume of the region of integration in orientation space (Mainprice et al. 2000).

For every individual measured orientation, g, each reference crystal co-ordinate frame has to be rotated into the specimens co-ordinate frame using the rotation matrix, g_{ij},

$$C_{ijkl}(g) = g_{ip}g_{jq}g_{kr}g_{lt}C_{pqrt}(g^0), \tag{6.5}$$

where $C_{ijkl}(g)$ (Section 1.3) is the elastic tensor of the crystal in the sample co-ordinate frame, $g_{ij} = g(\varphi_1, \phi, \varphi_2)$ the direction cosines based on the Euler angles, and $C_{pqrt}(g^0)$ is the elastic tensor in the crystal co-ordinate frame.

It is then possible to calculate the elastic tensor of the polycrystal by integrating the ODF over all possible orientations,

$$< C_{ijkl} >^m = \int C^m_{ijkl}(g) f(g) dg, \tag{6.6}$$

where, $< C_{ijkl} >^m$ is the bulk aggregate elastic tensor of mineral, m (Bunge 1982).

The single crystal elastic tensors for all minerals used in this study to determine aggregate seismic properties are listed in Appendix (D).

The elastic constants of the polycrystalline aggregate obtained from the averaging procedure of Hill (1952) are then used to calculate the seismic anisotropy attributed to the LPO of constituent mineral phases by solving the Christoffel equation (Christoffel 1910).

The equations of motion for elastic media, are written,

$$\frac{\partial \sigma_{ij}}{\partial x_j} = \rho \frac{\partial^2 u_i}{\partial t^2}, \tag{6.7}$$

at time t, where ρ is the density of the medium, σ_{ij} is the $3D$ stress tensor, u_i is the displacement, and x_j is the spatial coordinate system (Kendall 2000). Substitution of Equations (1.1 and 1.4) into Equation (6.7) gives for homogeneous media,

$$c_{ijkl}\frac{\partial^2 u_l}{\partial x_j \partial x_k} = \rho \frac{\partial^2 u_i}{\partial t^2}. \tag{6.8}$$

A plane-wave harmonic solution of (6.8) takes the form,

$$u_i = A_i e^{i\omega(t \pm x_i n_i / v_n)}, \tag{6.9}$$

where A is the amplitude and ω the frequency of a plane wave with unit normal, n_i and phase velocity, v_n. Substituting Equation (6.9) into Equation (6.8) gives,

$$c_{ijkl}(n_i n_l - \rho v_n^2 \delta_{jk} A_k) = 0, \tag{6.10}$$

where δ_{jk} is the Kronecker delta. Assuming A gives non-zero terms,

$$det|c_{ijkl}n_k n_l - \rho v_n^2 \delta_{ij}| = 0 \tag{6.11}$$

and

$$det|c_{ijkl}p_k p_l - \rho \delta_{ij}| = 0. \tag{6.12}$$

Thus the phase velocities of the three wave fronts can be determined from the three eigenvalues of $c_{ijkl}p_i p_j$ which correspond to one quasi-P wave and two quasi-S waves (Love 1944, Nye 1957).

The phase velocities in this study are presented as two lower hemispherical pole figure projections. These illustrate the P-wave velocity, and fast shear-wave polarisation orientation (denoted by black ticks) with the degree of shear-wave splitting contoured in the background (Figure 6.1). The seismic velocity pole figures were produced using open source software originally written by D. Mainprice (Mainprice 1990). Presented in Appendix (H) are the single crystal seismic properties for the constituent mineral phases.

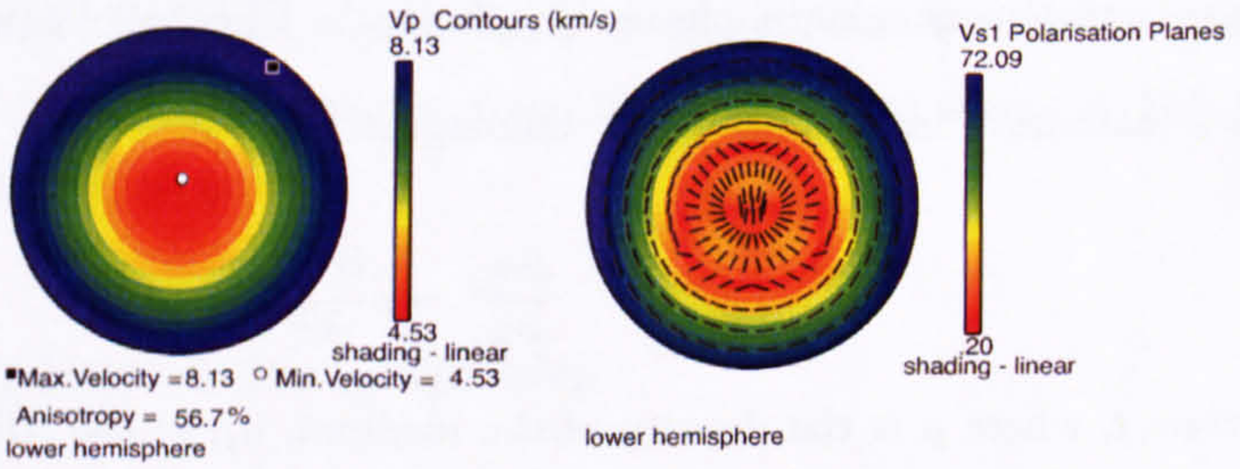

Figure 6.1: *Illustrative lower hemisphere velocity pole figures for single crystal muscovite (looking down onto the bedding plane/basal plane). The basal plane is represented by the perimeter of the circle. The pole figures from left-to-right represent: P-wave velocity distribution (km/s), and degree of shear-wave splitting (%), the black ticks represent the polarisation orientation of the fast shear-wave. Blue - High velocity/anisotropy, and Red - Low velocity/ansiotropy.*

6.4 Individual constituent mineral phase seismic anisotropy

6.4.1 Overview

Presented in this section are the results of the single mineral phase compressional and shear-wave velocity-anisotropy calculations. The single mineral phase calculations are

presented here to assist in the determination of the contribution made by a particular mineral phase to the bulk aggregate intrinsic seismic anisotropy.

6.4.2 Single mineral phase seismic anisotropy pole figures

The velocity and anisotropy single crystal pole figures for quartz are shown in Figures (I.1, I.2 and I.3) in Appendix (I). Presented in Figure (6.2) is an example of a typical quartz single mineral phase pole figure distribution. The velocity anisotropy symmetry patterns associated with quartz are broadly similar throughout samples that have a high quartz modal proportion ($> 50\%$). Figures (J.1, J.2 and J.3) in Appendix (J) show the consitentcy of alignment of feldspar maximum P-wave velocity and the consistent orientation of fast shear-wave polarisation throughout all the samples analysed. Presented in Figure (6.3) is an example of typical feldspar single mineral phase pole figure distributions. Calcite has rather more random velocity-anisotropy pole figure distributions as shown in Figures (K.1 and K.2) within Appendix (K). Presented in Figure (6.4) is an example of typical calcite single mineral phase pole figure distributions. A summary of the P- and S-wave single crystal seismic anisotropy calculations is shown in Table (6.1).

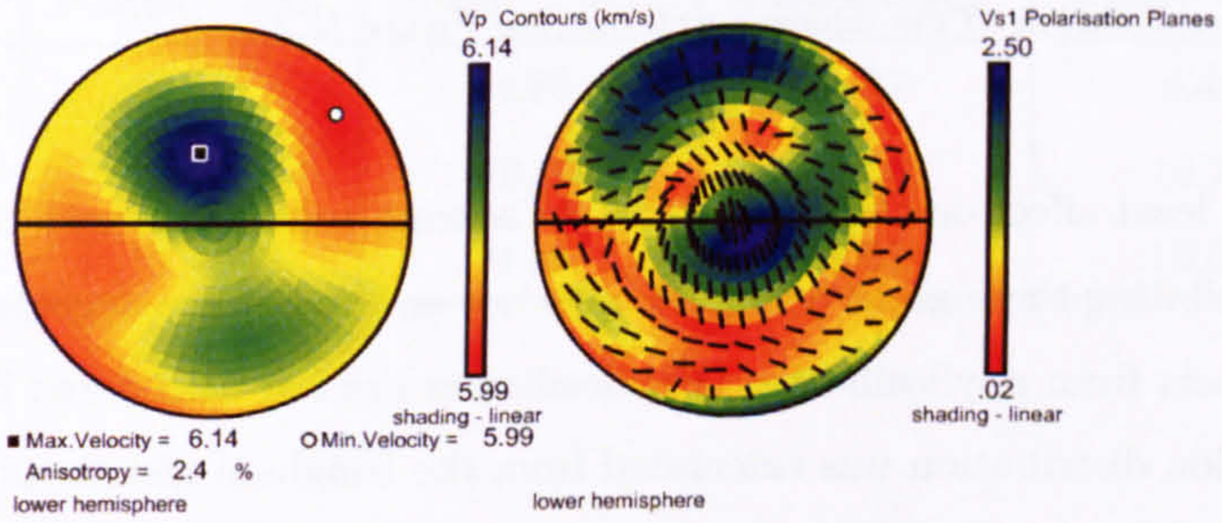

Figure 6.2: *Typical quartz single mineral phase velocity-anisotropy pole figure distributions. For an explanation of the diagram notation see Figure (6.1).*

A semi-log transform is shown to approximately linearise the relationship between fabric-intensity (J) (Chapter 5), and the maximum P- and S-wave anisotropy. Plotting the texture-index for all phases and samples versus degree of maximum P- and S-wave anisotropy results in the degree of anisotropy approaching a maximum achievable value which is probably dependent upon the particular mineral phase. Every individual phase has a maximum texture-index associated with a single crystal orientation and an associated maximum value for intrinsic seismic anisotropy. Quartz is predicted to have

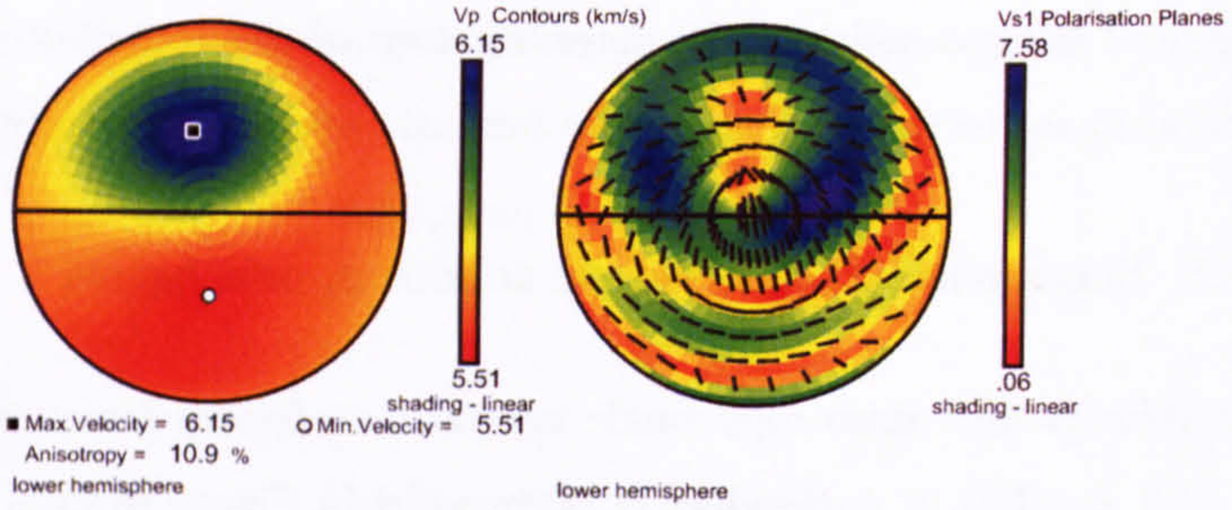

Figure 6.3: *Typical feldspar single mineral phase velocity-anisotropy pole figure distributions. For an explanation of the diagram notation see Figure (6.1).*

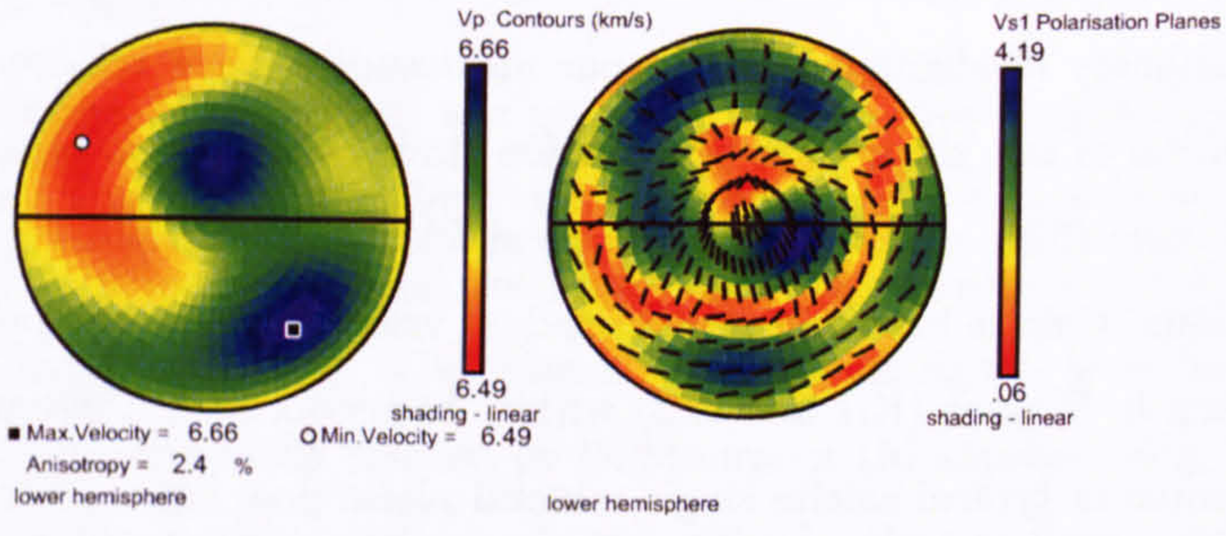

Figure 6.4: *Typical calcite single mineral phase velocity-anisotropy pole figure distributions. For an explanation of the diagram notation see Figure (6.1).*

the least affect on the bulk aggregate seismic anisotropy, with calcite next, and feldspar exhibiting the highest degree of influence on the P-wave aggregate anisotropy, excluding affects from phyllosilicates. Phyllosilicates are not considered here because their orientation distribution was calculated from the Bingham distribution and manual indexing. The relationship is such that the degree of P-wave anisotropy increases rapidly as the texture-index incrementally increases (Figure 6.5). Quartz produces a relatively tight cluster excluding a couple of outliers, that have low texture-indices and single mineral seismic anisotropy. Feldspar, however, is observed to have the higher variability in both texture-index and resulting single mineral anisotropy than quartz. On average the seismic anisotropy arising from the effect of feldspars is significant. The texture-indices and associated seismic anisotropy as a result of calcite is the most highly variable. In general, however, excluding potential sample anomalies (1663DY), calcite generally has a relatively low texture-index between 1-2 and thus resulting seismic anisotropy in the region of 2-4%. Quartz has the lowest amount of shear-wave splitting and has a signif-

Table 6.1: *Calculated minimum (min.) and maximum (max.) P- and S-wave anisotropy quoted in per cent attributed to a single mineral phase. Qtz. - quartz, Fspr. - feldspar, and Clc. - calcite.*

Phase	P-wave - min.	P-wave - max.	S-wave - min.	S-wave - max.
Qtz.	1.20	4.80	1.47	6.43
Fspr.	2.50	10.90	4.46	10.70
Clc.	1.40	9.20	1.61	13.04

icant variation. Feldspar is no longer the most anisotropic mineral phase, calcite has the greatest variation, and is predicted to have the highest shear-wave splitting (Figures 6.6).

6.5 Bulk aggregate seismic anisotropy predictions

6.5.1 Overview

The bulk aggregate seismic anisotropy predictions were calculated using QXRD determined modal proportions (Chapter 3), fine-clays (e.g., kaolinite) were approximated as having an isotropic distribution, an approximated phyllosilicate elastic tensor (as determined by taking an average of the Bingham approximation and EBSD manual indexing), and with the assumption of an isotropic distribution of a gas filled pore space.

6.5.2 Bulk aggregate seismic anisotropy pole figure predictions

The bulk aggregate velocity-anisotropy pole figures for the entire suite of samples analysed are presented in Figures (L.1, L.2 and L.3) in Appendix (L). Presented in Tables (6.2, 6.3 and 6.4) are the intrinsic seismic velocity and anisotropy predictions for all of the samples analysed using EBSD. A summary of the bulk aggregate P- and S-wave velocity and anisotropy predictions are shown in Table (6.5).

6.5.3 Ternary plots representing seismic anisotropy due to modal proportions

When a system, such as a clastic rock, can be considered to consist of only three main components the relative fractions of each component can be easily plotted on a simple ternary diagram. A typical rock with some composition will plot at the point that corresponds to the fractional volumes of the three components. Unfortunately, there are four components within the rocks in this study: quartz, feldspar, calcite and phyllosilicates. To construct a diagram as outlined previously some assumptions about a mineral phases fabric-intensity have to be made. Hence, quartz and calcite broadly have or as near to as possible a completely random mineral fabric, and, thus it was decided that there modal proportions would be added together on a single axis. Plotting phyllosilicate content and the combined total of quartz, calcite, and feldspar on a ternary diagram with the degree of both P- and S-wave seismic anisotropy as colour coded symbols clearly demonstrates that phyllosilicate content has a significant impact on the degree of predicted anisotropy

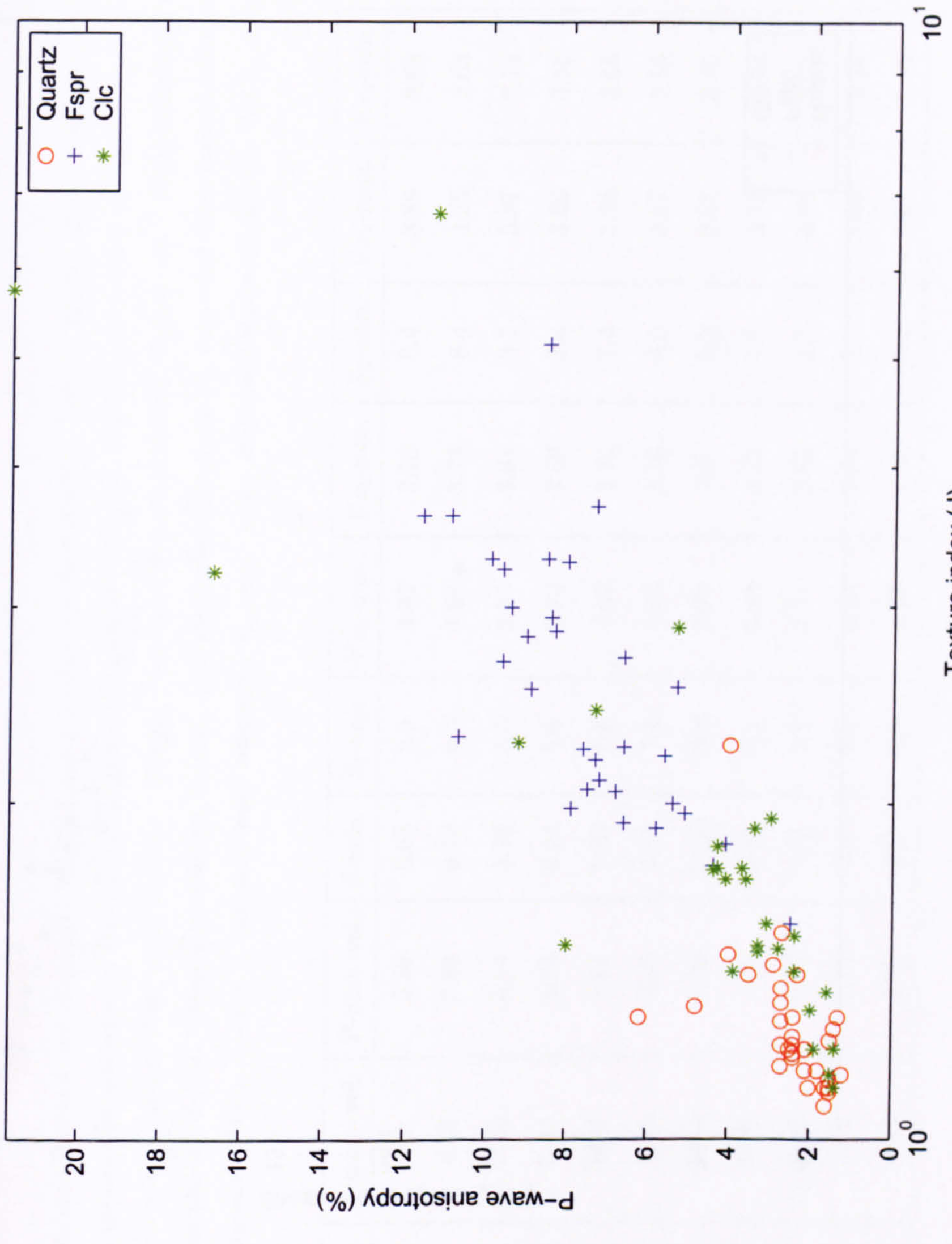

Figure 6.5: *A semi-log plot of the texture-index versus the calculated P-wave anisotropy for the individual constituent mineral phases. Notation: quartz - red circle, feldspar - blue cross, and calcite - green star. A semi-log transform approximately linearises the relationship between fabric strength intensity (J) and the degree of P-wave anisotropy. Hence, the model that describes the relationship between fabric intensity, and P-wave anisotropy is intrinsically linear.*

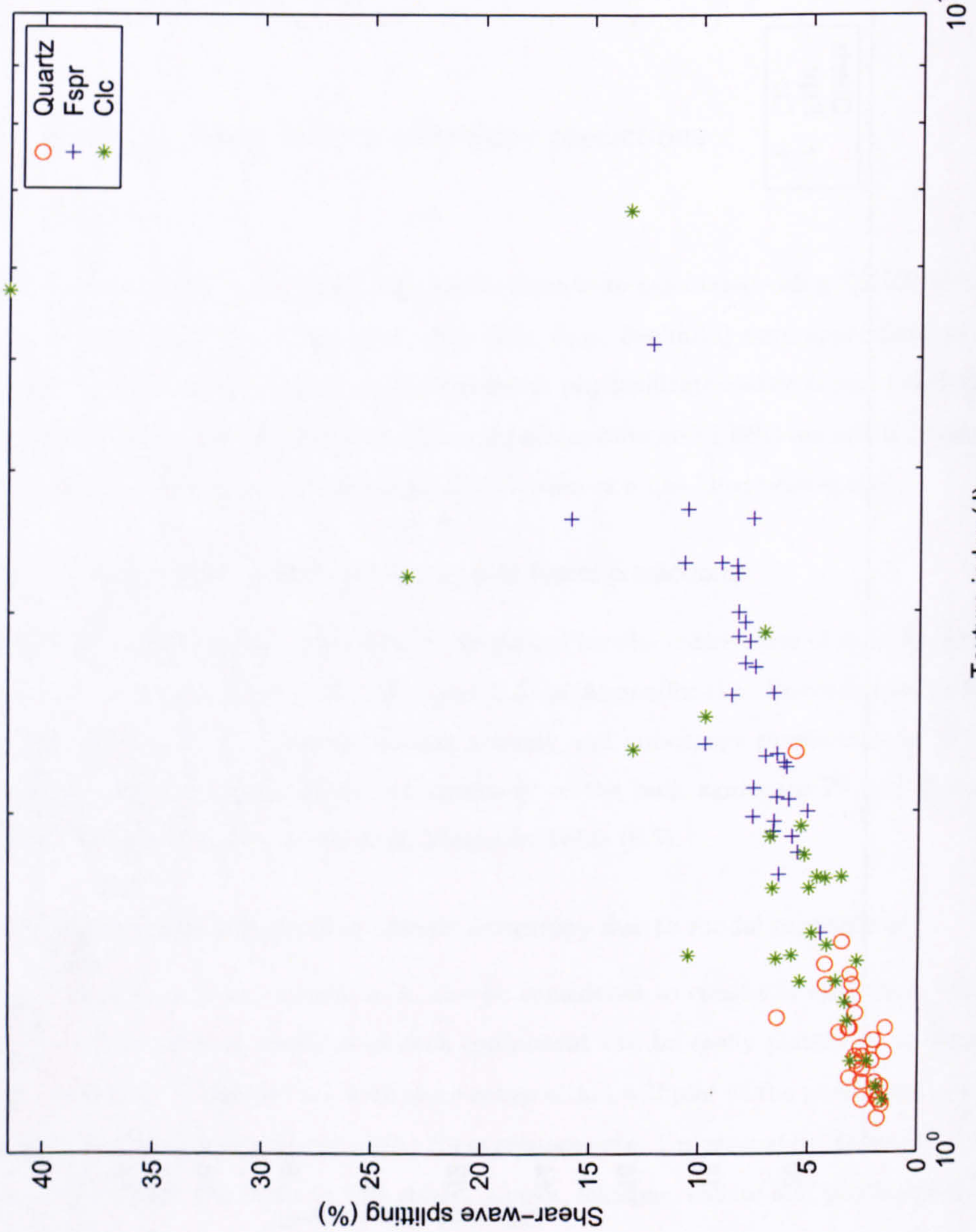

Figure 6.6: *A semi-log plot of the texture-index versus the calculated S-wave anisotropy for the individual constituent mineral phases. Notation: quartz -red circle, feldspar - blue cross, and calcite - green star. A semi-log transform approximately linearises the relationship between fabric strength intensity (J) and the degree of S-wave anisotropy. Hence, the model that describes the relationship between fabric intensity and S-wave anisotropy is intrinsically linear.*

Table 6.2: *Individual sample compressional and shear-wave velocity, and anisotropy for Well 206/8-8, 1663m - 1950m. For an explanation of sample notation see Appendix (B). Maximum and minimum are theoretically calculated in a complete 3D space. Velocities are in km/s and anisotropy is in percent. V_{s_1} is the fast shear-wave and V_{s2} is the slower shear-wave. Notation : P-anis. - maximum P-wave anisotropy, P-max. vel. - P-wave maximum velocity, P-min. vel. - P-wave minimum velocity, S-anis. - shear-wave splitting, S_1 anis. - fast shear-wave anisotropy, V_{s_1} max - fast shear-wave maximum velocity, V_{s_1}-min - fast shear-wave minimum velocity, S_2-anis. - slow shear-wave anisotropy, V_{s_2}-max. - slow shear-wave maximum velocity, and V_{s_1}-min. - fast shear-wave minimum velocity.*

Sample	P-anis.	P-max. vel.	P-min. vel.	S-anis.	S_1-anis.	Vs_1-max.	Vs_1-min.	S_2-anis.	Vs_2-max.	Vs_2-min.
1663b	7.3	6.3	5.86	6.68	5.0	3.97	3.78	5.4	3.89	3.69
1663DY	9.3	6.39	5.83	9.78	9.0	4.08	3.73	8.4	3.95	3.63
1663Z	6.3	6.22	5.84	5.28	3.5	3.95	3.81	3.7	3.87	3.73
1784	8.2	6.23	5.74	6.24	5.6	3.79	3.59	3.0	3.66	3.55
1784a	9.4	6.42	5.84	7.98	7.1	4.02	3.74	7.4	3.94	3.65
1784b	7.9	6.25	5.78	7.57	7.2	3.83	3.56	4.0	3.67	3.53
1841	14.3	6.49	5.63	13.65	12.8	3.98	3.5	5.9	3.67	3.46
1909	3.1	6.05	5.86	3.48	3.1	3.84	3.72	2.7	3.79	3.68
1909L3	3.1	6.04	5.86	2.31	2.1	3.81	3.73	1.3	3.76	3.71
1950	5.00	6.04	5.75	4.1	4.1	3.73	3.58	2.7	3.65	3.55
1950NY1	4.8	6.05	5.76	4.03	4.0	3.73	3.58	3.1	3.65	3.54

Table 6.3: *Individual sample compressional and shear-wave velocity and anisotropy for Well 206/8-8, 2073m - 2198m. For an explanation of sample notation see Appendix (B). Maximum, and minimum are theoretically calculated in a complete 3D space. Velocities are in km/s and anisotropy is in percent. V_{s_1} is the fast shear-wave and V_{s2} is the slower shear-wave. Notation : P-anis. - maximum P-wave anisotropy, P-max. vel. - P-wave maximum velocity, P-min. vel. - P-wave minimum velocity, S-anis. - shear-wave splitting, S_1 anis. - fast shear-wave anisotropy, V_{s_1} max - fast shear-wave maximum velocity, V_{s_1}-min - fast shear-wave minimum velocity, S_2-anis. - slow shear-wave anisotropy, V_{s_2}-max. - slow shear-wave maximum velocity, and V_{s_1}-min. - fast shear-wave minimum velocity.*

Sample	P-anis.	P-max. vel.	P-min. vel.	S-anis.	S_1-anis.	Vs_1-max.	Vs_1-min.	S_2-anis.	Vs_2-max.	Vs_2-min.
2073	11.1	6.33	5.66	10.15	8.5	3.96	3.63	4.7	3.74	3.57
2073Z	9.8	6.32	5.73	9.3	8.6	3.95	3.63	5.1	3.78	3.59
2129	3.5	6.09	5.88	3.42	3.5	4.03	3.89	2.7	3.95	3.85
2129G3	3.6	6.1	5.88	2.95	3.3	4.02	3.89	1.8	3.95	3.88
2192	4.6	6.13	5.85	4.1	3.8	3.98	3.83	2.2	3.89	3.8
2194	4.2	6.1	5.85	3.49	3.4	3.91	3.78	2.3	3.85	3.76
2194KY2	5.5	6.15	5.82	4.92	4.0	3.93	3.78	3.3	3.85	3.73
2198	7.1	6.19	5.76	6.11	5.8	3.95	3.72	2.7	3.8	3.7
2198M1	7.3	6.2	5.76	5.95	5.8	3.95	3.72	2.8	3.81	3.7
2198Z	6.0	6.17	5.81	4.61	4.0	3.9	3.75	2.5	3.82	3.72
2198Za	7	6.19	5.77	5.63	4.9	3.93	3.74	2.8	3.81	3.7

Table 6.4: *Individual sample compressional and shear-wave velocity and anisotropy for Well 206/13a-2. For an explanation of sample notation see Appendix (B). Maximum and minimum are theoretically calculated in a complete 3D space. Velocities are in km/s and anisotropy is in percent.* V_{s_1} *is the fast shear-wave and* V_{s2} *is the slower shear-wave. Notation : P-anis. - maximum P-wave anisotropy, P-max. vel. - P-wave maximum velocity, P-min. vel. - P-wave minimum velocity, S-anis. - shear-wave splitting,* S_1 *anis. - fast shear-wave anisotropy,* V_{s_1} *max - fast shear-wave maximum velocity,* V_{s_1}*-min - fast shear-wave minimum velocity,* S_2*-anis. - slow shear-wave anisotropy,* V_{s_2}*-max. - slow shear-wave maximum velocity, and* V_{s_1}*-min. - fast shear-wave minimum velocity.*

Sample	P-anis.	P max vel.	P min vel.	S-anis.	S_1 anis.	Vs_1 max	Vs_1 min	S_2 anis.	Vs_2 max	Vs_2 min
1959	5.60	6.16	5.83	5.16	4.9	3.74	3.56	3.5	3.65	3.52
1963a	10.2	6.41	5.79	9.68	9.5	3.98	3.62	4.3	3.77	3.61
1963a2	11.2	6.43	5.75	9.98	8.9	3.99	3.65	4.7	3.77	3.60
1963AX	10.3	6.41	5.78	9.62	9.5	3.99	3.63	4.0	3.77	3.62
2015	4.1	6.06	5.82	3.35	3.3	3.86	3.73	2.1	3.78	3.7
2023	5.7	6.11	5.78	4.15	3.9	3.86	3.71	3.5	3.8	3.67
2028	8.2	6.21	5.73	6.73	6.4	3.93	3.69	4.0	3.8	3.65
2028B2	7.2	6.16	5.73	5.9	5.7	3.91	3.69	2.8	3.77	3.67
2034	12.9	6.55	5.75	11.18	10.2	4.07	3.68	5.9	3.83	3.61
2070X	9.6	6.27	5.7	7.86	7.1	3.9	3.63	3.4	3.73	3.6

Table 6.5: *Statistical descriptives for the suite of samples for bulk aggregate P- and S-wave anisotropy quoted in %. S.D. = standard deviation, Var. = variance, Min.= minimum and Max. = maximum.*

Wave type	Mean	S.D.	Var.	Min.	Max.
P	7.29	2.91	8.48	3.10	14.30
S	6.42	2.80	7.86	2.31	13.65

(Figures 6.7 and 6.8). Moreover, by plotting different combinations of constituent minerals, such as, feldspar and calcite it becomes evident that the feldspar component is also a significant contributor to the bulk aggregate seismic anisotropy (Figures 6.9 and 6.10).

6.6 Predictions of seismic anisotropy using modal proportions

6.6.1 Velocity anisotropy-modal proportion model: predictions using the elastic tensor

With only a limited number of LPO SEM-EBSD measurements available and to allow estimates of the intrinsic seismic properties of sections of the reservoir not sampled, it is important to derive a predictive model. The following is a recipe that ultimately allows the prediction of the velocity-anisotropy (C_{ij} tensor) of any rock within the Clair field. This assumes, however, that the intrinsic nature of the mineral alignment does not vary significantly or consistently throughout the reservoir. In addition, individual sample directional information related to the C_{ij} is lost as it is only an average of the suite of mineral phase elastic tensors that is used in the calculations. The texture-index does not vary significantly with modal proportion nor are they correlated, which has been demonstrated in Chapter (5). Therefore it is possible to use a fixed value which describes the strength of fabric for each constituent mineral phase, and thus in turn, determine the relevant elastic tensor which describes the strength of fabric for the particular phase (Figures 6.5 and 6.6).

The program *rock.f* calculates the effective elastic constant of a rock comprised of quartz, feldspar, calcite/dolomite, micas (muscovite, biotite, and chlorite), fine-clays (kaolinite and illite), and pores (Appendix D). The quartz, feldspar, and calcite elastic tensors were determined by EBSD analyses. The mica elastic tensor was determined based upon an average of the Bingham model, manual EBSD indexing, and image analysis. The fine-clays were assumed to be isotropic in their distribution. The pores were assumed to be randomly distributed, and spherical in shape. The volume fractions were determined by QXRD analyses of core samples. The porosity was determined from Well logs, and *Hg* injection of core samples.

Calculation of the elastic stiffness tensor requires *a priori* information about the modal proportions. The program needs a data file containing all the modal fractions of the different mineral phases for the desired sample. The format is as follows with: modal

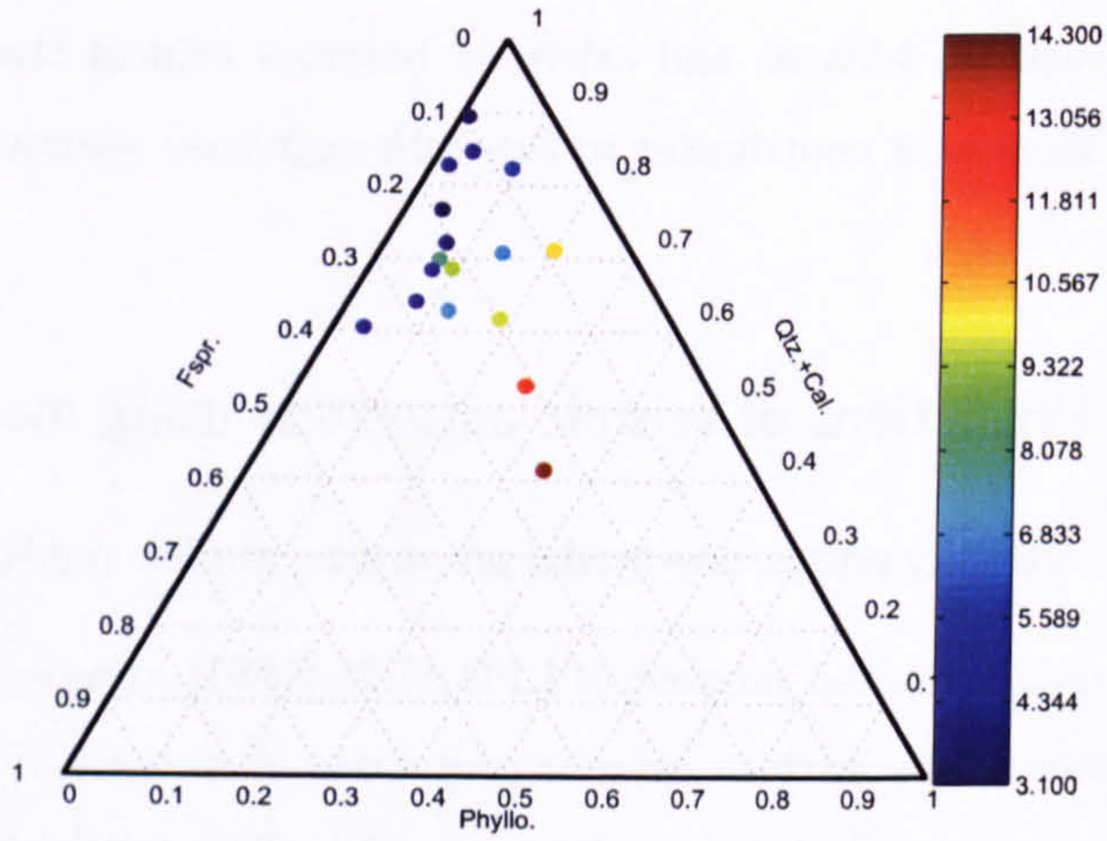

Figure 6.7: *Ternary diagram illustrating how the modal content controls absolute P-wave anisotropy. The colour scale bar represents the degree of anisotropy in per cent. The data points are coloured relative to their position on the scale bar. Fspr. - feldspar, Phyllo. - phyllosilicates, Qtz. - quartz and Cal. - calcite. The Matlab software used to produce this diagram was written by the current author.*

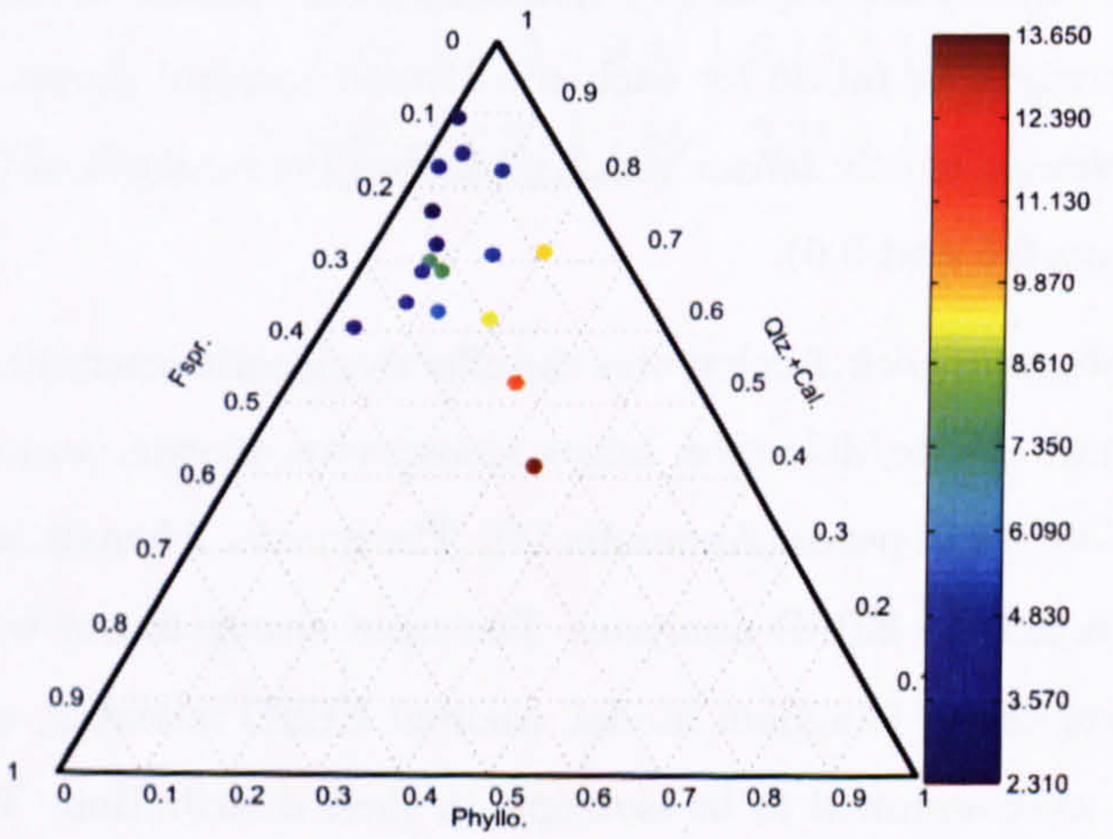

Figure 6.8: *Ternary diagram illustrating how the modal content controls absolute S-wave anisotropy (shear-wave splitting). The colour scale bar represents the degree of anisotropy in per cent. The data points are coloured relative to their position on the scale bar. Fspr. - feldspar, Phyllo. - phyllosilicates, Qtz. - quartz and Cal. - calcite. The Matlab software used to produce this diagram was written by the current author.*

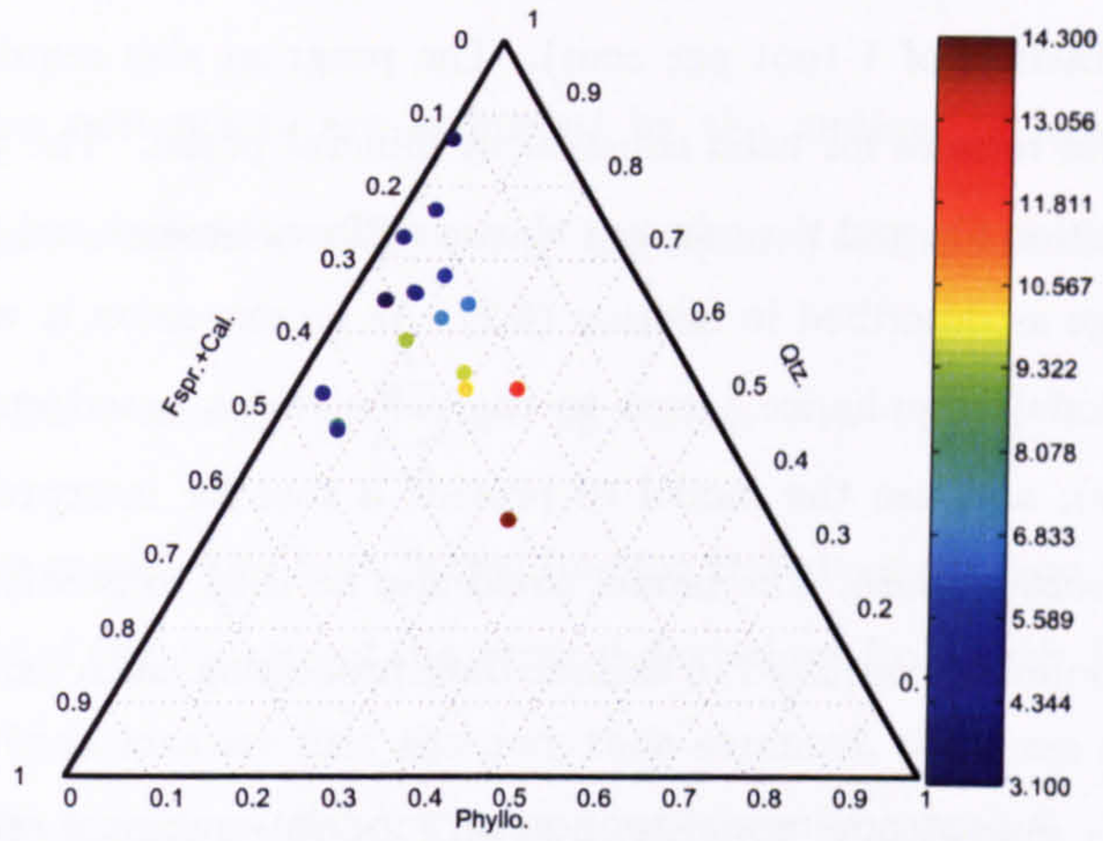

Figure 6.9: *Ternary diagram illustrating how the modal content controls absolute P-wave ansiotropy. The colour scale bar represents the degree of anisotropy in per cent. The data points are coloured relative to their position on the scale bar. Fspr. - feldspar, Phyllo. - phyllosilicates, Qtz. - quartz and Cal. - calcite. The Matlab software used to produce this diagram was written by the current author.*

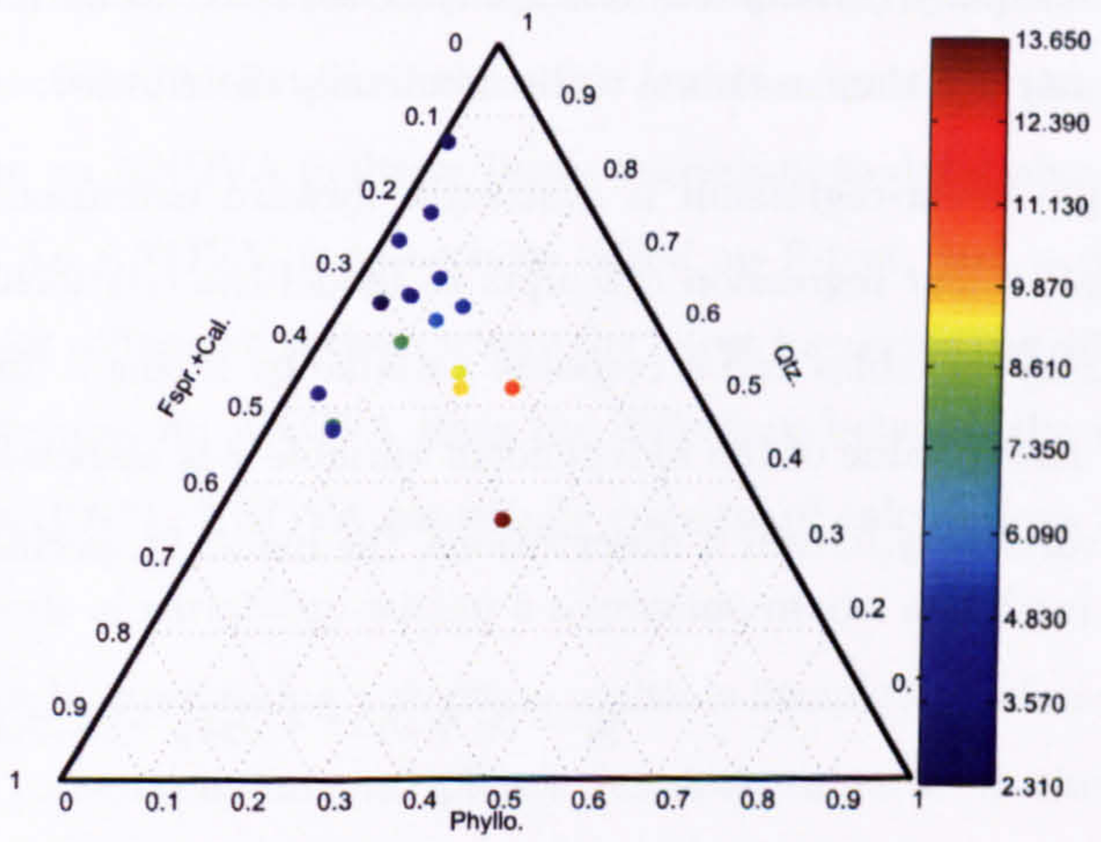

Figure 6.10: *Ternary diagram illustrating how the modal content controls absolute S-wave ansiotropy (shear-wave splitting). The colour scale bar represents the degree of anisotropy in per cent. The data points are coloured relative to their position on the scale bar. Fspr. - feldspar, Phyllo. - phyllosilicates, Qtz. - quartz and Cal. - calcite. The Matlab software used to produce this diagram was written by the current author.*

number (each mineral phase was assigned a number), and volume fraction expressed as a fraction of 1 (not per cent). The program also requires the single crystal elastic stiffness tensors for each constituent mineral phase. The program reads in the modal proportion file and the relevant elastic stiffness tensors and then performs a simple Voigt average as described in Section (6.2). As an extension it would also be possible to add additional compliance terms to the calculations based on auxiliary information (e.g., cracks), and use the model to provide a tool for interpreting estimates of anisotropy from seismic data. The model could also be used to predict anisotropy parameters that are commonly required in seismic data processing, such as, anisotropic depth migration.

6.6.2 Anisotropy-modal proportion models: empirical relations for siliciclastic rocks

Empirical relations have been devised which enable the interpretation of P- and S-wave anisotropy data in sections of reservoir not previously sampled. Using a simple multiple linear-regression combined with a test of ANOVA (analysis of variance) it was possible to calculate models which forward predict the approximate intrinsic P- and S-wave anisotropy attributed to modal proportion alone. This was conducted using Gauss-Markov assumptions. Gauss-Markov essentially states that the errors are not assumed to be normally distributed, nor are they assumed to be independent but only uncorrelated, nor are they assumed to be identically distributed.

Multiple linear-regression is a straight forward extension of the simple linear model. Multiple linear regression attempts to model the relationship between two or more explanatory variables and a response variable by fitting a linear equation to the observed data. Every value of the independent variable x is associated with a value of the dependent variable y. Given n observations, the model is specified as,

$$y_i = \beta_0 + \beta_1 x_1 + \beta_2 x_2 + \beta_m x_m, \tag{6.13}$$

where:

$x_j, j = 1, 2..., m,$	represent m different independent variables;
β_0	intercept;
$\beta_j, j = 1, 2, ..., m,$	represent the corresponding m regression coefficients;
$\beta_1, \beta_2, ..., \beta_m$	explanatory variables.

The values of these parameters are estimated by the method of least squares. The method of least squares minimises the sum of the squares of the residuals as follows,

$$SSE = min_{\beta_0,\ldots,\beta_p} \sum_{i=1}^{n} (y_i - \beta_0 - \beta_1 x_{i1} - \ldots - \beta_p x_{ip})^2. \quad (6.14)$$

In the least squares model, the best fitting line for the observed data is calculated by minimising the sum of the squares of the vertical deviations from each data point to the line. Because the deviations are first squared, then summed, there are no cancellations between positive and negative values. This is carried out by solving $p+1$ simultaneous equations for the $p+1$ unknowns. The estimates of β are given by the unstandardised coefficients. As in single regression the residuals are used to check the model assumptions.

Multiple linear regression attempts to fit a regression line for a response variable using more than one explanatory variable. The ANOVA (analysis of variance) calculations for multiple regression are nearly identical to the calculations for simple linear regression, except that the degrees of freedom are adjusted to reflect the number of explanatory variables included in the model. The modal proportions of quartz, feldspar, calcite/dolomite, phyllosilicates (muscovite, bioitite and chlorite), and the fine-clays (kaolinite and illite) were analysed using an ANOVA multiple linear regression to determine the appropriate input parameters. An ANOVA, is sometimes called an F-test, and is closely related to the t-test. The major difference is that, where the t-test measures the difference between the means of two groups, an ANOVA tests the difference between the means of two or more groups (Miller 1997). ANOVA essentially consists of calculations that provide information about levels of variability within a regression model and form a basis for tests of significance. Then by performing a stepwise multiple linear-regression using the modal proportions of the constituent mineral phases (as determined from the ANOVA test), and a 95% confidence interval, results in the following function

$$Y = 27.257 + 0.129_{x_1} - 0.288_{x_2} - 0.305_{x_3} - 0.189_{x_4}, \quad (6.15)$$

where:

Y predicted value for P-wave anisotropy (%);

x_1 phyllosilicate modal proportion (%);

x_2 quartz modal proportion (%);

x_3 feldspar modal proportion (%);

x_4 calcite modal proportion (%).

Using an ANOVA for multiple linear regression shows that to calculate the expected intrinsic compressional-wave anisotropy to within 95% confidence, the percentage of fine-clays and porosity are not required (Equation 6.15). The residuals of the regression (goodness of fit) can be assessed by examining the standardised normal probability plot (otherwise known as the P-P plot) (Figure 6.11). A probability-probability (P-P) plot is used to see if a given set of data follows a specified distribution. The P-P plot shows the observed cumulative probabilities of occurrence of the standardised residuals on the X-axis and the expected normal probabilities of occurrence on the Y-axis, such that a 45^o line will appear when the observed conforms to normality and the assumption of normally distributed error is met. Simply, the straighter the line formed by the P-P plot, the more the variable's distribution conforms to the selected test distribution. It is observed that the residuals approximate a normal distribution and as such show that the multiple regression is a reasonable fit.

The residuals of the P-wave multiple regression can further be assessed against a plot of standardised residuals against standardised predicted values (Figure 6.12). A standardised scatterplot of the standardised predicted dependent variable (ZPRED) by the standardised residuals (ZRESID) should show a random pattern across the entire range of ZPRED when, in regression, error is homoscedastic (a set of statistical distributions having the same variance). That is, when the regression model is equally accurate across the range of the dependent. The plot of standardised residuals shows a random distribution of data points and further supports the models adequacy in describing P-wave anisotropy from Equation (6.15).

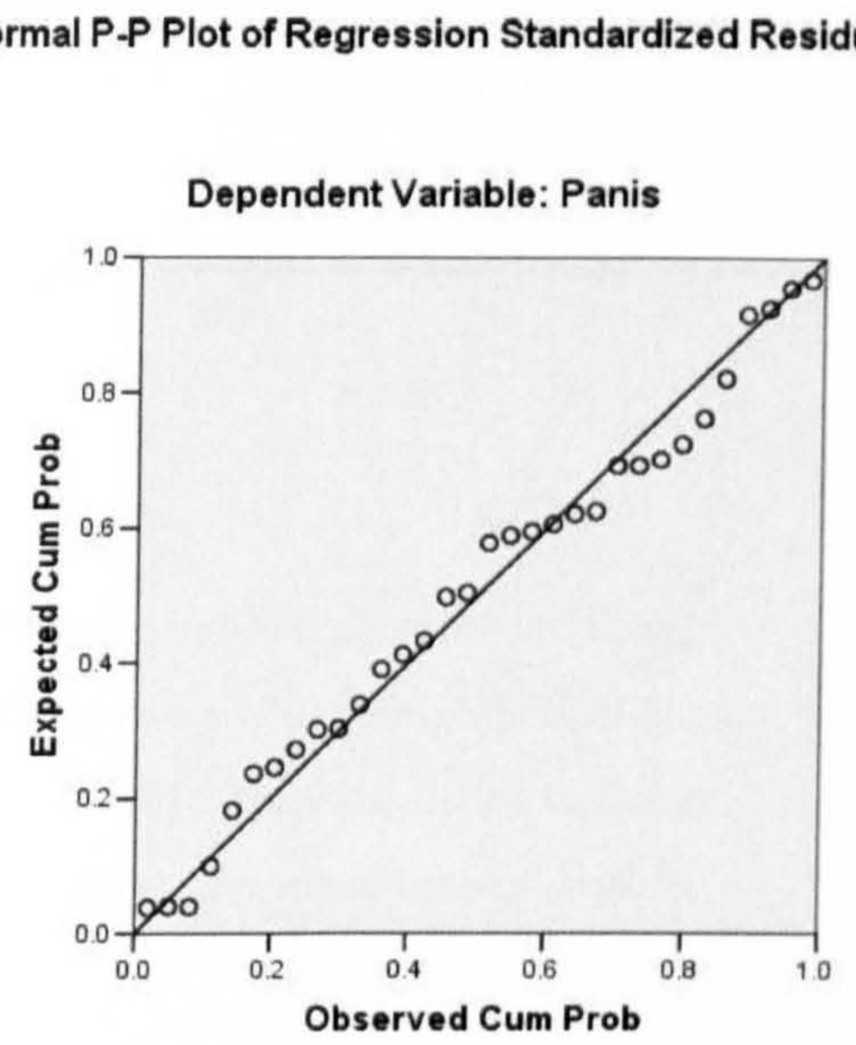

Figure 6.11: *Standardised normal probability plot of P-wave anisotropy. The P-P plot shows the observed cumulative probabilities of occurrence of the standardised residuals on the X-axis and the expected normal probabilities of occurrence on the Y-axis. The straighter the line formed by the P-P plot, the more the variable's distribution conforms to the selected test distribution. SPSS was used to produce this figure.*

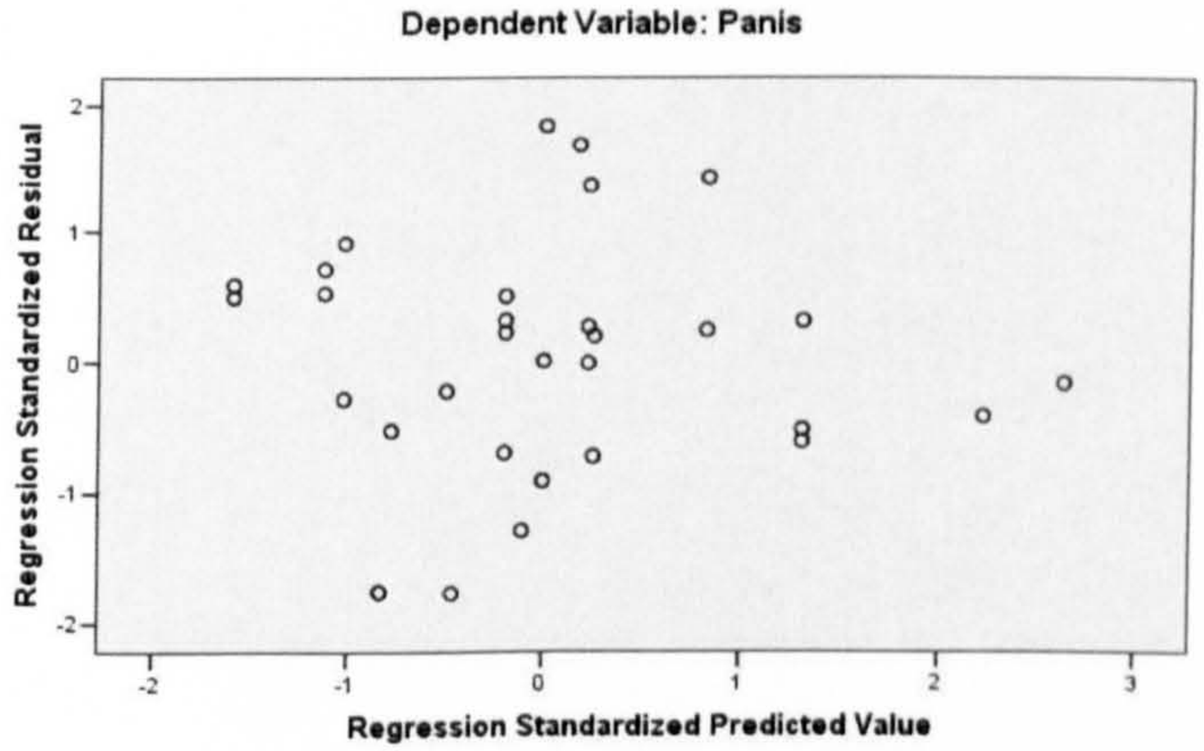

Figure 6.12: *Plot of P-wave standardised residuals. A standardised scatterplot of the standardised predicted dependent variable (ZPRED) by the standardised residuals (ZRESID) should show a random pattern across the entire range of ZPRED when, in regression, the error is homoscedastic (a set of statistical distributions having the same variance). SPSS was used to produce this figure.*

Performing the same procedure (ANOVA multiple linear regression) to predict the degree of shear-wave splitting results in,

$$Z = 14.73 + 0.244_{x_1} - 0.153_{x_2} - 0.166_{x_3}, \tag{6.16}$$

where:

Z	predicted value for shear-wave splitting (%);
x_1	phyllosilicate modal proportion (%);
x_2	quartz modal proportion (%);
x_3	feldspar modal proportion (%).

Using an ANOVA for multiple linear regression shows that to calculate the expected intrinsic shear-wave anisotropy to within 95% confidence, the percentage of fine-clays, calcite and porosity are not required (Equation 6.16). The same procedure for assessing the ability of the model to fully determine the S-wave anisotropy from modal proportions is shown in Figures (6.13; 6.14). It can be seen that the model does satisfactorily predict S-wave anisotropy from modal proportions.

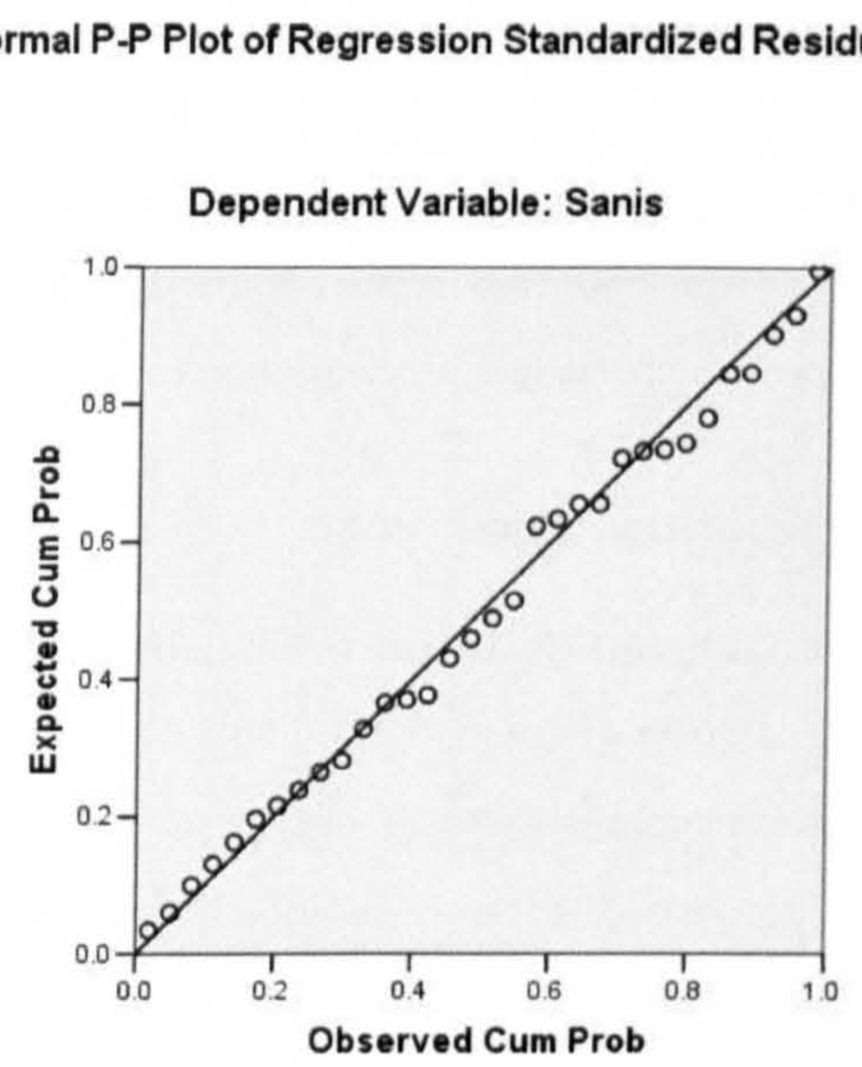

Figure 6.13: *Standardised normal probability plot of S-wave anisotropy. The P-P plot shows the observed cumulative probabilities of occurrence of the standardised residuals on the X-axis and of expected normal probabilities of occurrence on the Y-axis. The straighter the line formed by the P-P plot, the more the variable's distribution conforms to the selected test distribution. SPSS was used to produce this figure.*

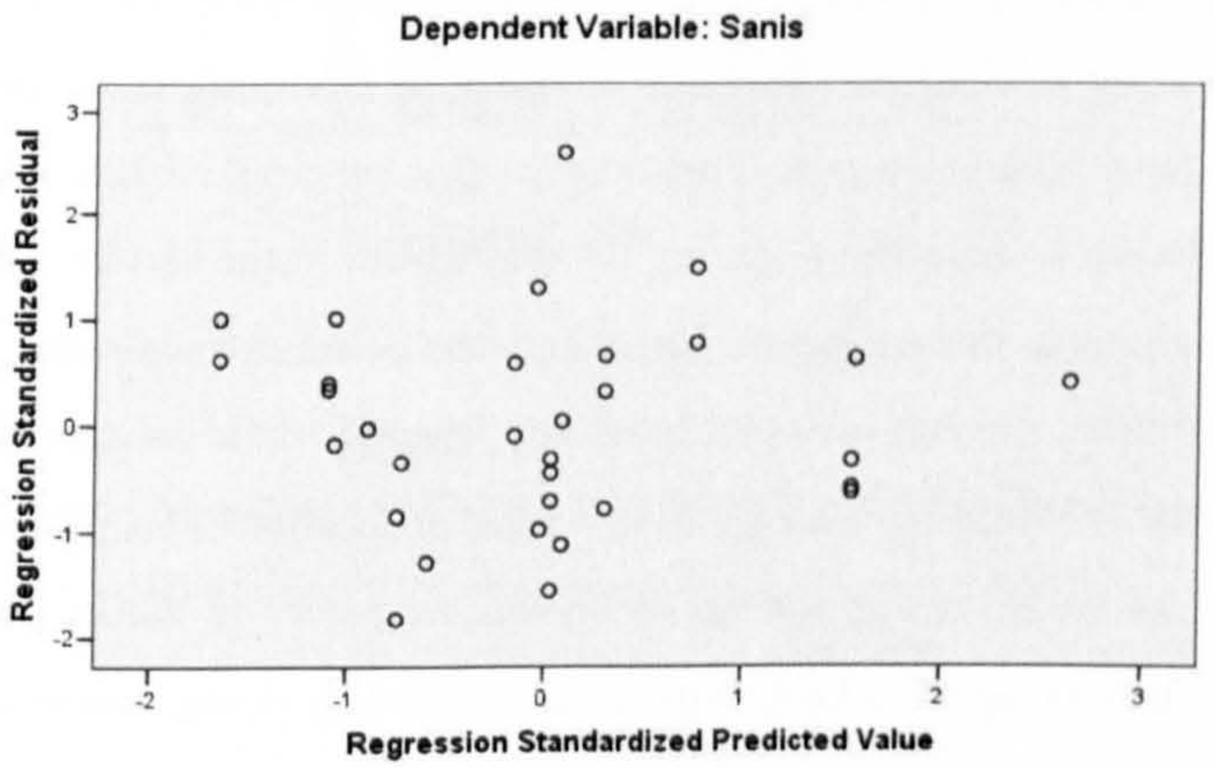

Figure 6.14: *Plot of S-wave standardised residuals. A standardised scatterplot of the standardised predicted dependent variable (ZPRED) by the standardised residuals (ZRESID) should show a random pattern across the entire range of ZPRED when, in regression, the error is homoscedastic (a set of statistical distributions having the same variance). SPSS was used to produce this figure.*

These relations are empirical and thus strictly speaking they only apply to the rocks studied. The result, however, should extend in general to many siliciclastic reservoir rocks. If possible the regression coefficients should be recalibrated at the site being studied. Note the extrapolation of the results to values of modal proportions outside the range of the experiments is not recommended.

6.6.3 Modal proportion model results

Presented within this section are the results obtained from the modal proportion models as described previously (Figures 6.15; 6.16). On average the multivariate linear regression model underestimates the bulk aggregate anisotropy when compared to the values predicted by the average of the elastic stiffness tensor. Nonetheless, it appears that qualitatively both models broadly agree. Simply plotting and taking an average of the compressional and shear-wave velocity anisotropies as a function of depth highlights the variation in bulk aggregate anisotropy throughout both wells (Figures 6.15; 6.16). The predicted anisotropy is high, at the top of both wells (in the overburden), as would be expected of phyllosilicate, and clay-rich rocks, whilst within the reservoir the predicted anisotropies are on average significantly lower (approximately $< 10\%$).

A simple average of the anisotropies within each horizon appears to serve as a good estimate of expected intrinsic anisotropy on a global field wide scale. Consider a wave which has a short wavelength compared to the layer thickness, the wave will then travel through each layer more-or-less independently. But, a problem arises because the fundamental underlying assumption ($\lambda/L << 1$) is not valid in the earth's subsurface as layers usually have a much shorter wavelength than the seismic wavelength. So when a long-period wave passes through a sequence of thin layers it deforms many layers at once and so the velocity is a different average of the layer properties. This problem was solved by Backus (Backus 1962). It was previously shown, however, by Valcke (2003), Valcke et al. (2006) that their appears to be no advantage gained by doing a more complicated Backus style average. Moreover, it was further shown by Valcke (2003) that no extra anisotropy is gained by taking into consideration the effect of microlayering as the difference between the clay-rich and sand-rich elastic tensors were not sufficiently different. Quite, possibly the difference in stiffness between the apparently notably different sand-rich and clay-rich layers were not in fact that different. Hence, when a layer is predominantly dominated by a stiff mineral phase such as quartz or calcite in comparison to say phyllosilicates

that a greater difference in stiffness may exist between the layers and thus the Backus style average might prove to be useful.

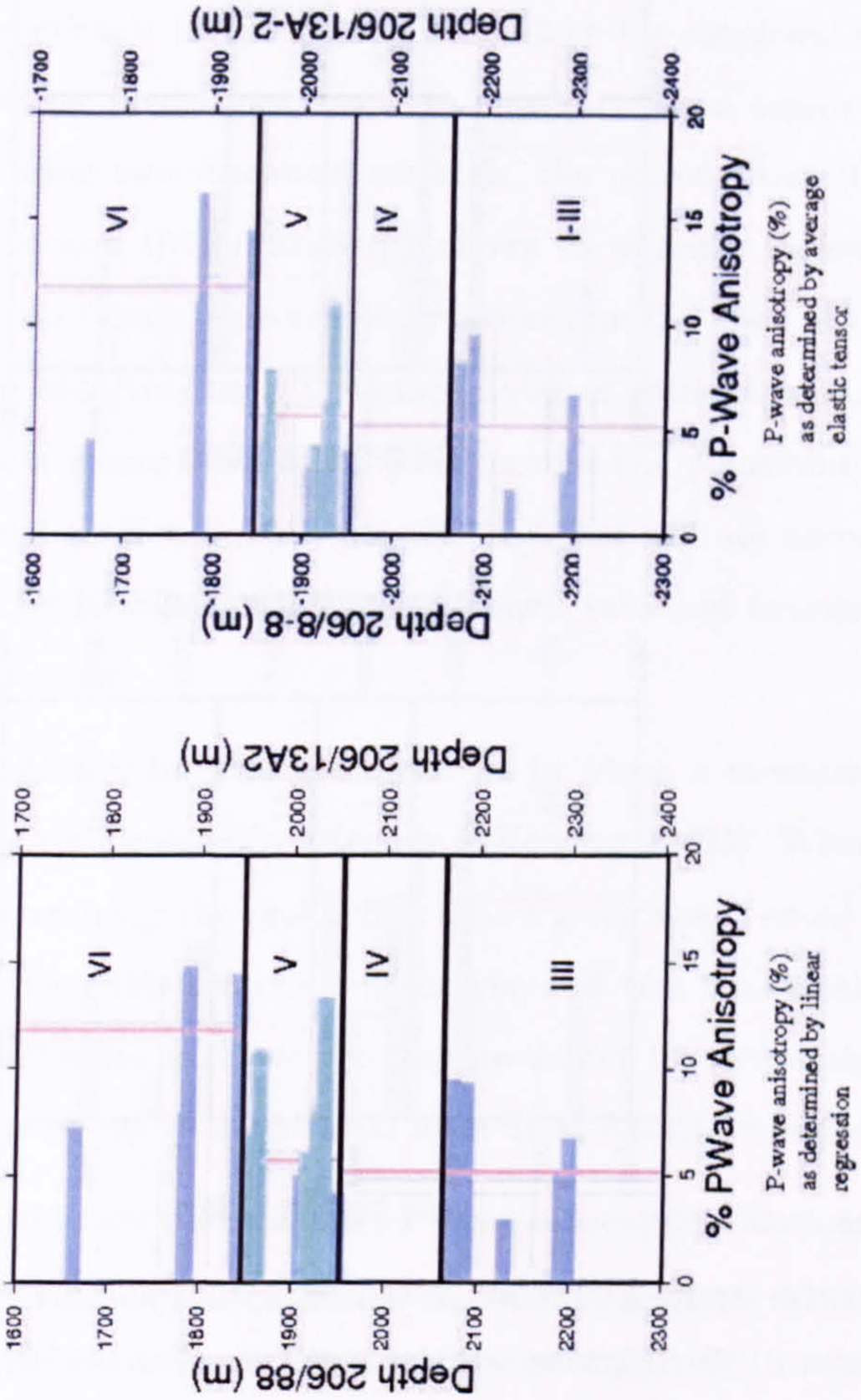

Figure 6.15: *Maximum compressional-wave seismic anisotropy as a function of depth due to crystal orientation effects alone. The left hand well log is the per cent anisotropy (%) as determined by linear regression methods whilst the right hand well log is as determined by averaging the elastic tensor. The GMT program used to produce this figure was written by Prof J-M. Kendall.*

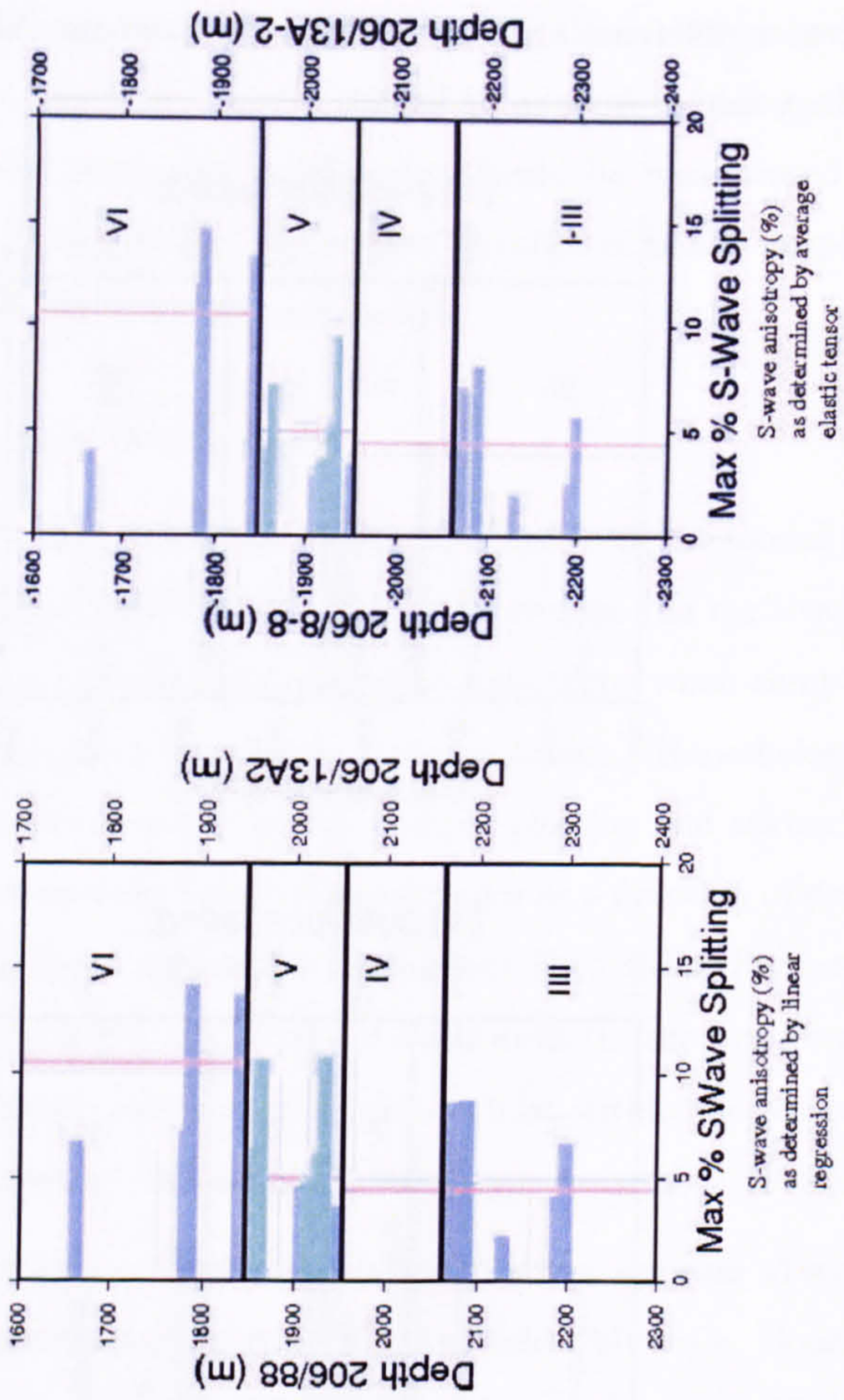

Figure 6.16: *Maximum shear-wave anisotropy as a function of depth due to crystal orientation effects alone. The left hand well log is the per cent anisotropy (%) as determined by linear regression methods whilst the right hand well log is as determined by averaging the elastic tensor. The GMT program used to produce this figure was written by Prof J-M. Kendall.*

6.6.4 Confidence intervals and significance tests: modal proportion-anisotropy forward models

Presented in this section is the procedure with which the empirical relation models (P- and S-wave anisotropy predictions) and the elastic stiffness tensor model are quantitatively criticised using two statistical methods, the paired t-test (Goulden 1956) and Wilcoxon test (Wilcoxon 1945). Statistics allows us to make inferences about the expected global data set (those expected observations) on the basis of the sample data set (limited number of observations). Statistics, however, cannot prove beyond all doubt but it does provide a means with which to determine the plausibility of competing hypotheses. The model predictions, are exactly that, and will not necessarily be identical to those predicted by EBSD, as EBSD determined values of anisotropy also take into account natural variation.

Quite simply a confidence interval is an interval in which a measurement or trial falls corresponding to a given probability (Kenney & Keeping 1962*b*). Whereas, a significance test is a test for determining the probability that a given result could not have occurred by chance. Essentially, this section will analyse and test the capabilities of the two models (empirical relations and average texture-index) to accurately determine those values of seismic anisotropy as determined from SEM-EBSD derived data.

Presented in Table (6.6) are the maximum P-wave anisotropy values as determined from the SEM-EBSD, empirical formula regressions, and elastic tensor averages. Furthermore, presented in Table (6.7) are the maximum shear-wave splitting (S-wave anisotropy) values as as determined from SEM-EBSD analyses, empirical formula regressions, and simple elastic tensor averages. The P- and S-wave tables of anisotropy predictions against the values of anisotropy as determined by EBSD provide a quick way to rapidly analyse how well the two models (empirical relations and elastic tensor average) predict anisotropy throughout all the samples. Where, no value for P- or S-wave anisotropy exists for EBSD analyses, it means that the sample was either not well consolidated or had a very high clay-mica content and thus could not be reliably analysed by electron microscopy. Presenting the information for comparison in tables is a relatively good method of analysing the fit of the data but it does not allow a quantitative comparison to be made.

The easiest way to determine whether a model accurately and correctly predicts the

as-measured data as predicted from SEM-EBSD analysis is by simply using an x-y cross-plot (Figure 6.17). It can be seen from a cross-plot of the different models that predict anisotropy that the results of the predictions are normally distributed about the line $x = y$. Ideally, the values would lie perfectly upon the line x-y, however, there does seem to be a little negative drag on the y-axis values. This suggests that the values of P- and S-wave anisotropy as predicted from the two models (empirical relations and elastic tensor average), on average, under predict the bulk aggregate anisotropy as expected from the LPO effect of grains alone. Figure (6.18) shows a comparison between the P- and S-wave seismic anisotropy predictions obtained from the average elastic tensor method and the linear regression method.

Presented in Tables (6.8; 6.9) are a comparison of the different statistical descriptives of the predictive models for P- and S-wave anisotropy. It is apparent from analysis of the P-wave anisotropy predictions in Table (6.8) that the empirical relation models most accurately predict the expected data set. In general, however, both the predictive models appear to under and over estimate the values of maximum and minimum P-wave anisotropy. As the empirical formulae were derived from a multiple linear regression it is expected that the predictions would be more accurate than those obtained from a simple linear average of the single mineral elastic stiffness tensors. Moreover, the empirical formulae used to derive seismic anisotropy were determined using a 95% confidence interval, and hence should on average better approximate the values obtained by EBSD analyses. As with the P-wave anisotropy predictions the predictions of S-wave anisotropy by the two models (empirical linear regression and average elastic stiffness tensor) appear to both under and over estimate the maximum and minimum values. As with the P-wave anisotropy predictions the empirical formula most accurately predict S-wave anisotropy. So far, analyses of the ability of the two different methods of predicting anisotropy were based upon relatively qualitative assessments. Here, relatively standard statistical tests have been applied to assist in the determination and verification of the ability of the two different mathematical models (empirical linear regression and average elastic stiffness tensor) to accurately and correctly predict bulk aggregate seismic anisotropy. A paired t-test (Goulden 1956) and the Wilcoxon Test (Wilcoxon 1945) were performed.

The t-test is described as follows, given two paired sets X_i and Y_i of n measured values, the paired t-test determines whether they differ from each other in a significant way under the assumptions that the paired differences are independent, and are identically

Table 6.6: *Comparison of the EBSD determined maximum P-wave anisotropy, empirically derived formula, and simple elastic tensor averages. Model refers to the predictive model used: EBSD - derived from LPO analysis, Emp. - empirical formula derived by linear regression and Cij - average of the single phase constituent elastic tensors. Depth is in metres and anisotropy is in per cent.*

Depth	EBSD	Emp.	Cij.
1663	7.63	7.30	4.60
1784	8.50	7.90	4.08
1788	-	-	16.2
1841	14.30	14.47	14.5
1909	3.10	5.03	3.3
1950	4.90	4.23	4
1959	5.60	7.00	4.70
1963	-	10.87	7.9
2015	4.10	6.04	4.40
2023	5.70	5.96	3.50
2028	7.70	7.99	6.40
2034	12.90	13.36	10.90
2070	9.60	7.76	4.9
2073	10.45	9.54	8.20
2088	-	-	9.5
2129	3.55	2.18	2.2
2192	4.60	5.18	3.00
2194	4.85	4.52	2.50
2198	6.85	6.77	6.7

Table 6.7: *Comparison of the EBSD determined maximum shear-wave splitting (S-wave anisotropy), empirically derived formula, and simple elastic tensor averages. Model refers to the predictive model used: EBSD - derived from LPO analysis, Emp. - empirical formula derived by linear regression and Cij - average of the single phase constituent elastic tensors. Depth is in metres and anisotropy is in per cent.*

Depth	EBSD	Emp.	Cij.
1663	7.25	6.77	4.08
1784	7.26	7.29	12.00
1788	-	-	14.78
1841	13.65	13.76	13.41
1909	2.89	4.56	2.93
1950	4.06	3.67	4.23
1959	5.16	6.46	4.23
1963	-	10.7	7.32
2015	3.35	5.00	3.80
2023	4.15	4.66	3.28
2028	6.32	6.19	5.35
2034	11.18	10.82	9.54
2070	7.86	6.44	4.28
2073	9.73	8.66	7.19
2088	-	-	8.17
2129	3.19	2.19	2.02
2192	4.10	4.17	2.57
2194	4.21	3.71	2.29
2198	5.58	6.73	5.76

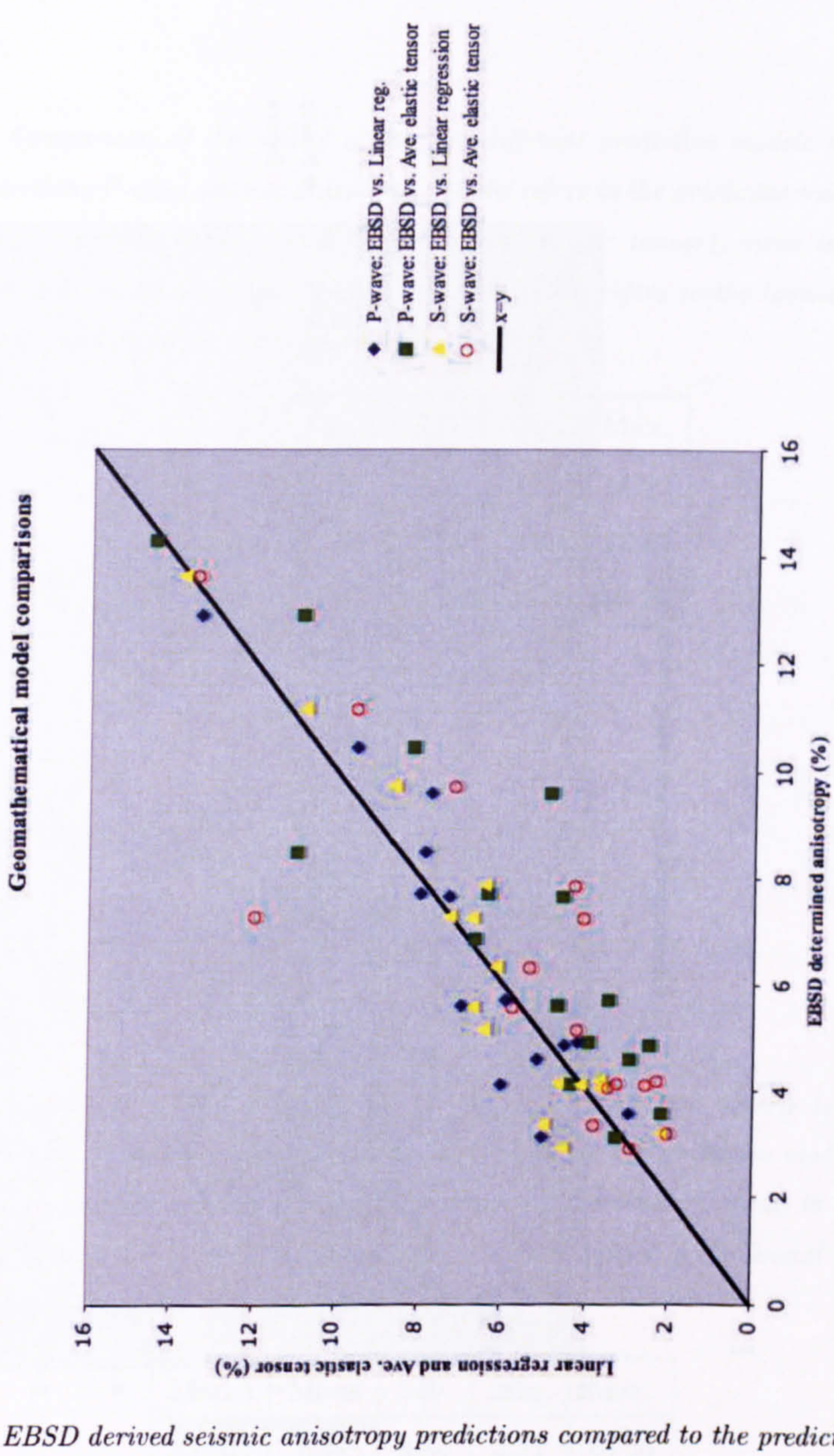

Figure 6.17: *EBSD derived seismic anisotropy predictions compared to the predictions obtained from the empirically derived formulae and the average of the constituent single mineral phase elastic tensors. The x-axis represents the values as predicted from calculations using EBSD and the y-axis represents those values calculated from the empirical formulae or by averaging the single constituent mineral phase elastic tensors. The black line represents* $x = y$.

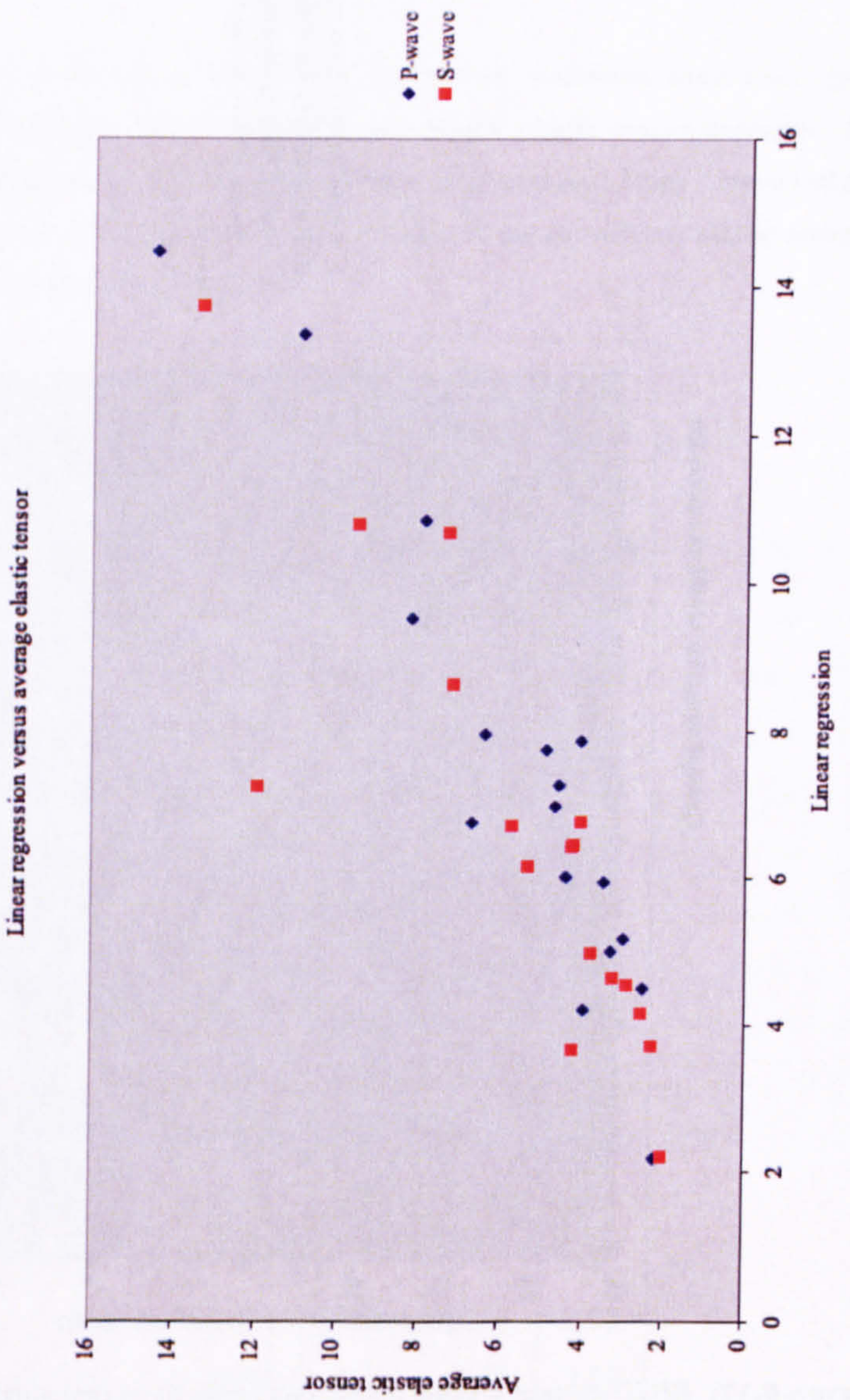

Figure 6.18: *Comparison of the P- and S-wave seismic anisotropy predictions obtained from the average elastic tensor method and the linear regression methodology.*

Table 6.8: *Comparison of the ability of the two different predictive models to correctly and accurately determine P-wave seismic anisotropy. Model refers to the predictive model used (EBSD derived, Emp. - empirical formula and Ave. - average elastic tensor), mean is the average of all predictions, S.D. is the standard deviation, the minimum refers to the lowest value, and the maximum the highest value for seismic anisotropy (%).*

Model	Mean	S.D.	Min.	Max.
EBSD	7.30	2.91	3.10	14.30
Emp.	7.30	2.72	2.98	14.48
Ave.	6.90	4.14	2.20	16.20

Table 6.9: *Comparison of the ability of the two different predictive models to correctly and accurately determine S-wave seismic anisotropy. Model refers to the predictive model used (EBSD derived, Emp. - empirical formula and Ave. - average elastic tensor), mean is the average of all predictions, S.D. is the standard deviation, the minimum refers to the lowest value, and the maximum the highest value for seismic anisotropy (%).*

Model	Mean	S.D.	Min.	Max.
EBSD	6.41	2.80	2.31	13.65
Emp.	6.57	2.68	2.18	13.76
Ave.	6.13	3.86	2.02	14.78

normally distributed.

To apply the test, let $\hat{X}_i = (X_i - \bar{X})$ and $\hat{Y}_i = (Y_i - \bar{Y})$.

Then define t by,

$$t = (\bar{X} - \bar{Y}) \sqrt{\frac{n(n-1)}{\sum_{i=1}^{n} (\hat{X}_i - \hat{Y}_i)^2}}. \tag{6.17}$$

With reference to the t-table at $(n_1 + n_2 - 2)$ degree of freedom (assuming p=0.05), if the calculated t value exceeds the tabulated value then the means are significantly different. For example, if the calculated t value exceeds the tabulated value for p=0.05 then there is a 95% chance of the means being significantly different (or 99% for p=0.001).

The Wilcoxon signed rank test is a non-parametric (no underlying assumptions about the distribution of the observed data) alternative to the paired t-test. It assumes there is information in the magnitudes of the differences between paired observations as well as the signs. A rank test uses statistical ranks of data points. The differences of the paired observations are calculated and then ranked from smallest to largest by absolute value. All the ranks associated with positive differences are added together giving the T_+ statistic.

Applying the paired t-test, and Wilcoxon signed rank test to the empirically derived formulae predicts that there is significant evidence to suggest that they both have comparable means, and variances. The results of the paired sample t-test for P-wave anisotropy have a paired difference: standard deviation of 1.02, mean of -0.01, and standard error mean of 0.18. Applying the same tests to the S-wave data as derived by the empirical formula also results in a positive assessment of means and variances with enough evidence to suggest that they are related. The results of the paired sample t-test for S-wave anisotropy have a paired difference: standard deviation of 1.15, mean of -0.16, and standard error mean of 0.20.

Applying the paired t-test to the P-wave anisotropy as determined by averaging the constituent single mineral elastic stiffness tensors results in a paired differences: mean of 1.22, standard deviation of 1.65, and a standard error of 0.41. Furthermore, performing the same paired samples test on the S-wave data results in a paired differences: mean of 0.85, a standard deviation of 1.88, and a standard error mean of 0.471. Using both the paired t-test, and Wilcoxon signed rank test there is sufficient evidence to suggest

that both P-wave, and S-wave anisotropy approximate the predictions of anisotropy as determined by EBSD mineral analyses.

It has been shown that both methods of determining bulk aggregate P- and S-wave anisotropy provide good approximations of anisotropy as determined experimentally by EBSD analyses.

6.7 Discussion

The Bingham approach provides a means of predicting phyllosilicate mineral orientation in samples which have a very high clay-mica modal proportion and which could not be examined by standard electron microscopy techniques, such as, SEM-EBSD. EBSD is restricted to samples which have a relatively low phyllosilicate content because of the uncertainty of EBSD to repeatedly and reliably index crystal orientations automatically. The Bingham model has been shown to be successful at determining the probability of the orientation distribution of platy-mineral grains. The success of the Bingham approximation, however, quickly breaks down in the circumstance whereby there is not a uniaxial symmetry of rotation about the vertical in the orientation of the platy surfaces. Moreover, it also falls down when there is not an uniaxial symmetry of orientation and reorientation of platy minerals during compaction. These assumptions would not necessarily hold in an environment of non-hydrostatic compaction or when there is a single dominant flow direction (e.g., turbidites). Nonetheless, when the results of the Bingham approach were compared to those as determined by manual EBSD analyses they did closely approximate one another. Similarly, the approximations of phyllosilicate orientation also compared favourably with those determined from the image analysis of thin-sections. This, however, is also based upon the assumption that the intersection of phyllosilicate basal planes is related to uniaxial symmetry of projection. This assumption would also break down and invalidate the results of the analysis if the phyllosilicate orientations were also controlled within the bedding plane by some exterior mechanism. As stated, however, the Bingham approach in this series of experiments did approximate the results obtained from image analysis and manual EBSD indexing thus suggesting that either the assumption of uniaxial symmetry of compaction is valid and, or that there was no mechanism within the bedding plane consistently orienting phyllosilicate basal planes.

The absolute values of velocity for the individual samples analysed as determined by the VRH (Voigt-Reuss-Hill) averaging scheme are high for porous sandstones and when compared to those obtained by laboratory testing (Chapter 4). The VRH scheme is based upon an approximation that all grains experience the same strain (Voigt) or the same stress (Reuss). However, to obtain a more sensitive and thus more accurate indication of the effect of LPO on elastic anisotropy a more detailed approximation is required which would take into account such variables as grain-shape, grain-orientation, and the spatial distribution of mineral phases. Such that, the stresses and strains at the grain scale vary in a manner which satisfies stress equilibrium and strain compatibility. To recover values which are physically realistic therefore the method of Ponte Castaneda and Willis is proposed as a means for examining the compositional and microstructural controls on the elastic properties of siliciclastic rocks (Castañeda & Willis 1995).

Presented are the bulk aggregate seismic anisotropy pole figure predictions for two distinct end member lithotypes; a clean sandstone (quartzo-feldspathic rich), and a mudstone (phyllosilicate rich) (Figure 6.19). The symmetries observed are typical of a Clair sandstone (orthorhombic) and mudstone (VTI). The sandstones are commonly completely dominated by a single point maximum of P-wave anisotropy and a complicated distribution of Vs_1 polarisations. The anisotropy observed within the bedding plane varies azimuthally, whist also varying with increasing inclination. Mudstones have a far simpler symmetry pattern, whereby they have maximum P- and S-wave anisotropy within the plane of bedding and minimum P- and S-wave anisotropy perpendicular to bedding. Vs_1 is aligned parallel to bedding within the bedding plane and at increasing intersection angles to bedding with increasing inclination. In general, samples near the top of the two Wells have VTI symmetry styles whilst those deeper down tend to be more orthorhombic.

The modal proportion empirical relations as determined by ANOVA multiple linear regression appear to provide a relatively good approximation of P- and S-wave anisotropy due to LPO mineral affects alone. The relations, however, only provide an absolute value of P- and S-wave anisotropy with no information provided about the overall expected symmetry of the sample. Furthermore, sensitivity issues will likely surround the phyllosilicate modal proportion parameter and a small difference in modal proportion will likely dramatically effect the output. No sensitivity analysis has been conducted on the various parameters and it is unclear as to effect of the error propagation and instability.

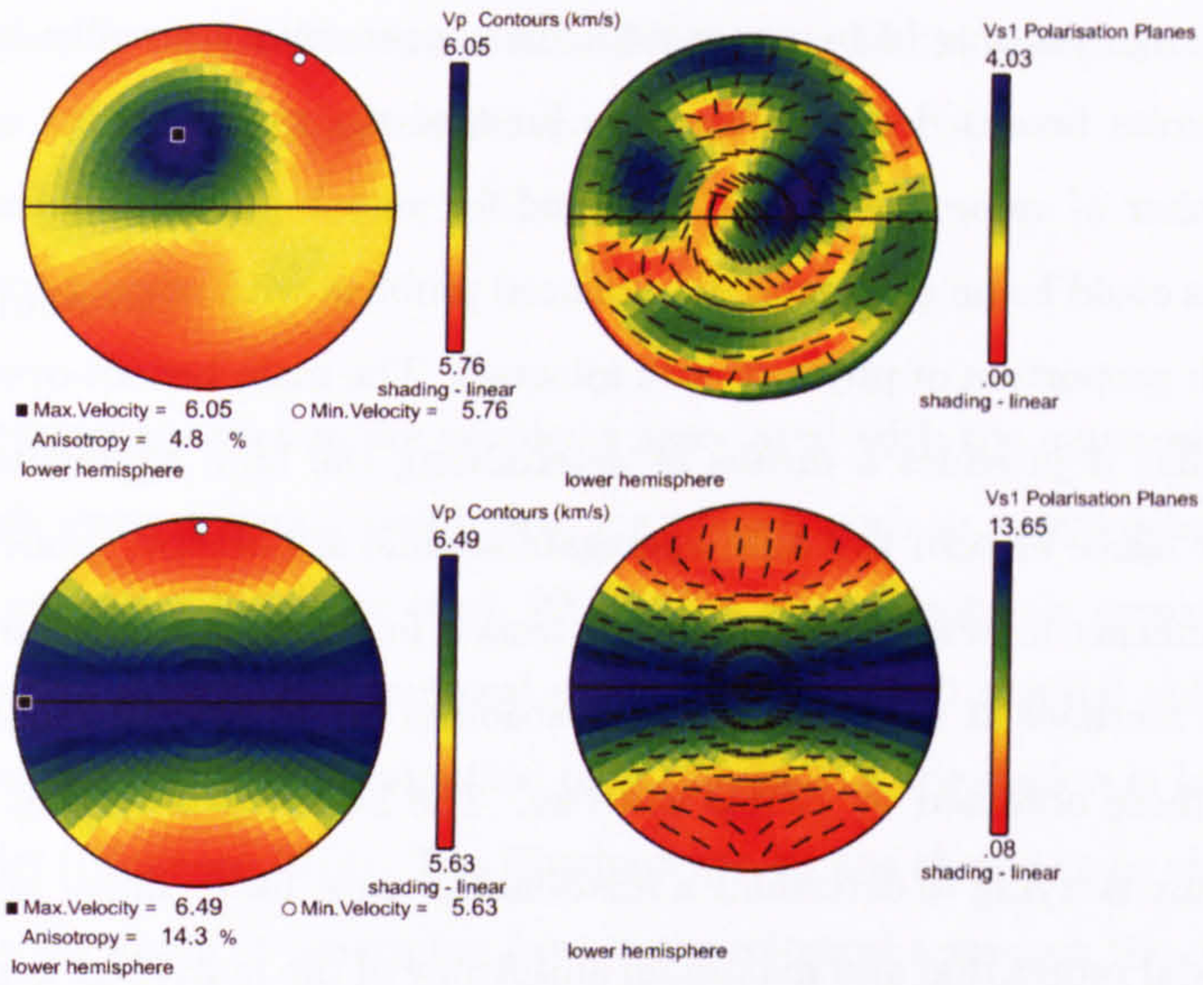

Figure 6.19: *Bulk aggregate seismic anisotropy pole figures typical of two end member lithotypes within the Clair field. Top - sandstone, and Bottom - mudstone. The sandstone has a complicated orthorhombic style of symmetry, whereas the mudstone is strongly vertically transversely isotropic. The maximum P-wave, and S-wave anisotropy is significant in both lithotypes. For diagram explanation see Figure (6.1).*

Therefore, it is suggested that an accurate determination of the phyllosilicate modal proportions with this methodology is absolutely paramount. Furthermore, it is be noted that these results, strictly only apply to the rocks analysed within this study and that extrapolation of the results outwith the samples analysed could yield erroneous results. These relations do provide a quick means of determining intrinsic anisotropy from modal proportions alone and therefore will prove to be a useful implement in the interpreters tool box. It is proposed that to re-apply these formulae in different hydrocarbon field areas that the regression coefficients should be re-calibrated. Furthermore, it is strongly suggested that sensitivity and instability analyses should be conducted to determine the robustness of the formulae and hence resolve the formulas limits of applicability.

The arithmetic average of elastic stiffness tensors provides a useful and reliable tool as a means of determining the effective elastic stiffness tensor of an aggregate. The methodology provides a convenient and yet simple means of upscaling the results of the small EBSD analyses to that of the scale of seismically observable horizons. As with the empirical relations no sensitivity analysis has been conducted and ideally a Monte-Carlo

investigation should be conducted. The approximation really falls down and hence the program breaks down at the very limit of the texture-index values as only a limited number of values have been obtained for very high single mineral content aggregates. This could be an even more pronounced problem with respect to a rock containing a very high proportion of phyllosilicate minerals. The main benefit over the empirical formulae is that it provides a means of determining the bulk aggregate elastic stiffness tensor and hence in turn the bulk aggregate seismic anisotropy. Nonetheless, as shown in the confidence interval and significance tests it has been shown to be the least accurate of the two methods at approximating the absolute values of seismic anisotropy when compared to those obtained by EBSD analyses. The best approach that could be applied in the future is trying to determine a relationship, most likely, linear between the texture-index, modal proportion and maximum anisotropy of the individual constituent mineral phases.

In the situation where an understanding of the nature of intrinsic seismic anisotropy of a unit within a hydrocarbon reservoir is required the empirical and elastic tensor averages offer a quick and easy way to roughly approximate the expected anisotropy. For example, interval velocities determined from wireline logs can be and are used when processing a field wide seismic survey. Likewise, estimates of seismic anisotropy and style of symmetry can be quickly determined from the average of the elastic stiffness tensor and used to assist in the interpretation of non-hyperbolic moveout data (typical of highly anisotropic horizons), for example, it would provide a useful starting point to aid the interpretation of the horizon being investigated.

Estimating anisotropy parameters from surface seismics is a very challenging topic. Knowledge of anisotropy is however required for accurate time-to-depth conversion and to improve quality of stacked and migrated sections. It is essential that as much *a priori* information is gathered as possible. For example, using P-P waves with a 2D data set is severely limited by the acquisition geometry as no azimuthal information can be extracted. It is therefore only possible to look for evidence of anisotropy from non-hyperbolic moveout. If non-hyperbolic moveout occurs then VTI anisotropy maybe present (Van der Baan & Kendall 2002). Successful estimation of actual anisotropy parameters can only be obtained with large offset/depth ratios ($x/z > 2$). The empirical and tensor averages provide the ability to forward predict anisotropy within units in the reservoir which have not been analysed or determined by field wide anisotropy analysis. Hence, an average of the individual layers individual seismic anisotropy predictions

within a seismically observable unit can be determined to aid interpretation of moveout characteristics, AVOA analysis and shear-wave splitting.

6.8 Conclusions

SEM-EBSD commonly encounters problems associated with the automated indexing of minerals which possess strong basal cleavage planes, such as, phyllosilicates and fine-grained clay minerals (Ullemeyer et al. 2000). The most commonly employed technique in the analysis of phyllosilicate mineral orientation is EBSD manual indexing. An alternative approach to the determination of phyllosilicate orientation is based upon the Bingham model (Bingham 1974). The Bingham model was chosen to be the most appropriate model with which to determine from a stereological approach the *3D* orientation distribution of phyllosilicates (Bingham 1974). Bingham's distribution represents the portion of a trivariate Gaussian distribution that intersects the surface of a unit sphere, with varying ellipsoidal shapes of the underlying Gaussian contours producing a variety of distributional forms on the sphere. Using the approach as determined by Bingham (Bingham 1974), phyllosilicate orientation was approximated from the probability distribution of thin-section intersections. It was also found that the Bingham approximation for phyllosilicate orientations compared well with those determined from EBSD manual indexing, and from image analysis of thin-sections. The absolute values of anisotropy obtained from image analysis, manual indexing and stereological determination were very similar. Moreover, the strength of the phylllosilicate orientation's as determined by the various methods was also coincident thus supporting the proposal that seterological determination of phyllosilicate orientation was an acceptable approach.

It has been shown in this chapter that undeformed siliciclastic hydrocarbon reservoir rocks can exhibit a substantial intrinsic seismic anisotropy due to the lattice preferred orientation of constituent mineral phases. With calculations of compressional-wave seismic anisotropy due to LPO effects varying from c.3.1% to c.14.0% for quartz-rich, clean sandstones and mudstones, respectively. Moreover, calculations of shear-wave anisotropy due to LPO effects alone varied from c.2.3% to c.13.6% for quartz-rich, clean sandstones and mudstones, respectively. Hence, this study of seismic anisotropy has proved that there exists a potential to reveal interesting attributes about a rocks microstructure and, or modal mineral content from field wide observations of seismic anisotropy alone. The

styles of symmetry observed within the seismic anisotropy calculations are strongly controlled by the constituent mineral phases. Samples which are rich in quartz and feldspar generally possess an orthorhombic style of symmetry. Whereas, those rich in clays and micas (> 15%) tend to have a very strong VTI style of symmetry. It is observed that the relationship that exists between maximum P- and S-wave seismic anisotropy is directly and linearly related to the log transform of the texture-index (J). Moreover, it was also shown that both feldspars and micas appear to have considerable control over the absolute values of bulk aggregate seismic anisotropy and thus the styles of symmetry produced.

To enable and constrain the interpretation of P- and S-wave anisotropy data a forward model was devised. The model is based upon a simple multiple-linear regression of the constituent mineral phases modal proportions and the resultant maximum seismic anisotropy as obtained from EBSD analyses. The resulting formulae have been shown to enable the accurate prediction of anisotropy and will in turn help guide the interpretation of the observed data. Two very simple empirical formuale were derived that enabled the prediction of the absolute values of maximum P- and S-wave anisotropy from modal proportions alone.

Furthermore, a similar model was derived from the basic underlying assumption that the strength of the texture-index for each individual mineral phase does not vary consistently or significantly throughout the reservoir. Based upon this simple observation it was possible to take a simple-average of the individual texture-indices for each mineral phase and hence determine it's average elastic stiffness tensor. The individual mineral phase averages were implemented into a simple calculation that enabled the forward prediction of the expected intrinsic elastic tensor and hence using the Christoffel equation the determination of the P- and S-wave velocity and anisotropy. A simple program was written which would use the modal proportions as an input and thus determine the expected intrinsic bulk aggregate elastic stiffness tensor. The input components were: quartz, feldspar, calcite/dolomite, phyllosilicates (muscovite, biotite and chlorite), clays (illite and kaolinite) and pore volume. The calculation was conducted using a Voigt average.

Qualitative and quantitative assessments were conducted on the two different predictive methodologies to quantify the accuracy and ability of the various models to predict anisotropy and velocity. The basic statistical descriptives such as mean, and standard

deviation of the various methods were compared to provide a broad understanding of the failings of the individual models. Moreover, paired t-tests and Wilcoxon tests were conducted to also ascertain quantitatively the ability of the techniques to predict anisotropy and velocity. Broadly, the empirical formulae have been shown to provide a more accurate description of the expected intrinsic anisotropy. Nonetheless, the empirical formulae only provide absolute values of anisotropy whereas the simple average of the elastic tensor provides insight into the symmetry of the expected sample.

Chapter 7

Crack density inversion

7.1 Introduction

The causes of seismic anisotropy are commonly considered to be the lattice preferred orientation of mineral phases (LPO), shape preferred orientation of grains (SPO), the non-random spatial distribution of mineral phases and preferentially aligned fractures, cracks and pores (Crampin 1981, Babuska & Cara 1991, Mainprice et al. 2000, Wendt et al. 2003, Kendall et al. 2006, Valcke et al. 2006). The controls of seismic anisotropy are therefore ultimately governed by a variety of factors including among others the depositional flow direction and the *in situ* stress field during lithification. Therefore, an understanding of seismic anisotropy could yield information useful for reservoir characterisation, such as, paleao-flow directions, *in situ* stress distributions and lithology. Nonetheless, most real-life rocks will contain a complicated mix of all the seismic anisotropy controlling features making it difficult to determine the impact of an individual feature. Hence, determining a method which allows the differentiation and quantification of the variables controlling extrinsic and intrinsic seismic anisotropy would provide useful information for the better interpretation of observations of seismic anisotropy.

Seismic velocities in rocks are sensitive to stress (Sayers 2002*b*). The presence of micro-cracks, and microporosity along grain boundaries greatly affects the velocity of elastic waves in rocks (Sayers 1994). This is generally attributed to the closing of compliant cracks and grain boundaries. Cracks are pushed together as the confining pressure increases. As more and more of the cracks are closed the mechanical stiffness and hence velocities of the rock increase (Sayers et al. 1990). It is well known that rocks containing

non-randomly oriented cracks or which have a strong grain shape fabric are commonly elastically anisotropic. Similarly, in the presence of non-isotropic stress fields seismic wave velocities in hydrocarbon reservoir rocks often show considerable stress-induced anisotropy (Sayers & Kachanov 1995). This is because the response of a discontinuity to the applied stress depends on its orientation relative to the applied stress field.

There have been numerous studies of seismic wave anisotropy as a consequence of applying an anisotropic stress, including Holt & Fjaer (1987), Sayers et al. (1990) and Scott et al. (1993). In general, most previous experimental work on the sensitivity of seismic wave velocities to an applied stress have largely concentrated upon the empirical relationships of the observed trends. Moreover, to fully characterise the anisotropy of a naturally occurring rock sample many different ultrasonic velocity measurements are required. In this study it is assumed that the sample has at least a VTI style of symmetry. A VTI symmetry can be considered as a reasonable assumption because of the predominance of horizontal layering within sedimentary rocks. Only five different measurements are required to characterise a VTI style of symmetry. However, it is more often than not that naturally occurring rock samples contain a variety of these lithological microstructures superimposed upon one another, such as, layering and a set of aligned fractures. Therefore, in sandstones which can contain horizontal layering, fracturing and grain boundary alignment can result in a less symmetric object, which would require significantly more measurements than that of VTI symmetry.

The work carried out in this chapter is an amalgamation of the results obtained from the ultrasonic analyses (Chapter 4) and the elastic tensor predictions obtained from EBSD analyses (Chapter 5). Sayers (2002*b*) showed that it was possible to predict crack density and orientation from P- and S-wave ultrasonic measurements from an approximated isotropic elastic tensor. In this chapter the inversion scheme of Sayers (2002*b*) has been expanded to include *a priori* knowledge of the elastic stiffness tensor as determined by EBSD. It is important to note that the resultant seismic anisotropy observations may not necessarily be related to cracks. It has to also be considered that similar observations of the sensitivity of elastic wave velocities to stress could be as a consequence of grain boundaries and the soft interparticle constituents of phyllosilicates (Sayers 2005).

7.2 Crack density inversion - theory

The approach used here in the determination of the orientation and density of crack-like micro-discontinuities (cracks, grain boundary micro-cracks and compliant phyllosilicate interparticle material) is largely based on Sayers (2002*b*) with added extensions to utilise the multi-axis velocity measurements (Chapter 4) and *a priori* knowledge of the rock matrix (Chapter 5). The anisotropy of the rock samples in this study are assumed to be at most orthorhombic. To fully characterise the elastic tensor requires P- and S-wave velocity measurements along the three principal axes, plus the off-axis P-wave velocities within each symmetry plane. The assumption that the background (intrinsic stiffness and symmetry of the sample) is orthorhombic seems reasonable for the samples considered since the LPO determined stiffness tensors show only small non-orthogonal terms. The following expressions as derived by Sayers & Kachanov (1991), allow ultrasonic velocity measurements to be inverted for to obtain the crack density tensor components.

As shown in Sayers & Kachanov (1991) the elastic compliance of a sandstone can be written as follows,

$$s_{ijkl} = s^{o}_{ijkl} + \Delta s_{ijkl}. \tag{7.1}$$

Where s^{o}_{ijkl} is the compliance of the rock matrix (which will be the aggregate anisotropic compliance of all the constituent grains). Δs_{ijkl} represents the additional compliance due to the presence of micro-discontinuities contained within the rock matrix (i.e., cracks, grain boundary micro-cracks and compliant interparticle phyllosilicate material) and can be given in terms of a second and fourth order crack density tensors α_{ij} and β_{ijkl} (Sayers & Kachanov 1991, Sayers 2002*b*). Where,

$$\Delta S_{ijkl} = \frac{1}{4}(\delta_{ik}\alpha_{jl} + \delta_{il}\alpha_{jk} + \delta_{jk}\alpha_{il} + \delta_{jl}\alpha_{ik}) + \beta_{ijkl}, \tag{7.2}$$

and δ_{ij} is the Kronecker delta. For a distribution of r planar discontinuities with surface areas $A^{(r)}$ and surface-normal vectors $n_i^{(r)}$ in a volume V, these crack density tensors can be defined in terms of two crack compliance terms describing the additional normal and tangential compliances, B_N and B_T, due to each discontinuity,

$$\alpha_{ij} = \frac{1}{V}\sum_{r} B_T^{(r)} n_i^{(r)} n_j^{(r)} A^{(r)}, \tag{7.3}$$

and

$$\beta_{ijkl} = \frac{1}{V}\sum_{r}(B_N^{(r)} - B_T^{(r)})n_i^{(r)}n_j^{(r)}n_k^{(r)}n_l^{(r)}A^{(r)}. \tag{7.4}$$

(Sayers & Kachanov 1991, Sayers 2002*b*). B_N and B_T are therefore the normal and tangential displacement discontinuities due to the normal and tangential traction's acting upon the crack faces. Therefore, α_{ij} and β_{ijkl} can be thought of as characterising the cumulative magnitude and orientation distribution function of the additional normal and shear compliances due to all the discontinuities present in the sample plus the relative ease to undergo shear or opening along different orientations. Additionally, the trace of α_{ij} normalised by a factor h (as given below for open, planar penny-shaped cracks, or an equivalent adapted for the specific crack conditions) is the commonly used crack density tensor $\frac{Na^3}{V}$, for N cracks of diameter a in a volume V (Gueguen & A. 2003). The trace of β_{ijkl} is similarly related to this crack density scalar but its definition also involves a term relating to the crack aperture and the moduli of crack fill.

For open, planar penny-shaped cracks of diameter a in a dry, isotropic rock with Young's modulus E_0 and Poisson's ratio υ_0, B_N and B_T are given by Sayers & Kachanov (1995),

$$B_N = \frac{16(1-\upsilon_0^2)\alpha}{3\pi E_0}, B_T = \frac{32(1-\upsilon_0^2)\alpha}{3\pi E_0(2-\upsilon_0)}. \tag{7.5}$$

Sayers & Kachanov (1995) point out that for the case, of dry penny-shaped cracks, B_N and B_T have approximately the same magnitude, and so can, for simplicity, often can be assumed to be equal (the validity of this approximation will be reduced if, for example, the cracks were fluid filled).

On the basis of Equations (7.5), a convenient normalising factor for the crack density terms can be defined,

$$h = \frac{3E_0(2-\upsilon_0)}{32(1-\upsilon_0^2)}, \tag{7.6}$$

which leads to non-dimensional crack density tensors that are only a function of their number density, diameter cubed and orientation (this is equivalent to the normalising parameter of Sayers & Kachanov (1995), Gueguen & A. (2003)). The first two factors can be combined to provide the well known crack density scalar, $\eta_c = \frac{Na^3}{V}$, as used by Hudson (1981), for example. For an anisotropic rock matrix with orthorhombic symmetry this

normalising factor must be defined for each of the three principal symmetry directions, $i = 1, 2, 3$,

$$h = \frac{3E_i(2 - \upsilon_i}{32(1 - \upsilon_i^2)}. \tag{7.7}$$

It can be assumed that irregular grain boundaries are generally only ever in partial contact and so the contribution from the fourth-rank tensor β_{ijkl} can be neglected (Sayers 2002*b*). Based upon the assumption that $\beta_{ijkl} = 0$ and the medium is isotropic, the C_{ij} can be described as follows,

$$C_{11} = (S_{12}^{o^2} - (S_{11}^o + \alpha_{22})(S_{11}^o + \alpha_{33}))/D \tag{7.8}$$

$$C_{22} = (S_{12}^{o^2} - (S_{11}^o + \alpha_{11})(S_{11}^o + \alpha_{33}))/D \tag{7.9}$$

$$C_{33} = (S_{12}^{o^2} - (S_{11}^o + \alpha_{11})(S_{11}^o + \alpha_{22}))/D \tag{7.10}$$

$$C_{12} = S_{12}^o(S_{11}^o - S_{12}^0 + \alpha_{33})/D \tag{7.11}$$

$$C_{13} = S_{12}^o(S_{12}^o - S_{12}^o + \alpha_{22})/D \tag{7.12}$$

$$C_{23} = S_{12}^o(S_{11}^o - S_{12}^o + \alpha_{11})/D \tag{7.13}$$

$$C_{44} = 1/(2S_{11}^o - 2S_{12}^o + \alpha_{22} + \alpha_{33}) \tag{7.14}$$

$$C_{55} = 1/(2S_{11}^o - 2S_{12}^o + \alpha_{11} + \alpha_{33}) \tag{7.15}$$

$$C_{66} = 1/(2S_{11}^o - 2S_{12}^o + \alpha_{11} + \alpha_{22}) \tag{7.16}$$

where

$$D = S_{12}^{o^2}(3S_{11}^o - 2S_{12}^o + \alpha_{11} + \alpha_{22} + \alpha_{33}) - (S_{11}^o + \alpha_{11})(S_{11}^o + \alpha_{22})(S_{11}^o + \alpha_{33}). \tag{7.17}$$

The components of α_{ij} can be estimated from C_{44}, C_{55} and C_{66} as,

$$2\mu\alpha_{11} = \frac{\mu}{C_{55}} + \frac{\mu}{C_{66}} - \frac{\mu}{C_{44}} - 1 \tag{7.18}$$

$$2\mu\alpha_{22} = \frac{\mu}{C_{44}} + \frac{\mu}{C_{66}} - \frac{\mu}{C_{55}} - 1 \tag{7.19}$$

$$2\mu\alpha_{33} = \frac{\mu}{C_{44}} + \frac{\mu}{C_{55}} - \frac{\mu}{C_{66}} - 1 \tag{7.20}$$

where $\mu = 1/(2S^o_{11} - 2S^o_{12})$ (Sayers 2002*b*).

The above equations as devised by Sayers (2002*b*) were modified to incorporate orthrhombic $C_{ij}s$ based on having *a priori* knowledge of the background matrix and the fourth-order crack density tensor terms (Hall et al. 2007).

$$C_{11} = ((S^o_{23} + \beta_{2233})^2 - (S^o_{22} + \alpha_{22} + \beta_{2222})(S^o_{33} + \alpha_{33} + \beta_{3333}))/D, \tag{7.21}$$

$$C_{22} = ((S^o_{13} + \beta_{1133})^2 - (S^o_{11} + \alpha_{11} + \beta_{1111})(S^o_{33} + \alpha_{33} + \beta_{3333}))/D, \tag{7.22}$$

$$C_{33} = ((S^o_{12} + \beta_{1122})^2 - (S^o_{11} + \alpha_{11} + \beta_{1111})(S^o_{22} + \alpha_{22} + \beta_{2222}))/D, \tag{7.23}$$

$$C_{12} = ((S^o_{12} + \beta_{1122})(S^o_{33} + \alpha_{33} + \beta_{3333}) - (S^o_{13} + \beta_{1133})(S^o_{23} + \beta_{2233}))/D, \tag{7.24}$$

$$C_{13} = ((S^o_{13} + \beta_{1133})(S^o_{22} + \alpha_{22} + \beta_{2222}) - (S^o_{12} + \beta_{1122})(S^o_{23} + \beta_{2233}))/D, \tag{7.25}$$

$$C_{23} = ((S^o_{23} + \beta_{2233})(S^o_{11} + \alpha_{11} + \beta_{1111}) - (S^o_{12} + \beta_{1122})(S^o_{13} + \beta_{1133}))/D, \tag{7.26}$$

$$c_{44} = (S^o_{44} + \alpha_{22} + \alpha_{33} + 4\beta_{2233})^{-1}, \tag{7.27}$$

$$c_{55} = (S^o_{55} + \alpha_{11} + \alpha_{33} + 4\beta_{1133})^{-1}, \tag{7.28}$$

$$c_{66} = (S^o_{66} + \alpha_{11} + \alpha_{22} + 4\beta_{1122})^{-1}, \tag{7.29}$$

and where

$$\begin{aligned} D = (S^o_{11}+\alpha_{11}+\beta_{1111})(S^o_{23}+\beta_{2233})^2+(S^o_{22}+\alpha_{22}+\beta_{2222})(S^o_{13}+\beta_{1133})^2+(S^o_{33}+\alpha_{33}+\beta_{3333}) \\ (S^o_{12} + \beta_{1122})^2 - 2(S^o_{12}\beta_{1122})(S^o_{13} + \beta_{1133})(S^o_{23} + \beta_{2233}) \\ - (S^o_{11} + \alpha_{11} + \beta_{1111})(S^o_{22} + \alpha_{22} + \beta_{2222})(S^o_{33} + \alpha_{33} + \beta_{3333}). \end{aligned} \tag{7.30}$$

7.3 Inversion Strategy

It is important to note that the inversion strategy is based upon the assumption that any heterogeneity that exists between samples is minimal. Furthermore, that the EBSD derived elastic properties are representative for all specimens of a single sample.

Equations (7.21 - 7.30) can be used to invert the multi-axial velocity data to derive the crack density tensors (Sayers 2002*b*). The approach involves two steps. The first step derives the α_{ij} terms for assumed scalar cracks (either using just the principal P-wave data or using all the data) and the second step derives β_{ijkl}, which is considered as a perturbation to the scalar crack model.

7.3.1 Step 1: Inversion for α_{ij}

The inversion uses Equations (7.21 - 7.23), when considering just the principal P-wave data, and Equations (7.21 - 7.29) when all the data are used. In both cases the β_{ijkl} are assumed to be zero in this initial step. The inversion uses the appropriate set of simultaneous Equations (7.21 - 7.23 or 7.21 - 7.29) and background elasticities (the S^0_{ij} terms from the EBSD-based calculations) to related the model vector, containing the three terms α_{11}, α_{22} and α_{33} to the data vector of the C^{obs}_{ij} which are the elastic properties determined from the measured velocities and density. The inversion is performed using an iterative, Newton-Raphson approach (Press et al. 1992) . The available velocity data, in this example, allow the definition of seven components of the observable stiffness

tensor, C_{ij}^{obs}: C_{11}^{obs}, C_{22}^{obs}, C_{33}^{obs}, C_{13}^{obs}, C_{44}^{obs}, C_{55}^{obs} and C_{66}^{obs}. Thus the Jacobian matrix which describes the variation of C_{ij}^{model} as a function of variations in the three non-zero components of α_{ij}, is 7 x 3. It is assumed that the principal axes of the background anisotropy and crack anisotropy are coincident and aligned with the axes of the velocity measurements.

7.3.2 Step 2: Peturbation analysis of β_{ijkl}

It is assumed that all of the deviations of the velocities back-calculated using the prior scalar-crack model, from the measured velocities are due to the influence of β_{ijkl} (i.e., due to unequal B_N and B_T). Thus, Equations (7.21 - 7.30) are used with the EBSD-based S_{ij}^0 and fixed values of α_{11}, α_{22} and α_{33} from Step 1 of the inversion. With the available velocity data, the components of β_{ijkl} that can be resolved are β_{1111}, β_{2222}, β_{3333}, β_{2233}, β_{1133} and β_{1122}.

7.3.3 Diagram notation

The results for the inversion procedures for α_{ij} and β_{ijkl} are presented in the next section using the following notation:

V_p^Z	Green circle
V_p^X	Red triangle
V_p^Y	Blue diamond
$V_p^{XZ^45}$	Black triangle
V_s^{xy}	Blue square
V_s^{xz}	Pink star
V_s^{yz}	Yellow cross
α_{11}	Red (x-direction)
α_{22}	Blue (y-direction)
α_{33}	Green (z-direction)

7.4 Results - Inversion for α_{ij}

7.4.1 Sample 1784

At low pressures $\alpha_{33} >> \alpha_{11}, \alpha_{22}$ therefore implying that it has a lot of horizontal microcracks. During loading it can be seen that the horizontal cracks close up but even at very high pressure there still exists a strong VTI symmetry (Figure 7.1).

7.4.2 Sample 1788

As $\alpha_{33} > \alpha_{11} > \alpha_{22}$ it has an orthorhombic symmetry at lower pressures but becomes VTI at higher pressures (Figure 7.1).

7.4.3 Sample 1841

It has a very strong VTI symmetry at low pressure, and an orthorhombic style of symmetry at high pressure where $\alpha_{33} > \alpha_{22} > \alpha_{11}$ (Figure 7.1).

7.4.4 Sample 1909

At low pressures it is weakly orthorhombic but at high pressures it has an approximately isotropic crack distribution. The change in α_{33} with pressure is significantly different to the other two and leads to higher densities of horizontal cracks at intermediate pressures (Figure 7.1).

7.4.5 Sample 1950

At low pressures it has an orthotropic crack distribution where $\alpha_{33} > \alpha_{11} > \alpha_{22}$. By approximately 10MPa the crack distribution changed to a HTI symmetry style (horizontal transverse isotropy) where $\alpha_{33} \sim \alpha_{11} > \alpha_{22}$ (Figure 7.1).

7.4.6 Sample 2129

At low pressures $\alpha_{33} \sim \alpha_{22} < \alpha_{11}$. As the pressure increases both α_{22} and α_{11} decrease at the same rate whilst α_{33} reduces much more rapidly, although they all level out at the same pressure. It could either be described as a CTI symmetry style, where there is a vertical distribution of cracks with their normals distributed in the x_1x_2 plane or there are two alignments of cracks with equal densities along the x_1 and x_2 planes (Figure 7.1).

7.4.7 Sample 2192

At low pressure $\alpha_{11} < \alpha_{22} \sim \alpha_{33}$ but at higher pressures it assumes a VTI symmetry with more horizontal cracks than vertical (Figure 7.1).

7.4.8 Sample 2194

In general, $\alpha_{33} >> \alpha_{22} \sim \alpha_{11}$ but it tends to a VTI style of symmetry at higher pressures (Figure 7.1).

7.4.9 Summary of the results for the inversion of α_{ij}

In general, it appears that the scalar-crack model provides a reasonable fit to the data particularly so at higher pressures but there does exist some slight deviations that may indicate there is some effect due to the fourth-order tensor terms.

7.4.10 Inversion using compressional and shear-wave data

Using both the P- and S-wave available data to invert for crack density it is found that there is only a small change in the derived α_{ij}. As would be expected with more data the fit of the back calculated velocities to measured velocities is far better (Figure 7.2).

7.5 Results - Inversion for β_{ijkl}

7.5.1 Sample 1788

Inclusion of the β_{ijkl} term leads to an improved fit of the velocity data and the back calculated velocities when compared to the scalar crack model. The fourth-order tensor magnitudes are significantly smaller than those determined for α_{ij} with the exception of β_{1133} which though smaller than the α_{ij} values is relatively large. Interpretation of the fourth-order term is not as simple as it is for the scalar term but importantly two of the principal components , β_{1111} and β_{3333} are positive indicating that the effective cracks with normals in x_1 and x_3 (horizontal cracks) have values of $B_N \lambda B_T$. This is most significant for the horizontal cracks at low pressure but $\beta_{1111} \approx \beta_{3333}$ at higher pressures.

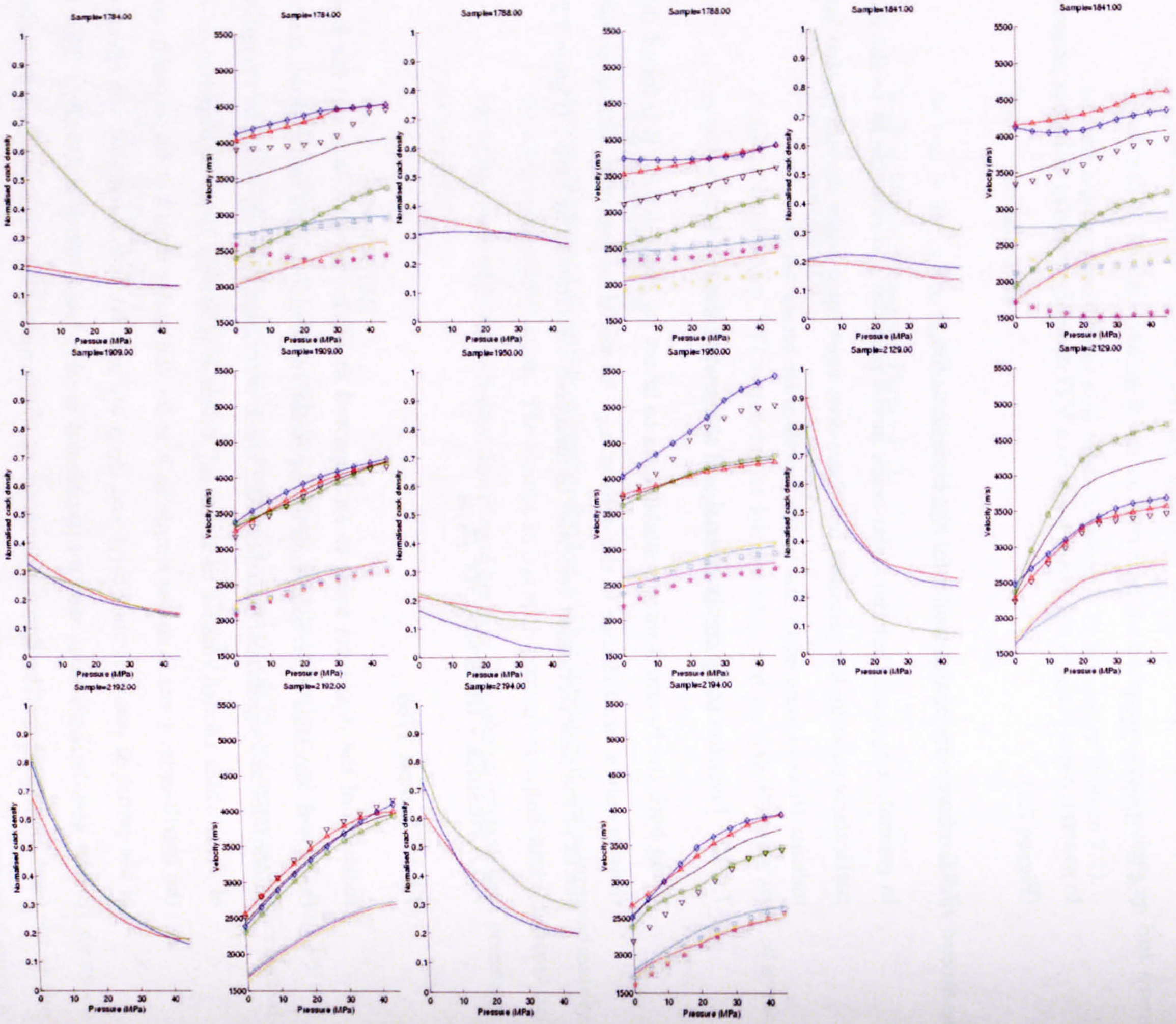

Figure 7.1: *Crack density tensor inversion using P-wave data (Hall et al. 2007).*

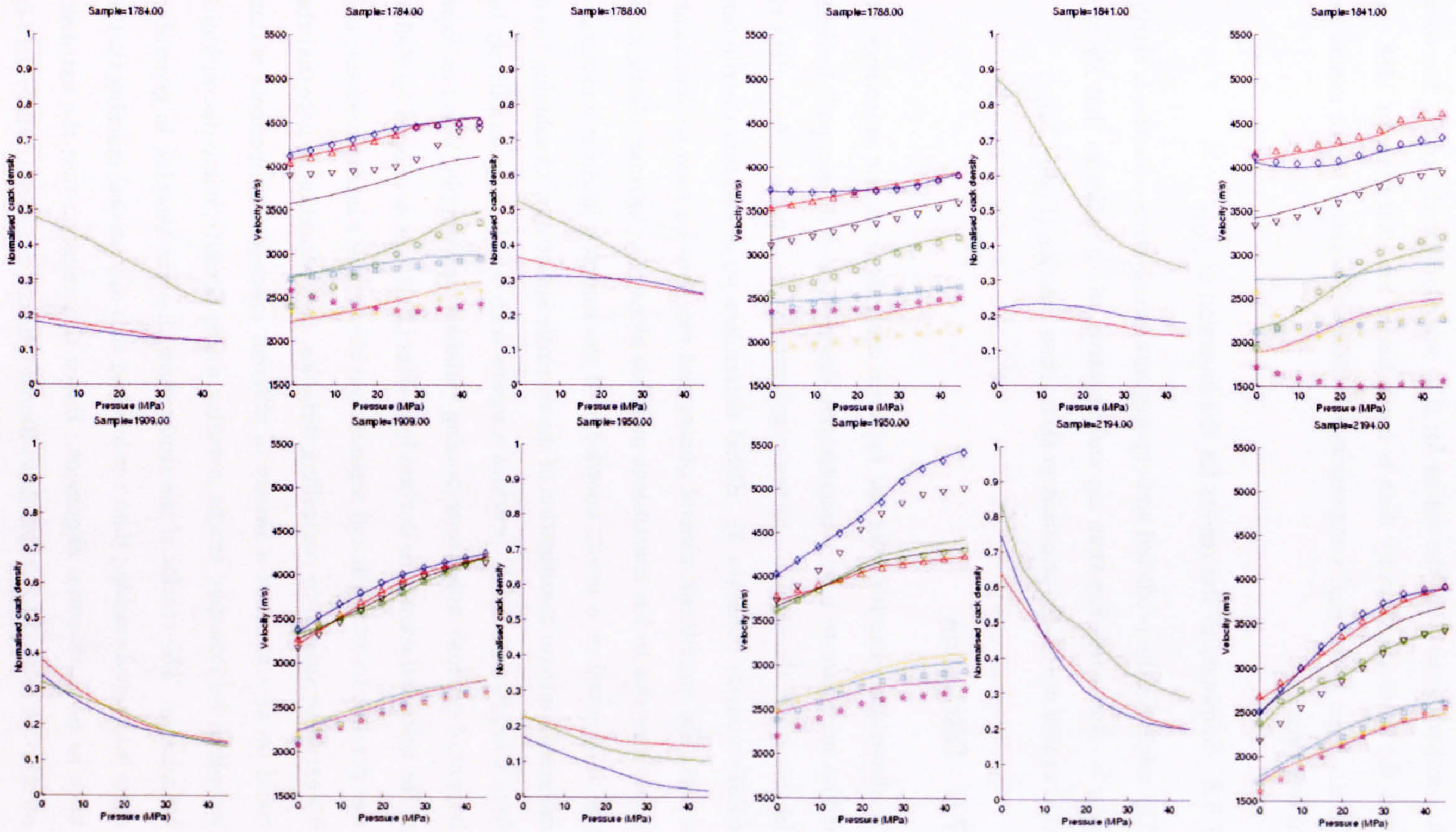

Figure 7.2: *Crack density tensor inversion using P- and S-wave data (Hall et al. 2007).*

7.5.2 Sample 1909

In comparison to 1788 the values for β_{ijkl} are significantly lower. Moreover, it appears that the fit to the velocity data is much better for 1909 than for 1788. All three β_{ijkl} (β_{1111}, β_{2222} and β_{3333}) components for 1909 are negative which means that $B_N < B_T$ at low pressures.

7.5.3 Summary of the results for the inversion of β_{ijkl}

The misfit for the predicted and experimental shear-wave velocities is attributed to β_{ijkl}. β_{ijkl} is often much less than α_{ij} and negative, which indicates that $B_T > B_N$, meaning that cracks are more compliant in shear than traction (Figure 7.3).

7.6 Discussion

To determine quantitatively the extrinsic controls of seismic anisotropy on a sample it is first necessary to have a quantitative description of the sample's intrinsic anisotropy. In this study the sample's intrinsic anisotropy was calculated from data obtained from EBSD analysis (Chapter 5). EBSD determines an orientation distribution function of a sample's constituent mineral phases and can thus be used to determine the samples anisotropy due to the constituent minerals alone (i.e., intrinsic elastic anisotropy). The pre-determined or *a priori* knowledge of the sample's intrinsic anisotropy can then be integrated into an investigation of the extrinsic anisotropy. Combining the data obtained from Chapters (4 and 5) provides a means with which to quantitatively investigate the impact of extrinsic anisotropy causing variables on a sample. Using an expanded version of the inversion scheme as devised by Sayers (2002*b*) as developed by Hall et al. (2007) it was possible to establish and separate out the sample's intrinsic seismic anisotropy from it's extrinsic anisotropy controlling variables. It is important to note that the crack effects could be as a result of a variety of different crack-like components within the sample, including, for example: cracks, porosity, micro-porosity, micro-discontinuities, and grain boundaries. The results of the study show that the samples, in general, contain much more horizontal cracking than vertical and that any vertical cracking that does occur has little or no preferential alignment. Hence this suggests that the extrinsic anisotropies seem to be related to simple depositional fabrics (bedding parallel micro-fabrics).

The velocity and crack anisotropy symmetries are notably similar with significant crack

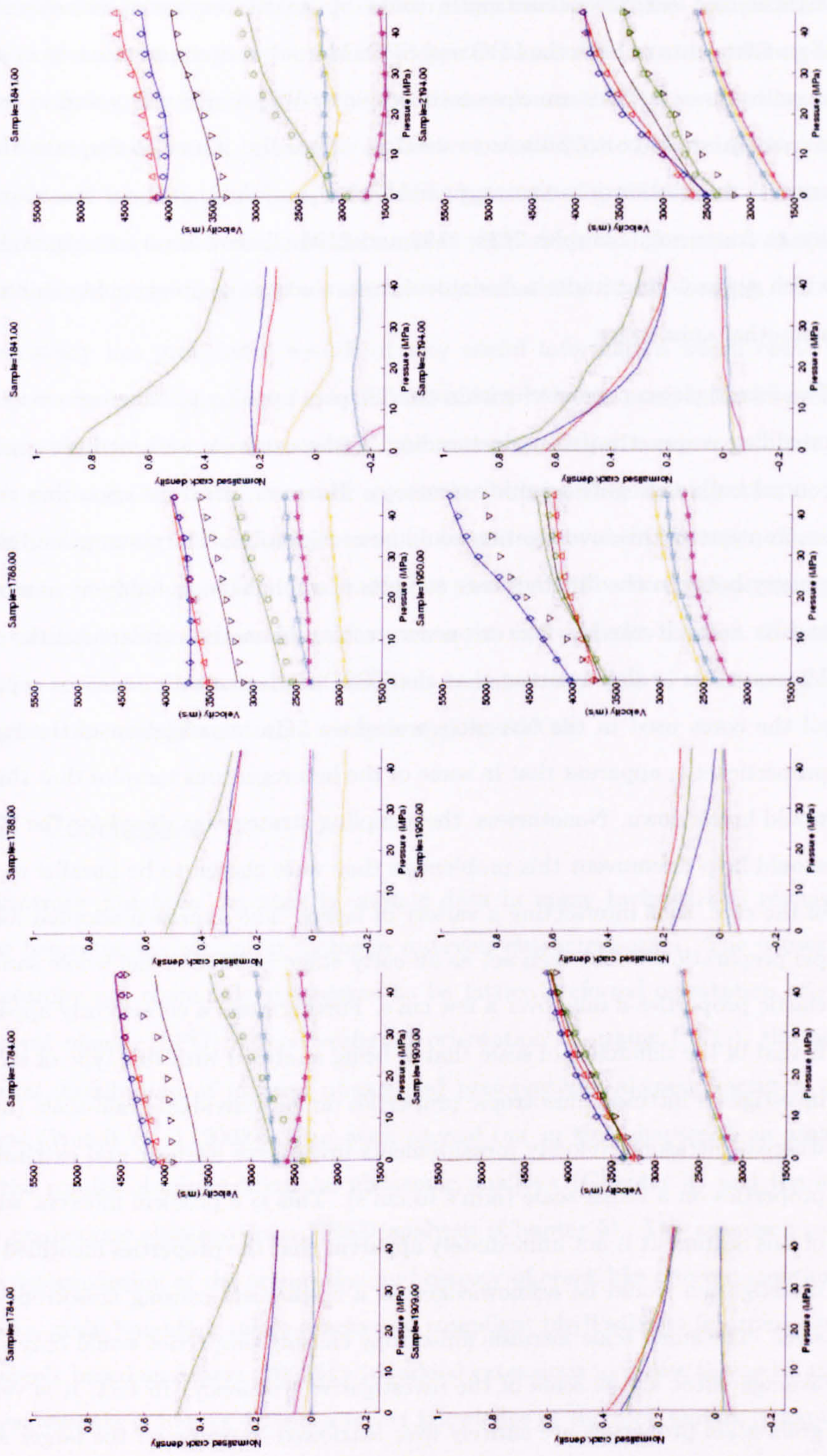

Figure 7.3: *Crack density tensor inversion for β_{ijkl} using P- and S-wave data (Hall et al. 2007).*

densities still remaining at approximately 50MPa. This observation suggests that the intrinsic and extrinsic anisotropies could be linked because it is believed that grain alignment controls both the LPO and SPO. Moreover, at approximately *in situ* confining pressure these samples are close to isotropic or VTI in symmetry and in some cases are extremely sensitive to pressure variation. Broadly, it seems the case then that any azimuthal variation in anisotropy could be observed *in situ* and would most likely be due to fracturing. Samples 2129, 2192 and 2194 all show a very strong stress sensitivity which suggests that under a deviatoric stress that the samples could exhibit a detectable azimuthal anisotropy.

The investigation presented within this chapter appears to have been very successful in providing a quantitative understanding of the extrinsic and intrinsic parameters that control bulk aggregate seismic anisotropy. However, concerns regarding the underlying assumptions of this investigation could be considerable. The assumption that the heterogeneity between the different core samples is minimal is probably an over simplification and as a result would yield erroneous results when the core's velocities are inverted. Moreover, its is also assumed that the EBSD derived elastic tensor is representative of all the cores used in the inversion procedure. On investigation of the individual core properties it is apparent that in some of the heterogeneous samples that this assumption would break down. Nonetheless, the sampling strategy employed for the EBSD analysis should help circumvent this problem as they were chosen to be parallel to the long axis of the core, thus intersecting a variety of layers. The approach adopted for EBSD sample preparation would then act as an early stage average of the whole samples intrinsic elastic properties if only over a few cm's. Furthermore, a consistently apparent problem is that of the difference in scale that is being analysed with this type of strategy. EBSD investigates intrinsic anisotropic properties on an individual grain-scale (nm's to mm's) whereas ultrasonic velocity measurements investigate intrinsic and extrinsic anisotropic properties on a larger scale (mm's to cm's). This is a problem inherent with all studies of this nature. It is not immediately apparent that the properties identified by ultrasonic investigation would be acknowledged as a mechanism causing anisotropy at the larger scale. The small scale intrinsic anisotropy causing properties would only show up as an average effect at the scale of the investigative frequency. In fact, it is very likely that grain-scale properties are entirely over shadowed by those on the larger scale, such as, cracks and micro-porosity.

Louis et al. (2005) determined the shape and spatial distribution of both grains and voids by computer image processing. Moreover, they also used X-ray computerised tomography and laser scanning confocal microscopy to characterise the inner *3D* structure of the rock samples. To fully support the hypotheses presented within this Chapter ideally a similar approach would be used as in Louis et al. (2005) to determine the internal grain shapes and whether there is a preferential alignment of grain contact regions. This type of investigation would then provide a means with which to differentiate the predominant mechanisms controlling elastic wave velocity sensitivity during loading.

This study has provided a wealth of very useful information which could be used to assist in the understanding of crack distribution within the samples and hence determine information which is fundamental to the understanding of a reservoir. It is postulated that any variation in the reservoir's pressure during either well injection or production would have a significant impact on the *in situ* reservoir anisotropy. Non-hyperbolic moveout analysis would be most suited to detect the observed anisotropies because of the predominantly horizontal cracks within the rock samples studied. Nonetheless, the ability to detect any azimuthal variation in anisotropy due to stress sensitivity would require some sort of azimuthal analysis such as AVOA.

7.7 Conclusions

Anisotropy has been detected in seismic data in many hydrocarbon reservoirs and is now becoming an important factor in reservoir characterisation. The causes of seismic anisotropy are commonly considered to be lattice preferred orientation of constituent mineral phases (LPO), shape preferred orientation of grains (SPO), the non-random spatial distribution of mineral phases and preferentially aligned fractures, cracks and pores (Wendt et al. 2003). The work carried out in this chapter is an amalgamation of the results obtained from the ultrasonic analyses (Chapter 4) and the elastic tensor predictions obtained from EBSD analyses (Chapter 5). The approach used here in the determination of the orientation and density of crack-like micro-discontinuities (i.e., cracks, grain boundary micro-cracks and compliant phyllosilicate interparticle material) is largely based on Sayers (2002*b*) with added extensions to utilise the multi-axis velocity measurements (Chapter 4) and *a priori* knowledge of the rock matrix (Chapter 5).

The results show that the extrinsic crack-induced anisotropy is strong relative to that of

the intrinsic anisotropy (i.e., LPO effects). In general, the predominant crack-set in the samples studied was aligned parallel to the depositional fabric. That is samples generally contained a much larger horizontal crack density than vertical. It is, however, observed that the LPO and extrinsic anisotropies appear in general to align, this indicates that they are very probably linked in some way. It is likely that the cracks are related to the grain boundary contacts which are aligned with the grains which are coincident with the LPO measurements. Furthermore, it was also determined that if any vertical cracking was detected that it had little or no preferential alignment.

There are several sample specific observations of interest. Sample 2129, for example, has a lot more vertical cracking than horizontal, although it is not clear whether the cracking is preferentially aligned. Analysis of thin-sections and core photos shows that the horizon was significantly fractured and also oil stained, both observations would support the conclusions drawn from the inversion (Smith & Lappin 1997, Knipe et al. 1998). Sample 2129, 2192, and 2194 all showed significant pressure sensitivity of the vertical crack sets. Moreover, these samples mentioned previously and samples 1784, 1788 and 1841 all show a strong variation in the horizontal crack set with loading.

Chapter 8

Magnetic Properties

8.1 Introduction

Technological developments, such as, *4D* seismic profiling, increasingly more complicated migration algorithms, and a proliferation of computational processing power mean that it is now possible to measure, amongst other attributes, seismic anisotropy of reservoir rocks in the subsurface. Measurements of seismic anisotropy offer a potentially powerful tool for remotely determining the properties of rocks and fluids prior to drilling. The interpretation of such data, however, is presently limited by our understanding of the causes of anisotropy in sedimentary rocks. Laboratory measurements of velocity and anisotropy currently provide important information on the seismic anisotropy of the bulk aggregate but do not discriminate the contributions from the numerous microstructural variables, such as, LPO, the non-random spatial distribution of mineral phases, aligned porosity, and fractures (Crampin 1981, Babuska & Cara 1991, Mainprice et al. 2000, Wendt et al. 2003, Kendall et al. 2006, Valcke et al. 2006).

Compressional and shear-wave velocity anisotropy measurements have been conducted on a suite of samples obtained from the Clair field, N.W. Scotland whose microstructure and mineralogical composition have been rigorously established (Chapter 5 and Chapter 3 respectively). To enable direct comparisons between the various analytical techniques used in this study and with independent studies of anisotropy the core samples were oriented using palaeomagnetic techniques. The minerals responsible for a magnetic fabric are weakly magnetic and are present in small proportions in most rocks (Hailwood & Ding 1995). Sedimentary rocks usually contain either one or two different components

of remanent magnetisation (Hailwood & Ding 2000). Viscous remanent magnetisation (VRM) gradually builds up over time and records the direction of mean magnetic North over the past several thousand years and provides the absolute direction of present-day geographic North. Whilst VRM builds up over time it also undergoes continuous decay and therefore must be continuously reacquired. The primary component magnetisation is acquired at the time of deposition (assuming the rock does not undergo significant re-working prior to lithification), and provides a record of palaeo-North. The primary component is used to orient the core, provided any significant post-depositional rotation of the region (due to plate motion) is known and accurately corrected. The palaeomagntic analysis of the core samples also provides useful information regarding sand transport directions and can help place important constraints on the positions of sand input points in sedimentary basins thus facilitating prediction of sand distribution and the geometry and direction of elongation of sand bodies.

Two independent methods were used to determine the anisotropy of magnetic susceptibility. One method measured the natural AMS of each individual sample, that is, the preferred orientation of naturally occurring magnetic minerals (e.g., magnetite). The second method measures the enhanced AMS, produced after a thin-film of magnetic particles have been precipitated onto the pore space. The information obtained from magnetic anisotropy is in many respects superior to optical microscopy, and complementary to electron microscopy methods as it provides *3D* information regarding grain orientation plus a quantitative assessment of the intensity of grain fabric (Hailwood & Ding 2000).

Presented in this chapter is an analysis of the palaeomagnetic properties of a suite of siliciclastic samples extracted from the Clair field, N.W. Scotland. The work was commissioned, analysed, and interpreted by myself but the measurements were performed by Dr. E. Hailwood of Core Magnetics, Cumbria. The chapter includes the results of palaeomagnetic core orientation and an investigation into the grain and pore fabric of the same set of core samples.

8.2 Methodology

Palaeomagnetic orientation, and anisotropic magnetic susceptibility measurements (AMS) were made on 1 inch diameter core plugs and enhanced AMS and magnetic porosity mea-

surements were made on $\frac{3}{4}$ inch cubes. Four plug samples had previously been drilled from each piece of half-core for the laboratory ultrasonic velocity measurements. Three of these core plugs (X, Y, and Z) were orthogonal to each other, while the fourth was inclined at 45^o to the borehole long axis (Figure 8.1). The samples for the palaeomagnetic study were cut from offcuts of the X, Y, and Z plugs.

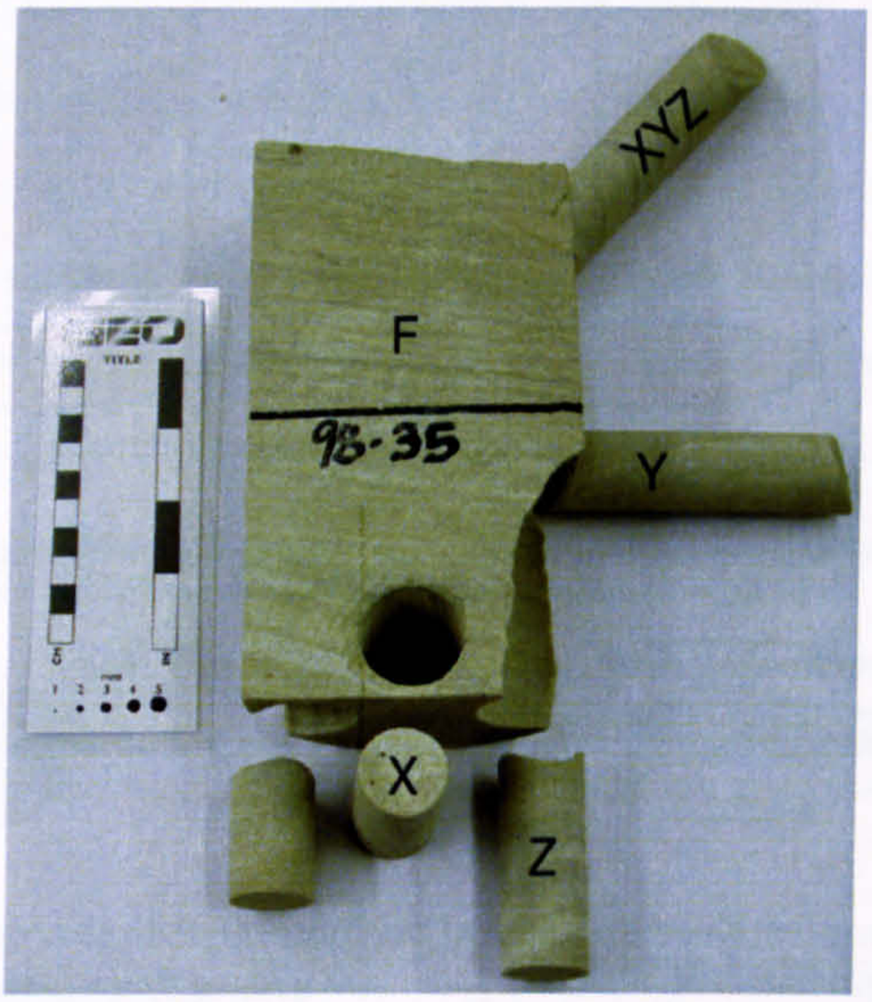

Figure 8.1: *The core sampling technique used in determining anisotropic magnetic susceptibility. Notation: X - perpendicular to the borehole axis (approximately parallel to bedding), Y - perpendicular to the borehole axis and perpendicular to the X-core (approximately parallel to bedding), Z - parallel to the borehole axis (approximately perpendicular to bedding), XYZ - 45° to bedding and the borehole axis, and F - perpendicular to the flat face of the borehole half core.*

In the plug samples used for palaeomagnetic orientation, spurious components of magnetisation associated with drilling are removed and the geologically-significant components are isolated from each other by incremental thermal demagnetisation. In most cases, the VRM is isolated by thermal demagnetisation at relatively low temperatures ($< 300^oC$) and the primary magnetisation at temperatures close to the Curie point of the magnetic constituents ($\sim 550^oC$).

In a core from a vertical or nearly-vertical well, as in this study (as determined from wellhead trajectory data), the mean horizontal component, J_h, of the VRM defines the direction of present-day geographic North (Figure 8.2A). The core plug is then rotated about the vertical axis until J_h coincides with geographic North (Figure 8.2B).

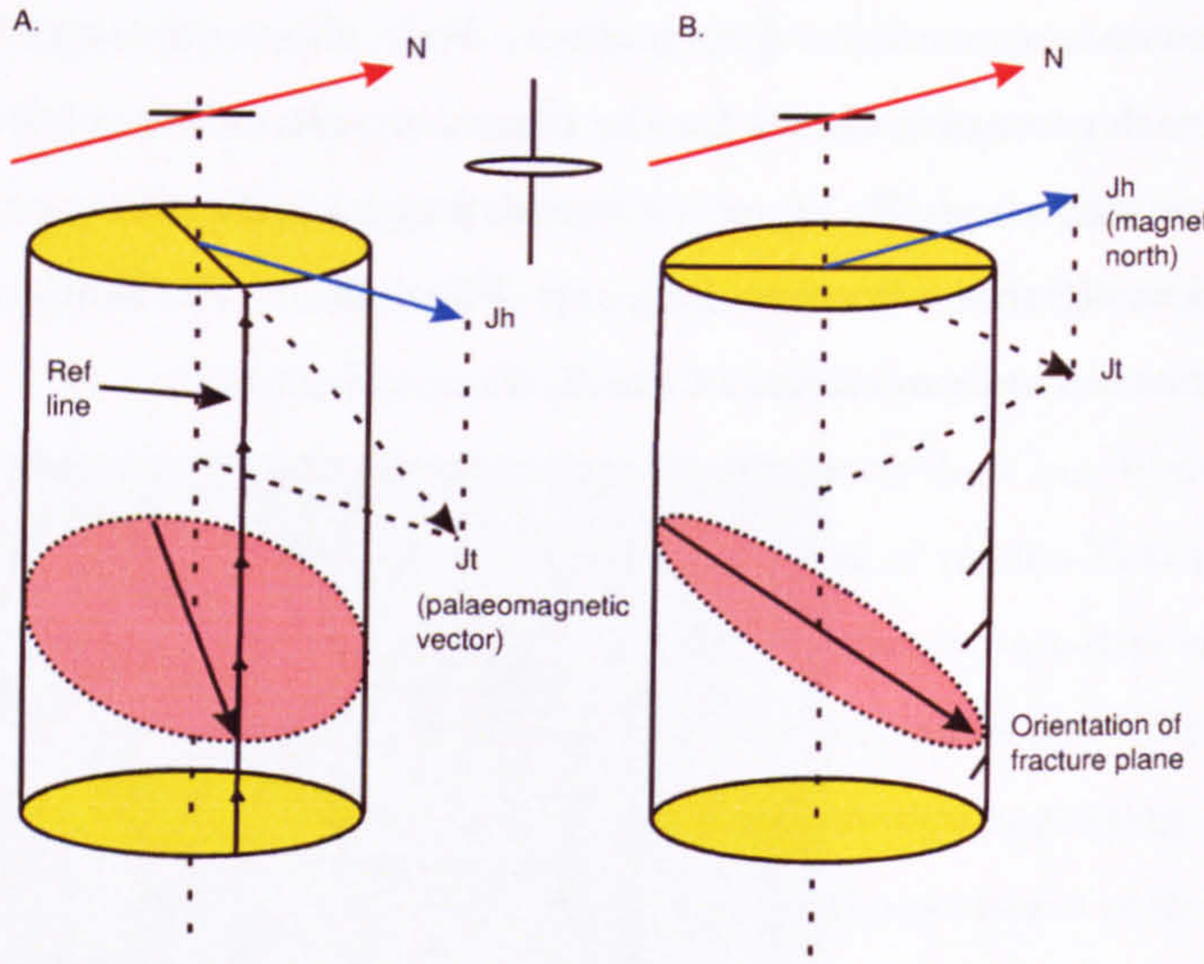

Figure 8.2: *Principle of palaeomagnetic core orientation in a vertical or near-vertical well. In a core from a vertical or near vertical well (as in this study, as determined from borehole trajectory data) the mean horizontal component J_h of the VRM defines the direction of present day North.*

All plug samples were subjected to incremental thermal demagnetisation using a Magnetic Measurements Thermal Demagnetiser (MMTD1). Their remanent magnetism was measured after each heating step with an automated high-sensitivity spinner magnetometer (AGICO JR5A). Both instruments were situated within the same magnetically shielded enclosure to minimise exposure of samples to external magnetic fields during laboratory handling.

During thermal demagnetisation, temperature increments in the range 25 to 40^{o}C were used, starting at 75^{o}C. Demagnetisation was continued until either the remanent magnetism became too weak for further reliable measurement or until magneto-mineralogical transformations began to occur. The thermal demagnetisation data was processed by *3D* principal component analysis (Kirschvink 1980).

8.3 Grain fabric determination by anisotropy of magnetic susceptibility

Anisotropic magnetic susceptibility provides a quick and accurate way of determining the statistical *3D* orientation of constituent grains (Hailwood & Ding 1995).

The method of measurement and calculation estimates a susceptibility (dimensionless sometimes denoted χ_m) in the form of a second rank symmetric tensor, K, which relates

the magnetisation J_i induced in a specimen by a field, H_j, (Equation 8.1).

$$J_i = K_{ij} H_j \tag{8.1}$$

This susceptibility can be specified by six terms, three relating to the magnitudes of its principal axes and three relating to their orthogonal directions.

For a single non-spherical grain of magnetite, the magnetic susceptibility has a maximum value K_{max} (grain long axis) and a minimum value K_{min} (grain short axis). In *3D* the variation of magnetic susceptibility with direction within the grain can be represented by a triaxial ellipsoid with principal axes K_{max}, K_{int}, and K_{min} where the intermediate susceptibility axis K_{min} is orthogonal to the other two (Figure 8.3).

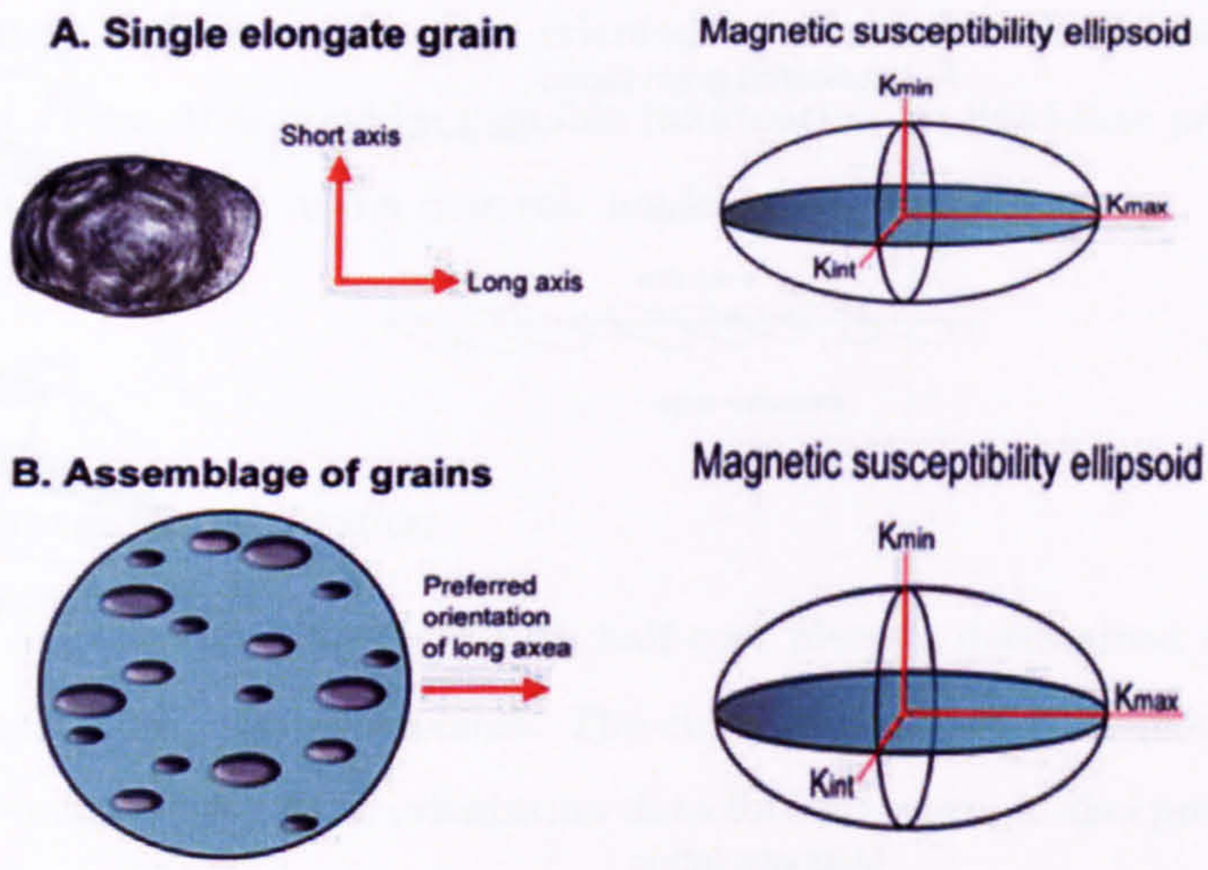

Figure 8.3: *Principle of grain fabric determinations from anisotropic magnetic susceptibility measurements. A single non-spherical grain of magnetite has a maximum susceptibility, K_{max}, the grain long dimension and K_{min} along its shortest axis. In 3D the variation can be represented by a triaxial ellipsoid with axes, K_{max}, K_{min}, and K_{int}, which is orthogonal to the other two axes.*

Depositional processes produce primary-style sedimentary fabrics from which sediment transport directions can be inferred (Hamilton & Rees 1970). Secondary-style fabrics, however, are caused by post-depositional processes, such as, slumping, bioturbation or de-watering. Samples which have a very weak natural AMS, however, can produce the secondary style fabrics as a result of a low signal-to-noise ratio. Consequently, secondary-style fabrics rarely provide reliable information on sediment transport directions (Hail-

wood & Ding 2000).

During deposition grains generally exhibit one of two orientations, either with their long axes parallel (FP - flow parallel) or perpendicular (FT - flow transverse) to the direction of deposition. These cases can be easily discriminated on the basis of their characteristic imbrication patterns (Hamilton & Rees 1970). When deposition occurs on an essentially flat bed, an upward imbrication of grain long axes (K_{max}) occurs in the down-current direction (Figure 8.4). Under conditions of traction (where grains roll along the substrate), however, it produces a flow-transverse alignment of grain long axes (Figure 8.4). In this case, K_{max} usually show no systematic imbrication (approximately equal numbers are distributed at either end of the flow-transverse axis), but K_{min} still show an upward imbrication in the up-current direction.

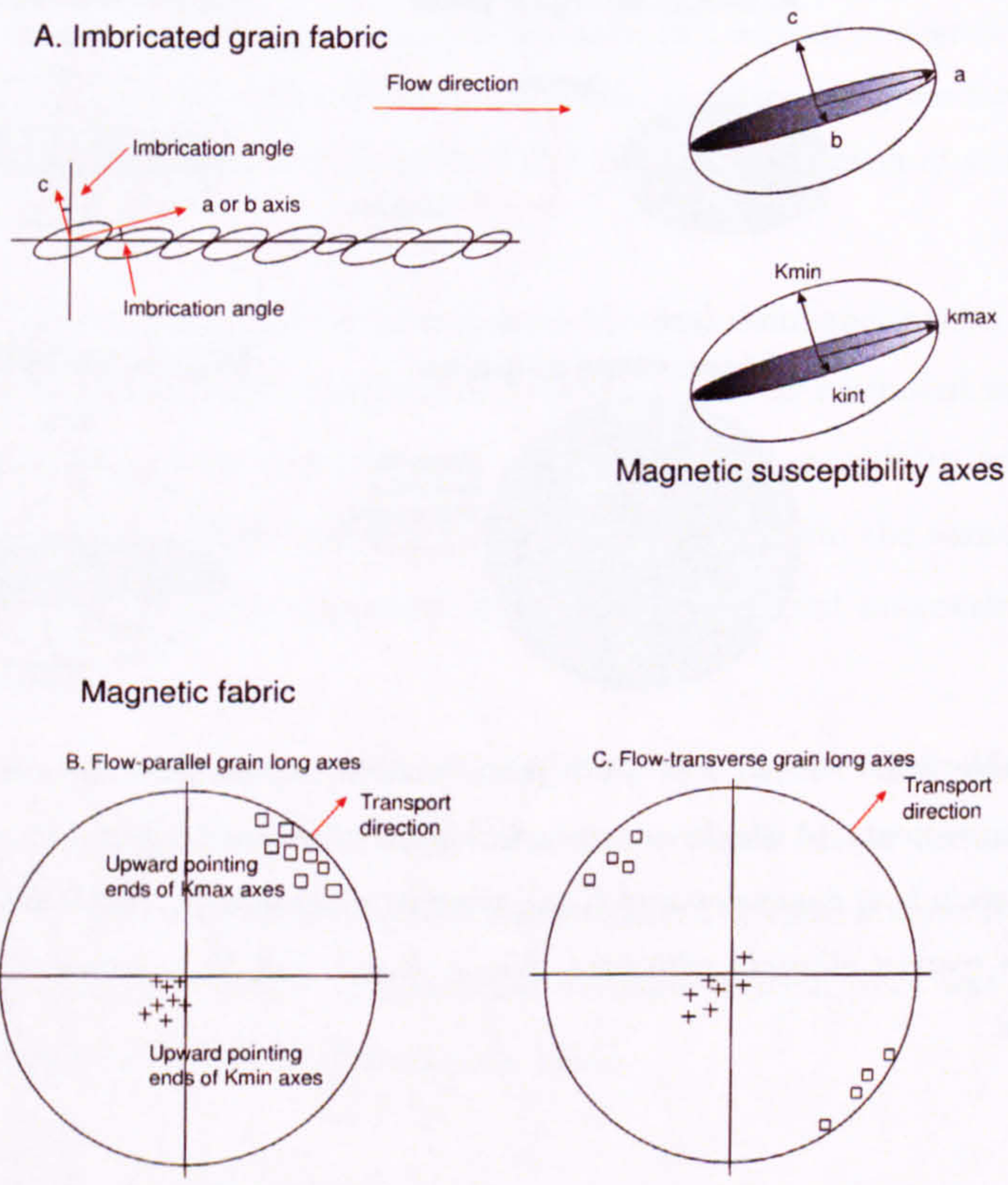

Figure 8.4: *(A) Production of grain imbrication by fluid flow. (B) Resulting magnetic fabric for a flow-parallel grain long axis alignment, and (C) magnetic fabric for a flow-transverse alignment. In (B) and (C), the AMS directions from individual plug samples are shown on upper hemisphere stereographic projections. Open squares and crosses represent maximum and minimum susceptibility axes respectively.*

8.4 Pore fabric and permeability anisotropy

Magnetic porosity analysis involves flooding a sample's pore network with a magnetic fluid. AMS measurements of the ferrofluid-saturated samples then define the pore fabric (i.e., the preferred orientation of pore long and short axes) (Hailwood & Ding 1995).

Furthermore, the degree of magnetic anisotropy has been suggested to be related to the degree of permeability anisotropy (Hailwood & Ding 2000). Consequently, this method provides precise information on the *3D* permeability anisotropy (Hailwood & Ding 1995). Magnetic porosity analysis qualitatively defines azimuthal permeability, whereas, routine permeability measurements only measure the vertical and horizontal permeability.

Measurements were made on core plugs to determine the degree and direction of permeability anisotropy and the results were oriented to geographic North using the palaeomagnetic data. Thus, this provides valuable information on fluid-flow properties of the reservoir, for incorporation into a reservoir model.

8.5 Results

8.5.1 Palaeomagnetic orientation

The direction of geographic North in each half-core piece is determined from the mean of the low temperature magnetic vectors. The circular standard error (c.s.e.), a measure of the angular uncertainty of the orientation data for each core, is also provided. On the basis of the c.s.e. and number of vectors contributing to the mean, the palaeomagnetic orientation data for each core piece has been assigned a reliability class ranging from 1 to 3. Class 1 represents the most reliable results, for which the angular reliability is $< 15^o$. Class 2 represents moderate reliability results with angular uncertainties in the range 15^o to 20^o, and class 3 represents poor reliability data with angular uncertainties $\geq 20^o$. The geographic azimuth of the reference direction, F, (measured in degrees clockwise from geographic North) for each core piece is listed in Table (8.1).

8.5.2 Anisotropy of magnetic susceptibility

The anisotropy of magnetic susceptibility directions have been referred to geographic North using the palaeomagnetic core orientation data and corrected for structural variation. K_{max} axes are shown as coloured squares and K_{min} axes as crosses.

Table 8.1: *Palaeomagnetic core orientation data. F - degrees East of North (perpendicular to the flat face of the borehole half core), Vectors - number of vectors contributing to the mean, c.s.e. - circular spherical error (measure of the angular uncertainty of the re-orientation data), and Class - reliability class of data (1 - $< 15^o$, 2 - $15^o - 20^o$ and 3 - $> 20^o$).*

Depth (m)	F (^{o}E of N)	Vectors	c.s.e.	Class
1663	032	5	9	1
1788	280	4	21	3
1841	348	2	25	3
1909	314	3	11	1
1950	050	3	6	1
1963	231	3	11	1
2028	041	3	9	1
2070	059	4	31	3
2073	004	5	15	2
2088	037	3	9	1
2129	047	3	14	1
2192	105	5	15	2
2194	327	5	10	1
2198	165	5	6	1

Natural and enhanced AMS upper hemisphere stereographic projections for Well 206/8-8 are shown in Figures (8.5; 8.6) respectively. K_{max} and K_{min} axes lie within $\sim 35^o$ of the horizontal and vertical respectively, typical of depositional fabrics. This suggests that the fabrics of these sediments have not been significantly disturbed by post-depositional processes. Both the natural and enhanced AMS plots show a broad clustering of upward pointing ends of K_{max} axes in the S or SE and a complementary offset of K_{min} axes from the vertical towards the NNW. These features are particularly clear for the enhanced AMS data from samples with Class 1 orientation. The mean sediment transport direction throughout Well 206/8-8 is toward the SSE.

Grain fabric data for 206/13a-2 obtained from natural and enhanced AMS measurements are shown in Figures (8.7; 8.8). The AMS results exhibit considerable dispersion but there is some indication of a weakly-defined flow parallel fabric in the enhanced AMS

data and flow tranverse fabric in the natural AMS data. This may reflect a tendency for dense particles to roll over the substrate in flow-transverse mode (reflected in natural AMS). In contrast, other less dense detrital grains (quartz etc.) are aligned flow parallel. The mean sediment transport direction of Well 206/13a-2 is also inferred to be towards the SE.

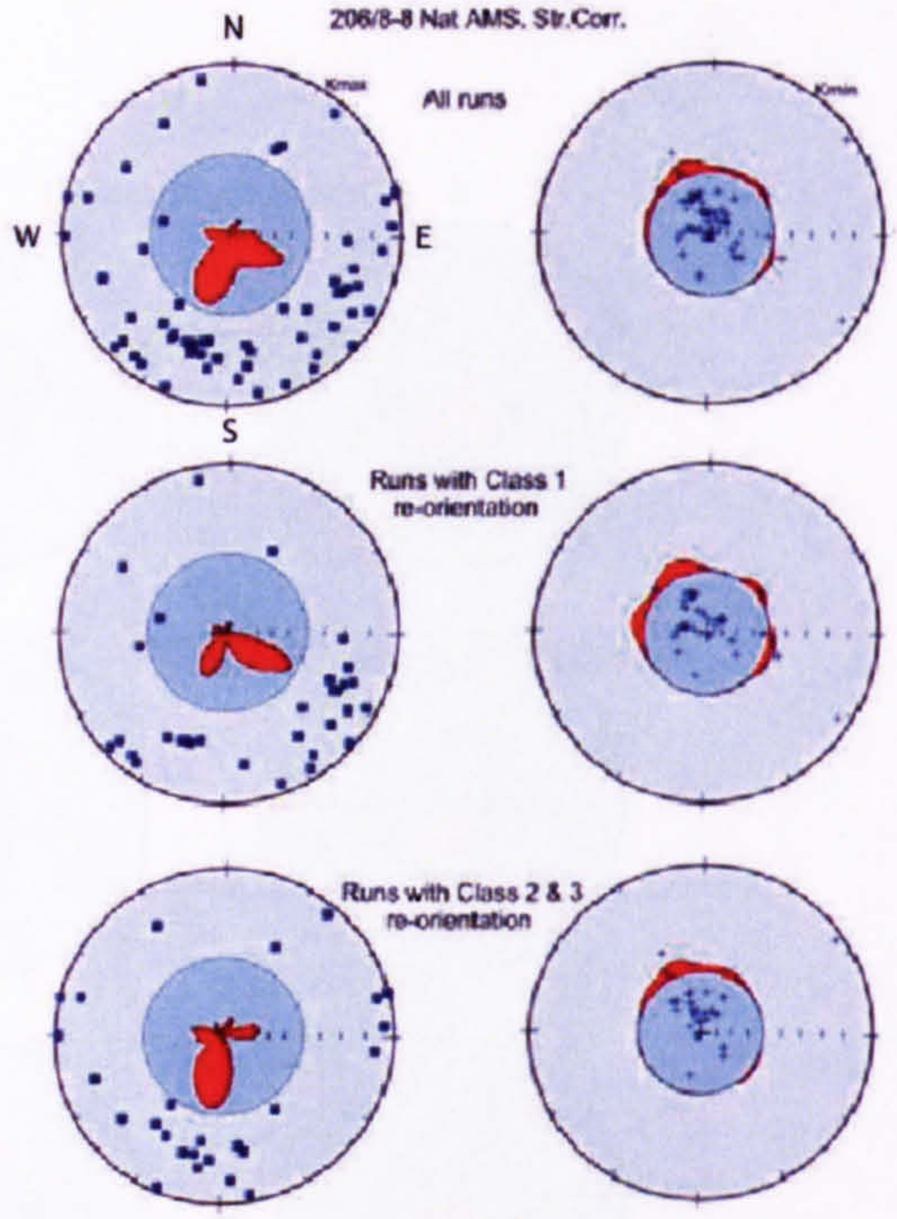

Figure 8.5: *Natural AMS data for all plug samples from Well 206/8-8 plotted on upper hemisphere stereographic projections after palaeomagnetic orientation and structural correction.* K_{max} *axes are shown as coloured squares and* K_{min} *axes as crosses. Azimuthal directions are shown on co-centred rose plots.*

8.5.3 Horizontal anisotropy

The azimuthal distribution of K_{max} axes sampled from 206/8-8 determined from enhanced AMS measurements are shown in Figure (8.9). These plots represent the preferred orientation of long dimensions of the dominant clastic grains. All directions have been oriented to geographic North using the palaeomagnetic data. The azimuths of the upward pointing end of the mean K_{max} axis and corresponding c.s.e for each individual core is shown in Table (8.2).

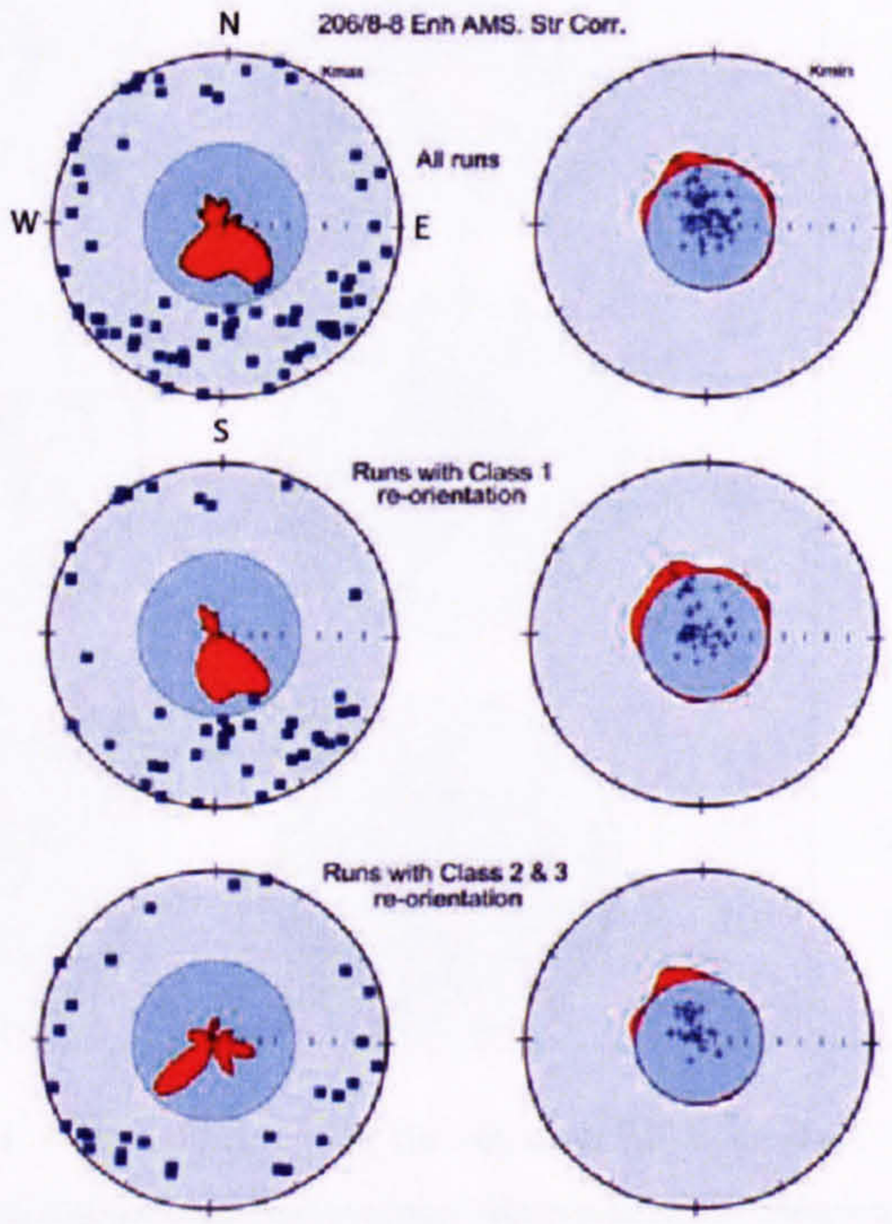

Figure 8.6: *Enhanced AMS data for all plug samples from Well 206/8-8 plotted on upper hemisphere stereographic projections after palaeomagnetic orientation and structural correction. K_{max} axes are shown as coloured squares and K_{min} axes as crosses. Azimuthal directions are shown on co-centred rose plots.*

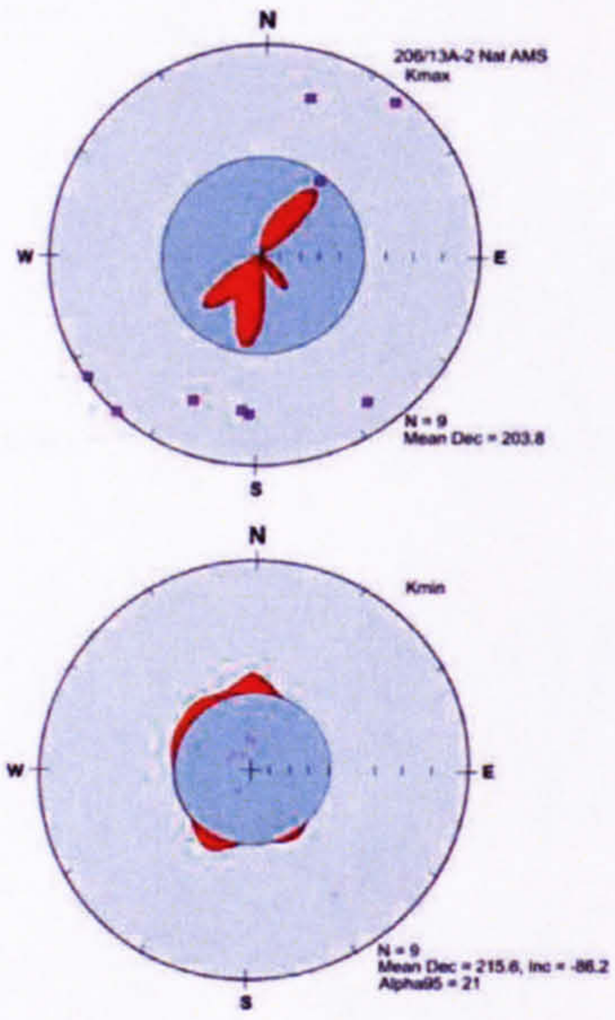

Figure 8.7: *Natural AMS data for all plug samples from Well 206/13a-2 plotted on upper hemisphere stereographic projections after palaeomagnetic orientation and structural correction. K_{max} axes are shown as coloured squares and K_{min} axes as crosses. Azimuthal directions are shown on co-centred rose plots.*

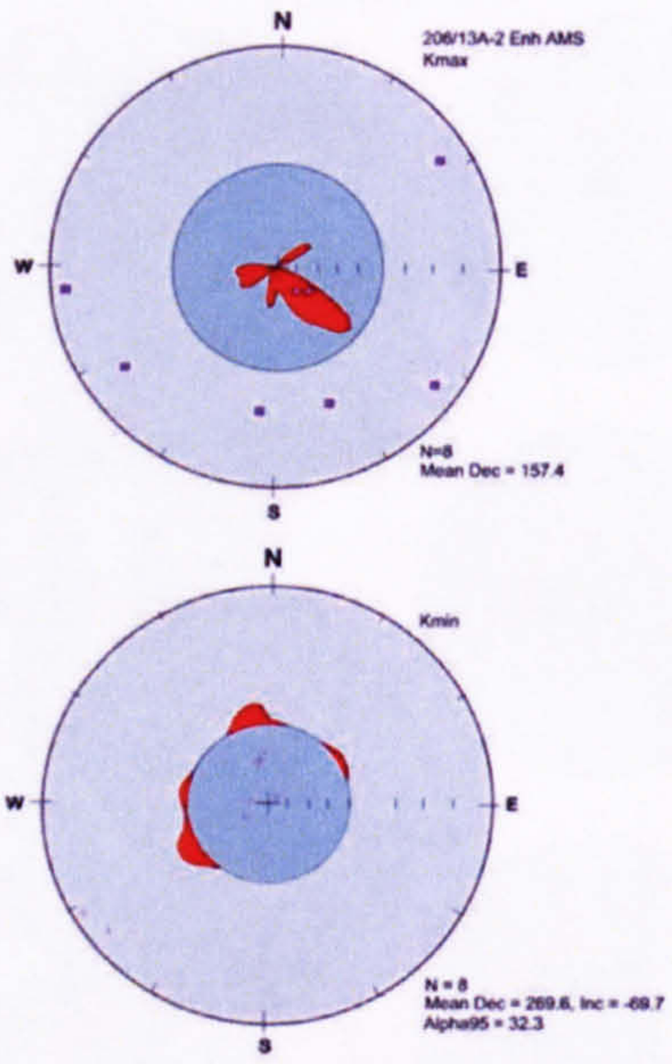

Figure 8.8: *Enhanced AMS data for all plug samples from Well 206/13a-2 plotted on upper hemisphere stereographic projections after palaeomagnetic orientation and structural correction. K_{max} axes are shown as coloured squares and K_{min} axes as crosses. Azimuthal directions are shown on co-centred rose plots.*

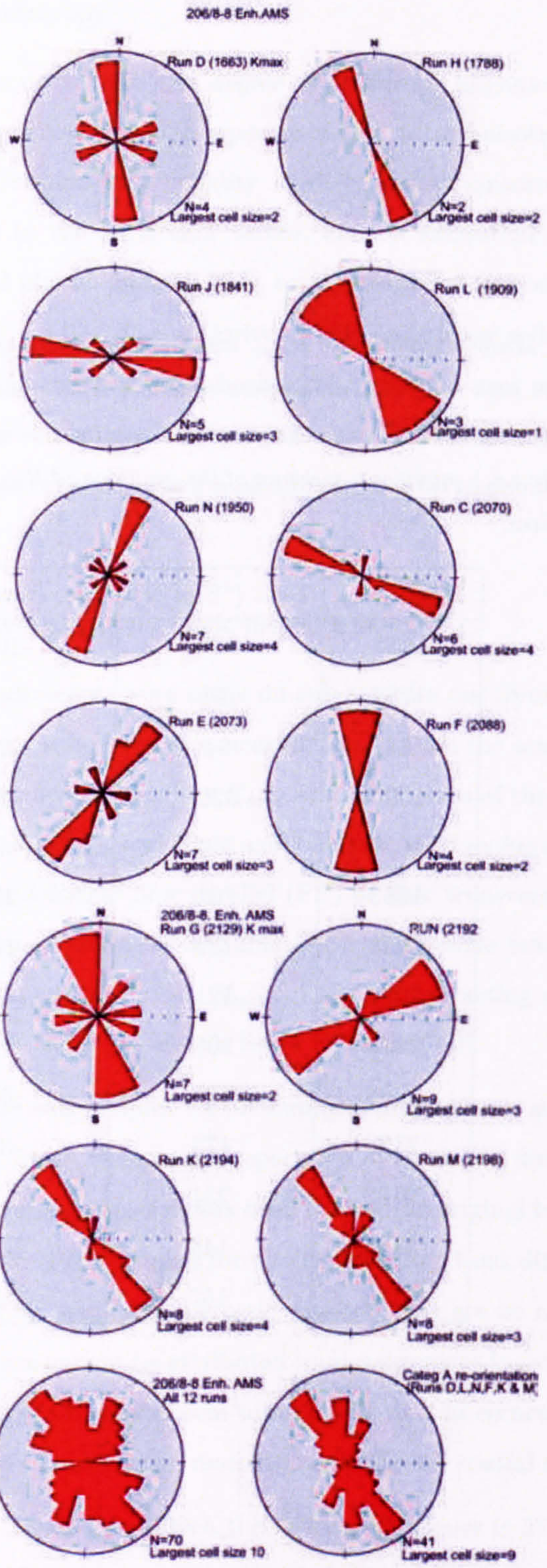

Figure 8.9: *Azimuthal preferred orientations of grain long axes determined from enhanced AMS measurements.*

Table 8.2: *Mean orientation of K_{max} axis (representing preferred orientation of grain long dimensions) in each core, determined from enhanced AMS measurements. The declination (Dec.) is referred to geographic North and the inclination (Inc.) is upward directed. The circular standard error (c.s.e.) provides a measure of the grouping of K_{max} axes of the sets of samples from each core piece.*

Depth (m)	Dec. (°E of N)	Inc. (upwards)	c.s.e.
1663	337	-10	26
1788	151	-8	2
1841	94	-2	12
1909	321	-2	11
1950	202	-6	15
1963	101	-29	21
2028	189	-16	21
2070	121	-5	17
2073	206	-13	14
2088	181	-30	5
2129	173	-33	17
2192	231	-2	10
2194	145	-7	7
2198	157	-6	12

8.5.4 Degree of anisotropy

The percent anisotropy reflects the degree of preferred alignment of the constituent grains. It can be specified in three separate ways: total anisotropy (the ratio of the maximum to the minimum susceptibility in *3D*), planar anisotropy (the ratio of the mean vertical value to the horizontal value), and as azimuthal anisotropy (variation within the horizontal plane). In both wells total anisotropy typically ranges from ~5 to 30% with a mean of ~ 11%. The majority of this anisotropy reflects the tendency for grains to lie with their long axes near horizontal and short axes near vertical, resulting in a dominant planar anisotropy with a mean of ~ 9%. Azimuthal anisotropy in these particular sediments is relatively weak typically ranging up to about 3% but with a mean of only ~ 1.5%.

8.5.5 Scale-dependence of grain fabric measurements

Enhanced AMS measurements were made on sub-samples cut from the core plugs. The enhanced AMS of these sub-cubes was measured to explore the scale-dependence of the grain fabric data. The directions of the K_{max} and K_{min} axes of the original samples are compared with the mean K_{max} and K_{min} axes of the corresponding sub-samples in Table (8.3). The fabric type, whether flow parallel (FP) or flow transverse (FT) alignment of grain long axes is also summarised in Table (8.3). The angle between the K_{max} axis of each original sample and the mean K_{max} of the corresponding sub-samples and the corresponding angle for the K_{min} axes is listed in Table (8.4).

The mean K_{min} of the sub-samples for all samples analysed are similar to that of the original sample. In all cases, the angular separation of these two directions is $\leq 6^o$. The mean K_{max} axis of the sub-samples differs from that of the original host sample by $\leq 15^o$ in most samples. In two of the samples for which these directions differ by larger angles, the percentage anisotropy and bulk magnetic susceptibility are no weaker than in other samples, so the difference cannot be attributed to measurement inaccuracies arising from a weak signal. Instead, these results seem to represent real differences in the grain fabric properties of these two samples when measured on different spatial scales.

In the case of sample 2194K1, for which the angular difference is 65.1°, it appears that this sample exhibits a flow transverse grain fabric style when measured on a scale of ~15mm, but a flow parallel style on a scale of ~5mm. This suggests that both flow

Table 8.3: *Comparison of K_{max} and K_{min} directions of original samples and mean directions for corresponding sets of sub-samples. Circular standard error (c.s.e) values for the mean K_{max} and K_{min} directions are listed and the fabric type, where FP = flow parallel and FT = flow transverse alignment of the grain long axes. See Appendix (B) for an explanation of sample notation.*

Sample	orig./sub.	K_{max} Dec.	K_{max} Inc.	K_{max} c.s.e.	K_{min} Dec.	K_{min} Inc.	K_{min} c.s.e.	Fabric
2129 G2.2	orig.	177.1	-27.5	-	325.5	-58.2	-	FP
2129 G2.2	sub	165.2	-30.7	10.2	329.9	-57.3	3.2	FP
2129 G1	orig.	151.5	-43.9	-	333.3	-46.1	-	FP
2129 G1	sub	130.8	-48.4	15.6	335	-45.7	6.4	FP
2192 IY	orig.	149.1	-22.8	-	332.5	-67.6	-	FP
2192 IY	sub	152.7	-26.4	5.4	340.1	-62.4	3.5	FP
2192 I2.3	orig.	61.6	-9.2	-	291.3	-74.9	-	FP
2192 I2.3	sub	50.3	-6.8	10.6	298.8	-73.5	2.0	FP
2194 K1	orig.	5.8	-0.7	-	274.5	-74.3	-	FT
2194 K1	sub	70.2	-14.7	9.3	280.9	-73.0	2.4	FP
2194 KY3.2	orig.	135.8	-10.3	-	297.7	-78.8	-	FP
2194 KY3.2	sub	131.1	-9.5	15.8	289.8	-82.9	2.9	FP
2198 M2	orig.	129.9	-3.2	-	14.4	-83.1	-	FT
2198 M2	sub	126.1	-0.6	6.6	33.2	-82.9	2.1	FT
2198 MY	orig.	167.5	-11.2	-	63	-50.7	-	FT
2198 MY	sub	159.4	11.9	7.4	59.7	-48.6	1.3	FT
1909 L2	orig.	326.4	-2.2	-	224.5	-78.2	-	FT
1909 L2	sub	333.1	-3.0	7.0	235.2	-77.8	2.6	FT

parallel and flow transverse grain fabrics exist within the original sediment, but one or the other dominates depending on the scale of the measurement.

Table 8.4: *Angular separation between AMS axes (K_{max} and K_{min}) of original (uncut) sample and the mean of the eight sub-samples cut from each.*

Sample	K_{max} ang. sep.	K_{min} ang. sep.
G2.2	10.9	2.5
G1	15	1.2
IY	4.9	6.0
I2.3	11.4	2.5
K1	65.1	2.2
KY3.2	4.7	4.3
M2	4.6	2.3
MY	24.5	3.0
L2	6.7	5.2

8.5.6 Permeability anisotropy

Maximum and minimum permeability directions in Wells 206/8-8 and 206/13a-2 determined by the magnetic porosity measurements are shown in Figures (8.10; 8.11).

In Well 206/8-8, the maximum permeability is relatively close to the horizontal and well grouped about a NW-SE axis. The minimum permeability directions in this well are nearly vertical. Permeability anisotropy is more variable in Well 206/13a-2. Maximum permeability directions in this well are generally steeper than in Well 206/8-8, dipping at 20^o to 40^o to the horizontal. Azimuthally, the directions fall into two main clusters with NW and SE orientations. These agree reasonably well with the azimuths of principal maximum permeability modes in Well 206/8-8. The plots for both wells also display subsidiary clusters in the NE and SW quadrants. Minimum permeability directions in Well 206/13a-2 are also more variable than Well 206/8-8 and the main cluster of directions is offset from the vertical by about 15^o.

For Well 206/8-8 the mean total and planar permeability anisotropy values, 13.7% and 11.2% respectively, are broadly similar to the corresponding grain fabric magnitudes,

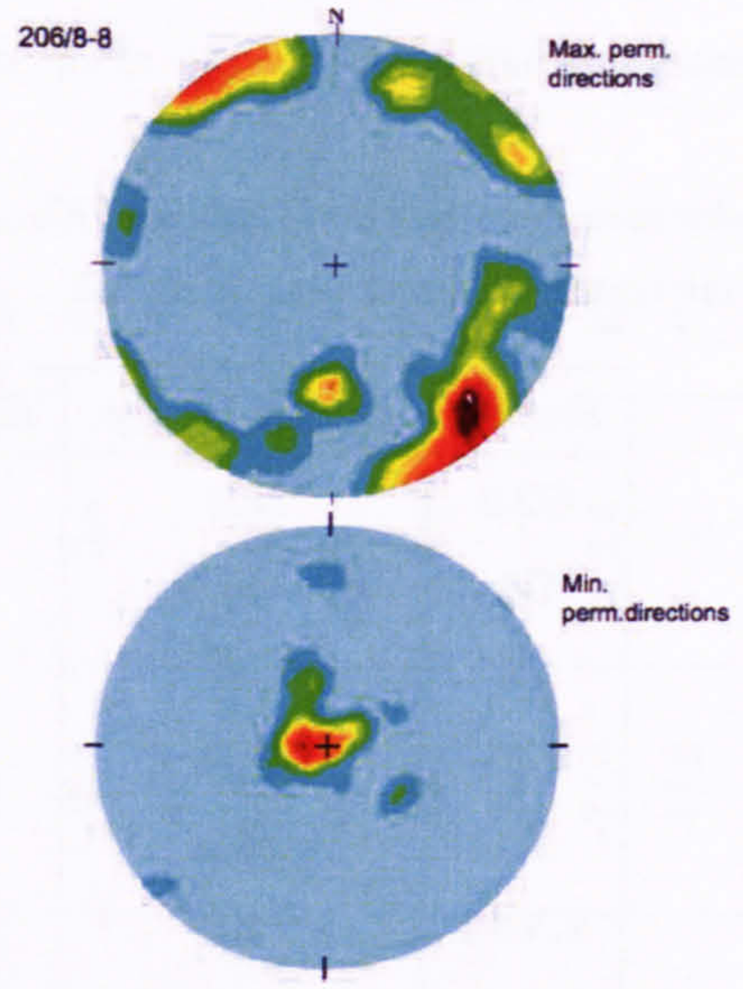

Figure 8.10: *Maximum (red) and minimum (blue) permeability directions in Well 206/8-8 as determined by magnetic porosity analyses.*

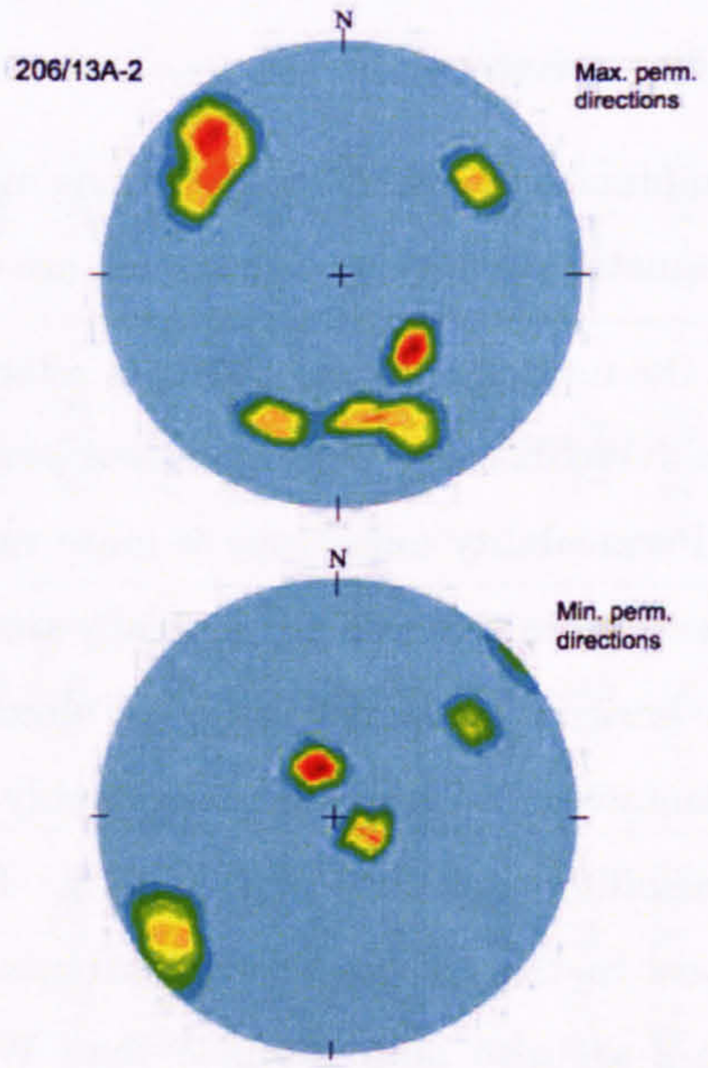

Figure 8.11: *Maximum (red) and minimum (blue) permeability directions in Well 206/13a-2 as determined by magnetic porosity analyses.*

11.1% and 9.6%. The mean azimuthal permeability anisotropy is 7.4%, which is significantly greater than the grain fabric linear anisotropy of 1.0%. This indicates that the strength of the pore fabric parallel to bedding is significantly greater than that of the grain fabric in this Well. This suggests that effective pore shapes tend to be more elongate or better aligned than grain shapes in these sediments.

Although the number of samples measured from Well 206/13a-2 is much smaller than from Well 206/8-8, the degree of permeability anisotropy of these samples is significantly greater with a mean total permeability of 20.8% and azimuthal anisotropy of 10.5%.

8.6 Discussion

The Clair field was first discovered back in 1977 but is as yet undeveloped. Essentially, the Clair reservoir is difficult to produce from for a variety of reasons: as it contains significant sedimentary heterogeneity, a viscous oil, and is heavily fractured (Coney et al. 1993). Hence to facilitate the efficient production of hydrocarbons from the Clair field's complicated reservoir structure requires a detailed knowledge of it's geometry, and architecture. To gain a full understanding of the geometry and architecture of hydrocarbon reservoirs requires a knowledge of the source of the reservoir sand and its dispersal pattern over the depositional area. This information is important for predicting continuity between reservoir sands in different wells and in seeking likely extensions of known reservoir sands into surrounding areas.

The most significant benefit and main reason for conducting palaeomagnetic core orientation was that the results obtained from the ultrasonic analyses and electron microscopy could be directly compared. Moreover, the seismic anisotropy predictions obtained from electron microscopy were also compared to the results obtained from the AVOA analyses and damage parameter tensor inversions.

Furthermore, the results of this study have also provided useful information that could be used to build working models of the Clair field's reservoir. The accuracy and precision of the high quality data allows the transport direction and dispersal pattern of the reservoir sands to be predicted. This suggests that more-detailed grain-fabric analyses could be used to distinguish individual flow units which are not apparent from visual observation. Moreover, studies of the natural and enhanced AMS of these sediments are both well defined with the majority of the samples characterised by depositional rather

than deformational style fabrics. This suggests that any fracturing that is prevalent throughout the Clair reservoir (which is shown to be the case from independent studies of seismic data and well log data) is on a larger scale than that of the samples studied. Likewise, pore fabric studies have shown that the maximum natural connectivity between units is within the horizontal plane with grains aligning with their long axes parallel to bedding. This is based upon the assumption that there exists a direct relationship between maximum permeability, grain shape and magnetic susceptibility. There is mounting evidence to suggest that a relatively simple relationship does exist between: permeability anisotropy, grain-shape orientation and magnetic susceptibility (Hamilton & Rees 1970, Hailwood & Ding 2000). Therefore, under this assumption it is possible that this information could be used to determine the most suitable well location. For example, maximum permeability is determined as being relatively close to the horizontal about a NW-SE axis whereas minimum permeability is shown to be near vertical. Moreover, large scale faulting is aligned NE-SW as determined from field wide seismic surveys and from field structural wide interpretation.

The azimuthal anisotropy has been shown to be only very slight approximately 1-3% where as the total anisotropy (difference between vertical and horizontal) ranges quite considerably from c.5-30%. These results are in broad agreement with those determined by EBSD and acoustic velocity measurements. It is unfortunately not possible to make a direct comparison between the results obtained from enhanced and natural AMS analyses with the individual mineral phase crystallographic pole figures because of the complexity and subtlety of the crystallographic pole figure patterns. It is, however, possible to compare the results obtained from the individual mineral phase seismic pole figures with the natural and enhanced AMS analyses. It is important to remember that when making a direct comparison between the two different techniques that the results of AMS are plotted in the upper-hemisphere whilst EBSD is conventionally plotted in the lower-hemisphere. The most reliable AMS results are those obtained from the class one samples, that is, with a standard deviation of less than 15^0. The results obtained from the class one samples from the natural and enhanced AMS analyses from well 206/8-8 and to a lesser degree 206/13-a2 (less sampling has possibly skewed the results) illustrate the predominant NW-SE orientation of the long-axis of the constituent grains. Whilst, no finite directional information can be extracted from the AMS analyses (i.e., it could possibly be a difference of 180^0) the orientation of the long-axes of the constituent

mineral grains are in agreement with the orientation of the maximum velocity of both the quartz and feldspar seismic velocity pole figures. Under the basic assumption that the long-axis of both the quartz and feldspar single crystals represent the maximum velocity (which is broadly true) it is evident then that both SPO and LPO are not only linked but coincident. This then leads to the conclusion that EBSD could be used to provide directional palaeoflow information or as a check for AMS analyses. Nonetheless, the assumption that the long-axis of the crystal represents the fastest direction is an oversimplification and indeed a further relationship may exist which is not immediately apparent using the pole figure plotting program used in this project.

Concerns regarding the reliability and accuracy of palaeomagnetic and magnetic susceptibility analyses are considered to be a problem whereby the data population is not sufficient enough to provide a detailed assessment of the magnetics of a sample. Furthermore, potential problems might include, compaction shallowing, and thermal overprinting. Errors may also include natural variations of the magnetisation directions at the scale of the sample. Under normal circumstances it is not possible to distinguish between the dispersion produced by natural directional variations of magnetisation and the dispersion due to experimental errors (Bohnel & Schnepp 1999). Sager & Singleton (1989) conducted a palaeomagnetic study of sediments in combination with a high resolution seismic survey in the Gulf of Mexico. It was observed from the seismic data that the samples extracted were from sites where the tilt due to diapiric uplift was about eight degrees. However, after structural corrections were made to the cored samples only six agreed with the geocentric axial dipole for the site whilst four showed significantly lower inclinations. It was suggested that the anomalous results could be because of sub-aerial exposure during a sea level low stand.

Detailed information regarding individual data population of production models is of great importance in accurately predicting fluid flow properties and individual well production rates. Information obtained from well logs has the benefit of providing scaleable data but unfortunately cannot provide information on a reservoirs depositional and dispersal pattern in *3D*. This study has shown that not only have the reservoir sands travelled from the NW to the SE but they have also travelled with their long axes in flow parallel (see Figure 8.4 for an illustration). The approximately horizontal orientation of the K_{max} axes and the vertically oriented K_{min} axes of the class 1 orientation data obtained from the natural and enhanced AMS analyses confirms that the fabrics

of these sediments have not been disrupted significantly by post depositional processes (Figure 8.6).

8.7 Conclusions

Compressional and shear-wave velocity anisotropy measurements have been conducted on a wide range of samples extracted from the Clair field, N.W. Scotland. The sample's microstructure and mineralogical composition have previously been established (Chapter 5 and Chapter 3). To be able to fully interpret the data obtained from the cores, such as, fracture directions and anisotropy orientations it is first necessary to restore the core pieces into their original *in situ* position with respect to North and vertical. The basic assumption is that almost all rocks contain one or more components of magnetisation which were aligned with the geomagnetic field at the time of deposition. These then provide a record of the direction of geographic North either in recent times of at the time of formation.

Palaeomagnetic core orientation has proven to be an useful and relatively successful technique in defining the direction of geographic North throughout all the samples analysed. Furthermore of those samples analysed each core orientation was assigned a reliability class from 1 (best) to 3 (poor). 64% of the samples analysed fell into class 1, 14% into class 2, and the remaining 22% into class 3. The palaeomagnetic core orientation can be thought of as being successful when considering that on average 64% of the orientation data had a circular error of less than or equal to 15^0. It was, unfortunately, not possible to conduct an independent study which analysed the reliability and accuracy of the palaeomagnetic orientations because of a shortage of suitable material.

It was determined from AMS analyses that in general K_{max} and K_{min} lay within 35^o of the horizontal and vertical respectively. This in turn means that the fabrics of the sediments deposited within the Clair field have not been disturbed significantly post-deposition. Furthermore, it has been shown that the mean sediment transportation direction is towards the SSE which is in accordance with independent studies of sediment pathway dispersal patterns at Clair.

Total grain anisotropy, that is, the difference between the vertical and horizontal throughout all the samples studied ranged from *c.*5−30% with a weighted mean of approximately 11%. Azimuthal anisotropy, the variation between the maximum and minimum orienta-

tions within the bedding plane, was significantly weaker than total anisotropy, ranging from $c.1 - 3\%$.

Enhanced AMS measurements were conducted to investigate the scale dependence of the samples but their was not sufficient evidence to suggest that the samples exhibited any scale-dependence. All but two of the samples analysed showed that their was no indication of a scale dependence. In the two samples which demonstrated a significant difference between the parent and daughter specimens the percentage anisotropy and bulk magnetic susceptibility were no weaker than any of the other samples. Hence, the observed difference of these samples is thought to be because the sample exhibits a flow transverse grain fabric and a flow parallel grain fabric but at different scales.

Permeability anisotropy analyses provides a qualitative assessment of the orientation of the maximum and minimum permeability directions. It is important to note that permeability anisotropy does not provide a quantitative assessment of the magnitude and orientation of the maximum and minimum permeability directions. It was determined in Well 206/8-8 that the maximum relative permeability was close to the horizontal and aligned about a NW-SE axis with the minimum permeability approximately vertical. The mean azimuthal anisotropy for Well 206/8-8 was significantly greater than that of the grain fabric anisotropy which suggests that the effective pore shapes tend to be more elongate or better aligned than the grain shapes in the Clair rocks. The data population for Well 206/13a-2 is sparse, however it can be deduced that the maximum permeability anisotropy was at about $20 - 30^{o}$ to the horizontal with the minimum permeability grouped into two clusters.

Chapter 9

Synthesis

9.1 Introduction

Seismic data is often used by the petroleum industry in an attempt to extract information and estimate uncertainty regarding the lithology and fluid distribution in the subsurface (Strandness 1991, Blangy 1992). Understanding the interaction between the various parameters that control rock properties is crucial to better interpretation of seismic data. In particular, to fully utilise seismic data it is vital to have a complete understanding of what seismic waves can reveal about the parameters that control *in situ* intrinsic and extrinsic rock properties. Technological developments, such as, *4D* seismic profiling, increasingly sophisticated migration algorithms, and a proliferation of computational processing power mean that it is now possible to measure, amongst other attributes, seismic anisotropy of reservoir rocks in the sub-surface (Helbig & Thomsen 2005). Seismic anisotropy in sedimentary rocks arises from the partial alignment of anisotropic minerals, fractures, bedding planes and heterogeneities on a length scale smaller than the seismic wavelength (Crampin 1981, Babuska & Cara 1991, Sayers 1994, Mainprice et al. 2000, Wendt et al. 2003, Kendall et al. 2006, Valcke et al. 2006). Therefore, observations of seismic anisotropy in the sub-surface could potentially be used to determine rock and fluid properties prior to drilling (Sayers 2002*a*, Kendall et al. 2006). However, for a more detailed interpretation of measures of anisotropy from field seismic data more quantitative information is required on the relative importance of the various factors thought to contribute to anisotropy.

Traditionally, acoustic laboratory measurements of velocity have been utilised to pro-

vide important information on bulk aggregate rock properties but they do not allow the discrimination of the various microstructural controls on anisotropy, such as, lattice preferred orientation, the non-random spatial distribution of mineral phases, aligned porosity, and fractures (Crampin 1981, Babuska & Cara 1991, Mainprice et al. 2000, Wendt et al. 2003, Kendall et al. 2006). The authors research presented in this thesis combined the results of a variety of different analytical and computational techniques to fully understand the extrinsic and intrinsic controls of seismic-wave velocity anisotropy of siliciclastic hydrocarbon reservoir rocks. The experimental techniques employed included: electron microscopy (SEM-EBSD), quantitative X-ray diffraction (QXRD), palaeomagnetism and ultrasonic velocity analysis. A break down of the individual sample analysis is presented in Appendices (C.1 and C.2). The results of the experimental techniques were then integrated by both the present author and research associates to provide a more complete understanding of the controls on seismic anisotropy. The present author conducted the petrofabric,and ultrasonic analysis whilst Dr Andrew Carter interpreted the field seismic data and Dr James Wookey, Dr Stephen Hall and Prof Michael Kendall conducted the reservoir modelling. The pre-processed sample data is contained within Appendices (Q and R). In particular, geomathematical models, which included, among others: crack density tensor inversion, Bingham distribution modelling, empirical relations, and upscaling techniques have been used to identify the key controls on seismic anisotropy of a suite of reservoir rocks from the Clair field.

Presented within this Chapter is a brief overview of the various analytical and computational techniques used in the determination of the controls of seismic anisotropy. Furthermore, this chapter also presents an analysis of the controls of seismic anisotropy and some potential uses of seismic anisotropy.

9.2 Methodologies

9.2.1 Petrophysical properties

Accurately predicting the petrophysical properties of a rock aggregate requires a quantitative description of the complex microstructure of the medium (e.g., Budiansky 1965, Brevik 1995, Castañeda & Willis 1995). Petrofabric analysis using SEM-EBSD has provided the means with which to fully characterise the strength of elastic anisotropy created by the orientation of minerals within a suite of siliciclastic hydrocarbon reservoir rocks.

A bulk aggregate elastic tensor is calculated for every sample analysed by EBSD; this is considered to represent the intrinsic anisotropy (i.e., matrix) of a specific siliciclastic reservoir specimen. The bulk aggregate elastic tensor is based upon the results of the EBSD analysis of fabric intensity, QXRD analysis of modal proportions, porosity analysis, and a Voigt-Reuss-Hill average (Voigt 1928, Reuss 1929, Hill 1952). The Voigt-Reuss-Hill average is used to estimate the effective elastic moduli of a rock in terms of it's constituents and pore space. Where LPO is the sole microstructural feature under investigation the Voigt and Reuss averaging schemes are the most suitable in which upper and lower bounds are placed on material properties by taking weighted arithmetic and harmonic means respectively of the single crystal elastic stiffness tensors of each constituent phase. The elastic constants of the polycrystalline aggregate obtained from the averaging procedure of Hill (1952) are then used to calculate the seismic anisotropy attributed to the LPO of constituent mineral phases by solving the Christoffel equation (Christoffel 1910).

9.2.2 Ultrasonic analysis

The theoretical calculation of the degree of of seismic anisotropy resulting from the LPO if mineral phases alone (Voigt 1928, Reuss 1929, Hill 1952, Budiansky 1965, Brevik 1995, Castañeda & Willis 1995) ignores other causes of elastic anisotropy, (e.g., the contribution from aligned grain boundaries are more difficult to model). As shown previously it is possible to theoretically calculate the amount of seismic anisotropy resulting from the LPO of mineral phases alone (Voigt 1928, Reuss 1929, Hill 1952, Budiansky 1965, Brevik 1995, Castañeda & Willis 1995) ignores other causes of elastic anisotropy (e.g., the contribution from aligned grain boundaries are more difficult to model). Laboratory measurements are therefore required to provide a comprehensive understanding of the controls of seismic anisotropy of rock aggregates (Kaarsberg 1959, Birch 1960, Tosaya & Nur 1982, Vernik & Nur 1992*b*). Compressional and shear-wave velocity anisotropy measurements were conducted on a suite of samples obtained from the Clair field, N.W. Scotland whose microstructure and mineralogical composition have been rigorously established. Compressional and shear-wave ultrasonic velocity measurements were conducted by the present author at the University of Manchester upon a suite of samples obtained from a siliciclastic reservoir. An extensive investigation of laboratory ultrasonic analyses was carried out under dry conditions at both atmospheric and elevated confin-

ing pressures (Birch 1960). Unfortunately, the interpretation of laboratory data in terms of the causes of anisotropy is often non-unique (Jizba 1991). It is therefore important to integrate laboratory measurements with the complete quantitative microstructural analyses (Louis et al. 2005, Valcke et al. 2006).

9.2.3 Palaeomagnetics

To enable direct comparisons between the various analytical techniques used in this study and with independent studies of anisotropy the core samples were oriented using palaeomagnetic techniques (Hailwood & Ding 1995, Hailwood 2004). The laboratory analyses were conducted by Dr. Ernie Hailwood at Core Magnetics but the interpretation and data representation was conducted by the present author. The primary component magnetisation is acquired at the time of deposition (assuming the rock does not undergo significant re-working prior to lithification), and provides a record of palaeo-North. The palaeomagnetic analysis of the core samples also provides useful information regarding sand transport directions and can help place important constraints on the positions of sand input points in sedimentary basins thus facilitating prediction of sand distribution and the geometry and direction of elongation of sand bodies (Hailwood & Ding 2000).

9.2.4 Damage tensor inversion

Rocks contain one or more feature that can cause seismic anisotropy. It is therefore difficult to quantitatively determine the impact of an individual feature on seismic anisotropy. Hence, determining a method that allows the differentiation and quantification of the variables controlling extrinsic and intrinsic seismic anisotropy would provide useful information for better interpretation of observations of seismic anisotropy (Sayers & Kachanov 1991, Sayers 2002*b*).

The presence of fractures, cracks, microcracks, and microporosity greatly affects the velocity of elastic waves in rocks (Sayers 1994). It is well known that rocks containing non-randomly oriented cracks or which have a strong grain shape fabric are commonly elastically anisotropic (Sayers & Kachanov 1995). It has to also be considered that similar observations of the sensitivity of elastic wave velocities to stress could be as a consequence of grain boundaries and the soft interparticle constituents of phyllosilicates (Sayers 2005). Studies that consider the extrinsic and intrinsic controls of seismic anisotropy on sedimentary rocks are rather rare with some recent exceptions (Louis et al.

2003, Han et al. 2004, Louis et al. 2005, Valcke et al. 2006). The present author gathered and interpreted all the data whilst Dr Stephen Hall wrote the computer programs and inverted the data (Hall et al. 2007). The theoretical framework, however, for considering multiple causes of anisotropy and in particular cracks and fractures in an anisotropic matrix have long been established (Sayers & Kachanov 1991). The main objective was to distinguish the intrinsic (LPO) from the extrinsic (SPO) effects and thus quantitatively describe the grain-boubdary architecture. The methodology used is based upon the approach of Sayers (2002*b*) but with added extensions to utilise multi-axis velocity measurements and a known matrix anisotropy (Hall et al. 2007).

9.2.5 Seismic anisotropy forward model

To circumvent the problems associated with EBSD analysis the microfabric and ultrasonic velocity data gathered during this study were provided to Prof Michael Kendall who created a geomathematical model to calculate the bulk aggregate elastic tensor from a given set of modal proportions as determined by either QXRD or well-log data (Kendall et al. 2006). The model was based upon a simple assumption that the strength of alignment of constituent mineral grains in each sample did not vary systematically throughout the reservoir. Therefore, a simple average of the single mineral phase elastic tensors were used as an input into a forward modelling program to calculate the bulk aggregate tensor. The program was designed to calculate the effective elastic constants of a rock comprised of quartz, feldspar, calcite/dolomite, micas (muscovite, biotite, and chlorite), clays (kaolinite and illite) and pores. The quartz, feldspar, and calcite elastic tensors were determined by EBSD analyses. The mica elastic tensors were determined based upon an average of the Bingham model, EBSD, and image analysis. The fine-grained clay components were assumed to have an isotropic distribution. Pores were also assumed to be isotropically distributed and spherical.

9.3 Results

9.3.1 Petrophysical Properties

The results from this study confirm that undeformed siliciclastic hydrocarbon reservoir rocks can exhibit a substantial intrinsic seismic anisotropy due to the lattice preferred orientation of constituent mineral phases. In particular, calculations show that

compressional-wave seismic anisotropy due to LPO effects vary from c.3.1% for quartz-rich, clean sandstones to c.14.0% for mudstones. The same calculations show that shear-wave anisotropy due to LPO effects vary from c2.3% for quartz-rich, clean sandstones to c.13.6% for mudstones. The styles of symmetry observed within the seismic anisotropy calculations are strongly controlled by the constituent mineral phases. Samples that are rich in quartz and feldspar generally possess an orthorhombic style of symmetry. Whereas, those rich in clays and micas (> 15%) tend to have a very strong VTI style of symmetry. This is a significant step beyond the achievements of previous similar projects (e.g., Han 1986, Eberhart-Phillips 1989, Jizba 1991, Strandness 1991, Blangy 1992) which have not investigated the mineral controls of anisotropy in sandstones. With the exception of Hornby (1998) very few studies have attempted to determined the link between anisotropy and LPO.

9.3.2 Ultrasonic analysis

The conclusions determined from the atmospheric ultrasonic analysis provide a detailed understanding of the azimuthal variation in velocity and anisotropy with respect to lithology. Investigation of the bulk aggregate seismic anisotropy pole figure plots shows that no azimuthal variation in velocity is expected for samples which contain in excess of c.15% phyllosilicates. On the other hand, investigation of the bulk aggregate seismic anisotropy pole figure plots also shows that samples which are quartz or feldspar rich are expected to show some azimuthal variation in velocity due to mineral grain alignment and hence grain boundary or micro-porosity alignment. The results of the atmospheric pressure ultrasonic analysis are in agreement with the high-pressure analysis, i.e., the style and relative magnitude of degree of seismic anisotropy is similar.

9.3.3 Palaeomagnetics

AMS analyses suggested that in general K_{max} and K_{min} lay within 35° of the horizontal and vertical respectively. This in turn means that the fabrics of the sediments deposited within the Clair field have not been disturbed significantly post-deposition. Broadly, a significantly higher and more inconsistent angle of orientation is observed for K_{max} in sedimentary environments which have undergone tectonic reworking. Total grain anisotropy, that is, the difference between the vertical and horizontal throughout all the samples studied ranged from $c.5 - 30\%$ with a weighted mean of approximately

11%. Azimuthal anisotropy, i.e., the strength of alignment of pore space within the bedding plane, (the variation between the maximum and minimum orientations within the bedding plane) was significantly weaker than total anisotropy, ranging from *c.*1−3%. The mean azimuthal anisotropy for Well 206/8-8 was significantly greater than that of the grain fabric anisotropy which suggests that the effective pore shapes tend to be more elongate or better aligned than the grain shapes in the Clair rocks. Whilst it has not been possible in this study to utilise pore shape data (VRH does not take such information into consideration) it could in future studies of this nature be incorporated into more complicated models and used as a direction of investigation.

9.3.4 Damage tensor inversion

The results of the data inversion by Dr Stephen Hall show that the extrinsic crack-induced anisotropy is strong relative to that of the intrinsic anisotropy (i.e., LPO effects). In general, the predominant crack-set in the samples studied was aligned parallel to the depositional fabric. In other words, samples generally contained a much larger horizontal crack density than vertical. It was, however, observed that the LPO and extrinsic anisotropies appear in general to align, indicating that they are very probably linked in some way. It is likely that the cracks are related to the grain boundary contacts which are aligned with the grains which are coincident with the LPO measurements. Furthermore, it was also determined that vertical cracks had little or no preferential alignment. This, however, is in contradiction to both previous field studies of seismic anisotropy (Coney et al. 1993, Smith & Lappin 1997) and the AVOA analyses suggesting that cracks or fractures exist on a larger scale than that of the ultrasonics. The presented results have provided an understanding of the crack distribution within the samples, which essentially relates to the architecture of the compliant grain contacts. Thus, from such results it is possible to determine the nature and significance of depositional features versus damage. In general, any azimuthal anisotropy observed *in situ* (using azimuthal amplitude/travel time or shear-wave splitting analyses) would most likely be due to damage, e.g., vertical fracturing (but as such damage is larger than the scale of this particular part of the study it is not assessed in detail here).

9.4 Controls of seismic anisotropy

Integration of petrofabric analysis with ultrasonic measurements has shown that the overall anisotropy of the samples is composed of both intrinsic and extrinsic components. The intrinsic components are the lattice preferred orientation of mineral phases, and the non-random orientation of grains. The extrinsic components of anisotropy are cracks, fracturing, and preferentially aligned porosity. Observations of seismic anisotropy by ultrasonic analysis are largely controlled by cracks and fractures with minor contributions from the affects of SPO and LPO. Whereas, calculations of anisotropy using EBSD only take LPO into consideration. Moreover, observations of porefabric anisotropy by anisotropic magnetic susceptibility (AMS) are broadly controlled by the alignment of pore space. Consequently, by taking the results of these different experimental techniques into consideration it is possible to derive a basic understanding of the controls of seismic anisotropy of siliciclastic reservoir rocks.

Examination of both the experimental and analytical results obtained from this study suggest that the principal intrinsic control of seismic anisotropy of siliciclastics is the partial alignment of highly anisotropic mineral grains, such as, phyllosilicates. However, the contribution LPO has towards bulk aggregate observations of seismic anisotropy is regarded as minor when compared to the effect of the alignment of cracks (i.e., grain boundaries and layer parallel cracks). Assuming the previous is true here it is postulated that even for highly phyllosilicate rich lithologies, such as, shales that LPO is still subordinate to the effect of fractures and cracks. For example, the maximum calculated anisotropy as a result of the LPO of mineral phases alone in this study was 14% P-wave anisotropy (Sample 1841m) for a phyllosilicate rich sample. In comparison, the maximum observed ultrasonic P-wave velocity anisotropy in the same phyllosilicate rich rock was approximately 70% at room temperature and pressure (Sample 1841m). Nonetheless, at approximately *in situ* pressures there still exists a significantly higher level of anisotropy. Therefore, it is likely that the significant difference between the two measurements of anisotropy is either due to the effects of grain boundaries or cracks. Seismic anisotropy due to mineral grain alignment alone, however, at *in situ* reservoir conditions could account for the degree of seismic anisotropy observed in field wide studies. It is also possible that the majority of the cracks and micro-fractures contained within the samples are as a result of uplift and that even after they have been returned to approximately *in situ* pressures that there still exists a high level of residual cracking that was not present in

reservoir. Moreover, at room temperature and pressure many shales do not contain any cracks and therefore any elastic anisotropy is assumed to be controlled by the fabric. For example, shear-wave splitting at the Valhall field is calculated to be approximately 1% and is thought to be related to dilation of grain boundaries. Whereas, non-hyperbolic moveout at the Valhall field records much higher levels of anisotropy which is believed to be related to the dominant horizontal fabric of the shale sequence. Analysis of the effects grain boundaries have on seismic anisotropy by crack density tensor inversion (i.e., inversion for the compliance matrix) by Dr Stephen Hall suggests that layer parallel (i.e., depositional bedding) cracks and fractures and not grain boundaries are the most predominant mechanism contributing to the observations of bulk aggregate anisotropy. However, in general the affects of grain boundaries on observations of seismic anisotropy may be significantly different in rocks which contain a stronger SPO.

It has become clear from the data obtained during this study that the intrinsic controls of elastic anisotropy (e.g., LPO and SPO) at the hand-specimen scale are subordinate when compared to the extrinsic controls of seismic anisotropy (e.g., layer parallel cracks and fractures) in siliciclastic rocks. The affects of vertically and sub-vertically aligned sets of cracks and fractures on seismic anisotropy on the scale of a seismic wavelength have not been fully investigated in this study which could provide more useful information in the better interpretation of field wide seismic surveys.

9.4.1 Upscaling

Petrofabric analysis was conducted upon cm scale samples. These cm scale samples are obviously not representative of the entire well section. The sampling strategy employed, however, for the EBSD analysis should have helped mitigate the issue concerning scale to some extent by only analysing samples that were extracted parallel to the long-axis of the core, thus interscting a variety of layers. Moreover, in a further attempt to help overcome the issue of scale, simple averages of several of the sample's intrinsic elastic tensors were used as inputs into the larger scale AVOA and non-hyperbolic moveout models.

The issue regarding the various scales of investigation with this project are difficult to overcome without producing a complex, multi-paramter self-consistent model. EBSD investigates intrinsic anisotropic properties on an individual grain-scale (nm's to mm's) whereas ultrasonic velocity measurements investigate intrinsic and extrinsic anisotropic

properties on a larger scale (mm's to cm's). It is not apparent that the properties identified by the ultrasonic investigation would be acknowledged as a mechanism causing anisotropy at the larger (seismics) or smaller scale (EBSD). The smaller scale intrinsic anisotropy causing properties would only show up as an average effect at the larger scale (ultrasonics and seismics). In fact, it is very likely that grain-scale properties are entirely over shadowed by those on the larger scale, such as, cracks and micro-porosity. Without building a completely integrated model which takes into account all the various seismic anisotropy controlling variables it will be difficult to definitively say which variables are the most dominant in the subsurface.

9.5 Application of results

9.5.1 Overview

This project has developed a framework for interpreting anisotropy on various length scales: crystal (LPO), intergrain (SPO), and fracture or bedding scale (seismics)(Hall et al. 2007, Kendall et al. 2006). These interpretations have only been made possible due to the high-quality of mineral orientation distribution and ultrasonic velocity measurements collected during this PhD study. A break down of the individual sample analysis is presented in Appendices (C.1 and C.2). The pre-processed sample data is contained within Appendices (Q and R).

9.5.2 Predictions of the symmetry of seismic anisotropy

Using the simple geomathematical model outlined previously it can be seen that the various horizons within the reservoir have a distinctly more VTI style of symmetry towards the top of the reservoir, near the overburden and a weaker more HTI style of symmetry (HTI has the same the symmetry properties as VTI except that it has been rotated ninety degrees about either of the horizontal axes, it can be thought of as a single vertical alignment of fracturing, cracks or micro-discontinuity) towards the bottom within the main reservoir unit. Acoustic wave velocity analysis, petrofabric analysis and field wide seismic analysis (conducted by Dr Andrew Carter) all broadly agree, in that, they all predict a VTI style of symmetry near the top of the wells with high expected P- and S-wave anisotropy. Whilst deeper down they all predict a more orthorhombic style of symmetry and significantly less P- and S-wave anisotropy. Even though the studies

investigate varying length scales they all appear to broadly agree in magnitude and style of symmetry of the observed anisotropy.

9.5.3 Indicators of reservoir quality

It has been demonstrated that rocks which contain in excess of 15% layer-parallel phyllosilicates have a very strong VTI style of symmetry associated with the preferential alignment of platy minerals. Therefore, non-hyperbolic moveout detected on P-wave reflectivity data may indicate the presence of a medium that has a VTI style of symmetry (Alkhalifah & Thomsen 1994, Alkhalifah 1997). Hence this could be as a result of the lithology possessing a significant proportion of clays or micas (e.g., shale or mudstone). Moreover, in areas which have very little to no seismic anisotropy detectable via non-hyperbolic moveout on P-wave reflectivity data it is highly likely that the unit is a clean, probably relatively randomly fractured sandstone. Consequently, seismic technology (e.g., non-hyperbolic moveout) could be used as an indication of reservoir quality. Previously, non-hyperbolic moveout has been used to distinguish sand from shale (e.g., Alkhalifah & Thomsen 1994, Alkhalifah 1997). This study, however, has suggested that it might also be possible to distinguish sands with varying clay locations and modal propoortions.

9.5.4 Palaeoflow indicators

The consistent dip and azimuth of the feldspar and quartz velocity and anisotropy maxima strongly supports the idea that seismic anisotropy could act as an indicator of palaeoflow direction in areas which contain little to no fracturing. The alignment identified from the results of the EBSD analysis seismic anisotropy predictions are in broad agreement with the anisotropic magnetic susceptibility analyses which were conducted independently (Hailwood 2004). Therefore, independent studies of the Clair field's reservoir palaeoflow direction concur that the depositional sands flowed from the NW towards the SE (Smith & Lappin 1997, Allen & Mange-Rajetzky 1992, Coney et al. 1993). These results are consistent with the work of Hamilton & Rees (1970) and Valcke et al. (2006). It should be noted that the anisotropy resulting from the palaeoflow direction would become swamped by fracture-induced anisotropy in areas containing slight to moderate densities of horizontal or vertical fractures. Moreover, the palaeoflow results obtained from this study are not necessarily representative of all siliciclastic hydrocarbon reser-

voirs for two reasons. First, the predominant depositional dispersal pattern for the Clair field was from the NW. Second, in general, throughout all the analysed samples constituent mineral grains showed parallel grain long axes alignment. For example, if their were to be multiple depositional dispersal patterns as in the Central Graben of the North Sea it could very quickly and easily complicate the observed patterns whether the grains were in traction or fluid shear. Nonetheless, in this study the maxima of anisotropy and velocity of the main constituent minerals have aligned in a constructive fashion and have agreed well with studies into AMS which were conducted independently.

9.5.5 Well position optimisation

The drilling of wells and production of hydrocarbons lead to changes in the stresses acting on the reservoir and surrounding rocks. These changes in stress may lead to such problems as well-bore instability, loss of permeability, reservoir compaction and surface subsidence (Caley et al. 2001). Elastic wave velocities in sandstones vary with stress due to the presence of discontinuities such as grain boundaries, micro-cracks and large scale fractures (Sayers & Kachanov 1991). The results of this investigation provide useful information on the significance of depositional features and damage properties. However, the nature of the damage parameters do not necessarily represent those features that would exist *in situ* because some, if not all, of those observed patterns may be as a result of core extraction and preparation. The samples, in general, show greatest pressure sensitivity with the micro-cracks that are aligned parallel to bedding (horizontally). This, however, is likely to be due to core damage on extraction and preparation and should be ignored. It is likely, therefore, that any azimuthal anisotropy observed within these rocks at depth would be due to the preferential alignment of fractures and would not be observed in the scale of this study. To be able to identify the anisotropies and potential changes with reservoir pressure would require analysis of nonhyperbolic moveout since the predominant crack set is layer parallel (Figure 9.1)(Alkhalifah & Thomsen 1994). The Clair field reservoir has deviatoric stresses (Smith & Lappin 1997) and therefore the response of the samples to loading could be significantly different to that identified in this study. However, below the damage threshold (i.e., below the threshold where applied stresses result in permanent damage to the rocks microstructure) it is possible that the observed trends could act as guidelines for identifying pressure sensitive zones. Conversely, by monitoring the changes in elastic wave velocities it may be possible to

monitor changes in the stress caused by drilling and production (Caley et al. 2001). This could lead to an optimised well position in highly stress sensitive units within producing reservoirs (Sayers & Kachanov 1995).

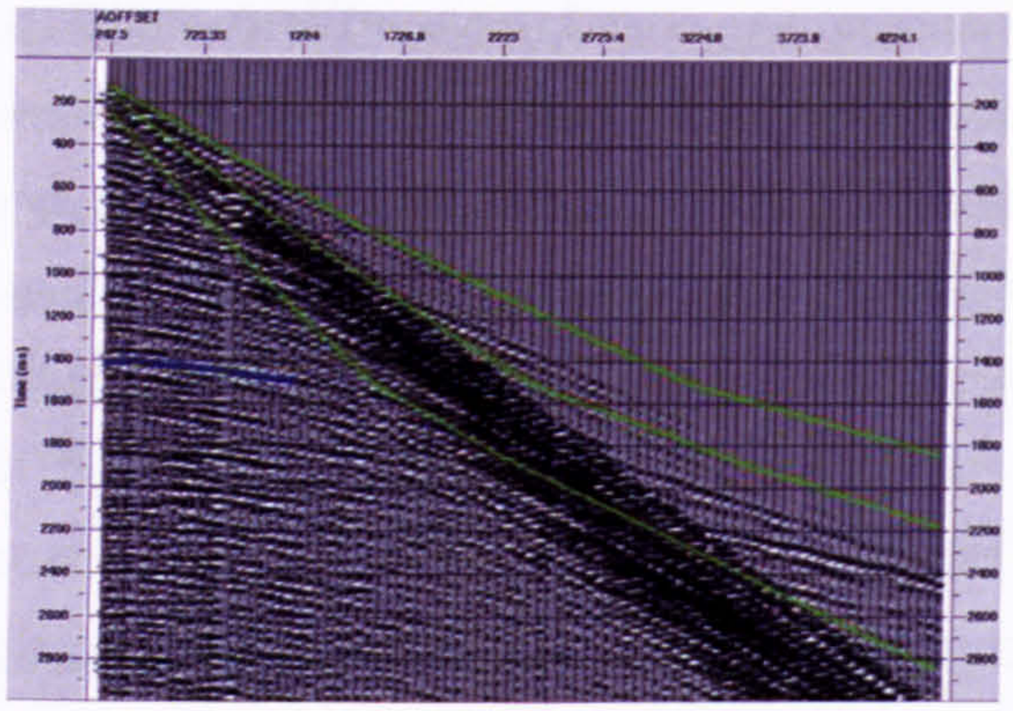

Figure 9.1: *An example of nonhyperbolic moveout inversion. X-axis - Two-way-time increases with depth. Y-axis - Offset from source in metres.*

9.5.6 Case Study: AVOA analysis of the Clair field, N.W. Scotland

In the presence of azimuthal anisotropy the velocity of the media bounding an interface will have an azimuthal dependence and therefore the amplitude of waves reflected from such an interface will vary with the angle of incidence and also with azimuth (Hall et al. 2002). AVOA (amplitude variation with offset and azimuth) analysis is now a commonly used tool in oil and gas exploration used to characterise fractures in the subsurface (Hall et al. 2002, Hall & Kendall 2003). AVOA analysis provides insight on the properties local to a reflector and therefore has the advantage of greater vertical resolution than analyses of shear-wave splitting (Hall & Kendall 2003). AVOA analysis has successfully been interpreted in terms of fracturing at the Valhall field where it showed spatial variability and variation in magnitude and good correlation with independent studies of fracture orientation (Hall et al. 2002).

Amplitude variation with offset (AVO) analysis has for a long time been recognised as a useful indicator of lithology and pore fluid. Figure (9.2c) shows the standard 2D AVO methodology, where the amplitude of a reflected wave varies as a function of incidence angle. In the presence of azimuthal anisotropy (Figure 9.2b), the velocity of the media bounding the interface will have an azimuthal depenedence and therefore the amplitude

of the waves reflected from this interface will vary with both angle of incidence and azimuth (Figure 9.2d). Thus azimuthal anisotropy may be characterised using amplitude variation with offset and azimuth.

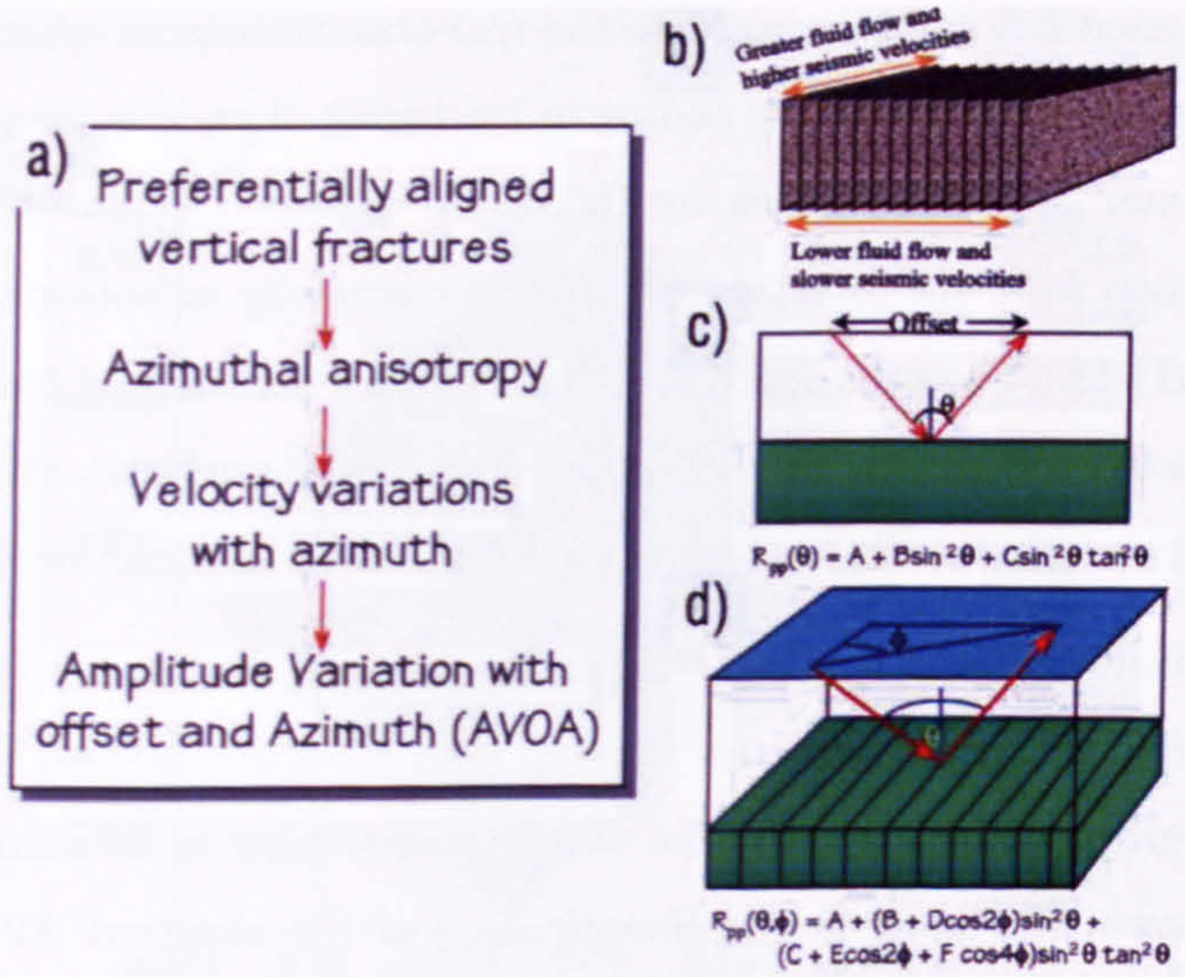

Figure 9.2: *a-b) The influence of aligned fractures on the elasticity and reflectivity of a medium. c) Standard offset-dependent reflectivity and AVO equation. d) Extension of the AVO methodology and equation to determine AVOA.*

SEM-EBSD analyses conducted by the present author on a limited number of samples have been provided to Dr James Wookey who used the SALAMI code to calculate the expected elastic anisotropy of various discrete horizons within the Clair field reservoir. As those calculated elastic stiffness tensors are for a particular specimen an average of several of them is required to calculate what would represent a seismically observable unit (several ten's of metres). Hence, the intrinsic elastic stiffness tensors, as determined by EBSD analysis, are then averaged over what is seismically observable horizons to derive elastic stiffness tensors representative of a unit. The elastic stiffness of the background matrix for Units IV and V are calculated by performing a VRH average of the relevant suite of elastic stiffness tensors (determined by EBSD analysis). Using the data obtained from the palaeomagnetics it was possible to orient all the elastic stiffness tensors into a geographic reference frame before calculating the VRH average. Unit V is relatively homogeneous as it is part of the main reservoir section whereas Unit IV is heterogeneous. This means that to calculate a general elastic stiffness tensor for Unit IV

would require many more samples which covered the entire range of lithologies encountered. An expected AVOA response is then calculated using the appropriate average of tensors for the specific unit of investigation. This then allows expected AVOA responses to be modeled and compared to the real observations based upon the quantification of the background matrix by adding in fracturing of various magnitudes (Hall 2000). The program, SALAMI written by Dr James Wookey, calculates the AVOA response of a reflection from the interface between two generally anisotropic layers. It uses the code RMATRIX (Thomsen 1998) to calculate the reflection and transmission coefficients between two sets of C_{ijs} (as determined from EBSD analysis), and can calculate the AVOA response for either an idealised or realistic survey acquisition geometry.

To illustrate the point Top Unit V will be used as an example. Figure (9.3) shows the observed AVOA response for the Top Unit V horizon around Well 206/8-8. A frequency histogram of the magnitude of absolute anisotropy as determined from AVOA analysis is shown in Figure (9.4). Examination of the observed AVOA response shows that on average the absolute anisotropy is approximately 0.2 to 0.6 (Figure 9.4). Figure (9.5) is a matrix scatter plot and represents the predicted AVOA response for varying magnitudes of fracturing within Top Unit V and the overlying Unit VI. The x-axis and y-axis represent the degree of fracturing within Unit VI and Unit V respectively. An increase in the positive direction on both the axes represents an increase in the magnitude of fracturing. The absolute magnitude of anisotropy is indicated by the colour scale bar. Therefore, to produce magnitudes of anisotropy similar to those observed within Unit V (Figure 9.4), Unit V is required to have strong fracturing whilst Unit VI is expected to have weak or little fracturing (Figure 9.5).

This methodology allowed the amalgamation of all the data sets (EBSD, ultrasonics and seismics) but it also meant that when performing the inversion procedure it was assumed that the actual AVOA response was as a consequence of all the seismic anisotropy causing variables. It was assumed that to a greater or lesser all the variables causing seismic anisotropy would appear in the actual observed AVOA. Hence, the observed AVOA contained information about the grain fabric, micro-porosity and larger scale fracturing.

On a local scale there can be significant variability in anisotropy orientation due, for example, to perturbation of stress fields around faults or across fold structures. thus, flexibility, such as avoiding prior assumptions about regional orientations is necessary in the AVOA analysis. AVOA may be interpreted in terms of fracturing but ambiguity

exists in this such that even azimuth of fracturing could be misinterpreted. Thus forward modeling is necessary to resolve this ambiguity. AVOA analysis interpreted in terms of fracturing and shows spatial variability in both orientation and magnitude that correlates with independently acquired data sets (Smith & Lappin 1997, Coney et al. 1993).

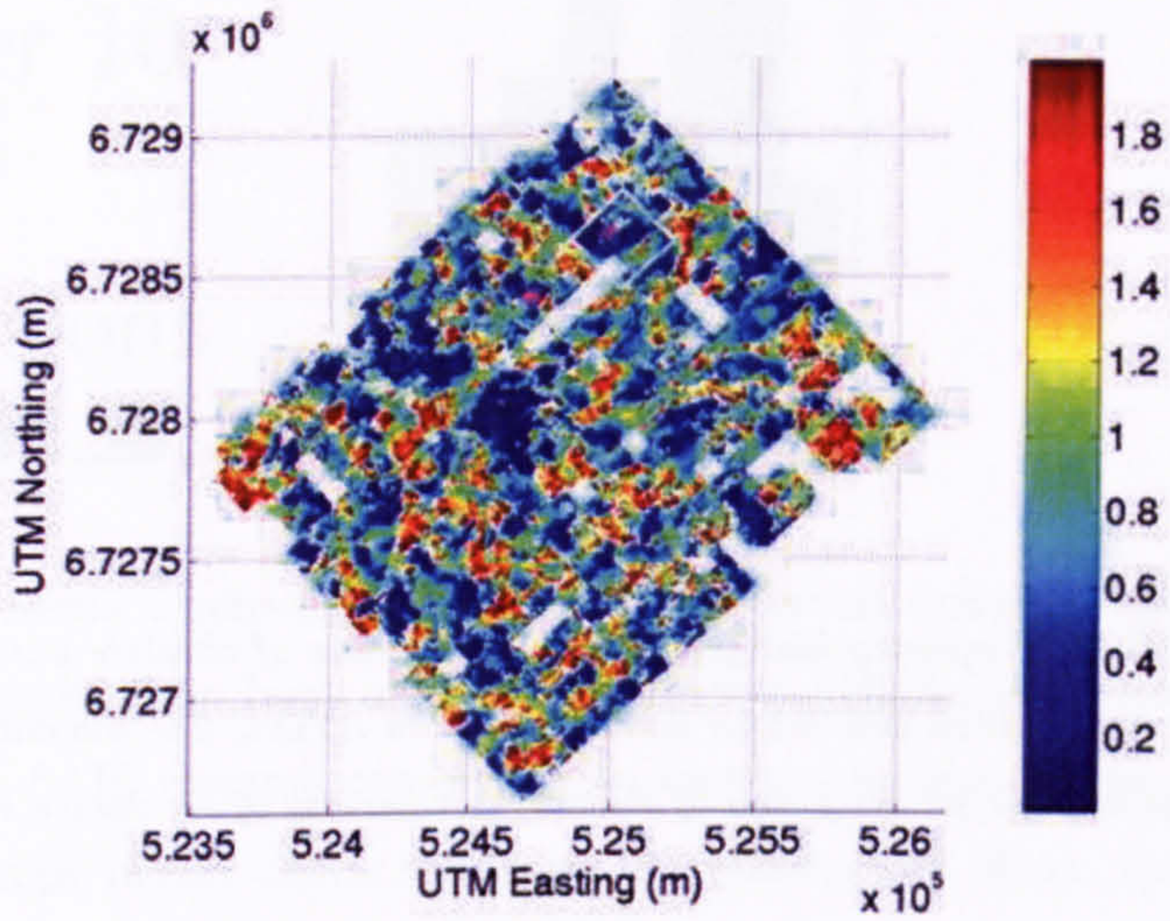

Figure 9.3: *Observed AVOA for the Top Unit V horizon within Well 206/8-8. The absolute magnitude of anisotropy is indicated by the colour bar. Courtesy of Dr Andrew Carter.*

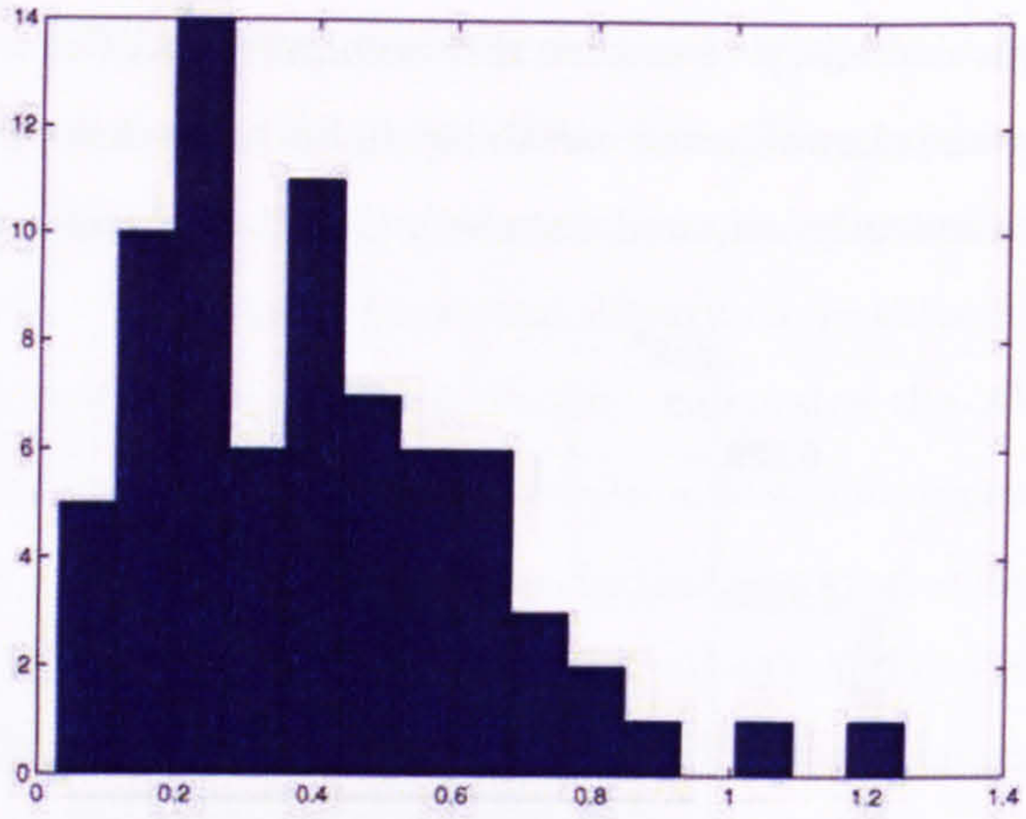

Figure 9.4: *Frequency histogram of the magnitude of absolute anisotropy for the Top Unit V horizon within Well 206/8-8 as determined from AVOA. The magnitude of anisotropy increases from left-to-right on the x-axis of the graph. Courtesy of Dr James Wookey.*

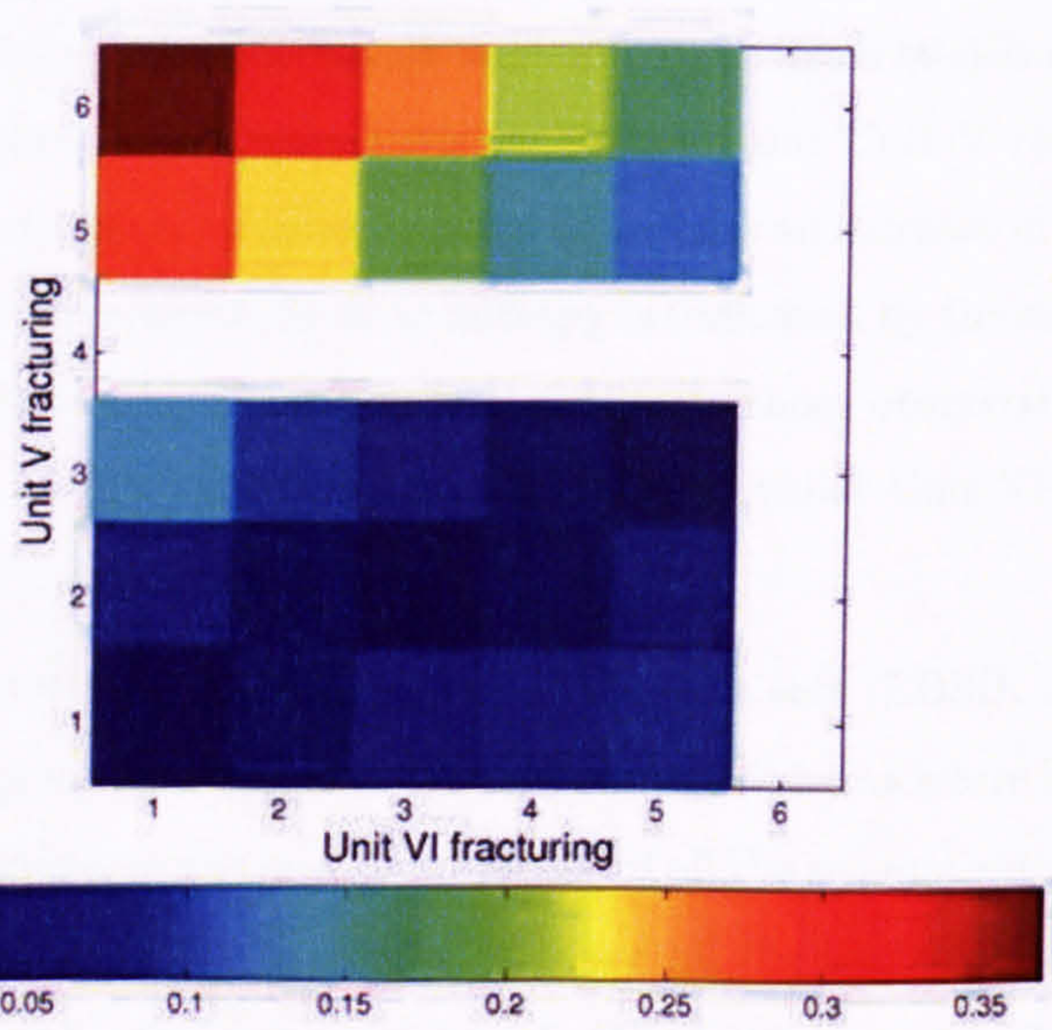

Figure 9.5: *Synthetic AVOA response using varying magnitudes of fracturing within Unit V and Unit VI with the assumption of an intrinsic anisotropy due to lattice preferred orientation. 1 - no fractures → 6 -highly fractured. The absolute magnitude of anisotropy is indicated by the colour bar. Courtesy of Dr James Wookey.*

Chapter 10

Conclusions

This thesis presents a petrofabric analysis of seismic aniostropy in siliciclastic reservoir rocks. The results have been used by the present authors and other researchers belonging to the SAIL research consortium to increase understanding of the controls of seismic anisotropy in siliciclastic reservoirs. As summarised below, the results raise the possibility that measures of seismic anisotropy from field seismic data can be used to predict reservoir parameters, such as, lithology, fracturing, and fracture orientation within siliciclastic rocks. Combining petrofabric analysis (conducted by the present author), ultrasonic velocity measurements (conducted by the present author at the University of Manchester), field seismic data (analysed by Dr Andrew Carter) via numerical modelling (conducted by Dr James Wookey, Dr Stephen Hall and Prof Michael Kendall) has highlighted some of the most important controls. This chapter will contain the main conclusions, outline the key contributions of this thesis and discuss potential future directions for the study of seismic anisotropy in sedimentary rocks.

Lattice preferred orientation determination methodologies

Automated EBSD proved to be a reliable technique for determining LPO of quartz, feldspar, and calcite. Manual EBSD indexing of phyllosilicates was required because of their platy structure, fine grain size and poorly crystallised structure. The predictive and analytical models that were both used to determine phyllosilicate orientation were consistent with each other. Overall, the studies conducted during this study may represent the most detailed petrofabric analyses conducted on a suite of sedimentary rocks.

Seismic anisotropy as a result of lattice preferred orientation

Undeformed clastic rocks exhibit a significant seismic anisotropy due to the LPO of their

mineral phases alone. The modal proportion of phyllosilicate minerals is the single most important control upon seismic anisotropy in the samples studied. Furthermore, both feldspar and calcite can have a significant impact on the bulk aggregate anisotropy. The fabric intensity of the constituent mineral phases is found to be directly proportional to the maximum P- and S-wave anisotropy. When the phyllosilicate modal content is approximately 15% they become the most dominant mineral phase with respect to the symmetry of the bulk aggregate anisotropy. A rock can be assumed to have a completely VTI style of symmetry when phyllosilicate content is $\leq 15\%$.

Palaeoflow indicators

The symmetry patterns of quartz and feldspar predicted throughout all the seismic velocity stereoplots align in a constructive fashion. The consistent plunge and azimuth of the both quartz and feldspar P- and S-wave maxima suggest a dominant palaeoflow direction. It is possible therefore that depositional flow direction of intra-reservoir units can be inferred from seismic anisotropy alone. This is the first study that has produced sufficient data to raise the possibility that seismic anisotropy could be used to identify palaeo-flow directions within reservoirs.

Mathematical models

High density EBSD analysis has enabled us to model any rock's seismic properties when given the modal proportions alone. The relationship between fabric intensity and maximum P- and S-wave anisotropy was the basis for a mathematical model of any of the Clair rocks. Furthermore, using a multiple linear-regression, empirical formulae were derived which predicted P- and S-wave anisotropy from modal proportions alone. This approach is a step further than the empirical correlations between porosity, clay content and velocity devised by *Han (1986)* as the geomathematical model allows the calculation of seismic velocities as a function of the entire rock mineralogy, the stress conditions as well as the direction of wave propagation.

Room pressure ultrasonic velocity measurements

P-wave velocities vary between 2 and 5 km/s, whilst S-wave velocities vary between 1 and 3 km/s. The velocities are typically transversely isotropic or isotropic. The samples could be grouped into three main categories: 1 - high velocities with strong anisotropy, 2 - high velocities and weak anisotropy, and 3 - low velocities with intermediate anisotropy. Group 1 samples typically had a significant phyllosilicate content and tended to part easily parallel to bedding. Group 2 samples were generally oil rich, and lacked any significant

amount of clay minerals. Group 3 samples were clean, high porosity sandstones.

High pressure ultrasonic velocity results

The anisotropy decreased rapidly for Group 1 samples over the first 50MPa and the velocity perpendicular to bedding increased faster than the velocities parallel to bedding which reflects the closure of the bedding parallel porosity. For the Group 2 samples there is a small decrease in anisotropy as the pressure increases but initially with a small anisotropy. Ultimately Group 2 samples are isotropic at the limit to elastic pore closure. The anisotropy initially increases and then drecreases as the pressure increases in Group 3 samples, suggesting that pores are more compliant in some directions than others and hence there is a different rate of pore closure with pressure in different directions; they are broadly isotropic. The rapid closure of the horizontally aligned (bedding parallel) cracks and micro-cracks are likely to have formed as a result of stress relaxation and probably not present in the reservoir.

Compliance tensor inversion

Extrinsic crack-induced anisotropy is much stronger relative to intrinsic LPO effects. In general, the predominant crack set is aligned parallel to the depositional fabric. Intrinsic and extrinsic anisotropies appear to be aligned. This indicates that they are linked in origin, for example, the cracks are related to grain boundary contacts and are aligned with the grains which give rise to the LPO and SPO.

Palaeomagnetic core orientation

Palaeomagnetic core orientation has proven to be an useful and relatively successful technique in defining the direction of geographic North throughout all the samples analysed. The palaeomagnetic orientation data was assigned a reliability class ranging from 1 to 3, where Class 1 represents an angular uncertainty of $< 15^o$, Class 2 15^o to 20^o, and Class 3 $> 20^o$. 64% of the samples analysed fell into class 1, 14% into class 2, and the remaining 22% into class 3. The palaeomagnetic core orientation can be thought of as being successful when considering that on average 64% of the orientation data had a circular error of less than or equal to 15^o.

Grain fabric and palaeoflow indicators

K_{max} and K_{min} axes lie within $\sim 35^o$ of the horizontal and vertical respectively. This confirms that these sediments have not been disturbed by post-depositional processes. The mean sediment transport direction for Well 206/8-8 was towards the SSE. The mean

sediment transport direction for Well 206/13a-2 was also towards the SE.

Grain fabric anisotropy

Total grain anisotropy in both wells typically ranges from ~ 5 to 30% with a mean of ~ 11%. The majority of this anisotropy reflects the tendency for grains to lie with their long axes near the horizontal and short axes near the vertical, resulting in a dominant planar anisotropy with a mean of ~ 9.5%. Azimuthal grain anisotropy is relatively weak ranging up to about only 3% but with an overall mean value of only 1%. The results of this analysis are consistent with the EBSD analysis of petrofabric intensity.

Developments in rock characterisation in both the laboratory and in field wide seismics have played an important role in the improvements made in both exploration and development of hydrocarbon reservoirs. Although many of these improvements have made seismic reservoir characterisation and monitoring possible there remains many significant challenges, such as, determining the relevance of the relationships between core, log and seismic measurements of seismic wave propagation and attenuation.

Future Directions

A Voigt-Reuss-Hill (VRH) average was applied throughout this project to calculate the bulk aggregate elastic properties. VRH is one of the simplest and best known averaging techniques, however, no information on shape or position of individual grains is used when determining the effective elastic constants. It is proposed that in future studies carried out in this area, a more complex averaging scheme could be applied such as the Ponte Castañeda and Willis method (Castañeda & Willis 1995). The Ponte Castañeda and Willis method provides a powerful method for a more detailed assessment of the causes of elastic property anisotropy in rocks with more complicated microstructures.

Automated EBSD is now a relatively well established technique but further work could be conducted on verifying the accuracy of its capabilities to identify low symmetry mineral phases, such as feldspars. Throughout this project new methodologies were developed to assist in the accurate and precise crystallographic orientation identification of low symmetry mineral phases. For example, it was decided that to correctly determine the orientation of phyllosilicates that they should be manually indexed. Furthermore, the crystallographic indexing files used by EBSD to identify feldspars, and muscovite orientation were also updated.

This study has provided a catalogue of results so that a mathematical model of any rock within the Clair field can be approximated on the basis of its mineralogy alone to aid the processing and understanding of field seismic data on what is a structurally complex reservoir. This study is however by no means exhaustive and has plenty of room for development. For example, approximately two thirds of the world's oil is produced from carbonate reservoirs. Therefore carrying out a similarly rigorous and detailed study on a suite of carbonates could also assist in the maximising of oil recovery from carbonate sequences.

The suite of samples that were studied were from an atypical clastic reservoir and further analytical work of the nature that has been carried out in this project is required to verify whether the assumptions made will in fact hold for all clastic reservoirs or whether they are unique to the Clair field. It is postulated that rock physics and their related seismic properties could be highly controlled by local geological factors. However it could be the case that rock physic trends are universal and therefore rock physic models can be used in a predictive way if they are constrained by local geological parameters.

Bibliography

Alkhalifah, T. (1997), 'Velocity analysis using nonhyperbolic moveout in transversely isotropic media', *Geophysics* **62**, 1839–1854.

Alkhalifah, T. & Rampton, D. (2001), 'Seismic anisotropy in Trinidad: A new tool for lithology prediction', *The Leading Edge* **20**(4), 420–424.

Alkhalifah, T. & Thomsen, L. (1994), 'Nonhyperbolic reflection moveout in anisotropic media', *Geophysics* **59**, 1290–1304.

Allen, P. & Mange-Rajetzky, M. (1992), 'Sedimentary evolution of the Devonian-Carboniferous Clair Field offshore North-Western UK: Impact of changing provenance', *Marine and Petroleum Geology* **9**, 29–52.

Babuska, V. & Cara, M. (1991), *Seismic anisotropy in the earth*, Kluwer Academic Publishers.

Backus, M. (1962), 'Long-wave elastic anisotropy produced by horizontal layering', *Journal of Geophysical Research* **67**, 4427.

Bayly, M. (1965), 'The sampling error in modal analysis', *American Mineralogist* **50**, 196–211.

Benson, P., Meredith, P., Platzman, E. & White, R. (2005), 'Pore fabric shape anisotropy in porous sandstones and its relation to elastic wave velocity and permeability anisotropy under hydrostatic pressure', *International Journal of Rock Mechanics and Mining Sciences* **42**, 890–899.

Berryman, J. (1979), 'Long-wave elastic anisotropy in transversely isotropic media', *Geophysics* **44**(4), 896–917.

Bingham, C. (1974), 'An antipodally symmetric distribution on the sphere', *The Annals of Statistics* **2**(6), 1202–1225.

Birch, F. (1960), 'The velocity of compressional waves in rocks to 10 kilobars', *Journal of Geophysical Research* **65**(4), 1083–1102.

Blackbourn, G. (1987), *European Dinantian Environments*, Wiley, chapter Sedimentary environments and stratigraphy of the Late Devonian-Early Carboniferous Clair basin, West of Shetland, pp. 75–91.

Blangy, J. (1992), Integrated seismic lithologic interpretation: the petrophysical basis, PhD thesis, Stanford University.

Bohnel, H. & Schnepp, E. (1999), 'Precision of the palcomagnetic method: An example from the Quaternary Eifel volcanics', *Earth, Planets, Space* **51**, 403–412.

Brevik, I. (1995), Chalk data, Workshop on effective media, Karlsruhe.

Budiansky, B. (1965), 'On the elastic moduli of some heterogeneous materials', *Journal of Mechanics and Physics of Solids* **13**, 223–227.

Bunge, H. (1982), *Mathematical methods of texture analysis*, Butterworths, London.

Burlini, L. & Kunze, K. (2000), 'Fabric and seismic properties of Carrara Marble mylonite', *Physical Chemistry of the Earth* **25**(2), 133–139.

Cadoret, T. (1986), *Effet de la Saturation Eau/Gaz sur les Proprietes Acoustiques des Roches*, PhD thesis, University of Paris.

Caley, A., Kendall, J.-M., Jones, R., Barkved, O. & Folstad, P. (2001), Monitoring fractures in 4D using micro-seismic data, EAGE 63rd Conference & Exhibition.

Carlson, C., Schaftenaar, C. & Moore, R. (1984), 'Causes of compressional-wave anisotropy in carbonate bearing, deep-sea sediments', *Geophysics* **49**, 525–532.

Castañeda, P. & Willis, J. (1995), 'The effect of spatial distribution of composite materials and cracked media', *Journal of the Mechanics and Physics of Solids* **43**, 1919–1951.

Castagna, J., Batzle, M. & Eastwood, R. (1985), 'Relationships between compressional-wave and shear-wave velocities in clastic silicate rocks', *Geophysics* **50**, 571–581.

Chayes, F. (1956), *Petrographic Modal Analysis*, John Wiley and Sons Inc., New York.

Cheeney, R. (1983), *Statistical methods in geology*, Allen & Unwin.

Christoffel, E. (1910), *Gesellschaft Technische Wissenschaftlische Adhandlungen*, Leipzig.

Chung, F. (1974), 'Quantitative interpretation of X-ray diffraction patterns', *Journal of Applied Crystallography* **7**, 519–525.

Coney, D., Fyfe, T., Retail, P. & Smith, P. (1993), 'Clair appraisal: the benefits of a co-operative approach', *Petroleum Geology of Northwest Europe: Proceedings of the 4th Conference* pp. 1409–1420.

Crampin, S. (1981), 'A review of wave motion in anisotropic and cracked media', *Wave Motion* **3**, 343–391.

Crampin, S. (1985), 'Evaluation of anisotropy by shear-wave splitting', *Geophysics* **50**(1), 142–152.

Crampin, S. & Lovell, J. (1991), 'A decade of shear-wave splitting in the earth's crust: what does it mean? what use can we make of it? and what should we do next?', *Geophysical Journal International* **107**, 387–407.

Crisp, R. (1997), Clair Southern Area Development, Clair Oils Geochemistry/PVT Review, Technical report, BP Exploration, Clair Development.

Dandekar, D. (1968), 'Pressure dependence of the elastic constants of calcite', *Physical Review* **172**(3), 873–877.

Day, A. (1993), Developments in the EBSP technique and their application to grain imaging, PhD thesis, University of Bristol.

Deer, W., Howie, R. & Zussman, J. (1999), *An introduction to the rock forming minerals*, Longman.

Eberhart-Phillips, D. (1989), Investigation of Crustal Structure and Active Tectonic Processes in the Coast Ranges, Central California, PhD thesis, Stanford University.

Eshelby, J. (1957), 'The determination of the elastic field of an ellipsoidal inclusion, and related problems', *Proceedings of the Royal Society of London, A.* **241**, 376–396.

Fresnel, A. (1821), 'Mémoire sur la double réfraction', *Académie des Sciences.*

Fynn, G. & Powell, W. (1979), *The cutting and polishing of electro-optic materials.*, Adams Hilger, London., chapter 1.

Galehouse, J. (1971), *Procedures in Sedimentary Petrology*, Wiley-Interscience, New York, chapter Point Counting, pp. 385–407.

Gassmann, F. (1951), 'Uber die elastizitat poroser medien', *Vier. der Natur. Gesellschaft in Zurich* **96**, 1–23.

Geertsma, J. (1961), 'Velocity-log interpretation: The effect of rock bulk compressibility.', *Society of Petroleum Engineering Journal* **1**, 235–248.

Goldstein, J., Newbury, D., Echlin, J., Joy, D., Romig, A., Lyman, C. J., Fiori, C. & Lifshin, E. (1992), *Scanning Electron Microscopy and X-ray Microanalysis*, Plenum, New York and London.

Goulden, C. (1956), *Methods of Statistical Analysis*, Wiley, New York.

Grechka, V., Tsvankin, I., Bakulin, A., Signer, C. & Hansen, J. (2002), 'Anisotropic inversion and imaging of PP and PS reflection data in the North Sea', *The Leading Edge* **21**(1), 90–97.

Green, G. (1837), 'On the laws of reflection and refraction of light at the common surface of two non-crystallised media', *Transaction of the Cambridge Philosophical Society.*

Gueguen, Y. & A., S. (2003), 'Elastic wave velocities and permeability of cracked rocks', *Tectonophysics* **370**, 163–176.

Gueguen, Y., Ravalec, M. L. & Ricard, L. (2006), 'Upscaling: Effective medium theory, numerical methods and the fractal dream', *Pure and Applied Geophysics* **163**, 1175–1192.

Hailwood, E. (2004), Palaeomagnetic re-orientation and magnetic anisotropy study of core, Technical report, Coremagnetics.

Hailwood, E. & Ding, F. (1995), *Palaeomagnetic Applications in Hydrocarbon Exploration and Production*, Geological Society London, Special Publication, chapter Palaeomagnetic re-orientation of cores and the magnetic fabric of hydrocarbon reservoir sands, pp. 245–258.

Hailwood, E. & Ding, F. (2000), 'Sediment transport and dispersal pathways in the Lower Cretaceous sands of the Britannian Field, derived from magnetic anisotropy', *Petroleum Geoscience* **6**, 369–379.

Hall, S. (2000), Rock fracture characterisation and seismic anisotropy: Application to ocean bottom seismic data, PhD thesis, University of Leeds.

Hall, S. & Kendall, J.-M. (2003), 'Fracture characterisation at Valhall: Application of P-wave AVOA analysis to a 3D ocean-bottom data set', *Geophysics* **68**, 1150–1160.

Hall, S., Kendall, J.-M. & Barkved, O. (2002), 'Fractured reservoir characterisation using P-wave AVOA analysis of *3D* OBC data', *The Leading Edge* **21**, 777–781.

Hall, S., Kendall, J.-M., Covey-Crump, S., Maddock, J., Fisher, Q. & Wookey, J. (2007), 'Crack density tensor inversion for analysis of rock frame architecture and its variation under hydrostatic loading in hydrocarbon reservoir rocks', *Geophysical Journal International.*

Hamilton, N. & Rees, A. (1970), *Palaeogeophysics*, London Academic Press, chapter The use of magnetic fabric in palaeocurrent estimation, pp. 445–464.

Han, D. (1986), Effects of porosity and clay content on acoustic properties of sandstones and unconsolidated sediments, PhD thesis, Stanford University.

Han, J., Schmitt, D., Collis, D. & Escertain, J. (2004), Laboratory determination of velocity anisotropy, CSEG National Convention.

Hearmon, R. (1984), *Landolt-Bornstein Tables*, Springer-Verlag, chapter The elastic constants of crystals and other anisotropic materials, pp. 1–154.

Helbig, K. & Thomsen, L. (2005), '75-plus years of anisotropy in exploration and reservoir seismics: A historical review of concepts and methods', *Geophysics* **70**(6), 9–23.

Helfing, D. (1970), 'Micro-fabrics of shales and their rearrangement by compaction', *Sedimentology* **15**, 247–260.

Hess, H. (1960), 'Seismic anisotropy of the uppermost mantle under oceans.', *Nature* **203**, 629–631.

Hill, R. (1952), 'The elastic behaviour of a crystalline aggregate', *Proceedings of the Physical Society* **A**(65), 351–354.

Hillier, S. (1999), 'Use of an air-brush to spray dry samples for X-ray powder diffraction', *Clay Minerals* **34**, 127–135.

Hillier, S. (2000), 'Accuarate quantitative analysis of clay and other minerals in sandstones by XRD; comparison of a rietveld and a reference intensity ratio (RIR) method and the importance of sample preparation', *Clay Minerals* **35**(1), 291–302.

Holt, R. & Fjaer, E. (1987), *North Sea Oil and Gas reservoirs*, Graham and Trotman, chapter Acoustic behaviour of sedimentary rocks during failure.

Hornby, B. (1998), 'Experimental laboratory determination of the dynamic elastic properties of wet, drained shales', *Journal of Geophysical Research* **103**, 29945–29964.

Hudson, J. (1981), 'Wave speeds and attenuation of elastic waves in material containing cracks', *Geophysical Journal of the Royal Astronomical Society* **64**, 133–150.

Jenkins, R. & Synder, R. (1996), *Introduction to X-ray Powder Diffractometry*, Wiley-Interscience, New York, chapter Quantitative analysis, pp. 355–384.

Jizba, D. (1991), Mechanical and acoustical properties of Sandstones and Shales, PhD thesis, Stanford University.

Johnston, J. & Christensen, N. (1995), 'Seismic anisotropy of shales', *Journal of Geophysical Research* **100**, 5991–6003.

Jones, L. & Wang, H. (1981), 'Ultrasonic velocities in Cretaceous shales from the Willingston basin', *Geophysics* **46**, 288–297.

Kaarsberg, E. (1959), 'Introductory studies of natural and artificial argillaceous aggregates by sound propagation and X-ray diffraction methods.', *Journal of Geology* **67**, 447–472.

Kendall, J.-M. (2000), *Seismic anisotropy in the boundary layers of the mantle*, AGU, chapter Earth's Deep Interior: Mineral Physics and Tomography From the Atomic to the Global Scale, pp. 133–159.

Kendall, J.-M., Ben-Ismail, W., Carter, A., Covey-Crump, S., Fisher, Q., Hall, S., Lloyd, G., Maddock, J. & Wookey, J. (2006), 'Seismic anisotropy and reservoir characterisation: contributions from the crystal, grain and fracture', *Geological Society of London, Special Publication, Structurally Complex Reservoirs.*

Kendall, R. & Kendall, J.-M. (1996), 'Shear-wave amplitude anomalies in south-central Wyoming', *Leading Edge* **15**, 913–920.

Kenney, J. & Keeping, E. (1962*a*), *Mathematics of Statistics*, Van Nostrand, Princeton, New Jersey.

Kenney, J. & Keeping, E. (1962*b*), *Mathematics of Statistics*, Vol. 1, Van Nostrand, Princeton, New Jersey, chapter Confidence limits for the binomial parameter, pp. 167–169.

King, M. (1966), 'Wave velocities in rocks as a function of changes in overburden pressure and pore fluid saturants', *Geophysics* **31**, 50–73.

Kirschvink, J. (1980), 'The least-squares line and plane and the analysis of palaeomagnetic data', *Geophysical Journal of the Royal Astronomical Society* **62**, 699–718.

Knipe, R., Porter, N., Fisher, Q., Jones, R. & Condliffe, D. (1998), *Structural core analysis of the Clair field*, Rock Deformation Research, Leeds University.

Kolsky, H. (1953), *Stress waves in Solids*, Clarendon Press, Great Britain.

Kommedal, J., Fowler, S. & McGarrity, J. (2004), Improved P-wave imaging with 3D OBS data at Clair, EAGE 66th Conference & Exhibition.

Krey, T. & Helbig, K. (1956), 'A theorem concerning anisotropy of stratified media and its significance for reflection seismics', *Geophysical Prospecting* **4**, 294–302.

Leyshon, P. & Lisle, R., eds (1996), *Stereographic Projection Techniques in Structural Geology*, Butterworth, Heinemann.

Lloyd, G. (1987), 'Atomic number and crystallographic contrast images with the SEM: a review of backscattered electron techniques', *Mineralogical Magazine* **51**, 3–19.

Lloyd, G. (2002), RMS Spring School - SEM Electron Backscattered Diffraction, Technical report, University of Leeds.

Lloyd, G. & Kendall, J.-M. (2005), *Petrophysical Properties of Crystalline Rocks*, Vol. 240, Geological Society London, Special Publications, chapter Petrofabric derived seismic properties of a mylonitic quartz simple shear zone: Implications for seismic reflection profiling.

Louis, L., David, C. & Robion, P. (2003), 'Comparison of the anisotropic behaviour of undeformed sandstones under dry and saturated conditions', *Tectonophysics* **370**, 193–212.

Louis, L., David, C., Metz, V., Robion, P. & Menendez, B. Kissel, C. (2005), 'Microstructural control on the anisotropy of elastic and transport properties in undeformed sandstones', *International Journal of Rock Mechanics and Mining Sciences* **42**, 911–923.

Love, A. (1944), *A treatise of the mathematical theory of elasticity*, Vol. 4th Edition, Dover Publications, New York.

Lucet, N. (1989), *Vitesse et attenuation des ondes elastiques soniques et ultrasoniques dans les roches sous pression de confinement*, PhD thesis, University of Paris.

Lucet, N. & Zinszner, B. (1992), 'Effects of heterogeneities and anisotropy on sonic and ultrasonic attenuation in rocks', *Geophysics* **57**(8), 1018–1026.

Maddock, J., Casey, M., Fisher, Q., Kendall, J.-M. & Lloyd, G. (2004), Petrofabric analysis of seismic anisotropy in siliciclastic sedimentary rocks, EAGE 66th Conference & Exhibition.

Mainprice, D. (1990), 'An efficient fortran program to calculate seismic anisotropy from the lattice preferred orientation of minerals', *Computers and Geosciences* (16), 385–393.

Mainprice, D., Barruol, G. & Ben-Ismail, W. (2000), *Earth's Deep Interior: Mineral Physics and Tomography From the Atomic to the Global Scale*, AGU, chapter The seismic anisotropy of the Earth's mantle: from single crystal to polycrystal, pp. 237–264.

March, A. (1932), 'Mathematische theorie der regelung nach der korngestalt bei affiner deformation', *Zeitschrift Kristallphysik* **81**, 285–297.

Mavko, G., Mukerji, T. & Dvorkin, J. (1998), *The Rock Physics Handbook*, Cambridge University Press.

Meskimin, H., Andreatch, P. & Thurston, R. (1965), 'Elastic moduli of quartz versus hydrostatic pressure at 25° to −198.5° C.', *Journal of Applied Physics* **36**(5), 1624–1632.

Miller, R. (1997), *Beyond ANOVA: Basics of Applied Statistics*, Chapman & Hall.

Morton, A., Knox, R. & Hallsworth, C. (2002), 'Correlation of reservoir sandstones using quantitative heavy mineral analysis', *Petroleum Geoscience* **8**, 251–262.

Nur, A. & Simmons, G. (1969), 'Stress-induced velocity anisotropy in rock: An experimental study', *Journal of Geophysical Research* **74**, 6667.

Nye, J. (1957), *Physical Properties of Crystals: their representation by tensors and matrices*, Oxford, Clarendon Press.

Olofsson, B., Kommedal, J., Barkved, O., Alexandre, R., Brunelliere, J. & Muyzert, E. (2002), Continuous progress in processing multicomponent data - a case study, EAGE 64th Conference & Exhibition.

Ostrander, W. (1984), 'Plane-wave reflection coefficients for gas sands at non-normal angles of incidence', *Geophysics* **49**, 1637–1648.

Pay, M., Astin, T. & Parker, A. (2000), 'Clay mineral distribution in the Devonian-Carboniferous sandstones of the Clair field, West of Shetland, and its significance for reservoir quality', *Clay Minerals* **35**, 151–162.

Plona, T. & Tsang, L. (1979), Determination of the average microscopic dimension in granular media using ultrasonic pulses: theory and experiments, SEG Expanded Abstracts.

Postma, G. (1955), 'Wave propagation in a stratified medium', *Geophysics* **20**, 780–806.

Press, W., Flannery, B., Teukolsky, S. & Vetterling, W. (1992), *Numerical recipes in Fortran*, Cambridge University Press.

Prior, D. & Wheeler, J. (1999), 'Feldspar fabrics in a greenschist facies albite-rich mylonite from electron backscatter diffraction', *Tectonophysics* **303**, 29–49.

Prior, D., Boyle, A., Brenker, F., Cheadle, M., Day, A., Lopez, G., Potts, G., Reddy, S., Spiess, R., Timms, N., Trimby, P., Wheeler, J. & Zetterstrom, L. (1999), 'The application of electron backscatter diffraction and orientation contrast imaging in the SEM to textural problems in rocks', *American Mineralogist* **84**, 1741–1759.

Randle, V. (2003), *Microtexture determination and its applications*, The Institute of Materials.

Raymer, D., Kendall, J.-M., Pedlar, D., Kendall, R., Mueller, M. & Beaudoin, G. (2000*a*), The significance of salt anisotropy in seismic imaging, SEG Expanded Abstracts.

Raymer, D., Tommasi, A. & Kendall, J.-M. (2000*b*), 'Predicting the seismic implications of salt anisotropy using numerical simulations of halite deformation', *Geophysics* **65**(4), 1272–1280.

Reed, S. (1996), *Electron Microprobe Analysis and Scanning Electron Microscopy in Geology*, Cambridge University Press.

Reuss, A. (1929), 'Berechnung der von mischkristallen auf grund der plastizitatsbedingung fur einkristalle', *Zeitschrift fur Angewandte Mathematik und Mechanik* **9**, 49–58.

Sager, W. & Singleton, S. (1989), 'Paleomagnetic inclination errors in sediments cored from a Gulf of Mexico salt dome - An indicator of ancient sea level', *Geology* **17**, 739–742.

Salisbury, M. (2000), *Atlantic rock properties database*, Geological Survey of Canada.

Sayers, C. (1994), 'The elastic anisotropy of shales', *Journal of Geophysical Research* **99**, 767–774.

Sayers, C. (2002*a*), 'Fluid-dependent shear-wave splitting in fractured media', *Geophysical Prospecting* **50**, 393–401.

Sayers, C. (2002*b*), 'Stress-dependent elastic anisotropy of sandstones', *Geophysical Prospecting* **50**, 85–95.

Sayers, C. (2005), 'Seismic anisotropy of shales', *Geophysical Prospecting* **53**, 667–676.

Sayers, C. & Kachanov, M. (1991), 'A simple technique for finding effective elastic constants of cracked solids for arbitrary crack orientation statistics', *International Journal of Solids and Structures* **27**(6), 671–680.

Sayers, C. & Kachanov, M. (1995), 'Microcrack-induced elastic wave anisotropy of brittle rocks', *Journal of Geophysical Research* **100**(B3), 4149–4156.

Sayers, C., van Munster, J. & King, M. (1990), 'Stress-induced ultrasonic anisotropy in berea sandstone', *International Journal of Rock Mechanics* **27**, 429–436.

Schmidt, N. & Olesen, N. (1989), 'Computer-aided determintaion of crystal lattice orientation from electron channeling patterns in the SEM', *Canadian Mineralogist* **27**, 15–22.

Schofield, P., Knight, K., Covey-Crump, S., Cressey, G. & Stretton, I. (2002), 'Accurate quantification of the modal mineralogy of rocks when image analysis is difficult', *Mineralogical Magazine* **66**, 189–200.

Schreiber, E. (1973), *Elastic constants and their measurement*, McGraw-Hill, New York.

Schwartz, A., Kumar, M. & Adams, B., eds (2000), *Electron Backscatter Diffraction in Materials Science*, Kluwer Academic Publishers.

Scott, T., Ma, Q. & Roegiers, J. (1993), 'Acoustic velocity changes during shear enhanced compaction of sandstone', *International Journal of Rock Mechanics and Mining Science and Geomechanical Abstracts* **30**, 763–769.

Sheriff, R. & Geldart, L. (1999), *Exploration Seismology*, Cambridge University Press.

Silver, P. & Chan, W. (1988), 'Implications for continental structure and evolution from seismic anisotropy', *Nature* **335**, 34–39.

Smith, R. & Lappin, J. (1997), Clair Subsurface Review, Technical report, BP Exploration, Clair Development.

Smith, R. & McGarrity, J. (2001), 'Cracking the fractures-seismic anisotropy in an offshore reservoir', *The Leading Edge* **20**(1), 18–26.

Strandness, S. (1991), Rock physics analysis of the Brent Group resservoir in the Oseberg field, PhD thesis, Stanford University.

Sturcken, J. & Croach, J. (1963), 'Predicting physical properties in oriented materials', *Transactions of the Metallurgical Society* **227**, 934–940.

Tabti, H., Tvedt, T. & Langhammer, J. (2004), Azimuth dependent processing - application to the Clair OBS data, EAGE 66th Conference & Exhibition.

Thomsen, C. (1998), *Seismic waves in complex 3D structures*, Department of Geophysics, Charles University Prague, chapter Notes on Rmatrix, a program to find the seismic-plane wave response of a stack of anisotropic layers, pp. 163–167.

Thomsen, L. (2002), *Distinguished instructor short course - Understanding Seismic Anisotropy in Exploration and Exploitation*, European Association of Geoscientists and Engineers.

Tosaya, C. & Nur, A. (1982), 'Effects of diagenesis and clays on compressional velocities in rocks', *Geophysical Research Letters* **9**, 5–8.

Trimby, P. & Prior, D. (1999), 'Microstructural imaging techniques: a comparison of optical and scanning electron microscopy inthe study of deformed rocks', *Tectonophysics* **303**, 71–81.

Ullemeyer, K., Braun, G., Dahms, M., Kruhl, J., Olesen, N. & Siegesmund, S. (2000), 'Texture analysis of a muscovite-bearing quartzite: a comparison of some currently used techniques', *Journal of Structural Geology* **22**, 1541–1557.

Urmos, J. & Wilkens, R. (1993), 'In situ velocities in pelagic carbonates: New insights from ocean drilling program leg 130, Ontong Java', *Journal of Geophysical Research* **98**(B5), 7903–7920.

Valcke, S. (2003), Towards the prediction of seismic anisotropy in sedimentary rocks, Master's thesis, University of Leeds.

Valcke, S., Casey, M., Lloyd, G., Kendall, J.-M. & Fisher, Q. (2006), 'Lattice preferred orientation and seismic anisotropy in sedimentary rocks', *Geophysical Journal International* **166**(2), 652–666.

Van der Baan, M. & Kendall, J.-M. (2002), 'Estimating anisotropy parameters and traveltimes in the tau-p domain', *Geophysics* **67**, 1076–1086.

Van der Plas, L. & Tobi, A. (1965), 'A chart for judging the reliability of point counting results', *American Journal of Science* **263**, 87–90.

Vargaftik, N., Vinogradov, Y. & Yargin, V. (1983), *Handbook of physical properties of liquids and gases: Pure substances and mixtures*, Taylor & Francis Inc.

Venables, J. & Harland, C. (1973), 'Electron backscattering patterns - a new technique for obtaining crystallographic information in the scanning electron microscope', *Philosophical Magazine* **27**, 1193–1200.

Vernik, L. & Liu, X. (1997), 'Velocity anisotropy in shales: A petrophysical study', *Geophysics* **62**(2), 521–532.

Vernik, L. & Nur, A. (1992*a*), 'Petrophysical classification of siliciclastics for lithology and porosity prediction from seismic velocities', *The American Association of Petroleum Geologists* **76**(9), 1295–1309.

Vernik, L. & Nur, A. (1992*b*), 'Ultrasonic velocity and anisotropy of hydrocarbon source rocks', *Geophysics* **57**, 727–735.

Vickers, B. & Thill, R. (1969), 'A new technique for preparing rock spheres', *Journal of Scientific Instrumentation* **2**, 901–902.

Voigt, W. (1928), *Lerrbuch der Kristallphysik*, Teubner-Verlag, Leipzig.

Wang, Z. (2002), 'Seismic anisotropy in sedimentary rocks, part 2: Laboratory data', *Geophysics* **67**, 1423–1440.

Wendt, A., Bayuk, I., Covey-Crump, S., Wirth, R. & Lloyd, G. (2003), 'An experimental and numerical study of the microstructural parameters contributing to the seismic anisotropy of rocks', *Journal of Geophysical Research* **108**(B8), 2365.

Wilcoxon, F. (1945), 'Individual comparisons by ranking methods', *Biometrics* **1**, 80–83.

Winterstein, D. (1986), 'Anisotropy effects in P-wave and SH-wave stacking velocities contain information on lithology', *Geophysics* **51**(3), 661–672.

Wookey, J., Kendall, J.-M. & Barroul, G. (2002), 'Mid-mantle deformation inferred from seismic anisotropy', *Nature* **415**, 777–780.

Xie, Y., Wenk, H.-R. & Matthies, S. (2003), 'Plagioclase preferred orientation by TOF neutron diffraction and SEM-EBSD', *Tectonophysics* **370**, 269–286.

Yale, D. & Jamieson, W. (1994), Static and dynamic rock mechanical properties in the Hugoton and Panoma fields, Society of Petroleum Engineers.

Appendix A

Quantifying microtexture

The integral of the texture function is used here to characterise the sharpness of a texture by a single parameter (Sturcken & Croach 1963),

$$J = \oint [f(g)]^2 dg. \tag{A.1}$$

If then the the series expansion is substituted for $f(g)$, it then follows that,

$$J = \sum_{l,\mu,\nu} \sum_{l,\dot{\mu}\dot{\nu}} C_l^{\mu\nu} C_l^{*\dot{\mu}\dot{\nu}} \oint T_l^{\mu\nu}(g) T_l^{*\dot{\mu}\dot{\nu}}(g) dg. \tag{A.2}$$

Because of the orthogonality of the generalised spherical harmonics, it logically follows that,

$$J = \sum_{l,\mu,\nu} \frac{1}{2l+1} [C_l^{\mu\nu}]^2. \tag{A.3}$$

In the instance of a random distribution of orientations,

$$J_r = 1, \tag{A.4}$$

and therefore for a single crystal,

$$J_{ideal} = \sum_{l,\mu,\nu} \frac{1}{2l+1} [T_l^{\mu\nu}(g_0)]^2 \rightarrow \infty. \tag{A.5}$$

The texture index therefore varies between 1 and ∞ in the case of random orientation and one or more ideal single crystals respectively (Bunge 1982).

It is also possible to define a measure of the sharpness of individual pole figures, similar to that of the texture index, by,

$$J_{hi} = \frac{1}{4\pi} \oint [P_{hi}(y)]^2 dy. \tag{A.6}$$

The measure of sharpness of an arbitrary pole figure can only be smaller than or at most equal to that of the *3D* ODF (Bunge 1982).

Appendix B

Sample notation

Sample number notation - small letter = refers to any number of repetitions of the same sample, X-Y-Z = refers to the direction of core that it was removed from, large letter possibly followed by a number = sample also used for palaeomagnetic re-orientation. Qtz. = quartz, Fspr. = feldspar, and Clc. = calcite. Where n/a appears, it means that the sample did not contain sufficient quantities of a mineral phase to enable its indexing. For example, 1663DY = sample number 1663, D the core was also used for palaeomagnetic re-orientation and was removed from core plug Y (parallel to bedding).

Appendix C

Experimental Analyses

Table C.1: *Sample mineralogy, porosity, permeability, and stratigraphic location. The Well refers to the number the samples was extracted from 206/8-8 or 206/13a2. Stratigraphic unit devised by Allen & Mange-Rajetzky (1992), sample depth (m), individual sample mineralogy (%), porosity (%) and permeability (mD). Qtz.- quartz, Fspr. - feldpsar, Clc./Dol. - calcite + dolomite, Phyllo. - muscovite + biotite + illite and Kaol. - kaolinite. Por. - Porosity was determined using helium porosimetry and Perm. - permeability by air porosity (Smith & Lappin 1997). The modal mineralogy of all the samples was established via quantitative X-ray diffraction. EBSD - analysed using Electron back scattered diffraction and a predicted intrinsic anisotropy was calculated. Hi P - ultrasonic analyses was conducted upon it at approximately reservoir (in situ) pressure (P-wave only). Lo P - ultrasonic analyses was conducted upon it at room temperature and pressure (P- and S-wave).* α_{ij} *- crack density tensor inversion for the* α_{ij} *parameter.* β_{ijkl} *- crack density tensor inversion for the* β_{ijkl} *parameter. Palmag - palaeomagnetic sample orientation. AMS - anisotropic magnetic susceptibility. - denotes that the sample was not analysed and * denotes that the sample was analysed using a particular technique.*

Well	Unit	Sample	Qtz.	Fspr.	Clc./Dol.	Phyllo.	Kaol.	Por.	Perm.	EBSD	Hi P	Lo P	α_{ij}	β_{ijkl}	Palmag.	AMS
8-8	VI	1663	57.60	6.81	12.37	8.13	0.00	15.10	0.65	*	-	*	-	*	*	*
8-8	VI	1763	17.02	20.64	1.90	47.35	1.18	11.90	0.00	-	-	-	-	-	-	-
8-8	VI	1784	38.64	18.26	18.26	6.20	6.65	12.00	24.00	*	*	*	*	-	-	-
8-8	VI	1788	30.89	25.41	1.32	34.38	0.00	8.00	0.02	-	*	*	*	*	*	*
8-8	VI	1841	30.97	21.77	5.92	30.24	0.00	11.10	0.07	*	*	*	*	*	*	*
8-8	V	1909	54.95	16.07	10.48	3.73	1.78	13.00	2.80	*	-	*	*	*	-	*
8-8	V	1950	44.19	30.46	7.45	3.10	0.00	14.80	84.00	*	*	*	*	*	*	*
13a2	V	1959	39.11	23.36	14.30	6.54	0.00	16.70	5.48	*	-	-	-	-	-	-
13a2	V	1963	45.77	7.69	16.46	17.43	5.55	7.10	0.15	*	-	*	-	*	*	*
13a2	V	2015	54.54	17.12	5.57	5.97	0.00	16.80	177.00	*	-	*	-	-	-	-
13a2	V	2023	54.00	19.88	2.53	6.15	1.35	16.10	12.30	*	-	*	-	-	-	-

Table C.2: *Sample mineralogy, porosity, permeability, and stratigraphic location. The Well refers to the number the samples was extracted from 206/8-8 or 206/13a2. Stratigraphic unit devised by Allen & Mange-Rajetzky (1992), sample depth (m), individual sample mineralogy (%), porosity (%) and permeability (mD). Qtz.- quartz, Fspr. - feldpsar, Clc./Dol. - calcite + dolomite, Phyllo. - muscovite + biotite + illite and Kaol. - kaolinite. Por. - Porosity was determined using helium porosimetry and Perm. - permeability by air porosity (Smith & Lappin 1997). The modal mineralogy of all the samples was established via quantitative X-ray diffraction. EBSD - analysed using Electron back scattered diffraction and a predicted intrinsic anisotropy was calculated. Hi P - ultrasonic analyses was conducted upon it at approximately reservoir (in situ) pressure (P-wave only). Lo P - ultrasonic analyses was conducted upon it at room temperature and pressure (P- and S-wave).* α_{ij} *- crack density tensor inversion for the* α_{ij} *parameter.* β_{ijkl} *- crack density tensor inversion for the* β_{ijkl} *parameter. Palmag - palaeomagnetic sample orientation. AMS - anisotropic magnetic susceptibility. - denotes that the sample was not analysed and * denotes that the sample was analysed using a particular technique.*

Well	Unit	Sample	Qtz.	Fspr.	Clc./Dol.	Phyllo.	Kaol.	Por.	Perm.	EBSD	Hi P	Lo P	α_{ij}	β_{ijkl}	Palmag.	AMS
13a2	V	2023	54.00	19.88	2.53	6.15	1.35	16.10	12.30	*	-	*	-	-	-	-
13a2	V	2028	49.60	19.98	0.71	9.72	1.18	18.80	4.84	*	*	*	-	*	-	*
13a2	V	2034	39.96	16.02	0.32	19.86	5.45	18.40	138.00	*	-	*	-	-	-	-
8-8	V	2070	47.46	17.57	7.75	7.75	7.06	12.40	3.80	*	-	*	-	*	*	*
8-8	V	2073	46.78	16.85	6.13	15.95	3.79	10.50	0.05	*	-	*	-	*	*	*
8-8	V	2088	53.79	14.57	2.30	19.34	0.00	10.00	1.20	-	*	*	-	*	*	*
8-8	I-III	2129	74.30	8.22	2.51	0.78	0.00	14.20	79.00	*	*	*	*	*	*	*
8-8	I-III	2192	63.76	9.51	6.43	3.17	1.63	15.50	55.00	*	*	*	*	*	*	*
8-8	I-III	2194	61.05	12.62	8.06	1.70	4.48	12.10	1.40	*	*	*	*	*	*	*
8-8	I-III	2198	58.49	13.58	6.32	13.11	0.00	8.50	0.36	*	*	*	-	*	*	*

Appendix D

Single crystal elastic tensors

Quartz, $\rho = 2.65$ (Mcskimin et al. 1965).

$$\begin{pmatrix} 0.8680 & 0.0704 & 0.1191 & -0.1804 & 0.0000 & 0.0000 \\ 0.0704 & 0.8680 & 0.1191 & 0.1804 & 0.0000 & 0.0000 \\ 0.1191 & 0.1191 & 1.0575 & 0.0000 & 0.0000 & 0.0000 \\ -0.1804 & 0.1804 & 0.0000 & 0.5820 & 0.0000 & 0.0000 \\ 0.0000 & 0.0000 & 0.0000 & 0.0000 & 0.5820 & -0.1804 \\ 0.0000 & 0.0000 & 0.0000 & 0.0000 & -0.1804 & 0.3988 \end{pmatrix} \tag{D.1}$$

Orthoclase, $\rho = 2.57$ (Hcarmon 1984).

$$\begin{pmatrix} 0.5960 & 0.3440 & 0.2800 & 0.0000 & -0.1700 & 0.0000 \\ 0.3440 & 1.5680 & 0.2160 & 0.0000 & -0.0590 & 0.0000 \\ 0.2800 & 0.2160 & 1.1950 & 0.0000 & -0.1290 & 0.0000 \\ 0.0000 & 0.0000 & 0.0000 & 0.1360 & 0.0000 & -0.0180 \\ -0.1700 & -0.0590 & -0.1290 & 0.0000 & 0.2260 & 0.0000 \\ 0.0000 & 0.0000 & 0.0000 & -0.0180 & 0.0000 & 0.3420 \end{pmatrix} \tag{D.2}$$

Calcite, $\rho = 2.71$ (Dandekar 1968).

$$\begin{pmatrix} 1.4627 & 0.5971 & 0.5076 & -0.2076 & 0.0000 & 0.0000 \\ 0.5971 & 1.4627 & 0.5076 & 0.2076 & 0.0000 & 0.0000 \\ 0.5076 & 0.5076 & 0.8531 & 0.0000 & 0.0000 & 0.0000 \\ -0.2076 & 0.2076 & 0.0000 & 0.3405 & 0.0000 & 0.0000 \\ 0.0000 & 0.0000 & 0.0000 & 0.0000 & 0.3405 & -0.2076 \\ 0.0000 & 0.0000 & 0.0000 & 0.0000 & -0.2076 & 0.4328 \end{pmatrix} \quad \text{(D.3)}$$

Muscovite, $\rho = 2.84$ (Bingham distribution).

$$\begin{pmatrix} 1.4648 & 0.3907 & 0.2970 & 0.0000 & 0.0000 & 0.0000 \\ 0.3907 & 1.4648 & 0.2970 & 0.0000 & 0.0000 & 0.0000 \\ 0.2970 & 0.2970 & 0.6505 & 0.0000 & 0.0000 & 0.0000 \\ 0.0000 & 0.0000 & 0.0000 & 0.2432 & 0.0000 & 0.0000 \\ 0.0000 & 0.0000 & 0.0000 & 0.0000 & 0.2432 & 0.0000 \\ 0.0000 & 0.0000 & 0.0000 & 0.0000 & 0.0000 & 0.2432 \end{pmatrix} \quad \text{(D.4)}$$

Kaolinite, $\rho = 2.64$ (Hearmon 1984).

$$\begin{pmatrix} 0.77867 & 0.30067 & 0.30067 & 0.000 & 0.0000 & 0.0000 \\ 0.30067 & 0.77867 & 0.30067 & 0.0000 & 0.0000 & 0.0000 \\ 0.30067 & 0.30067 & 0.77867 & 0.0000 & 0.0000 & 0.0000 \\ 0.0000 & 0.0000 & 0.0000 & 0.239 & 0.0000 & 0.0000 \\ 0.0000 & 0.0000 & 0.0000 & 0.0000 & 0.239 & 0.0000 \\ 0.0000 & 0.0000 & 0.0000 & 0.0000 & 0.0000 & 0.239 \end{pmatrix} \quad \text{(D.5)}$$

Gas, $\rho = 0.179$ (Vargaftik et al. 1983).

$$\begin{pmatrix} 0.00073 & 0.00073 & 0.00073 & 0.0000 & 0.0000 & 0.0000 \\ 0.00073 & 0.00073 & 0.00073 & 0.0000 & 0.0000 & 0.0000 \\ 0.00073 & 0.00073 & 0.00073 & 0.0000 & 0.0000 & 0.0000 \\ 0.0000 & 0.0000 & 0.0000 & 0.0000 & 0.0000 & 0.0000 \\ 0.0000 & 0.0000 & 0.0000 & 0.0000 & 0.0000 & 0.0000 \\ 0.0000 & 0.0000 & 0.0000 & 0.0000 & 0.0000 & 0.0000 \end{pmatrix} \quad \text{(D.6)}$$

Appendix E

Quartz pole figures

Figure E.1: *Non-polar, lower hemisphere, crystallographic stereonets of quartz poles to lattice planes (1663m - 1909m). For an explanation of figure details see Figure (5.14).*

Figure E.2: *Non-polar, lower hemisphere, crystallographic stereonets of quartz poles to lattice planes (1950m - 2028m). For an explanation of figure details see Figure (5.14).*

Figure E.3: *Non-polar, lower hemisphere, crystallographic stereonets of quartz poles to lattice planes (2028m - 2194m). For an explanation of figure details see Figure (5.14).*

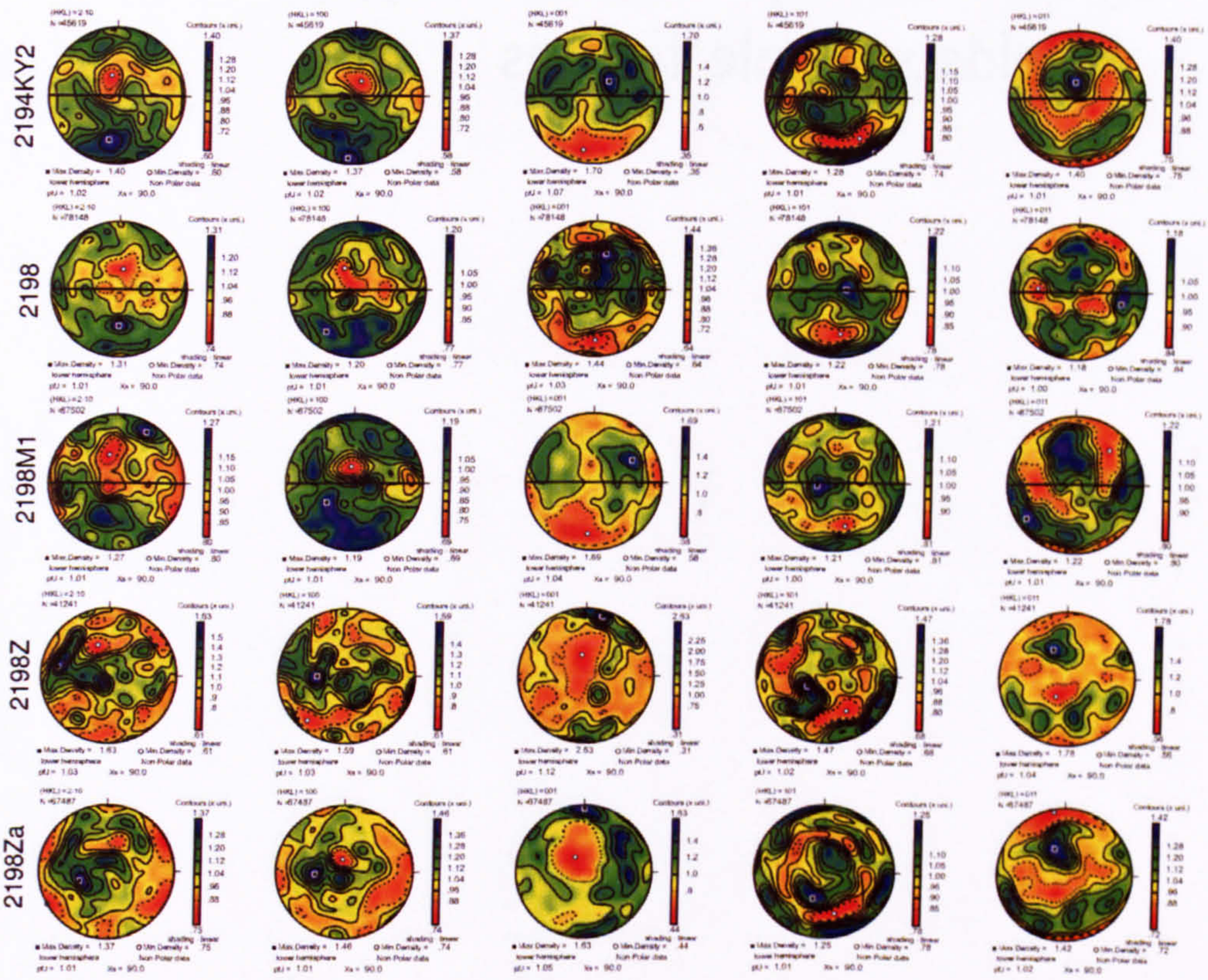

Figure E.4: *Non-polar, lower hemisphere, crystallographic stereonets of quartz poles to lattice planes (2194m - 2198m). For an explanation of figure details see Figure (5.14).*

Appendix F

Feldspar pole figures

Figure F.1: *Illustrative non-polar, lower hemisphere, crystallographic stereonets of feldspar (1663m - 1909m). For an explanation of figure details see Figure (5.15).*

Figure F.2: *Illustrative non-polar, lower hemisphere, crystallographic stereonets of feldspar (1950m - 2028m). For an explanation of figure details see Figure (5.15).*

Figure F.3: *Illustrative non-polar, lower hemisphere, crystallographic stereonets of feldspar (2028m - 2194m). For an explanation of figure details see Figure (5.15).*

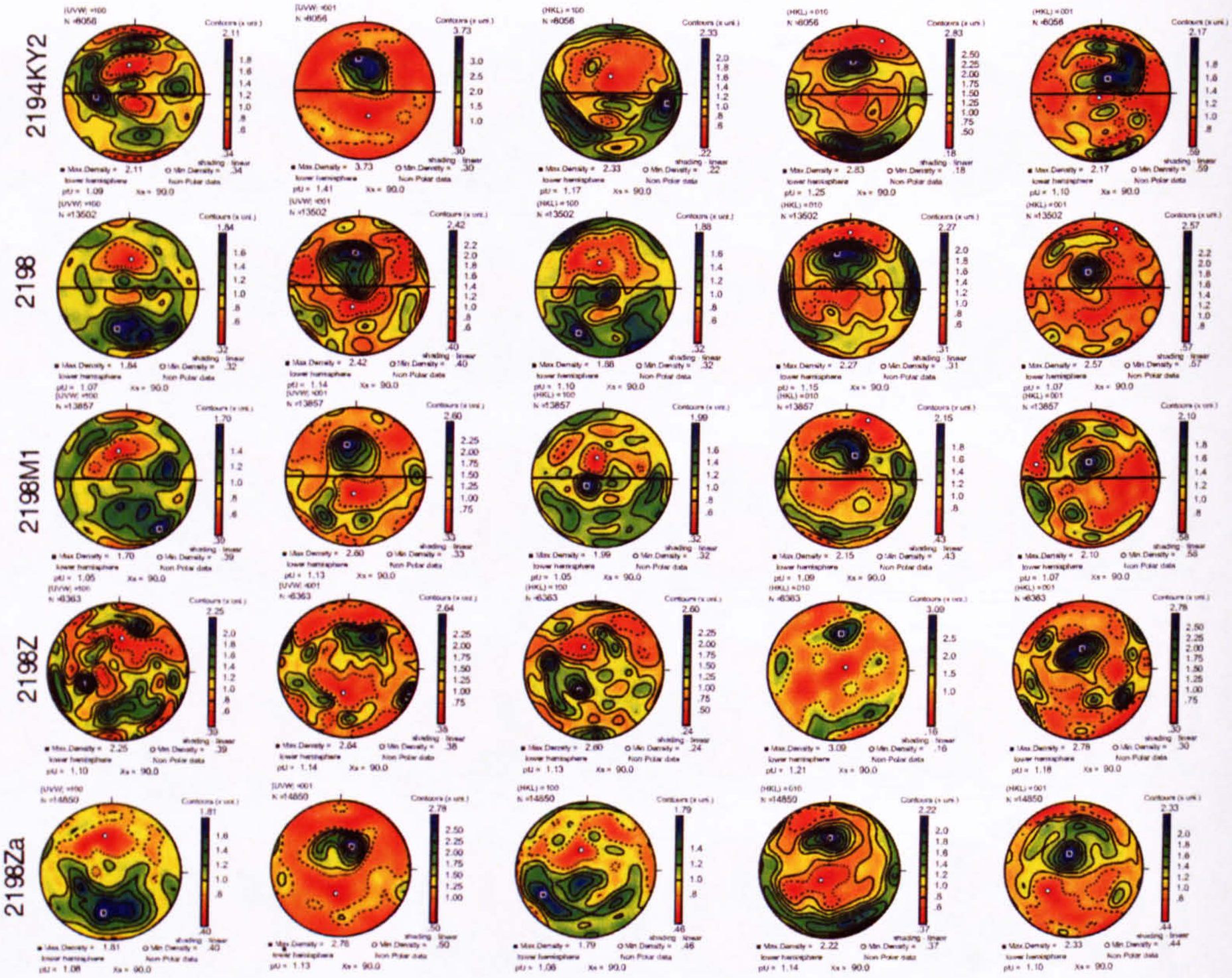

Figure F.4: *Illustrative non-polar, lower hemisphere, crystallographic stereonets of feldspar (2194m - 2198m). For an explanation of figure details see Figure (5.15).*

Appendix G

Calcite pole figures

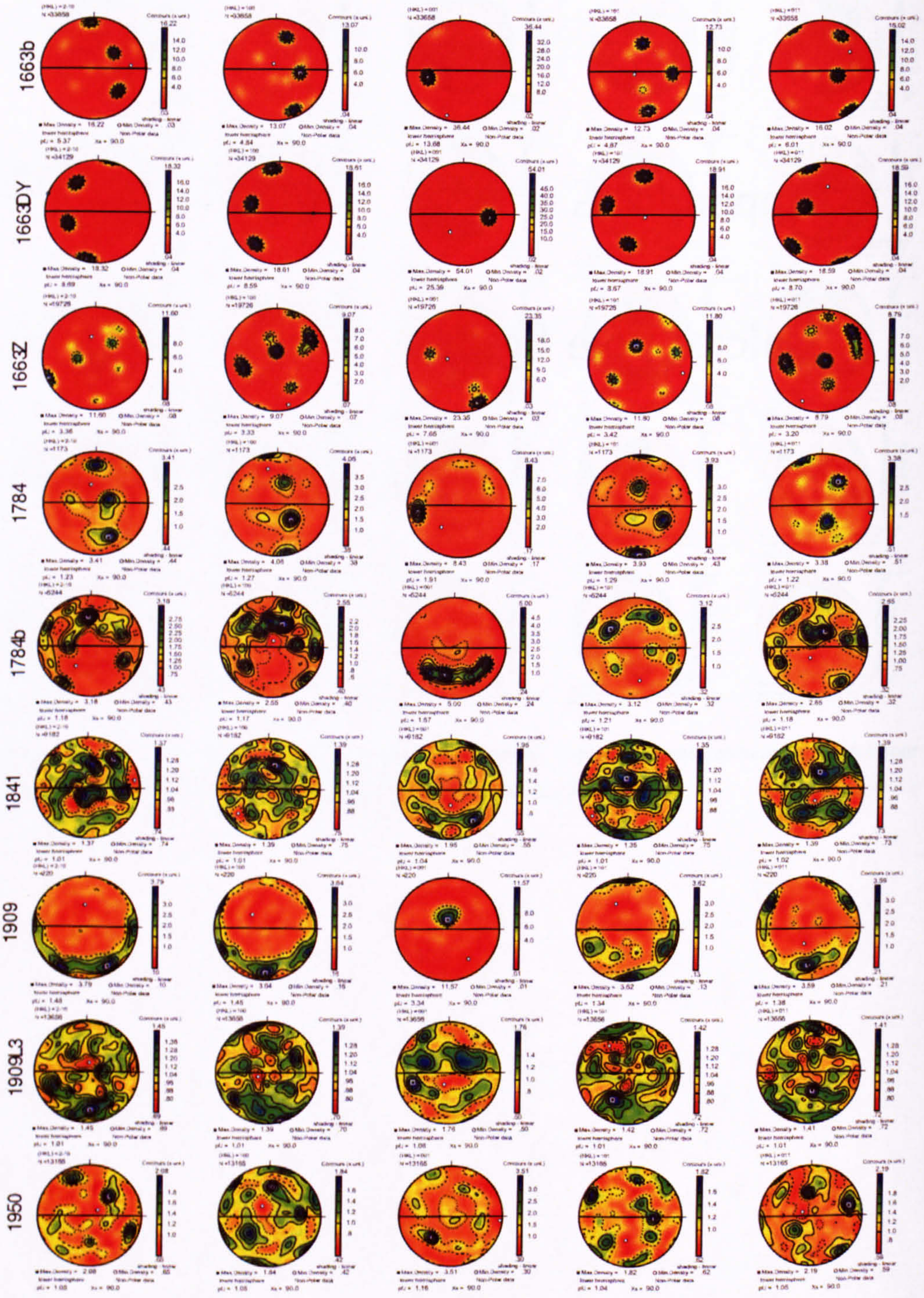

Figure G.1: *Illustrative non-polar, lower hemisphere, crystallographic stereonets of calcite (1663m - 1950m). For an explanation of figure details see Figure (5.16).*

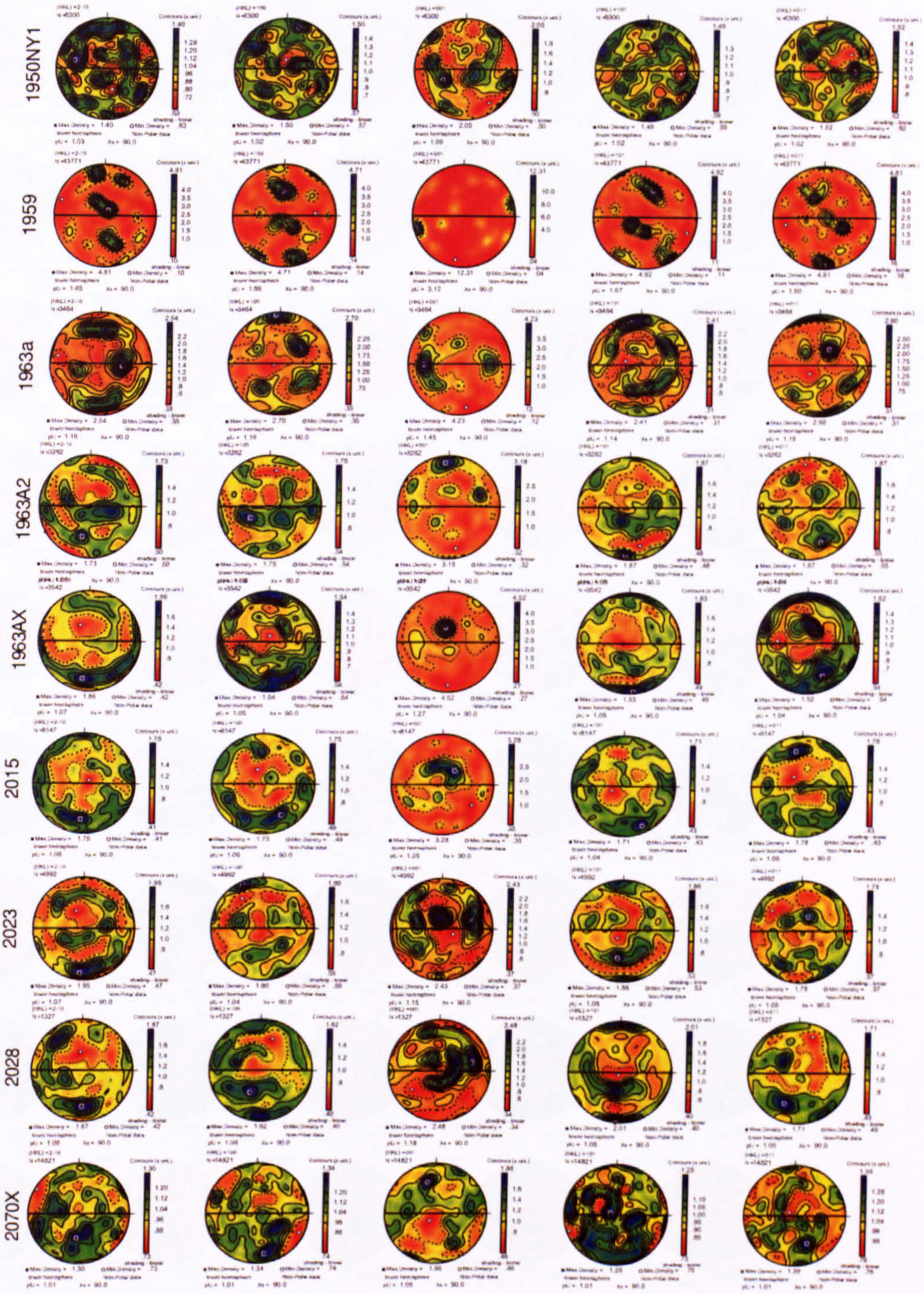

Figure G.2: *Illustrative non-polar, lower hemisphere, crystallographic stereonets of calcite (1950m - 2070m). For an explanation of figure details see Figure (5.16).*

Figure G.3: *Illustrative non-polar, lower hemisphere, crystallographic stereonets of calcite (2073m - 2198m). For an explanation of figure details see Figure (5.16).*

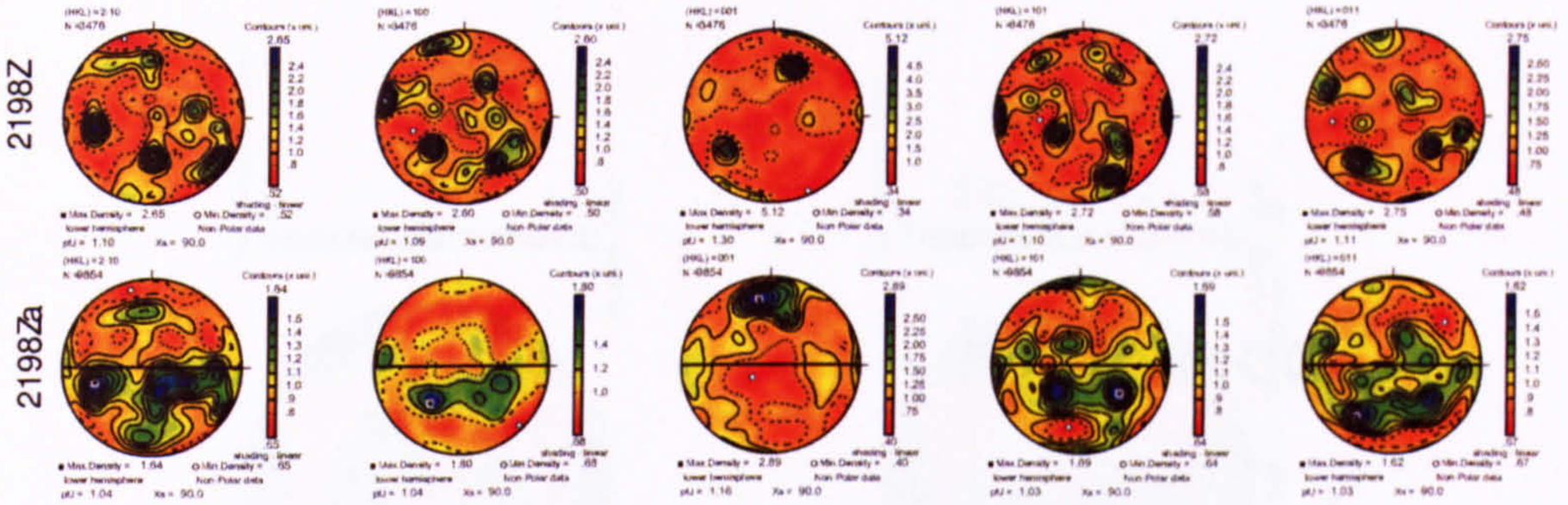

Figure G.4: *llustrative non-polar, lower hemisphere, crystallographic stereonets of calcite (2198m). For an explanation of figure details see Figure (5.16).*

Appendix H

Crystal velocity pole figures

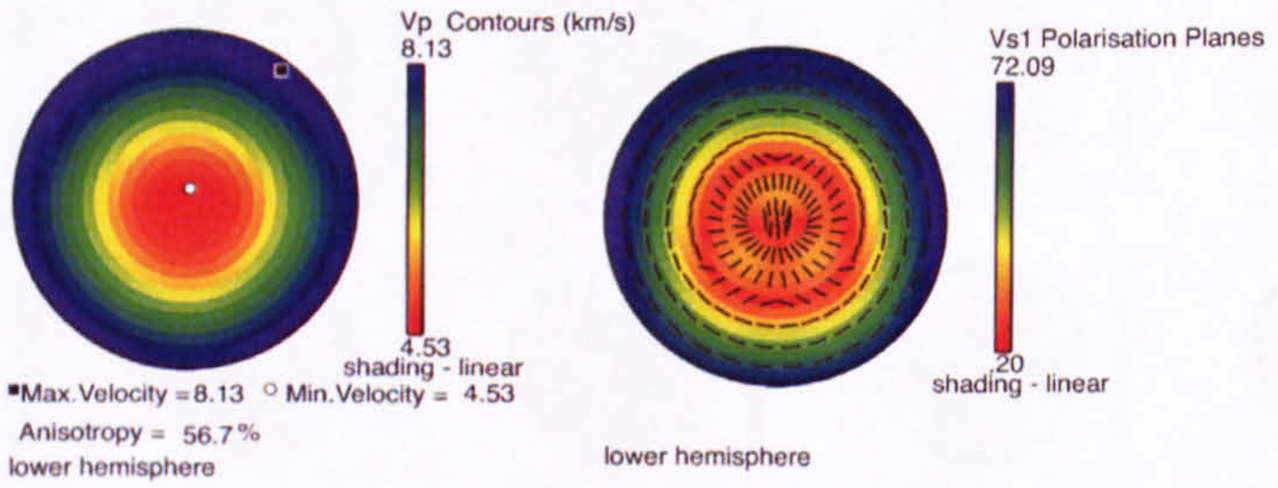

Figure H.1: *Illustrative lower hemisphere velocity pole figures for single crystal muscovite (looking down onto the bedding plane). Bedding is represented by the perimeter of the circle. The pole figures from left-to-right represent: P-wave velocity distribution, and degree of shear-wave splitting (%) , the black ticks represent the polarisation of the fast shear-wave. Blue - High velocity/anisotropy, and Red - Low velocity/ansiotropy. The P-wave pole figure also shows the location of the maximum (black square) and minimum anisotropy (white circle) with the degree of P-wave anisotropy calculated in per cent.*

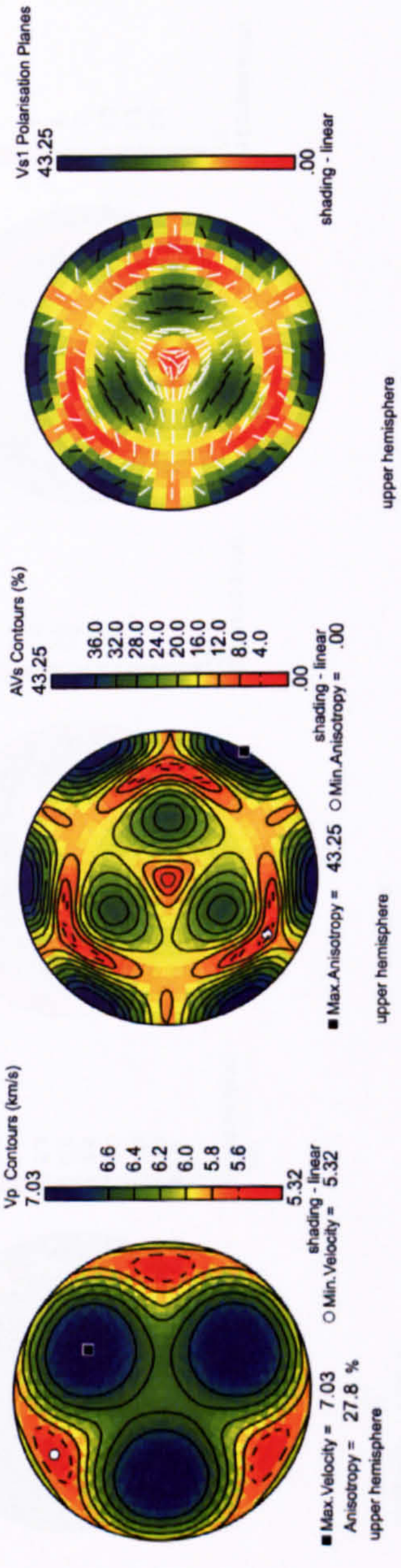

Figure H.2: *Single crystal seismic properties for quartz. Upper hemisphere, pole figure plots of maximum (black square) and minimum (white dot) velocity (km/s) and anisotropy (%). Black and white tick marks represent fast shear-wave polarisation orientation. Top (from L-R): Vp is the P-wave velocities, AVs indicates the degree of shear-wave splitting, and Vs_1 is the fast shear-wave anisotropy, and polarisation orientation. Bottom (from L-R): Vs_1 is the fast shear-wave velocity, Vs_2 is the slow shear-wave velocity, and dVs is the difference in velocity between the fast and slow shear-wave. Note that the contour intervals are not the same for every diagram.*

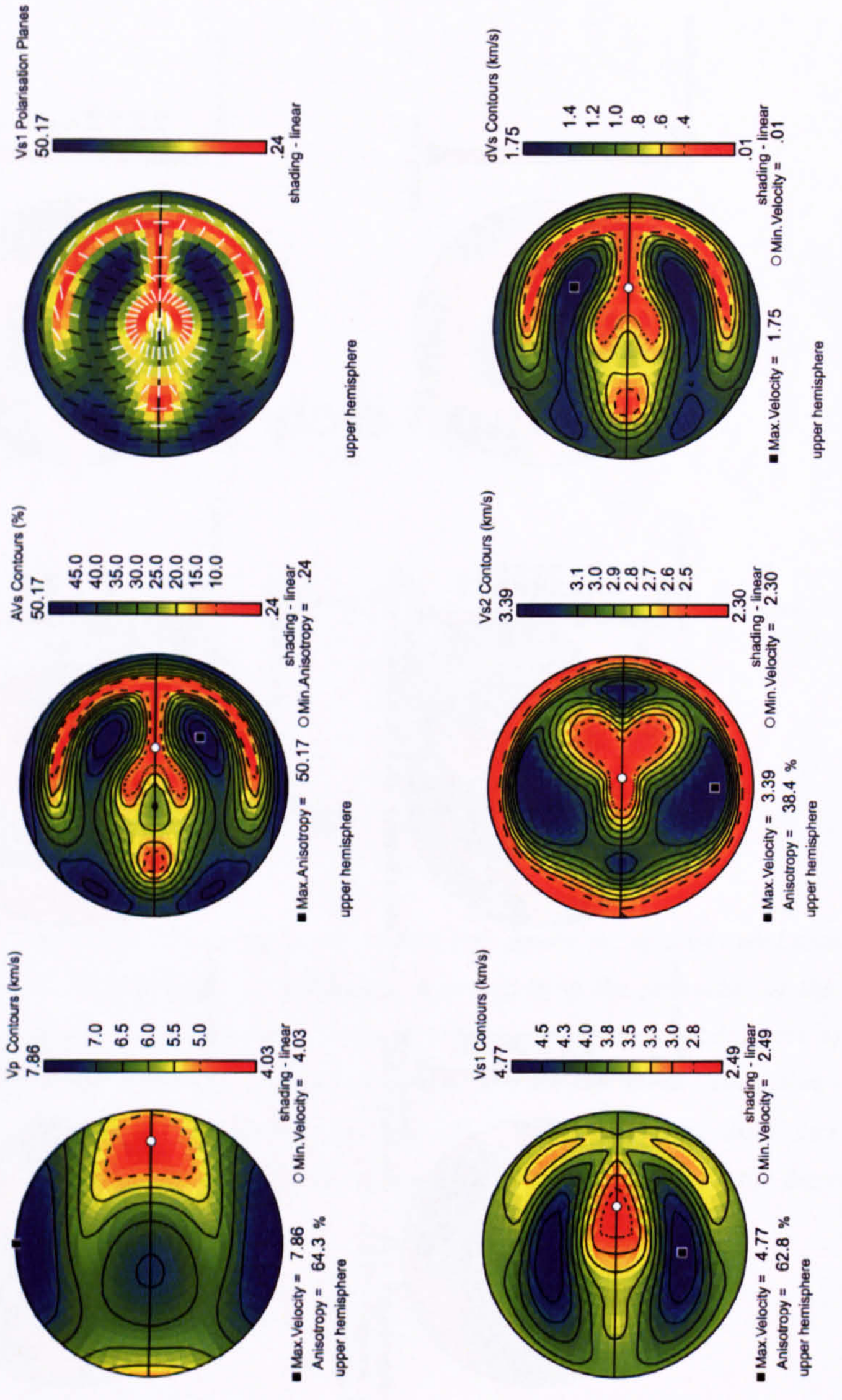

Figure H.3: *Single crystal seismic properties for orthoclase. Upper hemisphere, pole figure plots of maximum (black square) and minimum (white dot) velocity (km/s) and anisotropy (%). Black and white tick marks represent fast shear-wave polarisation orientation. Top (from L-R): Vp is the P-wave velocities, AVs indicates the degree of shear-wave splitting, and Vs_1 is the fast shear-wave anisotropy, and polarisation orientation. Bottom (from L-R): Vs_1 is the fast shear-wave velocity, Vs_2 is the slow shear-wave velocity, and dVs is the difference in velocity between the fast and slow shear-wave. Note that the contour intervals are not the same for every diagram.*

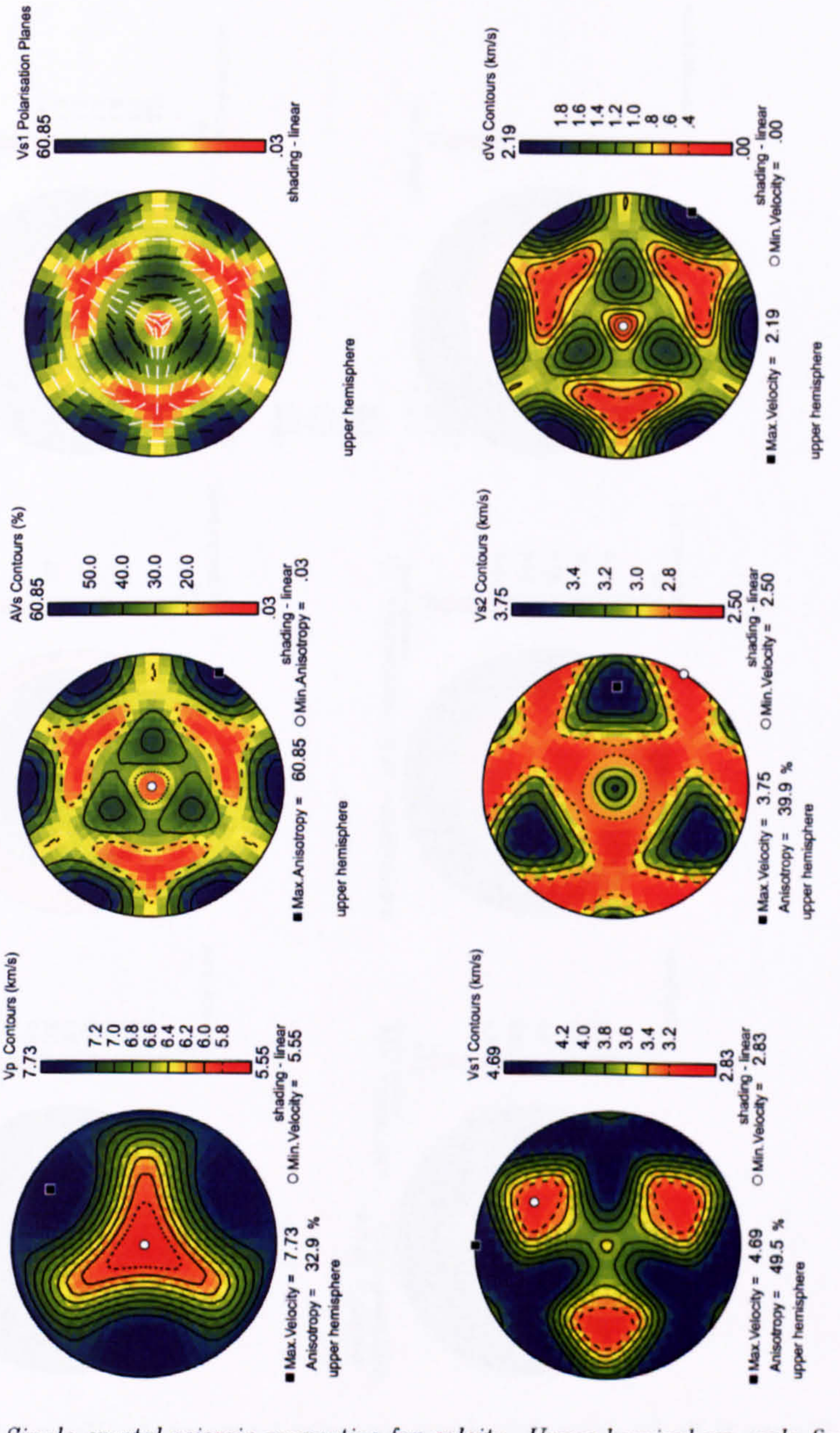

Figure H.4: *Single crystal seismic properties for calcite. Upper hemisphere, pole figure plots of maximum (black square) and minimum (white dot) velocity (km/s) and anisotropy (%). Black and white tick marks represent fast shear-wave polarisation orientation. Top (from L-R): Vp is the P-wave velocities, AVs indicates the degree of shear-wave splitting, and Vs_1 is the fast shear-wave anisotropy, and polarisation orientation. Bottom (from L-R): Vs_1 is the fast shear-wave velocity, Vs_2 is the slow shear-wave velocity, and dVs is the difference in velocity between the fast and slow shear-wave. Note that the contour intervals are not the same for every diagram.*

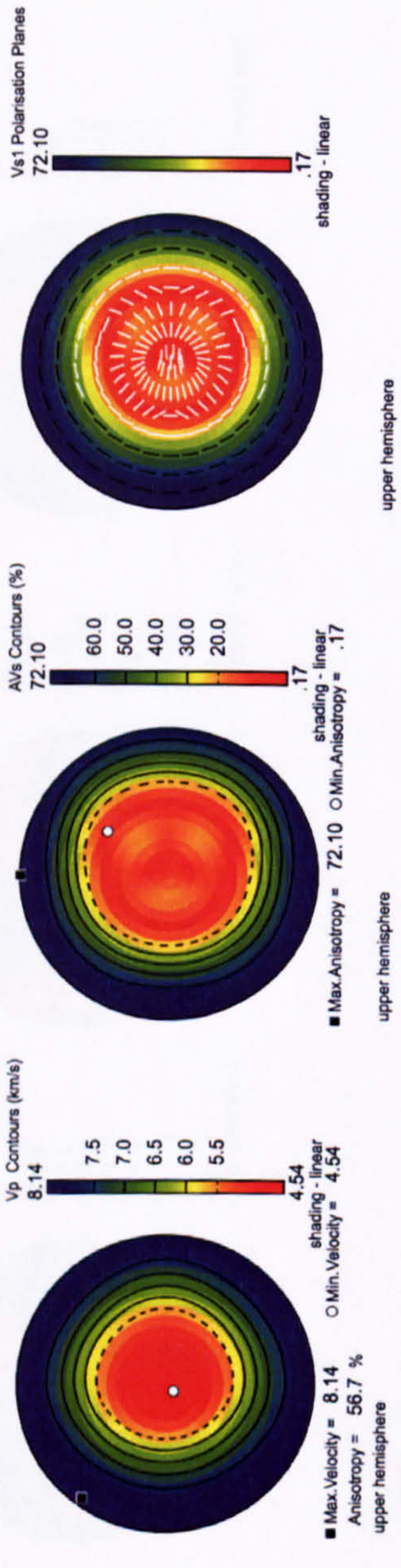

Figure H.5: *Single crystal seismic properties for muscovite. Upper hemisphere, pole figure plots of maximum (black square) and minimum (white dot) velocity (km/s) and anisotropy (%). Black and white tick marks represent fast shear-wave polarisation orientation. Top (from L-R): Vp is the P-wave velocities, AVs indicates the degree of shear-wave splitting, and Vs_1 is the fast shear-wave anisotropy, and polarisation orientation. Bottom (from L-R): Vs_1 is the fast shear-wave velocity, Vs_2 is the slow shear-wave velocity, and dVs is the difference in velocity between the fast and slow shear-wave. Note that the contour intervals are not the same for every diagram.*

Appendix I

Quartz velocity pole figures

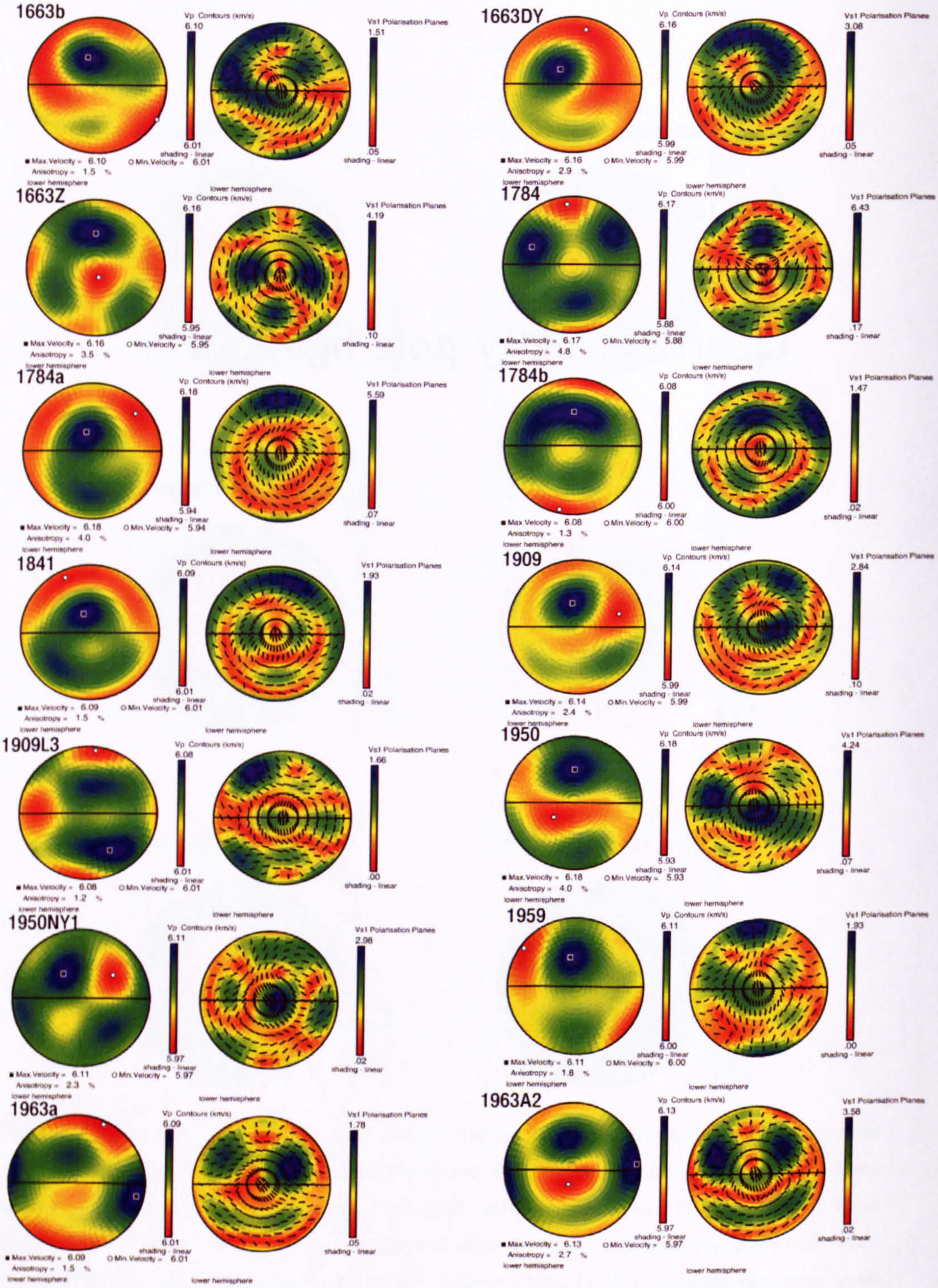

Figure I.1: *Quartz (1663m - 1963m) - P- and S-wave velocity-anisotropy pole figures. For an explanation of the diagram notation see Figure (H.1).*

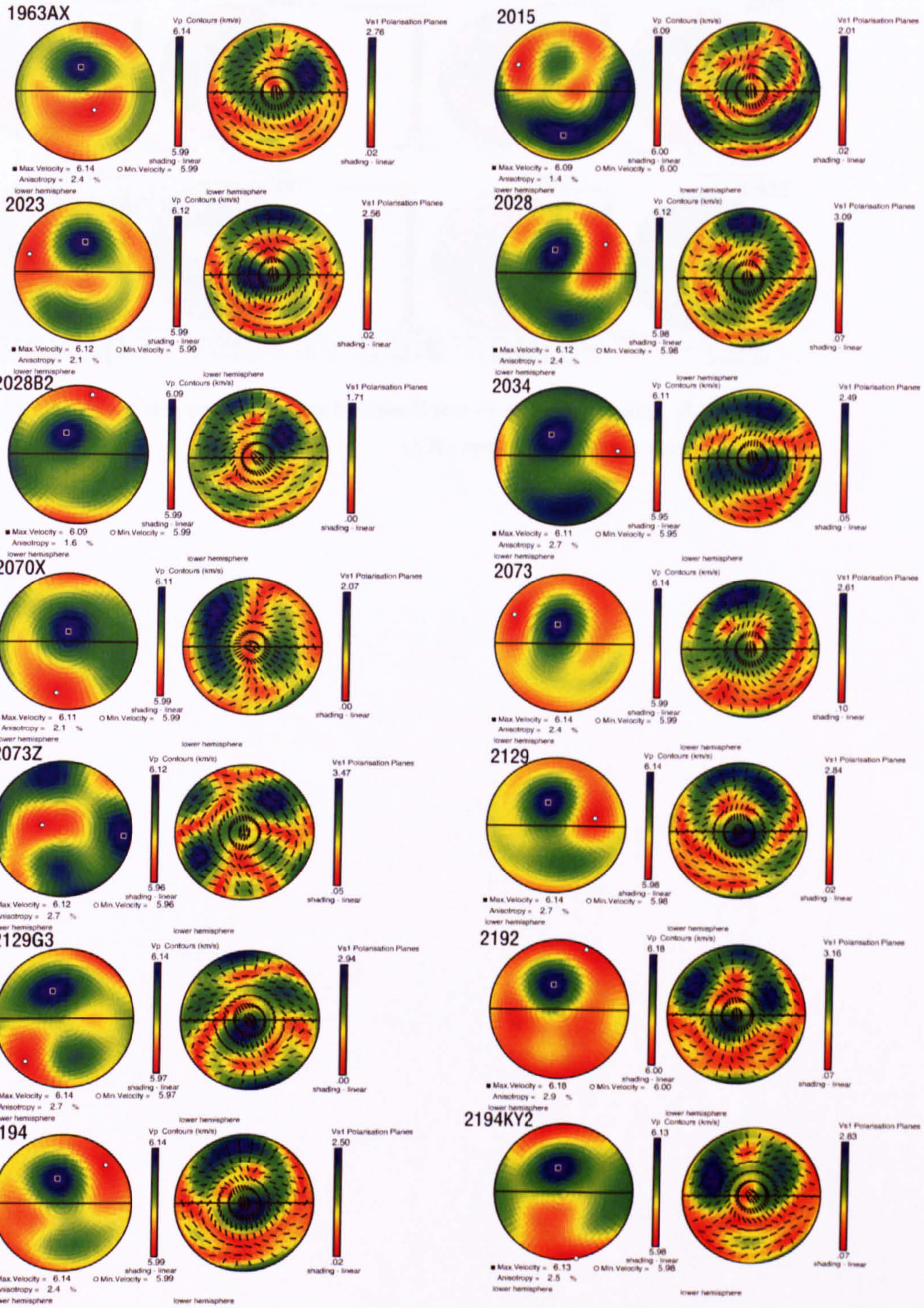

Figure I.2: *Quartz (1963m - 2194m) - P- and S-wave velocity-anisotropy pole figures. For an explanation of the diagram notation see Figure (H.1).*

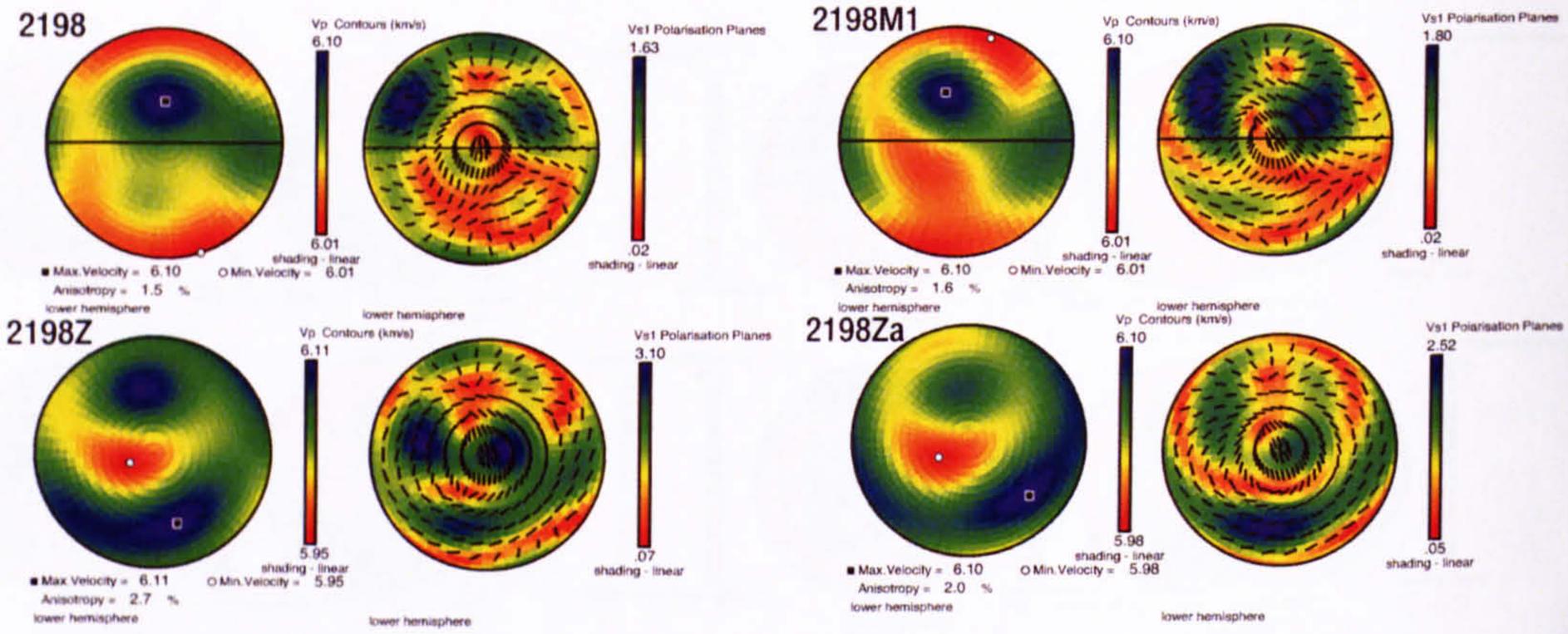

Figure I.3: *Quartz (2198m) - P- and S-wave velocity-anisotropy pole figures. For an explanation of the diagram notation see Figure (H.1).*

Appendix J

Feldspar velocity pole figures

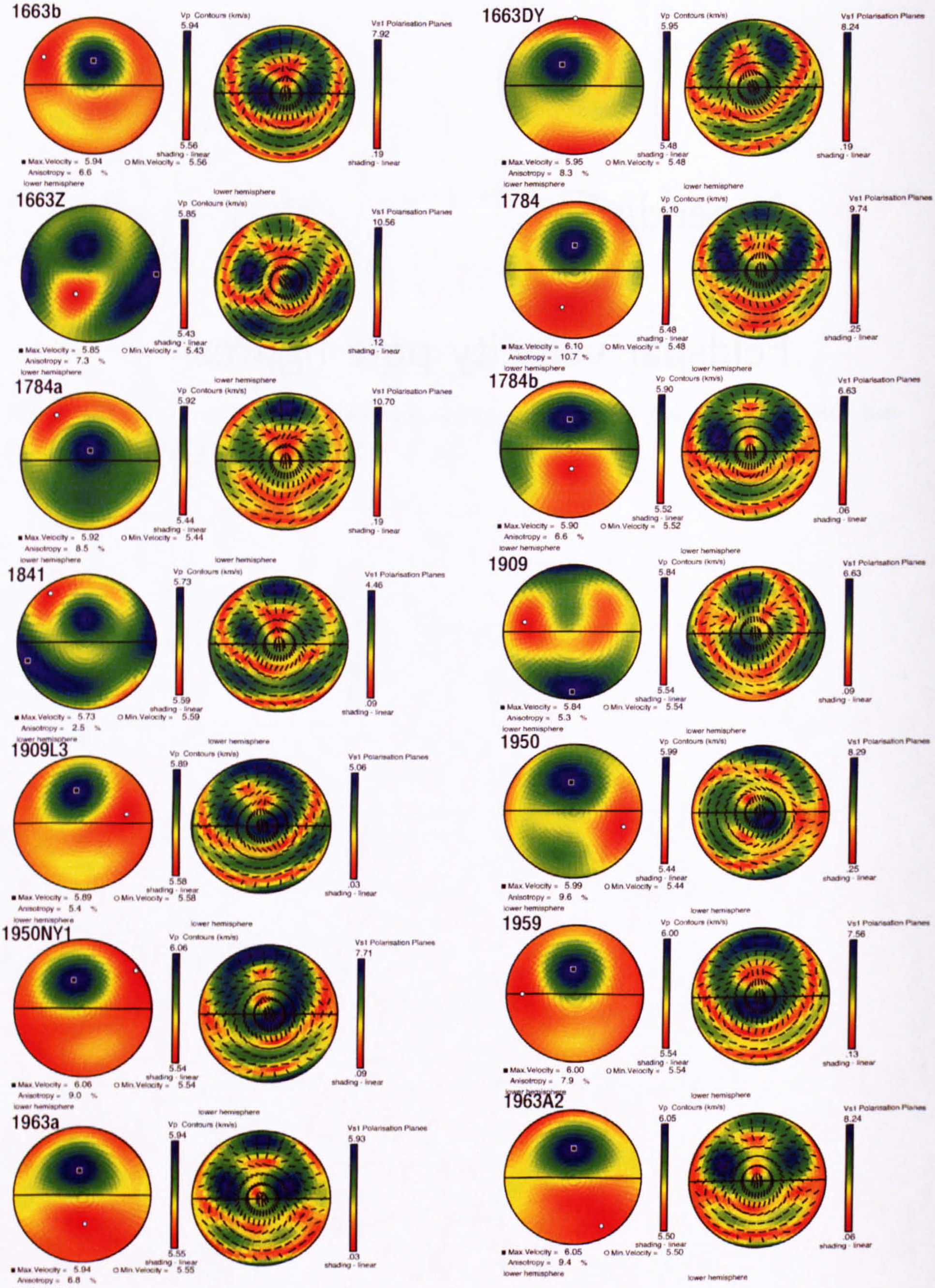

Figure J.1: *Feldspar (1663m - 1963m) - P- and S-wave velocity-anisotropy pole figures. For an explanation of the diagram notation see Figure (H.1).*

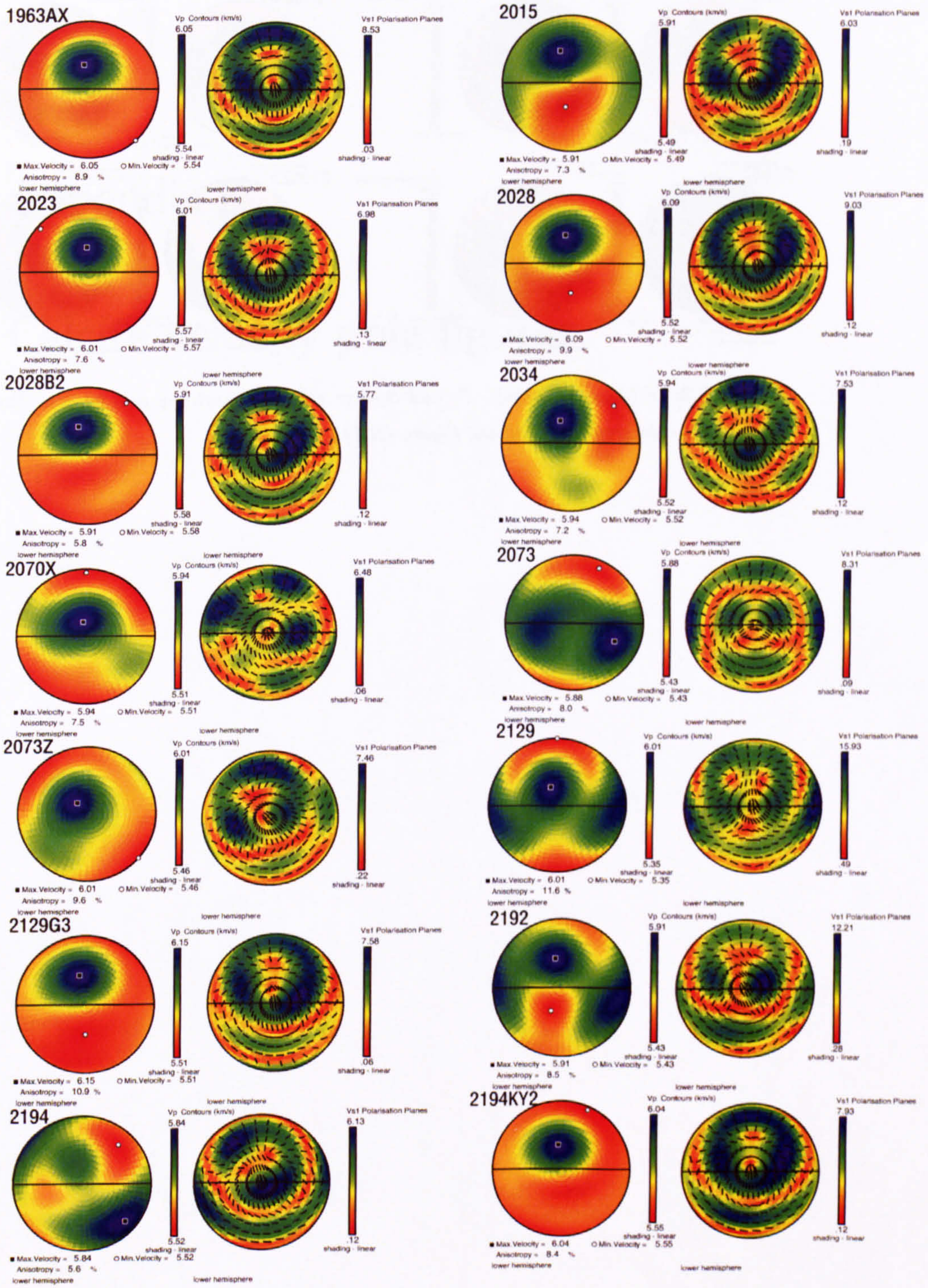

Figure J.2: *Feldspar (1963m - 2194m) - P- and S-wave velocity-anisotropy pole figures. For an explanation of the diagram notation see Figure (H.1).*

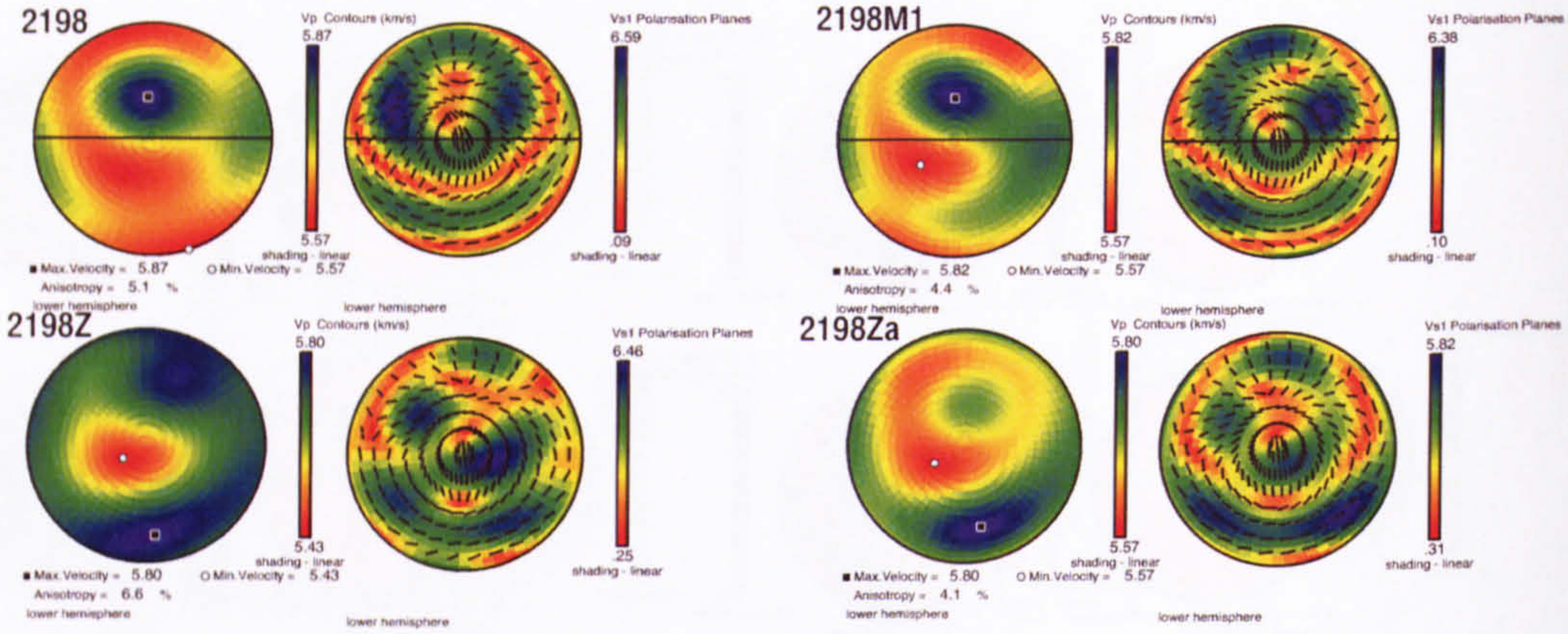

Figure J.3: *Feldspar (2198m) - P- and S-wave velocity-anisotropy pole figures. For an explanation of the diagram notation see Figure (H.1).*

Appendix K

Calcite velocity pole figures

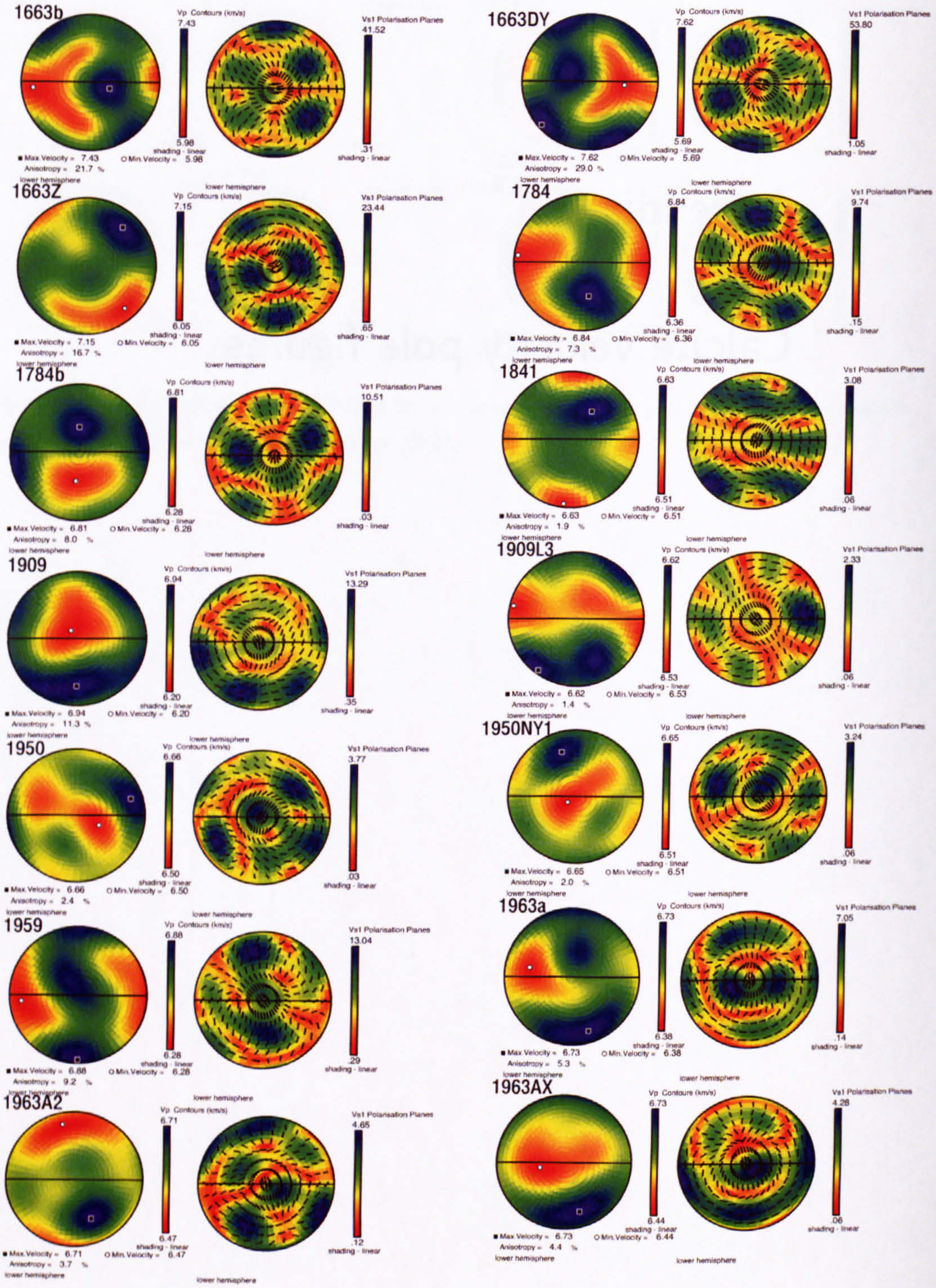

Figure K.1: *Calcite (1663m - 1963m) - P- and S-wave velocity, and anisotropy pole figures assuming 100% modal proportion. For an explanation of the diagram see Figure (H.1).*

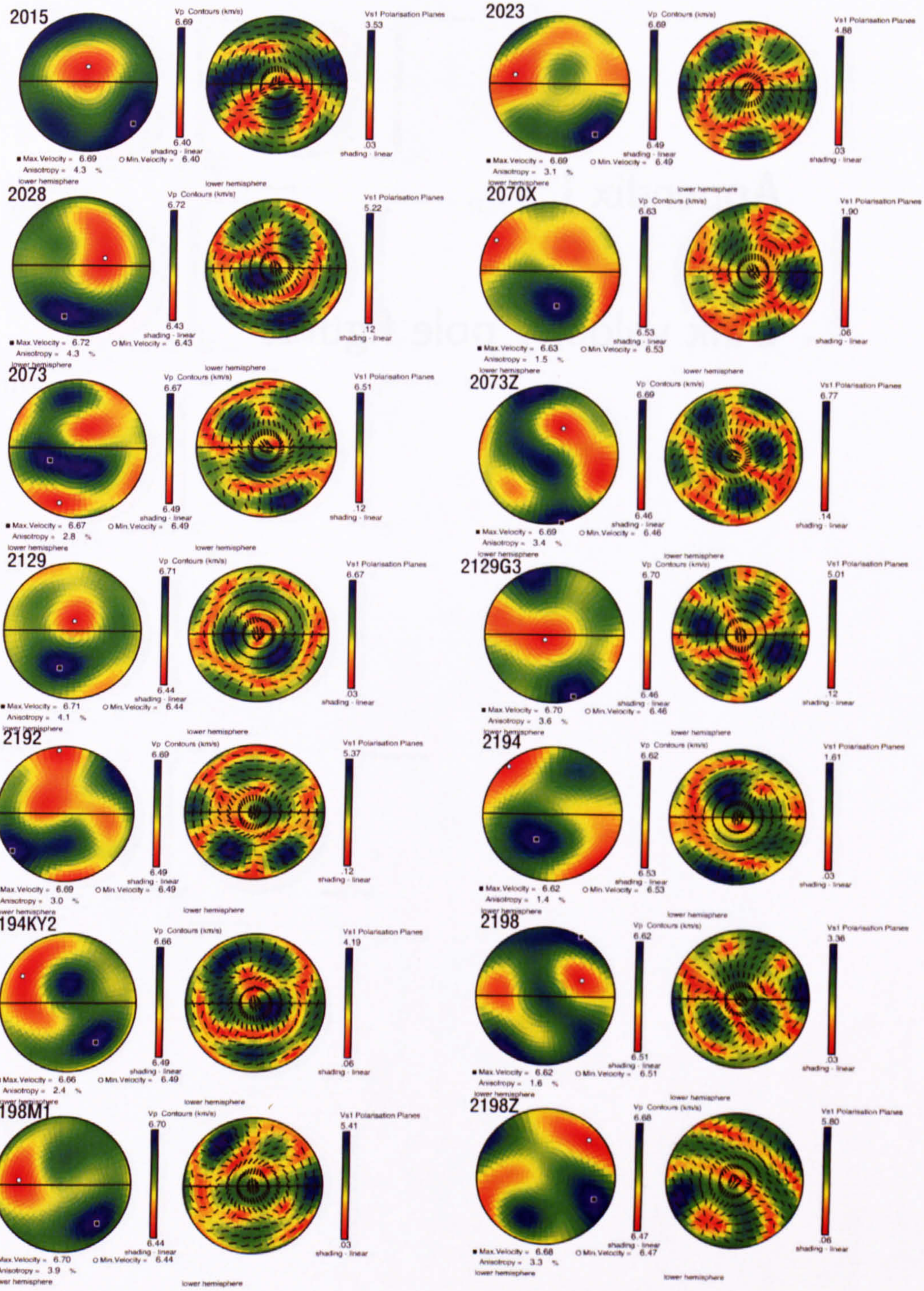

Figure K.2: *Calcite (2015m - 2198m) - P- and S-wave velocity, and anisotropy pole figures assuming 100% modal proportion. For an explanation of the diagram see Figure (H.1).*

Appendix L

Bulk velocity pole figures

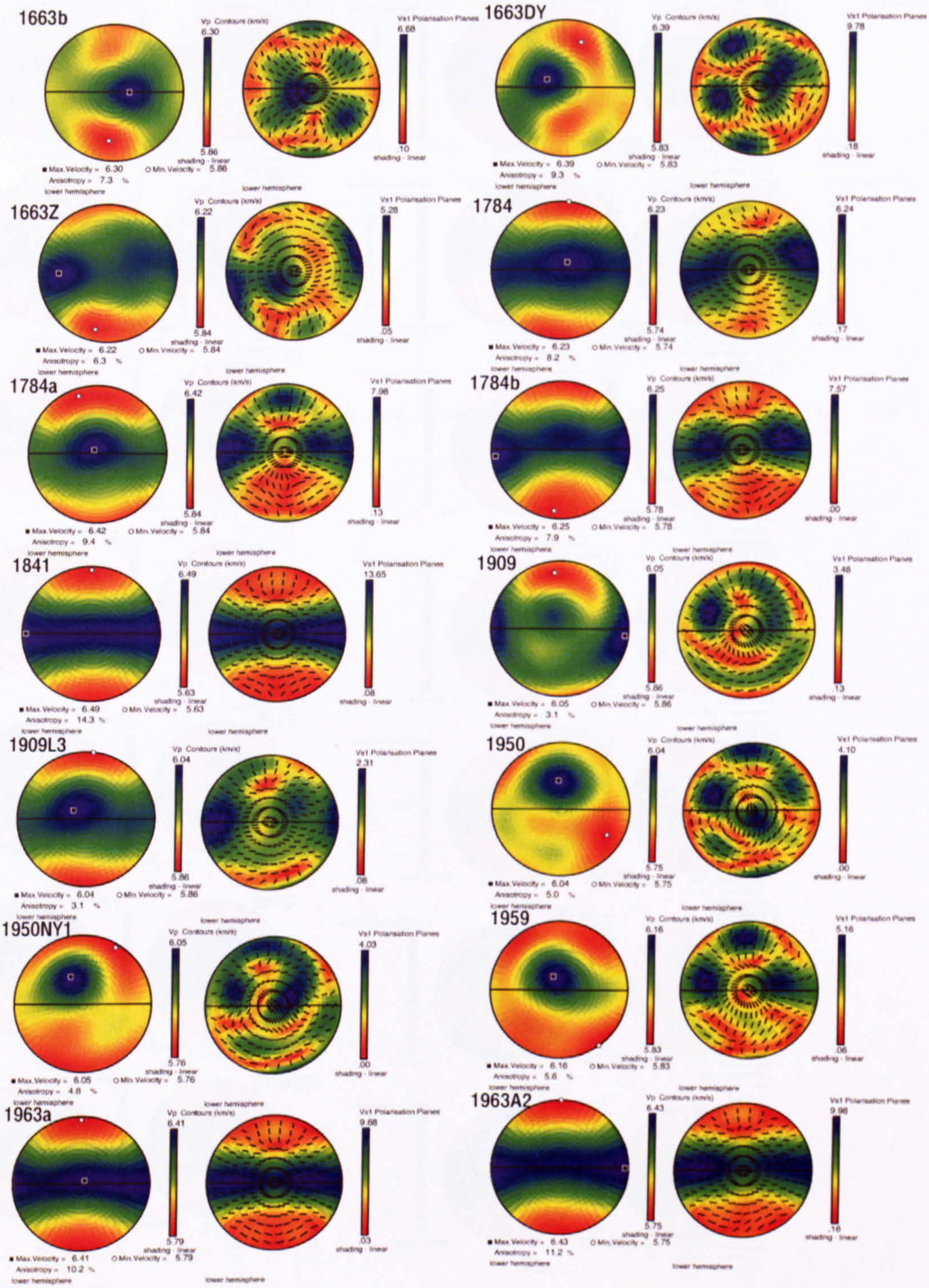

Figure L.1: *Bulk aggregate velocity, and anisotropy pole figure predictions from 1663m - 1963m. For diagram explanation see Figure (H.1).*

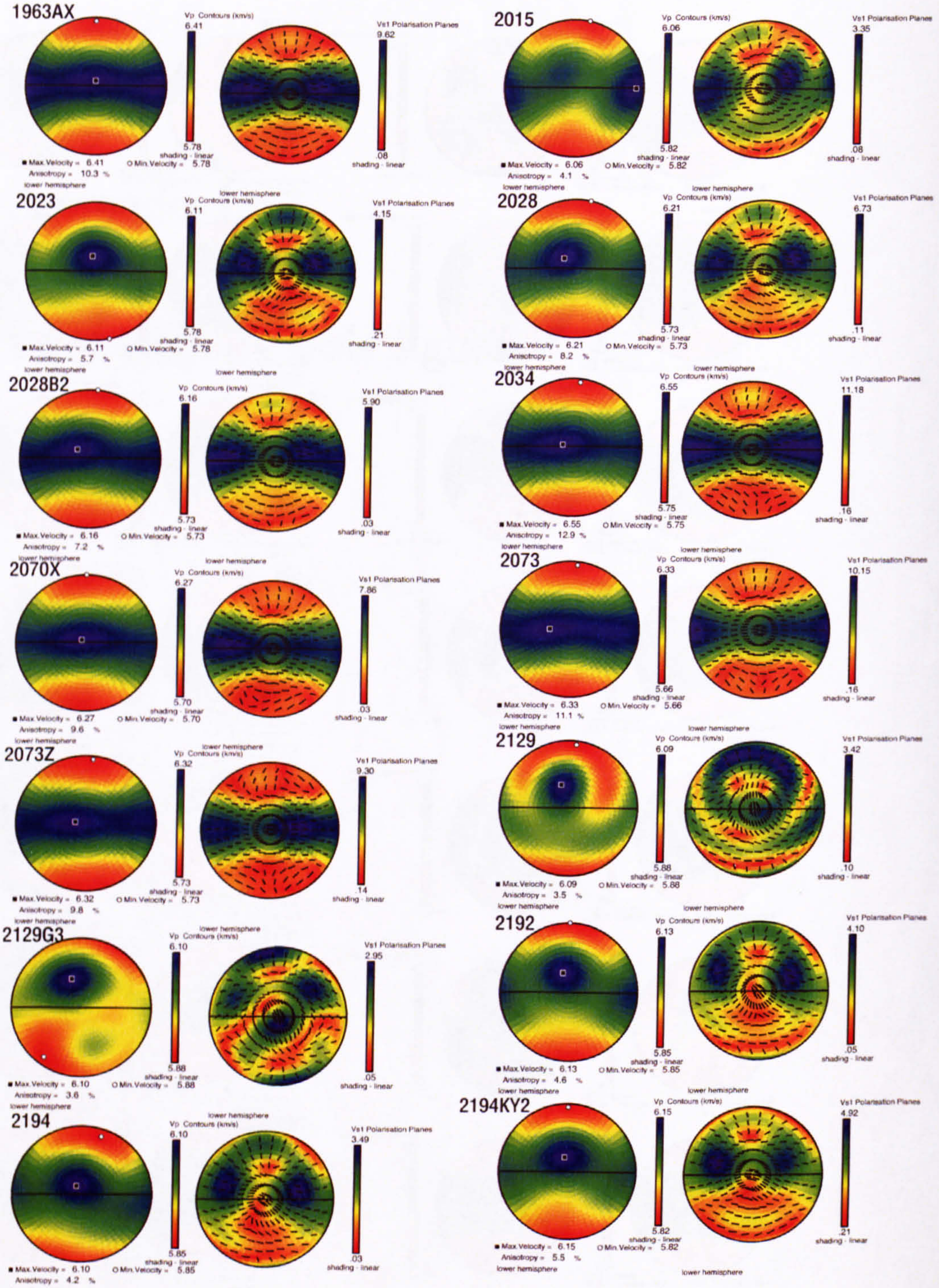

Figure L.2: *Bulk aggregate velocity and anisotropy pole figure predictions from 1963m - 2194m. For diagram explanation see Figure (H.1).*

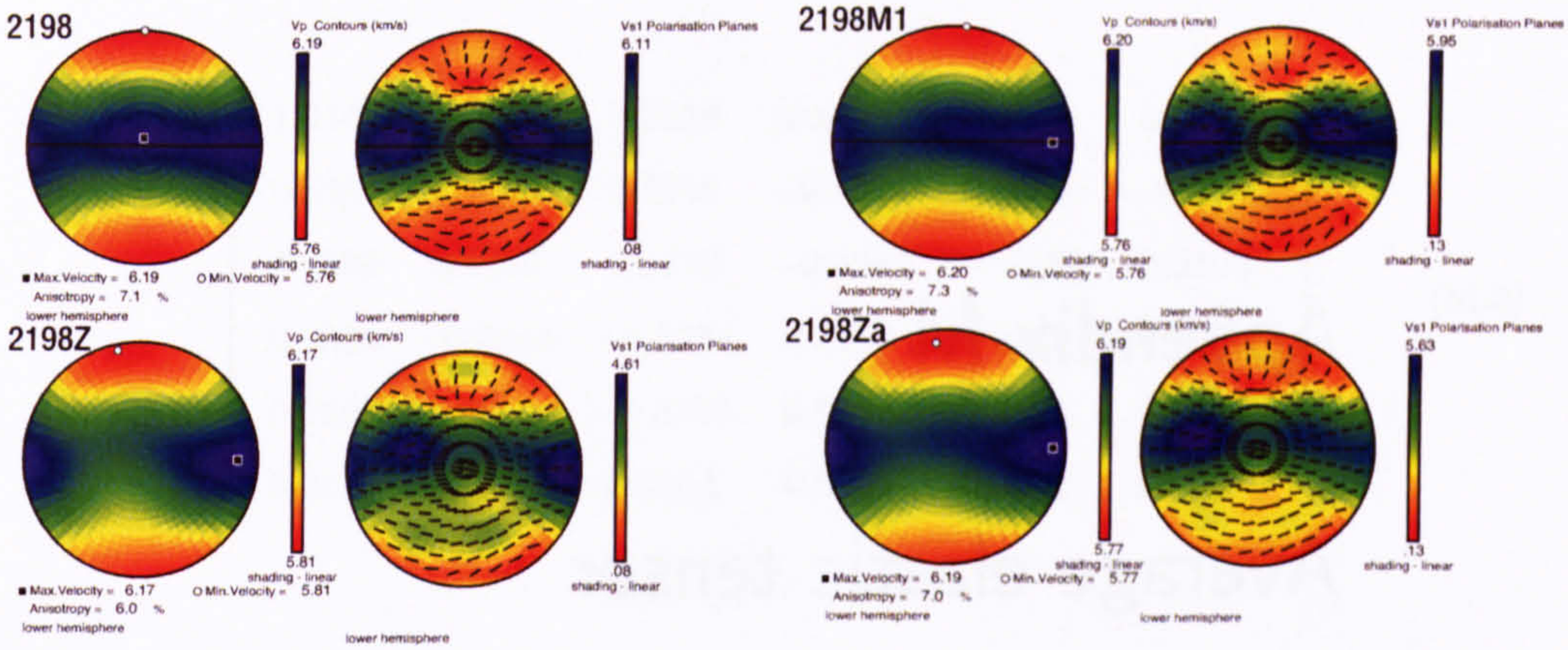

Figure L.3: *Bulk aggregate velocity and anisotropy pole figure predictions, for 2198m. For diagram explanation see Figure (H.1).*

Appendix M

Average elastic tensor

LPO determined average elastic tensors for the constituent mineral phases.

Quartz

$$\begin{pmatrix} 0.9587 & 0.0803 & 0.0860 & 0.0007 & 0.0029 & 0.0020 \\ 0.0803 & 0.9734 & 0.0764 & 0.0013 & 0.0031 & -0.0010 \\ 0.0860 & 0.0764 & 0.9715 & -0.0035 & -0.0098 & 0.0023 \\ 0.0007 & 0.0013 & -0.0035 & 0.4435 & 0.0045 & 0.0006 \\ 0.0029 & 0.0031 & -0.0098 & 0.0045 & 0.4498 & -0.0002 \\ 0.0020 & -0.0010 & 0.0023 & 0.0006 & -0.0002 & 0.4414 \end{pmatrix} \quad \text{(M.1)}$$

Orthoclase

$$\begin{pmatrix} 0.8012 & 0.2854 & 0.3269 & -0.0039 & -0.0059 & 0.0019 \\ 0.2854 & 0.8220 & 0.2971 & -0.0018 & -0.0064 & -0.0002 \\ 0.3269 & 0.2971 & 0.8475 & -0.0059 & -0.0422 & 0.0059 \\ -0.0039 & -0.0018 & -0.0059 & 0.2583 & 0.0051 & 0.0060 \\ -0.0059 & -0.0064 & -0.0422 & 0.0051 & 0.2480 & -0.0022 \\ 0.0019 & -0.0002 & 0.0059 & 0.0060 & -0.0022 & 0.2585 \end{pmatrix} \quad \text{(M.2)}$$

Calcite

$$\begin{pmatrix} 1.2147 & 0.5557 & 0.5239 & 0.0006 & 0.0160 & 0.0140 \\ 0.5557 & 1.1550 & 0.5258 & -0.0044 & 0.0070 & -0.0261 \\ 0.5239 & 0.5258 & 1.1719 & -0.0234 & -0.0176 & 0.0104 \\ 0.0006 & -0.0044 & -0.0234 & 0.3156 & 0.0102 & 0.0061 \\ 0.0160 & 0.0070 & -0.0176 & 0.0102 & 0.3115 & 0.0001 \\ 0.0140 & -0.0261 & 0.0104 & 0.0061 & 0.0001 & 0.3425 \end{pmatrix} \tag{M.3}$$

Appendix N

Ultrasonic Data - Group 1

1784

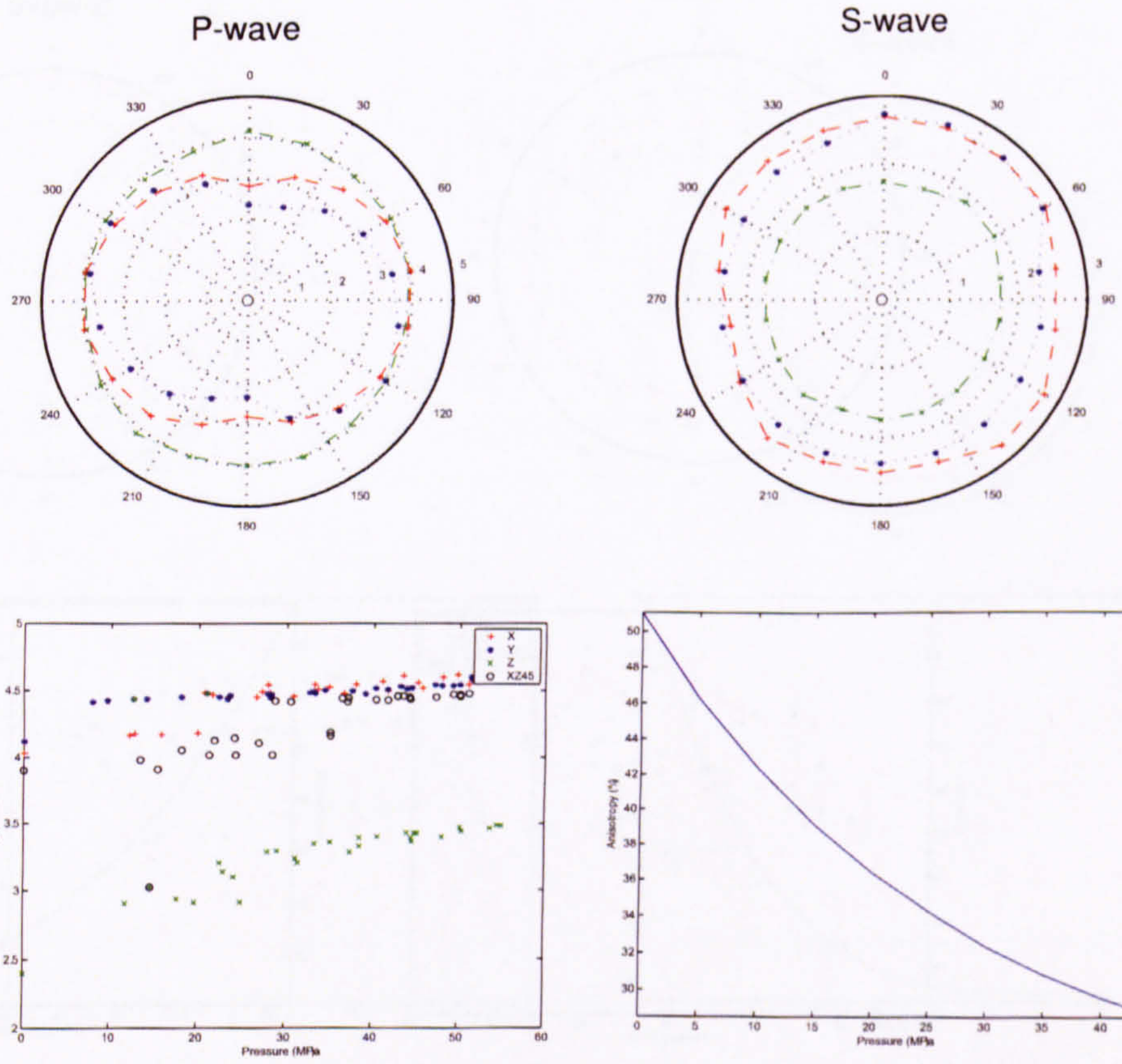

Figure N.1: *Group - 1. Well 206/8-8, sample 1784. Polar diagrams (top): atmospheric conditions compressional, and shear-wave velocity variation (km/s). Scatter plots (bottom): compressional-wave velocity (km/s) with respect to an increasing confining pressure for the X-, Y-, Z- and XZ45- (XYZ) cores (left hand plot). Compressional-wave anisotropy (%) with respect to an increasing confining pressure (MPa)(right hand plot).*

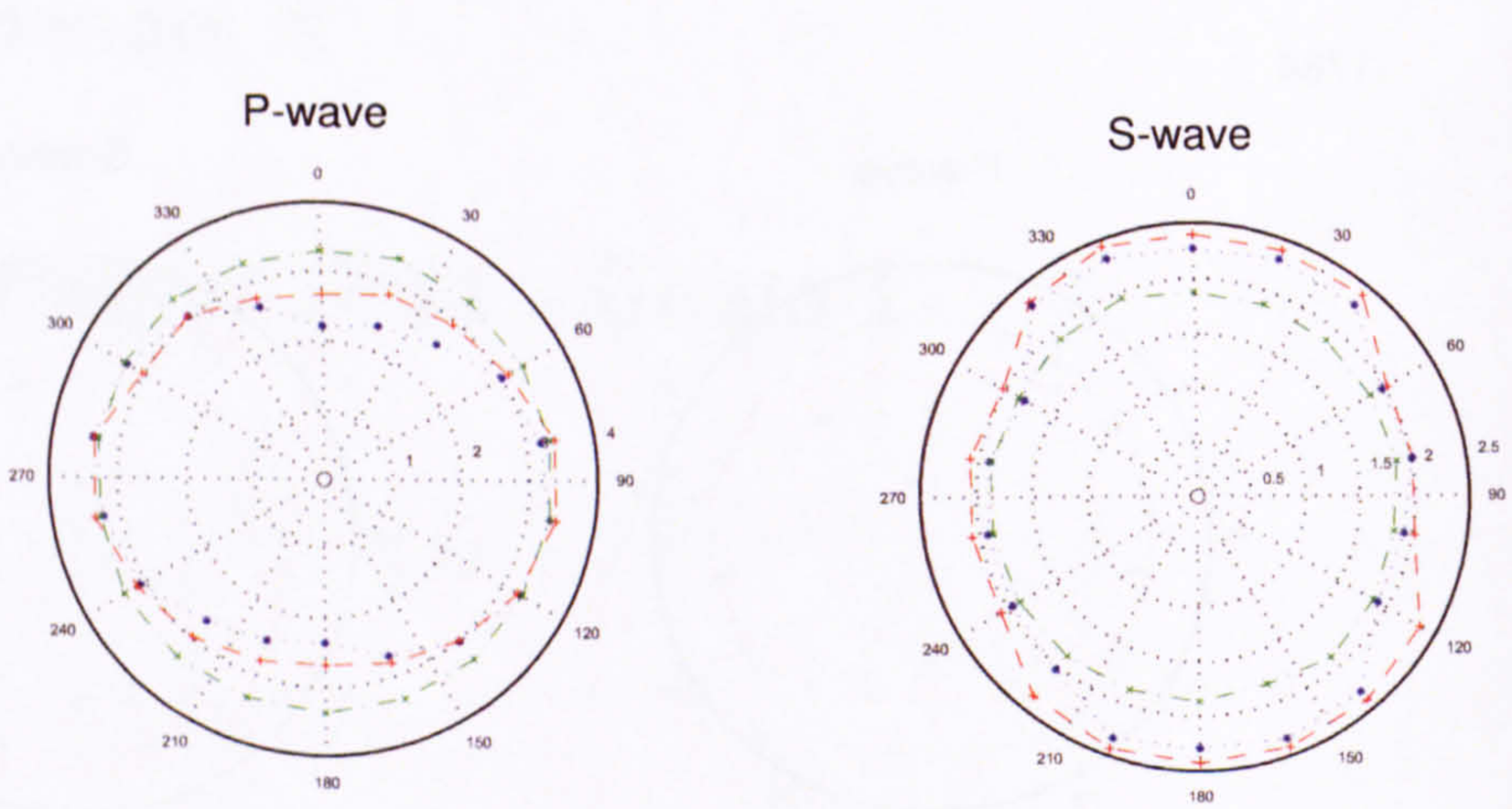

Figure N.2: *Group - 1. Well 206/8-8, sample 1788. Polar diagrams (top): atmospheric conditions compressional, and shear-wave velocity variation (km/s). Scatter plots (bottom): compressional-wave velocity (km/s) with respect to an increasing confining pressure for the X-, Y-, Z- and XZ45- (XYZ) cores (left hand plot). Compressional-wave anisotropy (%) with respect to an increasing confining pressure (MPa)(right hand plot).*

1841

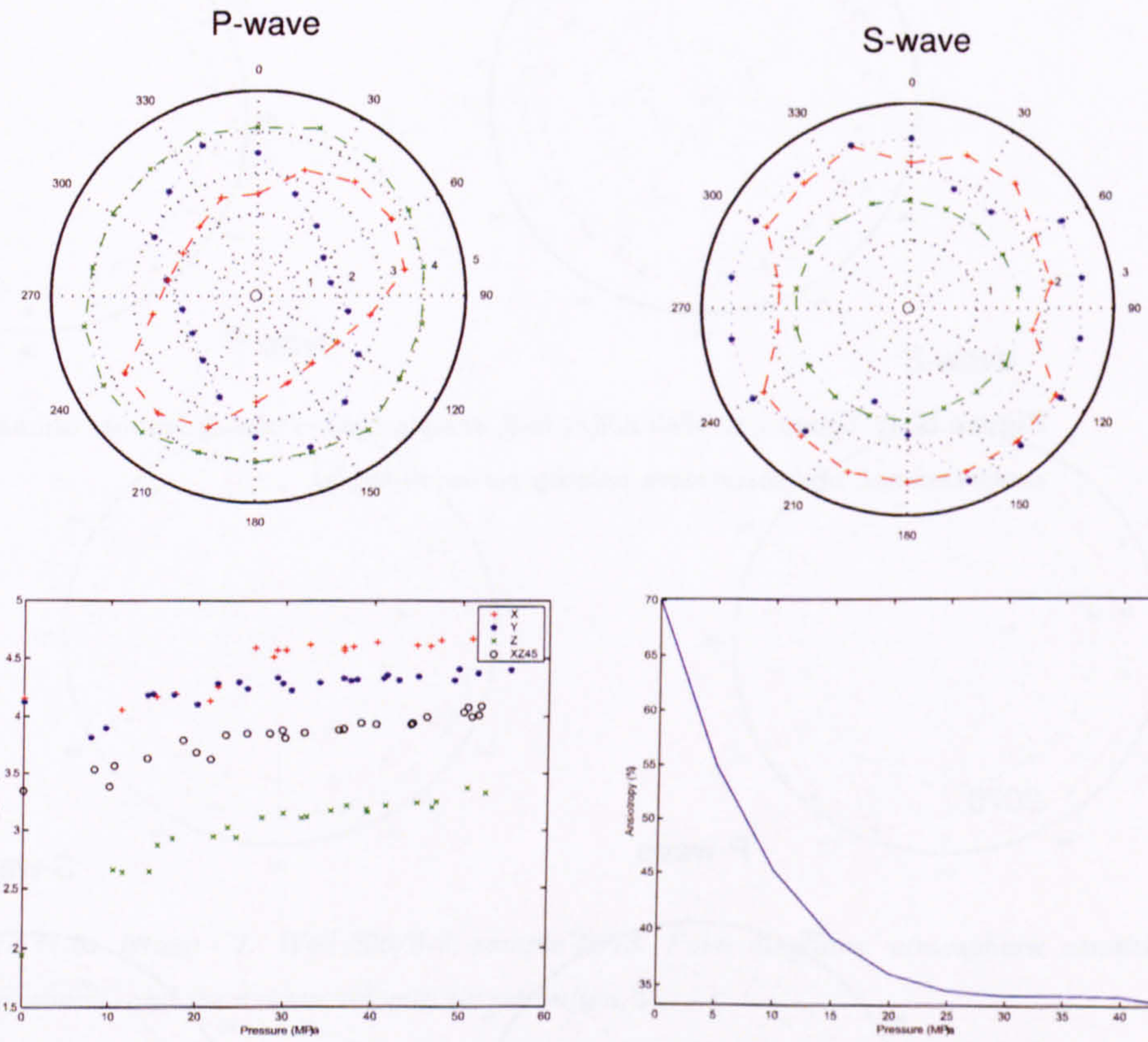

Figure N.3: *Group - 1. Well 206/8-8, sample 1841. Polar diagrams (top): atmospheric conditions compressional, and shear-wave velocity variation (km/s). Scatter plots (bottom): compressional-wave velocity (km/s) with respect to an increasing confining pressure for the X-, Y-, Z- and XZ45- (XYZ) cores (left hand plot). Compressional-wave anisotropy (%) with respect to an increasing confining pressure (MPa)(right hand plot).*

1963

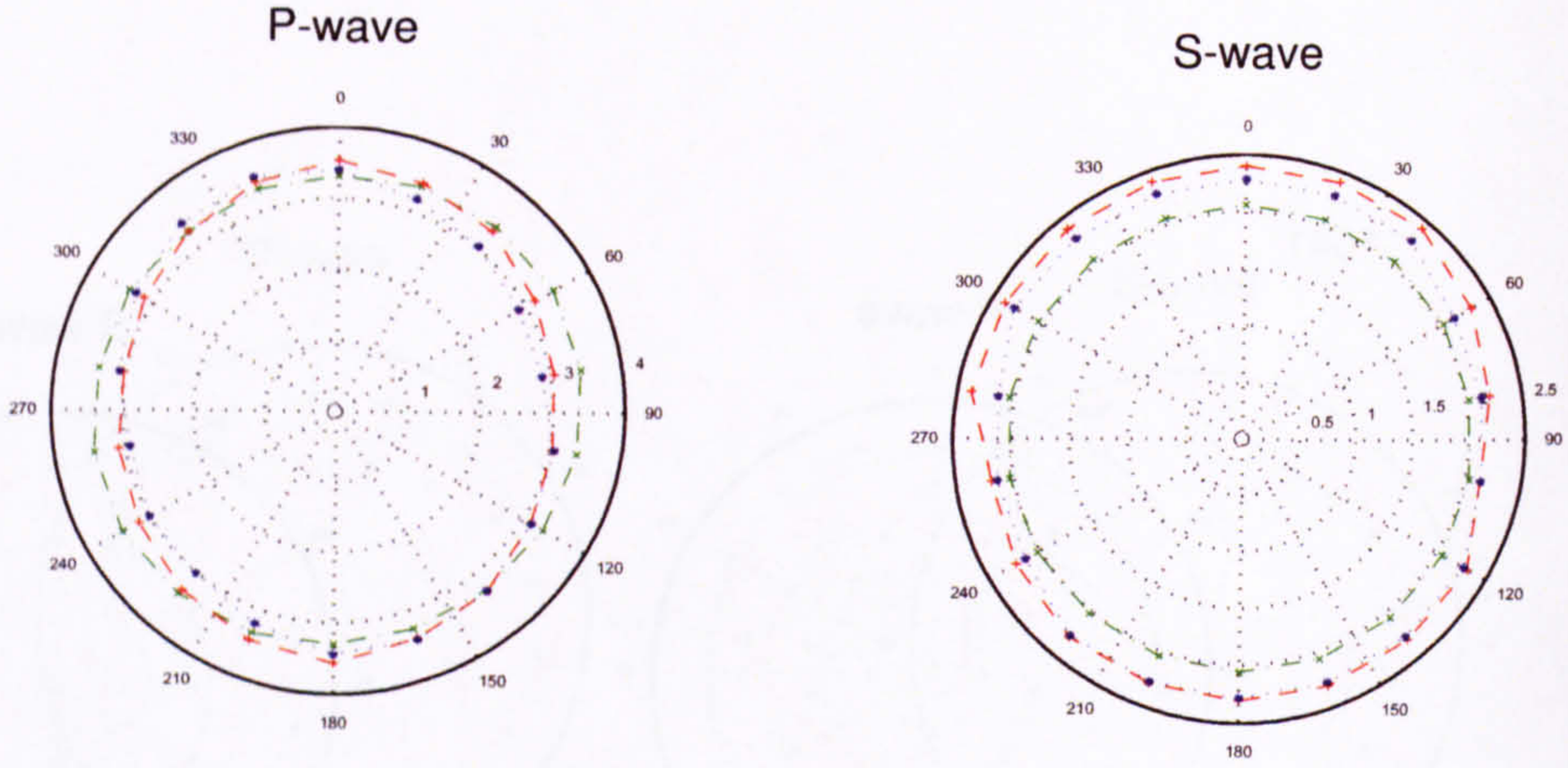

Figure N.4: *Group - 1. Well 206/13a-2, sample 1963. Polar diagrams: atmospheric conditions compressional, and shear-wave velocity variation(km/s).*

2070

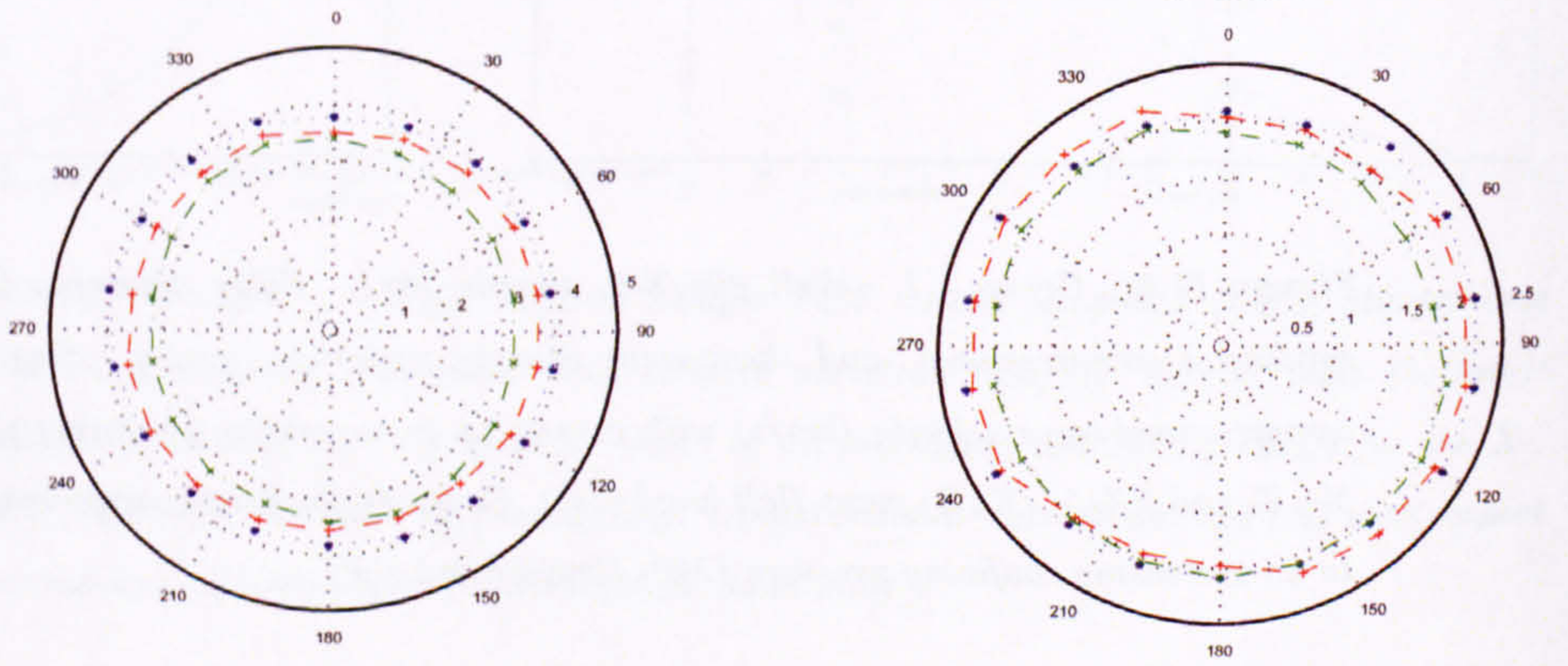

Figure N.5: *Group - 1. Well 206/8-8, sample 2070. Polar diagrams: atmospheric conditions compressional, and shear-wave velocity variation(km/s).*

2073

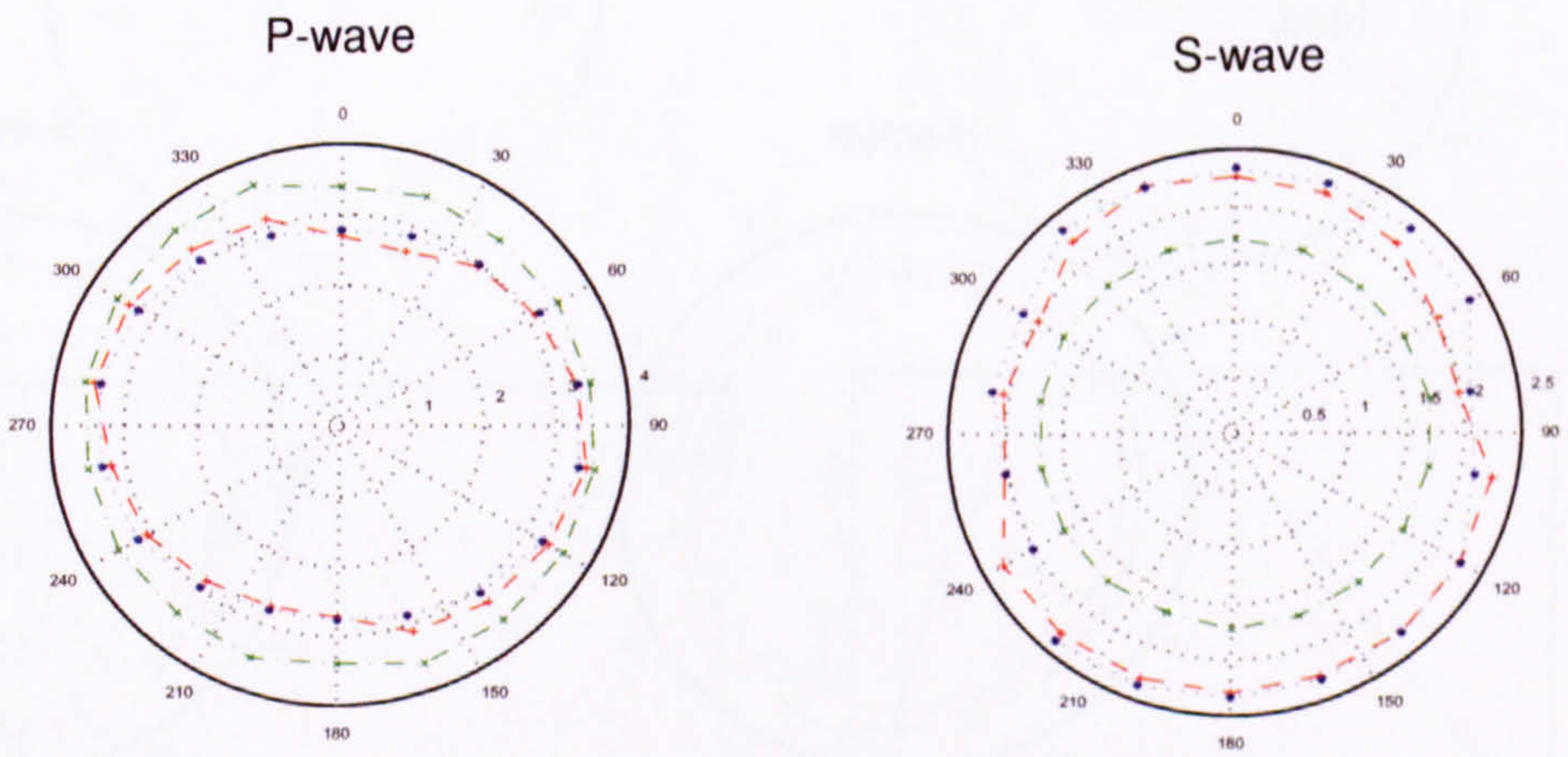

Figure N.6: *Group - 1. Well 206/8-8, sample 2073. Polar diagrams: atmospheric conditions compressional, and shear-wave velocity variation(km/s).*

Appendix O

Ultrasonic data - Group 2

1663

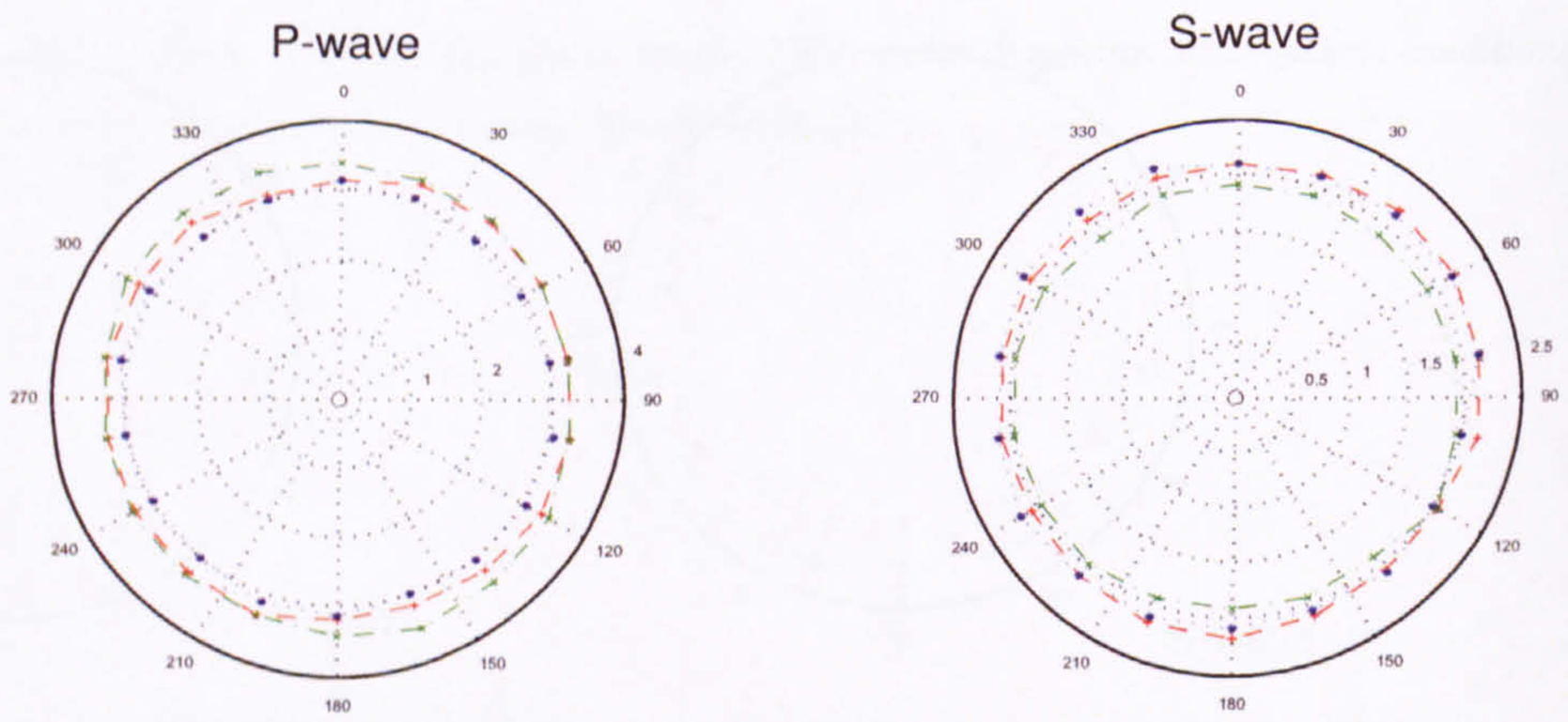

Figure O.1: *Group - 2. Well 206/8-8, sample 1663. Polar diagrams: atmospheric conditions compressional, and shear-wave velocity variation (km/s).*

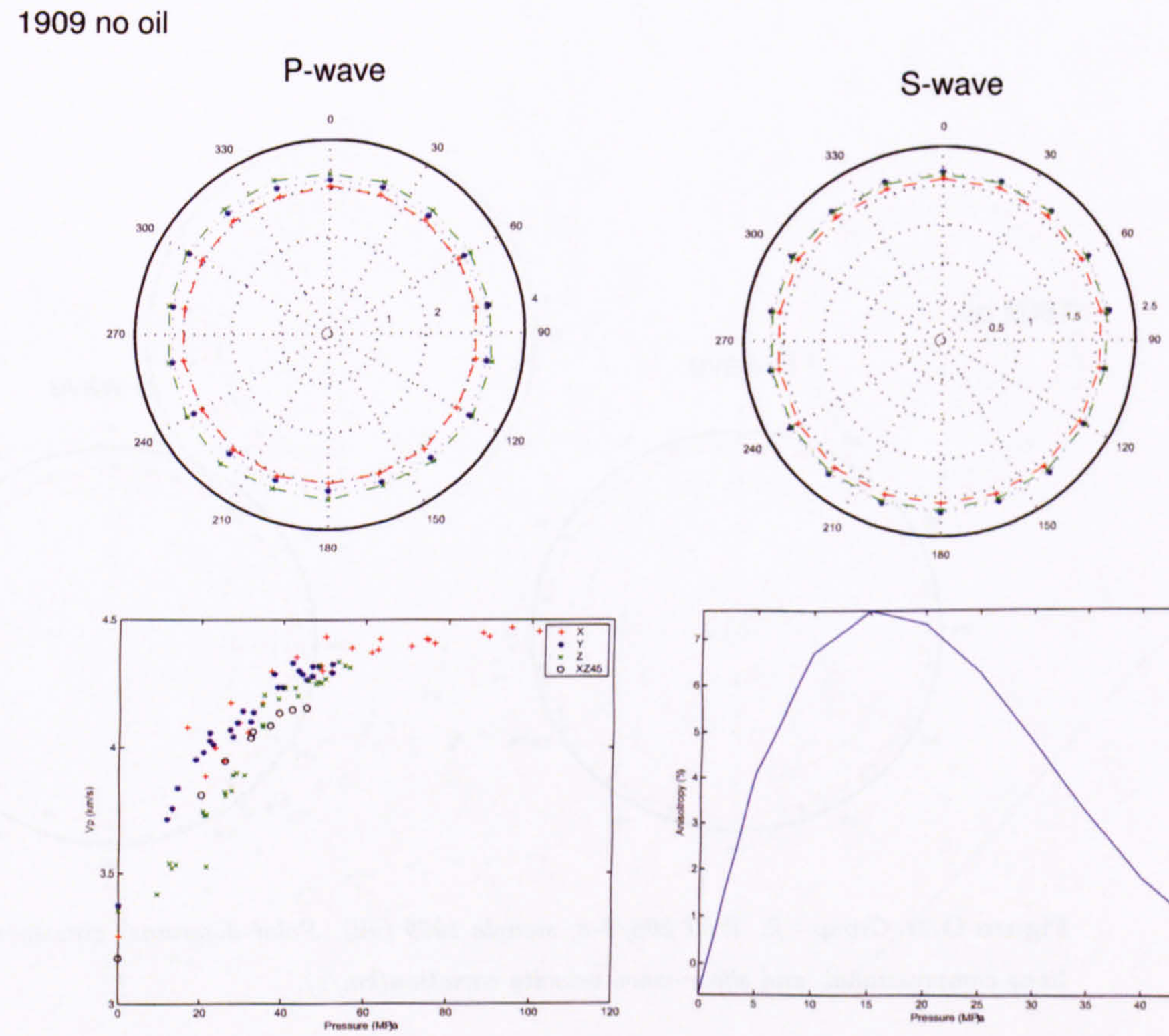

Figure O.2: *Group - 2. Well 206/8-8, sample 1909 (no oil). Polar diagrams (top): atmospheric conditions compressional, and shear-wave velocity variation (km/s). Scatter plots (bottom): compressional-wave velocity (km/s) with respect to an increasing confining pressure for the X-, Y-, Z- and XZ45- (XYZ) cores (left hand plot). Compressional-wave anisotropy (%) with respect to an increasing confining pressure (MPa)(right hand plot).*

1909 oil

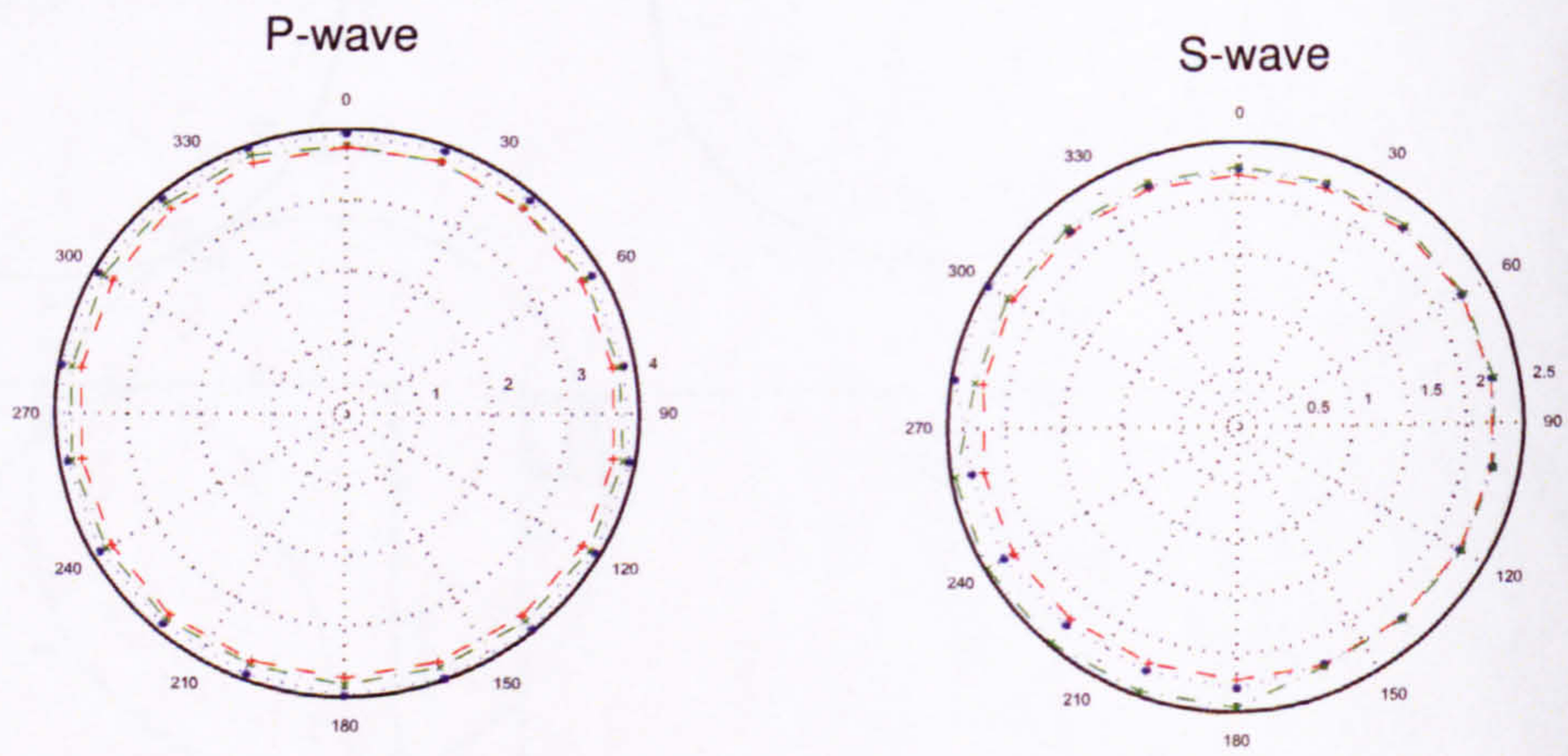

Figure O.3: *Group - 2. Well 206/8-8, sample 1909 (oil). Polar diagrams: atmospheric conditions compressional, and shear-wave velocity variation(km/s).*

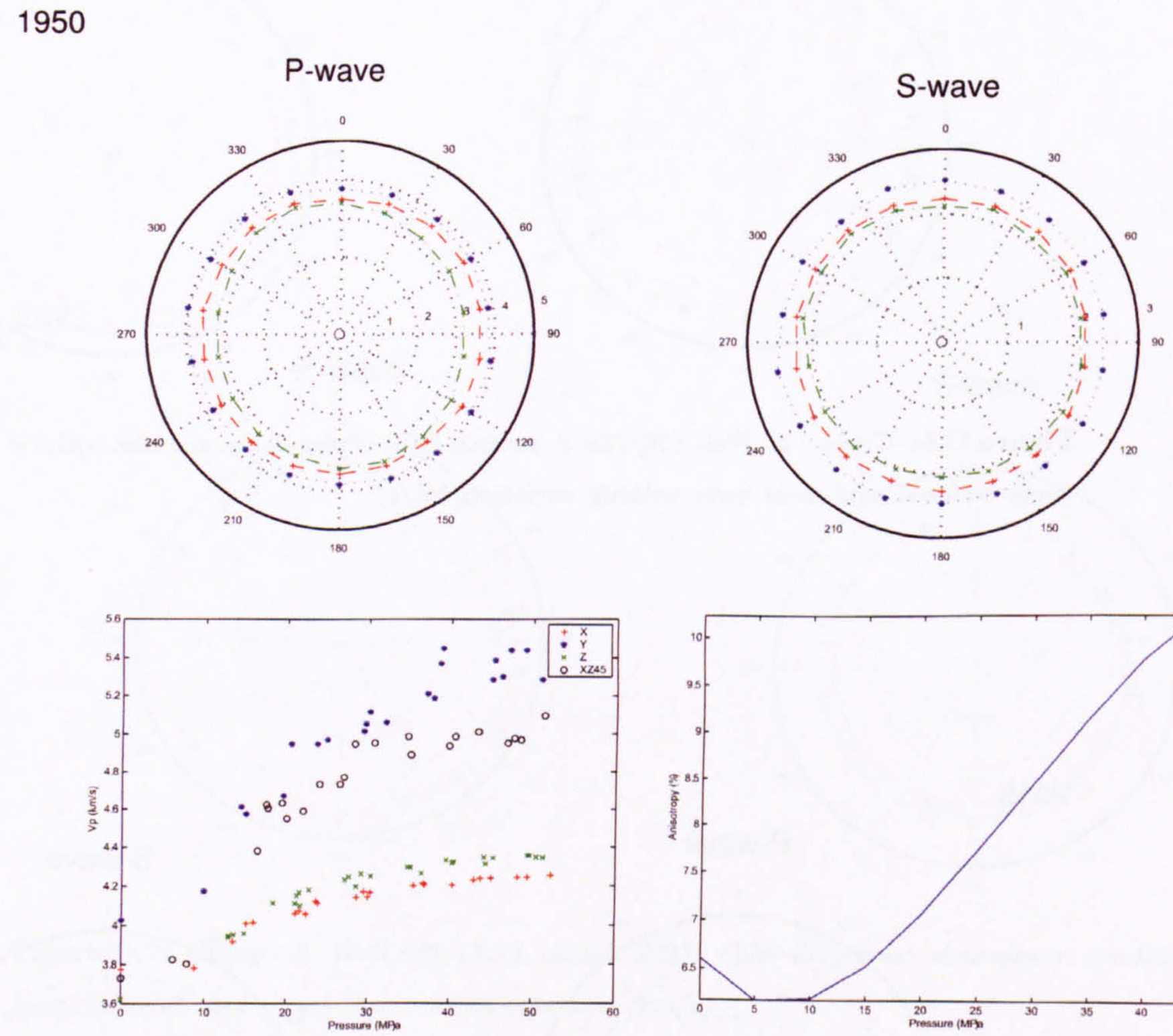

Figure O.4: *Group - 2. Well 206/8-8, sample 1950. Polar diagrams (top): atmospheric conditions compressional, and shear-wave velocity variation(km/s). Scatter plots (bottom): compressional-wave velocity (km/s) with respect to an increasing confining pressure for the X-, Y-, Z- and XZ45- (XYZ) cores (left hand plot). Compressional-wave anisotropy (%) with respect to an increasing confining pressure (MPa)(right hand plot).*

1959

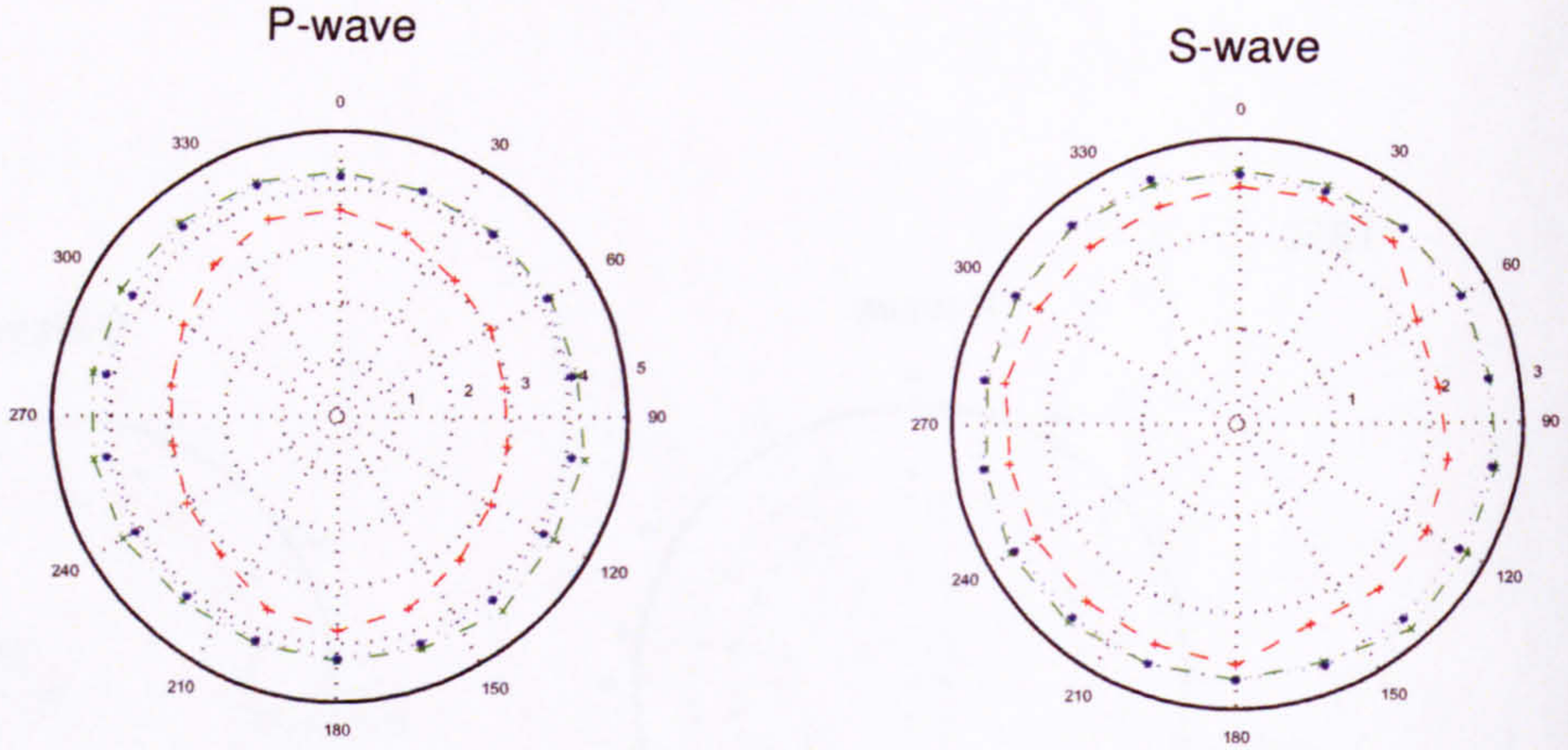

Figure O.5: *Group - 2. Well 206/13a-2, sample 1959. Polar diagrams: atmospheric conditions compressional, and shear-wave velocity variation(km/s).*

2015

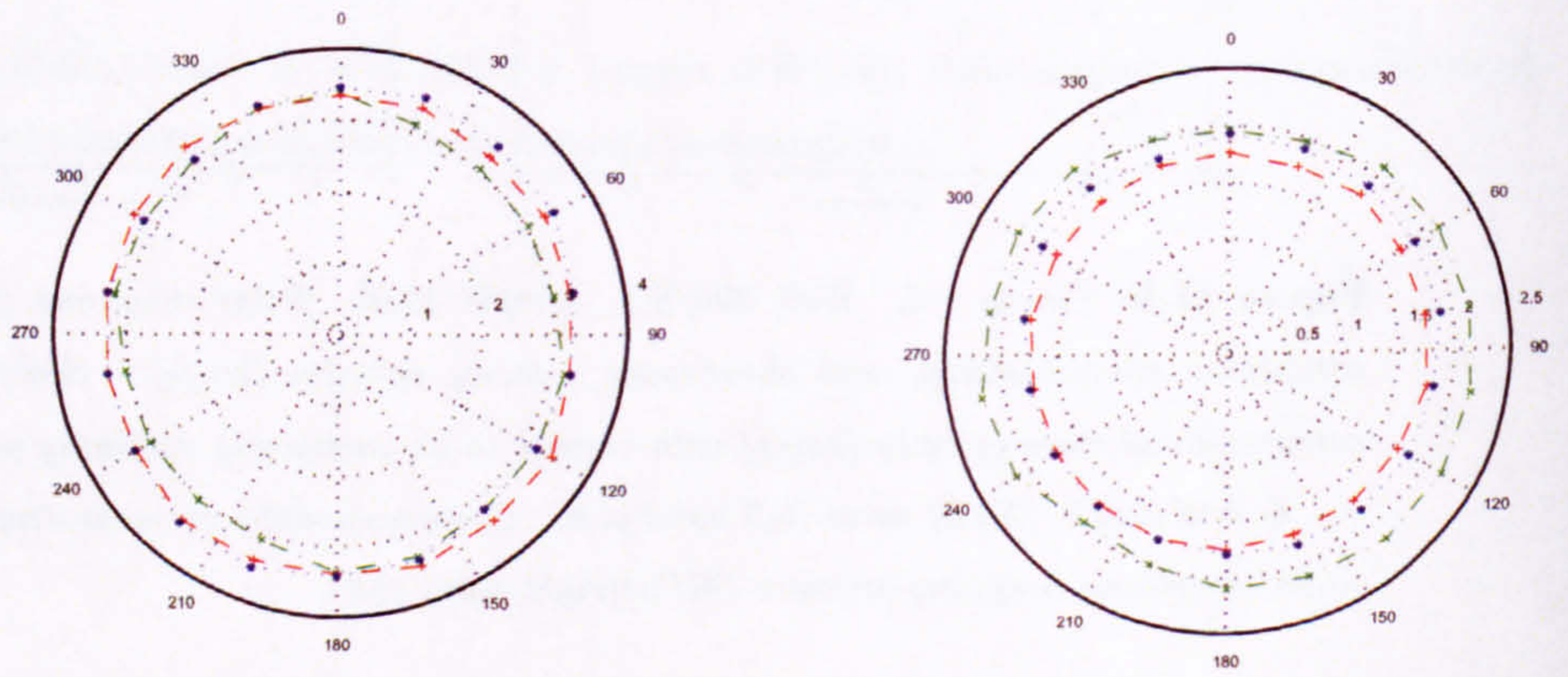

Figure O.6: *Group - 2. Well 206/13a-2, sample 2015. Polar diagrams: atmospheric conditions compressional, and shear-wave velocity variation (km/s).*

2023

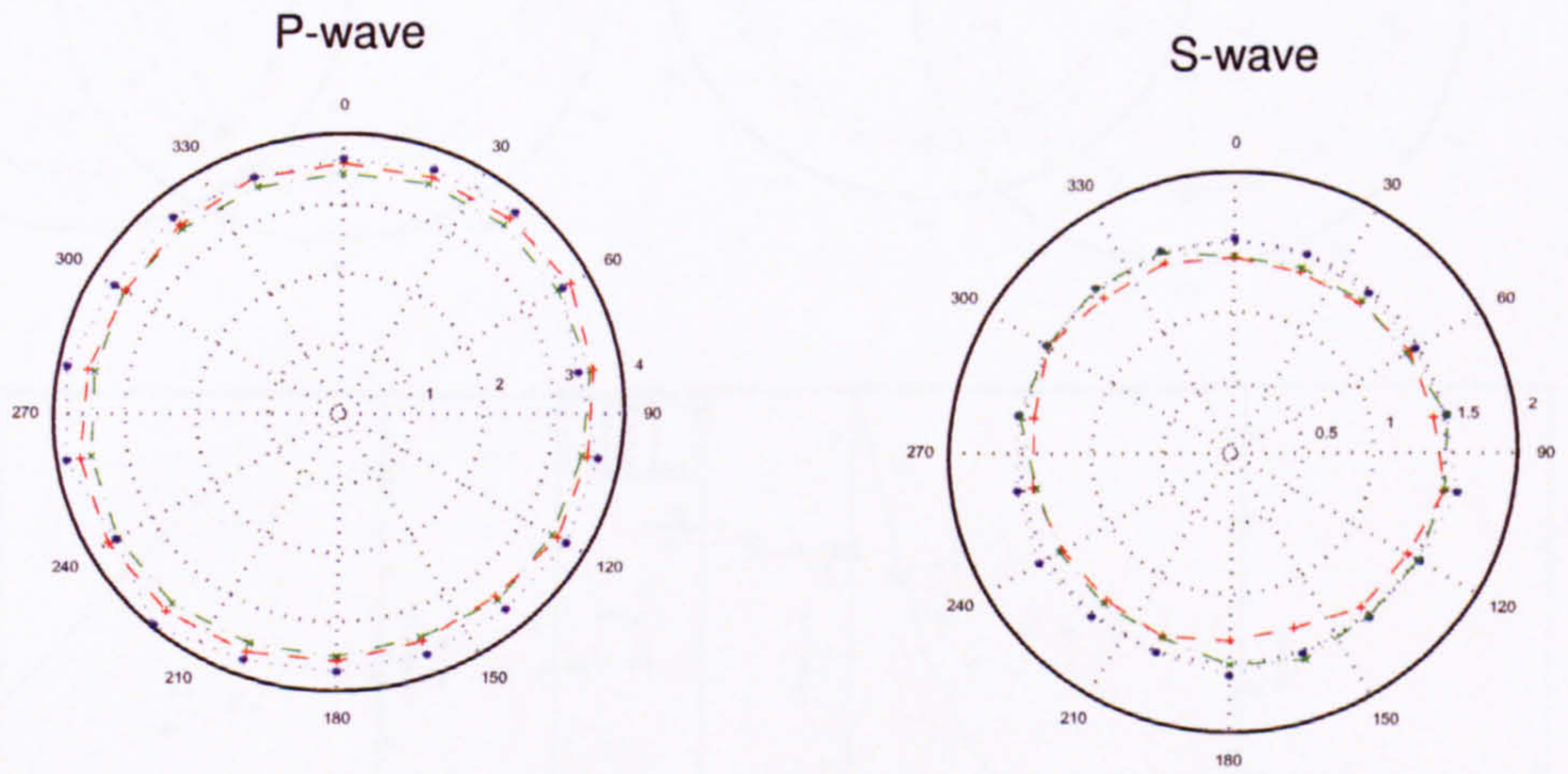

Figure O.7: *Group - 2. Well 206/13a-2, sample 2023. Polar diagrams: atmospheric conditions compressional, and shear-wave velocity variation (km/s).*

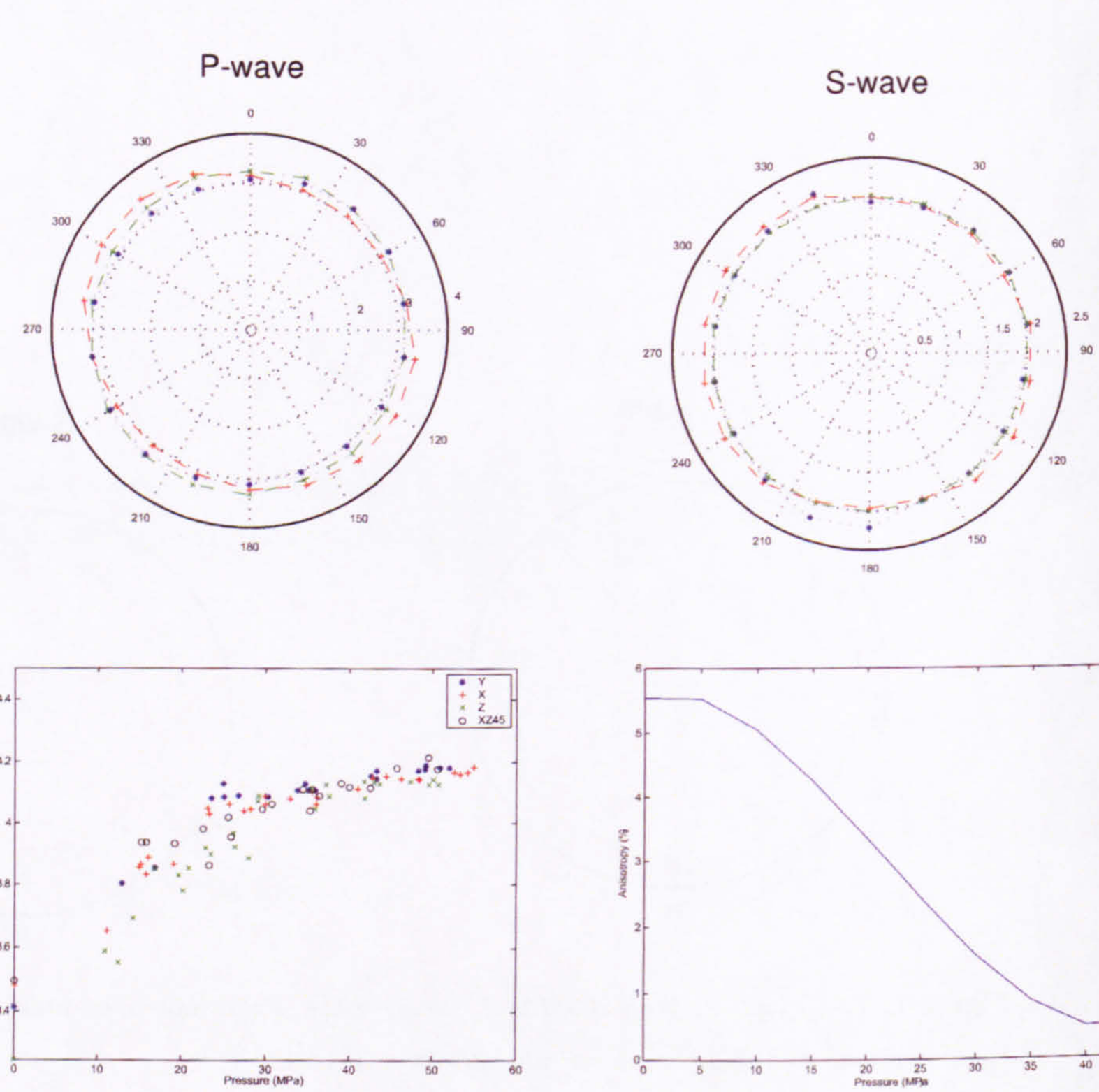

Figure O.8: *Group - 2. Well 206/13a-2, sample 2028. Polar diagrams (top): atmospheric conditions compressional, and shear-wave velocity variation(km/s). Scatter plots (bottom): compressional-wave velocity (km/s) with respect to an increasing confining pressure for the X-, Y-, Z- and XZ45- (XYZ) cores (left hand plot). Compressional-wave anisotropy (%) with respect to an increasing confining pressure (MPa)(right hand plot).*

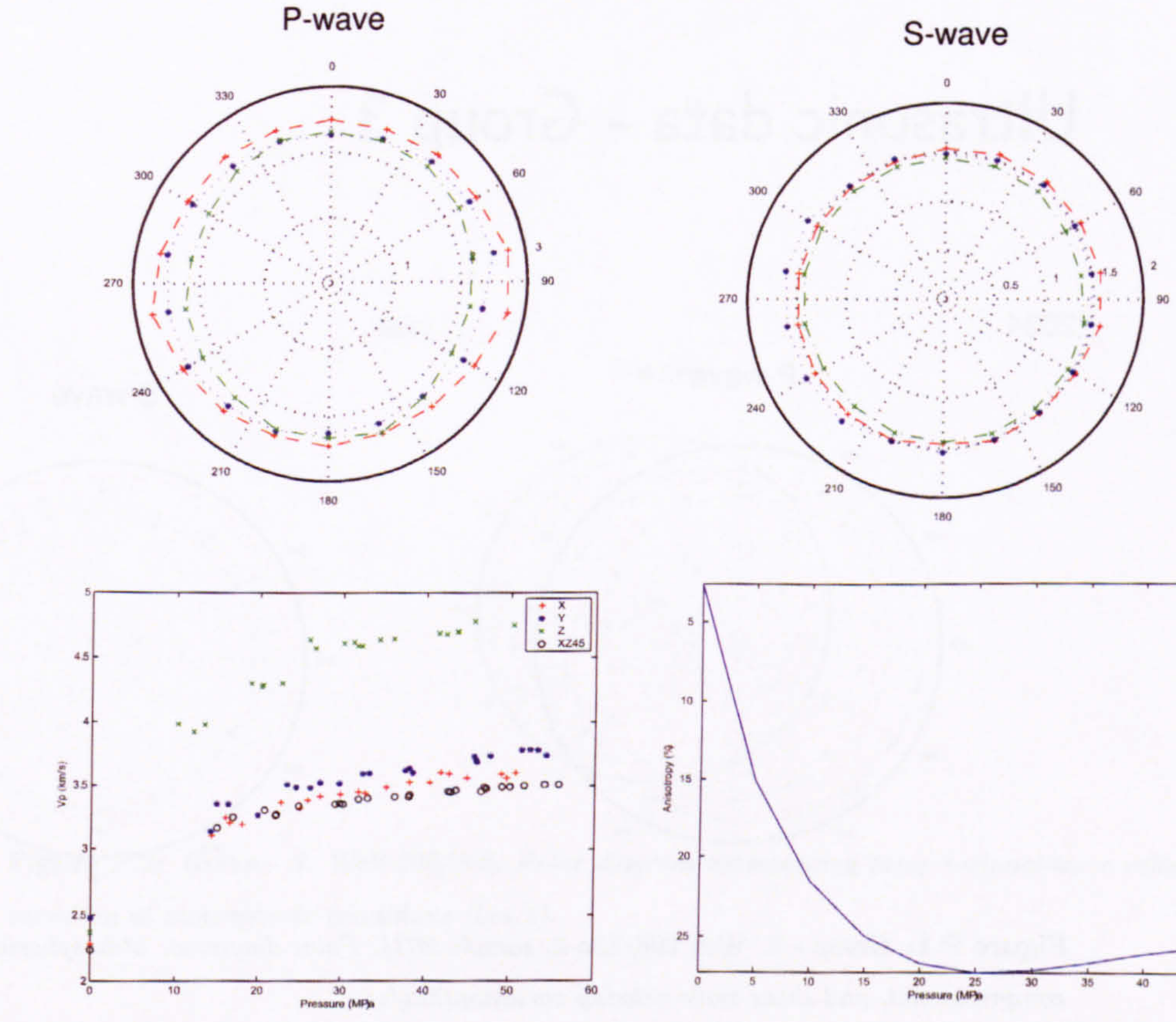

Figure O.9: *Group - 2. Well 206/8-8, sample 2129 (no oil). Polar diagrams (top): atmospheric conditions compressional, and shear-wave velocity variation(km/s). Scatter plots (bottom): compressional-wave velocity (km/s) with respect to an increasing confining pressure for the X-, Y-, Z- and XZ45- (XYZ) cores (left hand plot). Compressional-wave anisotropy (%) with respect to an increasing confining pressure (MPa)(right hand plot).*

Appendix P

Ultrasonic data - Group 3

2034

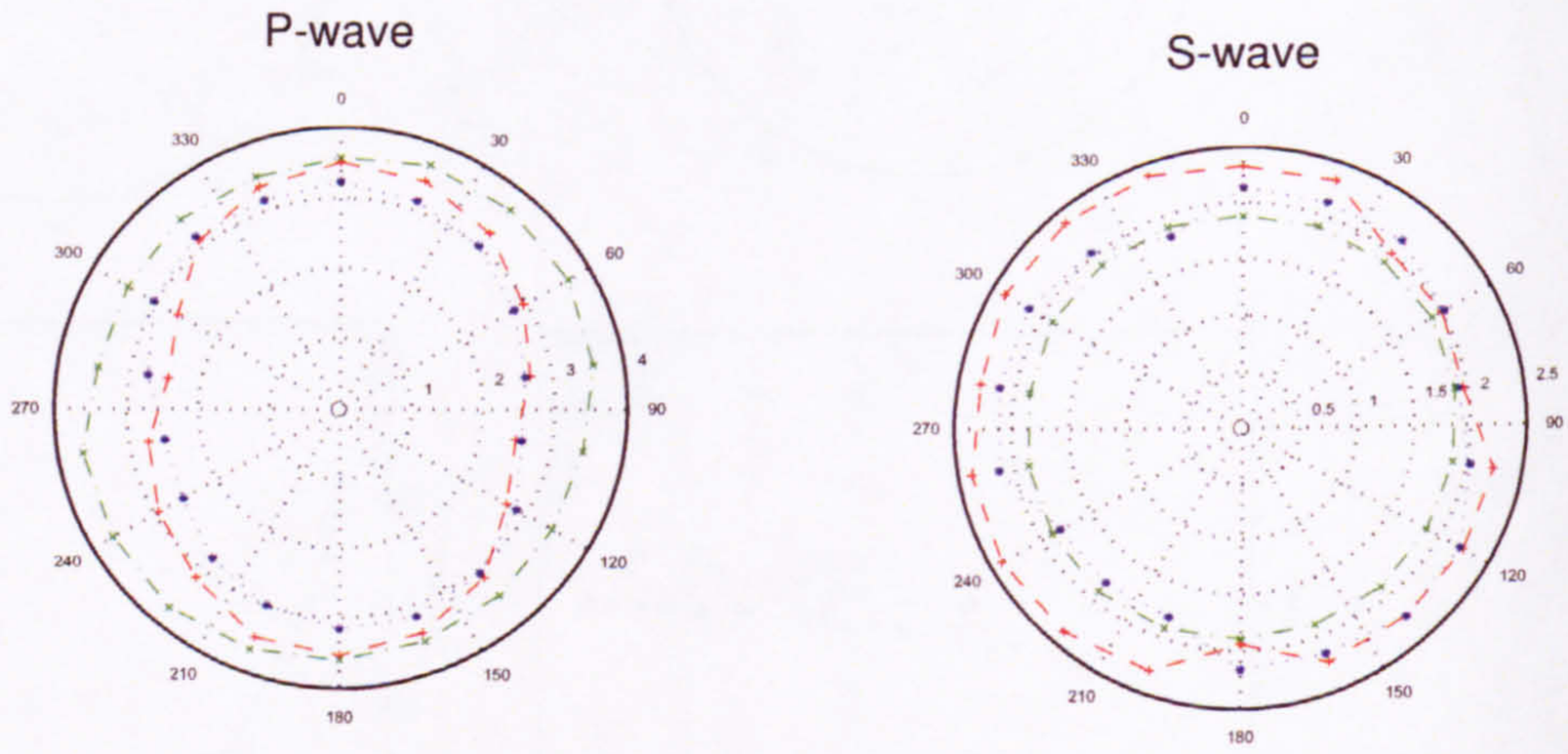

Figure P.1: *Group - 2. Well 206/13a-2, sample 2034. Polar diagrams: atmospheric conditions compressional, and shear-wave velocity variation(km/s).*

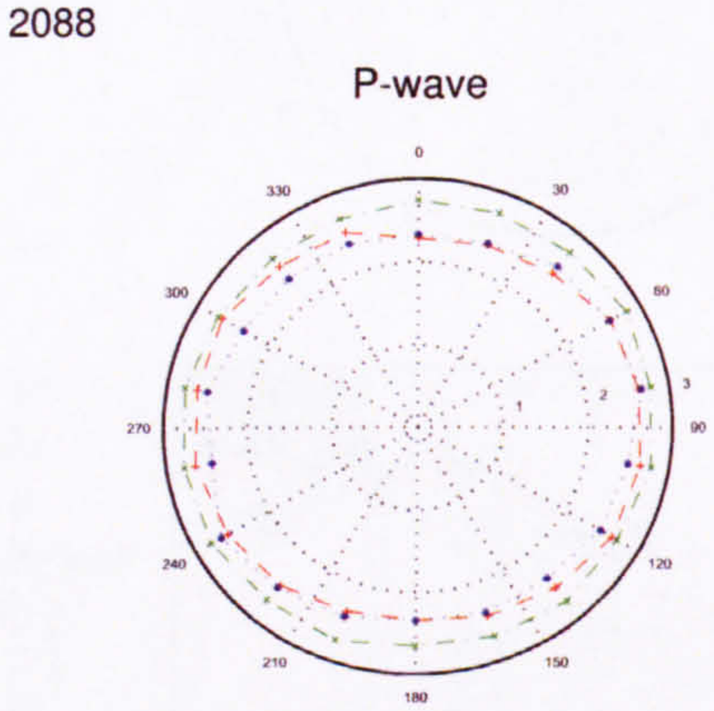

Figure P.2: *Group - 3. Well 206/8-8. Polar diagram representing compressional-wave velocity variation at atmospheric conditions (km/s).*

2192

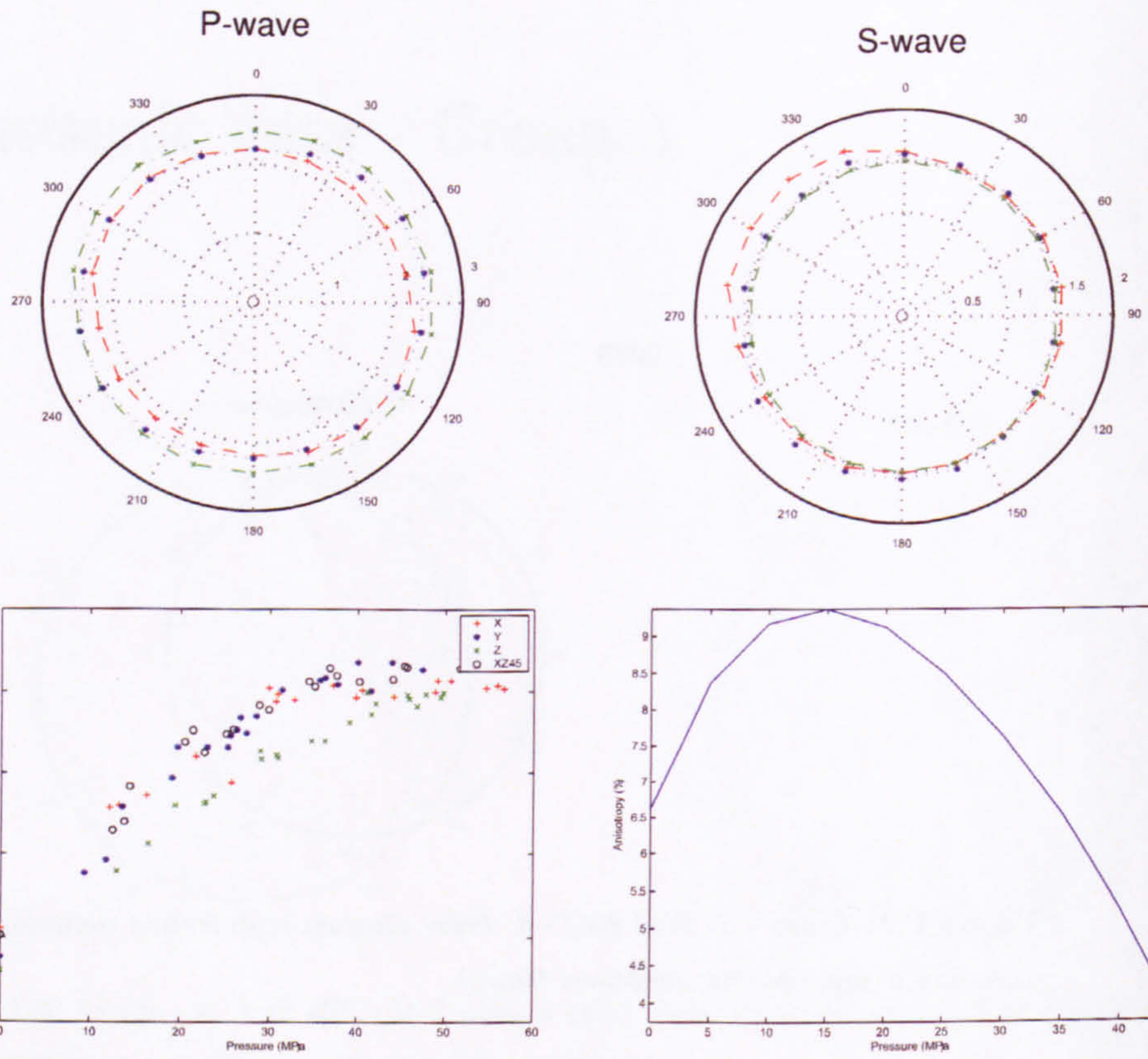

Figure P.3: *Group - 3. Well 206/8-8, sample 2192. Polar diagrams (top): atmospheric conditions compressional, and shear-wave velocity variation(km/s). Scatter plots (bottom): compressional-wave velocity (km/s) with respect to an increasing confining pressure for the X-, Y-, Z- and XZ45- (XYZ) cores (left hand plot). Compressional-wave anisotropy (%) with respect to an increasing confining pressure (MPa)(right hand plot).*

2194

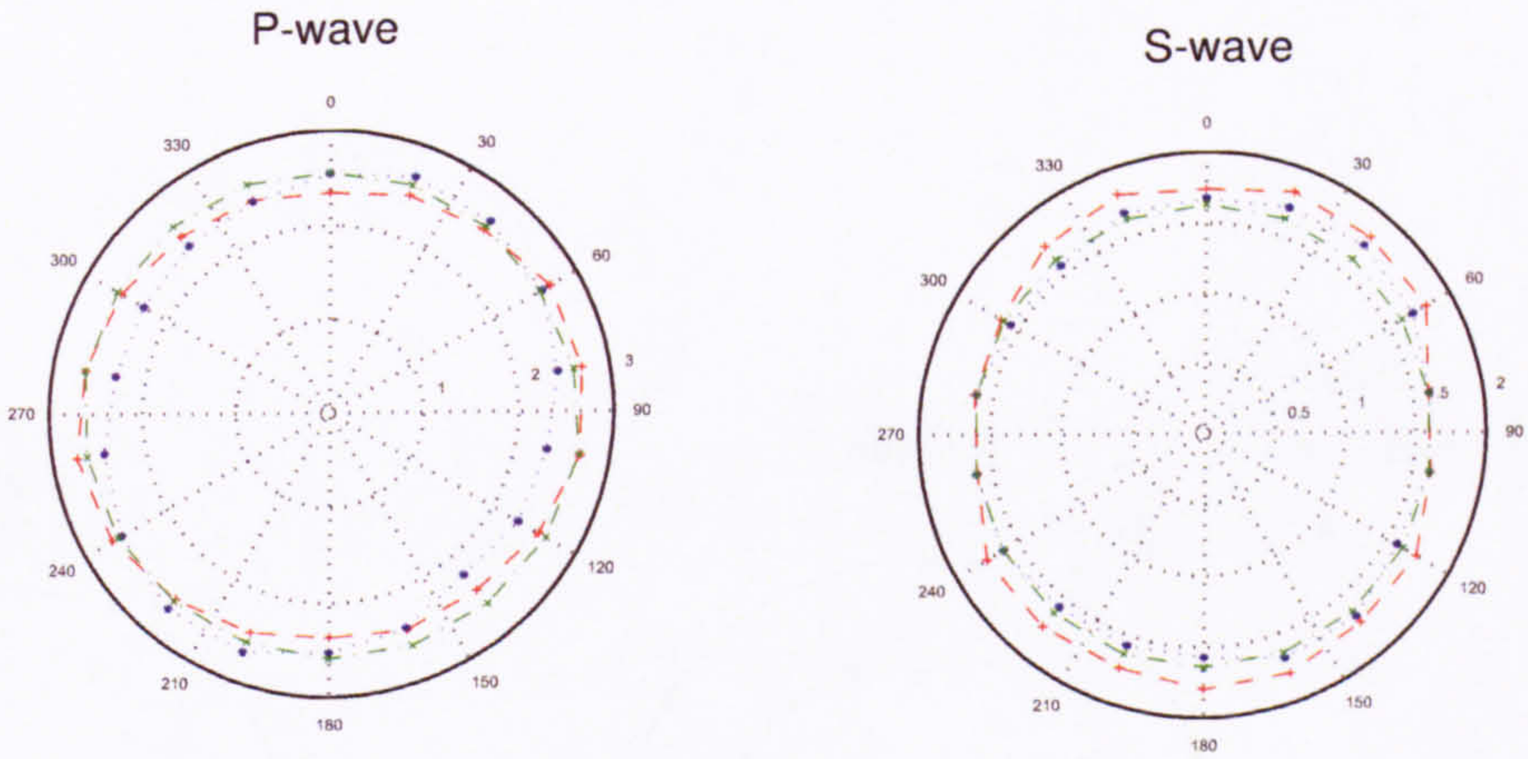

Figure P.4: *Group - 3. Well 206/8-8, sample 2194. Polar diagrams (top): atmospheric conditions compressional, and shear-wave velocity variation(km/s). Scatter plots (bottom): compressional-wave velocity (km/s) with respect to an increasing confining pressure for the X-, Y-, Z- and XZ45- (XYZ) cores (left hand plot). Compressional-wave anisotropy (%) with respect to an increasing confining pressure (MPa)(right hand plot).*

2198

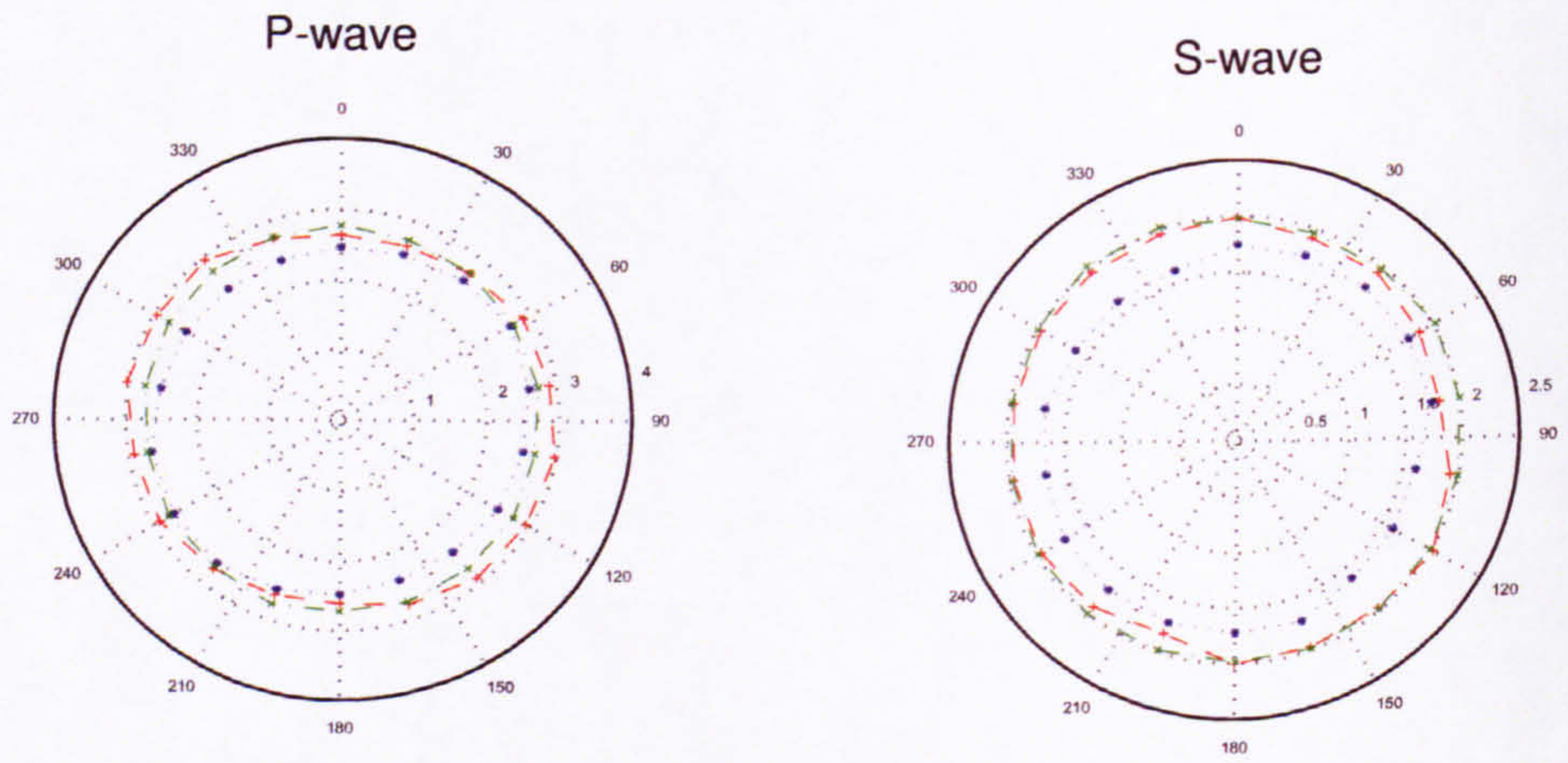

Figure P.5: *Group - 3. Well 206/8-8, sample 2198. Polar diagrams: atmospheric conditions compressional, and shear-wave velocity variation(km/s).*